Evaluation of Used Fuel Disposition in Clay-Bearing Rock

(FCRD-UFD-2016-000074)

Fuel Cycle Research & Development

Prepared for
U.S. Department of Energy
Used Fuel Disposition Campaign

Carlos F. Jové Colón, Glenn E. Hammond,
Kristopher L. Kuhlman (SNL)

Liange Zheng, Kunhwi Kim, Hao Xu,
Jonny Rutqvist (LBNL)

Florie A. Caporuscio, Katherine E. Norskog,
James Maner, Sarah Palaich, Michael Cheshire
(LANL)

Mavrik Zavarin, Thomas J. Wolery,
Cindy Atkins-Duffin (LLNL)

James Jerden, Jacqueline M. Copple,
Terry Cruse, William Ebert (ANL)

September 15th, 2016
SAND2016-10311 R

Prepared by:

Sandia National Laboratories

Albuquerque, New Mexico 87185

 U.S. DEPARTMENT OF **ENERGY**

 Sandia National Laboratories

APPENDIX E FCT
DOCUMENT COVER SHEET [1]

Name/Title of Deliverable/Milestone/Revision No:	Evaluation of Used Nuclear Fuel Disposition in Clay-Bearing Rocks M2FT-16SN080302071
Work Package Title and Number	DR Argillite Disposal R&D – SNL, FT-16SN08030207
Work Package WBS Number	1.02.08.03.02
Responsible Work Package Manager	Jove Colon, Carlos F. _(Name/Signature)_
Date Submitted	9/15/2016

Quality Rigor Level for Deliverable/Milestone[2]	☒ QRL-3	☐ QRL-2	☐ QRL-1 Nuclear Data	☐ Lab/Participant QA Program (no additional FCT QA requirements)

This deliverable was prepared in accordance with **Sandia National Laboratories**
(Participant/National Laboratory Name)

QA program which meets the requirements of
☒ DOE Order 414.1   ☐ NQA-1-2000   ☐ Other

This Deliverable was subjected to:

☒ Technical Review	☐ Peer Review
Technical Review (TR)	**Peer Review (PR)**
Review Documentation Provided	**Review Documentation Provided**
☐ Signed TR Report or,	☐ Signed PR Report or,
☐ Signed TR Concurrence Sheet or,	☐ Signed PR Concurrence Sheet or,
☒ Signature of TR Reviewer(s) below	☐ Signature of PR Reviewer(s) below

Name and Signature of Reviewers

Name	Signature
Yifeng Wang	9/15/16

NOTE 1: Appendix E should be filled out and submitted with the deliverable. Or, if the PICS:NE system permits, completely enter all applicable information in the PICS:NE Deliverable Form. The requirement is to ensure that all applicable information is entered either in the PICS:NE system or by using the FCT Document Cover Sheet.

NOTE 2: In some cases there may be a milestone where an item is being fabricated, maintenance is being performed on a facility, or a document is being issued through a formal document control process where it specifically calls out a formal review of the document. In these cases, documentation (e.g., inspection report, maintenance request, work planning package documentation or the documented review of the issued document through the document control process) of the completion of the activity, along with the Document Cover Sheet, is sufficient to demonstrate achieving the milestone. If QRL 1, 2, or 3 is not assigned, then the Lab / Participant QA Program (no additional FCT QA requirements) box must be checked, and the work is understood to be performed and any deliverable developed in conformance with the respective National Laboratory / Participant, DOE or NNSA-approved QA Program.

AKNOWLEDGEMENTS

SUMMARY

The R&D program from the DOE Used Fuel Disposition Campaign (UFDC) has documented key advances in coupled Thermal-Hydrological-Mechanical-Chemical (THMC) modeling of clay to simulate its complex dynamic behavior in response to thermal and hydrochemical feedbacks. These efforts have been harnessed to assess the isolation performance of heat-generating nuclear waste in a deep geological repository in clay/shale/argillaceous rock formations. This report describes the ongoing disposal R&D efforts on the advancement and refinement of coupled THMC process models, hydrothermal experiments on barrier clay interactions, used fuel and canister material degradation, thermodynamic database development, and reactive transport modeling of the near-field under non-isothermal conditions. These play an important role to the evaluation of *sacrificial zones* as part of the EBS exposure to thermally-driven chemical and transport processes. Thermal inducement of chemical interactions at EBS domains enhances mineral dissolution/precipitation but also generates mineralogical changes that result in mineral H_2O uptake/removal (hydration/dehydration reactions). These processes can result in volume changes that can affect the interface / bulk phase porosities and the mechanical (stress) state of the bentonite barrier. Characterization studies on bentonite barrier samples from the FEBEX-DP international activity have provided important insight on clay barrier microstructures (e.g., microcracks) and interactions at EBS interfaces. Enhancements to the used fuel degradation model outlines the need to include the effects of canister corrosion due the strong influence of H_2 generation on the source term.

As in previous deliverables, this report is structured according to various national laboratory contributions describing R&D activities applicable to clay/shale/argillite media. These activities are summarized as follows:

- **Evaluation of Used Fuel Disposition in Clay-Bearing Rock: Reactive-Transport Modeling of the Near Field Environment – SNL (Part I)**
    - Non-isothermal 1D reactive-transport modeling of the EBS using PFLOTRAN simulation code.
        - The thermally-driven phase transformation reaction gypsum $\rightarrow$ anhydrite (hydration/dehydration), in addition to dissolution/precipitation reactions, is captured by the reactive-transport model even with a fast temperature increase during the thermal pulse.
        - Gypsum $\rightarrow$ anhydrite phase transformation can generate volume differences of ~60% that could translate into porosity increases in the EBS bulk regions and at interfaces.
        - As exemplified by the Ca-SO_4-H_2O system, pore solution chemistry and temperature are key factors in determining the alteration mineral assemblage. For example, the formation of ettringite from cement alteration and reaction with Ca-SO_4 components in the pore solution.

- o International collaborations: FEBEX-DP chemical and micro-CT characterization work:
    - Micro-CT imaging reveals the wide occurrence of microcracks in bentonite as a result of dehydration and shrinkage. Microcracks can influence moisture transport and clay swelling.
    - FEBEX-DP samples in contact with the heater surface appears to produce unidentified Al-silicates with detectable amounts of K and Fe. Further work is needed on the characterization of these phases.
    - The application of scanning characterization techniques such as micro-XRF and SEM/EDS/BSEI to the compositional characterization of the shotcrete – bentonite interface suggests that much of the reaction appears to be confined to the shotcrete phase and little or no alteration was experienced by bentonite.

- **Argillite Disposal R&D at LBNL (Part II)**
    - o International Collaboration Activities: THM and Heater Test Modeling.
        - Successful completion of DECOVALEX-2015 modeling associated with the Mont Terri HE-E experiment and Horonobe EBS experiment.
        - Analysis of field data from the largest ongoing underground heater test in the world: Mont Terri FE experiment.
        - Improvement of the implementation and efficiency of the Barcelona Expansive Model (BExM) in TOUGH-FLAC as well as the interpretative modeling of field data from URL heater experiments.
    - o Investigation of the Impacts of High Temperature Limits with THMC modeling:
        - THMC model utilize dual structure Barcelona Expansive Clay Model (BExM) to link mechanical process with chemistry, allowing us to simultaneously incorporate the effects of exchangeable cations, ionic strength of pore water and abundance of swelling clay on the swelling stress of bentonite.
        - Corrosion of steel canister was considered in the chemical model to evaluate whether the iron-bentonite interaction would aggravate the negative impact on swelling stress through the formation of Fe bearing clay minerals.
        - The chemical changes as a whole reduce both total stress and effective/net stress in the bentonite buffer except the positions near the confinement rocks in the "high T" cases.
    - o Evolution of Bentonite in FEBEX-DP Coupled THMC Modeling:
        - THMC model outperformed the THC model in terms of matching measured THM data. Permeability and porosity changes due to mechanical process (swelling) were the key to matching all the THM data.

- The THMC model using complex double structure BExM (THMC-BExM) did not outperform the THMC model using linear swelling model (THMC-LS) in terms of matching the measured data.

- THMC models successfully matched the THM data, however, they failed to match the measured concentration profile of conservative species (chloride).

- A series of synchrotron X-ray microCT (SXR-μCT) examination of the microstructure of bentonite samples from FEBEX-DP project at the Grimsel site. SXR-μCT imaging was conducted for a sample in the "as is" (i.e., as received) and heated states. Heating completely modified the microstructure of the material, generating a pervasive network of fractures.

o Discrete Fracture Network (DFN) Approach for THM Damage Modeling in Argillaceous Rock:

- An effective coupling between the TOUGH2 and the RBSN approach has been implemented and applied to hydraulic fracturing simulations.

- Continued work on modeling damage and deformation in anisotropic rock and around tunnels, but have also made substantial effort in simulation of fluid driven fracture propagation.

- Current TOUGH-RBSN model is capable of modeling tightly coupled HM processes and the RBSN approach for mechanical anisotropy in elastic and fracture responses.

o **Experimental studies of Engineered Barrier Systems conducted at LANL (Part III)**

- Experimental work focus: Opalinus wall rock interactions with EBS backfill, copper alteration and corrosion rates, steel/bentonite interface phase reactions.

- Opalinus Clay upon heating develops wairakite along cracks and edges. Mine run bentonite contains clinoptilolite, and transforms to analcime at higher temperature, releasing both SiO_2 and water.

- Pit corrosion is the driving force in copper degradation. Copper reacts with H_2S (aq, g) to produce chalcocite and covellite. At latter times in the reaction pathway, Cl may combine with copper to produce atacamite.

- Systematic measurements (N>850) of copper corrosion cross sections have estimated corrosion reaction rates at experimental temperatures and pressures: At 6 weeks duration, corrosion rates ranged from 0.12 to 0.39 micron/day. However, in the 6 months experiment, the corrosion rate dropped by an order of magnitude, to 0.024 micron/day. We believe that complete coverage by the reaction product chalcocite pacifies the corrosion reaction.

- The interface between bentonite and steel develops a well characterized Fe-saponite (particularly at 300°C), that grows perpendicular to the steel surface. Pit corrosion of low carbon steel was common and resulted in a corrosion rate of 1083 µm/yr.

- **Update to Thermodynamic Database Development and Sorption Database Integration – LLNL & SNL (Part IV)**
  - Progress on the assessment of thermodynamic and sorption data:
    - A manuscript describing the evaluation of a thermodynamic data using concept of "links" to the chemical elements in their reference forms has been finally resubmitted to *Geochimica et Cosmochimica Acta* after responding to reviewer comments. This work has been carried in collaboration between LLNL and SNL.

    - A second manuscript, "Chemical Thermodynamic Data. II. Water in SUPCRT92 and Similar Codes: Thermochemical Properties in Relation to Equations of State" was recently submitted to *Computers & Geosciences*.

    - The coupling of the PHREEQC computer code with the parameter estimation / optimization software PEST was tested to fit U(VI)-quartz sorption dataset. Resulting fits are comparable with previous LLNL work efforts therefore providing a robust path forward for surface complexation database development.

    - Ongoing NEA TDB project activities include upcoming releases and/or ongoing review activities of chemical thermodynamic data: Ancillary data review, Fe – Part II review, Mo review, State-of-the-Art report (SOAR) on cements, SOAR Pitzer, Update Actinides review.

- **Fuel Matrix Degradation Model: Canister Corrosion and the Effect of Hydrogen on Used Fuel Degradation Rates – ANL (Part V)**
    - Formulated, coded and tested an electrochemical steel corrosion module that couples in-package steel corrosion with fuel degradation through the common solution.

    - Updated and optimized FMDM to improve the efficiency of integration with the GDSA PA model.

    - Performed scoping electrochemical tests to build confidence in modeling the H_2 effect mechanism which has a significant impact on source term calculations when in-package steel components are corroding simultaneously with used fuel.

- **Addition of Bromide to Radiolysis Model Formulation for Integration with the Mixed Potential Model – PNNL (Part VI)**
  - Update on the radiolysis model for calculating radiolytic generation of H_2O_2 with known concentration of H_2, O_2 and Br^-.
  - The radiolysis model is capable of accounting for the effects of bromide and the dependence on H_2. Comparisons between the full and the empirical radiolysis models were conducted to evaluate differences between these model representations.

Overall Future Perspectives:

- Expand integration of process model work with GDSA PA for case scenarios relevant to disposal in argillite in the presence of heat-generating waste.

- Expand non-isothermal reactive transport modeling of near-field chemical interactions to temperatures relevant to disposal concepts of interest in the assessment of thermal limits and the extent of *sacrificial zones*. This includes experimental and modeling efforts contributing to the elucidation of key processes affecting the fate and performance of barrier materials at elevated temperatures.

- Continue development and testing of coupled-process model representations of near-field chemical interactions, mechanical, and transport in barrier materials. Programmatic engagements and collaborations with international R&D activities (e.g., URL heater tests) in repository sciences are an integral part of these efforts.

- Development of a waste canister degradation plus other materials exerting important effects on EBS interfaces. This activity will leverage on the above-mentioned international collaborations particularly on the aspect of steel – bentonite interactions (e.g., FEBEX-DP) and sample characterization studies.

- Expand coupling of source term models (radiolysis and FMDM) that include the effects of waste package degradation and the presence aqueous species (e.g., Br^-). This is guided by the further integration of these models with GDSA-PA.

TABLE OF CONTENTS

Evaluation of Used Fuel Disposition in Clay-Bearing Rock: Reactive Transport and Barrier Interactions in the Near Field Environment - SNL (Part I)

Argillite Disposal R&D at LBNL (Part II)

Experimental studies of Engineered Barrier Systems conducted at LANL (Part III)

Update to Thermodynamic Database Development and Sorption Database Integration - LLNL & SNL (Part IV)

Fuel Matrix Degradation Model: Canister Corrosion and the Effect of Hydrogen on Used Fuel Degradation Rates - ANL (Part V)

Addition of Bromide to Radiolysis Model Formulation for Integration with the Mixed Potential Model - PNNL (Part VI)

TABLE OF FIGURES

Evaluation of Used Fuel Disposition in Clay-Bearing Rock: Reactive Transport and Barrier Interactions in the Near Field Environment – SNL (Part I)

Argillite Disposal R&D at LBNL (Part II)

xvii

xx

Experimental studies of Engineered Barrier Systems conducted at LANL (Part III)

Update to Thermodynamic Database Development and Sorption Database Integration (Part IV)

Fuel Matrix Degradation Model: Canister Corrosion and the Effect of Hydrogen on Used Fuel Degradation Rates (Part V)

Addition of Bromide to Radiolysis Model Formulation for Integration with the Mixed Potential Model (Part VI)

LIST OF TABLES

Evaluation of Used Fuel Disposition in Clay-Bearing Rock: Reactive Transport and Barrier Interactions in the Near Field Environment – SNL (Part I)

Argillite Disposal R&D at LBNL (Part II)

Experimental studies of Engineered Barrier Systems conducted at LANL (Part III)

Update to Thermodynamic Database Development and Sorption Database Integration – LLNL & SNL (Part IV)

Fuel Matrix Degradation Model: Canister Corrosion and the Effect of Hydrogen on Used Fuel Degradation Rates – ANL (Part V)

Addition of Bromide to Radiolysis Model Formulation for Integration with the Mixed Potential Model – PNNL (Part VI)

ACRONYMS

1D, 1-D	One Dimensional
2D, 2-D	Two Dimensional
3D, 3-D	Three Dimensional
ANDRA	Agence Nationale pour la Gestion Des Déchets Radioactifs (France)
ABM	Alternative Buffer Materials
ANL	Argonne National Laboratory
BBM	Barcelona Basic Model
BExM	Barcelona Expansive Model
CEC	Cation Exchange Capacity
CFRT	Colloid-Facilitated Radionuclide Transport
CIEMAT	Centro de Investigaciones Energéticas, Medioambientales y Tecnológicas (Spain)
CT	Computerized Tomography
DECOVALEX	DEvelopment of COupled Models and their VALidation against EXperiments
DFN	Discrete Fracture Network
DOE	Department of Energy
DOE-NE	Department of Energy, Office of Nuclear Energy
DRZ	Disturbed Rock Zone
DSEF	Disposal Systems Evaluation Framework
EBS	Engineered Barrier System
EBS-NS	Engineered Barrier System-Natural System
EC	European Community
EDL	Electric Double Layer
EDS	Energy dispersive X-ray spectroscopy
EDZ	Excavated Disturbed Zone
EMP(A)	Electron Microprobe (Analysis)
ENRESA	Empresa Nacional de Residuos Radioactivos SA
EoS or EOS	Equation of State
FCRD	Fuel Cycle Research and Development
FCT	Fuel Cycle Technologies
FCM	Fracture Continuum Model

FMDM	Fuel Matrix Degradation Model
FE	Full-Scale Emplacement Experiment
FEBEX	Full-scale Engineered Barriers Experiment
FEBEX-DP	Full-scale Engineered Barriers Experiment-Dismantling Project
FEP	Features, Events, and Processes
FTG	Flow Topology Graph
FY	Fiscal Year
GDSA	Generic Disposal System Analysis
GDSA-PA	Generic Disposal System Analysis – Performance Assessment
GTS	Grimsel Test Site
GW	Gigawatt
GWd	Gigawatt days
GWd/MT	Gigawatt (thermal) - days per Metric Ton
HC	Hydrological and Chemical
HE-E	Half-Scale Heater Test (Mont Terri)
HLW	High-Level nuclear Waste
HM	Heavy Metal
HPLC	High Pressure Liquid Chromatograph
IAEA	International Atomic Energy Association
IC	Ion Chromatography
I-S	Illite-Smectite
JAEA	Japan Atomic Energy Agency
JNC	Japan Nuclear Cycle Development Institute
LANL	Los Alamos National Laboratory
LBNL	Lawrence Berkeley National Laboratory
LC	Loading Collapse
LT	Local Thickness
LLNL	Lawrence Livermore National Laboratory
MC	Mechanical-Chemical
MT	Metric Ton
MTHM	Metric Tons Heavy Metal
Micro XR CT	Micro X-ray Computer Tomography

Micro-XRF	Micro X-ray Fluorescence
NAGRA	National Cooperative for the Disposal of Radioactive Waste
NBS	Natural Barrier System
NE	DOE-Nuclear Energy
NEA	Nuclear Energy Agency
NIST	National Institute of Standard and Technology
NMP	Noble Metal Particles
NS	Natural (Barrier) System
NW	Nuclear Waste
OECD	Organization for Economic Co-operation and Development
P	Pressure
PA	Performance Assessment
P-T-t	Pressure-Temperature-Time
PWR	Pressurized Water Reactor
QXRD	Quantitative X-ray Diffraction
R&D	Research and Development
RBSN	Rigid-Body-Spring Network
RH	Relative Humidity
SCM	Surface complexation model
SEM	Scanning Electron Microscopy
SIT	Specific Interaction Theory
SNF	Spent Nuclear Fuel
SNL	Sandia National Laboratories
SOAR	State of the Art Report
SXR-μCT	Synchrotron X-ray micro-Computer-Tomography
T	Temperature
t	time
TC	Thermal and Chemical
TDB	Thermodynamic Database
TEM	Transmission Electron Microscopy
TH	Thermal and Hydrological
THM	Thermal-Hydrological-Mechanical

THMC	Thermal-Hydrological-Mechanical-Chemical
TM	Thermal-Mechanical
TSPA	Total System Performance Assessment
UFD	Used Fuel Disposition
UFDC	Used Fuel Disposition Campaign
UOX	Uranium Oxide Fuel
UPC	University of Catalonia
URL	Underground Research Laboratory
WP	Waste Package
XRD	X-ray Diffraction
XRF	X-ray Fluorescence

Evaluation of Used Fuel Disposition in Clay-Bearing Rock:
Reactive Transport and Barrier Interactions in the Near Field Environment (Part I)

1. Evaluation of Used Fuel Disposition in Clay-Bearing Rock: Non-Isothermal Reactive-Transport Modeling of the Near Field Environment

1.1 Introduction

The ideal isolation qualities of clay/shale/argillaceous rock formations such as low permeability, geochemically reduced, crack/fracture self-healing, sorbtive mineralogy, and wide geological occurrence makes these a target media for hosting deep geological disposal of nuclear waste (Bianchi et al., 2013, 2014; Gonzales and Johnson, 1984; Hansen et al., 2010; Mazurek et al., 2003; Neuzil, 2013; Schurr, 1977). The R&D program from the DOE Used Fuel Disposition Campaign (UFDC) has documented advances in coupled Thermal-Hydrological-Mechanical-Chemical (THMC) modeling of clay to simulate its complex dynamic behavior in response to thermal and hydrochemical feedbacks (Jové Colón et al., 2014, 2015 and references therein). These modeling efforts leverage on the wide range of investigations on clay barrier materials and argillaceous rocks in particular by a number of international repository science programs (e.g., URLs) (Hansen et al., 2010). The DOE Used Fuel Disposition Campaign (UFDC) R&D program comprehends a suite of R&D topics aimed at model development and experimental work (Jové Colón et al., 2014; Rutqvist et al. 2014, Zheng et al. 2014). The objective is to build robust process models in support of high-fidelity performance assessment (PA) calculations of disposal concepts for nuclear waste. Some of the key items in support of the safety assessment for disposal in the argillite work package are:

- Experimental and modeling studies on hydrothermal interactions in clay.

- Coupled Thermal-Hydrological-Mechanical-Chemical (THMC) modeling.

- Experiments and model development of sorption and diffusion onto clay.

- Assessment of SNF and canister corrosion.

- Thermodynamic database development and analysis of fluid-mineral interactions on barrier materials.

An initial assessment of a reference case for disposal in argillite is given by Mariner et al. (2015) as part of the generic disposal system analysis performance assessment (GDSA-PA). The overall geological characteristics and repository dimensions along with the adopted stratigraphic sequences bounding the disposal are shown in Figure 1. The subsurface repository layout consists of horizontal disposal galleries emplaced end-to-end with waste packages in drifts lined with cement and/or metal support structures (Mariner et al., 2015). Numerical simulations in that work were conducted using PFLOTRAN with a 3D structured grid having variable spacings. The DAKOTA software toolkit is used for sampling, sensitivity analysis, and uncertainty quantification. Although this is an important first step in the direction of building up a GDSA-PA evaluation of disposal in argillaceous media, geochemical interactions that affect radionuclide chemistry and transport, and mineralogical alteration of barrier materials leading to changes in porosity/permeability properties still need to be evaluated. The following section describes a 1D reactive-transport model in PFLOTRAN focusing on barrier material interactions in the presence of SNF heating therefore producing a thermal pulse (see Greenberg and Wen, 2013). Such a thermal perturbation can last up to hundreds years therefore influencing barrier chemical interactions as well as moisture transport in the near-field.
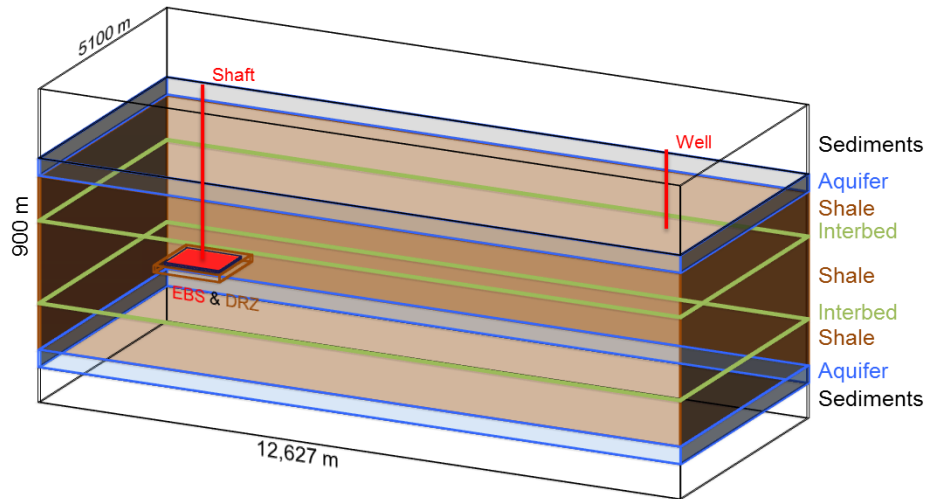
Figure 1. Schematic representation of the stratigraphy and repository footprint dimensions considered for the reference case for disposal in clay/shale/argillite rock (Mariner et al. 2015).

2.   Reactive Transport in the Near-Field Environment

Jové Colón et al. (2015) described a reactive-transport model to assess geochemical changes of pore solutions and mineral components plus variations in porosity. The objective of this simulation efforts is the evaluation of *sacrificial zones* in the EBS. A *sacrificial zone* refers to "barrier material that has undergone extensive geochemical alteration as a result of exposure to high temperatures" but not necessarily entails the destruction or compromise of the barrier isolation capacity at any specific location of the EBS (Jové Colón et al., 2013). Understanding the effects (long- and short-term) of heterogeneous chemical reactions (dissolution/precipitation), phase transformation phenomena, and the coupling of these with thermal effects are key to the overall barrier isolation performance in the near-field environment. In particular, chemical effects are expected to be intensified at EBS interfaces between dissimilar barrier materials inducing changes in the EBS porous properties. The main goal of the current stage of this work is to expand the 1D reactive-transport model to include the thermal perturbation caused by heat-generating waste along with chemical changes in the near-field. Within this objective, the goal is to also have a stable reactive-transport model with a comprehensive geochemical construct operating under such conditions to evaluate key interaction in the EBS.

As summarized in previous reports (e.g., Jové Colón et al., 2014), studies on EBS materials and their performance as a result of interactions with fluids have been conducted to evaluate cement-clay interactions (Dauzeres et al., 2010; Gaboreau et al., 2012; Sanchez et al., 2006; Savage, 2011; Trotignon et al., 2006), reactive-transport simulations of multi-barrier EBS concepts (Kosakowski and Berner, 2013; Marty et al., 2010; Marty et al., 2009; Montes-H et al., 2005), and characterization studies of reactive-diffusion and sorption in clay-bearing barrier materials (González Sánchez et al., 2008; Joseph et al., 2011; Joseph et al., 2013; Kozai et al., 2001; Kozaki et al., 2001; Van Loon et al., 2003). The UFD international collaboration with the FEBEX-DP project has provide the unique opportunity to study shotcrete / bentonite overcore samples from this long-term heater test and will be briefly discussed in a later section (Jové Colón, 2016).

3

The enhanced dissolution of clay and silicates in general when exposed to highly alkaline pore solutions as a result of cement-clay interactions presents a potential issue for repository sealing performance (Berner et al., 2013; Gaboreau et al., 2012; Kosakowski and Berner, 2013; Soler, 2012; Soler and Mader, 2010). The expected porosity enhancement and reduction (e.g., pore clogging) as a result of mineral dissolution and precipitation, respectively, have been evaluated in reactive-transport modeling efforts including benchmark test cases for computer code inter-comparisons (Marty et al., 2015; Xie et al., 2015). Moreover, EBS interfaces such as those defined by clay barriers and interactions with metal (steel) overpack/canister are also critical to the assessment waste package breaching given their close proximity to the SNF source and their importance to barrier material degradation (Jové Colón et al., 2013; Jové Colón et al., 2014; Marty et al., 2010; Wilson et al., 2015).

The main goal of this reactive-transport work is to build a non-isothermal 1D model representation of multilayered EBS capturing the complexity of geochemical interactions between various types of barrier materials and pore solutions with diffusive transport. A thermal source defined by the heat-generating waste is set to produce peak temperatures above 100°C on the canister surface. The chemical aspect of the model is to comprehensively capture the mineral composition of each barrier "layer" or zone as well as the pore solution chemistry. The code PFLOTRAN has been selected as the simulation platform for GDSA PA in the evaluation of disposal concepts (Mariner et al. 2015). The 1D reactive-transport model in PFLOTRAN exploits high performance computing (HPC) capabilities to ease simulation times thus allowing for rapid analysis of key input and output variables. Code run stability was an issue due to the rapid rise in temperatures and the reactive-transport part of the simulation.

2.1   1D Reactive-Transport Model Description of the EBS

The PFLOTRAN simulation tool is an open source, state-of-the-art massively parallel subsurface flow and reactive transport code with extensive modeling capabilities of THC processes (Lichtner et al., 2013). A major feature of PFLOTRAN is its performance on massively parallel or high performance computing (HPC) platforms where efficient scalability becomes important for large coupled process problems that otherwise could present a computational limitation in other simulation codes. Parallelization is achieved through domain decomposition using the PETSc (Portable Extensible Toolkit for Scientific Computation) libraries. Lichtner et al. (2013) provides details on PFLOTRAN simulation capabilities, reactive-transport formulations, and geochemical treatment of mineral-fluid interactions.

The 1D simulation case is similar to that described by Jové Colón et al. (2015) as depicted in Figure 2 but using the TH mode in PFLOTRAN. Some of the differences are in pore solution chemistry and geochemical constraints. The 1D structured grid has a cylindrical symmetry with 1000 grid cells in the horizontal direction covering a total near-field domain of 13 meters. The dimensional characteristics of each zone (also given in Figure 2) represent barrier thicknesses for the EBS concept proposed for the argillite reference case in Jové Colón et al. (2014). All zones are assumed to be fully saturated with a heating zone defined at the canister surface. Table 1 list some of the thermal and transport properties of each zone. Tables 2 and 4 provide the mineral volume fractions and initial pore solution chemical composition, respectively, for each barrier material zone. Three types of initial pore water chemistries for the cement liner, clay barrier, and clay-rock zones were considered: (a) dilute alkaline pH water (cement liner), (b) "FEBEX-like" pore water as described by Fernandez et al. (2001, 2004) (inner- and outer-clay), and (c) clay-rock pore water based on the work by Turrero et al. (2006). Some minor changes to the water

chemistry were considered to evaluate issues with code run stability during the heating. The $H_4SiO_4(aq)$ concentration in the inner clay zone is assumed to be in equilibrium with quartz given that 14% volume fraction of this mineral is present in this zone. The FEBEX pore water composition is considered nominal for bentonite pore waters reported in the literature. The clay rock pore water chemistry is based on the work of Turrero et al. (2006) for Opalinus Clay. Pore water compositions in the cement zone are mainly controlled by equilibria with respect to the calcite aggregate and the presence of CSH(1.6) and portlandite plus other cementitous phases. Although uraninite as a waste form source term is part of the EBS solid phase assemblage, the current simulations do not consider the constibutions of this phase to the solution chemistry. Future simulations will probe waste form and canister material interactions.

Canister material is currently represented in the model by Fe metal, similar to other reactive transport studies (Marty et al. 2010; Wilson et al. 2015). However, there are differences in the treatment of steel corrosion usually represented by an anaerobic corrosion reaction given by (Marty et al. 2010; Wilson et al., 2015):

$$Fe° + 2H_2O = Fe^{++} + H_2(g) + 2OH^-$$
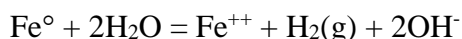
A similar reaction is adopted for the "Fe(element)" phase in the THERMODDEM thermodynamic database representing the steel material in this work:

$$Fe° + 2H^+ + 1/2O_{2(aq)} = Fe^{++} + H_2O$$
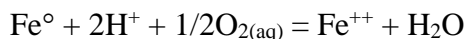
As expected, the above reaction results in an increase in pH due to H^+ consumption where $H_2(g)$ is controlled by the equilibria with other relevant species such as $O_2(aq)$, $O_2(g)$, and $H_2(aq)$. The current simulations show large reactivity, as expected, with a sharp increase in pH. At this moment, the reaction product for steel corrosion considered in the PFLOTRAN reactive-transport simulations is magnetite, goethite, and berthierine. Other phases like cronstedtite along with berthierine have been considered to investigate the predominant alteration phase assemblage but resulting in small precipitated volume fractions. Future work will focus on other Fe-bearing phases (oxides and silicates), however, lack of thermodynamic data at elevated temperatrures may be an obstacle for this assessment. Given the importance of these interactions to waste package degradation, future work will look at this issue in more detail to advance an adequate set of reaction products that include Fe oxy-hydroxides and Fe-bearing Al-silicates (e.g., Fe-clays). For example, the hydrothermal clay/stainless-steel experiments conducted by Cheshire et al. (2016, *in preparation*) described the formation of a chromite ($FeCr_2O_4$) passivation layer along with the minor formation of pentlandite (($Ni,Fe)_9S_8$) and millerite (NiS)). The presence of these S-bearing phases indicates the strong effect of the sulfide component in the alteration phase assemblage and potentially on corrosion mechanisms. This is somewhat similar to the case of copper corrosion and the formation of chalcocite (Cu_2S; see Part III of this report). Another important issue in waste canister corrosion is the fate of $H_2(g)$ and its impact on O_2 fluxes as result of aqueous chemical reactions and fluid transport at the clay-metal interface. This was noted by Wilson et al. (2015) whereby $H_2(g)$ being not well constrained in reactive-transport model scenarios it thus imposes important uncertainties in the chemical interactions at the clay-metal interface.

Table 1. Properties and dimensions of EBS components for the 1D PFLOTRAN simulation.

	Thickness (m)	Porosity (-)	Permeability (m^2)	Tortuosity (-)	Particle Density (kg/m^3)	Thermal Conductivity (Dry) (W/m K)	Remarks
Waste Form	0.475	0.3	1.0E-22	0.3	8720	11	Assumed to be inert
Metal Canister	0.1	0.001	1.0E-22	0.001	7850	46	Stainless steel overpack
Inner-Clay Barrier	1.24	0.3	1.0E-17	0.3	2700	1.7	Bentonite + Quartz
Outer-Clay Barrier	1.24	0.2	1.0E-20	0.2	2700	1.3	Bentonite
Cement Liner	0.75	0.15	1.0E-17	0.15	2700	1.7	Cement + aggregate
Clay Rock	9.2	0.12	5.0E-20	0.12	2700	1.7	Based on argillite properties

Table 2. Initial volume fractions inputs for the 1D PFLOTRAN simulations.

	Smectite (MX80)	Illite (IMt2)	Quartz (alpha)	Uraninite	Fe (element)	Pyrite	Calcite	Siderite	CSH(1.6)	Portlandite	Ettringite	Monosulfo aluminate	Gypsum	Remarks
Waste Form	-	-	-	0.7	-	-	-	-	-	-	-	-	-	Assumed to be inert
Metal Canister	-	-	-	-	0.999	-	-	-	-	-	-	-	-	Fe metal in the model
Inner-Clay Barrier	0.55	-	0.14	-	-	0.004	0.003	-	-	-	-	-	0.003	Bentonite + Quartz
Outer-Clay Barrier	0.79	-	-	-	-	0.004	0.003	-	-	-	-	-	0.003	Bentonite
Cement Liner	-	-	-	-	-	-	0.693	-	0.06	0.062	0.033	0.002	-	Cement + calcite aggregate
Clay Rock	0.06	0.43	0.24	-	-	0.01	0.139	0.001	-	-	-	-	-	Opalinus clay rock

Table 3. Initial molal concentration of aqueous components for each barrier zone in the PFLOTRAN input card.

	Na$^+$	K$^+$	Ca^{++}	Mg^{++}	H$_4$SiO$_4$(aq)	Al^{+++}	Fe^{++}	U^{++++}	Cl$^-$	SO$_4^{--}$	HCO$_3^-$	pH	Remarks
Waste Form	1.0E-07	1.0E-08	1.0E-07	1.0E-07	5.0E-06	6.0E-08	5.0E-15	trace	1.0E-07	1.0E-07	1.0E-05	7.51	Assumed to be inert
Metal Canister	1.0E-07	1.0E-08	1.0E-07	1.0E-07	5.0E-06	6.0E-07	5.0E-05	trace	1.0E-07	1.0E-07	1.0E-05	7.51	Stainless steel overpack
Inner-Clay Barrier	1.3E-01	1.7E-03	2.2E-02	2.30E-02	1.1E-04	6.0E-07	5.0E-06	trace	1.6E-01	1.0E-05	4.1E-04	7.72	FEBEX pore water;. H$_4$SiO$_4$(aq) in equilibrium with Quartz
Outer-Clay Barrier	1.3E-01	1.7E-03	2.2E-02	2.30E-02	1.1E-04	6.0E-07	5.0E-07	trace	1.6E-01	1.0E-05	4.1E-04	7.72	FEBEX pore water; Ca^{++} in equilibrium with calcite
Cement Liner	1.0E-05	1.0E-08	2.0E-03[a]	1.0E-04	6.0E-03	6.0E-07	5.0E-07	trace	1.0E-05	1.0E-09	1.0E-07[b]	11.2	Cement + calcite aggregate
Clay Rock	0.261	0.0027	0.0201	0.0165	2.95E-04	6E-07	2.3E-05	trace	0.332	1.0E-07	1.0E-06	7.6	Based on Turrero et al. (2006) for Opalinus Clay pore water

[a] Constrained by equilibrium with respect to CSH(1.6). [b] Constrained by equilibrium with respect to calcite. FEBEX pore water major ion composition after Fernandez et al. (2001).

Table 4. Kinetic rates and specific surface areas of mineral phases (see text).

Mineral Phase	Dissolution Rate (mol/ m^2 s)	Specific Surface Area (m^2/m^3)	Source	Remarks
Smectite(MX80)	8.0E-14	1	Marty et al. (2009)	-
Illite(IMt2)	1.585E-15	1	Köhler et al. (2003)	pH~7
Quartz(alpha)	1.99E-14	1	Rimstidt and Barnes (1980)	-
Uraninite	-	1	-	Assumed unreactive
Fe(element)	2.232E-12	1	Marty et al. (2010)	Rate constant for steel
Pyrite	2.884E-11	1	Williamson and Rimstidt (1994)	pH~7.5; 7.24E-7 molal dissolved oxygen
Calcite	1.778E-05	1	Pokrovsky et al. (2009)	-
Siderite	1.007E-09	1	Golubev et al. (2009)	pH~7
CSH(1.6)	2.75E-12	1	Baur et al. (2004)	pH range 11-12
Portlandite	5E-04	1	Giles et al. (1993)	Transport-independent rate
Ettringite	1.12E-12	1; 5E-04 (Arg.); 1E-02 (Cem.)	Baur et al. (2004)	Unity surface areas for all phases Except for cement (cem.) and clay rock (Arg.) – see text
Monosulfoaluminate	1.12E-12	1	-	Sames as ettringite
Gypsum	1.3d-3	1	Jeschke et al. (2001)	-

Diffusive transport in bentonite is still a subject of debate given the influence of clay interlayers and the description of porosity particularly in the compacted state (Wersin et al. 2015). For this reason, a much simpler form of diffusive flux is adopted focusing on assessing the thermal effect on reactive-transport. In these simulations, the diffusive flux in PFLOTRAN is then defined according to porosity, saturation, reference diffusivity, and tortuosity (Lichtner et al., 2013):

$$F_i = -\phi S D \tau \nabla C \tag{1}$$

where F_i is the diffusive flux of the solute constituent i, ϕ stands for porosity, S refers to saturation, τ represents tortuosity, D denotes the diffusion/dispersion coefficient, and C symbolizes solute concentration. Tortuosity in each zone is assumed to be equal to porosity following Archie's Law with the exponent n = 2. Boudreau (1996) compared tortuosity-porosity data for sedimentary environments along with formulations to represent tortuosity-porosity relations including Archie's Law. Considering the scatter in the data, Boudreau (1996) found that Archie's Law with n = 2.14 provides a reasonable description of this tortuosity-porosity relation. All media domains are fully saturated. The diffusion coefficient is set to 2.0 E-13 m^2/s to be consistent with the range of effective diffusion coefficient values adopted in the study of Kosakowski and Berner (2013). Although this value may seem to be on the lower end, diffusivities for compacted clay-rich barrier material and clay rock can be as low as 10^{-13} m^2/s. Sensitvity analyses on diffusion coefficients up to ~10^{-12} m^2/s resulted in stable code runs with the current inputs and material buildup. Porosities are updated in the simulations according to the volume fraction of minerals and their dissolution/precipitation rates.
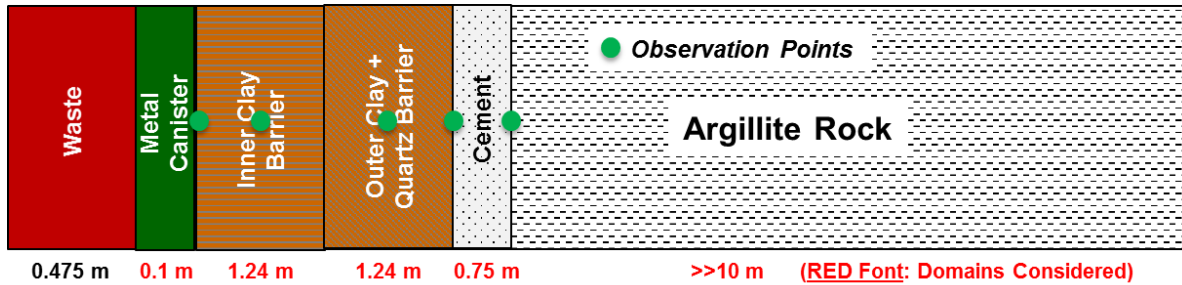
Figure 2. Schematic representation and dimensional characteristics of the 1D reactive-transport simulation domain including the EBS and argillite rock. Interactions with waste are not considered in this study. Green dots indicate observation points of code run data outputs presented in subsequent figures.

Mineral volume fractions of reactant minerals (Table 2) were defined consistent with porosities listed in Table 1. The specific surface areas of all constituent minerals are all set to unity except for ettringite in the cement and clay rock phases. The reason for treating specific surfaces areas differently for ettringite has to do with simulation stability during heating. Assuming unity surface areas as a modeling assumption deviates from other reactive-transport modeling studies but it allows for simpler evaluation of simulation outputs. PFLOTRAN updates surface area of minerals as a result of mineral dissolution and precipitation. This is captured in the code runs by changes in mineral volume fractions and hence porosity. Other modeling studies such as that of Marty et al. (2009) evaluated modeling sensitivities to specific surface areas. Given the range of surface areas adopted in reactive-transport simulation studies, it appears that these are mostly based on modeler choice built on literature values or estimates of specific and/or geometric mineral surface areas.

Sensitivity analyses were conducted with regards to specific surface areas of pyrite given its strong effect on pH. These sensitivities were also analyzed for ettringite in the cement liner and clay rock zones due to stability issues on simulation during the heating period. In the FEBEX pore water cases, specific surface areas were set in the order of ~10^{-3} to reduce the effects on pH which can be significant even when using relatively small pyrite volume fractions. According to Cheshire et al. (2014), the drop in pH as a result of pyrite decomposition is ~2 pH units based on clay hydrothermal experiments. In the cases for the FEBEX pore water chemistry, the drop in pH was observed but of lesser magnitude than in the diluted pore water case.

Thermodynamic data for all mineral phases were obtained from the THERMODDEM database (Blanc et al., 2012; Blanc et al., 2006). This database contains a comprehensive set of relevant mineral solids and aqueous species such as smectite (MX-80) and illite (IMt2) clays among other silicates. Many datasets contain logK for reactions extrapolated to elevated temperatures which is appropriate for these simulations. Its development is borne out from the traceability requirements demanded by rigorous assessment of data to be used in (geo)chemical modeling of radioactive waste and engineered barrier materials. THERMODDEM also contains a comprehensive set of solid phases relevant to cementitious materials such as CSH(1.6), portlandite, and ettringite among others. The cement liner composition considered in these simulations approximates that of ordinary Portland cement (OPC) with ~70% volume of calcite aggregate (see Table 2).

The PFLOTRAN simulations were conducted in TH mode (coupled thermal-hydrological flow) assuming full saturation. The non-isothermal simulations were conducted using a SNF decay heat data based on the thermal analysis approach by Greenberg et al. (2013). The decay heat curve is inititally based on 12 UOX PWR assemblies with a 50-year storage. The resulting temperatures in the thermal profile were scaled down to produce reasonable peak temperatures above 100°C without compromising code run stability. The thermal scale-down was done as to retain the overall shape of the thermal profile. The heating period after 50 years generating a sharp increase in temperature up to ~125°C with a slow decrease afterwards then approaching near-ambient temperatures within a period of several hundreds of years (Figure 3). The sharp increase in temperature resulted in code stability problems due to convergence issues. Many attempts to surpass peak temperatures above ~125°C failed and this limitation will be investigated further in FY17 since much higher temperatures at the canister surface need to be investigated. Figure 3 show the temperature profiles at different observation points (Figure 2) from the waste canister surface to the interface between cement liner and clay rock.

Dissolution rates of mineral solids are listed in Table 4. A linear dissolution rate law without temperature dependency is assumed for simplicity. Adding activation energies for the full set of minerals is being considered in future simulations. Several simulations specifying activations energies of few phases were performed with minimal effects on code run stability. Although the assumption of ignoring temperature dependencies adds to the simulation uncertainty, adding ill-constrained values to a rate law would also result in uncertain results. It should be noted that activation energies for some silicate and oxide phases can be estimated within reasonable bounds but this is not the case for certain types of clay or cementitious phases. It is assumed that precipitation rates are the reverse of dissolution rates given the very limited kinetic data available. This is consistent with the PFLOTRAN implementation of transition-state theory (TST) where the equilibrium constant can be defined as the ratio of backward and forward rates.

9

The dissolution rate for pyrite is obtained from Williamson and Rimstidt (1994) for a near-neutral pH 7.5. The smectite (MX-80) dissolution rate is taken from Marty et al. (2009) and it's based on the work of Amram and Ganor (2005), Huertas et al. (2001), and Golubev et al. (2006). The illite dissolution rate for pH~7 is from the experimental work of Kohler et al. (2003). The aqueous dissolution rate for magnetite is obtained from the electrochemical work of White et al. (1994) at pH 7. Dissolution rates for calcite and siderite were obtained from the studies of Pokrovsky et al. (2009) and Golubev et al. (2009), respectively.

The dissolution rate of the CSH phases was obtained from Baur et al. (2004) for pH 11-12. Dissolution rates for ettringite is based on the rates given for ettringite-Ca(2) in Baur et al. (2004). The dissolution rate tobermorite(11) is assumed to be equal to that of ettringite. The dissolution rate of portlandite was obtained from Giles et al. (1993). This rate was retrieved from spinning disk dissolution experiments for the "reaction-controlled" or transport-independent rate. The portlandite dissolution rate obtained from this study is orders of magnitude faster than that adopted by Marty et al. (2009). It's also more realistic for a pure portlandite phase since the spinning disk methodology provides insight into transport effects on dissolution rates which in this case are attributed to Ca diffusion through the interface (Giles et al., 1993). The dissolution rate of gypsum was taken from the study by Jeschke et al. (2001). Simulations were conducted up to time lengths of 1,000, 5,000, 10,000, and 20,000 years. Due to the length of the simulations, only results of up to 15,000 years are considered even with the use multiple processors. Observation points were located at the center of each zone and at interfaces between EBS material domains.

2.2   Results and Discussion

The code simulations results in the first 50 years consistent with isothermal ambient temperature interactions reported in Jové Colón et al. (2015) which include (1) rapid increase in pH and H_4SiO_4(aq) concentration in pore water is observed at the interfaces between cement and outer-clay buffer, and between cement and clay rock; and (2) effects on aqueous speciation by the thermal pulse (after 50 years) imposing sharp changes in the computed pore solution chemistry. This is evidenced by the combined effects on pH, aqueous speciation, and mineral precipitation (e.g., gypsum and anhydrite).

At the onset of heating (50 years), the rapid increase in temperature reaches a peak of 125°C (~100 years) and a slower decay afterwards (Figure 3). At this stage, the largest porosity changes occur at the cement – outer-clay interface with a small decrease after the peak porosity increment. The outer-clay center region experiences similar changes in porosity. The relative porosity enhancement at the outer-clay – cement liner interface is due to the gypsum to anhydrite dehydration. On the other hand, the cement – clay rock interface doesn't indicate this type of porosity changes (Figure 5). The reason for this dissimilar porosity behavior is related to different pore solution chemistries where depletion of Ca and SO_4 in clay rock pore water doesn't lead to gypsum-anhydrite formation. The FEBEX bentonite contains ~92% Ca-bearing smectite with pore solutions having higher concentrations of Ca and SO_4 than those of the clay rock. SO_4^{--} concentration in the cement region needed to be inititally constrained in equilibrium with respect to gypsum for code run stability reasons. As shown in Figure 4, The Ca^{++} concentrations drop consistently for inner- and outer-clay center regions as well as the interface of cement liner interfaces with outer-clay and clay rock regions. In the case of cement liner interfacial regions, this is due gypsum precipitation. Figure 4 also shows the SO_4^{--} concetration profiles mapping a similar relationship in the same regions.

The captured phase transformation reactions in this rapid temperature increase is important for thermally-driven hydration-dehydration reactions that can contribute to significant changes in permeability/porosity. This is reflected by a rapid drop in gypsum and the near-simultaneous increase in anhydrite volume fractions (Figure 6a). This transformation occurs at a temperature of ~44°C where the overall dehydration reaction produces a slight increase in porosity (Figure 5b). As mentioned previously, simulation stability during the heat pulse was also affected by the formation of ettringite at the cement liner interface regions. Ettringite formation is consistent with the reaction of $CaSO_4$ phases in the presence of Ca and Al as described in the cement literature. This outlines the importance of Ca-SO_4 and their equilibria in reactive systems particularly at elevated temperatures. Stable simulations were attained by reducing specific surface areas for enttringite. Also, sensitivity analyses with respect to the inclusion/suppression of other cementitious phases were conducted to search for additional dependencies on cement phase assemblage and code run stability.

Porosity reduction as a result of gypsum formation is observed with the temperature decrease in the outer-clay – cement interface and the outer-clay center regions. The timing of such changes differ due to their spatial locations with respect to temperature. Overall, the volume fractions of precipitated minerals were too small as to generate any significant reduction in porosity. The volume difference between gypsum and anhydrite is ~60% which can be significant depending on the relative amount of these phases, particularly when they are common to cementitious materials. These volume changes can induce mechanical effects where hydration/dehydration reactions can also influence H_2O transport in the EBS. Future work will assess the aspect of porosity changes in more detail from the standpoint of the chemical contributions due to dissolution/precipitation and hydration/dehydration reactions.
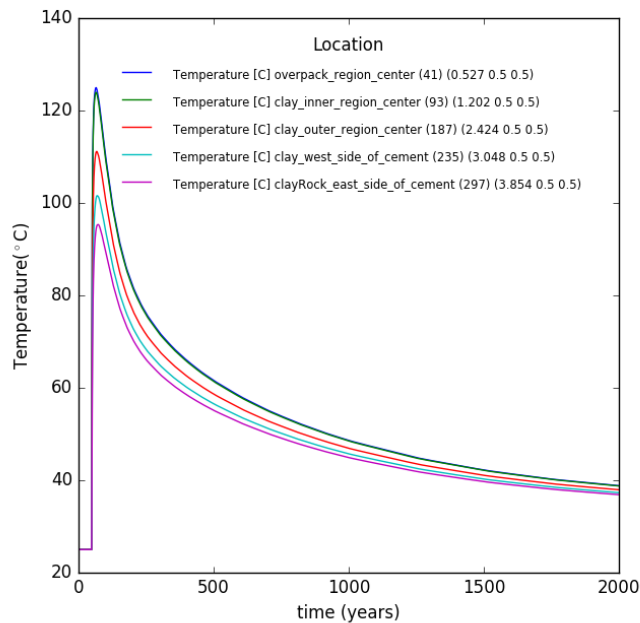
Figure 3. Profile of temperature vs. time (up to 1,000 years) for the reactive transport calculations of the multi-layered EBS. The number triplet in the second set parentheses in the legend refers to the

11

observation location (x, y, z) distances starting from the waste leftmost coordinate. A 50-year storage time prior to the thermal load.
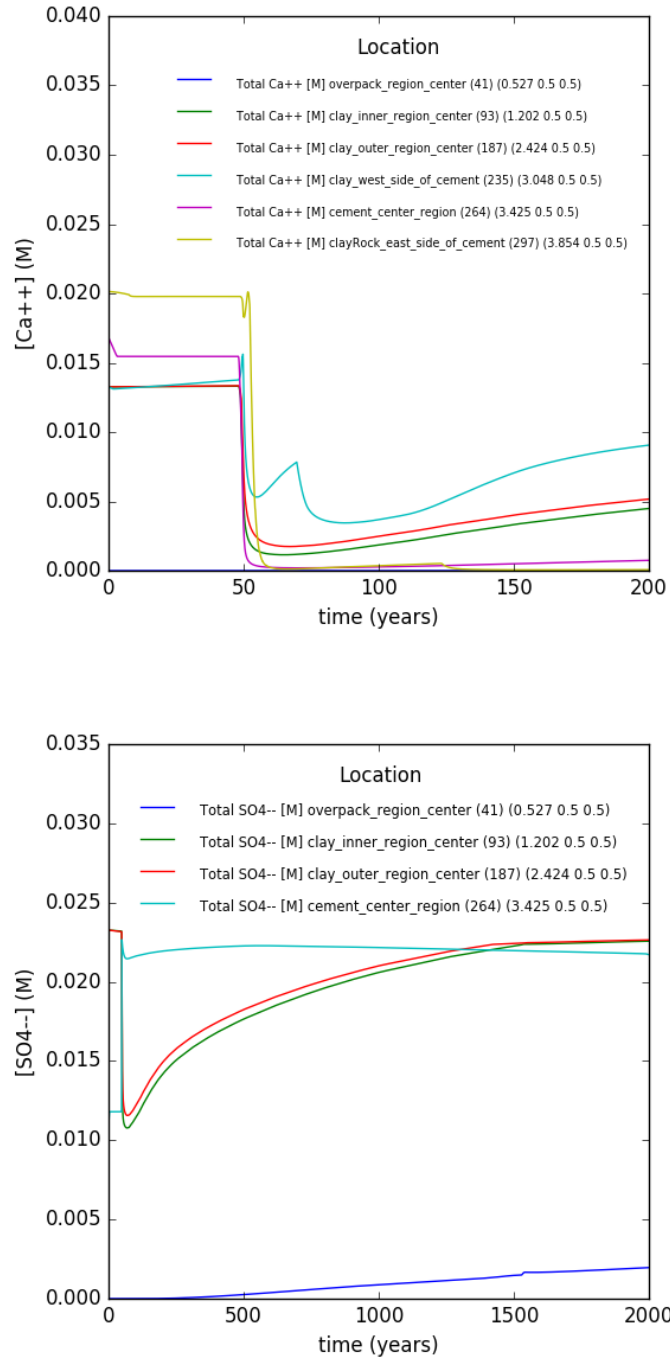
Figure 4. Ca^{++} and SO$_4^-$ concentration profiles as a function of time for various regions. Notice the effect of the heat pulse in the time range after 50 years.
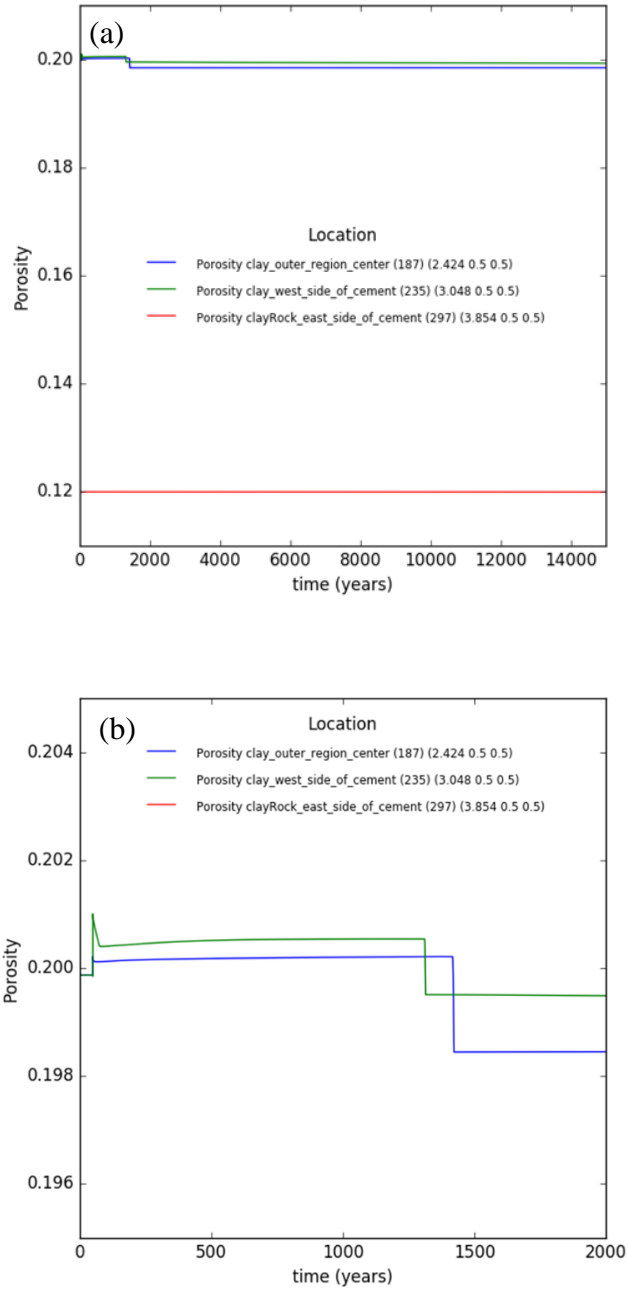
Figure 5. Profile of porosity vs. time of the reactive transport calculations for the multi-layered EBS at the identified observation points: (a) shows the longest simulation time period up to 15,000 years; (b) shows an enlarged view (up to 2,000 years) to outline the largest change in porosity. Porosity increase/decrease is more marked at the interfaces but their overall magnitude is relatively minimal in these simulations (see text).
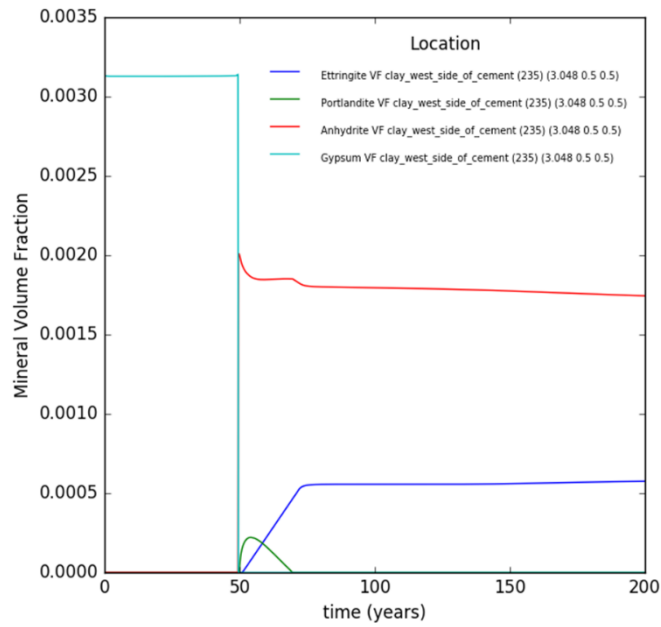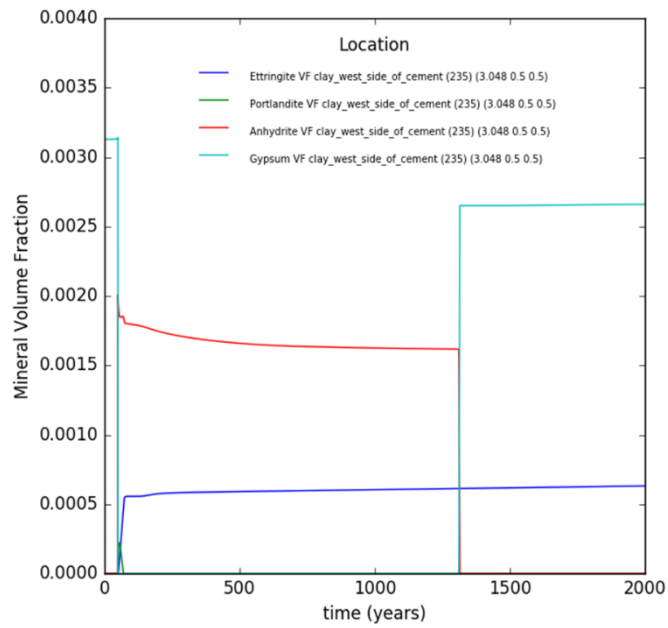
Figure 6. Volume fraction of gypsum, anhydrite, portlandite, and attringite at different time ranges.

14

Observations from FEBEX-DP Heater Test Samples

Cement – bentonite interactions is being investigated by the FEDEX-DP international collaboration activity by the characterization of overcore samples between the shotcrete seal/plug and bentonite. A preliminary characterization study by Jové Colón (2016) shows some observations on the compositional nature of cement-bentonite interface using scanning probe techniques – a brief summary follows. Figure 7 shows a BSEI micrograph and an EDS line scan of Ca across the shotcrete-bentonite interface. The sample is a polished thin section of the overcore material cut at the shotcrete-bentonite interface. The BSEI analysis show the granular texture of shotcrete with angular grains having a fairly wide size range embedded in a fine-grained matrix. The purpose of the line scan an X-ray maps is to probe for elemental distributions indicative of a reactive front or mineral phase alteration along the interface region. Ca is a ubiquitous component in many of both FEBEX bentonite and shotcrete phases and its overall distribution should serve as an indicator of alteration at the interface as shown in Figure 7. The peak Ca counts observed along the line scan transect are for a grain which is presumably portlandite based on the detection of elevated Ca and O only in X-ray maps. Based on various EDS X-ray maps and line scans, there is no indication of pervasive alteration or mineralization in the analyzed interface regions. Notice that on both sides of the Ca peak in Figure 7, elemental counts decreased to nominal levels that are comparable to both sides of the interface. This indicates little or low levels of alteration within the interface region. Other elemental profiles also show a similar behavior across the shotcrete-bentonite interface. Likewise, analysis of textures using BSEI and EDS at the micron level also indicates little or no alteration along the interface.
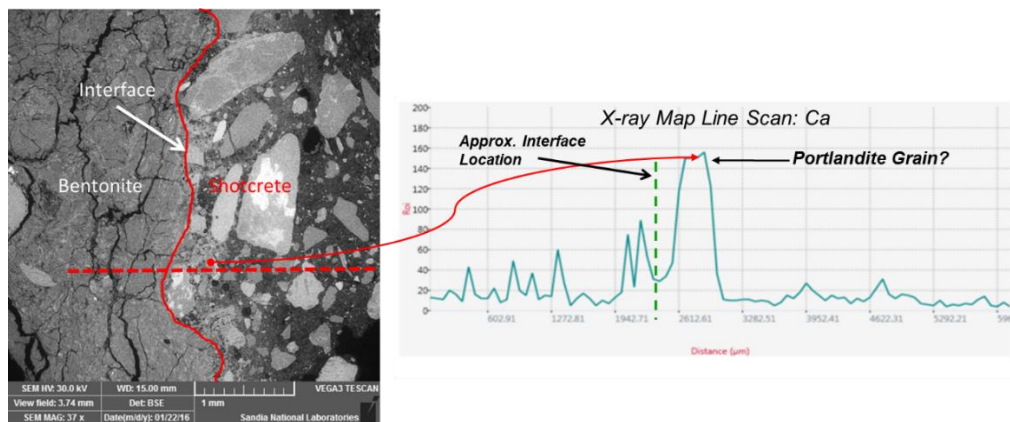
Figure 7. BSEI with Ca element profile line scan retrieved from X-ray map of the shotcrete-bentonite interface region. The horizontal red dashed-line in the BSEI is an approximate position of the line scan.

Compositional analysis using micro – X-ray Fluorescence (XRF) was conducted on the same polished thin section sample described above for SEM/BSEI/EDS analyses. Figure 8 shows micro-XRF maps for Ca and S indicating slight or virtually no alteration in the bentonite side. This observation is consistent with the SEM/EDS X-ray map analyses described previously. These Ca and S compositional maps also suggest the existence of an apparent millimeter-scale depletion zone in shotcrete close to the interface. The depletion zone is demarcated by some gradation from the bulk shotcrete towards the bentonite interface which is depicted by the Ca map. The depletion zone doesn't appear to traverse the bentonite side suggesting a reaction zone confined mainly to the shotcrete side. However, this observation is very preliminary and more

micro-XRF maps are needed to assess spatial compositional heterogeneities of shotcrete in the bulk. Another aspect of the characterization study of these samples is the use of micro X-ray CT (micro computerized tomography) imaging. This non-destructive scanning technique provides the ability to analyze relatively large specimens (in the order of cm in length), excellent resolution (e.g., ~10 microns), and the generation of 2D-3D digital image data for textural evaluation. A noticeable feature in this interfacial domain of the overcore sample is the wide occurrence of microcracks in bentonite and pores (no cracks) in shotcrete (Figure 9). "tree" branch networks evolving into craquelure or "chickenwire" patterns in many cases connected by rectilinear and jagged segments (Jové Colón, 2016). In some cases, these connected segments evolve into larger void spaces. The occurrence and distribution of these microcracks in bentonite due to drying/shrinkage is key to evaluating clay barrier performance given its strong influence to moisture transport, clay swelling, and therefore permeability/porosity properties of the barrier. This is particularly important in the assessment of barrier performance during dry/wet cycles as anticipated for HLW upon emplacement in disposal galleries. Part II of this report describes similar observations using synchrotron X-ray micro CT (SXR-μCT). More details of this micro X-ray CT work is given in Jové Colón (2016).
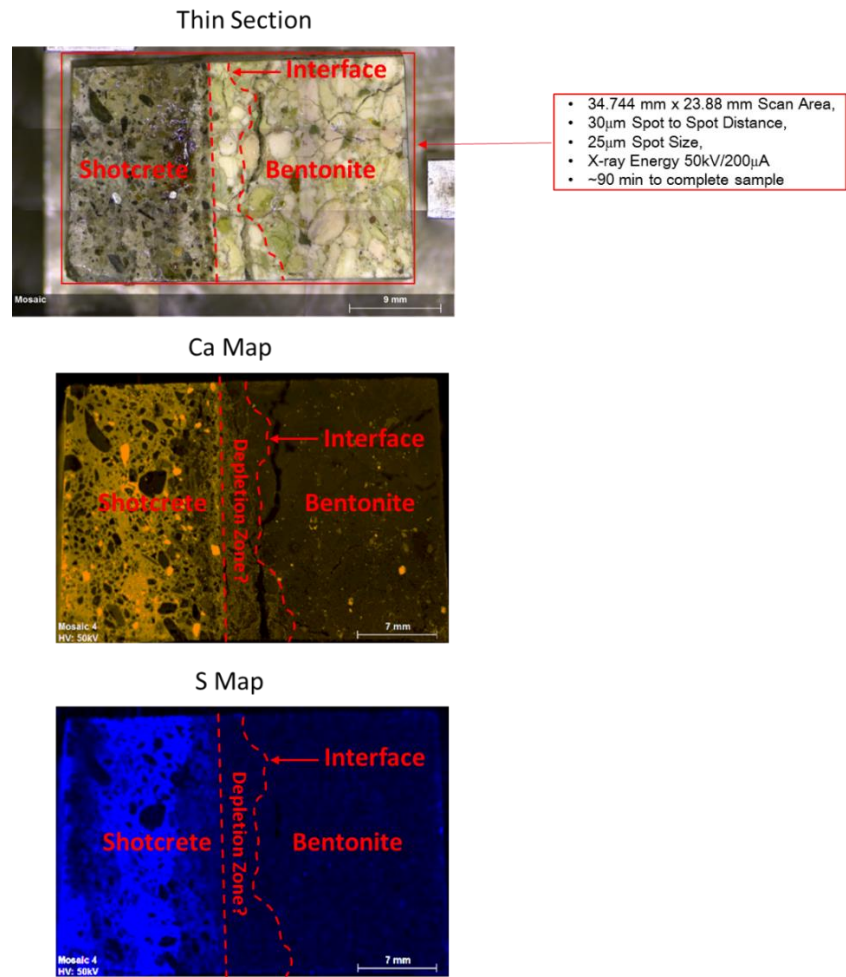
Figure 8. Micro-XRF maps for Ca and S at the shotcrete-bentonite interface. An apparent depletion zone close to the shotcrete-bentonite interface is delineated by red-dashed lines.
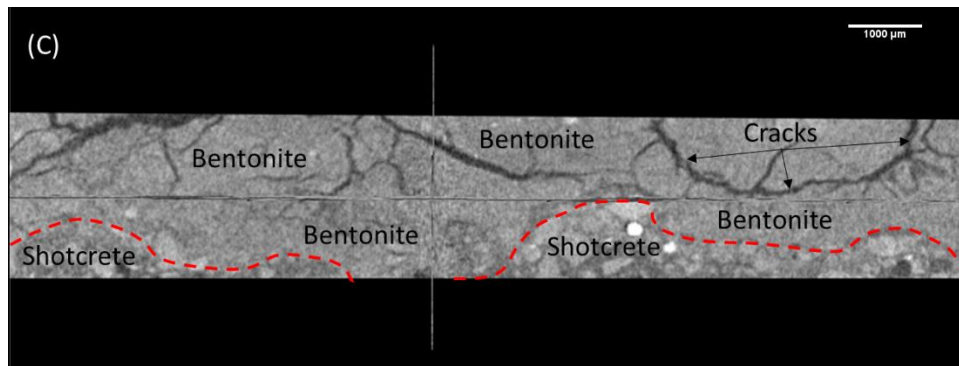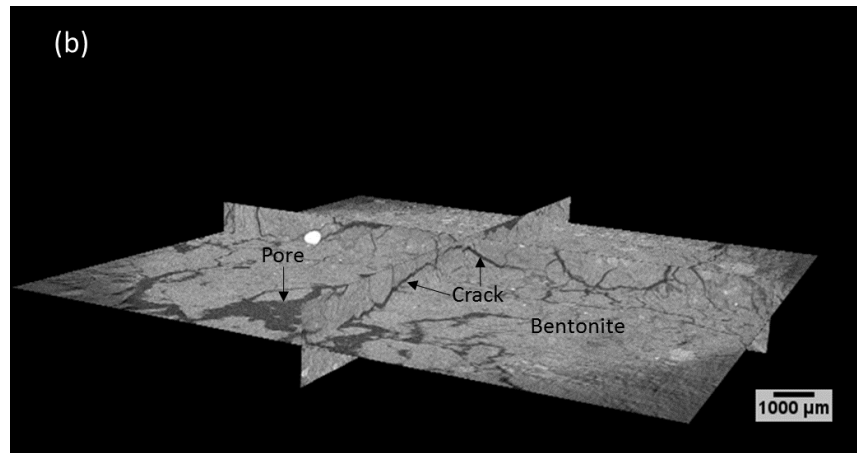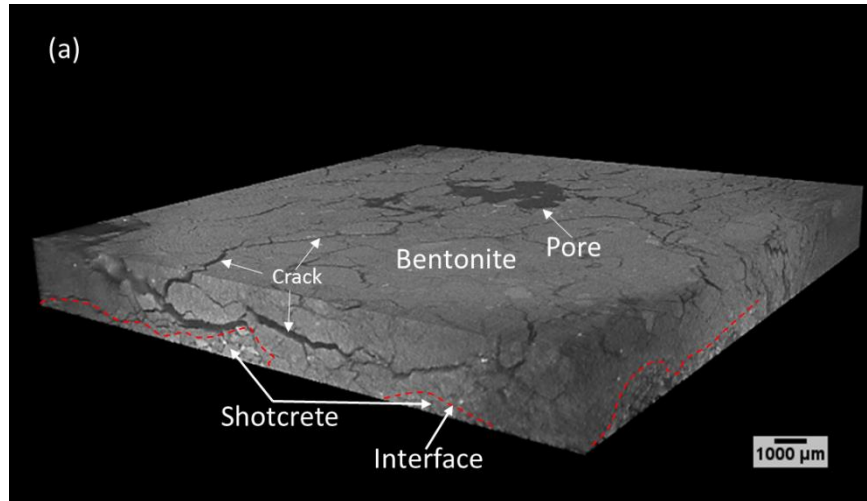
Figure 9. (a) 3D rendered volume of X-ray CT image data for sample C-C-32-6 at the shotcrete-bentonite interface (red dashed line) region. Notice the 3D crack network connectivity to other cracks and large pores in the bentonite region; (b) orthoslice projection of the volume in (a) with the horizontal plane near the shotcrete-bentonite interface; (c) 2D orthoslice (plan view) projection of the shotcrete-bentonite interface (red dashed line) showing its irregular nature. The length of the rectangular front face in (c) is ~1.3 cm.

3.   Canister Corrosion and Fe – Clay Interactions

The studies by Guillaume et al. (2004), Bildstein et al. (2006), Perronnet et al. (2008), Schlegel et al. (2008), Mosser-Ruck et al. (2010), Jodin-Caumon et al. (2012), Bourdelle et al. (2014), Pignatelli et al. (2014), Cheshire et al. (2014, 2016), Le Pape et al. (2015), Ngo et al. (2015), Rivard et al. (2015), Villa-Alfageme et al. (2015), Wilson et al. (2015), and Wersin et al. (2015) among others have provided key information on Fe-clay interactions based on corrosion experiments, geochemical modeling, and the effects of Fe on clay mineralogical changes and stability. These studies have identified alteration phases from metallic Fe – clay interactions leading to the formation of smectitic Fe-bearing silicates (e.g., berthierine, chamosite, Fe-saponite, vermiculite) whose stability is dictated by solution chemistry (e.g., aqueous silica activity), co-exisiting mineralogy, redox chemistry, and temperature conditions. As described in Section 2.1, future work will look at details on the alteration mineral assemblage as to advance an adequate set of reaction products that include Fe oxy-hydroxides and Fe-bearing Al-silicates (e.g., Fe-clays). However, lack of thermodynamic data at elevated temperatures may be an obstacle for this assessment The hydrothermal experiments conducted by Cheshire et al. (2016, *in preparation*) on clay/stainless-steel interactions described the formation of Fe-saponite (see Part III) and a chromite ($FeCr_2O_4$) passivation layer. Minor formation of pentlandite (($Ni,Fe)_9S_8$) and millerite (NiS)) was also part of the alteration assemblage. The presence of these S-bearing phases indicates the strong effect of the sulfide component in determining alteration phases, redox chemistry, and potentially on corrosion mechanisms. The use of activity phases relations has elucidated the sensitivities of Fe aqueous activities on the clay stability and temperature given the common presence of this component in clay chemistries (Jové Colón et al., 2015). Even with thermodynamic data limitations for clays at elevated temperature, our objective is to at least evaluate key stability relations consistent with observations between alteration mineralogy that include clays and zeolites. Guided by the aforementioned studies and the availability of bentonite clay samples (FEBEX-DP; Jové Colón, 2016) closely interacting with steel at elevated temperatures (100°C) provide the basis for clay mineral characterization of Fe-bearing phases and corrosion products.

Jové Colón (2016) reported a preliminary study on bentonite samples obtained from the FEBEX-DP International collaboration activity that were in contact with the corroded low carbon steel mesh liner. BSEI/EDS analyses were conducted samples from Section 49 (samples BM-D-49-1,2,3) close to the steel mesh surrounding the heater. These samples were in contact with the corroded carbon steel mesh as indicated by the rusty-colored circular rind on bentonite (Figures 10 a,b). EDS elemental analyses of bentonite sampled from this rind area show mainly clay with variable K content and a few grains with relatively enriched regions in Fe and K (Figures 10 c-e). Although there seems to be some correlation between K and Fe based on X-ray maps (Figures 10 c,d), these results are still preliminary and more analyses are needed to further evaluate such correlation or whether these are Fe-rich coatings or just Fe-bearing clay. Other correlations to be investigated are Si and Fe for comparison against analyses of naturally-occuring Fe-bearing illites and glauconitic clays. Overall, EDS spot analyses of these samples indicate levels of K at detectable levels whereas Fe tends to be more localized on certain regions. Phase identification using XRD on these rusty-colored samples is planned for FY17.
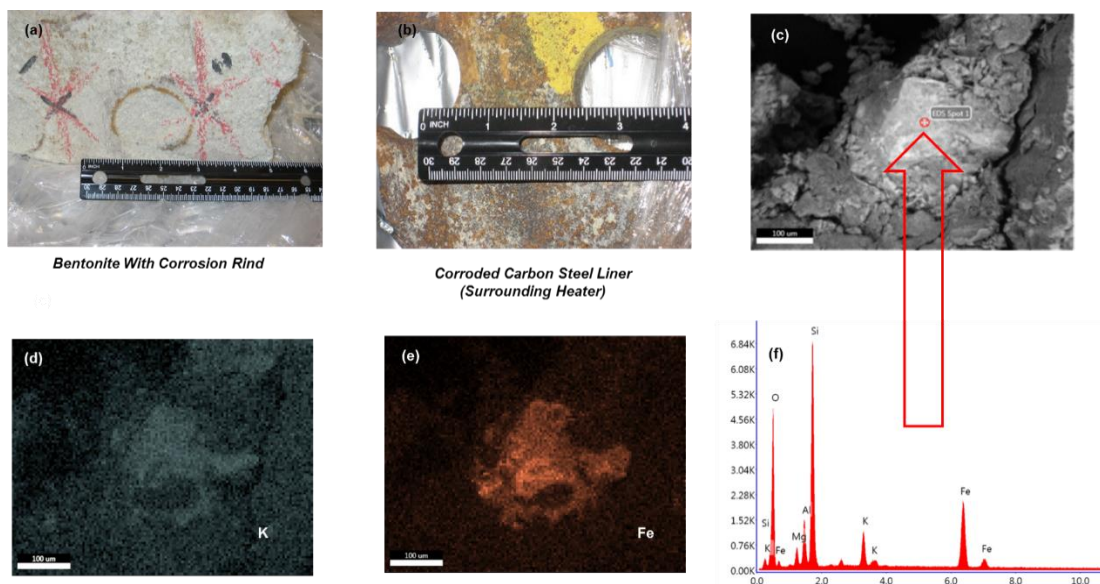
Figure 10. Sample set BM-D-49-(1,2,3) in close contact with perforated steel mesh liner surrounding heater assembly – see Fig. 8 for sample location; (a) rusty-colored corrosion rind delineating the region in contact with steel perforation; (b) corroded carbon steel mesh liner with perforations; (c) BSEI micrograph of bentonite grain sampled from corrosion rind; (d) and (e) EDS X-ray map for K and Fe, respectively, of region shown in (c); (f) EDS spectrum of spot analysis on grain denoted by the red dot-cross symbol in (c), also marked by red arrow symbol (Jové Colón, 2016).

The above observations plus previous work suggests that the Fe-bearing mineral assemblage can be complex and their characterization is difficult. The presence of these alteration zones is key to canister steel corrosion and could serve as potential getters of actinides. Also, the type and extent of these Fe-bearing secondary phases can be complex according to thermal and saturation state of bentonite barrier as reported in the characterization studies by FEBEX-DP partners. It is envisioned that a reactive-tranport process model capturing thermal and hydrological features of the near-field could provide the foundation to represent key EBS interactions and provide feeds to GDSA-PA (Figure 11). Capturing such feedbacks and providing "updates" to solution chemistry as a result of EBS interactions would allow for more realism in the source term.
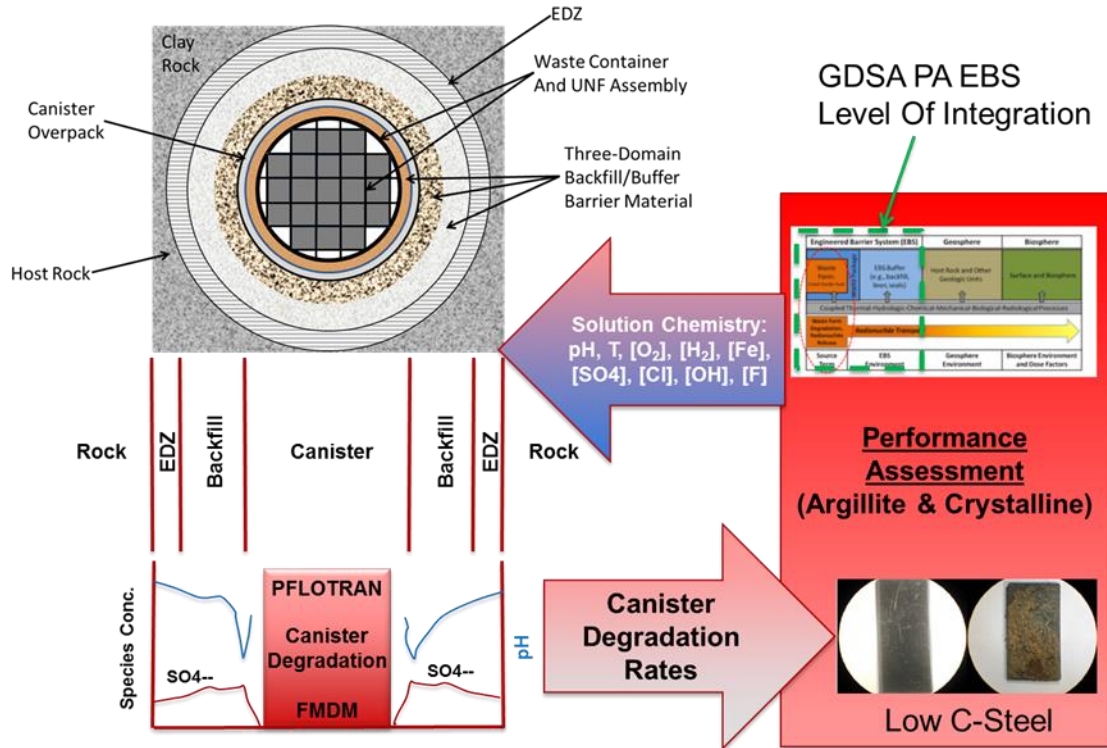
Figure 11. Idealized GDSA-PA integration scheme coupling EBS interactions including bentonite buffer, waste canister, and host rock.

4.   Concluding Remarks

The 1D reactive-transport model developed in PFLOTRAN has been expanded to evaluate non-isothermal scenarios such as the effects of a thermal pulse in a repository producing peak temperatures above 100°C along with thermal gradients affecting chemical interactions at the EBS and NS interfaces. Some key observations on the geochemical behavior of barrier materials in the presence of a heat pulse are:

- The thermally-driven phase transformation reaction gypsum $\rightarrow$ anhydrite (hydration/dehydration), in addition to dissolution/precipitation reactions, is captured by the reactive-transport model even with a fast temperature increase during the thermal pulse. Such a phase transformation can generate volume differences of ~60% that could translate into significant porosity changes (enhancement/reduction) in the EBS bulk regions and at interfaces.

- As exemplified by the $Ca-SO_4-H_2O$ system, pore solution chemistry and temperature are key factors in determining the formation of alteration mineral assemblage. For example, FEBEX pore waters richer in SO_4^{--} lead to precipitation of Ca-sulfate phases. This could have implications to cement product phases such as ettringite during the thermal pulse.

- Stable non-isothermal PFLOTRAN simulations are currently limited to a peak temperature of ~125°C. This limitation will be investigated further in FY17 since higher temperatures at the canister surface need to be investigated.

- Product cement phases such as ettringite had an effect on the stability of the reactive-tranport part of the simulation, particularly at high temperatures. Ettringite formation is consistent with $CaSO_4$ phase reaction in the presence of Ca and Al as described in the cement literature.

- Preliminary observations of metallic Fe interactions with bentonite in FEBEX-DP samples in contact with the heater surface appears to produce unidentified Al-silicates with detectable amounts of K and Fe. The extent of this alteration seems rather limited but interesting thus furthering the need to expand this characterization work.

The application of scanning characterization techniques such as micro-XRF and SEM/EDS/BSEI to the compositional characterization of the shotcrete – bentonite interface suggests that much of the reaction appears to be confined to the shotcrete phase and little or no alteration was experienced by the bentonite. This has implications to processes such as secondary mineralization and pore clogging in the bulk or at interfaces. Such processes are considered in reactive-transport models in the assessment of barrier performance for interactions with cementitious materials. Micro C-ray CT also provides key information on the distribution and morphology of microcracks in bentonite formed as result of shrinkage. Such micro-structures could influence clay barrier performance on processes like moisture transport, clay swelling, and permeability/porosity properties of the barrier.

Figure 11 shows a slightly updated version of the chronological evolution of thermal-chemical (TC) processes relevant to barrier performance in a clay/shale/argillite repository. The only update from the version in Jové Colón et al. (2015) is the addition of hydration/dehydration diagenetic reactions (e.g., gypsum → anhydrite phase transformation; clay/zeolite dehydration) that can influence H_2O during the heating period (dryout) and porosity changes. Hydrological and mechanical processes are omitted for simplicity. The temporal extents of the chemical processes outlined in this figure are roughly based on their expected predominance from the thermal pulse and beyond. The timing is also highly uncertain since it can be specific to mineral types, their relative abundances, thermal regimes, and solution chemistries. However, it still provides a reasonable picture of key chemical processes affecting the EBS.

4.1   Proposed Research Outlook for FY17

Extension of the current work within the clay/shale/argillite work package is planned but also towards integration with the GDSA PA work package. The 1D non-isothermal reactive transport model is used to elucidate thermal and chemical aspects influencing repository design on the basis of EBS interactions, radionuclide transport, and thermal-hydrological (TH) processes.

1D reactive-transport modeling at the scale of the EBS using PFLOTRAN is a powerful tool to evaluate the effects of diffusive reaction fronts at EBS interfaces. This work should be extended to examine the following:

- Integration with GDSA-PA: Evaluate needs for the coupling of chemical processes during and beyond the heat pulse period, and how it affects the EBS (e.g., waste canister degradation).
- Development of a waste canister degradation model gauged by observations from metal-clay interaction experiments and URL heater test samples (FEBEX-DP).
- Expand non-isothermal PFLOTRAN simulations to temperatures above 125°C. Some repository design concepts considered heat loads that will generate temperatures of up to and above 200°C.
- Expand kinetic (e.g., activation energies) and transport parameter representation for reactive-transport analyses at elevated temperatures; characteristic of the heat pulse period.
- Porosity reduction / clogging and reaction zones: Utilize observations from characterization studies of international collaboration activities such as FEBEX-DP to constrain modeling of EBS interactions.
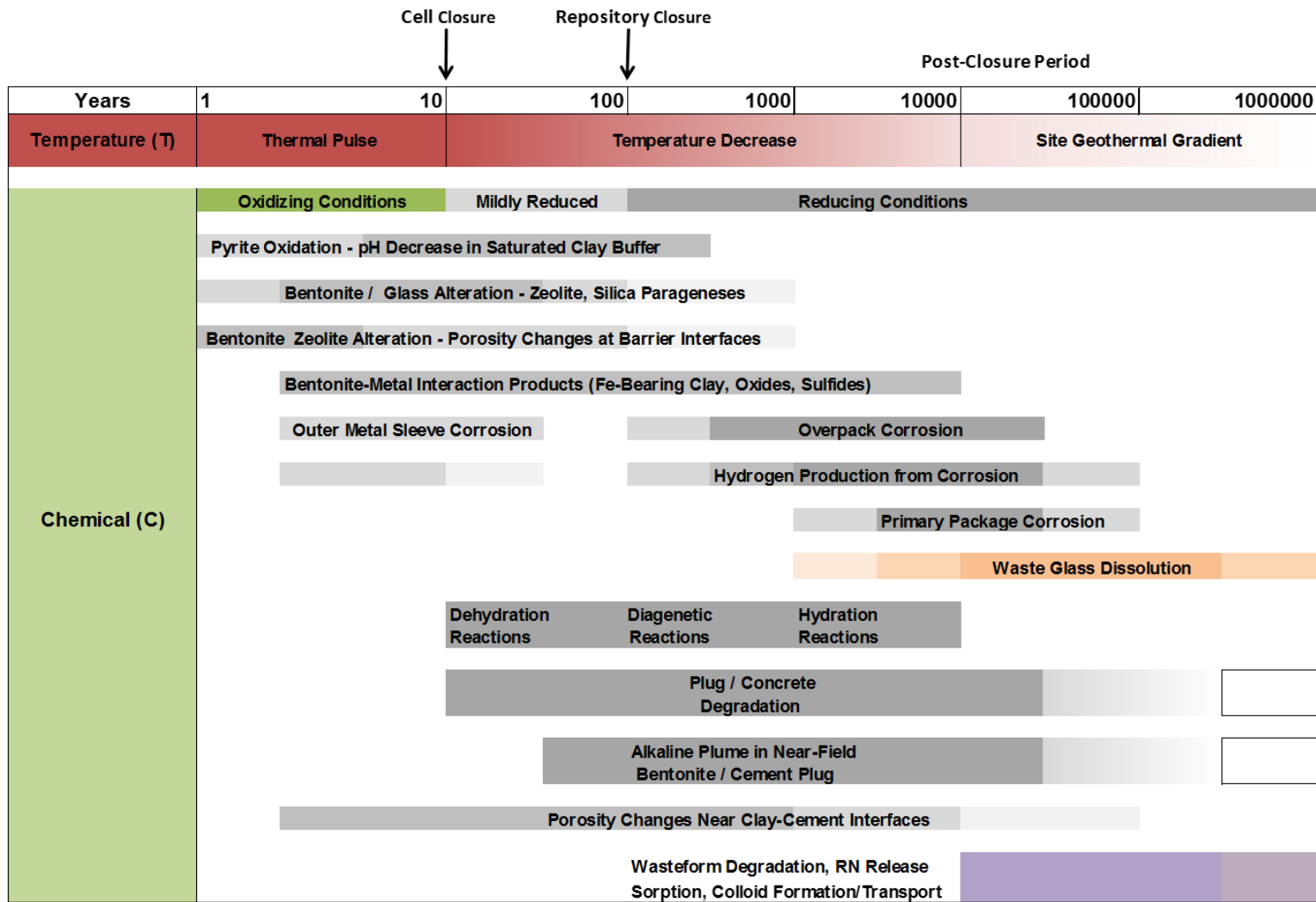
Figure 11. Chronological evolution of Thermal-Chemical processes in a shale/argillite repository (modified after Jové Colón et al., 2014). Hydrological and mechanical processes are not shown for simplicity.

5. References

Amram, K., and Ganor, J., 2005, The combined effect of pH and temperature on smectite dissolution rate under acidic conditions: Geochimica et Cosmochimica Acta, v. 69, no. 10, p. 2535-2546.

Baur, I., Keller, P., Mavrocordatos, D., Wehrli, B., and Johnson, C. A., 2004, Dissolution-precipitation behaviour of ettringite, monosulfate, and calcium silicate hydrate: Cement and Concrete Research, v. 34, no. 2, p. 341-348.

Berner, U., Kulik, D. A., and Kosakowski, G., 2013, Geochemical impact of a low-pH cement liner on the near field of a repository for spent fuel and high-level radioactive waste: Physics and Chemistry of the Earth, Parts A/B/C, v. 64, no. 0, p. 46-56.

Bianchi, M., H.-H., Liu, and J. T. Birkholzer. (2013). Diffusion Modeling in a Clay Repository: FY13 Report. . FCRD-UFD-2013-000228 Report, Lawrence Berkeley National Laboratory, Berkeley, USA.

Bianchi, M., H.-H., Liu, and J. T. Birkholzer. (2014). Radionuclide Transport Behavior in a Generic Geological Radioactive Waste Repository. Groundwater. doi: 10.1111/gwat.12171.

Bildstein, O., L. Trotignon, M. Perronnet, and M. Jullien, 2006, Modelling iron–clay interactions in deep geological disposal conditions. Physics and Chemistry of the Earth, Parts A/B/C, 31(10): p. 618-625.

Blanc, P., Lassin, A., Piantone, P., Azaroual, M., Jacquemet, N., Fabbri, A., and Gaucher, A., 2012, Thermoddem: A geochemical database focused on low temperature water/rock interactions and waste materials: Applied Geochemistry, v. 27, p. 2107-2116.

Blanc, P., Piantone, P., Lassin, A., and Burnol, A., 2006, Thermochimie : Sélection de constantes thermodynamiques pour les éléments majeurs, le plomb et le cadmium, Rapport final BRGM/RP-54902-FR: France, BRGM, p. 157.

Boudreau, B. P., 1996, The diffusive tortuosity of fine-grained unlithified sediments: Geochimica et Cosmochimica Acta, v. 60, no. 16, p. 3139-3142.

Bourdelle, F., L. Truche, I. Pignatelli, R. Mosser-Ruck, C. Lorgeoux, C. Roszypal, and N. Michau, 2014, Iron–clay interactions under hydrothermal conditions: Impact of specific surface area of metallic iron on reaction pathway. Chemical Geology, 381: p. 194-205.

Cheshire, M., Caporuscio, F. A., Rearick, M. S., Jové Colón, C. F., and McCarney, M. K., 2014, Bentonite evolution at elevated pressures and temperatures: An experimental study for generic nuclear repository designs: American Mineralogist, v. 99, p. 1662-1675.

Cheshire, M., F.A. Caporuscio, C.F. Jové Colón, and M.K. McCarney, 2016, Fe-saponite growth on low-carbon and stainless steel in hydrothermal-bentonite experiments. *in preparation*.

Jodin-Caumon, M.-C., R. Mosser-Ruck, A. Randi, O. Pierron, M. Cathelineau, and N. Michau, 2012, Mineralogical evolution of a claystone after reaction with iron under thermal gradient. Clays and Clay Minerals, 60(5): p. 443-455.

Dauzeres, A., Le Bescop, P., Sardini, P., and Coumes, C. C. D., 2010, Physico-chemical investigation of clayey/cement-based materials interaction in the context of geological

waste disposal: Experimental approach and results: Cement and Concrete Research, v. 40, no. 8, p. 1327-1340.

Dick, J. M., 2008, Calculation of the relative metastabilities of proteins using the CHNOSZ software package: Geochemical Transactions, v. 9, no. 10.

Fernandez, A.M., J. Cuevas, and P. Rivas, 2001, Pore water chemistry of the Febex bentonite. Scientific Basis for Nuclear Waste Management XXIV, 663: p. 573-588.

Fernandez, A.M., B. Baeyens, M. Bradbury, and P. Rivas, 2004, Analysis of the porewater chemical composition of a Spanish compacted bentonite used in an engineered barrier. Physics and Chemistry of the Earth, 29(1): p. 105-118.

Gaboreau, S., Lerouge, C., Dewonck, S., Linard, Y., Bourbon, X., Fialips, C. I., Mazurier, A., Pret, D., Borschneck, D., Montouillout, V., Gaucher, E. C., and Claret, F., 2012, In-Situ Interaction of Cement Paste and Shotcrete with Claystones in a Deep Disposal Context: American Journal of Science, v. 312, no. 3, p. 314-356.

Giles, D. E., Ritchie, I. M., and Xu, B. A., 1993, The Kinetics of Dissolution of Slaked Lime: Hydrometallurgy, v. 32, no. 1, p. 119-128.

Golubev, S. V., Bauer, A., and Pokrovsky, O. S., 2006, Effect of pH and organic ligands on the kinetics of smectite dissolution at 25 degrees C: Geochimica Et Cosmochimica Acta, v. 70, no. 17, p. 4436-4451.

Golubev, S. V., Benezeth, P., Schott, J., Dandurand, J. L., and Castillo, A., 2009, Siderite dissolution kinetics in acidic aqueous solutions from 25 to 100 degrees C and 0 to 50 atm pCO_2, Chemical Geology, v. 265, no. 1-2, p. 13-19.

Gonzales, S. and K.S. Johnson, (1984). Shale and other argillaceous strata in the United States. Oak Ridge National Laboratory. ORNL/Sub/84-64794/1.

González Sánchez, F., Van Loon, L. R., Gimmi, T., Jakob, A., Glaus, M. A., and Diamond, L. W., 2008, Self-diffusion of water and its dependence on temperature and ionic strength in highly compacted montmorillonite, illite and kaolinite: Applied Geochemistry, v. 23, no. 12, p. 3840-3851.

Guillaume, D., A. Neaman, M. Cathelineau, R. Mosser-Ruck, C. Peiffert, M. Abdelmoula, J. Dubessy, F. Villieras, and N. Michau, 2004, Experimental study of the transformation of smectite at 80 and 300 degrees C in the presence of Fe oxides. Clay Minerals, 39(1): p. 17-34.

Hansen, F.D., E.L. Hardin, R. P. Rechard, G. A. Freeze, D.C. Sassani, P.V. Brady, C. M. Stone, M. J. Martinez, J. F. Holland, T. Dewers, K.N. Gaither, S. R. Sobolik, and R. T. Cygan, 2010, Shale Disposal of U.S. High-Level Radioactive Waste. SAND2010-2843. Albuquerque, NM: Sandia National Laboratories.

Hardin, E., T. Hadgu, D. Clayton, R. Howard, H. Greenberg, J. Blink, M. Sharma, M. Sutton, J. Carter, M. Dupont, and P. Rodwell, 2012, Repository Reference Disposal Concepts and Thermal Load Management Analysis. FCRD-UFD-2012-000219 Rev. 2. U.S. Department of Energy, Office of Used Nuclear Fuel Disposition, Washington, DC.

Holland, T. J. B., and Powell, R., 2011, An improved and extended internally consistent thermodynamic dataset for phases of petrological interest, involving a new equation of state for solids: Journal of Metamorphic Geology, v. 29, p. 333-383.

Huertas, F. J., Caballero, E., de Cisneros, C. J., Huertas, F., and Linares, J., 2001, Kinetics of montmorillonite dissolution in granitic solutions: Applied Geochemistry, v. 16, no. 4, p. 397-407.

Jeschke, A. A., Vosbeck, K., and Dreybrodt, W., 2001, Surface controlled dissolution rates of gypsum in aqueous solutions exhibit nonlinear dissolution kinetics: Geochimica Et Cosmochimica Acta, v. 65, no. 1, p. 27-34.

Joseph, C., Schmeide, K., Sachs, S., Brendler, V., Geipel, G., and Bernhard, G., 2011, Sorption of uranium(VI) onto Opalinus Clay in the absence and presence of humic acid in Opalinus Clay pore water: Chemical Geology, v. 284, no. 3–4, p. 240-250.

Joseph, C., Van Loon, L. R., Jakob, A., Steudtner, R., Schmeide, K., Sachs, S., and Bernhard, G., 2013, Diffusion of U(VI) in Opalinus Clay: Influence of temperature and humic acid: Geochim. Cosmochim. Acta, v. 109, p. 74-89.

Jové Colón, C.F., International Collaboration Activities on Engineered Barrier Systems (FCRD-UFD-2016-000628), 2016, Sandia National Laboratories: Albuquerque, NM, SAND2016-8935 R. p. 26.

Jové Colón, C.F., P.F. Weck, G.E. Hammond, K. Kuhlman, L. Zheng, J. Rutqvist, K. Kim, J. Houseworth, F.A. Caporuscio, M. Cheshire, S. Palaich, N. K., M. Zavarin, T.J. Wolery, J.L. Jerden, J.M. Copple, T. Cruse, and W.L. Ebert, Evaluation of Used Fuel Disposition in Clay-Bearing Rock (Vols. I & II) (FCRD-UFD-2015-000124), 2015: Albuquerque, NM, SAND2015-7827 R. p. 318.

Jové Colón, C. F., Greathouse, J. A., Teich-McGoldrick, S., Cygan, R. T., Weck, P. F., Hansen, G. A., Criscenti, L. J., Caporuscio, F. A., Cheshire, M., Rearick, M. S., McCarney, M. K., Greenberg, H. R., Wolery, T. J., Sutton, M., Zavarin, M., Kersting, A. B., Begg, J. B., Blink, J. A., Buscheck, T., Benedicto-Cordoba, A., Zhao, P., Rutqvist, J., Steefel, C. I., Birkholzer, J., Liu, H.-H., Davis, J. A., Tinnacher, R., Bourg, I., Zheng, L., and Vilarrasa, V., 2013, EBS Model Development and Evaluation Report (FCRD-UFD-2013-000312): Albuquerque, NM, Sandia National Laboratories, SAND2013-8512 P, p. 508.

Jové Colón, C. F., Weck, P. F., Sassani, D. C., Zheng, L., Rutqvist, J., Steefel, C. I., Kim, K., Nakagawa, S., Houseworth, J., Birkholzer, J., Caporuscio, F. A., Cheshire, M., Rearick, M. S., McCarney, M. K., Zavarin, M., Benedicto-Cordoba, A., Kersting, A. B., Sutton, M., Jerden, J. L., Frey, K. E., Copple, J. M., and Ebert, W. L., 2014, Evaluation of Used Fuel Disposition in Clay-Bearing Rock (FCRD-UFD-2014-000056): Albuquerque, NM, Sandia National Laboratories, SAND2014-18303 R, p. 434.

Kohler, S. J., Dufaud, F., and Oelkers, E. H., 2003, An experimental study of illite dissolution kinetics as a function of pH from 1.4 to 12.4 and temperature from 5 to 50 degrees C: Geochimica Et Cosmochimica Acta, v. 67, no. 19, p. 3583-3594.

Kosakowski, G., and Berner, U., 2013, The evolution of clay rock/cement interfaces in a cementitious repository for low- and intermediate level radioactive waste: Physics and Chemistry of the Earth, v. 64, p. 65-86.

Kozai, N., Inada, K., Kozaki, T., Sato, S., Ohashi, H., and Banba, T., 2001, Apparent diffusion coefficients and chemical species of neptunium (V) in compacted Na-montmorillonite: Journal of Contaminant Hydrology, v. 47, no. 2–4, p. 149-158.

Kozaki, T., Inada, K., Sato, S., and Ohashi, H., 2001, Diffusion mechanism of chloride ions in sodium montmorillonite: Journal of Contaminant Hydrology, v. 47, no. 2–4, p. 159-170.

Le Pape, P., C. Rivard, M. Pelletier, I. Bihannic, R. Gley, S. Mathieu, L. Salsi, S. Migot, O. Barres, and F. Villiéras, 2015, Action of a clay suspension on an Fe (0) surface under anoxic conditions: Characterization of neoformed minerals at the Fe (0)/solution and Fe (0)/atmosphere interfaces. Applied Geochemistry, 61: p. 62-71.

Lichtner, P. C., Hammond, G. E., Lu, C., Karra, S., Bisht, G., Andre, B., Mills, R. T., and Kumar, J., 2013, PFLOTRAN User Manual: http://www.pflotran.org.

Mariner, P.E., W.P. Gardner, G.E. Hammond, D. Sevougian, and E. Stein, Application of Generic Disposal System Models (FCRD-UFD-2015-000126), 2015, Sandia National Laboratories: Albuquerque, NM.

Marty, N. C., Bildstein, O., Blanc, P., Claret, F., Cochepin, B., Gaucher, E. C., Jacques, D., Lartigue, J.-E., Liu, S., and Mayer, K. U., 2015, Benchmarks for multicomponent reactive transport across a cement/clay interface: Computational Geosciences, p. 1-19.

Marty, N. C. M., Fritz, B., Clement, A., and Michau, N., 2010, Modelling the long term alteration of the engineered bentonite barrier in an underground radioactive waste repository: Applied Clay Science, v. 47, no. 1-2, p. 82-90.

Marty, N. C. M., Tournassat, C., Burnol, A., Giffaut, E., and Gaucher, E. C., 2009, Influence of reaction kinetics and mesh refinement on the numerical modelling of concrete/clay interactions: Journal of Hydrology, v. 364, no. 1-2, p. 58-72.

Mazurek, M., F.J. Pearson, G. Volckaert, and H. Bock, Features, Events and Processes Evaluation Catalogue for Argillaceous Media, (2003). Organisation for Economic Co-operation and Development (OECD) - Nuclear Energy Agency (NEA): Paris, France. 379 pp.

Miller, H., 2004, Initial Radionuclide Inventories (ANL-WIS-MD-000020 REV 01): Las Vegas, Nevada, Bechtel SAIC Company, LLC, U.S. Department of Energy, Office of Civilian Radioactive Waste Management, Office of Repository Development, p. 178.

Montes-H, G., Marty, N., Fritz, B., Clement, A., and Michau, N., 2005, Modelling of long-term diffusion-reaction in a bentonite barrier for radioactive waste confinement: Applied Clay Science, v. 30, no. 3-4, p. 181-198.

Mosser-Ruck, R., M. Cathelineau, D. Guillaume, D. Charpentier, D. Rousset, O. Barres, and N. Michau, 2010, Effects of temperature, pH, and iron/clay and liquid/clay ratios on experimental conversion of dioctahedral smectite to berthierine, chlorite, vermiculite, or saponite. Clays and Clay Minerals, 58(2): p. 280-291.

NAGRA (2002) Project Opalinus Clay: safety report. Demonstration of disposal feasibility for spent fuel, vitrified high-level waste and long-lived intermediate level waste (Entsorgungsnachweis). Nagra Technical Report NTB 02-05, Wettingen, Switzerland.

Neuhoff, P. S., Hovis, G. L., Balassone, G., and Stebbins, J. F., 2004, Thermodynamic properties of analcime solid solutions: American Journal of Science, v. 304, no. 1, p. 21-66.

Neuhoff, P. S., and Ruhl, L. S., 2006, Mechanisms and geochemical significance of Si-Al substitution in zeolite solid solutions: Chemical Geology, v. 225, no. 3-4, p. 373-387.

Neuzil, C. (2013). Can Shale Safely Host US Nuclear Waste? Eos, Transactions American Geophysical Union 94(30): 261-262.

Perronnet, M., M. Jullien, F. Villiéras, J. Raynal, D. Bonnin, and G. Bruno, 2008, Evidence of a critical content in Fe (0) on FoCa7 bentonite reactivity at 80 °C. Applied Clay Science, 38(3): p. 187-202.

Pignatelli, I., F. Bourdelle, D. Bartier, R. Mosser-Ruck, L. Truche, E. Mugnaioli, and N. Michau, Iron–clay interactions: Detailed study of the mineralogical transformation of claystone with emphasis on the formation of iron-rich T–O phyllosilicates in a step-by-step cooling experiment from 90° C to 40° C, 2014, Chemical Geology, 387: p. 1-11.

Pokrovsky, O. S., Golubev, S. V., Schott, J., and Castillo, A., 2009, Calcite, dolomite and magnesite dissolution kinetics in aqueous solutions at acid to circumneutral pH, 25 to 150 degrees C and 1 to 55 atm pCO_2: New constraints on CO_2 sequestration in sedimentary basins: Chemical Geology, v. 265, no. 1-2, p. 20-32.

Pusch, R., Takase, H., and Benbow, S., 1998, Chemical processes causing cementation in heat-affected smectite-the Kinnekulle bentonite, Svensk Kärnbränslehantering.

Rimstidt, J. D., 1997, Quartz solubility at low temperatures: Geochimica Et Cosmochimica Acta, v. 61, no. 13, p. 2553-2558.

Rutqvist, J., L. Zheng, F. Chen, H.-H. Liu and J. Birkholzer, 2014a, Modeling of Coupled Thermo-Hydro-Mechanical Processes with Links to Geochemistry Associated with Bentonite-Backfilled Repository Tunnels in Clay Formations. Rock Mechanics and Rock Engineering 47(1): 167-186.

Sanchez, L., Cuevas, J., Ramirez, S., De Leon, D. R., Fernandez, R., Dela Villa, R. V., and Leguey, S., 2006, Reaction kinetics of FEBEX bentonite in hyperalkaline conditions resembling the cement-bentonite interface: Applied Clay Science, v. 33, no. 2, p. 125-141.

Savage, D., 2011, A review of analogues of alkaline alteration with regard to long-term barrier performance: Mineralogical Magazine, v. 75, no. 4, p. 2401-2418.

Shurr, G.W., 1977, The Pierre Shale, Northern Great Plains; A Potential Isolation Medium for Radioactive Waste. United States Geological Survey Open File Report 77-776.

Schlegel, M.L., C. Bataillon, K. Benhamida, C. Blanc, D. Menut, and J.-L. Lacour, Metal corrosion and argillite transformation at the water-saturated, high-temperature iron–clay interface: A microscopic-scale study, 2008, Applied Geochemistry, 23(9): p. 2619-2633.

SNL, 2014, Evaluation of Options for Permanent Geologic Disposal of Spent Nuclear Fuel and High-Level Radioactive Waste in Support of a Comprehensive National Nuclear Fuel Cycle Strategy (FCRD-UFD-2015-000125), Volume I: Albuquerque, NM, Sandia National Laboratories, p. 302.

Soler, J. M., 2012, High-pH plume from low-alkali-cement fracture grouting: Reactive transport modeling and comparison with pH monitoring at ONKALO (Finland): Applied Geochemistry, v. 27, no. 10, p. 2096-2106.

Soler, J. M., and Mader, U. K., 2010, Cement-rock interaction: Infiltration of a high-pH solution into a fractured granite core: Geologica Acta, v. 8, no. 3, p. 221-233.

Tagirov, B., and Schott, J., 2001, Aluminum speciation in crustal fluids revisited: Geochimica Et Cosmochimica Acta, v. 65, no. 21, p. 3965-3992.

Trotignon, L., Peycelon, H., and Bourbon, X., 2006, Comparison of performance of concrete barriers in a clayey geological medium: Physics and Chemistry of the Earth, v. 31, no. 10-14, p. 610-617.

Turrero, M., Fernández, A., Peña, J., Sánchez, M., Wersin, P., Bossart, P., Sánchez, M., Melón, A., Garralón, A., and Yllera, A., 2006, Pore water chemistry of a Paleogene continental mudrock in Spain and a Jurassic marine mudrock in Switzerland: Sampling methods and geochemical interpretation: Journal of Iberian Geology, v. 32, no. 2, p. 233-258.

Van Loon, L. R., Soler, J. M., and Bradbury, M. H., 2003, Diffusion of HTO, $^{36}Cl^-$ and $^{125}I^-$ in Opalinus Clay samples from Mont Terri: Effect of confining pressure: Journal of Contaminant Hydrology, v. 61, no. 1–4, p. 73-83.

Villa-Alfageme, M., S. Hurtado, S. El Mrabet, M.C. Pazos, M.A. Castro, and M.D. Alba, Uranium immobilization by FEBEX bentonite and steel barriers in hydrothermal conditions. Chemical Engineering Journal, 2015. 269: p. 279-287.

Wersin, P., Johnson, L. H., and McKinley, I. G., 2007, Performance of the bentonite barrier at temperatures beyond 100ºC: A critical review: Physics and Chemistry of the Earth, v. 32, no. 8-14, p. 780-788.

Wersin, P., A. Jenni, and U.K. Mäder, Interaction of Corroding Iron with Bentonite in the ABM1 Experiment at Äspö, Sweden: A Microscopic Approach, 2015, Clays and Clay Minerals, 2015. 63(1): p. 51-68.

White, A. F., Peterson, M. L., and Hochella, M. F., 1994, Electrochemistry and Dissolution Kinetics of Magnetite and Ilmenite: Geochimica Et Cosmochimica Acta, v. 58, no. 8, p. 1859-1875.

Williamson, M. A., and Rimstidt, J. D., 1994, The Kinetics and Electrochemical Rate-Determining Step of Aqueous Pyrite Oxidation: Geochimica Et Cosmochimica Acta, v. 58, no. 24, p. 5443-5454.

Wilson, J. C., Benbow, S., Sasamoto, H., Savage, D., and Watson, C., 2015, Thermodynamic and fully-coupled reactive transport models of a steel-bentonite interface: Applied Geochemistry.

Wolery, T. J., and Jarek, R. L., 2003, EQ3/6, Version 8.0: Software User's Manual: Sandia National Laboratories.

Xie, M. L., Mayer, K. U., Claret, F., Alt-Epping, P., Jacques, D., Steefel, C., Chiaberge, C., and Simunek, J., 2015, Implementation and evaluation of permeability-porosity and tortuosity-porosity relationships linked to mineral dissolution-precipitation: Computational Geosciences, v. 19, no. 3, p. 655-671.

Zheng, L., James Houseworth, Carl Steefel, Jonny Rutqvist, Jens Birkholzer (2014), Investigation of Coupled Processes and Impact of High Temperature Limits in Argillite Rock. FCRD-UFD-2014-000493, U.S. Department of Energy, Washington DC.

Argillite Disposal R&D at LBNL (Part II)

1. Introduction

Shale and clay-rich geological formations have been considered as potential host rock for geological disposal of high-level radioactive waste throughout the world because of their low permeability, low diffusion coefficient, high retention capacity for radionuclides, and capability to self-seal fractures. The low permeability of clay and shale rock are well-known in the hydrogeology community where these rock types represent aquitards that severely limit groundwater movement, and in petroleum geology, where they act as caprocks limiting the rise of buoyant petroleum fluids. While fractures can occur, clay and shale often demonstrate the tendency to self-seal fractures, which reduces the effects of fractures on bulk permeability. Other favorable characteristics of clay/shale rock are the strong sorptive behavior for many radionuclides, reducing conditions because of the lack of oxygen transport from the surface, and chemical buffering of introduced materials.

Engineered barrier system (EBS) with bentonite backfilled is also a critical component in most repository concepts. A large body of information concerning the behavior of clay/shale geologic environments using bentonite backfill/buffers for nuclear waste disposal has been developed through the repository programs with underground research laboratories in Switzerland, France, Belgium, and Japan. In this report we document modeling of tests conducted at Mont Terri underground rock laboratory and Grimsel underground rock laboratory in Switzerland, and the Horonobe underground research laboratory in Japan.

The focus of research within the Used Fuel Disposal (UFD) Campaign is on repository-induced interactions that may affect the key safety characteristics of EBS bentonite and an argillaceous rock. These include thermal-hydrological-mechanical-chemical (THMC) process interactions that occur as a result of repository construction and waste emplacement. Some of the key questions addressed in this report include the development of fracturing in the excavation damaged zone (EDZ) and THMC effects on the near-field argillaceous rock and buffer materials and petrophysical characteristics, particularly the impacts of induced temperature rise caused by waste heat.

Within the Used Fuel Disposition (UFD) Campaign at the Department of Energy's (DOE) Office of Nuclear Energy, LBNL's research activities have focused on understanding and modeling EDZ evolution and the associated coupled processes and impacts of high temperature on parameters and processes relevant to performance of a clay repository to establish the technical base for the maximum allowable temperature. This report documents results from some of these activities. These activities address key Features, Events, and Processes (FEPs), which have been ranked in importance from medium to high, as listed in Table 7 of the Used Fuel Disposition Campaign Disposal Research and Development Roadmap (FCR&D-USED-2011-000065 REV0) (Nutt, 2011). Specifically, they address FEP 2.2.01, Excavation Disturbed Zone, for clay/shale, by investigating how coupled processes affect EDZ evolution; FEP 2.2.05, Flow and Transport Pathways; and FEP 2.2.08, Hydrologic Processes, and FEP 2.2.07, Mechanical Processes, and FEP 2.2.09, Chemical Process—Transport, by studying near-field coupled THMC processes in clay/shale repositories. The activities documented in this report also address a number of research topics identified in Research & Development (R&D) Plan for Used Fuel Disposition Campaign (UFDC) Natural System Evaluation and Tool Development (Wang 2011), including Topics S3, Disposal system modeling – Natural System; P1, Development of discrete fracture network (DFN) model; P14, Technical basis for thermal loading limits; and P15 Modeling of disturbed rock zone (DRZ) evolution (clay repository).

This report documents the following research activities:

- Section 2 presents THM modeling of underground heater experiments in clay formations, including studies related to the <u>D</u>evelopment of <u>C</u>oupled Models and their <u>Val</u>idation against <u>Ex</u>periments (DECOVALEX)-2015 project and the Mont Terri FE (Full-scale Emplacement) Experiment. The FE Experiment is undertaken as an ultimate test for the performance of geologic disposal in Opalinus Clay; it will be one of the largest and longest running heater tests worldwide. Coupled THM model for FE test was developed using TOUGH-FLAC, which provides a unique opportunity to validate and test the models at realistic, large-scale, in-situ conditions, including the interactions between the host rock and EBS.

- Section 3 presents the development and application of thermal-hydrological-mechanical-chemical (THMC) modeling to evaluate bentonite EBS and clay rock NS responses under higher temperatures (200 °C). Model results are presented to help to understand the impact of high temperatures on the properties and behavior of bentonite and clay rock.

- Section 4 presents coupled THMC modeling for an *in situ* test conducted at Grimsel underground laboratory in Switzerland in the FEBEX-DP project. The data collected in the test after almost two decades of heating and two dismantling events provide a unique opportunity of validating coupled THMC models and enhancing our understanding of coupled THMC process in EBS bentonite.

- Section 5 presents development, testing, and applications of a discrete fracture network (DFN) approach for modeling THM induced damage and fracturing in argillaceous rocks. The modeling work was conducted using TOUGH-RBSN, a simulation code combines TOUGH2 with the rigid-body-spring network (RBSN) model. The code is validated against the laboratory experiments for hydraulic fracture propagation in rock-analogue samples and used to model anisotropic failure characteristics of a uniaxial compression tests and a tunnel excavation process in the presence of discrete faults. In addition, the ongoing work on the dynamic simulation code development is presented.

- Section 6 summarizes the main research accomplishments for FY, 2016 and proposes future work activities.

2. THM Modeling: FE Heater Test and DECOVALEX

In this section, we present LBNL's activities related to THM modeling of underground heater experiments in clay formations, including studies related to the Development of Coupled Models and their Validation against Experiments (DECOVALEX)-2015 project and the Mont Terri FE (Full-scale Emplacement) Experiment. DECOVALEX-2015 is an acronym for the sixth phase of the "Development of Coupled Models and their Validation against Experiments" project, from 2012 through 2015. Thus, the DECOVALEX-2015 was completed in December 2015, although some reporting was done during the spring of 2016 and some joint journal papers are still being prepared summarizing the results. In DECOVALEX-2015, LBNL participated in a modeling task denoted Task B, which included:

Subtask B1—Mont Terri HE-E Experiment: A heating experiment to evaluate sealing and clay-barrier performance, in a micro-tunnel at the Mont Terri URL in Switzerland; and,

Subtask B2—Horonobe Engineered Barrier System (EBS) Experiment: A heating experiment to study the thermo-hydro-mechanical-chemical (THMC) behavior of the EBS and its interaction with the mudstone host rock, in a vertical emplacement hole at the Horonobe URL in Japan.

In addition to the modeling work in these two DECOVALEX tasks, LBNL participates in the Mont Terri FE Experiment as one of the participating modeling teams. The FE Experiment is undertaken as an ultimate test for the performance of geologic disposal in Opalinus Clay, focusing on both the EBS components and the host-rock behavior; it will be one of the largest and longest running heater tests worldwide.

UFD objectives for participating in these international activities are to develop expertise and test advanced models of coupled processes in clay-based backfill in interaction with clay host rock. Through participation in modeling these field experiments, the models will be developed and experience will be gained for a range of different backfill materials (e.g., bentonite pellets and sand/bentonite mixture), as well as different host rocks (e.g., Opalinus clay and mudstone). The main software developed and used for these simulations is the numerical simulator TOUGH-FLAC (Rutqvist et al. 2002; 2011; 2014b). For nuclear waste isolation, TOUGH-FLAC provides UFD with a model framework for modeling coupled THM processes in the EBS and host rock and their interactions using state-of-the-art macroscopic constitutive models for bentonite, crushed rock salt backfill, clay, salt and crystalline host rocks. For rigorous modeling of the THM behavior of bentonite-based (swelling) buffer and back-fill materials, the BBM (Barcelona Basic Model) and BExM (Barcelona Expansive Model) have been implemented into TOUGH-FLAC (Rutqvist et al., 2011; 2014b; Vilarrasa et al., 2015). Modeling of the in situ heater experiments provides a unique opportunity to validate and test the models at realistic, large-scale, in-situ conditions, including the interactions between the host rock and EBS. Finally, through the numerical modeling of these experiments and being at the forefront of modeling coupled THMC processes our goal is also to advance the state-of-the-science internationally in the field of coupled processes modeling of clay barriers.

In the following Subsection 2.1, the modeling approach and the status of model development will be summarized, and in Subsection 2.2 the work related to improvement and validation of the BExM implementation in TOUGH-FLAC will be presented. Then the modeling work conducted associated with field experiments is presented in Subsections 2.3 through 2.5. Finally, in Subsection 2.6, the current status and future plans for THM modeling are summarized.

2.1   Modeling Approach

LBNL uses two independent numerical simulators (TOUGH-FLAC and ROCMAS) for modeling of coupled THM processes associated with nuclear waste disposal and for modeling of the aforementioned heater experiments. The TOUGH-FLAC simulator developed at LBNL is the primary analysis tool, because this simulator has the required capabilities to model a large variety of problems associated with nuclear waste disposal for various engineering and natural systems. The ROCMAS code, also developed at LBNL, is used for confidence building through code-to-code verification. That is, models of a particular problem might be built in both TOUGH-FLAC and ROCMAS, and if the simulation results agree, they provide confidence in the models.

Both the TOUGH-FLAC and ROCMAS codes solve THM coupled problems, but are two different codes with different characteristics. TOUGH-FLAC can simulate coupled THM processes under multiphase flow conditions through a sequential coupling of the TOUGH2 multiphase flow simulator with the FLAC3D geomechanical code (Rutqvist et al. 2002; Rutqvist 2011). TOUGH-FLAC has recently been modified for applications related with to bentonite-backfilled repositories in clay host formations (Rutqvist et al., 2014b). ROCMAS simulates coupled THM processes in unsaturated media, including single-phase liquid flow and vapor diffusion in a static gas phase (Rutqvist et al. 2001a). The code has been extensively applied in earlier phases of the DECOVALEX project for THM analysis in bentonite-rock systems (Rutqvist et al., 2001b; 2005; 2009). Thus, ROCMAS is simplified compared to that of TOUGH-FLAC, foremost in the handing of multiphase fluid flow processes and in the geomechanical constitutive models, which are much more advanced in TOUGH-FLAC. Another difference is ROCMAS uses full implicit coupling between fluid flow and geomechanics, whereas sequential coupling technique is adopted in TOUGH-FLAC. In the following, the TOUGH-FLAC simulator (primary analysis tool) is described in more detail.

The TOUGH-FLAC simulator (Rutqvist 2011), is based on linking the TOUGH2 multiphase flow and heat transport simulator (Pruess et al., 2012) with the FLAC3D geomechanical simulator (Itasca 2011). In this approach, TOUGH2 (Pruess et al., 2012) is used for solving multiphase flow and heat transport equations, whereas FLAC3D (Itasca, 2011) is used for solving geomechanical stress-strain equations. The two codes are sequentially coupled so that a TOUGH-FLAC simulation runs seamlessly.

For analysis of coupled THM problems, TOUGH2 and FLAC3D are executed on compatible numerical grids and linked through a coupled THM model (Figure 2.1) with coupling functions to pass relevant information between the field equations that are solved in the respective codes. In the coupling scheme between TOUGH2 and FLAC3D, the TOUGH2 multiphase pressures, saturation, and temperature are provided to update temperature, and pore pressure to FLAC3D (Figure 2.1). After data transfer, FLAC3D internally calculates thermal expansion, swelling, and effective stress. Conversely, element stress or deformation from FLA3D is supplied to TOUGH2 to correct element porosity, permeability, and capillary pressure for the fluid-flow simulation in TOUGH2. The corrections of hydraulic properties are based on material-specific functions.

In a TOUGH-FLAC simulation, the calculation is stepped forward in time with the transient multiphase fluid flow analysis in TOUGH2, and at each time step or at the TOUGH2 Newton iteration level, a quasi-static mechanical analysis is conducted with FLAC3D to calculate stress-induced changes in porosity and intrinsic permeability (Figure 2.2). In this scheme, the fluid-

flow sequence is solved first under fixed stress, and the resulting pressure and temperature are prescribed in the mechanical sequence. This corresponds to so-called stress-fixed iterations in the sequential scheme, in which the solution becomes unconditionally stable. The resulting THM analysis may be explicit sequential method, meaning that the porosity and permeability is evaluated only at the beginning of each time step, or the analysis may be implicit sequential method, with permeability and porosity updated on the Newton iteration level towards the end of the time step using an iterative process.
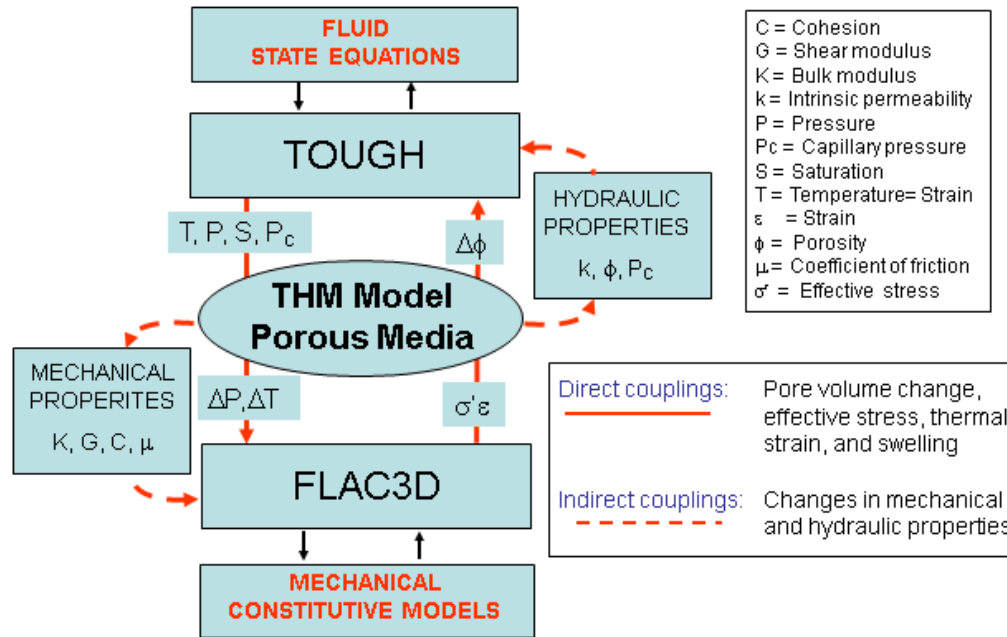
Figure 2.1. Schematic of linking of TOUGH2 and FLAC3D in a coupled TOUGH-FLAC simulation.
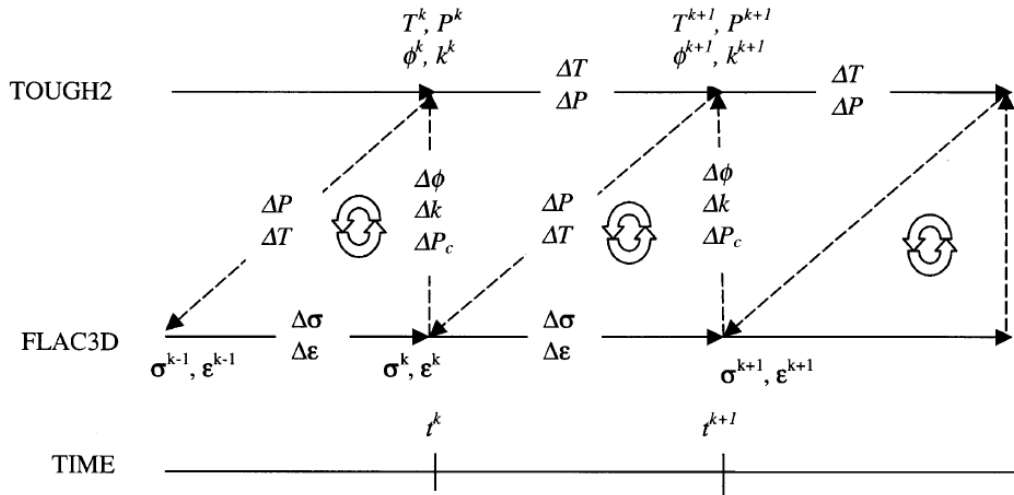
Figure 2.2. Numerical procedure of a linked TOUGH2 and FLAC3D simulation with subscript k signifying time step.

A great advantage with TOUGH-FLAC is that both TOUGH2 and FLAC3D are continuously developed and widely used in both academia and industry. In TOUGH2, a large number of fluid equation-of-state modules are available, while in FLAC3D, a large number of geomechanical constitutive models are available. This means that the simulator can be relatively easily extended to new application areas.

As part of the UFD effort, the TOUGH-FLAC simulator has been extended and applied to issues related to nuclear waste disposal with bentonite backfilled tunnels (Rutqvist et al., 2011; 2014b). This includes implementation of the Barcelona Basic Model (BBM) (Alonso et al., 1990), for the mechanical behavior of unsaturated soils, which has been applied for modeling of bentonite backfill behavior (Rutqvist et al., 2011). The BBM was first developed and presented in the early 1990s as an extension of the Modified Cam Clay (MCC) model to unsaturated soil conditions (Alonso et al., 1990). The model can describe many typical features of unsaturated-soil mechanical behavior, including wetting-induced swelling or collapse strains, depending on the magnitude of applied stress, as well as the increase in shear strength and apparent preconsolidation stress with suction (Gens et al., 2006). More details about the BBM model are given in Section 2.2.1.

The BBM has been used for modeling bentonite-buffer behavior in various national nuclear waste programs in Europe and Japan. For example, the BBM was successfully applied to model the coupled THM behavior of unsaturated bentonite clay associated with the FEBEX *in situ* heater test at the Grimsel Test Site, Switzerland (Gens et al., 2009). The BBM has also been applied to other types of bentonite-sand mixtures based on MX-80, considered as an option for an isolating buffer in the Swedish KBS-3 repository concept (Kristensson and Åkesson 2008). As part of the UFD program, the BBM was also used by Rutqvist et al. (2014b), for modeling of coupled THM processes around a generic repository in a clay host formation.

In the last few years, as part of the UFD EBS program, the BBM has been extended to a dual structure model, corresponding to the Barcelona Expansive Model (BExM). In a dual-structure model, the material consists of two structural levels: a microstructure in which the interactions occur at the particle level, and a macrostructure that accounts for the overall fabric arrangement

of the material comprising aggregates and macropores (Figure 2.3) (Gens et al., 2006; Sánchez et al., 2005; Gens and Alonso 1992). A dual-structure model has important features for modeling the mechanical behavior of a bentonite buffer, such as irreversible strain during suction cycles. However, most importantly, a dual-structure model provides the necessary link between chemistry and mechanics, enabling us to develop a coupled THMC model for the analysis of long-term EBS behavior. This approach enables mechanistic modeling of processes important for long-term buffer stability, including effects of pore-water salinity on swelling (loss of swelling), conversion of smectite to nonexpansive mineral forms (loss of swelling), and swelling pressure versus exchangeable cations. Details of the development, testing and applications of the dual structure model, were presented in the FY2014 milestone report titled "Investigation of Coupled THMC Processes and Reactive Transport: FY14 Progress" (Rutqvist et al. 2014a) and has also recently been published in a journal paper (Vilarrasa et al., 2015).

Based on model simulation in the DECOVALEX-2015 project with TOUGH-FLAC, considering full multiphase flow (gas and liquid) we found that a gas intrinsic permeability several orders of magnitude higher than the intrinsic permeability related to liquid flow would be required for accurate modeling of the evolution of the moisture content in the buffer. In the following simulations of the three heater experiments we simulated high intrinsic gas permeability in the bentonite through the Klinkenberg parameter according to:

$$K_g = K_l\left(1 + b/P\right) \qquad\qquad 2.1$$

where K_g is intrinsic permeability for gas flow, K_l is intrinsic permeability of water flow, b is the Klinkenberg parameter, and P is pressure. In this case, we assigned a high value of the Klinkenberg parameter of 2.5×10^{11} Pa^{-1}, which means that the intrinsic permeability for gas flow would be about 6 orders of magnitude higher than the intrinsic permeability for water flow. This was necessary as otherwise it is not possible to simulate the drying that usually occurs near the heaters.

(a)   (b)
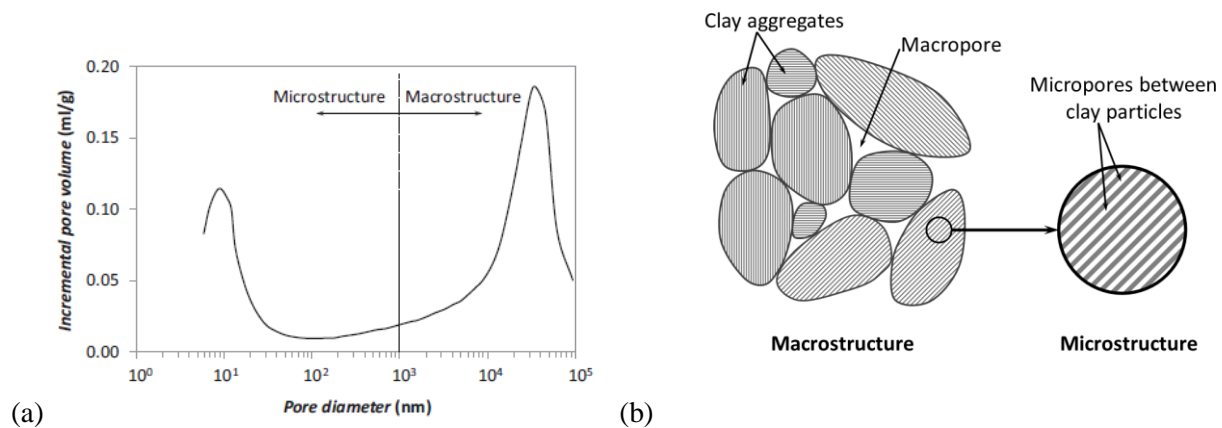
Figure 2.3. (a) Pore size distribution and (b) schematic representation of the two structural levels considered in the dual structure model. Clay particles are represented by the gray lines (Vilarrasa et al., 2015).

In FY2015, a substantial effort has been dedicated to improve the implementation of the BExM model into TOUGH-FLAC and to validate this implementation. The new implementation has resulted in increased efficiency.

2.2 Improvement and Validaiton of BExM in TOUGH-FLAC

The dual structure model proposed by Alonso et al. (1999) and Sánchez et al. (2005) has been implemented into TOUGH-FLAC (Vilarrasa et al., 2015), by extending the previous implementation of the BBM (Rutqvist et al., 2011) to include the microstructural level and its interactions with the macrostructure. This year, the model has been implemented into the simulation tool, TOUGHREACT-FLAC3D, and has been improved to enhance the capability for modeling swelling behavior of bentonite:

1. The framework to compute dual-structural model has been revised to be compatible with FLAC3D, and a new solve command can be used for better efficiency and convergence.
2. The micro-structural strain evolution under anisotropic stress has been implemented in FLAC3D.
3. The interface for chemical-mechanical interaction has been integrated, so BExM can be linked with TOUGHREACT to account for chemical effects.
4. Some minor bugs have been fixed in the new version.

The implementation of the dual structure model in FLAC3D was done using the User Defined constitutive Model (UDM) option in FLAC3D, including C++ coding and dynamic link libraries. This also involves consideration of the sequential coupling of the TOUGH2/TOUGHREACT and FLAC3D simulators (Rutqvist, 2011), and constitutive stress-strain behavior in FLAC3D. With these improvements, the new simulator TOUGHREACT-FLAC3D can be used to study coupled THMC processes in bentonite-based backfill material. In this section, we present one swelling pressure test on Boom clay pellets, two cyclic wetting-drying tests, and two tests with combination of loading paths on compacted bentonite samples to validate the model implementation. The numerical analysis is launched with the set of material parameters calibrated by the model development team against laboratory experiments from published literature. The applications of BExM for THMC processes in expansive clays are presented in Sections 3 and 4.

2.2.1 The dual structure approach

Expansive clays present a bimodal or trimodal pore size distribution (Figure 2.3(a)). This pore size distribution leads to the differentiaion of a microstructure, which is made of the active clay minerals, and a macrostructure, which is formed by the global distribution of clay aggregates and the macropores between them (Figure 2.3(b)). Thus, in the dual structure model, the total volume (V), the total void ratio (e), and porosity (ϕ), of the material are divided into micro-structural parts (V_{micro}, e_{micro}, ϕ_{micro}) and macro-structural parts (V_{macro}, e_{macro}, ϕ_{macro}). The microstructure can swell to invade the macroporosity, depending on the mechanical confinement and load level.

2.2.1.1 Macrostructural level

The macrostructural behavior is modeled based on the BBM, in which the yield surface is defined in the p-q-s space, where p is net mean stress (i.e., total stress minus gas-phase pressure), q is deviatoric stress (or shear stress), and s is suction (i.e., gas pressure minus liquid pressure)

(Figure 2.4). The rate of the increase of the elastic domain, represented by the loading-collapse (LC) curve according to

$$f_{LC} = \frac{q^2}{g_y(\theta)^2} - \frac{M^2}{g_y(\theta=0)^2}(p+p_s)(p_0-p)=0$$

2.2

where θ is the Lode angle, the function $g_y(\theta)$ describes the shape of the yield surface in the deviatoric plane, M is the constant slope of the critical state line, $p_s = k_s s$ represents the increase in cohesion with suction, k_s is an empirical material constant and function

$$p_0 = p_c\left(\frac{p_0^*}{p_c}\right)^{[\lambda(0)-\kappa]/[\lambda(s)-\kappa]}$$

2.3

is the net mean yield stress at current suction, where p_0^* is the net mean yield at full saturation, p_c is a reference stress, $\lambda(0)$ is a compressibility parameter in virgin soil states at zero suction, $\lambda(s) = \lambda(s)[(1-r)\exp(-\zeta s)+r]$ is a compressibility parameter in virgin soil states at suction s, r is a constant related to the maximum stiffness of the soil (for an infinite suction), ζ is a parameter that controls the rate of increase of soil stiffness with suction and κ is the elastic stiffness parameter for changes in net mean stress at current suction. The flow rule is given by

$$g_{LC} = \frac{\alpha_a q^2}{g_y(\theta)^2} - \frac{M^2}{g_y(\theta=0)^2}(p+p_s)(p_0-p)$$

2.4

where α_a is a parameter that gives rise to a non-associative model, i.e., $g_{LC} \neq f_{LC}$.
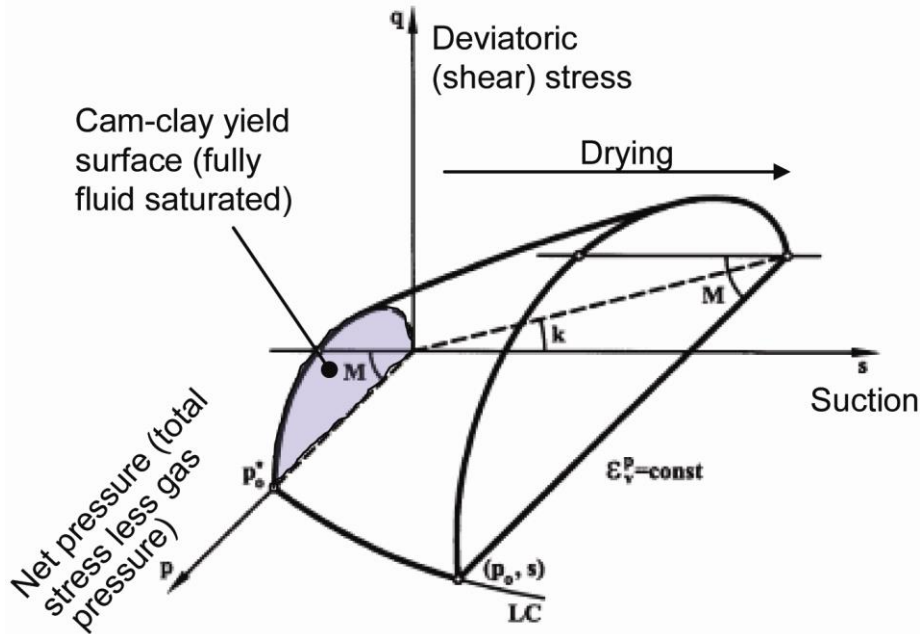
Figure 2.4. BBM constitutive model showing the yield surface in q-p-s space.

2.2.1.2 Microstructural level

The microstructure is controlled by the effective stress.

$$\hat{p} = p + \chi s \qquad\qquad 2.5$$

where $\hat{p}$ is mean effective stress, p is the mean net stress, and χ is a constant ($\chi > 0$) which is dependent on saturation. The microstructural strains $d\varepsilon_{vm}^e$ are elastic and volumetric, but will induce irreversible strains in the macroporosity. These irreversible macrostructural deformations induced by microstructural effects are considered proportional to the microstructural strain through interaction functions as

$$d\varepsilon_{v\beta}^p = f d\varepsilon_{vm}^e \qquad\qquad 2.6$$

where $\varepsilon_{v\beta}^p$ is the macrostructural plastic strain arising from the interaction between both structures. Two interaction functions are defined: $f = f_c$ for microstructural compression or shrinkage paths and $f = f_s$ for microstructural swelling paths. These functions can adopt several forms (Sánchez et al., 2005), but they always depend on the ratio p_r/p_0

$$f_c = f_{c0} + f_{c1}(p_r / p_0)^{n_c} \text{ and } f_s = f_{s0} + f_{s1}(1 - p_r / p_0)^{n_s}, \qquad\qquad 2.7$$

or

$$f_c = f_{c0} + f_{c1} \tanh[f_{c2}(p_r / p_0 - f_{c3})] \text{ and } f_s = f_{s0} - f_{s1} \tanh[f_{s2}(p_r / p_0 - f_{s3})], \qquad 2.8$$

where f_{ij} and n_i ($i = \{c, s\}$ and $j = \{0,1,2,3\}$) are constants. p_r is an isotropic stress status projected from the current stress status. The ratio p_r/p_0 is a measure of the distance from the current stress state to the yield locus for the macrostructure LC and has the same meaning as the over consolidation ratio for an isotropically consolidated soil. A low p_r/p_0 implies a dense packing of the material, while a high p_r/p_0 implies a looser macrostructure.

2.2.1.3 Elastic Strain

The macrostructural volumetric elastic strain increment for the dual structure model is associated with changes in net mean stress dp and suction ds (Alonso et al., 1999)

$$d\varepsilon_{vM}^e = \frac{1}{K_M} dp + \frac{1}{K_s} ds, \qquad\qquad 2.9$$

where K_M is the macrostructural bulk modulus and K_s is the macrostructural modulus associated with suction strain. K_M and K_s are defined as

$$K_M = \frac{(1+e_M)p}{\kappa}, \qquad\qquad 2.10$$

$$K_s = \frac{(1+e_M)(s + p_{atm})}{\kappa_s}, \qquad\qquad 2.11$$

where e_M is macro-structural void ratio, $\kappa = \kappa_0(1 + s\alpha_{ps})$, $\kappa_s = \kappa_{s0}(1 + \alpha_{sp} \ln(p_r/p_0)) \exp(\alpha_{ss}s)$, κ_0, κ_{s0} are compressibility parameters for changes in net mean stress and suction, respectively, p_{ref} is a reference stress state for relating elastic compressibility to suction,

and α_{ps}, α_{sp} and α_{ss} are empirical parameters. The microstructural volumetric strain depends on the change in the microstructural effective stress

$$\mathrm{d}\varepsilon_{vm}^e = \frac{1}{K_m}\mathrm{d}\hat{p}\,, \qquad\qquad 2.12$$

where K_m is the microstructural bulk modulus for changes in mean effective stress. Alonso et al. (1999) define two alternative expressions for the microstructural modulus

$$K_m = \frac{(1+e_m)\hat{p}}{\kappa_m} \quad \text{or} \qquad K_m = \frac{e^{\alpha_m \hat{p}}}{\beta_m} \qquad\qquad 2.13$$

where e_m is micro-structural void ratio, κ_m, α_m and β_m are compressibility parameters. Thermal strains are purely volumetric

$$\mathrm{d}\varepsilon_v^T = (\alpha_0 + 2\alpha_2 \Delta T)\mathrm{d}T\,, \qquad\qquad 2.14$$

where α_0 and α_2 are material parameters corresponding to a temperature-dependent volumetric thermal expansion coefficient and T is temperature. The deviatoric elastic strain increment is defined as

$$\mathrm{d}\varepsilon_q^e = \frac{1}{3G}\mathrm{d}q\,, \qquad\qquad 2.15$$

where G is the shear modulus and may be obtained using a constant Poisson ratio ν in

$$G = \frac{3(1-2\nu)}{2(1+\nu)}K_M\,. \qquad\qquad 2.16$$

2.2.1.4 Plastic Strain

Macrostructural plastic strain occurs by two possible mechanisms: either when the stress lies on the LC yield surface, or as a result of microstructural shrinkage/swelling. While the plastic strain by microstructural shrinkage/swelling is described by Equation 2.5, the LC plastic strains are obtained from the plastic flow rule

$$\mathrm{d}\varepsilon_{vLC}^p = \mathrm{d}\Lambda\frac{\partial g_{LC}}{\partial p}\,, \qquad\qquad 2.17$$

$$\mathrm{d}\varepsilon_{qLC}^p = \mathrm{d}\Lambda\frac{\partial g_{LC}}{\partial q}\,, \qquad\qquad 2.18$$

where $\mathrm{d}\Lambda$ is the plastic multiplier obtained from the consistency condition $\mathrm{d}f_{LC} = 0$ (recall Eq. 2.2). The calculation of the plastic multiplier $\mathrm{d}\Lambda$ is detailed in Rutqvist et al. (2011). The total plastic volumetric strain is the sum of both plastic mechanisms

$$\mathrm{d}\varepsilon_v^p = \mathrm{d}\varepsilon_{vLC}^p + \mathrm{d}\varepsilon_{v\beta}^p \qquad\qquad 2.19$$

The hardening variable of the macrostructure - the pre-consolidation pressure p_0^* - depends on the total plastic volumetric strain ε_v^p as

$$\frac{\mathrm{d}p_0^*}{p_0^*} = \frac{(1+e)\mathrm{d}\varepsilon_v^p}{\lambda(0)-\kappa}.$$

2.20

2.2.2 Swelling pressure test

The swelling pressure test is used to investigate the swelling capacity of expansive soils, which can be placed as a buffer in EBS to isolate the radioactive waste. In this section, we test the dual structure model by modeling a laboratory experiment carried out by Romero (1999) on a sample of Boom clay pellets. The microstructure in these materials is associated to the high density pellets (dry density 1.96 Mg/m^3), and the macrostructure corresponds to the granular-like arrangement of these pellets (dry density 1.37 Mg/m^3) with macro-pores between the pellets. Table 2.1 presents the values of soil parameters and initial values of state variables which are calibrated and suggested by Sánchez et al. (2005).

Table 2.1. Parameters used for swelling pressure test (Sánchez et al., 2005)

Parameters defining the Barcelona basic model for macrostructural behavior						
$\kappa = 0.02$	$\kappa_s = 0.01$	$\lambda(0) = 0.65$	$p_c = 0.01$ MPa	$r = 0.78$	$\zeta = 5$ MPa^{-1}	$p_0^* = 0.11$ MPa

Parameters defining the law for microstructural behavior	
$\kappa_m = 0.01$	$\chi = 1$

Interaction functions	
$f_c = -0.10 + 1.10\left(\dfrac{p_r}{p_0}\right)^{0.5}$	$f_s = -0.10 + 1.1\left(1-\dfrac{p_r}{p_0}\right)^2$
$e_{macro} = 0.6$	$e_{micro} = 0.35$
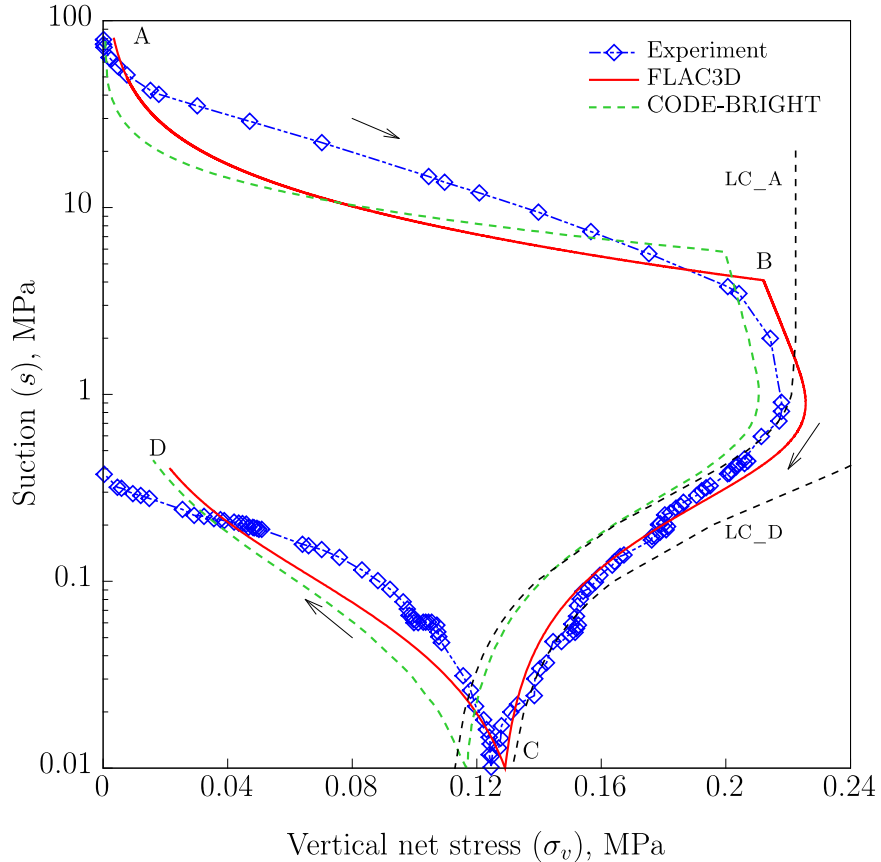
Figure 2.5. Observed (Romero, 1999) and computed stress path in the $\boldsymbol{\sigma_v}$–$\boldsymbol{s}$ plane. LC_A (LC_D) represents the loading-collapse yield surface corresponding to the stress state at point A (point D) (calculated by FLAC3D). To the left of LC_A (LC_D) is elastic domain while to the right of LC_A (LC_D) corresponds to the plastic domain. The result noted as "CODE-BRIGHT" presents the work by Sánchez et al. (2005).

This swelling pressure test was operated under constant volume conditions, while the suction (s) was controlled as external loading changes. In Figure 2.5, the observed behavior during the test (noted as "Experiment") and the numerical simulation results (noted as "FLAC3D") are displayed with vertical net stress-suction (σ_v–s) path. The same simulation done by CODE-BRIGHT (Sánchez et al. 2005) is also presented in Figure 2.5 for comparison.

The experiment includes two loading steps. It started with an initial suction of 80 MPa and a low vertical stress (σ_v) (point A). First, a wetting path was followed up by decreasing the suction to 0.01 MPa (point C). In the second step (C-D), the sample was subjected to drying, up to a maximum suction of 0.4 MPa.

The numerical analysis has been carried out prescribing the same suction changes as in the test. Figure 2.6 shows the evolution of the hardening parameter, p_0^*, in the simulation, and Figure 2.7 displays the evolution of the interaction functions f_c and f_s. Three phases can be observed:
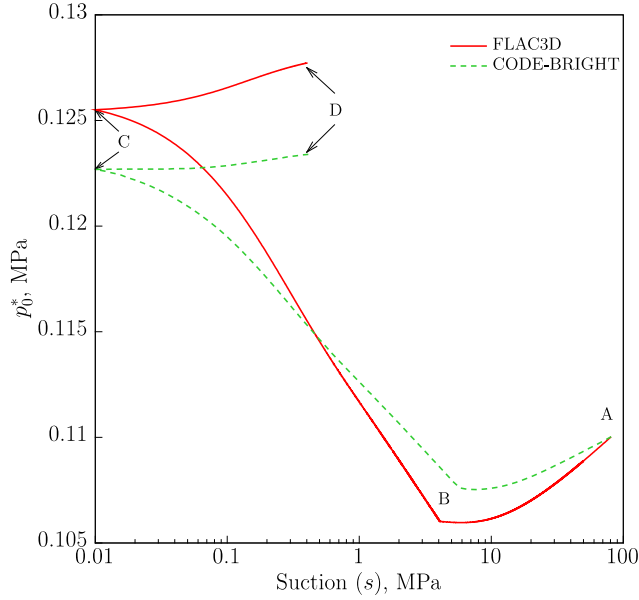
Figure 2.6. Evolution of the hardening parameter, $\boldsymbol{p_0^*}$, in the simulation. The result noted as "CODE-BRIGHT" presents the work by Sánchez et al. (2005).
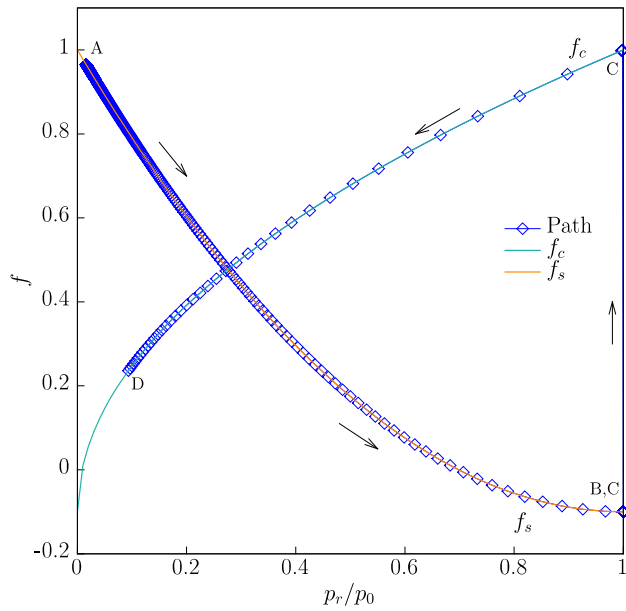
Figure 2.7. Evolution of the $\boldsymbol{f_c}$ and $\boldsymbol{f_s}$ interaction functions. (The function in A-B stage is plotted with every 2000th point, and the one in C-D stage is plotted with every 100th point.)

- From A to B: During this period, the suction decreases from 80 MPa to about 4MPa. When computation starts at point A, the initial collapse yield surface is at the position where LC_A locates (Figure 2.5). Thus, the initial state of material is inside the elastic domain of the macrostructure. In this stage, the material sample remains inside the LC yield surface but suction reduction induces that the microstructural-swelling (ms) mechanism is active. As a result, the stress increases to

45

compensate the swelling strains. The ms interaction function f_s is positive during most of this stage (Figure 2.7), which implies the induced macrostructural plastic strains due to ms mechanism are in expansion. The hardening parameter, p_0^*, decreases as well (Figure 2.6) and the material becomes a more open macrostructure (the structure is looser than before). The LC yield curve moves from the initial position LC_A to the left where point B locates. Negative values of f_s are obtained and result in the very slight change of tendency of p_0^* just before reaching point B (close to collapse). Point B corresponds to the contact point between the stress path and the LC curve.

- From B to C: During this period, the suction continues decreasing to 0.01 MPa. From point B, a collapse of the macrostructure occurs (plastic yield surface of macro-structures is reached) with a hardening of the material (an increase of p_0^* in Figure 2.6).

- Finally, from C to D, the suction increases, inducing the microstructural-contraction (mc) mechanism is active. The LC yield curve moves right to the final position LC_D with a increase of hardening parameter, p_0^*. This corresponds to compressive plastic macrostructural strains associated with macrostructural hardening, and the final state of the sample is a denser macrostructure.

The model can reproduce satisfactorily the main trends observed during the swelling pressure test. The computation results obtained by our implementation (FLAC3D) is close to the result by CODE-BRIGHT which simulator used by the model developers (Sánchez et al. 2005). The fact that the results are slightly different might be a result of difference in numerical methods, including integration algorithms used in different simulators are distinct. The hardening of parameter p_0^* we obtained is higher than Sánchez et al. (2005) simulated. Moreover, it is observed that the stress path calculated with FLAC3D is dependent on the value of initial vertical stress, which may be due to the high non-linearity of BExM.

2.2.3 Cyclic wetting-drying test

In this section, we model cyclic wetting-drying laboratory experiments carried out by Pousada (1982). This kind of test provides valuable information on the behavior of expansive soil subjected to cyclic suction changes. The samples were prepared with a dry density of 1.34 Mg/m^3 and with an initial water content of 24%. Two tests have been operated under oedometric conditions at two different vertical stress levels. Then samples were subjected to six wetting-drying suction cycles (12 loading-unloading steps in total) with suction changing from 0.2 to 1.7 MPa and back, in which expansive clays show a non-reversible behavior. Table 2.2 summarizes the parameters of the dual structure model resulting from the calibration of the laboratory experiments.

Table 2.2. Parameters used for cyclic wetting-drying tests (Sánchez et al., 2005).

Parameters defining the Barcelona basic model for macrostructural behavior							
$\kappa = 0.05$	$\kappa_s = 0.01$	$\lambda(0) = 0.065$	$p_c = 0.01$ MPa	$r = 0.96$	$\zeta = 0.2$ MPa^{-1}	$p_0^* = 0.11$MPa	

Parameters defining the law for microstructural behavior		
$\alpha_m = 0.8$ MPa^{-1}	$\beta_m = 0.02$ MPa^{-1}	$\chi = 1$

Interaction functions

$$f_c = 1.6 + 0.6 \tanh\left[10\left(\frac{p_r}{p_0} - 0.54\right)\right] \qquad f_s = 1.6 - 0.6 \tanh\left[10\left(\frac{p_r}{p_0} - 0.54\right)\right]$$

$e_{macro} = 0.55$	$e_{micro} = 0.45$

The experimentally observed responses of the material at two different vertical stresses (0.01 and 0.1 MPa) are presented in terms of volumetric deformations (Figures 2.8(a) and 2.9(a)) and compared with the numerical results with FLAC3D. Estimations of the micro- and macro-void ratios calculated during the numerical simulations using the dual structure model are plotted as well in both figures. The simulation results obtained are good in qualitative terms with experiment data. The upper points in each figure represent the strains or deformation associated with the suction reduced to 0.2 MPa, while the lower points correspond to the state for suction up to 1.7 MPa. A are in agreement is obtained between simulated and observed volumetric deformations for the sample. The microstructural behavior is reversible and the changes in the microstructural void ratio are not greatly affected by the stress level (Figures 2.8(a) and 2.9(a)). On the other hand, the macrostructural void ratio is influenced by the values of applied stress. This can be attributed to the increased difficulty of modifying the macrostructural arrangement when the material confinement is higher. With cycles accumulate, the increments of the irreversible strains decrease as well in both tests. Figure 2.8(b) and 2.9(b) display the evolution of the micro-macro interaction function for first two cycles of suction changes. The tests started at the initial position A. Then suction decreases, so ms mechanism occurs (positive value of f_s function), inducing expansive macrostructural plastic strains (the path curves in Figures 2.8(b) and 2.9(b)). During the drying path, the sample shrinks with activate mc mechanism. Due to this effect (with positive interaction function f_c), the external suction change induces compressive macrostructural plastic strains.
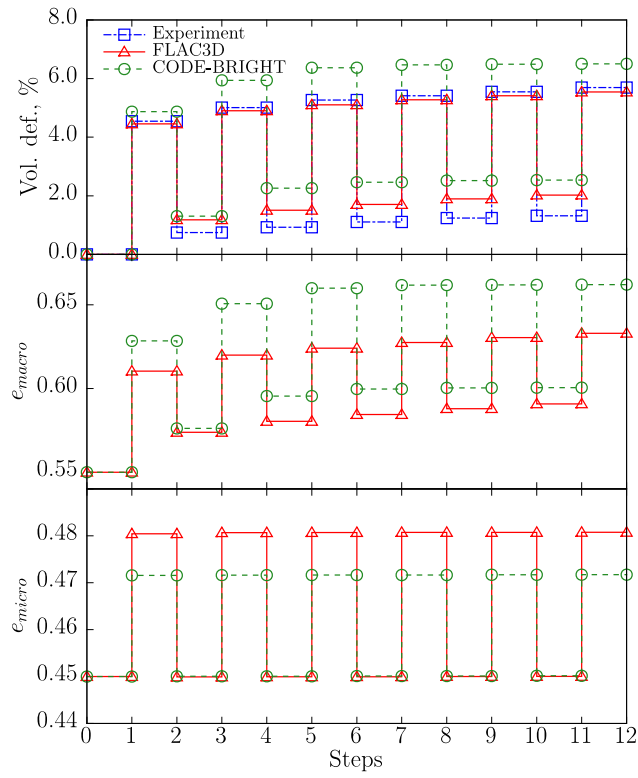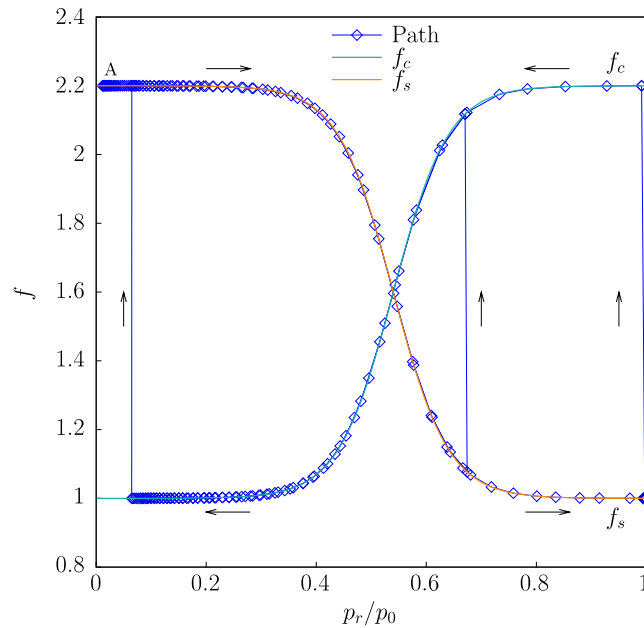
Figure 2.8. Observed and computed results of cyclic suction loading test with $\boldsymbol{\sigma_v = 0.01}$ MPa. (a) Values of volumetric deformations (observed and computed), micro- and macro-void ratios induced by loading-unloading steps. (b) Evolution of the interaction functions for first two cycles of suction changes (plotted with every 200th points during each loading cycle).
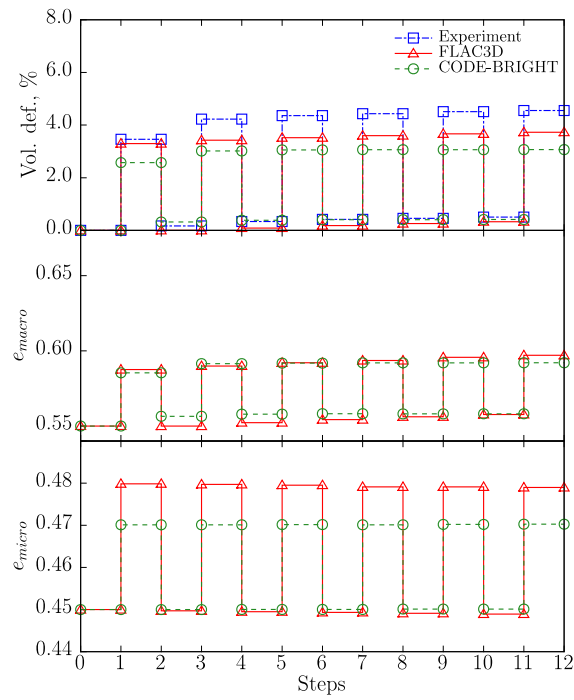
a)
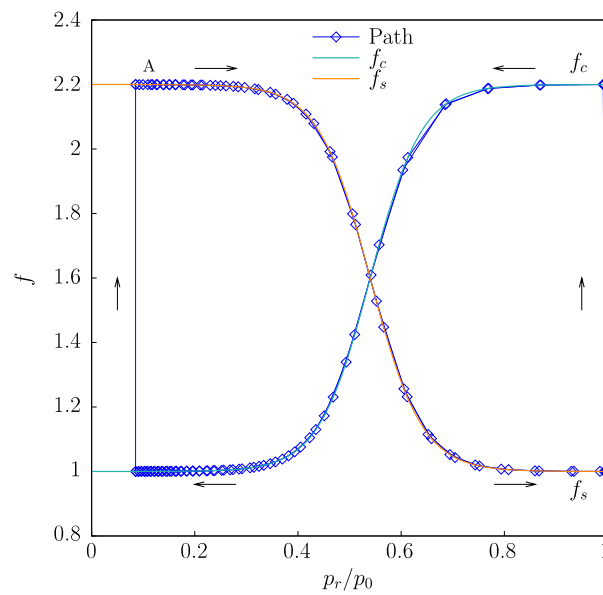
b)

Figure 2.9. Observed and computed results of cyclic suction loading test with $\sigma_v = 0.1$ MPa. (a) Values of volumetric deformations (observed and computed), micro- and macro-void ratios induced by loading-unloading steps. (b) Evolution of the interaction functions for first two cycles of suction changes (plotted with every 200th points during each loading cycle).

49

The model implemented on TOUGHREACT-FLAC3D can satisfactorily reproduce the main trends observed during the cyclic wetting-drying tests. The evolution of the micro-macro interaction function (Figures 2.8(b) and 2.9(b), we obtain from the simulation with FLAC3D is quite similar with the results by CODE-BRIGHT (Sánchez et al. 2005). To be clear, here we do not present their results of interaction functions. However, other mechanical deformation results by two simulators are slightly different (Figures 2.8(a) and 2.9(a)). The micro-void ratios we obtain at suction of 0.2 MPa in both experiments are higher than their results. The macro-void ratios we obtain in the test under low vertical stress ($\sigma_v = 0.01$ MPa) are lower than CODE-BRIGHT's results, while two simulators obtain close results of macro-void ratio results in the test under high vertical stress ($\sigma_v = 0.1$ MPa). The volumetric deformations we obtain match better with experiment data than theirs.

2.2.4　Tests with combination of loading paths

Two oedometer tests carried out at Centre for Energy, Environment and Technology (CIEMAT) with suction control are simulated with BExM in this section. Samples were compacted statically to a dry density of 1.70±0.02 Mg/m^3 with the material at hygroscopic water content. In the tests, a combination of loading paths at constant suction and wetting and drying paths at constant load were applied. A special technique (axistranslation technique) required by suction control procedure has been used in the oedometer cell. Suction values have been applied by prescribing a value of the relative humidity of the atmosphere in contact with the sample. The oedometer cell used in this case is depicted in Figure 2.10.
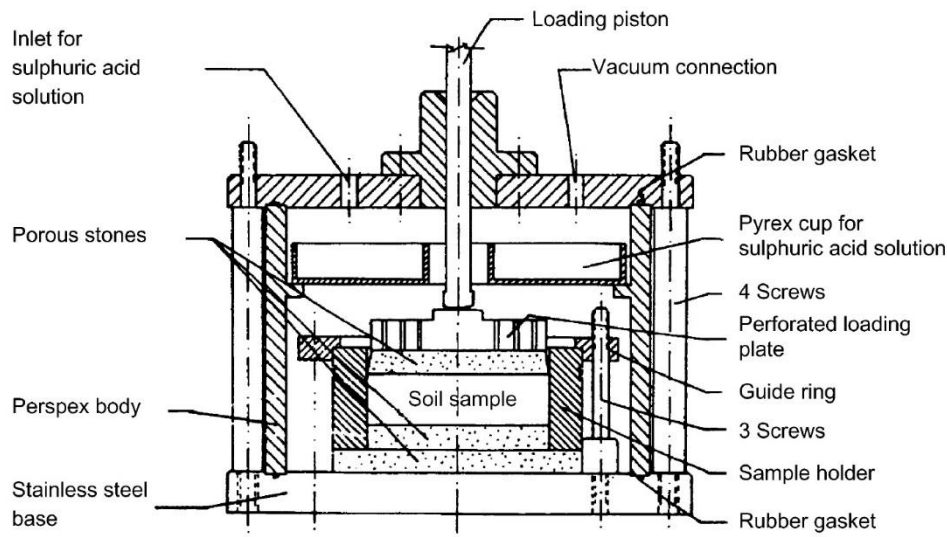
Figure 2.10. Schematic layout of the high-suction oedometer used in the CIEMAT laboratory (Esteban, 1990)

Table 2.3 presents the initial conditions, in terms of dry densities (ρ_d) and water contents (w), and the stress paths, in terms of applied suction and vertical loads, of two tests performed at CIEMAT laboratory. In order to use a logarithmic scale a constant value of 0.1 MPa has been added to all suction values plotted in Figure 2.11. The same convention has been used in other figures (Figures 2.12, 2.13, 2.15 and 2.16) plotted with suction.

Table 2.3. Stress paths of the tests, in which a combination of loading paths was applied. Tests performed at CIEMAT laboratory. (Lloret et al., 2003)

Test	Initial conditions		Path							
	ρ_d Mg/m^3	w %	A		B		C(S1) or D(S5)		E	
			σ_v Mpa	s Mpa	σ_v Mpa	s Mpa	σ_v Mpa	s Mpa	σ_v Mpa	s Mpa
S1	1.72	13.0	0.1	138	0.1	550	5.1	460	5.1	0
S5	1.72	13.2	0.1	138	0.1	520	0.1	0	5.0	0

The parameters of BExM used in the modelling are shown in Table 2.4. As Lloret et al. (2003) illustrated, the calibration of the material parameters for compacted bentonite was determined by the behavior of tests S1 and S5.

Table 2.4. Parameters used for combination of loading paths tests (Lloret et al., 2003).

Parameters defining the Barcelona basic model for macrostructural behavior
$\kappa = 0.005$ $\qquad \kappa_s = 0.001$ $\qquad \lambda(0) = 0.08$ $\quad p_c = 0.5$ Mpa $\quad r = 0.90$ $\quad \zeta = 1$ MPa^{-1} $\quad p_0^* = 12$ MPa

---

Parameters defining the law for microstructural behavior
$\alpha_m = 0.021$ MPa^{-1} $\quad \beta_m = 2.3 \times 10^{-3}$ MPa^{-1} $\quad \chi = 1$

Interaction functions

$$f_c = 1 + 0.9 \tanh\left[20\left(\frac{p_r}{p_0} - 0.25\right)\right] \qquad f_s = 0.8 - 1.1 \tanh\left[20\left(\frac{p_r}{p_0} - 0.25\right)\right]$$

$e_{macro} = 0.11$ $\hspace{8cm}$ $e_{micro} = 0.45$

Here we present the numerical analysis on tests S1 and S5, which can be compared with the corresponding experimental results. The two tests share the same initial and final generalized stress states but their trajectories are different (Figure 2.11). Test S1 was loaded up to a 5.1 MPa vertical load under a high suction of 550 MPa and was then wetted to full saturation. In contrast, test S5 was first wetted to saturation at a low vertical stress of 0.1 MPa and then was loaded to a vertical stress of 5.0 MPa. Figure 2.12 shows the computed variation of void ratio over the stress paths and over suction changes for the two tests, together with the experimental results.

a) b)
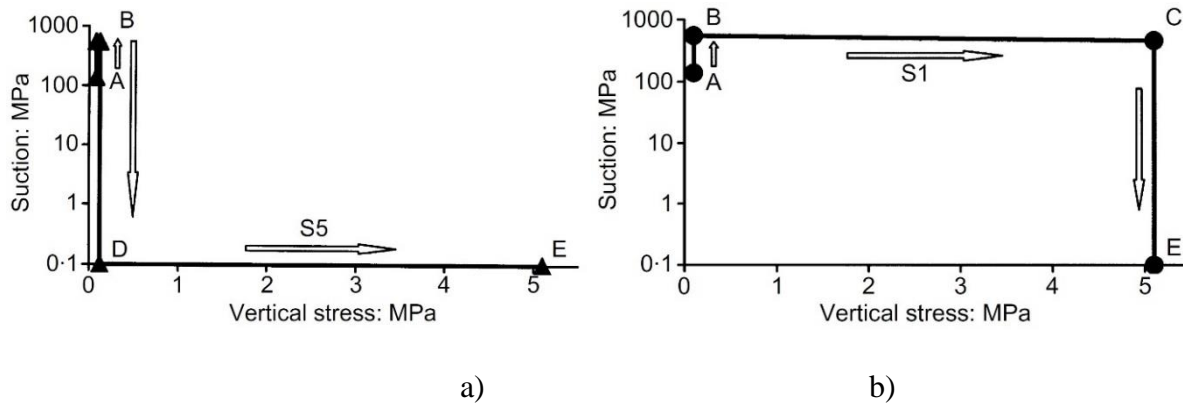
Figure 2.11. Stress paths of tests (a) S5 and (b) S1 from Lloret et al.(2003).
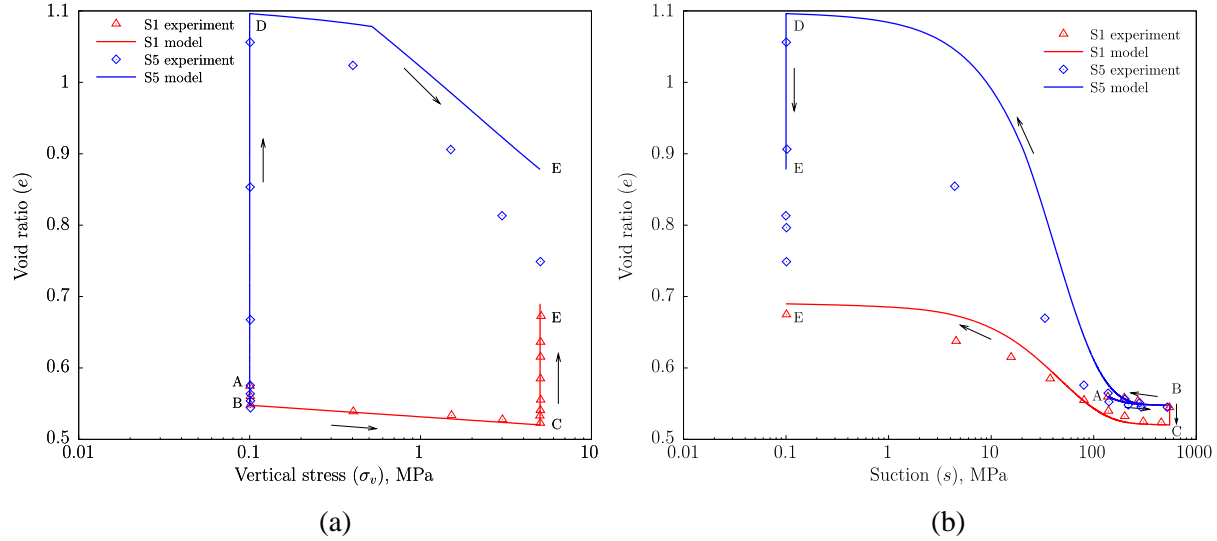
Figure 2.12. Experimental results and computed variation of void ratio for tests S1 and S5: (a) variation over stress paths; (b) variation over suction changes.

Figure 2.12 presents the evolution of total void ratio for test S5 against vertical stress change (Figure 2.12 (a) and against suction changes (Figure 2.12 (b)). The evolution of the microstructural and macrostructural void ratio computed for test S5 is displayed in Figure 2.13. Figure 2.14 shows the evolution of the interaction functions during the test S5. The first drying process (from A to B) does not induce much changes of total void ratio (Figures 2.12 (a) and 2.12 (b)) as well as micro- and macro-void ratio changes (Figure 2.13). With the reduction of suction, both micro- and macro-structures contract during this period. Since the stiffness is high at this stage, due to high suction, the compressive strains of both structures are small. The interaction effect between two scales is low with a small value of f_c (Figure 2.14). During the following swelling stage (path B-D), the microstructure swells, inducing larger plastic strains in the macrostructure (Figure 2.13) because of the positive value of the interaction function f_s (Figure 2.14). As a result of that, the total void ratio during this stage changes from about 0.55 to 1.1 (Figure 2.12). During the final loading stage (path D-E), the specimen is already saturated, so the external loading induces small compressive strains. In contrast, the compression of the macrostructure is significant, which is dominant during this stage.

52
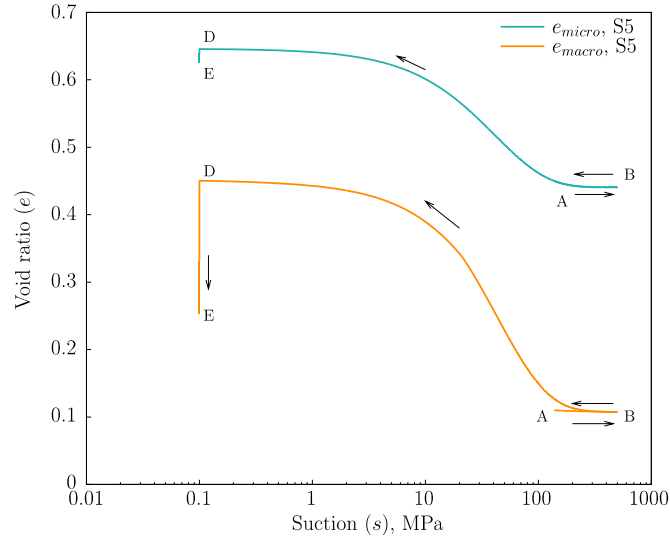
Figure 2.13. Evolution of computed microstructural and macrostructural void ratio for test S5.
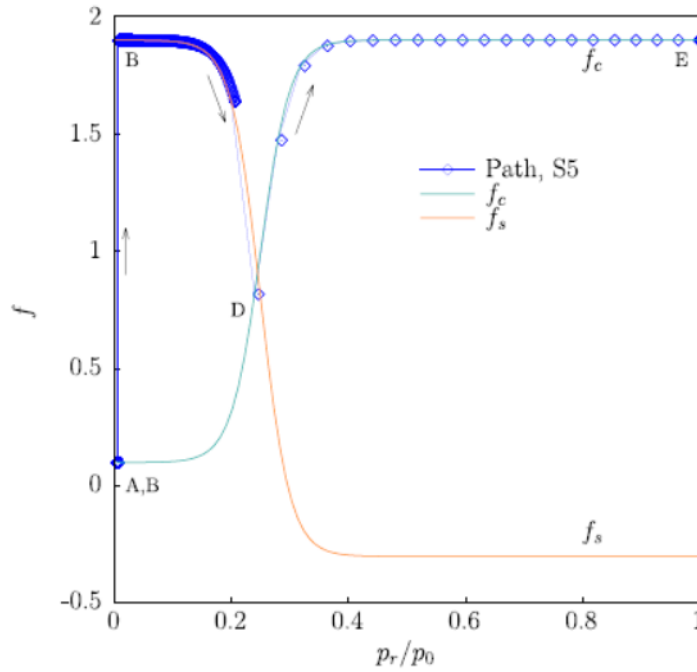
Figure 2.14. Interaction functions involved in the various stages of test S5.

The yield point observed and computed (between points D and E in Figure 2.12(a)) corresponds to the crossing of the LC yield curve during the final loading stage (from D to E). The evolution of the hardening parameter, p_0^* is plotted in Figure 2.15. This parameter is reduced during the swelling stage (path B-D) and then increases in the subsequent loading stage (path D-E).
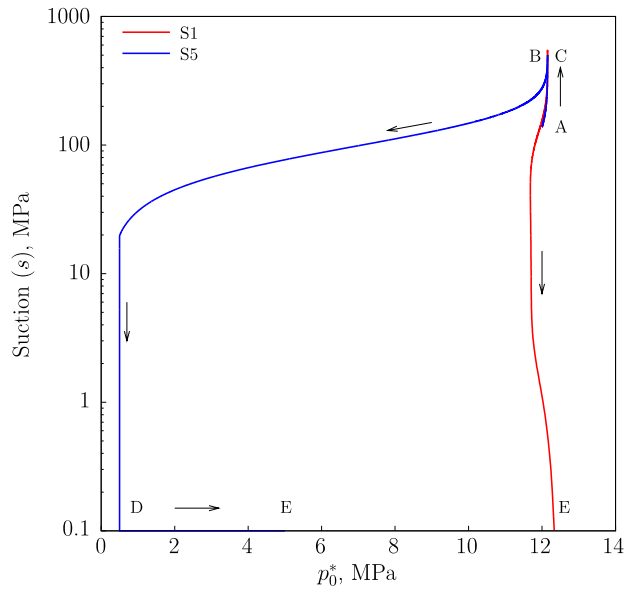
Figure 2.15. Evolution of hardening parameter p_0^* for tests S1 and S5.

The behavior of sample S1 is quite different from the sample S5. The evolution of microstructural strains and macrostructural strains is presented in Figure 2.16, and the evolution of total void ratio against vertical stress change and against suction changes for test S1 is presented in Figure 2.12. During the first drying stage (path A to B) and subsequent loading stage (path B to C), the deformations of microstructure and macrostructure are both very small, inducing the change of total void ratio is also small (Figure 2.12). During the swelling stage (path C to E), the microstructural strains are significant. However, the macrostructural strains are small. The plot of interaction function (Figure 2.17) shows the macro-strains induced by micro-swelling strains are small contraction because of the negative values obtained before reaching point E. As a result, the total void ratio changes from about 0.52 to 0.7 during this stage (Figure 2.12). The evolution of the hardening parameter for test S1 has also been plotted in Figure 2.15 and the changes are very slight.
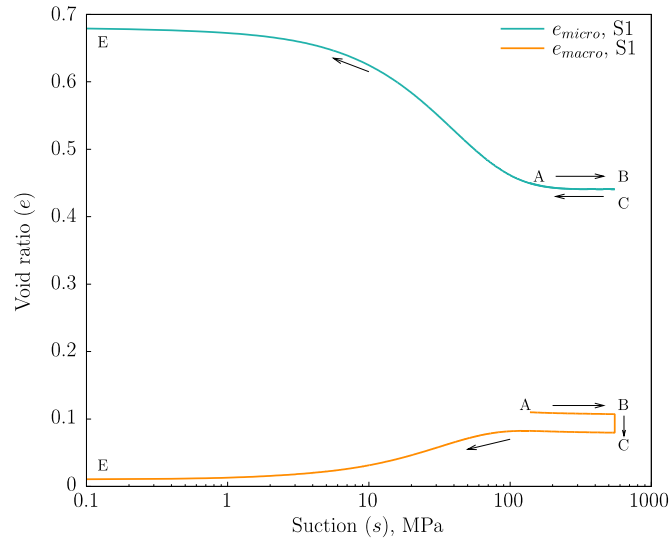
Figure 2.16. Evolution of computed microstructural and microstructural void ratio for test S1.
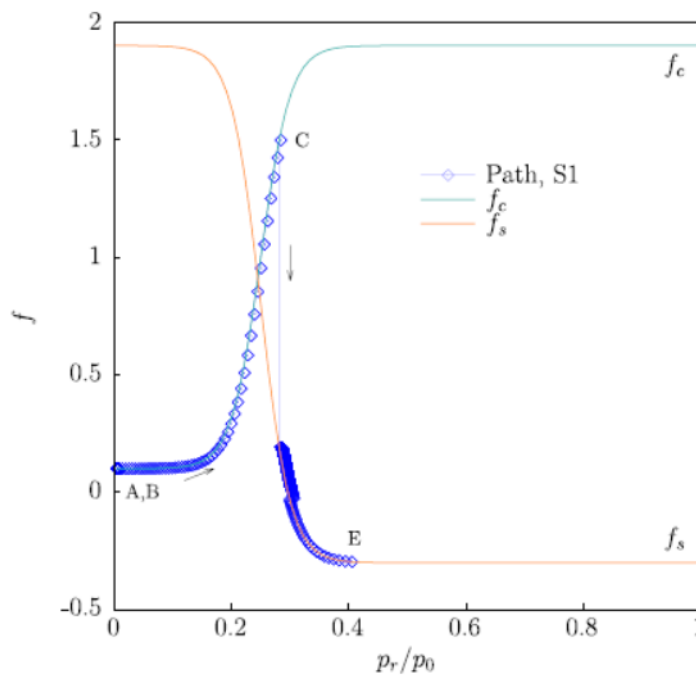
Figure 2.17. Interaction involved in the various stages of test S1.

Good reproduction of behavior between model computation and experimental results was achieved for test S1. However, some deviations are observed at intermediate and final stages of the swelling of test S5, especially the final contraction of S5 is less than the experiment observed (Figure 2.12). The model is capable of simulating observed results with the set of parameters adopted. It takes into account the two levels of structure in the material. Most of the main features of behavior are correctly reproduced and the two levels of structure in the material are taken into account by the model. The limitation of this case is that the model is used one-dimensionally, so the simulations provided by Lloret et al. (2003) and here are under isotropic

55

conditions, which actually cannot represent the stress states in oedometer testing with constrained lateral displacements. The oedometer testing does not provide full information on the stress state of the material, as the horizontal confining stress is not usually measured. In addition, in the case of unsaturated soils, there is also uncertainty regarding the degree of saturation of the soil, which is always unknown, although the retention curves obtained at constant volume may provide an approximate water content for every suction value. These limitations may affect the model calibration on parameters.

2.2.5 Summary and status of BExM in FLAC3D

The dual structure model is implemented into FLAC^{3D} using the UDM option. The model implementation has been validated by modeling one swelling pressure test on Boom clay pellets, two cyclic wetting-drying tests on one type of expansive clay and two tests with combination of loading paths on compacted bentonite samples. Based on the simulation results, the model is capable repoducing the observed behavior of expansive clays during experiments associated with suction changes. The computation results we obtained with BExM agree well with the experiment data, and also follow the same tendency of results presented by BExM developers. In conclusion that the implementation of dual- structure model, BExM, on FLAC^{3D} is validated and can be used for more complicated cases including THM or THMC processes for clays in a repository environment.

2.3   Modeling of Mont Terri HE-E Experiment (DECOVALEX-2015)

The Mont Terri HE-E Experiment focuses on the THM behavior of bentonite barriers in the early nonisothermal resaturation stage and their THM interaction with Opalinus Clay (Figure 2.18). The objective is to better understand the evolution of a disposal system for high level waste in the early post-closure period, with emphasis on the thermal evolution, buffer resaturation (*in situ* determination of the thermal conductivity of bentonite and its dependency on saturation), pore-water pressure in the near field, and the evolution of swelling pressures in the buffer (Gaus et al., 2014). Because the test is conducted in a micro-tunnel, it is considered a validation, not a demonstration experiment. The heating test involves two types of bentonite buffer materials: (i) a bentonite pellets and (ii) a sand bentonite mixture emplaced in two sections isolated from the rest of the micro-tunnel (Figure 2.18 (b)) by three plugs. The heater-buffer interface is heated to a maximum temperature of 135°C and a temperature of 60–70°C is expected at the buffer-rock interface. A dense instrumentation network was in place in the host rock surrounding the micro-tunnel from a previous experiment testing the impact of ventilation on the clay host rock, and has been improved for the purpose of the HE-E Heater Test (up to 40 piezometers in total); various sensors have also been placed in the buffer material. The heating phase started in the late summer of 2011 and is still ongoing.
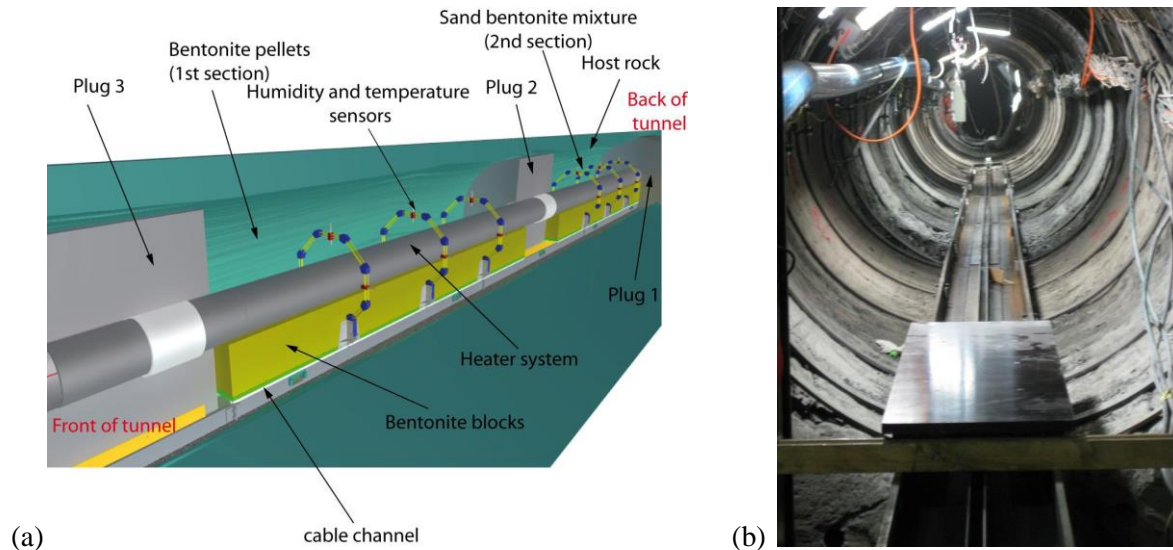
Figure 2.18. (a) Schematic setup of HE-E experiment at Mont Terri and (b) photo of micro-tunnel (Garitte, 2012).

2.3.1 DECOVALEX-2015 Task B1 and international modeling teams

In DECOVALEX-2015 (Task B1), eight international research teams were participating in the modeling of the HE-E experiment. Task B1, which was running over three years (2012 to 2015), was divided into the following steps:

- Step 1a: Opalinus Clay study including HE-D experiment, literature study, processes understanding and parameter determination.

- Step 1b: Buffer material study including CIEMAT column cells, literature study, processes understanding and parameter determination.

- Step 2: HE-E predictive modeling using as-built characteristics and true power load.

- Step 3: HE-E interpretative modeling and forward analysis

Step 1a started in 2012 with the modeling of the previous HE-D experiment for *in situ* characterization of THM material parameters for the Opalinus Clay and was completed in November 2013. The HE-D experiment involved one year of heating of the Opalinus Clay without any bentonite buffer. The modeling of the HE-D experiment and comparison of the TOUGH-FLAC modeling results to the results of other modeling teams were reported in the FY2013 milestone report titled "Report on THMC modeling of the near field evolution of a generic clay repository: Model validation and demonstration" (Liu et al., 2013). Step 1b, which is a study of buffer material properties through modeling of laboratory experiments on buffer material samples, has been completed by all the modeling teams in DECOVALEX-2015. LBNL's final analysis of the CIEMAT column experiments associated with Step 1b was presented in the FY2014 milestone report entitled "Investigation of Coupled Processes and Impact of High Temperature Limits in Argillite Rock" (Zheng et al., 2014). In FY2015 milestone report titled "Investigation of Coupled Processes and Impact of High Temperature Limits in Argillite Rock" we presented the TOUGH-FLAC model prediction of the Mont Terri HE-E experiment with some initial comparison to field data.

In this section we provide a summary of results related to DECOCALEX-2015 Task B1, Steps 1 to 3, including comparison with other research teams in the DECOVALEX-2015 project. Table 2.5 shows an overview of the eight modeling teams, including their codes and models for Step 1 to 3 in DECOVALEX 2015 Task B1. The predictive analysis involved a blind prediction of the responses during the three years of heating using material properties determined from modeling of the HE-D and column experiments. Then a refined or interpretative analysis was done once the field data had been distributed to the research teams. Finally, the forward analysis involved a prediction of the time to full saturation of the bentonite buffer, if the heating were to be turned off after eight years.

Table 2.5. Modeling teams, codes and models of DECOVALEX-2015 Task B1 related to the Mont Terri HE-E experiment.

Team	Code	HE-D	Column test	HE-E (all 3D THM, excepted CNWRA)		
				Predicted	Refined	Forward
BGR/UFZ	OpenGeoSys	3D THM	2D THM	√	√	√
CAS	EPCA3D	3D THM	3D THM	√	√	-
LBNL	TOUGH-FLAC	3D THM	2D THM	√	√	√
ENSI	OpenGeoSys	3D THM	2D TH	√	-	-
CNSC	COMSOL	3D THM	1D THM	√	-	-
JAEA	THAMES	3D THM	2D THM	√	-	-
KAERI	FLAC	3D THM	2D TH	√	√	-
CNWRA	xFlo-FLAC	2D THM	2D THM	√	√	√

2.3.2 Modeling of the HE-D Experiment for THM Characterization of Opalinus Clay

Step 1 of DECOVALEX-2015 involved modeling of the Mont Terri HE-D experiment with main purpose of determining and validating in situ THM properties of Opalinus Clay. The HE-D experiment was conducted between March 2004 and June 2005 by *in situ* heating of Opalinus Clay from two heaters placed in a horizontal borehole (Figure 2.19) (Wileveau, 2005; Gens et al., 2007). Around this heating borehole, about 30 temperature sensors, 10 water pressure sensors, and 3 extensometers were placed, which allowed for monitoring the evolution of the variables induced by the heating (Wileveau, 2005; Gens et al., 2007). Approximately one month after installation, the heaters were switched on with a total power of 650 W (325 W per heater). The heaters were then left under constant power for 90 days. Afterwards, the power was increased threefold, to 1950 W (975 W per heater), and maintained at that level for a further 248 days. At the end of this second heating stage, the heaters were switched off and the clay was allowed to cool down. Temperature, pore pressure, and deformation were measured throughout. In Figure 2.19, the positions of the main temperature and pore pressure sensors with respect to the heater axis are indicated.
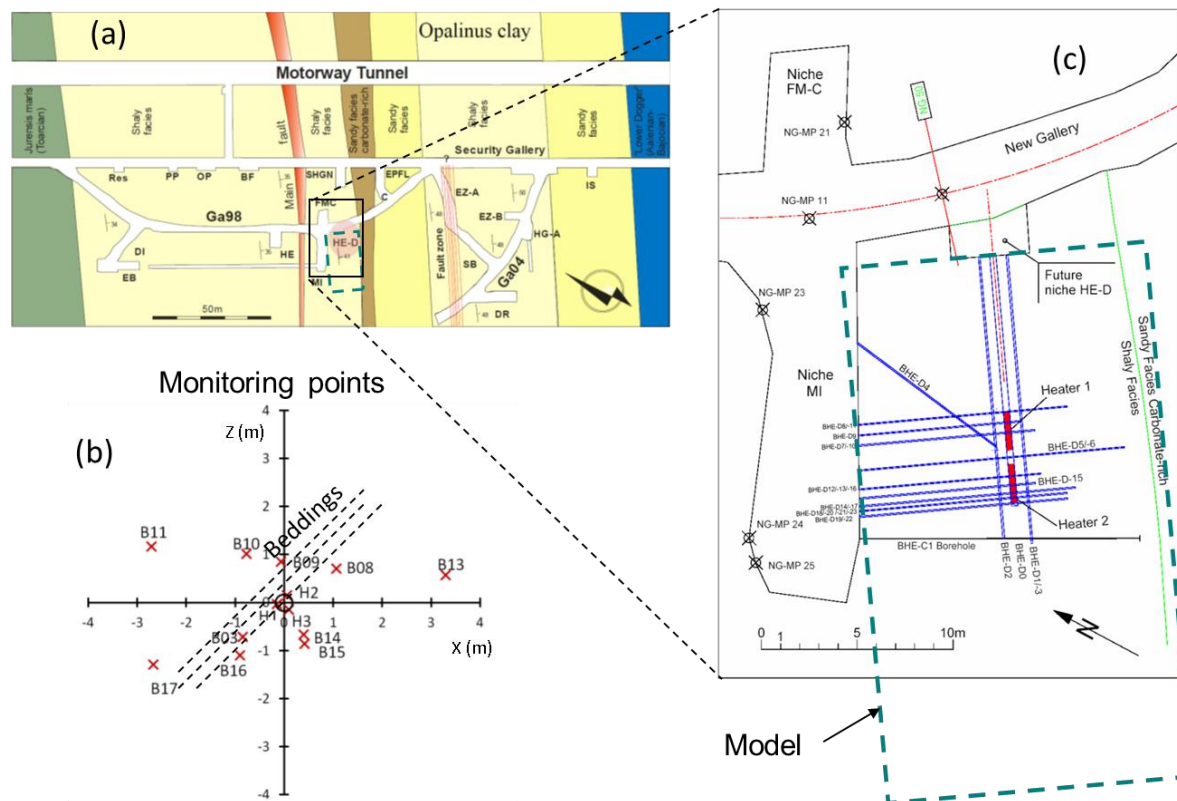
Figure 2.19. Layout of the HE-D experiment including. (a) Horizontal cross-section showing the location of the HE-D experiment in the Mont Terri URL. (b) Vertical cross-section showing monitoring points and directions of bedding planes, and (c) top view of experiment including monitoring borehole layout (Wileveau, 2005).

2.3.2.1   LBNL Model Setup of HE-D experiment

We modeled the HE-D experiment using the TOUGH-FLAC simulator employing an anisotropic material model considering the beddings of the Opalinus Clay. To accurately model anisotropic

thermal behavior in TOUGH2, the mesh was inclined along with the beddings (Figure 2.20). Anisotropic mechanical material behavior is simulated using a so-called ubiquitous joint model, available in FLAC3D, with properties derived from published work (Corkum and Martin, 2007). These included parameters for the FLAC3D ubiquitous joint model defining anisotropic strength properties, a bulk modulus of 4.17 GPa, and a shear modulus 1.92 GPa. The thermal expansion coefficient was set to 1.4×10^{-5} °C^{-1} which is a representative isotropic average value of the Opalinus Clay (Gens et al., 2007). Finally, we assigned an isotropic permeability of 5×10^{-20} m^2, and pore compressibility of 1×10^{-9} Pa^{-1}, based on Gens et al. (2007). In the simulation presented here the permeability was set to an isotropic value 5×10^{-20} m^2 according to previous simulations by Gens et al. (2007), although permeability at the Mont Terri is anisotropic by a factor of about 4.
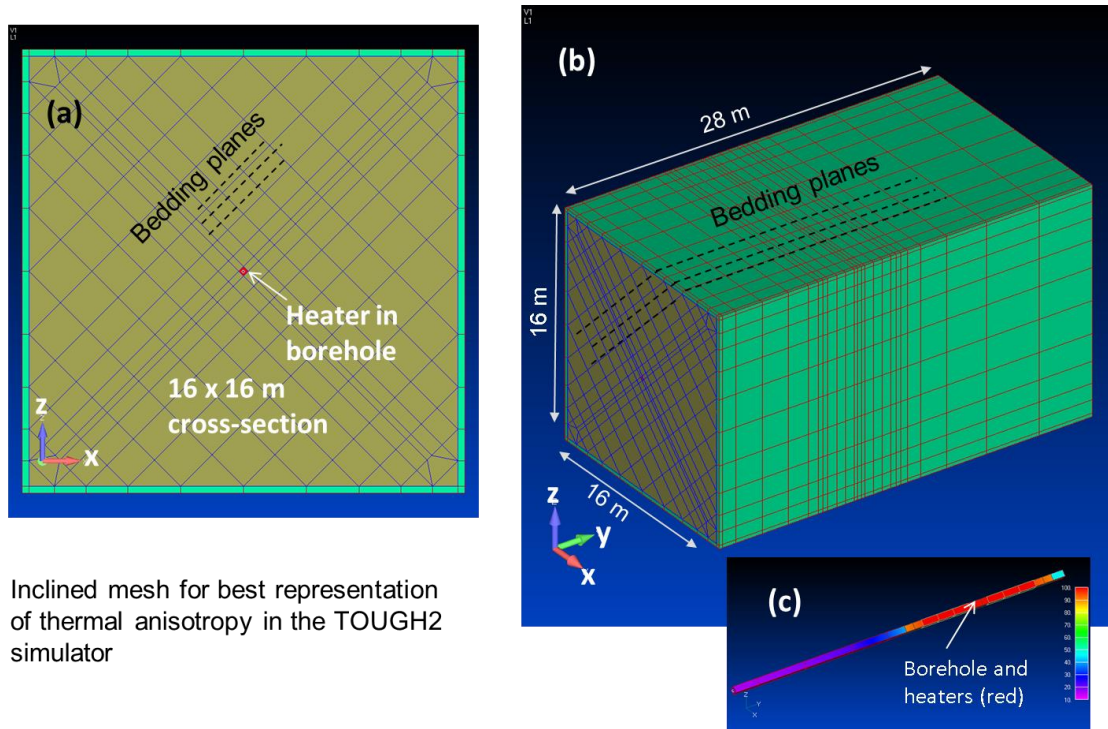
Figure 2.20. TOUGH-FLAC model for the analysis of coupled THM processes at the HE-D experiment.. (a) vertical cross-section showing the inclined mesh along bedding, (b) Entire 3D model, and (c) view of the micro-tunnel with heater shown in red.

The initial hydraulic and thermal conditions for the model simulation were 0.9 MPa in pore fluid pressure and 15°C in temperature within the host rock. The 0.9 MPa of pore pressure is not under hydrostatic conditions, and the process is affected by the existing tunnel system at the site. A stress field was applied based on the best estimated Mont Terri *in situ* stresses. The vertical stress was set to 7 MPa, whereas the maximum and minimum horizontal stresses were respectively set to 5 MPa (along x-axis) and 2 MPa (along y-axis, which correspond to the strike of bedding) (Figure 2.20 (b)).

2.3.2.2 LBNL Results with Comparison to HE-D Field Data

The modeling shows that the heating of the rock mass is the driving force for the THM responses in the HE-D experiment. Temperature changes strongly affect hydraulic and mechanical responses whereas thermal processes are not significantly impacted by the hydraulic and mechanical processes. Heat transfer is dominated by thermal conduction and the temperature evolution can be calculated independently of the hydraulic and mechanical processes. In this case we input the measured heat load and then calibrated the transversely anisotropic thermal conductivity until a are in agreement was obtained between simulated and measured temperature evolution at 31 locations in the rock mass. A good overall temperature match was obtained for thermal conductivity parallel to the bedding planes, $K_\parallel = 2.15$ W/m-K, and perpendicular to bedding planes, $K_\perp = 1.19$ W/m-K; a thermal conductivity anisotropy factor, $K_\parallel/K_\perp = 1.8$. Moreover, an additional heating-system power loss of 5% was assumed for achieving the best overall match between simulated and measured temperature evolution.

Figure 2.21 shows comparison of LBNL simulated and measured temperature (Figures 2.21 (a) and (b) and pressure (Figure 2.21 (c) and (d)) at two monitoring points (B16 and B15), and strain at another location close to B04. The simulation shows a correlation between temperature and fluid pressure as a result of thermal pressurization, which occurs as a result of the differences in the coefficient of thermal expansion between the fluid and the solid rock. As previously mentioned, a good temperature agreement is achieved using an anisotropic thermal conductivity. A reasonably are in agreement between simulated and measured pressure is achieved with the permeability set to 5×10^{-20} m^2 and a pore compressibility of 1×10^{-9} Pa^{-1}. This pore compressibility was estimated from the elastic properties of the rock assuming uniaxial strain conditions (Rutqvist et al., 2014a). The strain results shown in Figure 2.21(e) were measured from the relative displacement between two anchor points located about 1 m from each other and in the radial direction from the heater hole (represented in Figure 2.21(e) by endpoints of the green line. The fact that these anchor points are located in the radial direction means the radial strain can be back calculated from the relative displacements between these anchor points. The radial strain mainly shows a compression during heating as rock is expanded from the heated borehole.
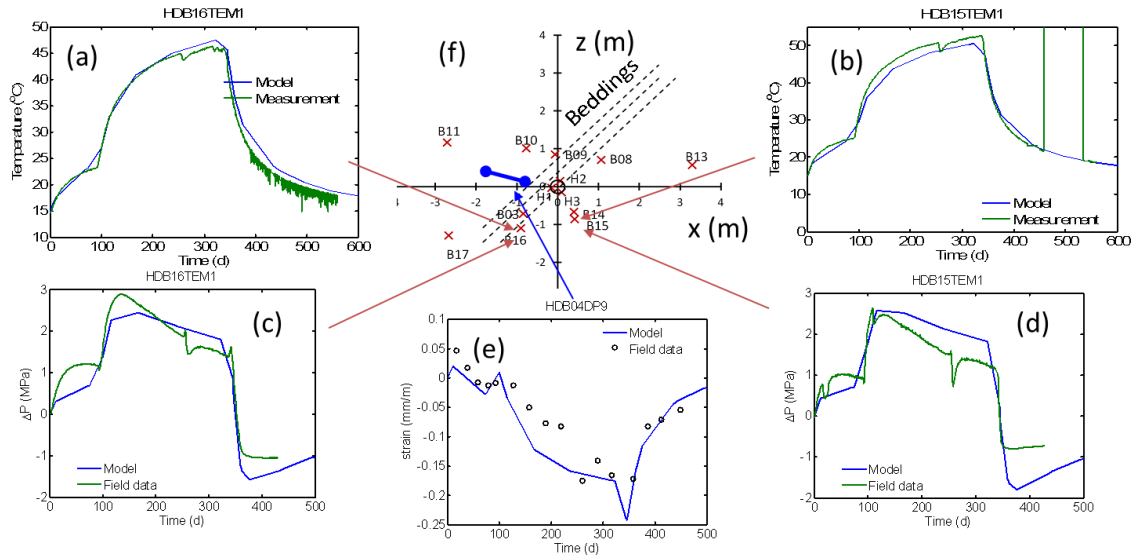
Figure 2.21. Comparison of simulated and measured (a and b) temperature and (c and d) pressure at two monitoring points (B15 and B16) and €strain at a location close to the heater. (f) location of the monitoring points relative to the heater and position of the two anchor points used to estimate the radial strain.

2.3.2.3 Comparison between 8 DECOVALEX-2015 modeling teams and HE-D data

As previously mentioned, a total of eight modeling teams were involved in comparative calculations of the THM processes with different codes (Table 2.5). The comparison of the results for the temperature field shows a are in agreement between the teams and the simulated temperatures are close to the measurements. One example is shown in Figure 2.22 for two temperature sensors. Sensor HEDB03 is located at a distance of 1.11 m away from the center of the heater parallel to bedding, whereas sensor HEDB14 is located 0.775m away perpendicular to bedding. Figure 2.22 shows a are in agreement between the results of the different groups as well as between simulations and observations. The comparison of these sensors also illustrates the effect of the anisotropic heat conductivity of Opalinus clay. Despite the different distance to the heater, both sensors show a similar course of temperature evolution over time. The largest disagreement shown is for one team at sensor HEDB14 in which the temperature was overestimated because the simulation was conducted with an axisymmetric model in which the thermal anisotropy could not be considered. Other comparisons of thermal pressurization and displacements were not as good for temperature, though the main THM responses were captured by all the modelling teams (Garitte, 2016).

62

(a)

(b)
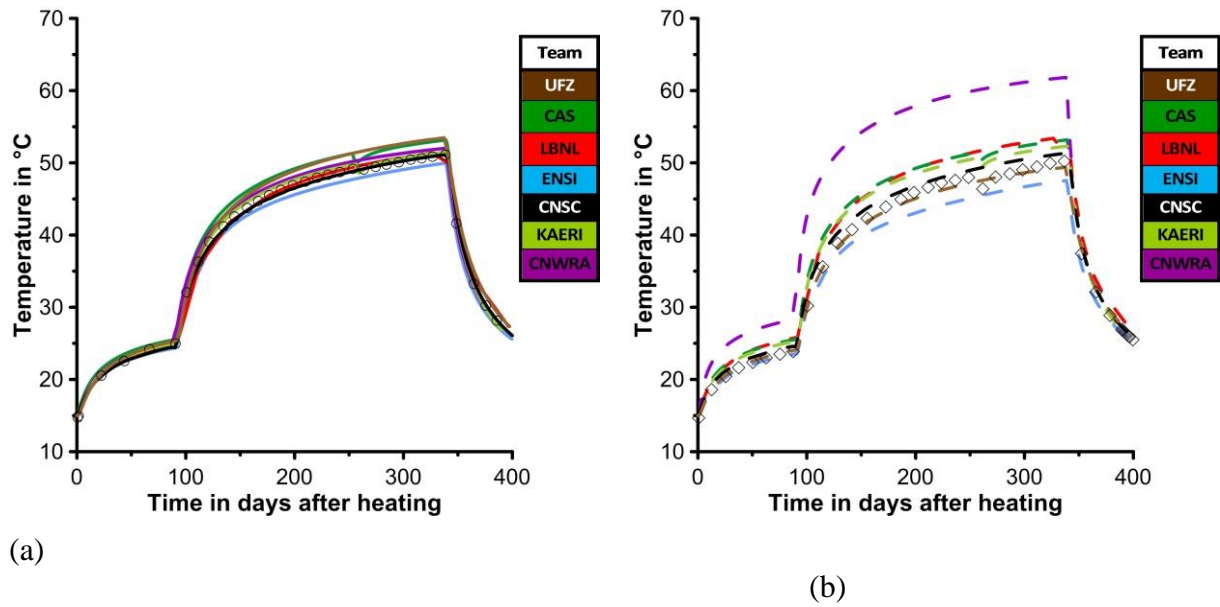
Figure 2.22.Comparison of measurements and model results of for the temperature evolution over time at sensors (a) HEDB03 and (b) HEDB14 (Graupner et al., 2013).

2.3.3 Buffer material characterization using CIEMAT column experiments

In this subsection we summarize the results of the modeling of CIEMAT column experiments (Villar 2012). The modeling of the CIEMAT column experiments are done for characterization of the buffer material. In CIEMAT column experiments, two buffer materials, granular bentonite (or bentonite pellets) and sand/bentonite mixture, were tested. However, in DECOVALEX-2015, only the granular bentonite experiment was required to be modeled by the research teams, whereas it was optional to model the sand/bentonite experiment.

The design of the column experiments mimicked the HE-E conditions, with the height of the column equal to the thickness of the buffer filled between the canister and host rock (Figure 2.23). A heater was placed at the bottom and a cooler was placed at the top of the column, so that the column was heated while the top remains at an ambient temperature of approximately 21.5 ˚C. During the experiments, temperature and relative humidity were measured at three points along the axis of the column (T1, T2, and T3, and Fig. 2.23). The wall of the column is made up of Teflon. The column was wrapped with a layer of foam, which was later replaced with rock wool and BT-LV insulation materials (Villar, 2012). The power input was monitored as well. In this study, the objectives were to model the fluid flow and heat transfer processes that occur in the experiment, and to calibrate the flow and thermal properties of the two buffer materials against the experimental measurements. The initial modeling of the experiment revealed substantial heat loss through the equipment and it was necessary to consider this heat loss in the numerical modeling. Actually, the model simulation indicated that only about 20% of the power input entered the bentonite sample.
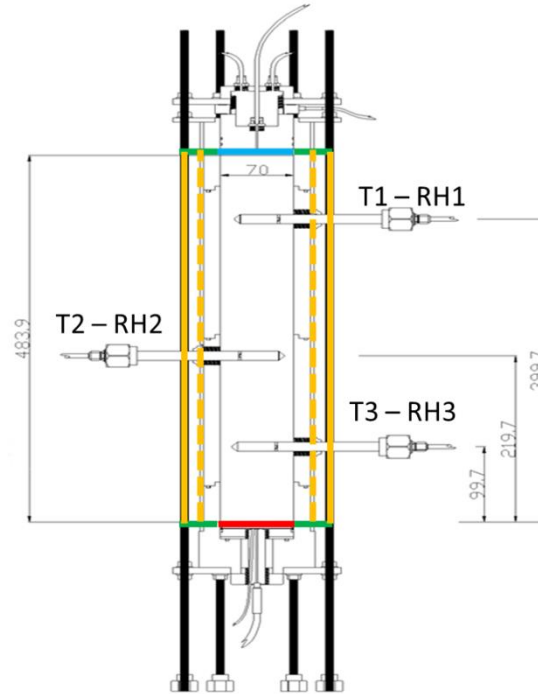
Figure 2.23. Experiment layout of the CIEMAT column test, dimensions given in mm (Garitte, 2016). Heater is in red at the bottom and cooler in blue on top.

2.3.3.1 LBNL model setup of column experiment

A 2D radial symmetric mesh of 9×28 elements was created for the modeling of this column experiment (Figure 2.24). Bentonite is represented in a zone of 4×25 elements (grey zone in Figure 2.24). The multiple stages of the experiment were simulated sequentially and the boundary conditions of each step were adjusted according to the experiment. This also includes the aforementioned addition of more insulation materials after 1566 hours of heating. During the experiment, the hydration valve was closed and therefore no water flowed into the column before the start of heating. Fixed temperature conditions at the heater were simulated by assigning a large heat capacity to the heater elements. To simulate the temperature increase at the heater elements, e.g., from 21.5 to 100 ºC, and from 100 to 140 ºC, a heating rate was applied to the heater element, such that the heating rate equal to the experiment. Hydration was simulated by assigning a constant absolute pressure of $1.1×10^4$ Pa at the top boundary.
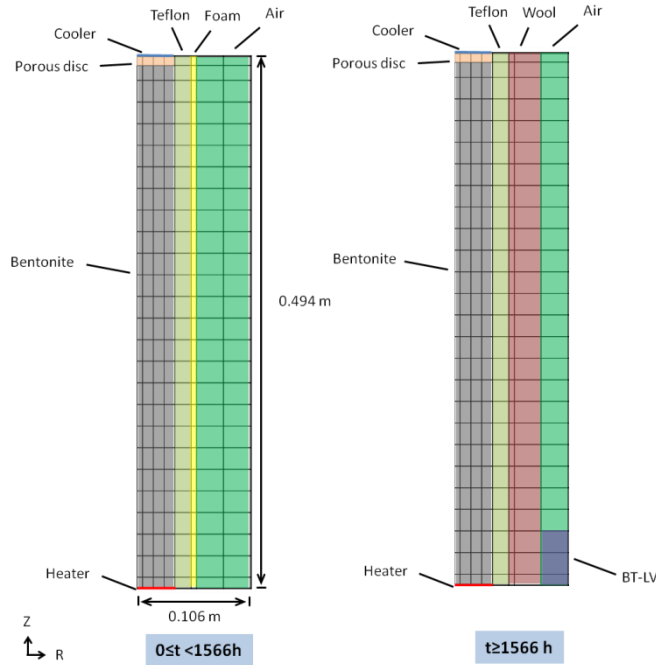
Figure 2.24. Model mesh and the materials represented in the model at different steps for column experiment on bentonite pellets. The reference time (t = 0) is the start of heating.

The granular bentonite has a solid grain density of 2700 kg/m^3 and a porosity of 0.46 (Villar, 2012). The specific heat of the bentonite is 950 J/kg°C. The pores were initially saturated with 22% of water and the measured relative humidity was 40% uniformly along the column. Olivella and Gens (2000) reported that the measured permeabilities of FEBEX and Boom clay samples to gas are about 6-7 orders of magnitude higher than those to liquid. To account for the increased gas permeability, we considered vapor and air diffusion and Klinkenberg effect in the model. A diffusion coefficient of 2.13×10^5 m^2/s was used for both vapor and air and a tortuosity factor of 0.67 was used in the model. An artificial Klinkenberg parameter of a very high value of 2.5×10^{11} Pa was used. This high value of the Klinkenberg parameter was applied to simulate the effect of a very high gas intrinsic permeability.

2.3.3.2 LBNL Back-analysis of THM properties

The model analysis of the column experiment was conducted to back-analyze a number of THM properties of the granular bentonite. The most important parameters back-analyzed were

1) Thermal conductivity of the granular bentonite and its dependency on water saturation was back-calculated by examining the transient and steady state behavior

2) A temperature dependent capillary pressure curve was determined using previous experimental results of water retention and by further model calibration against moisture movements in the column experiment.

3) Calibration of intrinsic permeability against and initial infiltration test on the column

Figure 2.25 shows the best match simulation results and measured data. After the heater was turned on (t=0h), the simulated relative humidity increased rapidly at 10 cm (orange curve on Fig. 2.25a). This is caused by the upward-flowing vapor from the heated zone beneath the sensor. Over time, the relative humidity decreases at the 10-cm location, as a result of drying that occurred at the 10-cm location caused by continued heating. A discrepancy between the simulated and measured relative humidity appears after 3527 h, when insulation was improved (foam replace by wool, see Fig. 2.24). This might be caused by the fact that the van Genuchten function overestimates the increase of capillary pressure at low water saturations, causing the underestimation of relative humidity at the 10-cm location. The upflow of vapor is evidenced by the continuous increases in relative humidity at the 22- and 40-cm locations (blue and red curves, respectively). Overall, the simulated relative humidity and the temperature evolution (Fig.2.25b) at these three locations are in are in agreement with the measured ones.

(a)

(b)
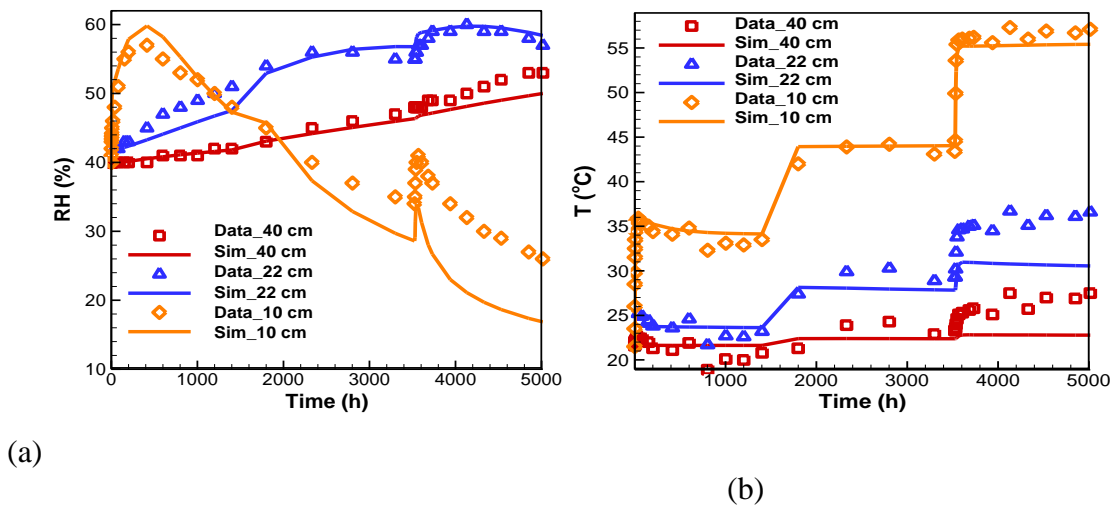
Figure 2.25. Simulated and measured (a) relative humidity and (b) temperature at 10, 22, and 40 cm from the heater.

2.3.3.3   *Comparison between 8 DECOVALEX-2015 modeling teams*

Figure 2.26 shows the comparison of relative humidity evolution calculated by eight DECOVALEX-2015 research teams and measured data. Figure 2.26 shows two stages of data and modelling results

1) The initial 5000 hours (208 days) of data during heating that was used to calibrate the THM properties of the bentonite

2) The following 5000 to 20000 hours (208 to 833 days) of data that was given to teams after their modelling and thus represent a model prediction of the longer term resaturation.

The initial 5000 hour part in Figure 2.26 is the same as shown in Figure 2.25 (the yellow diamonds, triangle and circle in Figure 2.26 correspond to the orange, blue and red lines in Figure 2.26 (b). The modelling teams could model the general responses of drying near the heat source and wetting near the cold and end of the column and infiltration boundary. Note that there

was no infiltration before 5000 days, meaning that increased relative humidity at the cold end as seen in Figure 2.25 (a) (blue triangle) is a result of vapor transport in the gas phase from the hot end towards the cold end where condensation takes place. The overall agreement between models and measurement is very good. This is also clear from Figure 2.27, which shows a are in agreement of the overall relative humidity distribution profile at 5000 and 10000 hours.
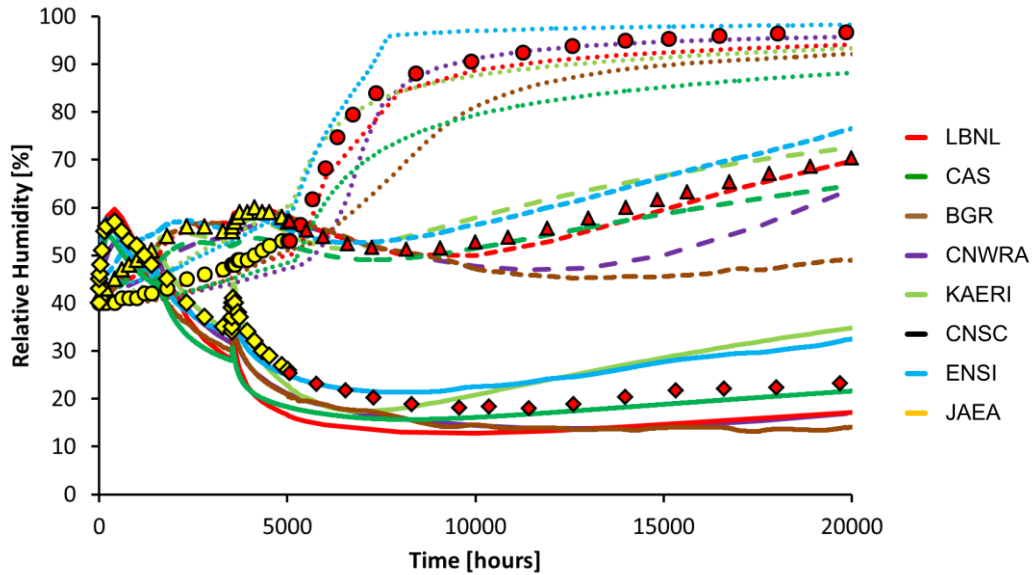
Figure 2.26. Measured and modelled relative humidity in the column at RH1 (circles and dotted lines), RH2 (triangles and dashed lines) and RH3 (diamonds and full lines) during the heating and hydration phase. (Yellow measurement dots, before hydration phase were used by the teams to calibrate the models; red measurement dots were acquired during the hydration phase and the corresponding modelling results are predicting results) (Garitte, 2016).
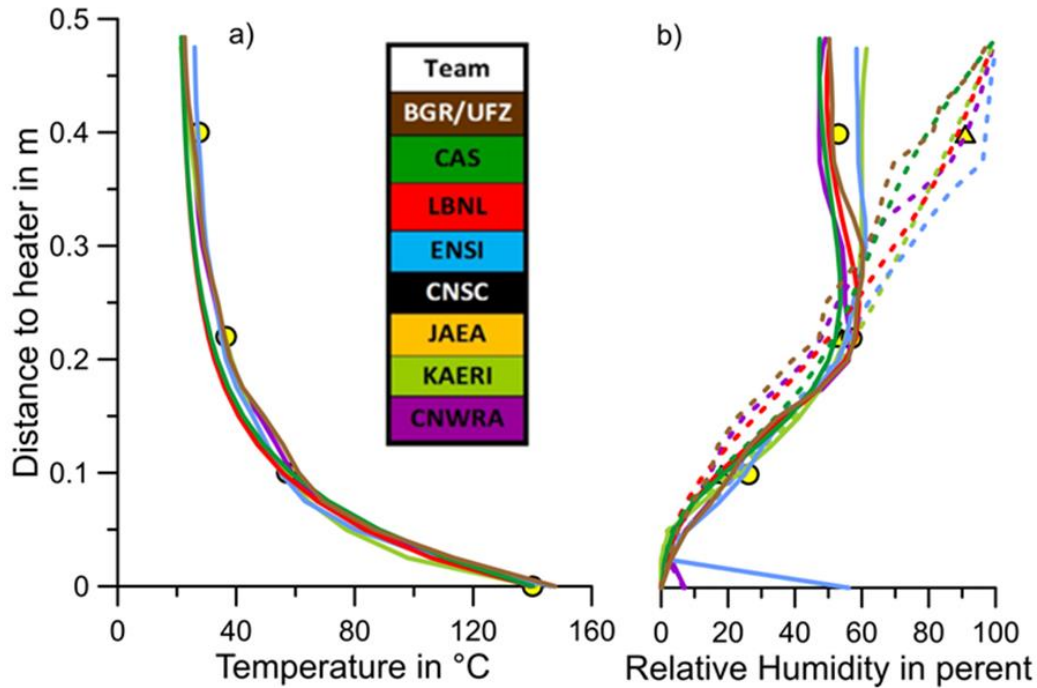
Figure 2.27. Vertical measured and modelled profiles for (a) temperature at 5000 hours and (b) relative humidity after 5000 and 10000 hours. The measurements at 5000 hours are shown as discrete points marked with circles whereas measured relative humidity at 10000 hours are marked with triangles. Solid lines are modeling results at 5000 hours and dashed lines are relative humidity modeling results at 10000 hours (Garitte, 2016).

2.3.4   Predictive Modeling of the Terri HE-E experiment

In the predictive modeling of the HE-E experiment, the models applied and input material parameters were based on those determined and validated using data from the HE-D experiment and the CIEMAT laboratory column experiment as described in the previous section.

2.3.4.1   *LBNL Model setup of the Mont Terri HE-E experiment*

Figure 2.28 shows a 3D model grid for the HE-E experiment and its location within the Mont Terri URL, whereas Figure 2.29 shows more details of the materials in a vertical cross-section that is also the geometry of a 2D plane strain model. It is a half symmetric model with a vertical symmetry plane along the tunnel axis. In the model, the relevant materials are represented, including the different types of bentonite materials. The most important thermal and hydraulic properties, listed in Table 2.6, were derived from modeling of the Mon Terri HE-D and CIEMAT column laboratory experiment as well as literature data.
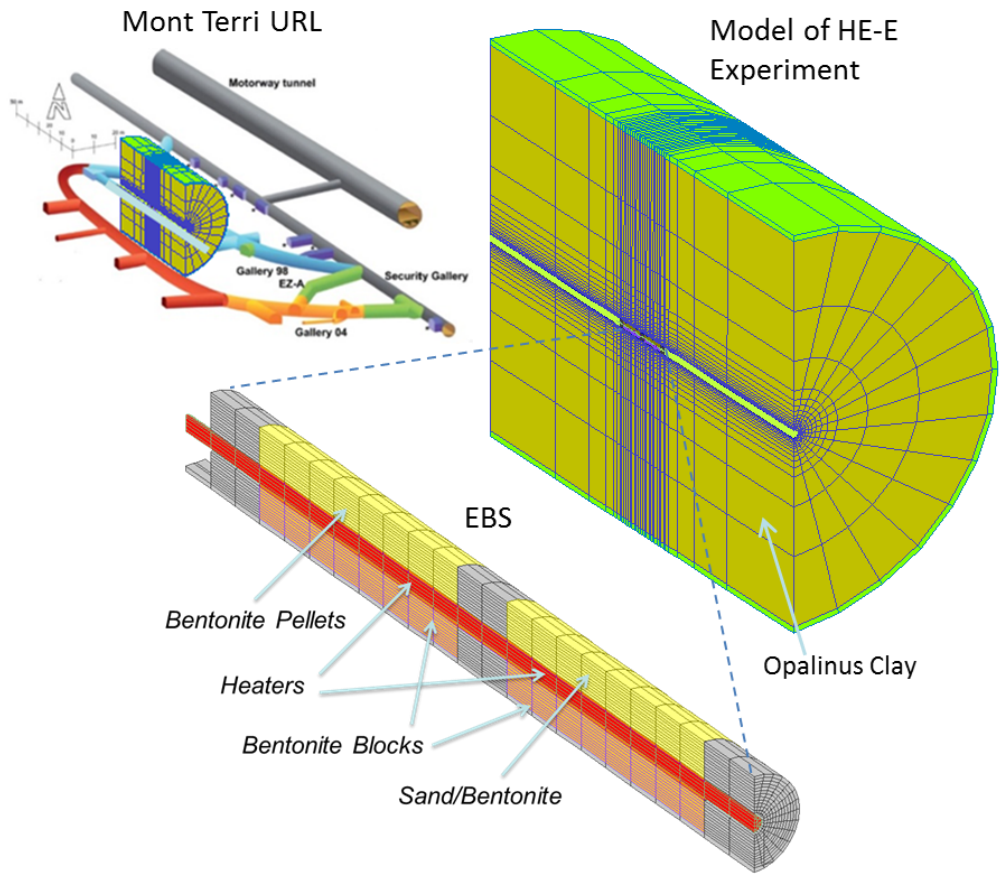
Figure 2.28. TOUGH-FLAC 3D model of the Mont Terri HE-E experiment.
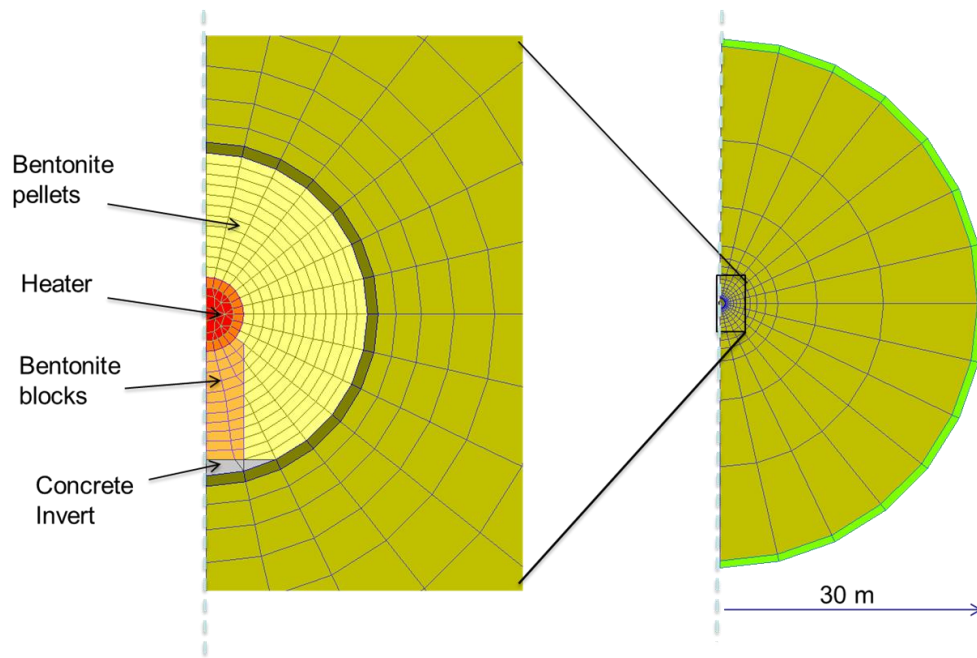
Figure 2.29. Vertical cross-section through the model grid.

Table 2.6. Parameters used in the predictive modeling of the Mont Terri HE-E experiment.

Parameters	Symbol	Opalinus Clay	Granular Bentonite	Bentonite blocks	Concrete (shotcrete and plugs)	Unit
Grain density	ρ_g	2.7×10^3	2.7×10^3	2.7×10^3	2.7×10^3	kg/m³
Porosity	Ø	0.15	0.46	0.389	0.15	-
Intrinsic permeability	k	5.0×10^{-20}	5.0×10^{-21}	2.0×10^{-21}	3.5×10^{-21}	m²
Liquid relative permeability (van Genuchten, 1980) $k_{lr}(S_l) = \left(\frac{S_l - S_{lr}}{S_{ls} - S_{lr}}\right)^A$	A	-	5	3	-	-
Liquid relative permeability (van Genuchten, 1980) $k_{lr}(S_l) = \left(\frac{S_l - S_{lr}}{S_{ls} - S_{lr}}\right)^{1/2}\left[1 - \left\{1 - \left(\frac{S_l - S_{lr}}{S_{sl} - S_{lr}}\right)^{1/m}\right\}^m\right]^2$	m	0.52	-	-	0.52	-
Capillary curve (van Genuchten, 1980) $\psi(S_l) = P0\left\{\left(\frac{S_l - S_{lr}}{S_{ls} - S_{lr}}\right)^{-1/m} - 1\right\}^{1-m}$	P_0	1.09×10^7	1.0×10^7	3.0×10^7	1.09×10^7	Pa
	M	0.29	0.4	0.32	0.29	-
	S_{ls}	1.0	1.0	1.0	1.0	-
	S_{lr}	0.01	0.0	0.0	0.01	-
Thermal conductivity (wet)	λ_{sat}	1.7	1.3	1.0	1.7	W/m°K
Thermal conductivity (dry)	λ_{dry}	1.06	0.3	0.5	1.06	W/m°K
Grain specific heat	C	800	950	950	800	J/kg°K

The modeling of the HE-E experiment was conducted in several steps (Figure 2.30), including

1) The tunnel being open for thirteen years at a constant relative humidity of 98%
2) Bentonite buffer and heaters emplaced for 75 days before start of heating
3) Heating for 1000 days

The simulation of the tunnel open for thirteen years at a constant relative humidity of 98% is simulated applying a constant suction value of 2.6 MPa at the tunnel wall. In reality, the tunnel was exposed to a complex history including ventilation experiments, and the average 98% relative humidity was inferred from information in Gaus et al. (2014). This created a pressure sink around the tunnel with a slight desaturation of the near field rock. The bentonite buffer and heaters where then simulated into the model by changing material properties for elements within the tunnel. Also the initial saturation of about 20% in the granular bentonite buffer was assumed based on in-situ observations Gaus et al. (2014). Finally, after another 75 days, the heaters were turned on following the heater power used in the actual experiment. In the simplified 2D model simulations used for the initial model predictions, the actual heat power was scaled down to represent the heat input per meter tunnel.
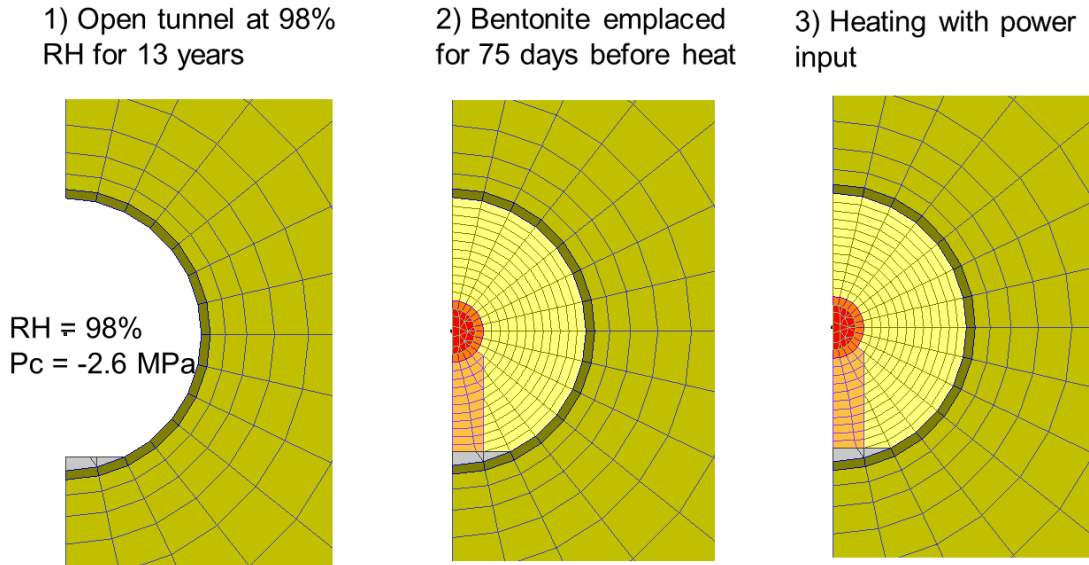
Figure 2.30. Steps for modeling the Mont Terri HE-E experiment. (RH= relative humidity, Pc = capillarity pressure)

2.3.4.2   *LBNL model prediction results with comparison to measurements*

Figure 2.31 shows the simulation results related to the evolution of liquid saturation and temperature from -100 to 1000 days, i.e. from 100 days before the start of the heating. Figure 2.31a shows that as soon as the bentonite buffer is installed (at -75 day), water is sucked into the bentonite from the adjacent rock. This is seen as a drop in liquid saturation in the rock (orange curve), while the saturation in the bentonite adjacent to the rock wall increases (blue curve). When the heating is turned on, a typical drying occurs at the inner part of the buffer (e.g. red line). Using the given heat power input, the maximum temperature of about 140°C is reached in less than 400 days, while the temperature at the rock wall gradually increases to about 60°C.

Figure 2.32 compares the simulated responses at two points located in the granular bentonite section with two points located within bentonite blocks, but located at about same distance from the heater. In this case the results are presented in terms of relative humidity and temperature. At the initial saturation of 20% in the granular bentonite, the relative humidity is about 40%, whereas in the bentonite block initial saturation was about 65% with a relative humidity of about 60%. The relative humidity for a given degree of saturation depends on the capillary pressure and hence the water retention curve. A higher saturation in the bentonite blocks, results in a higher thermal conductivity which explains the difference in the temperature between the monitoring points in the granular bentonite and the bentonite blocks.

A comparison of the predicted and observed evolutions of relative humidity and temperature is shown in Figure 2.33. The figure shows that the general humidity behavior of the bentonite at the rock wall and drying of the inner parts of the bentonite buffer are captured in the modeling. Modeling results for relative humidity, which is related to saturation, show very are in agreement with measurements for the blue and red curves (i.e., close to the rock wall and close to the heater). However, the model overestimates relative humidity in the mid part of the bentonite buffer (green curve). Nevertheless, the overall evolution of relative humidity was reasonably predicted by the modeling.

71

Figure 2.34a shows the evolution of fluid pressure within Opalinus Clay at a monitoring point located 3.54 m from the tunnel wall. This increase in fluid pressure is a result of so-called thermal pressurization, caused by thermal expansion of the pore fluid that cannot escape in the relatively low-permeability host rock. The magnitude and duration of this excess pressure pulse depends on parameters such as rock permeability and compressibility of water and rock (Rutqvist et al., 2014b). Using the Opalinus Clay properties determined from the modeling of the HE-D experiments, it appears that the model could predict this pressure increase fairly well. However, when considering the initial pressure we can observe some more deviation between modeling and measurements.

Figure 2.34 (b) shows the pressure evolution in two other points that where selected as part of the model comparison for the DECOVALEX-2015, Task B1. Although these points are located in a borehole adjacent to the pressure changes are much smaller and the initial fluid pressure is much smaller. A better agreement might be obtained by reducing the initial fluid pressure in the model.

(a)

(b)
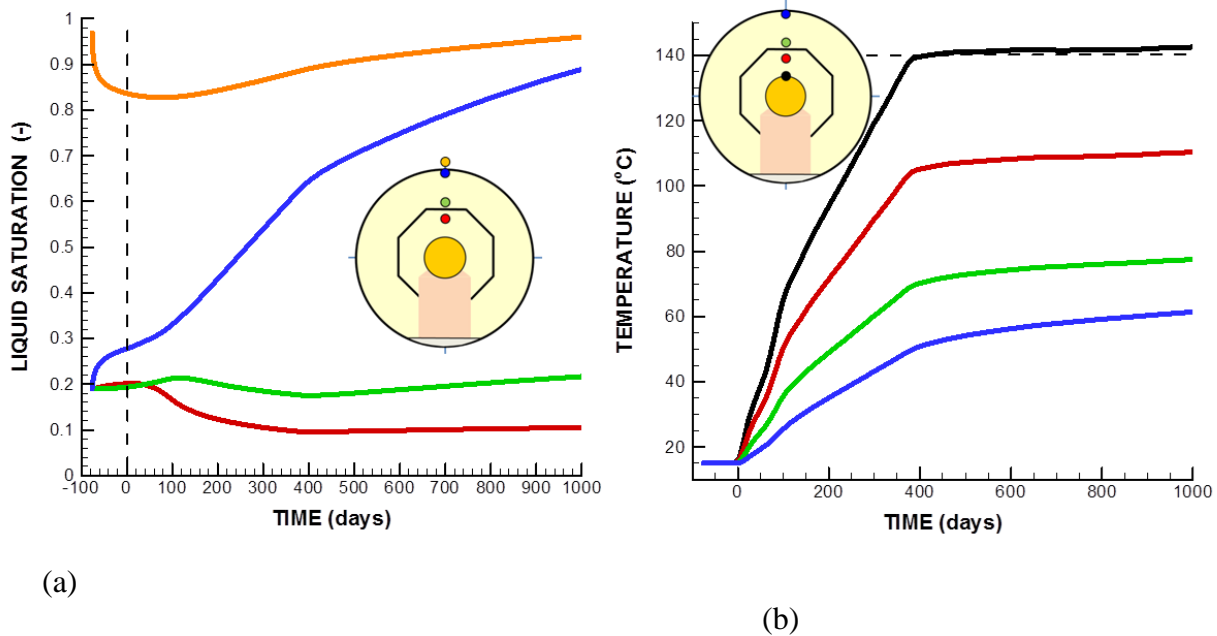
Figure 2.31. Calculated evolution of (a) liquid saturation and (b) temperature.
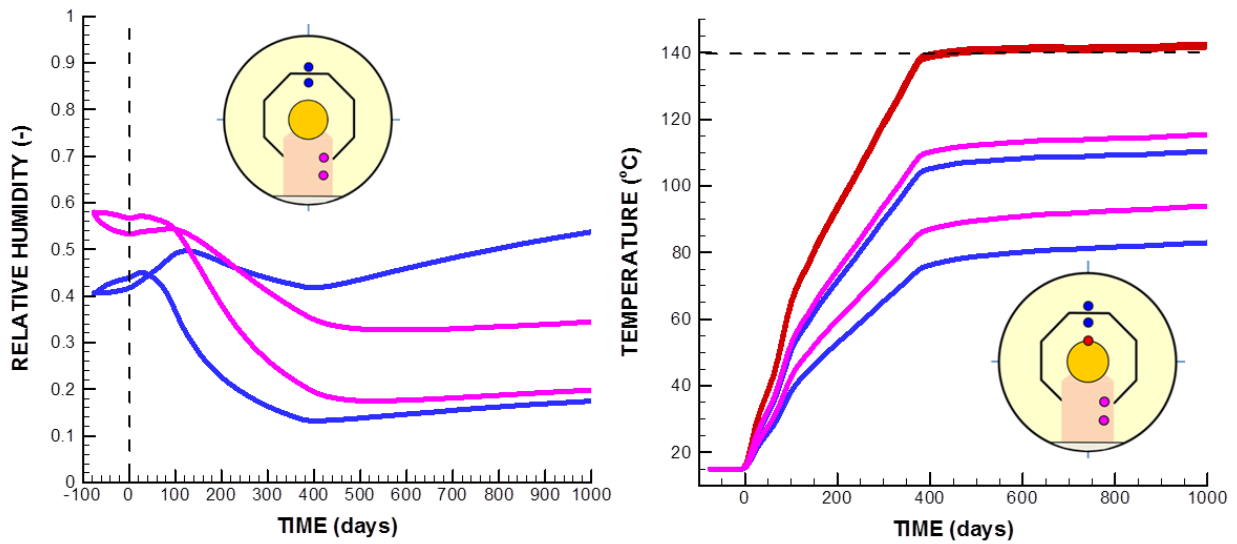
Figure 2.32. Calculated evolution of (a) liquid saturation relative humidity and (b) temperature at monitoring points in the granular bentonite (above heater) and bentonite blocks (below heater).
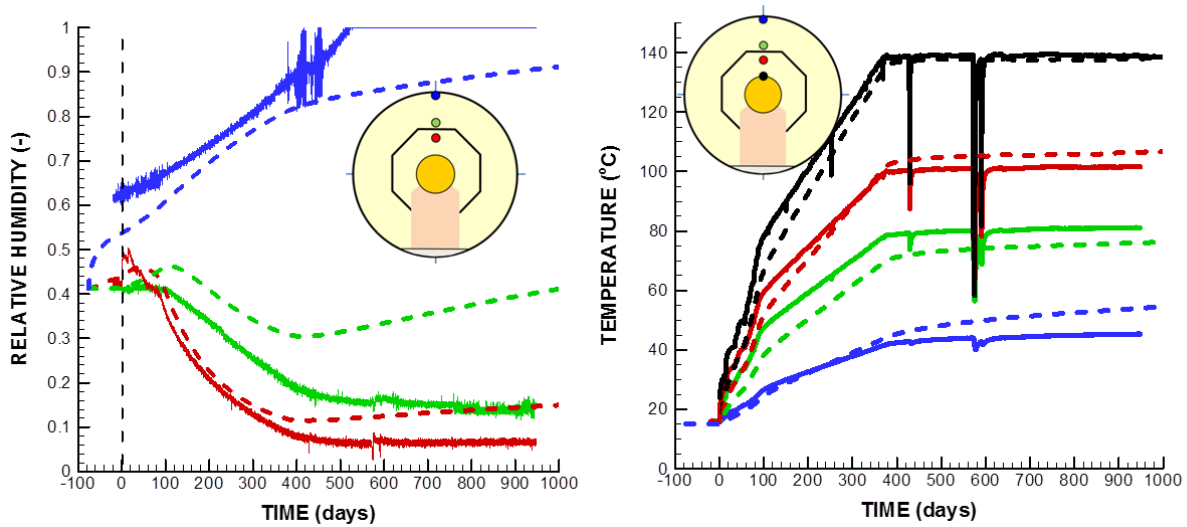
Figure 2.33. Comparison of predicted (dashed lines) and measured (solid lines) evolutions of (a) liquid saturation relative humidity and (b) temperature.

(a)

(b)
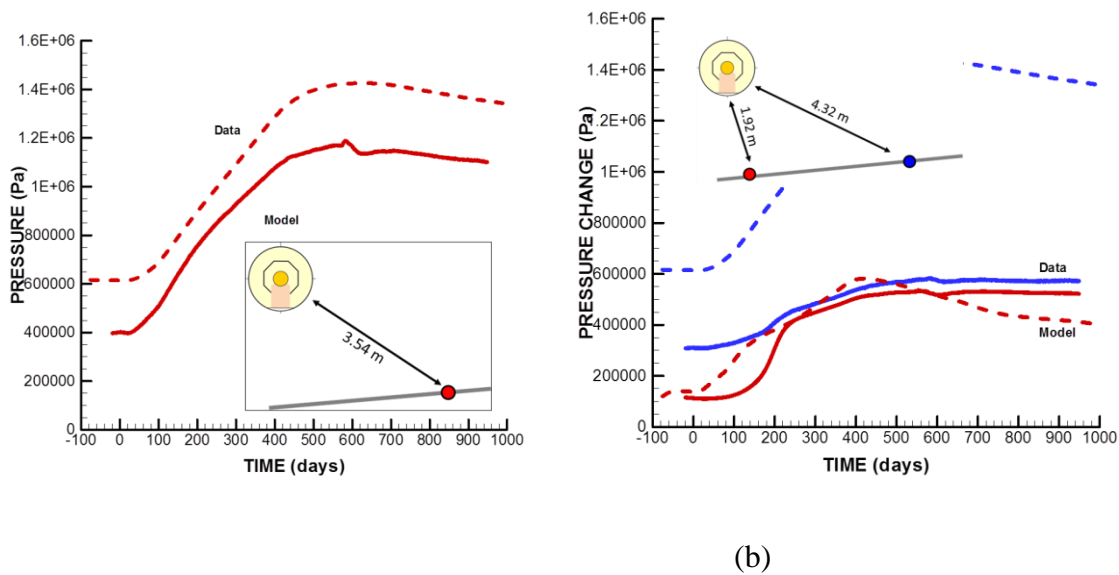
Figure 2.34. Comparison of predicted (dashed lines) and measured (solid lines) evolutions of pore pressure in Opalinus Clay at a various distances from the tunnel.

2.3.4.3   *Comparison between 8 DECOVALEX-2015 modeling teams*

Figures 2.35 and 2.36 show the comparison of the modeling predictions by eight DECOVALEX-2015 modeling teams and measured data at different locations within granular bentonite and bentonite blocks. The results in Figure 2.35 for locations closest to the heater show are in agreement between models and measurements. Some larger deviations between models and measurements can be observed in Figure 2.36 for locations at the mid-distance between heater and rock wall. Such disagreement is consistent with what can be observed in Figure 2.33 (a). Thus, it appears that the transient moisture movement in the buffer at the mid-distance between the heater and the rock wall is not captured very well in the model. There are a number of potential reasons for this which will be the subject of future studies.
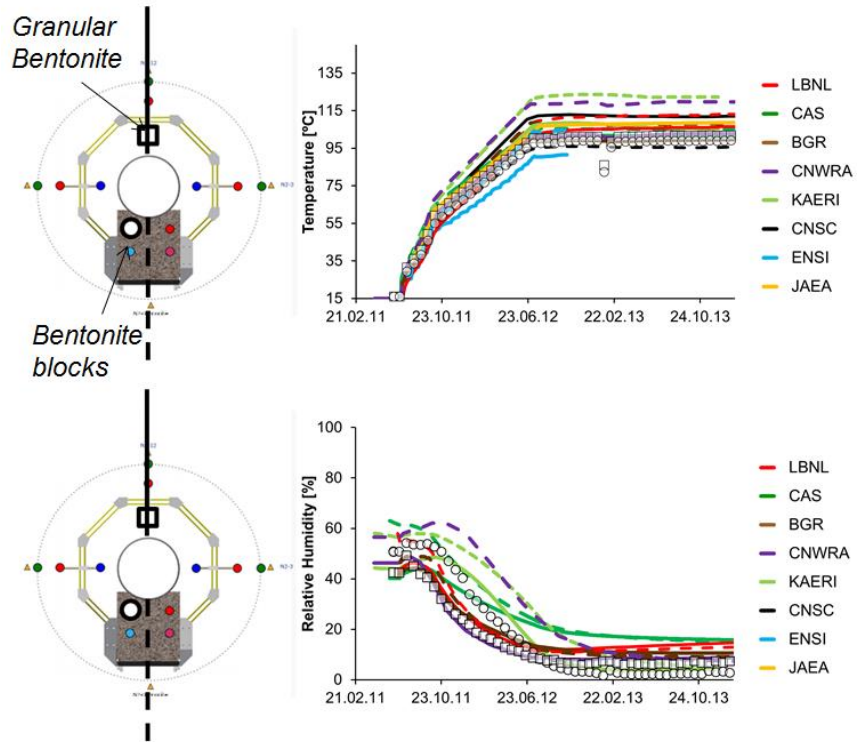
Figure 2.35. Comparison of predicted (lines) and measured (symbols) evolutions of temperature and relative humidity at points located 10 cm (in granular bentonite, white square in left figures) and 7 cm (in bentonite blocks, bigger white circle in left figures)) for eight modeling teams within the DECOVALEX-2015 project. Solid lines for modeling results in granular bentonite and dashed lines for modeling results in bentonite blocks (Garitte, 2016)
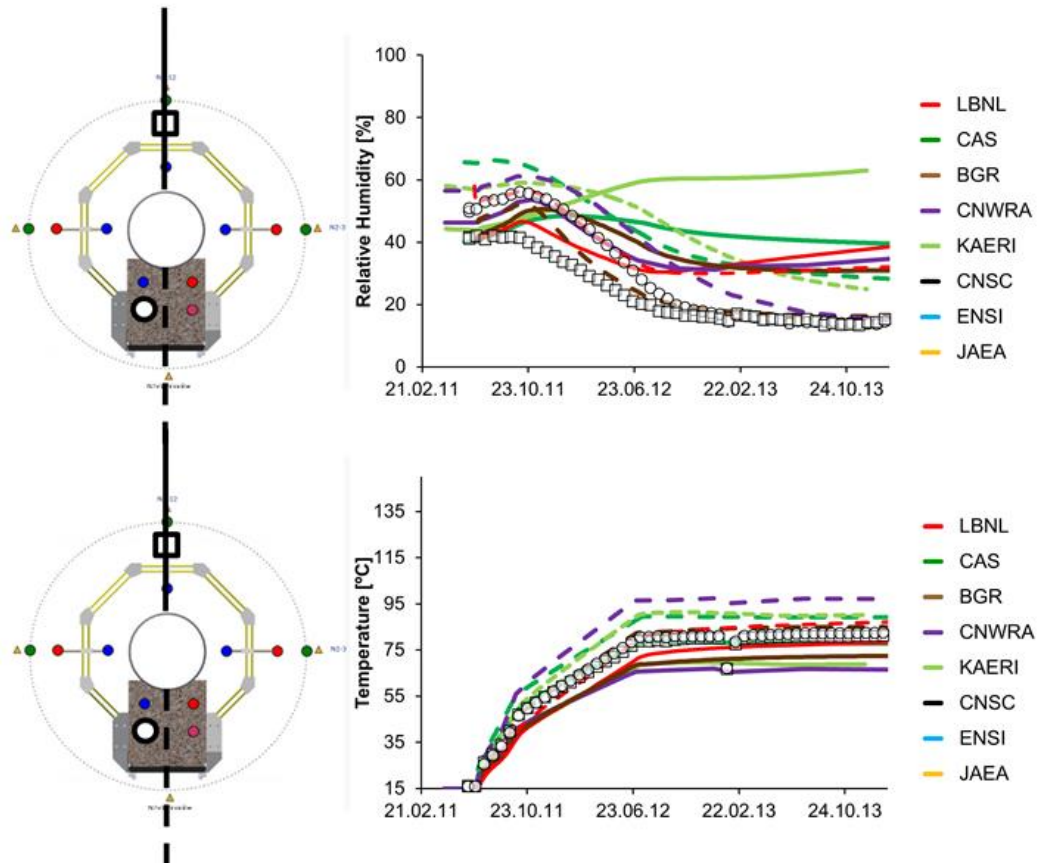
Figure 2.36. Comparison of predicted (lines) and measured (symbols) evolutions of temperature and relative humidity at points located 25 cm (in granular bentonite, white square in left figures) and 17 cm (in bentonite blocks, bigger white circle in left figures) for 8 modeling teams within the DECOVALEX-2015 project. Solid lines for modeling results in granular bentonite and dashed lines for modeling results in bentonite blocks (Garitte, 2016)

2.3.5 Interpretative Modeling of the Terri HE-E experiment

This section presents some of the interpretative modeling conducted in order to try to improve the modeling and material properties by calibration. This was defined as Step 3 in the DECOALEX-2015, Task B1 as described above. One obvious deviation between the initital predictive modeling (blind prediction in DECOVALEX-2015 Step 2) and measurements is the evolution of relative humidity in the mid-section of the buffer (green lines in Figure 2.33 (a). A parameter study was performed in order to try to find a way to improve the match of the relative humidity in the buffer mid-section, but it turned out that it was not possible to achieve a better match with the current model. The parameter study can be summarized as follows:

1) Buffer absolute permeability (no significant effect)
2) Diffusion coefficient (did not help)
3) Buffer relative permeability (lowered but did not help)
4) Water retention curve (varied but did not help)

The modeling showed that the moisture content in the inner and mid parts of the buffer achieves a pseudo steady state dictated by two-way diffusion, i.e. thermally driven vapor diffusion and a counter flow by capillary driven diffusion as been observed and modeled previously (e.g. Rutqvist et al., 2001b).

Another item that was studied in the interpretative modeling of the field data was an observed slight unsymmetrical temperature in the buffer. In the measurements, the temperature is somewhat lower in the lower part of the buffer, where buffer consists of pre-compacted blocks. A lower temperature was also observed at the heater surface on the lower part of the heater. This lowering of the temperature at the lower part of the heater could be modeled by reducing the thermal conductivity of the heater in the model from 12 W/ms to 6 W/ms. These appear to be artificially low values for steel, but it was sufficient to create spatially different temperatures around the heater surface in the model. On the other hand, using this approach it was not possible to model the observed lower temperature within the bentonite blocks compared to that of the granular bentonite buffer section.

The results of temperature and relative humidity with the updated parameters as a result of the interpretative modeling are presented in Figure 2.37 for the upper parts of the buffer. Compared to the model prediction shown in Figure 2.33, there are some improvements related to the relative humidity near the rock interface (blue curves), whereas there are only minor changes otherwise. The improvement near the rock interface was a result of a slight change in the water retention curve for the bentonite pellets.
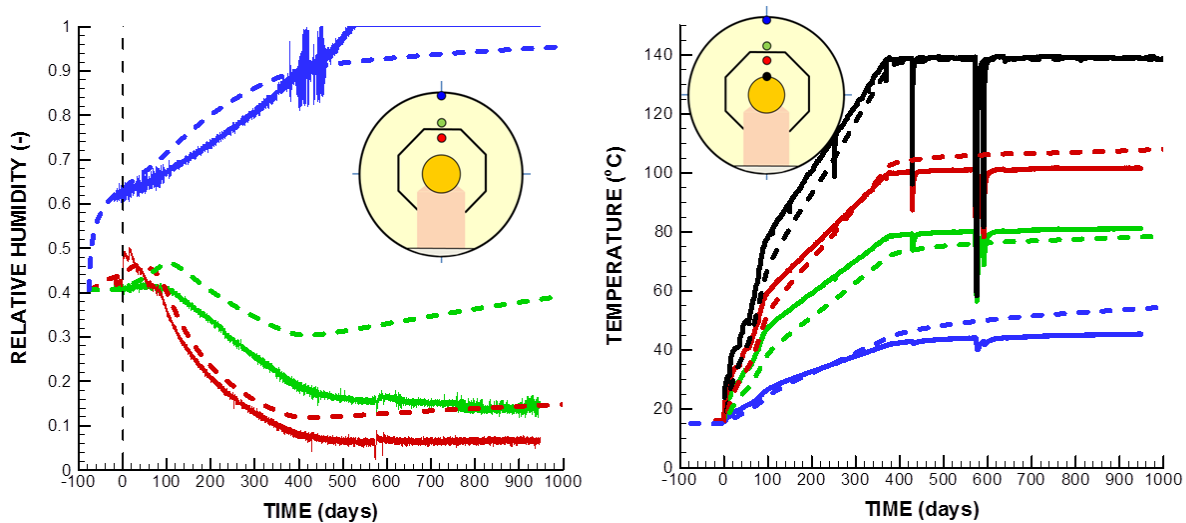
Figure 2.37. Comparison of calculated (dashed lines) and measured (solid lines) evolutions of (a) liquid saturation relative humidity and (b) temperature after interpretative modeling.

Figure 2.37 shows the data comparison, including both upper and lower parts of the buffer for the improved model parameters set obtained by the interpretative analysis. There is an excellent agreement for the heater temperature both on top and bottom of the heater. The temperature evolution in the upper part of the buffer, i.e., within the granular bentonite is also in are in agreement with measured data. The temperature evolution in the lower part of the buffer, i.e., in

77

bentonite block section is not as satisfactory as the temperature is somewhat overestimated in the model simulations. The evolution of relative humidity are in general agreement with the data in trends, showing drying at the heater and wetting from the rock surface, but the measurement indicates more drying in the mid part of the buffer.
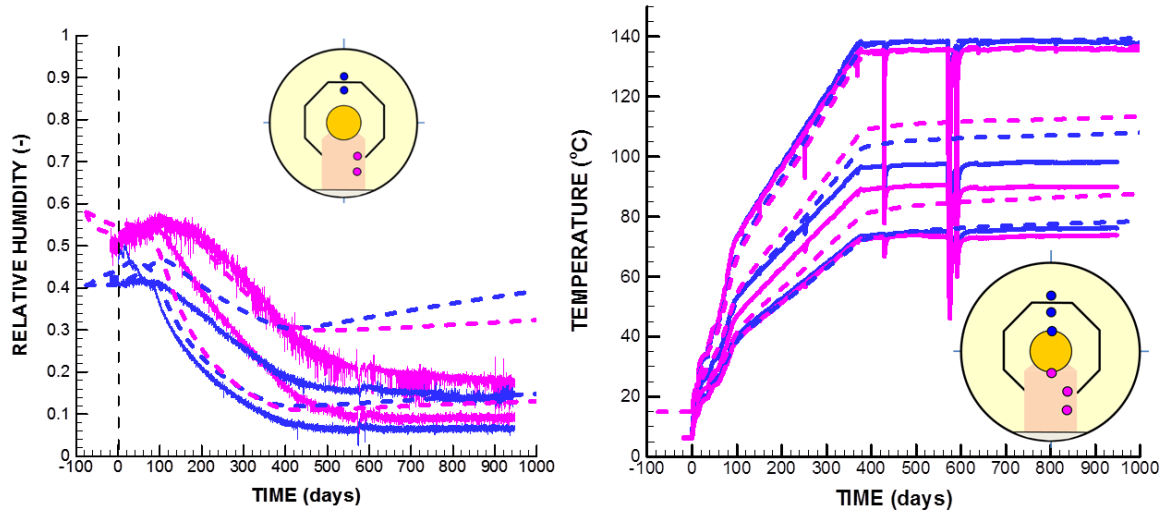
Figure 2.38. Comparison of calculated (dashed lines) and measured (solid lines) evolutions of (a) liquid saturation relative humidity and (b) temperature after interpretative modeling at top and bottom of buffer.

Finally, in order to establish an initial fluid pressure in the rock at some of the measurement point for the thermal pressurization, the pressure at the outer boundary of the model was reduced from 1.7 MPa to 1.2 MPa. Using such a low boundary pressure a low pressure similar to that observed was established in the model. The simulation results in Figure 2.39 show excellent agreement for one point (Figure 2.39 (a)), and mixed results for two other locations shown in Figure 2.39 (b). Thus the pressure increase may depend on local heterogeneities in the rock.
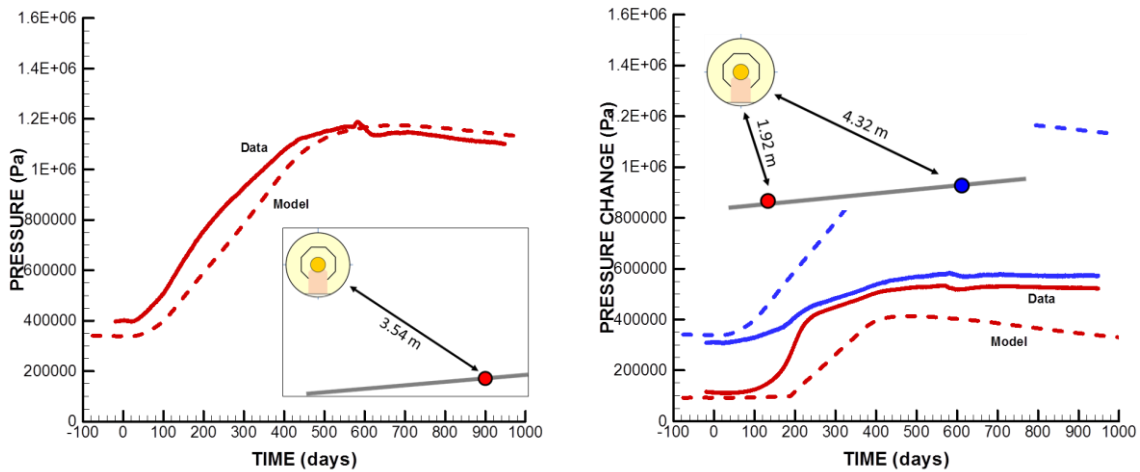
Figure 2.39. Comparison of modeled (dashed lines) and measured (solid lines) evolutions of pore pressure in Opalinus Clay at a various distances from the tunnel after interpretative modeling.

2.3.6   Longer-Term Modeling of the HE-E experiment

The modeling teams in DECOVALEX-2015 Task B1 were asked to perform a long-term simulation to estimate when the buffer will be completely resaturated if the heaters are turned off after eight years. The time to full resaturation is relevant as full resaturation will ensure complete and uniform swelling and tightness of the buffer. This was conducted by extending the simulation with the model from the interpretive modeling. Figure 2.40 shows a distinct saturation response when the heaters are turned off and the time to full resaturation is eighty two years. Figure 2.41 shows that after eighty two years the pressure is still low but would eventually increase to 1.2 MPa which is the pressure at the outer boundary of the model.
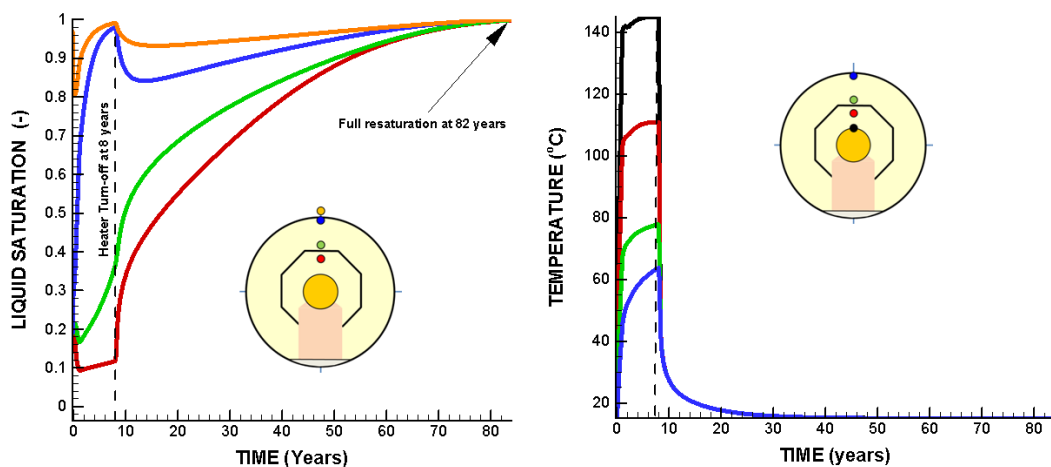
Figure 2.40. Calculated long-term evolution of (a) liquid saturation and (b) temperature.

79
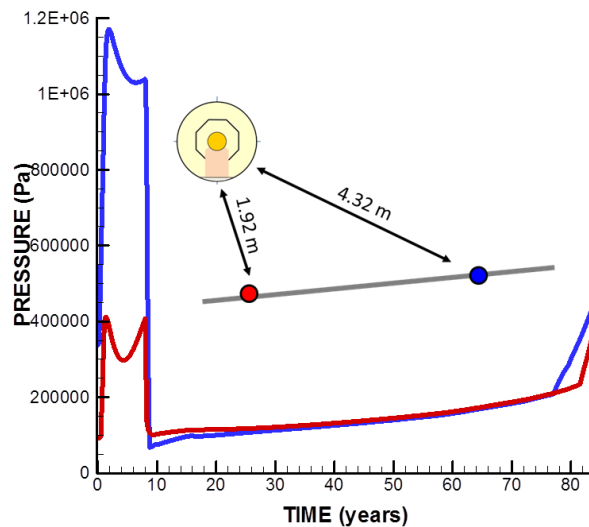
Figure 2.41. Calculated long-term evolution of pore pressure in the Opalinus Clay host rock.

2.3.7 Concluding remarks on Mont Terri HE-E modeling

Over the past three years, as part of the DECOVALEX-2015 project we have conducted modeling of coupled THM processes in bentonite backfill and Opalinus host rock associated with the Mont Terri HE-E experiment. Listed below are a few important findings and lessons learned from LBNL's participation in this modeling task:

- As one of 2 teams out of eight, we applied full two-phase (gas and liquid) flow modeling, whereas other teams used single (liquid) phase flow modeling with an additional flow term for vapor flow in a static gas phase. Our modeling using fully two-phase flow modeling revealed that very high intrinsic gas permeability of the bentonite is required to match observations of drying near the heat source. Such high gas intrinsic permeability has also been observed in laboratory experiments and reported in the literature and it is one of the assumptions for simplifying to single phase flow models. The fact that gas permeability is high in bentonite means that both full two-phase flow models and single phase flow models are adequate for modeling TH responses in the buffer.
- The HE-D Experiment was modeled with a 3D TOUGH-FLAC model with good match to experimental data. This was important for determining *in situ* TMH properties of Opalinus Clay, including anisotropic thermal conductivity and permeability. Based on the are in agreement between models and data for HE-D, we are confident about the THM parameters characterized for the Opalinus Clay.
- The modeling of the CIEMAT column experiment using a detailed transient analysis provided a unique back-analysis of bentonite thermal conductivity and a very good match with experimental data was obtained, including long term hydration. The are in agreement between model and CIEMAT experimental data shows adequate modeling of thermal-hydrological processes in bentonite.
- With the THM parameters determined from HE-D and CIEMAT experiments, the modeling of the HE-E experiment resulted in good prediction, though some disagreement occurred in the evolution of moisture content at the mid distance between heater and rock. The reason for these local disagreements in moisture evolution is still an open question.

80

- The modeling of these experiments has provided important model validation and THM properties of granular bentonite and Opalinus Clay that are currently being applied in the modeling of the larger scale Mont Terri FE experiment.

2.4   Honorobe EBS Experiment (DECOVALEX-2015)

This task focuses on coupled THM modeling of a full-scale EBS experiment conducted by the Japan Atomic Energy Agency (JAEA) at the Horonobe URL, Hokkaido, Japan (Figure 2.42). The EBS experiment is carried out at a depth of 350 m in a very porous and soft, siliceous mudstone with the following basic properties:

- Porosity 35-60%
- Permeability $10^{-20} – 10^{-18}$ m^2
- UCS (Strength) 5-25 MPa
- Young's Modulus 1-4 GPa
- Thermal Conductivity 1.34-1.53 W/mK

Figure 2.43 shows the experimental layout with a vertical heater emplacement installed in a test pit at the bottom of an experimental drift. The detailed sequence of the experiment is given in Table 2.7. The experimental drift was backfilled after the installation of the heater and bentonite buffer into the test pit. Bentonite buffer and backfill materials are based on the Japanese Kunigel V1 bentonite. For the buffer, Kunigel V1 bentonite is mixed with sand and emplaced at a dry density of 1600 kg/m^3, whereas for the backfill rock debris is mixed in for an emplacement dry density of 1400 kg/m^3. The experimental area was then isolated by a concrete plug and the heater was finally turned on January 15, 2015. Sensors have been installed in buffer, backfill and rock to monitor temperature, stress, strain, pore pressure, humidity, displacement, pH, resistivity, electric potential, and seismic velocity.

Figure 2.44 shows some early-time measurements of pressure at the bottom of the test pit (within the sand layer) and temperature at the three points on the heater. The locations of these monitoring points for both pressure and temperature are shown in Figure 2.44 (a) insert. During the construction and installation of the buffer, backfill and plug, water was pumped out of the test pit. The pump was turned off on December 22, 2014, i.e., 24 days before the heater was turned on. Figure 2.44 (a) shows that the water pressure increases due to inflow from the rock and reaches a steady value about 60 kPa after 15 to 20 days. Figure 2.44 (b) shows the temperature at the side and top of the heater stabilizes at a temperature slightly less the 100°C, whereas the temperature at the bottom of the heater stabilizes at about 80°C.
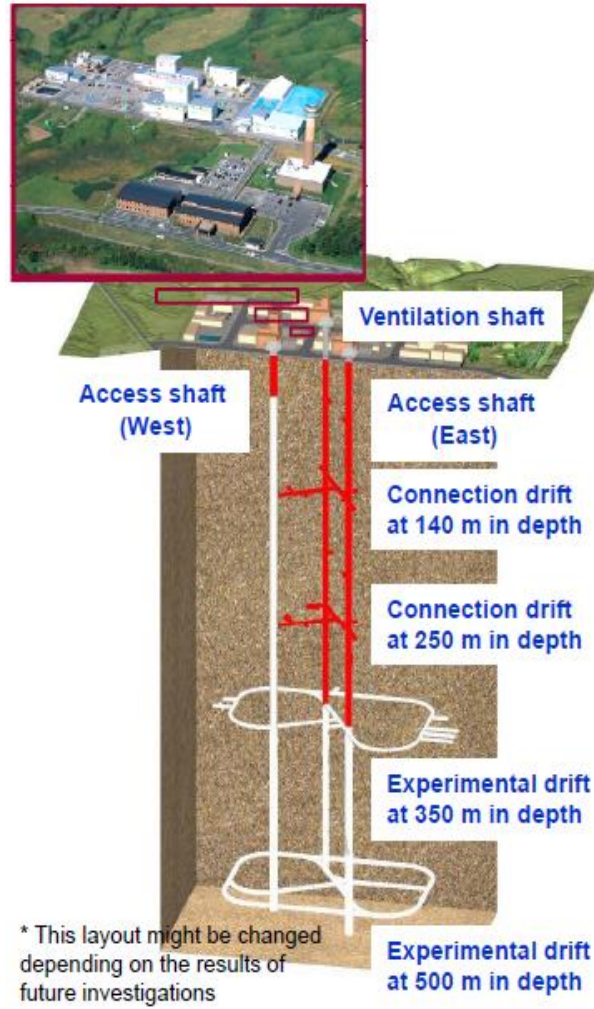
Figure 2.42. Layout of the Horonobe URL in Hokkaido, Japan (Sugita et al., 2016).

(a)

(b)
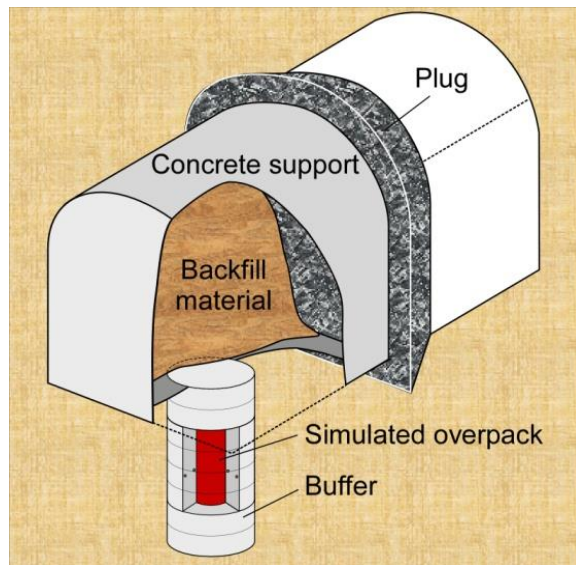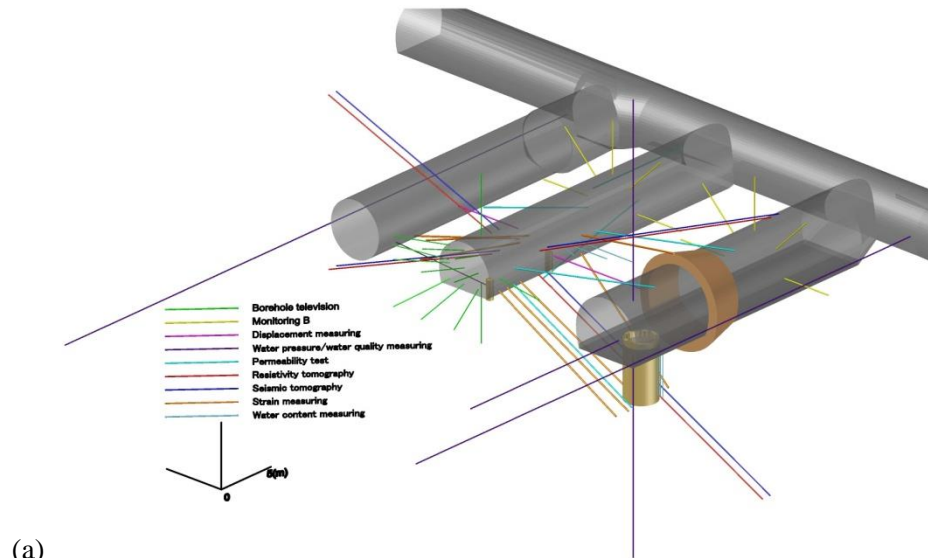
Figure 2.43. General description of the EBS experiment at the Horonobe URL Project in Japan (Sugita et al., 2016).

Table 2.7. Details on the sequence of construction and installation of the Horonobe EBS experiment

Sequence of the Horonobe EBS Experiment	
Excavation of the experimental gallery	Oct 29 – Dec 6, 2013
Opening of the test pit	Feb 3 – 8, 2014
Emplacement of the buffer	Aug 18 – Sept 6, 2014
Emplacement of the backfill	Sep 8 – Oct 3, 2014
Plugging	Oct 9 – 27, 2014
Stop pumping up water from pit	Dec 22, 2014 at 14:00
Start of heating	Jan 15, 2015 at 14:20
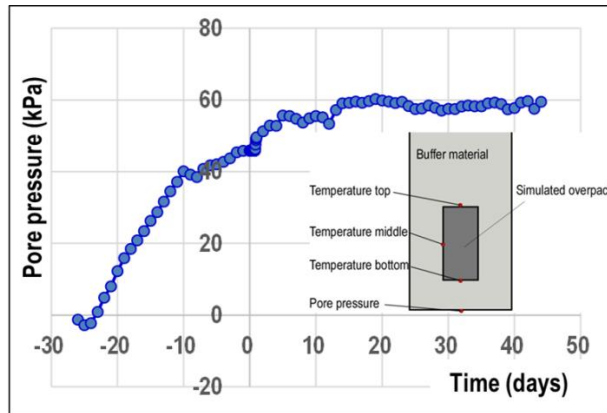
(a)
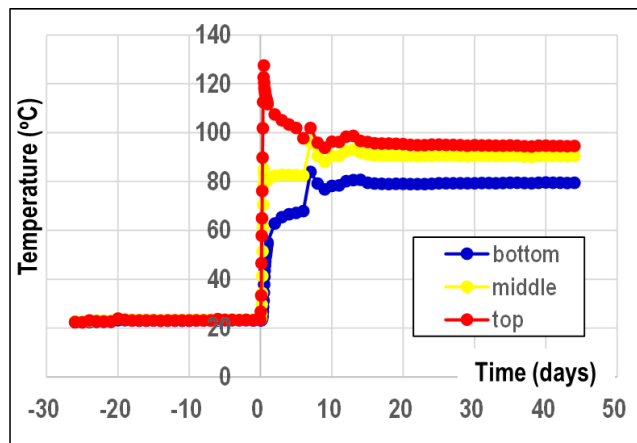
(b)

Figure 2.44. Early time monitored (a) fluid pressure in the test pit and (b) temperature evolution at three points located on the heater surface. The location of monitoring points for both pressure and temperature are shown in figure (a) insert.

2.4.1 DECOVALEX-2015 modeling tasks related to Horonobe EBS experiment

The DECOVALEX Task B2 related to the Horonobe EBS experiment was divided into the following steps;

- Step 1 (1D benchmark test with comparison of numerical models)
- Step 2 (Prediction analysis)
- Step 3 (Calibration analysis)

The 1D benchmark test (Step 1) was defined with exact properties and boundary conditions given by the JAEA. The benchmark test was conducted for the teams to familiarize themselves with the problem and for precise comparison of computer codes before going into the more complex full-scale case. Thereafter, in Step 2, a model of the real experimental design should be constructed and a first predictive analysis will to be performed for several years from the start of the heating. The heating started on January 15, 2015, and the plan was that JAEA would eventually provide the monitored data for the first six months of heating to the research teams. The research teams should then calibrate their models against this first sixmonths of field data

and then carry out coupled numerical analysis for long-term predictions (100 – 1,000 years) using the test conditions of the EBS experiment.

JAEA provided reports from the investigations at the Horonobe URL for input parameters related to the mudstone host rock and buffer material properties for the Kunigel V1 bentonite from the previous H12 project, whereas properties for the backfill were investigated along with the project.

In the FY14 milestone report titled "Investigation of Coupled Processes and Impact of High Temperature Limits in Argillite Rock" (Zheng et al., 2014), we presented the final results of the Step 1 benchmarking with comparison to the results of other DECOVALEX-2015 teams. In the FY15 milestone titled "Investigation of Coupled Processes and Impact of High Temperature Limits in Argillite Rock" (Zheng et al., 2015) we presented Step 2 model predictions of the full-scale EBS experiment with comparison of the results to other DECOVALEX-2015 modeling teams. In this report we present comparison of model prediction with actual measured data during the first 75 day of heating. The data used and provided to the research teams included temperature, suction, stress and displacement in the buffer. However, the suction and displacement data were very limited so we focused our comparison to temperature and stress. We also present comparison of modeling results from other DEOCOVALEX-2015 research teams participating in this task. In total five DECOVALEX-2015 research teams have participated in the modeling of the Horonobe EBS experiment with the models listed in Table 2.8. Some of the models listed in Table 2.8 have been extensively applied in previous DEOCOVALEX project phases, whereas some are new and being developed.

Table 2.8. DECOVALEX research teams and numerical simulators in modeling Horonobe EBS experiment

Research Team	Numerical Simulator	Brief Description of Numerical Simulator
DOE U.S. Department of Energy's Research Team: Lawrence Berkeley National Laboratory (LBNL)	TOUGH-FLAC	TOUGH-FLAC is a simulator for analysis of coupled THM processes under multiphase fluid flow conditions being developed at the LBNL (Rutqvist et al., 2002). The simulator is based on linking of the existing computer codes TOUGH2 and FLAC3D, and has been extended for modeling of coupled THM and THMC processes associated with nuclear waste disposal with backfilled emplacement tunnels in clay formations (Rutqvist et al., 2014b).
	ROCMAS	ROCMAS is a finite element program for analysis of coupled THM processes in porous and fractured rock developed at LBNL (Rutqvist et al., 2001a). It can model unsaturated media with single-phase liquid flow and vapor diffusion in a static gas phase. The code has been extensively applied in earlier phases of the DECOVALEX project for THM analysis in bentonite-rock systems (Rutqvist et al., 2001 (b); 2005).
BGR Bundesanstalt für Geowissenschaften und Rohstoffe's Research Team: University of Tübingen	GeoSys/Rockflow	GeoSys/Rockflow is based on object-oriented programming (Kolditz et al., 2003). It was first applied in previous DECOVALEX phases for analysis of thermal-hydrological and thermal-mechanical processes and has been extended to THM (Wang et al., 2006). For the present study, an unsaturated single-phase liquid flow and vapor diffusion is considered.
CAS Chinese Academy of Sciences' Research Team	EPCA3D	The EPCA code (Elasto-Plastic Cellular Automata) uses the concept of cellular automata inspired by the self-organizing theory in biology. This code has been successfully used to simulate the failure process of heterogeneous rocks with and without consideration of hydro-mechanical coupling (Feng et al., 2006; Pan et al., 2008).
JAEA Japan Atomic Energy Agency's Research Team, including Hazama Cooperation	THAMES	THAMES is a finite element program for analyzing coupled THM processes in porous and fractured rock developed at the Kyoto University. The code has been extended to unsaturated media with single-phase liquid flow and vapor diffusion in a static gas phase (Chijimatsu et al., 2005).
KAERI Korean Atomic Energy Research Institute	FLAC/FLAC3D/Tough2	Simulation tools being developed along with the DECOVALEX-2015 project based on FLAC and FLAC3D linked with TOUGH2.

2.4.2 Model predictions of the full scale Horonobe EBS experiment

A 3D model was developed for prediction of the THM responses at the Horonobe EBS experiment. The model is half symmetric, including half of the tunnel, and half of the deposition hole (Figure 2.45). It contains all relevant materials, including mudstone rock, buffer, backfill, a sand layer at the rock/buffer interface, concrete lining and plug. In this model prediction, we use the properties of the buffer and rock developed associated with the 1D benchmark calculation (Table 2.9). Additional properties for the backfill, sand layers, concrete lining and plug were provided by the JAEA to DECOVALEX-2015 modeling teams. The intrinsic permeability of gas flow in the bentonite is about six orders of magnitude higher than the intrinsic permeability for liquid flow and this is simulated in TOUGH2 using a high value of the Klinkenberg parameter.
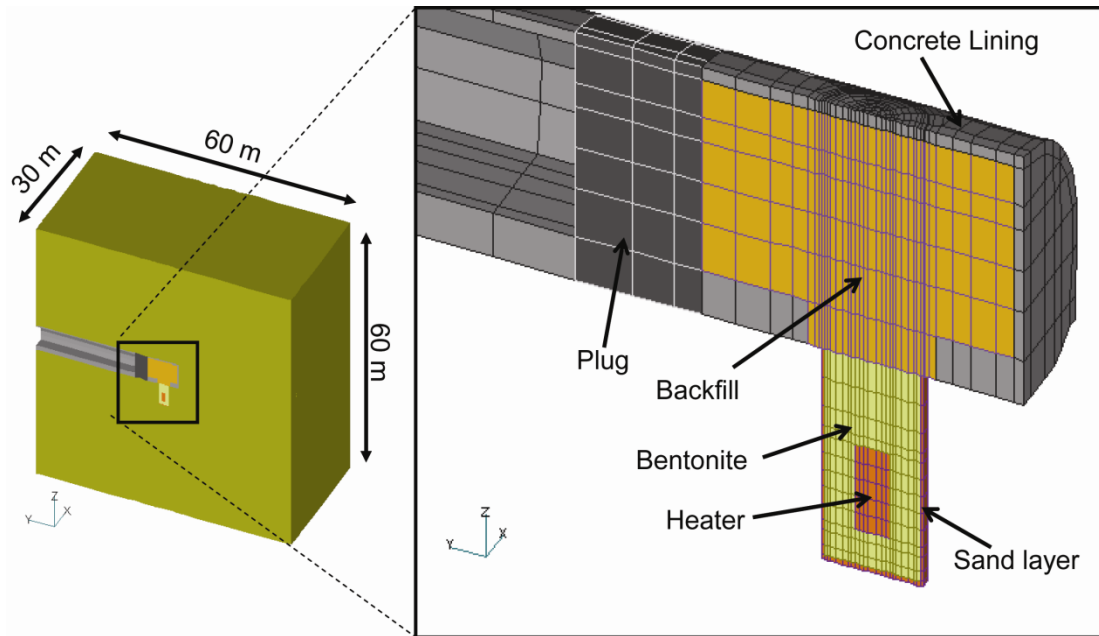
Figure 2.45. TOUGH-FLAC 3D numerical grid of the Horonobe EBS experiment.

Table 2.9. Material parameters for modeling Horonobe EBS experiment.

Parameter	Symbol	Overpack	Buffer	Backfill	Rock
Grain density (kg/m³)	ρ_g	10,000.	2680.	2680.	2454.
Porosity	ϕ	0.403	0.403	0.460	0.4482
Permeability (m²)	K	5×10^{-51}	4×10^{-20}	1.5×10^{-19}	1.33×10^{-15}
Thermal conductivity (saturated) (W/m°C)	λ_{wet}	20	1.986	1.250	1.231
Specific heat (solids) (J/kg°C)	C	10,000	341	341	626
Thermal conductivity (desaturated) (W/m°C)	λ_{dry}	20	0.444	0.444	0.579
Liquid relative permeability (van Genuchten, 1980)	A	1.3	1.3	1.3	NA
$k_{rl}(S_l) = \left(\dfrac{S_l - S_{,r}}{S_{ls} - S_{,r}}\right)^A$	S_{lr}	0	0	0	NA
	S_{ls}	1	1	1	NA
Water relative permeability parameters (van Genuchten, 1980)	m	NA	NA	NA	0.503
$k_{rl}(S_l) = \left(\dfrac{S_l - S_{lr}}{S_{ls} - S_{lr}}\right)^{1/2}\left[1 - \left\{1 - \left(\dfrac{S_l - S_{lr}}{S_{ls} - S_{lr}}\right)^{1/m}\right\}^m\right]^2$	S_{lr}	NA	NA	NA	0
	S_{ls}	NA	NA	NA	1
Capillary pressure parameters using van-Genuchten equation	$\alpha \, (m^{-1})$	8×10^{-3}	8×10^{-3}	8×10^{-3}	9.928×10^{-3}
$\psi(S_l) = 1/\alpha\left\{\left(\dfrac{S_l - S_{lr}}{S_{ls} - S_{lr}}\right)^{-1/m} - 1\right\}^{1-m}$	M	0.375	0.375	0.375	0.503
	S_{lr}	0	0	0	0
	S_{ls}	1	1	1	1
Vapor diffusion coefficients (m²/s)	D_v	3.5×10^{-6}	3.5×10^{-6}	3.5×10^{-6}	3.5×10^{-6}
Young's modulus E, (GPa)	E	200.000	37	3	1820.0
Poisson's ratio (-)	ν	0.3	0.3	0.4	0.21
Linear thermal expansion coefficient (C⁻¹)	C^{-1}	1×10^{-6}	1×10^{-6}	1×10^{-6}	1.33×10^{-5}
Moisture swelling coefficient, β_{sw}	β_{sw}	0	0.0108	0.0108	0

We simulated the experiment in 3 steps:

1)   Excavations are open for three months.

2)   Excavations are filled with backfill and the heater, buffer and plug are all installed for 6 months.

3)   Heating with heater temperature of 100°C.

Figures 2.46 and 2.47 show comparisons of LBNL predicted and measured evolution of temperature and radial stress during the first 75 days of heating at six different points. The temperature predictions are excellent, whereas stress predictions are not as perfect. However, we can state that both the modeling predictions and measurements show stress changes in the buffer are small during this initial phase. On the other hand the trends of the stress evolutions are quite different between the model predictions and measurements. This might be, because in this case a simple linear swelling model was applied in which the swelling strain is a linear function of changes in liquid saturation. Such a model maybe used to predicte the final swelling stress, but may not be accurate in prediction the path of the swelling strain and stress along with changes in saturation.
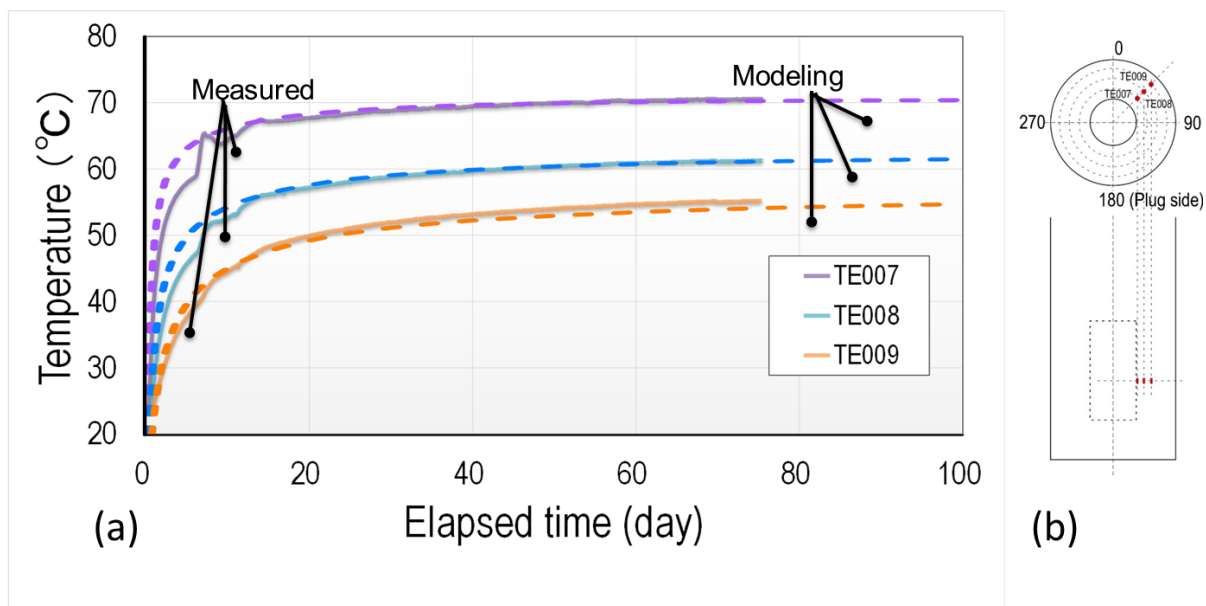
Figure 2.46. (a) Predicted and measured temperature evolution at three monitoring points in the buffer and (b) map view and vertical cross-section of the test pit with the locations of the monitoring points.
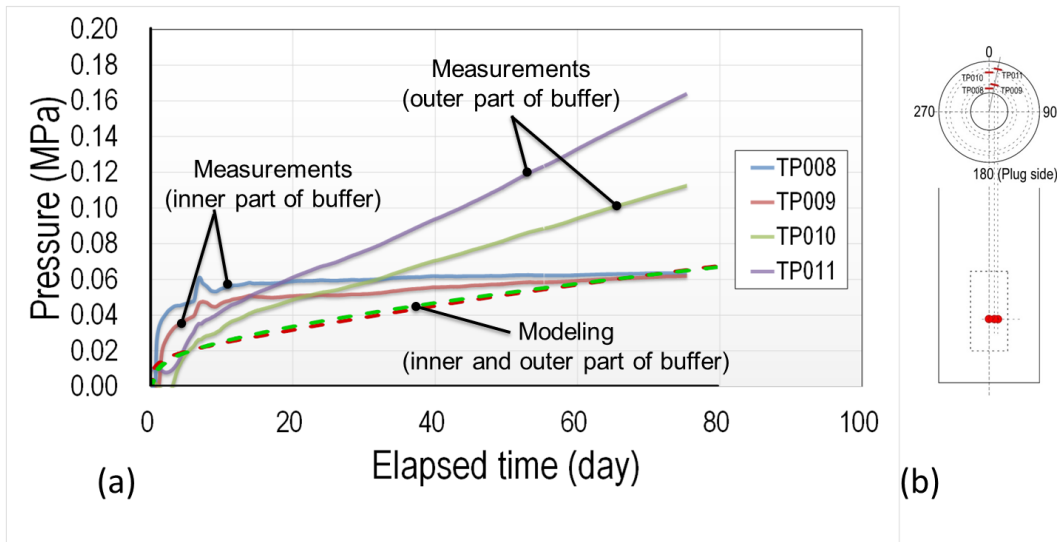
Figure 2.47. (a) Predicted and measured stress evolution at four monitoring points in the buffer and (b) map view and vertical cross-section of the test pit with the locations of the monitoring points

Figure 2.48 shows the comparison of the model prediction by five DECOVALEX-2015 modeling teams and measurements of temperature and radial stress in the buffer. The results again show the temperature evolution could be predicted in close agreement with the measurements, whereas the calculated stress results are not as consistent. Again, we emphasize these are very early time data and swelling stress have not developed very substantially at such an early time, because the buffer is far from being fully saturated.
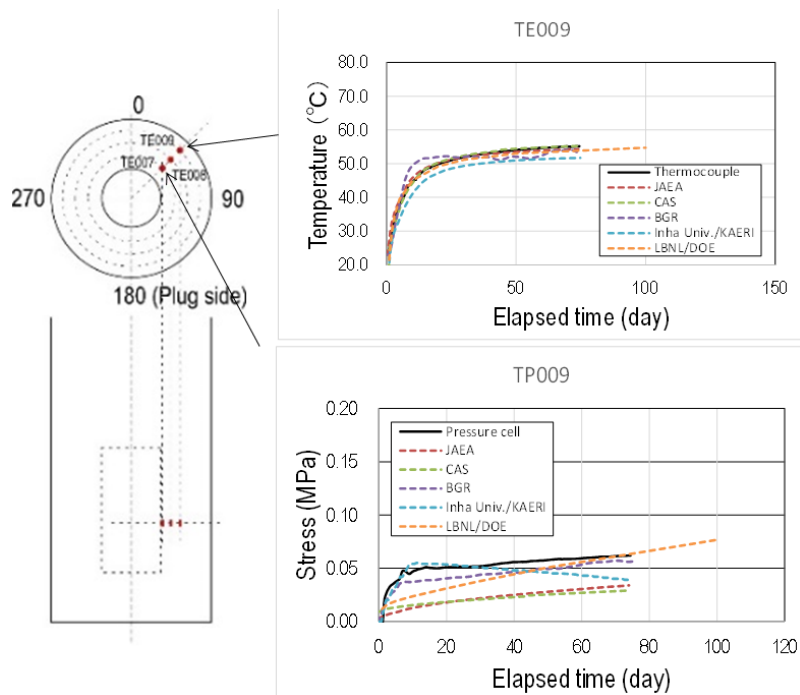
Figure 2.48. Simulated evolution of temperature and stress evolution in the buffer for five DECOVALEX-2015 modeling teams with comparison to measured data during the first 75 days of heating (modified from Sugita et al., 2016).

2.4.3 Interpretative modeling of early time buffer stress evolution

The TOUGH-FLAC model prediction showed a very are in agreement related to temperature evolution, whereas the calculated early time evolution of stress in the buffer could be improved. We therefore decided to conduct some interpretative modeling of the buffer stress evolution. We observe early on, during the first ten days, the buffer stress increase seems to be correlated with temperature increase in the buffer. For example, a temporal stress peak at about seven days is very well correlated with temporal temperature peak (Figure 2.49). On the other hand, at the outer boundary there is a gradual increase in stress that seems to be correlated with increasing saturation near the outer boundary. Thus, initial stress increase during the first 10 days seems to be due to thermal expansion while the following slow increase in compressive stress occurring at the outer boundary maybe a result of moisture swelling.

Figure 2.50 shows modeling results for two different model simulations. In one case the moisture swelling coefficient was set to zero (no moisture swelling) and thermal expansion coefficient was increased as to provide a stress response of pure thermal expansion (red dashed line), which matches measured data at the inner parts of the buffer. In the second simulation the moisture swelling coefficient was increased to give higher moisture swelling stress and this matched the measurements in the outer part of the buffer. However, the modeling using this simple linear swelling approach always produced a uniform swelling stress resulting in equivalent swelling stress evolution at the inner and outer parts of the buffer. Thus, a model should be applied that can result in different stress evolution in the inner and outer parts of the buffer. This will be further investigated in future studies.
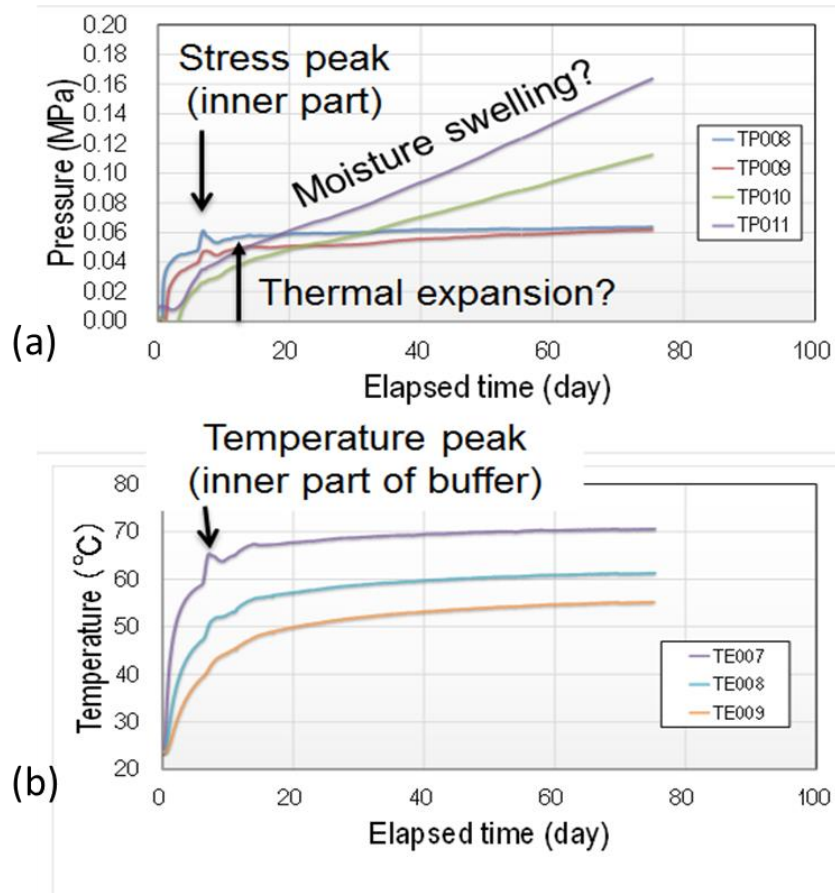
Figure 2.49. Measured (a) buffer stress and (b) temperature evolution indicating thermal and moisture swelling effects on the stress evolution (modified from Sugita et al., 2016).
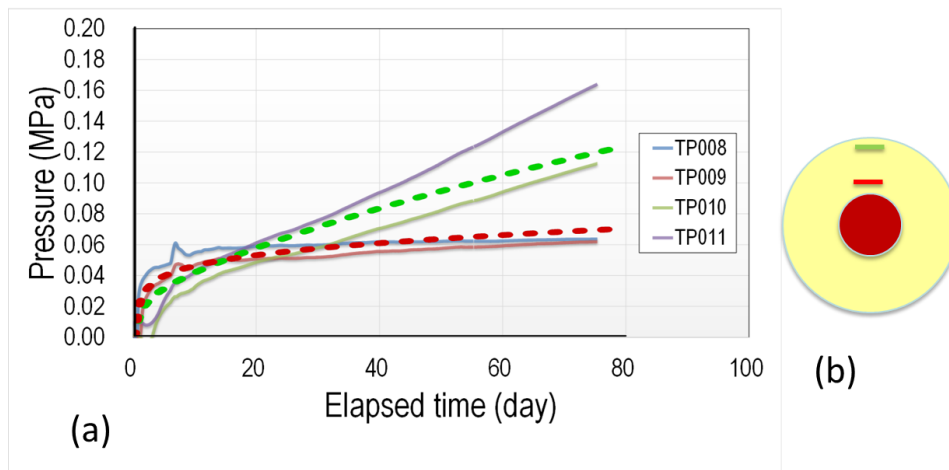
Figure 2.50. Interpretative model simulation of radial buffer stress (pressure) showing in (a) the results of two different simulations (red and green dashed lines) with different parameters for thermal expansion and moisture swelling that can each provide a good match to measured data with the approximate locations shown in (b) on a plane view of the buffer (field data from Sugita et al., 2016).

2.4.4 Summary and lessons learned from modeling the Horonobe EBS experiment

Over the past three years, as part of the DECOVALEX-2015 project, we conducted modeling of coupled THM processes in bentonite backfill and mud stone at the Horonobe site. Here we list a few important findings and lessons learned from LBNL participation in this modeling task:

- We applied full two-phase (gas and liquid) flow modeling which again revealed a very high intrinsic gas permeability is required to match observations of drying near the heat source. As mentioned, such high gas intrinsic permeability has been observed in laboratory and reported in the literature and is one of the assumptions when simplifying to single phase flow models.
- The Horonobe EBS experiment was modeled with a 3D TOUGH-FLAC model, in this case applied to system of vertical emplacement, a backfilled tunnel, a different type of bentonite, and relatively high permeability and high porosity host rock.
- With the THM parameters determined from laboratory scale experiments on bentonite and backfill, and based on site investigations on mudstone properties, the modeling of the Horonobe EBS experiment resulted in good prediction in temperature, whereas some disagreement occurred in the stress evolution. The reason for these local disagreements in stress evolution is still an open question.
- The Horonobe EBS experiment provides good mechanical measurement data in the buffer, including stresses and displacements at various parts of the buffer that with longer time data can be used to evaluate different constitutive models for bentonite mechanical behavior.
- The 75 days of measured data is too short and it will be important to continue to follow the evolution and compare with modeling much beyond 75 days.

2.5   FE Experiment at the Mont Terri Site (Mont Terri Project)

Presented in this section is the current status of the FE Experiment and modeling. For the Mont Terri FE experiment is that all the heaters, bentonite buffer and instrumentation have been installed, the tunnel has been plugged, and the final heater was turned on February 15, 2015 (Figure 2.51). Field data from the first year of heating was distributed to the international modeling teams participating in the modeling of the FE experiment were distributed in February 2016. LBNL as a modeling team is currently in the midst of interpretative modeling of the first year of data in preparation for the next modeling meeting expected to be held in November 2016.
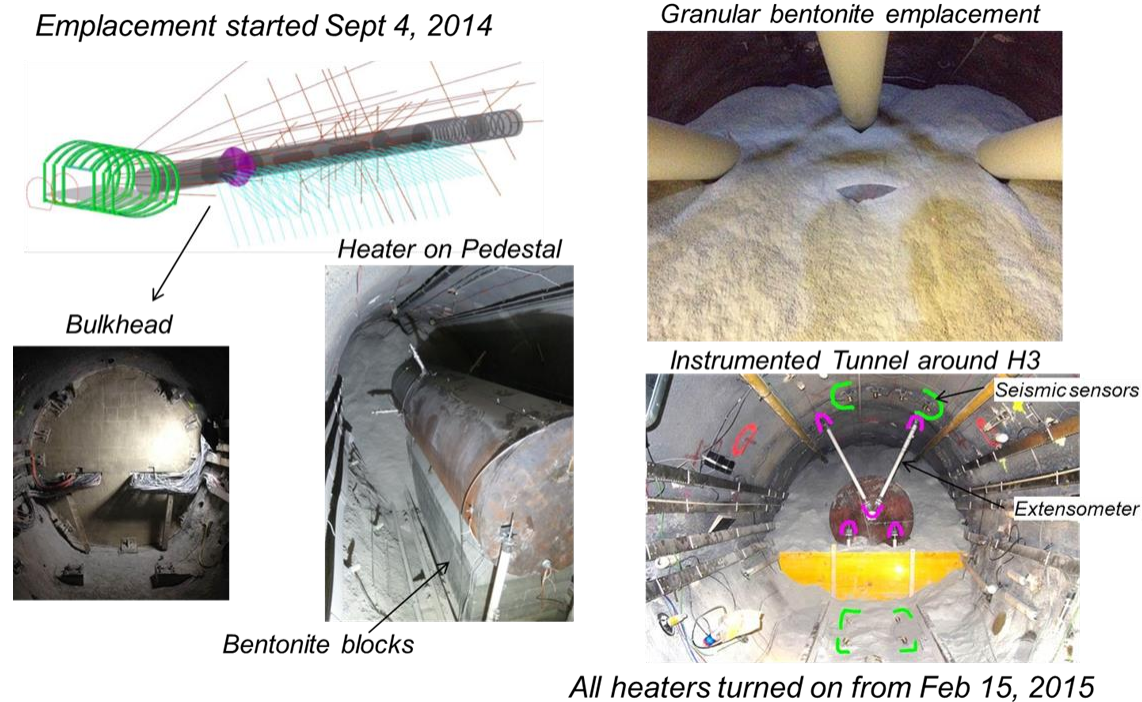
Figure 2.51. Images from the construction and installation of heaters, bentonite buffer and plugs from NAGRA daily reports by Herwig Müller, NAGRA on FE experiment progress during its construction.

As mentioned, the Mont Terri FE Experiment will be one of the largest and longest-duration heater tests worldwide, with focus on both the EBS components and the host-rock behavior. The FE experiment is conducted in a side tunnel at Mont Terri, excavated along the claystone bedding planes for this purpose, extending 50 m in length and about 2.8 m in diameter (Figure 2.52). Heating from emplaced waste will be simulated by three heat-producing canisters of 1500 W maximum power. The temperature is expected to exceed 100°C, with a target temperature 125 to 135°C at the inner parts of the buffer. A sophisticated monitoring program is planned, including dense pre-instrumentation of the site for *in situ* characterization, dense instrumentation of the bentonite buffer and host rock, and extensive geophysical monitoring (seismic and electric tomography).

The experiment will provide data useful for the validation of THM coupling effects regarding the processes in the host rock, while correctly accounting for (and examining) the conditions in the emplacement tunnel (temperature, saturation, and swelling pressure). Due to the 1:1 scale of the experiment, it will be possible to achieve realistic temperature, saturation, and stress gradients. It will also be possible to test backfilling technology with granular bentonite, as well as lining technology with shotcrete, anchors, and steel ribs. Processes examined in the test cover many aspects of repository evolution, such as creation and desaturation of the EDZ during tunnel excavation and operation (including ventilation for about one year), as well as reconsolidation of the EDZ, resaturation, thermal stresses, and thermal pore-pressure increase after backfilling and heating (heating and monitoring period > ten years).
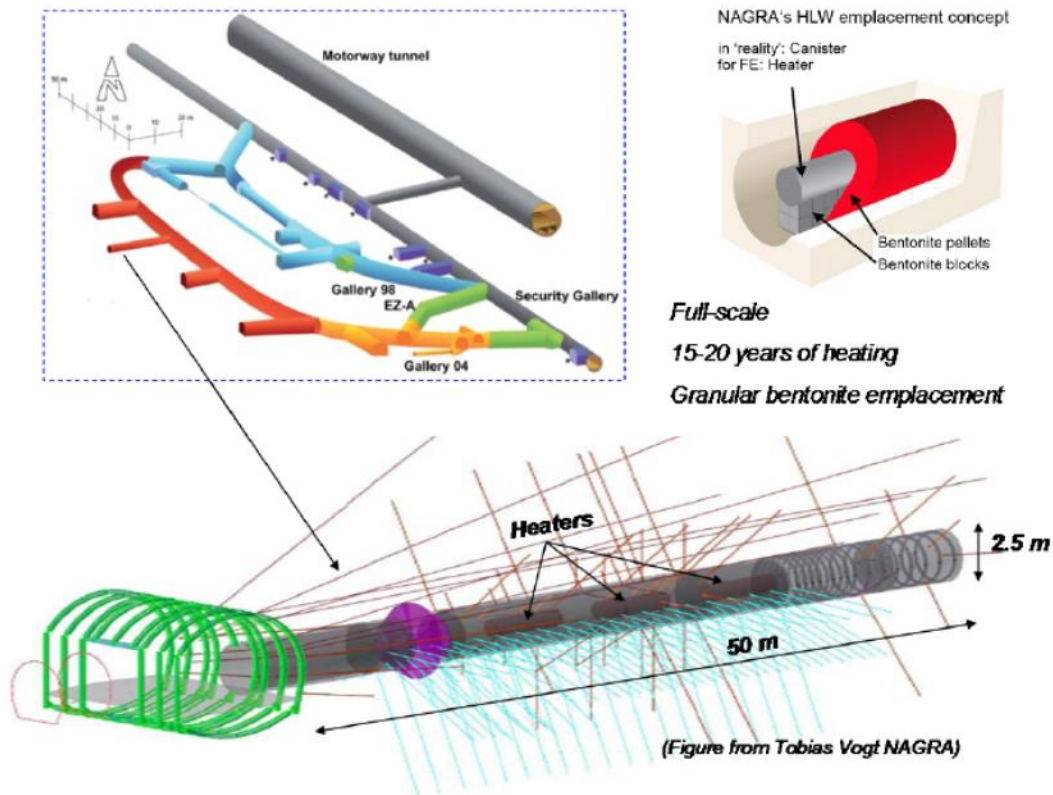
Figure 2.52. Plan view of FE experiment setup and borehole layout.

In 2011, a niche in front of the FE tunnel was constructed, followed by a first phase of instrumentation of the rock mass surrounding the tunnel, using boreholes from the niche. The FE tunnel was then excavated by road-header in 2012; this was followed by another phase of instrumentation. The tunnel was open for a one year ventilation period. This was followed by the emplacement of the heaters, bentonite buffer, and a concrete plug, after which the heating was gradually turned on during the fall of 2014. The heating is then expected to go on for at least fifteen years, with continuous monitoring of THM processes in both the bentonite buffer and surrounding rock.

2.5.1 FE-E experiment modeling tasks

DOE is one of the experimental partners for the FE heater experiment, and LBNL is one of the modeling teams. In addition to LBNL, six other modeling teams are currently involved in the Mont Terri FE experiment from Germany (2 teams), United Kingdom, Spain, Switzerland, and Canada.

The THM modeling program includes three types of computations:

1) Scoping calculations

2) Bench Marking

3) Predictive computations

The scoping calculations include brainstorming on potential ongoing processes, evaluating their significance and parameter range, comparing simulation results and input parameters derived by each team, and lessons learned (parameter range, importance, expected response). The benchmarking uses well-defined geometry problems with exact parameter values given to the teams, focusing on process modeling with precise comparison of codes. In the predictive calculations, likely parameters values and the as-built information of the experiment will be frozen.

Each modeling team developed conceptual models and material properties using available literature (papers and reports) on lab experiments and previous Mont Terri *in situ* tests, etc. Moreover, this is complemented with a restricted benchmark test for code comparison, in which properties and model geometry are set by NAGRA. The FY13 UFD milestone report titled "Report on International Collaboration Involving the FE Heater and HG-A Tests at Mont Terri (Houseworth et al., 2013), presented results on the scoping calculations and the benchmarking which was completed in April 2014. We also made a first full THM 3D simulation of the FE heater test, was created including the BBM model for calculating the mechanical responses. These were scoping and preliminary predictions with the material properties available at the time, though in some cases including a different kind of bentonite.

The FY2015 UFD milestone report title "Investigation of Coupled Processes and Impact of High Temperature Limits in Argillite Rock" (Zheng et al., 2015), presented simulation results related to the thermal evolution for different heat power schemes. This included a staged heating during the first few months of the experiment. A staged heating schedule was also adopted in the real experiment to be able to use early data for determining the maximum heat load so that temperatures would not exceed certain limits. For example, the maximum temperature should not exceed 150°C as such high temperature could potentially damage the monitoring system. The modeling presented in the FY15 UFD milestone report indeed showed that temperature could increase about 150°C in the maximum heat power of 1500 W would be applied on each of the heaters. It was decided by NAGRA, to limit the maximum heat power to 1380 W to be well below 150°C in maximum temperature.

This report presents initial interpretative modeling of the FE experiment with comparison to field data for the first year of heating. The approach was to use the previously developed 3D model of the FE experiment but with THM properties updated and determined from the modeling of the smaller scale HE-E experiment.

2.5.2   TOUGH-FLAC model of the Mont Terri FE Experiment

For the modeling of the FE experiment, conceptual model and modeling approach that was presented and used for model predictions in previous milestone reports (Houseworth et al., 2013; Zheng et al., 2014; Zheng et al., 2015). The host rock is modeled using TOUGH-FLAC with anisotropic properties considering bedding planes of the Opalinus Clay. To accurately model anisotropic thermal and hydrological behavior, we created an inclined TOUGH2 mesh. Anisotropic mechanical material behavior is simulated using the FLAC3D ubiquitous joint model, with initial properties of those derived from the excavation design analysis of the experimental tunnels. In the ubiquitous joint model weak planes are assumed along the bedding planes of the Opalinus Clay in which the shear strength properties are different along bedding versus across bedding (Housworth et al. 2013). For the bentonite, we started with the BBM model as applied by the CIEMAT and UPC (Garitte and Gens, 2012), and derived specific input

material parameters for the MX-80 bentonite pellets that is used as the emplaced bentonite buffer around the heaters. With this modeling approach, we are able to simulate THM processes in both the bentonite and host rock, as well as their interactions.

Figure 2.53 presents the 3D TOUGH-FLAC numerical grid of the FE experiment. This model grid includes all vital material components for the modeling of the FE experiment, including layered Opalinus Clay host rock, excavation disturbed zone, tunnel, three heaters, bentonite buffer, concrete liner, and concrete plug. The initial conditions for the model simulation are 2 MPa pore-fluid pressure and 15°C temperature for the host rock. The 2 MPa pore pressure is not under hydrostatic conditions, and the process is affected by the existing tunnel system at the site. In our simulations, we first run a simulation with an open tunnel at atmospheric pressure for one year, creating a pressure drop and hydraulic gradient around the tunnel. Thereafter, we assume instantaneous emplacement of the heater and buffer, and start our heating simulation.
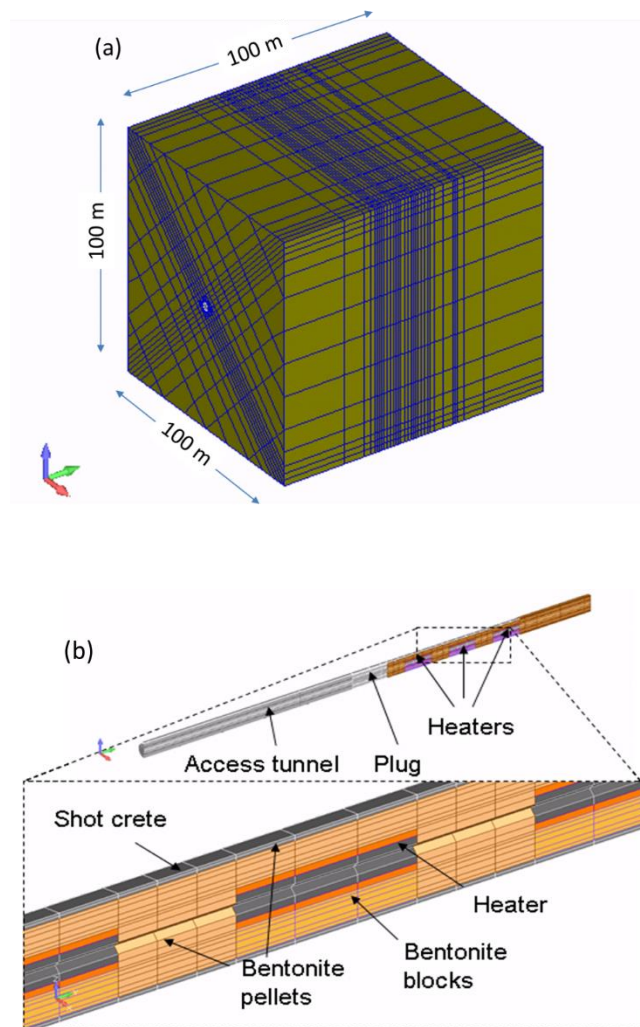
Figure 2.53. TOUGH-FLAC 3D numerical grid of the FE experiment. (a) entire model and (b) details of the materials and gridding of the EBS.

The thermal and hydraulic material properties for modeling the FE experiment are identical to those given in Table 2.6 for the HE-E experiment. These properties are based on the modeling studies of several other smaller scale heater experiments, including the HE-D and HE-E experiments and are therefore expected to be the best estimate of properties at the FE experiment. The intrinsic permeability of gas flow in the bentonite is about six orders of magnitude higher than the intrinsic permeability for liquid flow and this is simulated in TOUGH2 using a high value of the Klinkenberg parameter.

Our initial approach was to use the initial saturation in the buffer corresponding to the one observed in HE-E experiment, which based on an initial measured relative humidity and the adopted retention curve would be about 20% in the granular bentonite and 65% in the bentonite blocks. However, as it turned out from the relatively humidity measurement, the initial buffer saturation was slight different in the FE experiment compared to that of the HE-E experiment. To match the initial relative humidity in the FE experiment, the initial saturation was set to 16.5% for granular bentonite and to 75% for bentonite blocks.

Figures 2.54 and 2.55 shows the comparison of modeling and measured data for the evolution of temperature and relative humidity within the buffer at the middle heater. Figure 2.54 shows that the modeled evolution of temperature is in excellent agreement with measurements, while Figure 2.55 shows a reasonable are in agreement between modeled and measured relative humidity. These results show that the modeling in general very well captures the TH responses in the buffer during the first year of heating.

The modeling results in Figures 2.54 and 2.55 are not strictly blind predictions as a few model parameters were adjusted in an interpretative analysis to achieve the best possible agreement between model and measurements. As mentioned, the starting point was to use the material properties determined from the previous modeling of the HE-E experiment. Using these properties, an excellent agreement was indeed achieved for the temperature evolution. However, the thermal properties of the heater assembly were adjusted to achieve the observed difference in temperature between the granular bentonite and bentonite bocks and to achieve a rapid increase in temperature during the initial phase of the heating. This was achieved by reducing both the thermal conductivity and heat capacity of the heater assembly compared to that of solid steel. As shown in Figure 2.54, the temperature at the heater surface is substantially lower below the heater (adjacent to bentonite blocks, around 118°C after 400 days) compared to the temperature at the side of the heater (adjacent to granular bentonite, around 125°C after 400 days). From the modeling we can explain this difference by the fact that the thermal conductivity of the compacted bentonite blocks are much higher than that of the granular bentonite at the initial saturation. To achieve a are in agreement between modeled and measured evolution of relative humidity, a porous medium tortuosity factor of 0.14 was multiplied to the diffusion coefficient. No other material parameter for bentonite or Opalinus Clay was modified compared to that of the HE-E experiment. As a sensitivity case we may try to use a medium tortuosity factor of 1.0 that results in a higher effective diffusion coefficient. The result in Figure 2.56 shows that the modeled and measured relative humidity evolution strongly deviated for such a case indicating too high effective diffusion coefficient.

98
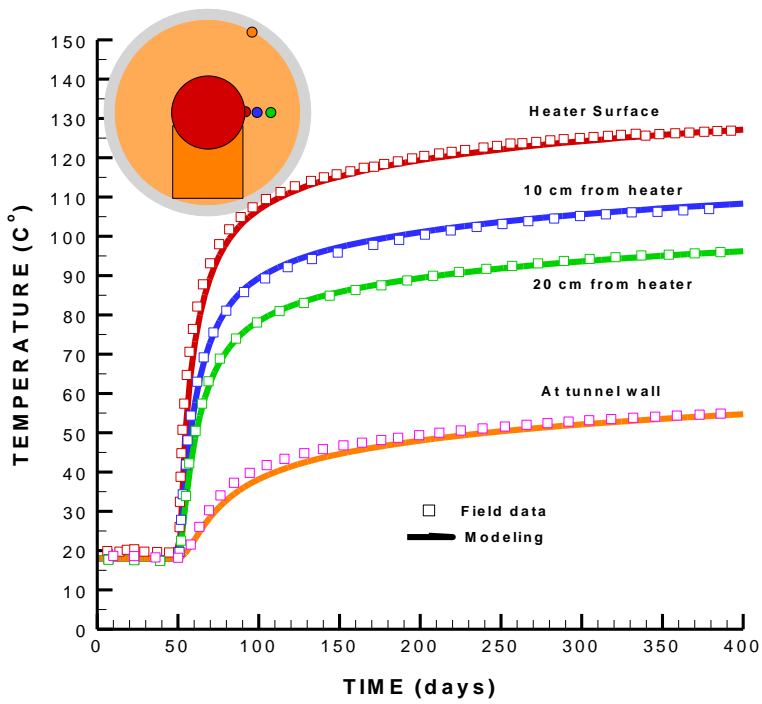
(a)
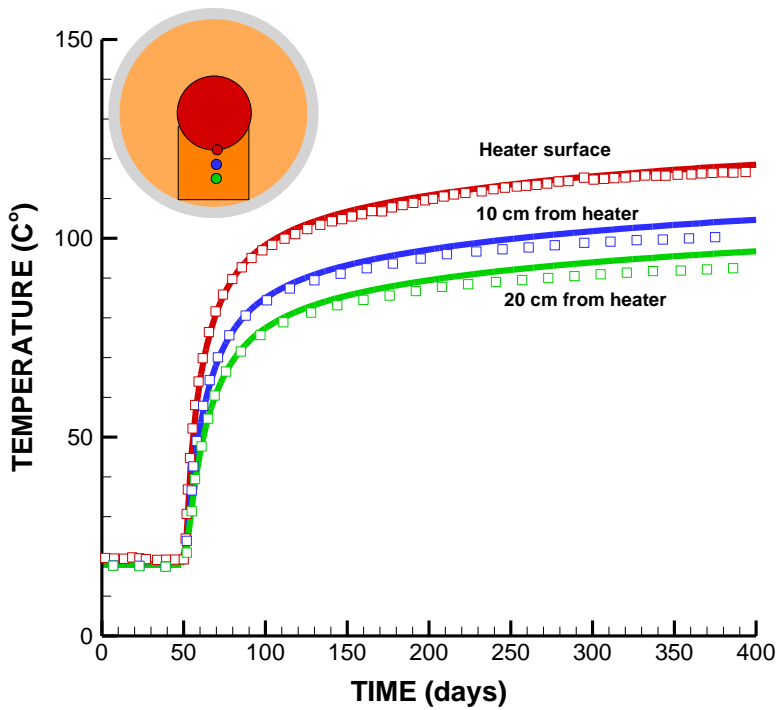
(b)

Figure 2.54. Comparison of modeled (lines) and measured (symbols) evolutions of temperature at monitoring point located in (a) granular bentonite and (b) bentonite blocks.
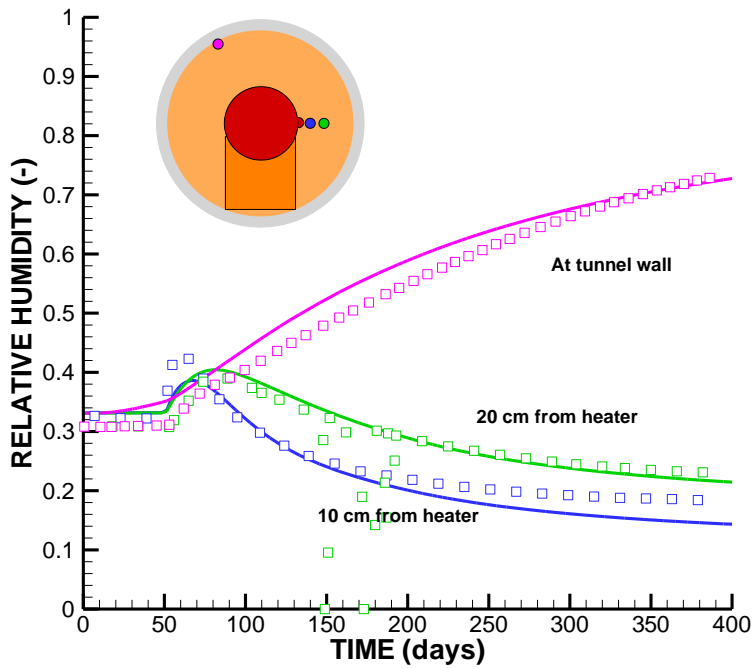
(a)
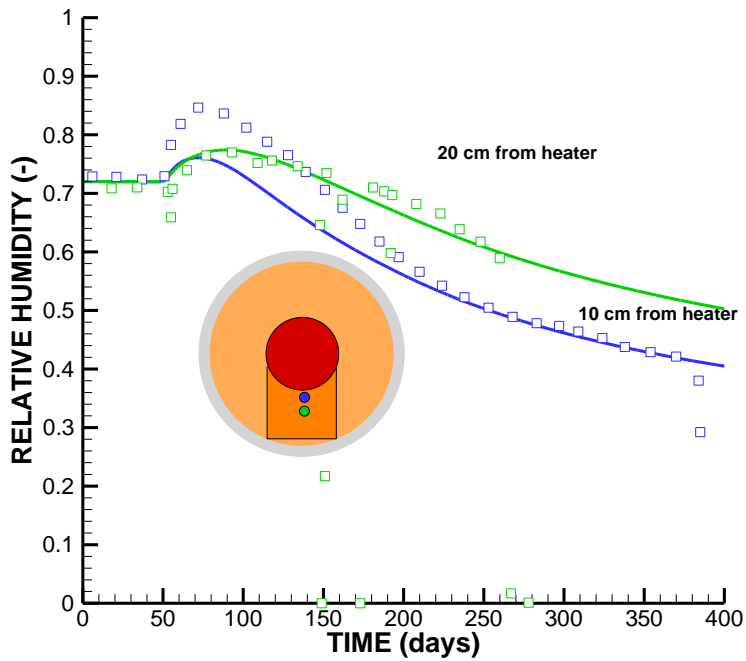
(b)

Figure 2.55. Comparison of modeled (lines) and measured (symbols) evolutions of relative humidity at monitoring point located in (a) granular bentonite and (b) bentonite blocks for a diffusion tortuosity factor of 0.14.
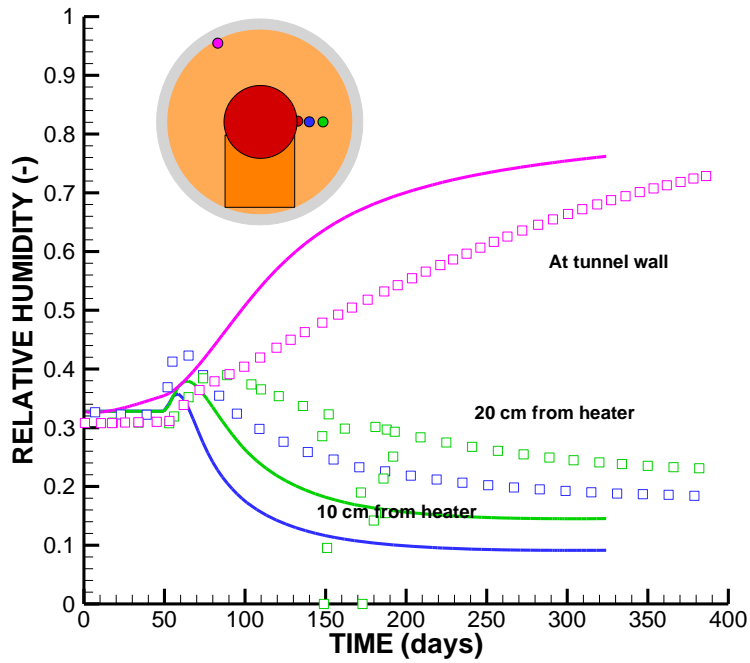
(a)
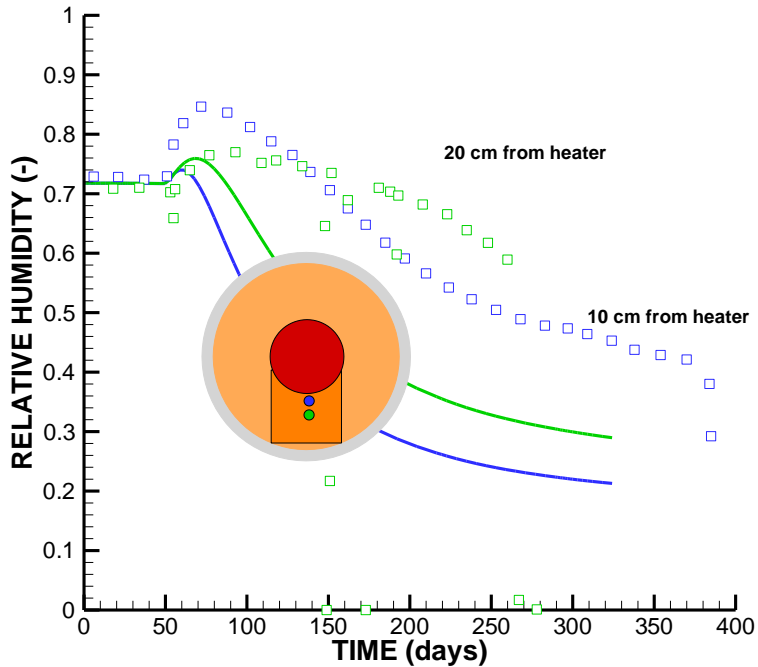
(b)

Figure 2.56. Comparison of modeled (lines) and measured (symbols) evolutions of relative humidity at monitoring point located in (a) granular bentonite and (b) bentonite blocks for a diffusion tortuosity factor of 1.0 showing the sensitivity to this parameter.

2.5.4 Summary and status the FE experiment modeling

As a modeling team in the Mont Terri FE experiment, we have conducted various types of modeling over the past few years, including benchmarking, heating design modeling, and model predictions and interpretations of the first year of heating data. We have done some initial comparison of the basic temperature and relative humidity evolution in both granular bentonite and bentonite blocks. Some finding and lessons learned from this:

The initial relative humidity in the FE experiment was slightly different from that of the HE-E experiment, although the buffer materials were the same. The reason for this difference is an open question. Maybe related to the initial relative humidity in the Mont Terri URL depending on season.

A are in agreement between modeled and measured evolutions in buffer temperature and relative humidity was achieved at the FE experiment based on a model prediction using properties of bentonite and Opalinus Clay determined associated with the previous HE-E experiment.

A value of the effective vapor diffusion coefficient (and medium tortuosity factor) could be precisely calibrated against measured relative humidity evolution, but their values were much lower than those used for modeling of the HE-E experiment. This difference and the potential role of enhanced thermal diffusion of the early time TH response in the buffer are open questions.

By studying field data going beyond one year, we will be able to model stress evolution in the buffer and validate mechanical models as well as study the questions related to diffusion mentioned in the previous bullet.

2.6   Summary and Status of THM and Heater Test Modeling

UFD and LBNL greatly benefit from participating in these international activities for developing expertise and testing advanced models for coupled THM processes to be used for predicting long-term THM evolution of a multibarrier nuclear waste repository system, involving backfilled emplacement tunnels in argillite host formations. FY16 work has been focused on modeling of large scale in situ heater experiments involving both bentonite and rock, including the Mont Terri HE-E, Horonobe EBS, and Mont Terri FE experiments. Modeling these experiments require large 3D models, involving all relevant components, such as simulated waste package, bentonite buffer, and host rock, as well as their interactions. Modeling a real system at full scale is the ultimate test of the numerical models and provides valuable experience in preparation for the performance assessment of future high-level nuclear waste disposals sites in the U.S.

In FY16 we have been able to successfully complete the DECOVALEX-2015 modeling associated with the Mont Terri HE-E experiment and Horonobe EBS experiment, and for the first time able to analyze field data from the largest ongoing underground heater test in the worlds; the Mont Terri FE experiment. The main accomplishments in FY16 include the improvement of the implementation and efficiency of the Barcelona Expansive Model (BExM) in TOUGH-FLAC as well as the interpretative modeling of field data from all the three underground heater experiments included in LBNL's international commitments on heater experiments.

The interpretative analyses of heater experiments as well as the evaluation of the outcome of predictive modeling have confirmed that the temperature and moisture evolution can be predicted with confidence. Related to the evolution of moisture content and buffer resaturation some questions remain related to the thermally driven diffusion, how strong this process is and why we observe some apparent inconsistencies between the modeling of different experiments; we observed some difference in moisture evolution between the Mont Terri HE-E and FE experiments that should be studied further.

Related to the mechanical evolution of the buffer, it is well known this is more complex as it depends on a number of processes such as moisture swelling, pore pressure and thermal expansion in turn depends on the evolution of saturation, temperature, pressure and 3D geometrical mechanical confinement effects. No mechanical measurements were conducted in the buffer for the HE-E experiment, whereas the stress in the buffer has not yet been developed very much in the case of the Horonobe EBS experiment and Mont Terri FE experiment. The stress in the buffer will take years to develop and this should be modeled in the future, especially related to the Mont Terri FE experiment which is comprehensively monitored regarding mechanical changes in both buffer and host rock.

2.7   Future Work

In FY17 we plan to continue our work on participating in major international underground heating experiments, by continuing modeling of the Mont Terri FE experiment as one of the international modeling teams and starting on a new modeling tasks in the new DECOVALE-2019 project. These commitments in the new DECOVALEX-2019 project will replace our previous commitments related to the Mont Terri HE-E and Horonobe EBS experiments in the DECOVALEX-2015, which has been completed.

The DECOVALEX-2019 tasks to be started in FY17 are denoted Task A and Task E in the new DECOVALEX-2019 project. Task A is related to gas migration in bentonite, and TOUGH-FLAC with dual-structure model is one of the approach that will be tested. Task E is related to upscaling of modeling results from small scale to one-to-one scale based in heater test data in Callovo-Oxfordian claystone (COx) at MHM underground research laboratory in France. This will be a perfect task for our development and application of the model capabilities we have developed and tested over the last few years within the UFD Campaign. Upscaling is an important issue for the repository design and safety calculation. The question is how to go from sample to a repository scale? This task will include modeling at difference scales, from laboratory scale to field scale heater experiments and all the way to repository scale.

The FY17 work on the Mont Terri FE experiment will be focused on modeling of the mechanical evolution of the buffer and host rock, including the application of the BExM model at a large scale. It will be a great opportunity to apply and test the BExM at the larger scale on the FE experiment, in particular because one the other international modeling teams is the University of Catalonia group in Barcelona, Spain that is the origin of the BExM model and they will apply BExM for the modeling of the Mont Terri FE experiment, but using a different numerical simulator. At the same time we will continue to validate and gain experiences in the use of the BExM.

In addition to these tasks related to underground heater experiments, in FY17 we intend to study a few important technical issues that arose from the DECOVALEX-2015 work on HE-E and Horonobe experiments. The first is related to the strength of thermally driven diffusion which did not seem consistent between different experiments, such as the HE-E and FE experiments. We will investigate different options of enhanced thermal diffusion which may resolve the small deviation between modeling and measurements of the evolution of relative humidity the buffer as observed for the HE-E experiment. The second is related to the small inconsistencies we observed in the early time stress evolution at the Horonobe EBS experiment. We now have longer term measurement data from the experiment and using this we plan to try different constitutive mechanical models, such as BBM instead of simple swelling, to investigate whether a more consistent mechanical behavior can be modeled.

Finally, the implementation and application of a continuum damage model for the evolution of the excavation disturbed zone is another needed addition to the current model for the calculating the evolution of permeability along with damage as well as sealing and healing. Different approaches can be tested, including continuum damage models considering fracture evolution implicitly. Such a model can be benchmarked against discrete fracture modeling of damage zone fractures using TOUGH-RBSN. The goal is to build a pragmatic continuum model that can be validated against field experiments such as sealing experiments conducted in underground research laboratories.

2.8   References

Alonso EE, Gens A, Josa A (1990) A constitutive model for partially saturated soils. Geotechnique. 40: 405-430.

Alonso, E. E., Vaunat, J., Gens, A. (1999). Modelling the mechanical behaviour of expansive clays. Engng Geol. 54, 173–183.

Chijimatsu M, Nguyen TS, Jing L, de Jonge J, Kohlmeier M, Millard A, Rejeb A, Rutqvist J, Souley M, Sugita Y (2005) Numerical study of the THM effects on the near-field safety of a hypothetical nuclear waste repository – BMT1 of the DECOVALEX III project. Part 1: Conceptualization and characterization of the problems and summary of results. Int. J Rock Mech & Min Sci 42:720–730.

Corkum A.G., Martin C.D. (2007) The Mechanical Behaviour of Weak Mudstone (Opalinus Clay) at Low Stresses, International Journal of Rock Mechanics and Mining Sciences, 44, 196-209.

Esteban, F. (1990). Caracterización experimental de la expansividad de una roca evaporítica. PhD thesis, Universidad de Canabria, Santander (in Spanish).

Feng Xia-Ting, Pan Peng-zhi, Zhou Hui (2006) Simulation of rock microfracturing process under uniaxial compression using elasto-plastic cellular automata. Int J Rock Mech & Min Sci 43: 1091–1108.Garitte B. and Gens A. (2012). TH and THM Scoping computations for the definition of an optimal instrumentation layout in the Full-scale Emplacement (FE) experiment NAGRA NIB 10-34, March 2012.

Garitte B. DECOVALEX-2015 Task B1 Final Report. May (2016). Garitte, B. (2012) HE-E experiment - In situ Heater Test, Presentation given at 1th DECOVALEX 2015 workshop, April 2012, Berkeley.

Garitte B. and Gens A. (2012) TH and THM Scoping computations for the definition of an optimal instrumentation layout in the Full-scale Emplacement (FE) experiment NAGRA NIB 10-34, March 2012.

Gaus I, Wieczorek K, Schuster K, Garitte B, Senger R, Vasconcelos R and Mayor JC (2014) EBS behaviour immediately after repository closure in a clay host rock: HE-E experiment (Mont Terri URL). Geological Society, London, Special Publications, first published March 7, 2014; doi 10.1144/SP400.11

Gens A, Sánchez, M Sheng, D (2006) On constitutive modelling of unsaturated soils. Acta Geotechnica. 1, 137-147.

Gens, A, Alonso, E. A framework for the behaviour of unsaturated expansive clays. Can. Geotech. J. 29, 1013–1032 (1992).

Gens, A., Garitte, B., Wileveau, Y. (2007) In situ Behaviour of a Stiff Layered Clay Subject to Thermal Loading: Observations and Interpretation, Geotechnique, 57, 207-228.

Gens, A., Sánchez, M., Guimaraes, L.D.N., Alonso, E.E., Lloret, A., Olivella, S., Villar, M.V., Huertas, F. (2009) A full-scale in situ heating test for high-level nuclear waste disposal: observations, analysis and interpretation. Geotechnique 59, 377–399

Graupner, B.J., Lee, C., Manepally, C., Pan, P., Rutqvist, J., Wang, W., Garitte, B. (2013) The Mont Terr HE-D Experiment as a Benchmark for the Simulation of Coupled THM Processes. Extended abstract for the European Association of Geoscientists & Engineers (EAGE) International Workshop Geomechanics & Energy, Lausanne, Switzerland, 26-28 November, 2013.

Houseworth J., Rutqvist J., Asahina D., Chen F., Vilarrasa V., Liu H.H., Birkholzer J. Report on International Collaboration Involving the FE Heater and HG-A Tests at Mont Terri. Prepared for U.S. Department of Energy, Used Fuel Disposition Campaign, FCRD-UFD-2014-000002, Lawrence Berkeley National Laboratory (2013).

Itasca, FLAC3D V5.0, Fast Lagrangian Analysis of Continua in 3 Dimensions, User's Guide. Itasca Consulting Group, Minneapolis, Minnesota (2011).

Kolditz O, Bauer S, Beinhorn M, de Jonge J, Kalbacher T, McDermott C, Wang W, Xie M, Kaiser R, Kohlmeier M (2003) ROCKFLOW - Theory and Users Manual, Release 3.9, Groundwater Group, Center for Applied Geosciences, University of Tübingen, and Institute of Fluid Mechanics, University of Hannover.

Kristensson, O., Åkesson, M., (2008) Mechanical modeling of MX-80 – Quick tools for BBM parameter analysis. Phys Chem Earth, Parts A/B/C. 33, Supplement 1: S508-S515.

Liu H.H., Houseworth J., Rutqvist J., Zheng L., Asahina D., Li L., Vilarrasa V., Chen F., Nakagawa S., Finsterle S., Doughty C., Kneafsey T., Birkholzer J. Report on THMC Modeling of the Near Field Evolution of a Generic Clay Repository: Model Validation and Demonstration. Prepared for U.S. Department of Energy, Used Fuel Disposition Campaign, FCRD-UFD-2013-000244, Lawrence Berkeley National Laboratory (2013).

Lloret A, Villar MV, Sánchez M, Gens A, Pintado X, Alonso EE. Mechanical behaviour of heavily compacted bentonite under high suction changes. Géotechnique 2003; 53(1):27–40.

Olivella, S., Gens, A., 2000. Vapour transport in low permeability unsaturated soils with capillary effects. Transp. Porous Media 40, 219e241.

Pan Peng-zhi, Feng Xia-Ting, Huang Xiao-Hua, Cui Qiang, Zhou Hui (2008) Study of coupled THMC processes in crystalline rock in the EDZ using an ECPA code. Environmental Geology.

Pousada P.E. Deformabilidad de arcillas expansivas bajo succión controlada. Ph.D. Thesis, Technical University of Madrid, Spain, 1982.

Pruess, K., Oldenburg, C.M., Moridis, G. (2012) TOUGH2 User's Guide, Version 2.1, LBNL-43134(revised), Lawrence Berkeley National Laboratory, Berkeley, California.

Romero E. Characterisation and thermal-hydro-mechanical behaviour of unsaturated Boom clay: an experimental study. Ph.D. Thesis, Technical University of Catalonia, Spain, 1999.

Rutqvist J. Status of the TOUGH-FLAC simulator and recent applications related to coupled fluid flow and crustal deformations. Computers & Geosciences, 37, 739–750 (2011).

Rutqvist J., Barr D., Birkholzer J.T., Fujisaki K., Kolditz O., Liu Q.-S., Fujita T., Wang W. and Zhang C.-Y. A comparative simulation study of coupled THM processes and their effect on fractured rock permeability around nuclear waste repositories. Environ Geol, 57, 1347–1360 (2009)

Rutqvist J., Börgesson L., Chijimatsu M., Nguyen T. S., Jing L., Noorishad J., Tsang C.-F. (2001b) Coupled Thermo-hydro-mechanical Analysis of a Heater Test in Fractured Rock and Bentonite at Kamaishi Mine – Comparison of Field Results to Predictions of Four Finite Element Codes. Int. J. Rock Mech. & Min. Sci. 38, 129-142.

Rutqvist J., Chijimatsu M., Jing L., De Jonge J., Kohlmeier M., Millard A., Nguyen T.S., Rejeb A., Souley M., Sugita Y. and Tsang C.F. Numerical study of the THM effects on the near-field safety of a hypothetical nuclear waste repository – BMT1 of the DECOVALEX III project. Part 3: Effects of THM coupling in fractured rock Int. J. Rock Mech. & Min. Sci, 42, 745-755 (2005).

Rutqvist J., Davis J., Zheng L., Vilarrasa V., Houseworth J.,Birkholzer J. Investigation of Coupled THMC Processes and Reactive Transport: FY14 Progress. Prepared for U.S. Department of Energy, Used Fuel Disposition, FCRD-UFD-2014-000497, Lawrence Berkeley National Laboratory, LBNL-6720E (2014a).

Rutqvist J., Zheng L., Chen F, Liu H.-H, and Birkholzer J. Modeling of Coupled Thermo-Hydro-Mechanical Processes with Links to Geochemistry Associated with Bentonite-Backfilled Repository Tunnels in Clay Formations. Rock Mechanics and Rock Engineering, 47, 167–186 (2014b).

Rutqvist, J., Börgesson, L., Chijimatsu, M., Kobayashi, A., Nguyen, T.S., Jing, L., Noorishad, J., Tsang, C.-F. (2001a) Thermohydromechanics of partially saturated geological media – Governing equations and formulation of four finite element models. Int. J. Rock Mech. & Min. Sci. 38, 105-127.

Rutqvist, J., Ijiri, Y. and Yamamoto, H. Implementation of the Barcelona Basic Model into TOUGH-FLAC for simulations of the geomechanical behavior of unsaturated soils. Computers &Geosciences, 37, 751-762 (2011).

Rutqvist, J., Wu, Y.-S., Tsang, C.-F. and Bodvarsson, G. (2002). A modeling approach for analysis of coupled multiphase fluid flow, heat transfer and deformation in fractured porous rock. International Journal of Rock Mechanics & Mining Sciences, 39, 429-442.

Sánchez, M., Gens, A., Guimarães, L. do N., Olivella, S. A double structure generalized plasticity model for expansive materials. Int. J. Numer. Anal. Meth. Geomech., 29, 751–787 (2005).

Sugita Y., Kwon, S., Lee C., Maßmann J., Pan P., and Rutqvist J. DECOVALEX-2015 Task B2 Final Report. May (2016).

van Genuchten, M.T. (1980) A closed-form equation for predicting the hydraulic conductivity of unsaturated soils. Soil Sci Soc Am J 1980, 44, 892-898.

Vilarrasa V., Rutqvist J., Blanco-Martin L., and Birkholzer J. (2015). Use of a dual structure constitutive model for predicting the long-term behavior of an expansive clay buffer in a nuclear waste repository. Int. J. Geomech., D4015005.

Villar, M.V. (2012) THM Cells for the HE-E Test: Setup and First Results; PEBS Report D2.2.7a. CIEMAT Technical Report CIEMAT/DMA/2G210/03/2012; Euratom 7th Framework Programme Project: PEBS: Madrid, Spain.

Wang W, Xie M, Nowak T, Kunz H, Shao H, Kolditz O (2006) Modeling THM coupled problem of Task D of the DECOVALEX project. Proc. GEOPROC2006 International symposium: 2nd International Conference on Coupled Thermo-hydro-mechanical-chemical processes in Geosystems and Engineering, HoHai University, Nanjing, China, May 22-25, 2006, 226–232, HoHai Univers

Wileveau, Y. THM behaviour of host rock: (HE-D experiment): Progress Report September 2003–October 2004. Mont Terri Project, TR 2005-03 (2005).

Zheng L., Rutqvist J., Kim K., Houseworth J. Investigation of Coupled Processes and Impact of High Temperature Limits in Argillite Rock. Prepared for U.S. Department of Energy, Used Fuel Disposition, FCRD-UFD-2015-000362, Lawrence Berkeley National Laboratory, LBNL-187644 (2015).

Zheng L., Rutqvist J., Steefel C., Kim K., Chen F., Vilarrasa V., Nakagawa S., Houseworth J., and Birkholzer J. Investigation of Coupled Processes and Impact of High Temperature Limits in Argillite Rock. Prepared for U.S. Department of Energy, Used Fuel Disposition, FCRD-UFD-2014-000493, Lawrence Berkeley National Laboratory, LBNL-6719E (2014).

3. Investigation of the Impacts of High Temperature Limits With THMC Modeling

3.1 Introduction

Radioactive waste from spent fuel emanates a significant amount of thermal energy due to decay processes, which causes temperature increases in the surrounding environment particularly in the early stages of waste emplacement. The temperature to which the EBS (engineered barrier system) and natural rock can be exposed is one of the most important design variables for a geological repository, because it determines waste package spacing, distance between disposal galleries, and therefore the overall size (and cost) of repository for a given amount of heat-emanating waste (Horseman and McEwen, 1996). This is especially important for a clay repository, because argillaceous rocks have relatively small heat conductivity. Temperature governs chemical alteration and the subsequent changes in mechanical properties of the EBS. A high temperature could result in chemical alteration of buffer and backfill materials (bentonite) within the EBS through illitization and cementation, which compromise the function of these EBS components by reducing their plasticity and capability to swell when wetting (Pusch and Karnland, 1996; Pusch et al., 2010; Wersin et al., 2007). The swelling capability of clay minerals within the bentonite is important for sealing gaps between bentonite blocks, between bentonite and other EBS components, and between the EBS and the surrounding host rock. Chemical alteration may also occur in the near-field host rock, which could reduce the clay capability for self-sealing within the excavation damaged zone (EDZ). Because the permeability of clay rock is low, a high temperature may induce significant pore pressure build-up (through pore water expansion and vaporization) in the near field, which could generate adverse mechanical deformation (such as fracturing), damaging the integrity of the host rock (Horseman and McEwen, 1996).

All disposal concepts throughout the world, despite their differences in design, unanimously impose a temperature limit of about 100°C (Hicks et al., 2009). However, Wersin et al. (2007), after reviewing a number of data sets, concluded that the criterion of 100°C for the maximum temperature within the bentonite buffer is overly conservative. Their conclusion was based on their findings that no significant changes in bentonite hydraulic properties occur at temperatures of up to 120°C under wet conditions and that bentonite is chemically stable to much higher temperature under dry conditions. The impact of high temperature on bentonite and clay host rock behavior, and consequences on repository performance, remain largely an open question for a clay repository system. While various studies have shed light on certain aspects of this question, there is no study that integrates the relevant THMC processes and considers the interaction between EBS and host rock.

In UFDC, LBNL has used coupled THMC modeling to evaluate the chemical alteration and mechanical changes in EBS bentonite and the NS (natural system) clay formation under various scenarios, attempting to provide necessary information for decisions on temperature limits. After an extensive review of the THMC alteration of EBS and argillite under various temperature conditions, fully coupled THMC simulations were developed for a nuclear waste repository in a clay formation with a bentonite-backfilled EBS (Liu et al., 2013). Two scenarios were simulated for comparison: (1) a case in which the peak temperature in the bentonite near the waste canister is about 200°C and, (2) a case in which the temperature in the bentonite near the waste canister peaks at about 100°C. In these simulations, it was assumed that the host rock properties were

representative of Opalinus Clay (Bossart 2011; Lauber et al., 2000) and the EBS bentonite was Kunigel-VI bentonite (Ochs et al., 2004) or FEBEX bentonite (ENRESA, 2000). Simulations were first conducted for one thousand years (Liu et al., 2013; Zheng et al., 2014) and then were extended to one hundred thousand years thanks to improvement of efficiency of TOUGHREACT-FLAC3D simulator (Zheng et al., 2015). Model results (Liu et al., 2013; Zheng et al., 2014; Zheng et al., 2015) found out the illitization is enhanced at high temperature. However, the magnitude of illitization varies a great deal and has to be evaluated case by case. In general, illitization leads to reduction in swelling stress but the degree of reduction varies with the type of bentonite.

The coupling between chemical and mechanical processes is the key part of THMC model that allow us to evaluate the direct impact of chemical changes on mechanical behavior. In previous THMC model (e.g. Zheng et al., 2015), the coupling between chemical and mechanical processes was carried out via an extended linear swelling model which is simple and key parameters are relatively easy to be calibrated. However, such model does not accurately describe the transient state of swelling, neglect the history of mechanical change and is unable to account for the impact of cations exchange on the swelling. In FY16, THMC models uses double structure Barcelona Expansive Clay Model (BExM) (Sánchez et al., 2005) to link mechanical process with chemistry. As a result, the model can simultaneously incorporate the effects of exchangeable cations, ionic strength of pore water and abundance of swelling clay on the swelling stress of bentonite. In addition, the corrosion of steel canister was considered in the chemical model to evaluate whether the iron-bentonite interaction would aggravate the negative impact on swelling stress by forming some Fe bearing clay minerals. In this report, we first summarize the key findings from previous modeling work (Liu et al., 2013; Zheng et al., 2014; Zheng et al., 2015) which set the stage for the simulations conducted in FY16; second, we present the THMC model that takes into account of the interaction between corroded steel canister and bentonite, and third we discuss the coupled THMC model using BExM and the chemical effect on stress.

3.2   Model Development

Because the model used in this report is similar to that in previous years (Liu et al., 2013; Zheng et al., 2014; Zheng et al., 2015), we briefly describe each element of the THMC model here, focusing on the updates in FY16. Additional details on the THMC model are presented in Liu et al. (2013).

3.2.1   Simulator

Although codes that can simulate THMC processes are fairly sparse, numerous codes that are capable of simulating either THC or THM process have been developed in the last two decades. Examples of THC codes include: TOUGHREACT (Xu et al., 2006; 2011), RETRASO (Saaltink et al., 2004), CRUNCH (Steefel, 2001), NUFT (Nitao, 1996), GEOCHEMIST'S WORKBENCH (Bethke, 2002), and examples of THM codes are ROCMAS (Noorishad and Tsang, 1996; Rutqvist et al., 2001), CODE_Bright (Olivella et al., 1994), and Open-Geosys (Wang et al. 2011). In recent years, some codes have also been expanded to have THMC capability such as versions of CODE_BRIGHT (Guimaraes et al., 2007; 2013); FADES-CORE (Zheng and Samper, 2008) and TOUGH2-CSM (Zhang et al., 2012), TR-FLAC (Taron et al., 2009), TOUGHREACT-FLAC (Zheng et al., 2014), and TOUGHREACT-ROCMECH (Kim et al., 2015). The OPEN-GEOSYS (Wang et al., 2011) and MOOSE (Gaston et al., 2009) model

frameworks are open and flexible software environments that allow coupling of THMC processes.

Consideration of the coupling between chemistry and mechanics differs depending on the application, e.g. geothermal versus nuclear waste disposal, and various simplifications have been employed in order to focus on relevant couplings and processes for the specific problem to be solved. The numerical simulations in this study are conducted with TOUGHREACT-FLAC3D, which sequentially couples the multiphase fluid flow and reactive transport simulator, TOUGHREACT (Xu et al., 2011), with the finite-difference geomechanical code FLAC3D (Itasca, 2009). The coupling of TOUGHREACT and FLAC3D was initially developed in Zheng et al. (2012) to provide the necessary numerical framework for modeling fully coupled THMC processes. It included a linear elastic swelling model (Zheng et al., 2012; Rutqvist et al., 2014) to account for swelling as a result of changes in saturation and pore-water composition and the abundance of swelling clay (Liu et al., 2013; Zheng et al., 2014). The major improvement in TOUGHREACT-FLAC3D is the implementation of a time-step management scheme to reduce the simulation time. Figure 2.1 shows the coupling scheme of TOUGHREACT-FLAC3D. In each time step, TOUGHREACT calculates the primary variables for THC processes including temperature (T), liquid pressure (P_l) or gas pressure (P_g), water saturation (S_l), ion concentrations of pore water (C_i) and concentration of exchangeable cations and/or abundance of swelling clay minerals (X_i). These primary variables are then passed to FLAC3D via a coupling module to conduct stress and strain analysis (see Figure 3.1). The coupling between THC processes (provided by TOUGHREACT) and the mechanical part (FLAC3D) is carried out at every time step. The FLAC3D stress and strain analysis constitutes a large portion of the total computation time. For example, in the base case for FEBEX bentonite described below, a THC run took about 4.5 hours but the THMC run (which calls FLAC3D at every time step) took about 4 days. The length of time step is constrained by the chemical calculation to accommodate small changes in the concentrations. However, such small changes in chemical conditions lead to very minimal changes in stress and it is unnecessary to update the stress every time step. Therefore, a time step management scheme was implemented in TOUGHREACT-FLAC3D. A subroutine was inserted in TOUGHREACT to check the change of primary variables from the previous time step and decide if the change is large enough to warrant an update in stress/strain based on the predetermined criteria. An optimal criteria that reduces computational time but also minimizes error was determined. A criteria of 2% reduces computation time significantly and the calculated stress is very close (within 0.1% difference) to that obtained by updating stress/strain every time step.
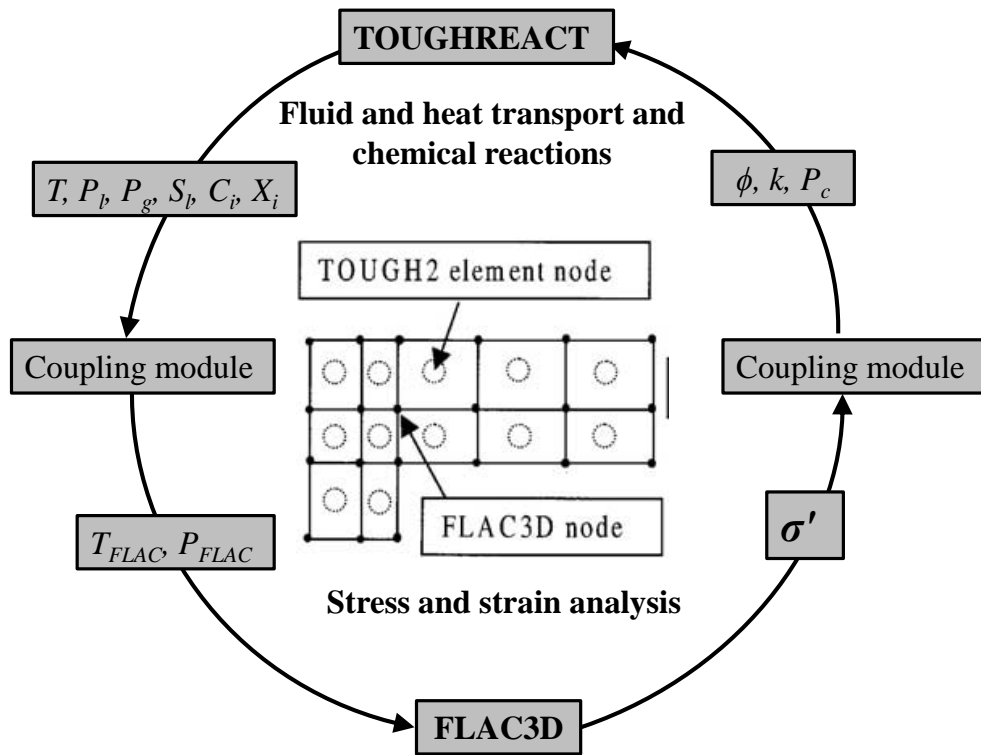
Figure 3.1.The coupling scheme for TOUGHREACT-FLAC3D.

Modeling scenario

The model scenario is still the same as in Liu et al. (2013) and Zheng et al., (2014). The model is applied to a hypothetical bentonite-backfilled nuclear waste repository in clay rock, a repository example that involves a horizontal nuclear waste emplacement tunnel at 500 m depth (Figure 3.2) (Rutqvist et al., 2013). The Z-axis is set as vertical, while the horizontal Y- and X-axes are aligned parallel and perpendicular to the emplacement tunnel, respectively (Figure 3.2) in this 2-D model. Note that while the canister is modeled as a heat source with mechanical properties of steel, the THC changes in the canister and their interactions with EBS bentonite are not considered here for the sake of simplicity.

An initial stress field is imposed by the self-weight of the rock mass. Zero normal displacements are prescribed on the lateral boundaries of the model. Zero stress is applied to the top and vertical displacements are prevented at the bottom. An open boundary is applied to the liquid pressure at top and bottom and initially the model domain is in a hydrostatic state. The initial temperature at the top is about 11 $^\circ$C, with a thermal gradient of 27 $^\circ$C/km, the initial temperature at the bottom is 38 $^\circ$C. The model simulation was conducted in a nonisothermal mode with a time-dependent heat power input (Rutqvist et al., 2014). The power curve in Figure 3.2 was adopted from representative heating data from the U.S. DOE's Used Fuel Disposition campaign for pressurized water reactor (PWR) used fuel. This heat load is then scaled in the 2D model to represent an equivalent line load, which depends on the assumed spacing between individual waste packages along an emplacement tunnel. The heat load for the "low-T" case corresponds to an initial thermal power of 3144 W for a 4-PWR-element waste package after aging for sixty years, a 50-m spacing between emplacement tunnels, and 3-m spacing between the 5-m long packages. The heat load for the "high T" case represents similar waste package and spacing, except with only twenty years of aging. Initially the EBS bentonite has a water saturation of 65% and the clay formation is fully saturated. From time zero, the EBS bentonite undergoes simultaneously re-saturation, heating, chemical alteration, and stress changes.
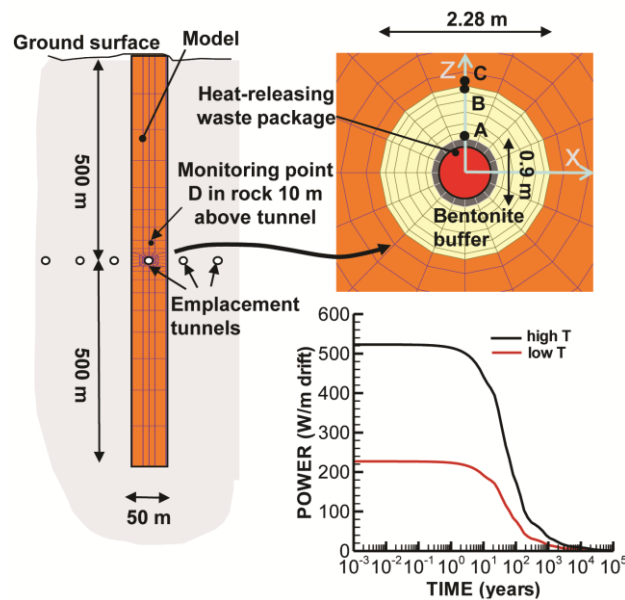
Figure 3.2. Domain for the test example of a bentonite back-filled horizontal emplacement drift at 500 m (Rutqvist et al 2013). Modeling monitoring points: A: inside the bentonite near the canister, B: inside the

112

bentonite and near the EBS-NS interface, C: inside the clay rock formation and near the EBS-NS interface, D: inside the clay rock formation at a distance of 10 m from the canister. "High T": 200 ºC; "Low T": 100ºC.

3.2.2 Mechanical Model

3.2.2.1 Linear elastic model

Details of mechanical model implemented in the TOUGHREACT-FLAC3D are given in Rutqvist et al., (2014). Here we briefly describe the mechanical models for the EBS bentonite and clay formation. For nonisothermal behavior of unsaturated soils, we may partition the total incremental strain into elastic

(ε^e), plastic (ε^p), suction (ε^s), thermal strains (ε^T) and chemical strains (ε^c):

$$d\varepsilon = d\varepsilon^e + d\varepsilon^p + d\varepsilon^s + d\varepsilon^T + d\varepsilon^c \tag{1}$$

where the suction strain represents the strain associated with changes in suction and chemical strain represents the strains associated with change in chemical conditions, including changes in ion concentration and abundance of swelling clays. Each of these types of strain, except chemical strain, is described in Rutqvist et al., (2014).

Similar to thermally induced strains, chemical strains are purely volumetric:

$$d\varepsilon^c = -A_n^* \, dC + A_{sc}^* dMs \tag{3.2}$$

where A_n^* is a constant that linearly relates ion concentration (C) variation and the corresponding strain change. A_{sc}^* is a constant that relates the change in mass fraction of swelling clay, m_s, to change in strain.

A linear elastic swelling model essentially defines the suction stress as a function of water saturation:

$$d\varepsilon^s = \beta_{sw} dSl \tag{3.3}$$

where Sl is the water saturation and β_{sw} is a moisture swelling coefficient.

Under mechanically constrained conditions and considering the linear relationship between swelling stress and suction strain, $d\sigma_s = 3K d\varepsilon^s$, we have a swelling stress that is linearly proportional to the saturation:

$$d\sigma_s = 3K\beta_{sw}dSl \qquad\qquad 3.4$$

where K is the bulk modulus. Equation (4) is what was used for EBS bentonite in Rutqvist et al. (2011). In this report, β_{sw} is 0.048, calibrated based using the swelling pressure of 1 MPa for Kunigel-VI bentonite (Börgesson et al. 2001) under the condition that bentonite is saturated with dilute solution (e.g. deionized water), and K is 20 MPa (Rutqvist et al., 2011).

To consider the swelling due to both moisture and chemical changes, we include the stress due to a change of ion concentration in the pore water and abundance of swelling clay:

$$d\sigma_s = 3K(d\varepsilon^s + d\varepsilon^c) = 3K(\beta_{sw}dSl + A_n^*dC + A_{sc}^*dMs) = 3K\beta_{sw}dSl + A_n dC + A_{sc}dMs \qquad 3.5$$

where $A_n = 3KA_n^*$ is a constant that linearly relates ion concentration (C) variation and the corresponding swelling stress change. $A_{sc} = 3KA_{sc}^*$ is a constant that relates the change in mass fraction of swelling clay, Ms, to change in swelling stress.

A_n is typically calculated from swelling pressures measured using a different solution (e.g. deionized water versus 1 M NaCl solution) to saturate the bentonite. Laredj et al. (2010) proposed the following expression for A_n:

$$A_n = \frac{(5.312\ln C - 23.596)}{\sqrt{C}} - \frac{7.252 \times 10^{-4}}{C^2} \qquad\qquad 3.6$$

An empirical value for A_{sc} is derived through a linear regression of swelling pressure versus smectite mass fractions as shown in Figure 3.3, and A_{sc} is the slope of the linear correlation. However, probably because these bentonite materials differ not only in the mass fraction of smectite but also in other properties, these data points are fairly scattered. This makes it impossible to establish a unique linear regression between swelling pressure change and mass fraction change of smectite. Therefore, we chose a linear correlation line that crosses the measured swelling pressure for Kunigel VI bentonite and used the slope of this line as the value

of A_{sc} which is 2.5×10^6 Pa. For FEBEX bentonite, we used the slope of line that crosses the measured swelling pressure of FEBEX bentonite as the value of A_{sc} which is 6.5×10^6 Pa.
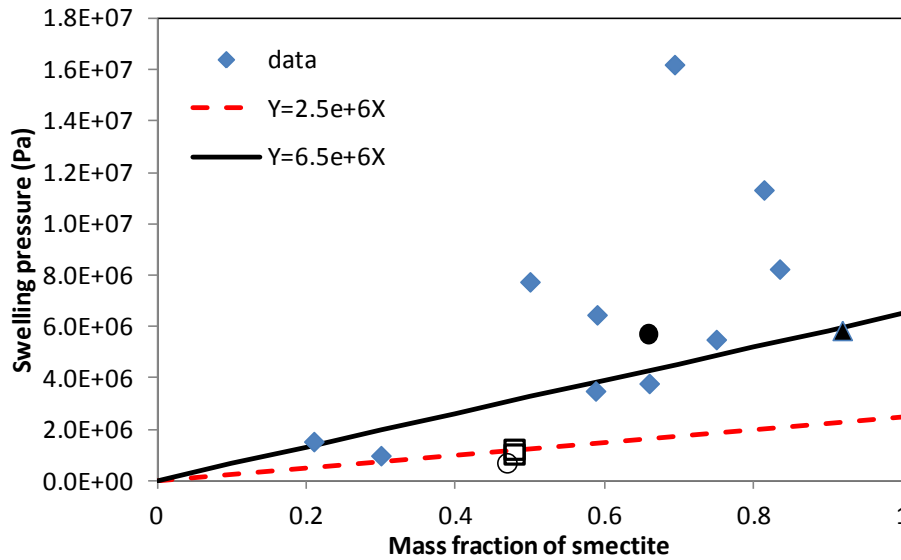
Figure 3.3. Swelling pressure versus mass fraction of smectite for various bentonites. ▲, FEBEX bentonite (ENRESA, 2000); ●, Montigel bentonite (Bucher and Muller-Vonmoos, 1989); □, Kunigel VI bentonite (JNC, 1999); ○, Kunigel bentonite (Komine and Ogata, 1996), ♦ are data for reference material from Czech, Danish, Friedland, Milos Deponit CA-N, Kutch (Indian) and Wyoming MX-80 (Karnland et al., 2006).

For clay formations, we extend the elastic model used in Rutqvist et al., (2014) to consider the chemical strain as in Equation (2). The parameters, A_n and A_{sc}, are same as those used for bentonite, with an assumption that compact bentonite and clay rock behave similarly in terms of the effect of chemical change on strain. However, the validity of this assumption needs to be confirmed with more data.

3.2.2.2   *Double structure BExM*

In the dual structure model, the macrostructure is modeled with a constitutive model for unsaturated soils, such as the Barcelona Basic Model (BBM). The microstructure is incorporated to extend BBM to a dual structure model, which enables simulating the behavior of expansive soils, such as the dependency of swelling strains and swelling pressures on the initial stress state and on the stress path, strain accumulation upon suction cycles and secondary swelling. Thus, in the dual structure model, the total volume (V), the total void ratio (e), and porosity (ϕ), of the material are divided into a micro-structural part and a macro-structural part. The micro-structure can swell to invade the macro-porosity, depending on the mechanical confinement and load level. This is relevant when considering permeability changes during the soil swelling, because fluid flow takes place mostly through the macro-porosity, which is not proportional to the total strain and deformation of the expansive soil. Equations to describe the mechanical behavior of micro-structural and macro-structural levels and the interaction between structural levels are given in Section 2.

Chemical-mechanical coupling via BExM

We develop a one-way coupling approach, in which chemical changes affect mechanical behaviors of bentonite through the evolution of volume fraction of smectite, exchangeable cation concentration, and ionic strength (via osmotic suction). In this report, these effects are taken into account using a dual-structure model (BExM). The mathematical formulations for CM coupling are summarized below.

The original BExM predicts the micro-strains induced by the effective stress for the whole micro-structure, ignoring the effects of smectite. When the material is hydrated, instead of the whole micro-structure, only the parts of the smectite within the micro-structures that interact with the water invasion swell. Here, we introduce the volume fraction of smectite, f_s, into the micro-structure in BExM for C-M coupling. The swelling capacity of the material should decreases with the reduction of the volume fraction of smectite. Thus, the micro-structural volumetric strains are assumed to depend on the change in the microstructural effective stress as follows:

$$\mathrm{d}\varepsilon_{vm}^{e} = \frac{f_s}{K_m}\mathrm{d}\hat{p} \qquad\qquad 3.7$$

where $\hat{p} = p + s_m$, p is the effective mean stress, and s_m is the microstructural suction. K_m is using Equations (3.8):

$$K_m = \frac{e^{\alpha_m \hat{p}}}{\beta_m} \qquad\qquad 3.8$$

The total suction, s_m, contains two components, matric suction, s, and osmotic suction, s_o, i.e. $s_m = s + s_o$. The effect of ionic strength of the pore water on microstructural strain is carried out via the osmotic suction. It is computed as:

$$s_o = -10^{-6}\frac{RT}{V_w}\ln a_w \qquad\qquad 3.9$$

where V_w is the molar volume of water (in m³/mol), and a_w is the activity of water. a_w is calculated in TOUGHREACT (Xu et al. 2011) as follows:

$$\ln a_w = -\Phi m^{*}\frac{1}{55.51} \qquad\qquad 3.10$$

where Φ is osmotic coefficient of the solution and m^* is the sum of the molalities of all species in solution. The effect of exchangeable cations is linked to mechanics through the dependence of β_m (Equation 3.11) on exchangeable cation concentration as shown in the following equation (Gens, 2010):

116

$$\beta_m = \sum_i \beta_m^i x_i \qquad\qquad 3.11$$

As shown in Equation 3-11, the larger the β_m, the more soil swells. Gens (2010) and Guimaraes et al. (2013) proposed that β_m^i is proportional to the ionic hydrated radius and inversely, proportional to its valence, and typically $\beta_m^{Li} > \beta_m^{Na} > \beta_m^K$. Thus, Na-smectite which contains exclusively Na in the interlayer space should swell more than Ca-smectite, provided that other conditions are the same.

Parameters of BExM used for the FEBEX bentonite

The parameters of BExM utilized for these studies are summarized in Table 3.1 The set of parameters are calibrated based on compacted bentonite by Lloret et al. (2003), and are used in the numerical analysis for Mock-up test by Sanchez et al. (2012). In Lloret et al.'s work, the simulation is one-dimensional, which can be treated as an isotropic case in 3D. However, the lateral displacements are constrained in oedometer test but the vertical loading is controlled by stresses. Thus, the stress status in oedometer test is anisotropic and the assumption of isotropy is not appropriate for this test. In Sanchez et al.'s work, although a are in agreement between numerical results and observed behavior during experiments is obtained, the macro-structural bulk modulus of bentonite can reach as high as 2 GPa. Based on the report by Rutqvist and Tsang (2002), the bulk modulus of FEBEX bentonite should be in the order of 10 MPa~100 MPa. Therefore, the bulk modulus evolved too high during the simulation. Here we determine the parameters related to macro-structural bulk modulus, κ, which gives reasonable bulk modulus (in the order of 10 MPa~1000 MPa), from the observed results during experiment. In order not to affect the hydraulic effects on macro-structures, we increase the parameters κ_s to keep the same ratio of $\frac{\kappa}{\kappa_s}$ as Lloret et al. (2003) and Sanchez et al. (2012) used in their simulations. The void ratios e_{micro} and e_{macro} are recalculated based on the experiment data. To match the order of magnitude of β_m which is related to exchangeable cation concentration, a smaller α_m suggested by Sanchez et al. (2012) is used here.

Table 3.1. Parameters used for combination of loading paths tests (Lloret et al., 2003; Sánchez et al., 2012a).

Parameters defining the Barcelona basic model for macrostructural behavior

$\kappa = 0.018$ $\kappa_s = 0.0036$ $\lambda(0) = 0.08$ $p_c = 0.5$ MPa $r = 0.90$ $\zeta = 1$ MPa^{-1} $p_0^* = 6.5$ MPa

$\alpha_a = 0.5$ $\alpha_0 = 1 \times 10^{-5}\,°C$

Parameters defining the law for microstructural behavior

$\alpha_m = -2.1 \times 10^{-6}$ MPa^{-1} $\chi = 1$

Interaction functions

$f_c = 1 + 0.9 \tanh\left[20\left(\frac{p_r}{p_0} - 0.25\right)\right]$ $f_s = 0.8 - 1.1 \tanh\left[20\left(\frac{p_r}{p_0} - 0.25\right)\right]$

Initial conditions

$e_{macro} = 0.21$ $e_{micro} = 0.48$ $f_s = 0.6164$ MPa $s_o = 0.777$ MPa $\beta_m = 2.74 \times 10^{-6}$ MPa^{-1}

Note that the parameters (κ and κ_s) related to macro-structural bulk modulus is higher than original ones used in (Lloret et al., 2003; Sánchez et al., 2012a)

3.2.3 Chemical Model

In these generic cases, it is assumed that that the host rock properties are representative of Opalinus Clay (Bossart 2011; Lauber et al., 2000). Two cases are used for the EBS backfill: one is Kunigel-VI bentonite (Ochs et al., 2004) and the other is FEBEX bentonite (ENRESA, 2000). The mineral compositions of the bentonite and clay formation are listed in Table 3.2. The pore-water compositions of the Kunigel-VI bentonite (Sonnenthal et al., 2008), FEBEX bentonite (Fernández et al., 2001) and the clay formation (Fernández et al., 2007) are listed in Table 3.3. The initial redox potential, expressed as the concentration of dissolved O_2 (O_2(aq)) in the model.

Table 3.3 lists the thermal and hydrodynamic parameters used in the model. The majority of these parameters are taken from Sonnenthal et al. (2008) for Kunigel-VI bentonite and from Thury (2002) for the EBS bentonite and the NS clay formation. Permeability for the clay formation is from Soler (2001) and bentonite permeability is from JNC (1999).

In this report, we used the same thermal conductivity and permeability for both FEBEX and Kunigel-VI bentonites. These parameters are actually fairly similar for the two types of bentonite — thermal conductivity for saturated Kunigel-VI bentonite is 1.5W/m-ºC (see Table 3.2) and that for FEBEX bentonite is 1.3 W/m ºC (ENRESA, 2000); permeability for Kunigel-VI bentonite is 2E-21 m^2 and that for FEBEX ranges from 1E-21 to 3.75E-21 m^2 (ENRESA, 2000; Zheng et al., 2011; Chen et al. 2009). Moreover, by using the same values of thermal conductivity and permeability for both bentonites, we can isolate the effect of variations in chemical and CM coupling parameters on the stress changes.

Table 3.2. Mineral volume fraction (dimensionless, ratio of the volume for a mineral to the total volume of medium) of the Kunigel-VIbentonite (Ochs et al., 2004), FEBEX bentonite (ENRESA, 2000; Fernández et al., 2004; Ramírez et al., 2002) and Opalinus Clay (Bossart 2011; Lauber et al., 2000).

Mineral	EBS Bentonite: Kunigel-VI	EBS Bentonite: FEBEX	Clay Formation: Opalinus Clay
Calcite	0.016	0.0065	0.093
Dolomite	0.018	0.0	0.050
Illite	0.000	0.0	0.273
Kaolinite	0.000	0.0	0.186
Smectite	0.314	0.6	0.035
Chlorite	0.000	0.0	0.076
Quartz	0.228	0.026	0.111
K-Feldspar	0.029	0.0065	0.015
Siderite	0.000	0.0	0.020
Ankerite	0.000	0.0	0.045
Pyrite	0.000	0.01	0.000
Greenrust	0.000	0.000	0.000
Magnetite	0.000	0.000	0.000
Hematite	0.000	0.000	0.000
Goethite	0.000	0.000	0.000
Fe(oh)3(s)	0.000	0.000	0.000
Fe(oh)2	0.000	0.000	0.000
Vermiculites	0.000	0.000	0.000
Berthierine(Fe^{+2})	0.000	0.000	0.000
Berthierine(Fe^{+3})	0.000	0.000	0.000
Saponite(Fe, Ca)	0.000	0.000	0.000
Saponite(Fe,K)	0.000	0.000	0.000
Saponite(Fe, Na)	0.000	0.000	0.000
Saponite(Fe, Mg)	0.000	0.000	0.000

Table 3.3. Pore-water composition (mol/kg water, except pH) of Kunigel-VI bentonite(Sonnenthal et al., 2008), FEBEX bentonite (Fernández et al., 2001) and Opalinus Clay (Fernández et al., 2007).

	EBS Bentonite: Kunigel-VI	EBS Bentonite: FEBEX	Clay formation : Opalinus Clay
pH	8.40	7.72	7.40
Cl	1.50E-05	1.60E-01	3.32E-01
SO_4^{-2}	1.10E-04	3.20E-02	1.86E-02
HCO_3^-	3.49E-03	4.1E-04	5.18E-03
Ca^{+2}	1.37E-04	2.2E-02	2.26E-02
Mg^{+2}	1.77E-05	2.3E-02	2.09E-02
Na^+	3.60E-03	1.3E-01	2.76E-01
K^+	6.14E-05	1.7E-03	2.16E-03
Fe^{+2}	2.06E-08	2.06E-08	3.46E-06
$SiO_2(aq)$	3.38E-04	1.1E-04	1.10E-04
AlO_2^-	1.91E-09	1.91E-09	3.89E-08
$O_2(aq)$	2.57e-4	2.57e-4	1.2E-51

Table 3.4. Thermal and hydrodynamic parameters.

Parameter	Clay formation : Opalinus Clay	EBS Bentonite
Grain density [kg/m^3]	2700	2700
Porosity ϕ	0.162	0.33
Saturated permeability [m^2]	2.0×10^{-20}	2.0×10^{-21}
Relative permeability, k_{rl}	$m = 0.6$, $S_{rl} = 0.01$	$K_{rl} = S^3$
Van Genuchten α [1/Pa]	6.8×10^{-7}	3.3×10^{-8}
Van Genuchten m	0.6	0.3
Compressibility, β [1/Pa]	3.2×10^{-9}	5.0×10^{-8}
Thermal expansion coeff., [1/^{o}C]	1.0×10^{-5}	1.5×10^{-4}
Dry specific heat, [J/kg- ^{o}C]	860	800
Thermal conductivity [W/m-^{o}C] dry/wet	1.48/1.7$^\$$	1.1/1.5
Tortuosity for vapor phase	$\phi^{1/3}S_g^{10/3}$	$\phi^{1/3}S_g^{10/3}$
Bulk modulus, (GPa)	4.17	0.02
Shear modulus, (GPa)	1.92	0.0067

From http://www.mont-terri.ch/internet/mont-terri/en/home/geology/key_characteristics.html

In previous simulations (Liu et al., 2013; Zheng et al., 2014; 2015), the corrosion of canister was neglected because the chemical model focused on the illitization in bentonite and it is assumed that corrosion of canister won't interfere the illitization processes. In this report, in order to test this assumption, corrosion of a steel canister is included in the chemical model using the following reaction:

$$\text{Iron} + 2H^+ + 0.5O2(aq) \leftrightarrow Fe^{+2} + H_2O \qquad\qquad 3.12$$

The corrosion of steel canister might lead to formation of Fe-oxides and Fe-hydroxides. In current model, we added greenrust (fougerite), magnetite, hematite, goethite, Fe(OH)$_3$(s) and Fe(OH)$_2$. If the Fe ion released by corrosion is not been consumed by the precipitation of Fe-oxides and Fe-hydroxides, there is a chance that some Fe bearing clay minerals could be formed, such as vermiculite, berthierine, saponite with different type of cations. These minerals are also listed in Table 3.2 as secondary minerals such that they could be formed.

Mineral dissolution/precipitation is kinetically controlled. The kinetic law for mineral dissolution/precipitation is given in Xu et al. (2011):

$$r = kA \left| \left(1 - \left(\frac{K}{Q} \right)^{\theta} \right) \right|^{\eta}$$

3.13

where r is the kinetic rate, k is the temperature-dependent rate constant (mol/m^2-s), A is the reactive surface area per kg water, K is the equilibrium constant for the mineral–water reaction (written for the destruction of one mole of mineral), and Q is the reaction quotient. Here, for simplicity, the exponents θ and η are assumed equal to 1.

The kinetic rate constants can usually be summed for three mechanisms (Lasaga et al., 1994):

$$k = k_{25}^{nu} \exp \left[\frac{-E_a^{nu}}{R} \left(\frac{1}{T} - \frac{1}{298.15} \right) \right] + k_{25}^{H} \exp \left[\frac{-E_a^{H}}{R} \left(\frac{1}{T} - \frac{1}{298.15} \right) \right] a_H^{n_H}$$
$$+ k_{25}^{OH} \exp \left[\frac{-E_a^{OH}}{R} \left(\frac{1}{T} - \frac{1}{298.15} \right) \right] a_{OH}^{n_{OH}}$$

3.14

where superscripts *nu*, *H* and *OH* indicate neutral, acid, and alkaline mechanisms, respectively, E is the activation energy, k_{25} is the rate constant at 25 °C, R is the gas constant, T is the absolute temperature, α is the activity of the species, and n is a power term (constant). It should be noted that reaction rates depend on the reactive surface area A in Equation (3-13), which is a function of the product of the specific surface area and the volume fraction of each mineral. Therefore, the calibrated values of specific surface area and volume fraction should be viewed as arbitrary and non-unique (co-linearly varying) values, the product of which is relevant but not each value separately.

The kinetic rates and surface areas for the minerals considered in the model were taken mostly from Xu et al. (2006) (Table 3.5). However, the illitization rate (the rate of illite precipitation and smectite dissolution) was calibrated (Liu et al., 2013) based on the measured illite percentage in an illite/smectite (I/S) mixed layer from Kinnekulle bentonite, Sweden (Pusch and Madsen, 1995). The kinetics data for iron is taken from Birgersson and Wersin (2013). Surface areas and reaction rates for greenrust (fougerite), magnetite, hematite, goethite, $Fe(OH)_3$(s) and $Fe(OH)_2$ are taken the same as ankerite. The kinetic data for vermiculite, berthierine, saponite are the same as smectite. The thermodynamic data were taken from the Data0.dat.YMPv4.0, an EQ3/6 (Wolery 1993) database qualified by the U.S. Department of Energy for the Yucca Mountain Project.

Table 3.5. Kinetic properties for minerals considered in the model (Xu et al., 2006).

Mineral	A (cm²/g)	Parameters for Kinetic Rate Law								
		Neutral Mechanism		Acid Mechanism			Base Mechanism			
		k_{25} (mol/m²/s)	E_a (kJ/mol)	k_{25} (mol/m²/s)	E_a (kJ/mol)	$n(H^+)$	k_{25} (mol/m²/s)	E_a (kJ/mol)	$n(H^+)$	
Quartz	9.8	1.023×10^{-14}	87.7							
K-feldspar	9.8	3.89×10^{-13}	38	8.71×10^{-11}	51.7	0.5	6.31×10^{-12}	94.1	-0.823	
Kaolinite	151.6	6.91×10^{-14}	22.2	4.89×10^{-12}	65.9	0.777	8.91×10^{-18}	17.9	-0.472	
Illite	1.5×10^{2} [1]	1.3×10^{-11}	105 [2]							
Chlorite	9.8	3.02×10^{-11}	88	7.76×10^{-12}	88	0.5				
Calcite	3.5	1.63×10^{-7}	23.5							
Dolomite	12.9	2.52×10^{-08}	62.76	2.34×10^{-7}	43.54	1				
Ankerite	0.3	1.26×10^{-9}	62.76	6.46×10^{-4}	36.1	0.5				
Smectite	1.5×10^{2} [1]	1.3×10^{-11}	105 [2]							
Pyrite	0.3	$2.5\text{X}10^{-12}$	62.76							
Iron	1.68	4.47×10^{-9}	0.0							
Greenrust	0.3	1.26×10^{-9}	62.76							
Magnetite	0.3	1.26×10^{-9}	62.76							
Hematite	0.3	1.26×10^{-9}	62.76							
Goethite	0.3	1.26×10^{-9}	62.76							
Fe(oh)3(s)	0.3	1.26×10^{-9}	62.76							
Fe(oh)2	0.3	1.26×10^{-9}								
Vermiculites	1.5×10^{2}	1.3×10^{-11}	105							
Berthierine(Fe^{+2})	1.5×10^{2}	1.3×10^{-11}	105							
Berthierine(Fe^{+2})	1.5×10^{2}	1.3×10^{-11}	105							
Saponite(Fe, Ca)	1.5×10^{2}	1.3×10^{-11}	105							
Saponite(Fe,K)	1.5×10^{2}	1.3×10^{-11}	105							
Saponite(Fe, Na)	1.5×10^{2}	1.3×10^{-11}	105							
Saponite(Fe, Mg)	1.5×10^{2}	1.3×10^{-11}	105							

[1] calibrated based on the field illitization data (Liu et al., 2013)

[2] from Pusch and Madsen (1995)

3.3 Model Results

In Liu et al. (2013) and Zheng et al. (2014) the model results for first one thousand years, expressed as the evolution of temperature, pore pressure, water saturation, concentration and stress, were discussed in detail and a sensitivity analyses to key chemical and mechanical parameters were conducted to understand the coupling processes. In Zheng et al. (2015), the simulations were conducted for one hundred thousand years thanks to the improvement in the efficiency of TOUGHREACT-FLAC3D, which helped to answer questions like when illitization stabilizes in the long run. In the following sections, we first briefly summarize these results in Sections 3.3.1 and 3.3.2, and then present new model results from FY16 effort in Section 3.3.3.

3.3.1   Key Findings from Previous Models Using Extended Linear Elastic Model

In the generic cases we used to study the effect of high temperature on the THMC evolution in bentonite and clay formation, two bentonites have been simulated: Kunigel-VI and FEBEX bentonite, and two scenarios were simulated for comparison: a case in which the temperature in the bentonite near the waste canister can reach about 200ºC and a case in which the temperature in the bentonite near the waste canister peaks at about 100ºC. All these simulations used extended linear elastic model to link chemistry with mechanics. In this section, we summarize the key findings from Liu et al. (2013), Zheng et al. (2014), and Zheng et al. (2015).

3.3.1.1   *Enhancement of Illitization under Higher Temperature*

The very first question we were attempting to answer by this series of simulations was whether illitization would occur in the EBS bentonite and host clay formation. Illitization, the transformation of smectite to illite, has caught great attention of researchers because it results in a loss of smectite which in turn causes a loss in the swelling capacity. Illitization is evident in geological systems (Wersin et al., 2007), as exemplified by several natural analogue studies (Pusch and Madsen, 1995; Kamei et al., 2005; Cuadros 2006; Casciello et al., 2011). Illite/smectite mixed-layer clay is commonly observed in clayey sediments, and deep formations typically contain more illite than shallow formations (Cuadros 2006), which leads to a conclusion that smectite is gradually transformed to illite during diagenesis and become of the basis for assuming the illitization would occur in EBS bentonite. Liu et al. (2013) did an extensive review of laboratory experiments (e.g. Mosser-Ruck and Cathelineau 2004; Pacovsky et al. 2005) and field tests (Pusch et al., 2010) and modeling studies (e.g. Montes-H et al., 2005), and found out there was no conclusive evidence that illitization will occur and swelling capacity will be lower in bentonite. While various studies shed light on certain aspects of this question, there is no study that integrates the relevant THMC processes and considers the interaction between EBS and host rock. One of the key findings from our simulations is that illitization does occur in the two bentonites we tested: Kunigel-VI (Ochs et al., 2004) and FEBEX (ENRESA 2000) bentonite and it is enhanced at higher temperature, as shown in Figure 3.4. In addition, we also have the following observations:

- The quantity of illitization, expressed as the smectite volume fraction change, is affected by many chemical factors and as a result varies over a wide range. The most important chemical

factors for illitization are the concentration of K and dissolution rate of K-feldspar, as revealed by the sensitivity analyses conducted in Liu et al. (2013) and Zheng et al., (2014).

- The geochemical interaction between EBS bentonite and the clay formation has a strong effect on long term illitization in bentonite. Figure 3.4 shows that bentonite near the EBS-NS interface undergo more illitization than that near the waste package by the end of one hundred thousand years for the "high T" scenarios (Figure 3.4). The reason is that after two thousand –three thousand years, the illitization process ceases in the clay formation and the K ion is not consumed by the local illitization and is, therefore, transported into the EBS bentonite to facilitate further illitization.

- Illitization is more pronounced for Kunigel-VI bentonite than FEBEX bentonite (Figure 3.5) due to their difference in chemical properties, indicating illitization in EBS bentonite has to be evaluated case by case. The key chemical properties that lead to different degree of illitization is the supply of K and Al, for example by the dissolution of K-feldspar (Figure 3.6).

- In additions to illitization, other chemical alterations include the dissolution of K-feldspar and calcite, and the precipitation of quartz, chlorite, and kaolinite. And, precipitation of quartz could affect the mechanical property of bentonite.

- The type of smectite contained in the bentonite, i.e., whether it is Na-smectite or Ca-smectite does not have a strong effect on illitization.

- Illitization also occurs in clay formation and is significantly enhanced under higher temperature (see Figure 3.4).

Figure 3.4. The temporal evolution of smectite volume fraction at points A, B, C, and D for the "high T" and "low T" cases, and a simulation that assumes no heat release from the waster package (A: inside the bentonite near the canister, B: inside the bentonite and near the EBS-NS interface, C: inside the clay rock formation and near the EBS-NS interface, D: inside the clay rock formation at a distance of 10 m from the canister).

Figure 3.5. The temporal evolution of smectite volume fraction at points A and B for Kunigel and FEBEX bentonite.

Figure 3.6. The temporal evolution of K-feldspar volume fraction at points A, B, C, and D in the base case with Kunigel bentonite and a sensitivity case with FEBEX bentonite.

3.3.1.2 *Impact of Illitization on Swelling Stress*

The mechanical-chemical coupling implemented in the model allows us to evaluate how the chemical changes may affect the mechanical behavior of the EBS bentonite in terms of swelling and total stress. Because of the extended linear swelling model used, we limit our analysis to the effects of ion concentration and illitization on swelling and do not include other potential effects of chemical changes on mechanics, such as changes in mechanical properties due to cementation.

Several processes combine to drive stress up in bentonite and peak at around one hundred years, and then decrease and stabilized after twenty to thirty thousand years. Reasons for the stress increase include the increase in pore pressure due to hydration and thermal pressurization (a processes caused by the difference in thermal expansion of the fluid and solid host rock), bentonite swelling, and thermal expansion. The stronger thermal pressurization in the "high T" case leads to much higher stress in the bentonite than the "low T" case. For both the "high T" and "low T" cases, the major contribution to total stress within the buffer is pore pressure, with smaller contributions from swelling and thermal stresses.

The constitutive relationship described by Equation (3.5) provides an opportunity to evaluate the effect of chemical changes on swelling stress. In order to isolate the contributions of ion concentration changes versus smectite changes on swelling stress changes, we present three sets of calculated swelling stress. In the first set, denoted in Figure 3.7 as "$\sigma=f(Sl,C,Ms)$", the swelling stress is calculated according to Equation (3.5) as a function of liquid saturation changes (Sl), ion concentration (C) changes, and smectite (Ms) changes. In the second set, denoted as "$\sigma=f(Sl,C)$", the contribution from smectite changes in Equation (3.5) is disregarded, and the swelling stress is only a function of liquid saturation and ion concentration. In the third set, denoted as "$\sigma=f(Sl)$", all chemical effects are neglected, and the swelling stress is only a function of liquid saturation changes. By the comparing the simulated swelling stresses in these three sets of simulations, we can calculate the swelling stress reduced by ion concentration and smectite dissolution, which are listed in Table 3.7 for both Kunigel-Vi and FEBEX bentonite.

127

Figure 3.7. Simulation results of swelling stress at point A for the "low T" and "high T" scenarios for Kunigel-VI bentonite (Zheng et al., 2015), respectively.

Table 3.6. The geochemically induced swelling stress for Kunigel-VI and FEBEX bentonite at points A and B for "high T" scenario. Stress reduction by ion concentration is the difference between the swelling stress obtained with "σ=f(Sl)" and "σ=f(Sl,C)", and the stress reduction by smectite dissolution is the difference between the swelling stress obtained with "σ=f(Sl,C)" and "σ=f(Sl,C,Ms)" (see Figure 3.7), where the relative amount (%) use the results from "σ=f(Sl)" as the basis.

	Kunigel-VI bentonite				FEBEX bentonite			
	Stress reduction by ion concentration		Stress reduction by smectite dissolution		Stress reduction by ion concentration,		Stress reduction by smectite dissolution	
	MPa	%	MPa	%	MPa	%	MPa	%
Point A	0.07	7%	0.09	9%	0.006	0.1%	0.17	3.4%
Point B	0.08	8%	0.45	45%	0.06	1.1%	0.6	12%

In terms of the effect of chemical changes on swelling stress for bentonite, the modeling results (Zheng et al., 2015) leads to the following observations:

- More swelling stress reduction take place near the near the EBS-NS interface as more illitization occurs in this area, expressed as the smectite volume fraction change, For the "high T" case, Kunigel-VI bentonite near the EBS-NS loses as much as 53% swelling capacity and FEBEX bentonite near the EBS-NS has about 13% reduction in swelling stress whereas bentonite near the waste package undergoes a small reduction in swelling stress — 16% reduction for Kunigel-VI and 3.4% for FEBEX bentonite, respectively.

- High temperature leads to higher reduction in swelling stress. For the "low T" case, the stress reduction by chemical change is relatively homogeneous, 16% reduction for Kunigel-VI bentonite and around 3% reduction for FEBEX bentonite after one hundred thousand years, as opposed to as high as 53% swelling stress reduction for Kunigel-VI bentonite and 13% reduction for FEBEX bentonite.
- Although Kunigel-VI and FEBEX bentonite undergo similar magnitude reduction in swelling stress in absolute values (as in MPa), relative to their corresponding swelling capacity, it is a much minor reduction for FEBEX bentonite because FEBEX bentonite has a swelling capacity about 5 folds of that of Kunigel-VI bentonite. Using EBS bentonite with higher swelling capacity could alleviate the negative consequence of illitization.
- Despite the swelling stress is noticeably affected by illitization, the total stress is much less affected by the chemical change because swelling stress only accounts for a relatively small proportion of total stress.
- Chemical change leads to about a 2.6% decrease in stress near the EBS-NS interface and about 0.7% in the far field. In general, chemical change does not have significant impact on the stress in the clay formation.

3.3.2   Impact of iron-bentonite interaction on swelling stress

While the type of material for waste canister is a still open question, steel canister has been selected as one of the potential canister. For example, based on a series of selection criteria including canister lifetime, avoidance of detrimental impacts on other barrier, retrievability during the operational phase, etc, NAGRA proposed to use steel canister (NAGRA, 2002). In order to ensure very limited impact of the other barriers, extensive research have been conducted on the interaction of corroding iron with bentonite (e.g. Wersin et al., 2015; Shibata et al., 2014; Martin et al., 2014). Corrosion of steel under the repository conditions is a very complex process and affected by the both the environment inside and outside the canister. In addition to deterioration of canister itself, corrosion of steel could lead the generation of H_2(gas) and alteration of bentonite. In this report, it is for the first time that Fe-corrosion was simulated in conjunction with coupled THMC model for bentonite barrier, therefore we start with several simplifications such that we can focus on the alteration of smectite in bentonite barrier caused by steel corrosion. First, a constant reaction rate is applied to iron dissolution reaction, using a surface area of 1.68 cm^2/g and a rate constant of $10^{-8.35}$ mol/m^2/s which corresponds to an average corrosion rate of 1 μm/a (Birgersson and Wersin, 2014). It is known that corrosion rate is affected by the geochemical and bacterial conditions in vicinity of canister (Landolt et al., 2009) and such conditions should be built in the reaction rate. However, we neglect this effect and use a constant rate in this report. Second, focused corrosion is neglected. Focused or localized corrosion processes result from the establishment of electrochemical cells due to spatial differences in the local environment or in the material properties. To simplify our simulation, we assume the corrosion is homogeneous at the canister surface.

Previous THMC models (Liu et al., 2013; Zheng et al., 2014; 2015) were conducted using both Kunigel-VI and FEBEX bentonite as the EBS bentonite. In FY16, because corrosion of steel canister and interaction of bentonite and corroded steel is very complex and information about the iron-bentonite interaction for Kunigel-VI bentonite is very sparse, coupled THMC model with iron-bentonite was only conducted for the case using FEBEX bentonite as EBS. As presented in Section 4, extensive geochemical characterization of FEBEX bentonite after the dismantling of FEBEX in situ test was conducted. Once the geochemical data is available, they will be used to constrain our iron-bentonite interaction conceptually model such that model prediction would be more reliable. In the remaining part of this section, the THMC model that takes into account iron-bentonite interactions (for example, named "hgh T, with Fe-ben") are compared to the THMC model (Zheng et al. 2015) that did not consider iron-bentonite interactions (for example, named "hgh T, no Fe-ben").

In the model, it is assumed that the steel canister is 1.5 cm. With an average corrosion rate of 1 μm/a, the canister is totally corroded in about fifteen thousand years, as shown in Figure 3.8. Corrosion of steel typically undergoes an initial aerobic corrosion and then become anaerobic once oxygen is consumed. Because of the longer aerobic corrosion (due to longer unsaturation time in bentonite) and higher temperature in the "high T" case, the corrosion is faster in the "high T" case (Figure 3.8) than that in "low T" case, but eventually both cases have similar corrosion rate as the canister cool down.

Figure 3.8. Simulation results of the corrosion of steel canister for the "low T" and "high T" scenarios for FEBEX bentonite.

Anaerobic corrosion of steel is an oxidation that involves direct formation of magnetite (Fe_3O_4) via a solid state reaction. $Fe(OH)_2$ can also be transformed to magnetite through Schikkor reaction:

$$3Fe(OH)_2 \rightarrow Fe_3O_4 + 2H_2O + 2H^+$$
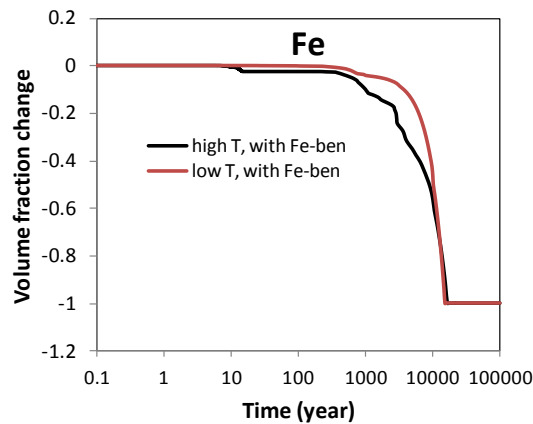
Eventually the production of corrosion is dominated by the magnetite, with small amount of $Fe(OH)_3(s)$ and $Fe(OH)_2$ remaining (Figure 3.9). Over the course of transferring steel to magnetite and iron-hydroxides, Fe^{+2} moves into bentonite via diffusion and current model shows the formation of goethite at the vicinity of canister (point A in Figure 3.10). At point B, the formation of goethite is firstly caused by the interaction between bentonite and host rock, but after about one thousand years, the formation of goethite is caused by arrival of Fe^{+2} front from the corrosion of steel canister.
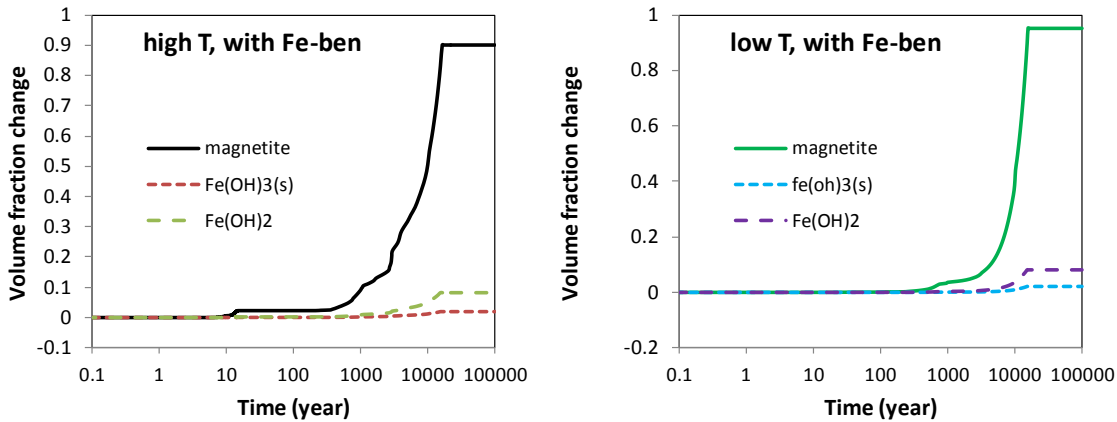
Figure 3.9. Simulated volume fraction change of magnetite, $Fe(OH)_3(s)$ and $Fe(OH)_2$ for ion for the "low T" (right) and "high T" scenarios (left) for FEBEX bentonite.
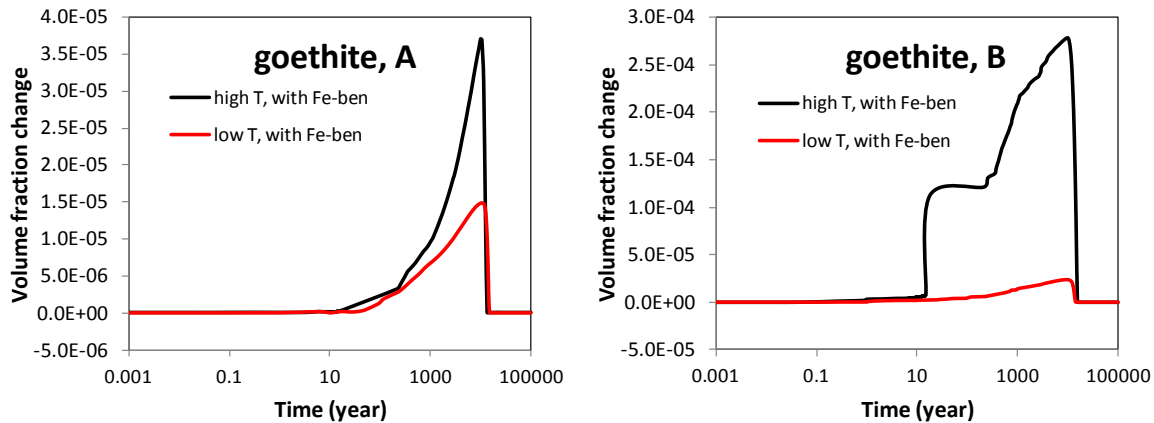
Figure 3.10. Simulated volume fraction change of goethite at point A and B for the "low T" (right) and "high T" scenarios (left) for FEBEX bentonite.

Although the formation of Fe-oxide and Fe-hydroxides as a result of corrosion of steel canister is relatively well understood, the Fe-bentonite interaction is far from conclusive. In the Alternative Buffer Materials (ABM) test conducted in the Aspo hard rock laboratory, Sweden, saturated MX-80 bentonite was in contact with steel canister and samples were collected after 881 days. Wersin et al. (2015) analyzed the samples and found no transformation of montmorillonite or newly formed clay phase. But Cheshire et al., (2014) showed that there were significant changes

to the phyllosilicates at the metal-bentonite interface due to metal corrosion producing either Fe-phyllosilicates (i.e., Fe-saponite and chlorite) on steel surfaces. Based on Mosser-Ruck et al (2010), at 80 and 150 °C, montmorillonite underwent weak enrichment of Fe and depletion of Si. At 300 °C, vermiculite became dominant. Vermiculite is structurally similar to montmorillonite but has higher interlayer charge (0.5 to 0.7 per $O_{10}(OH)_2$ unit vs that of 0.2 to 0.5 in montmorillonite and therefore swells much less). Under neutral pH conditions, Mosser-Ruck et al (2010) concluded the possibility of forming Fe-rich dioctahedral smectite or berthierine or Fe-saponite depending on Fe/bentontie ratios and Liquid/bentonite ratios and temperature. In the current model, we therefore added as vermiculite, berthierine, saponite with different type of cations as secondary minerals that they could be formed (Table 3.1). However, thermodynamically all these minerals are under-saturated, for example, as shown in Table 3.7 for their saturation indices at point A at ten thousand years for the "high T" case. Therefore, current model does not show the formation of these minerals.

Table 3.7. Saturation index (log(Q/K)) of some Fe bearing clay minerals at point A at ten thousand years for "high T" case.

	Vermiculite	Berthierine (Fe^{+2})	Berthierine (Fe^{+3})	Saponite (Fe, Ca)	Saponite (Fe, K)	Saponite (Fe, Mg)	Saponite (Fe, Na)
Saturation index	-11.6	-7.2	-7.5	-6.9	-7.0	-7.3	-5.7

In previous THMC model (Zheng et al., 2015), although Fe-bentonite interaction was not considered, the excessive silicates and aluminum produced by the dissolution K-feldspar and smectite led to the precipitation of chlorite. In the current model in which Fe-bentonite interaction is considered, as more Fe^{+2} is diffuse into bentonite, chlorite precipitation is enhanced slightly (see Figure 3.11), especially for the "high T" case. Consequently, more precipitation of chlorite seems to drive more dissolution of smectite (see Figure 3.12). However, the difference in smectite dissolution between models that consider Fe-bentonite interaction and that did not consider Fe-bentonite interaction is fairly moderate.
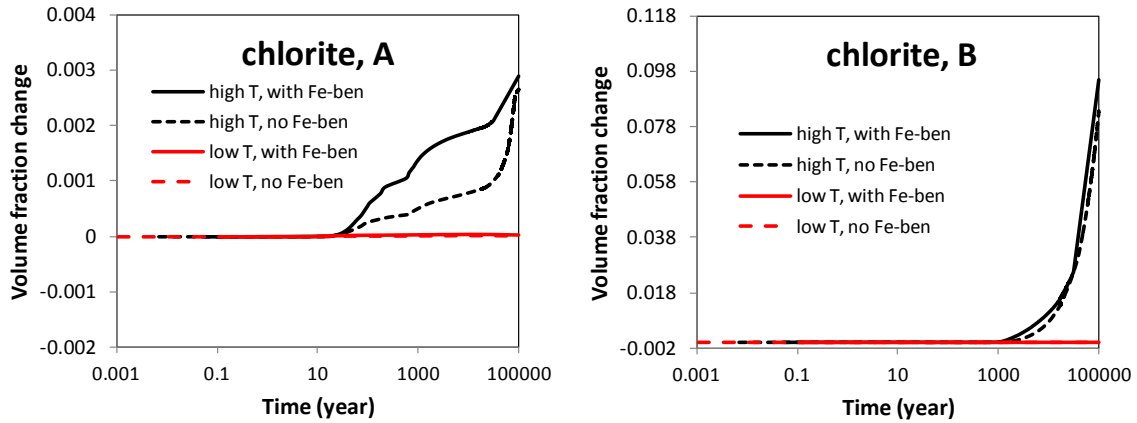
Figure 3.11. Simulated volume fraction change of chlorite at point A and B for the "low T" (right) and "high T" scenarios (left) for FEBEX bentonite, with Fe-bentonite interaction and without Fe-bentonite interaction (Zheng et al., 2015).
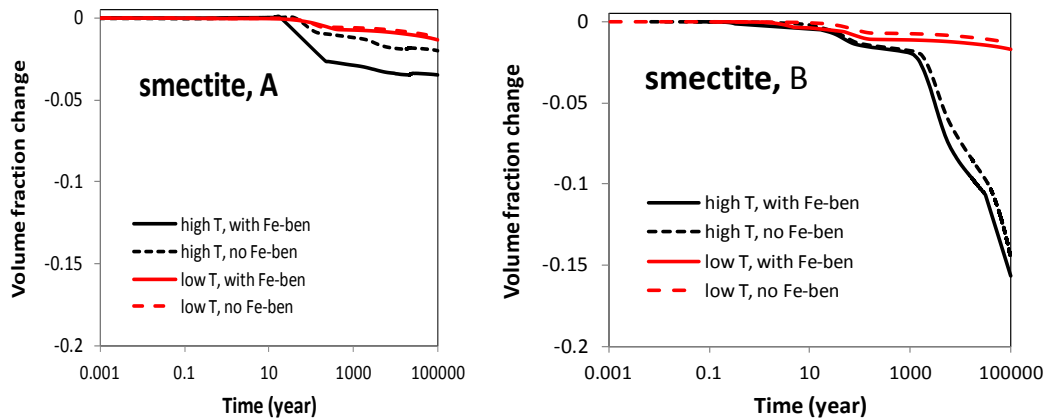
Figure 3.12. Simulated volume fraction change of smectite at point A and B for the "low T" (right) and "high T" scenarios (left) for FEBEX bentonite, with Fe-bentonite interaction and without Fe-bentonite interaction (Zheng et al., 2015).

As shown in Figure 3.12, model considering the Fe-bentonite interaction has slight more dissolution of smectite, which lead to a slightly more reduction in swelling stress. Table 3.8 lists the swelling stress reduction for the model with and without Fe-bentonite interaction. At point A, when Fe-bentonite interaction is considered in the model, the swell stress reduction by smectite dissolution is 7.2% in comparison with 3.4% for the model without considering Fe-bentonite interaction. At point B, the difference in stress reduction by smectite dissolution between the model with and without Fe-bentonite interaction is about 2%.

Table 3.8. The geochemically induced swelling stress for FEBEX bentonite with and without considering Fe-bentonite interaction at points A and B for "high T" scenario. Stress reduction by ion concentration is the difference between the swelling stress obtained with "σ=f(Sl)" and "σ=f(Sl,C)", and the stress reduction by smectite dissolution is the difference between the swelling stress obtained with "σ=f(Sl,C)" and "σ=f(Sl,C,Ms)", where the relative amount (%) use the results from "σ=f(Sl)" as the basis.

	with Fe-bentonite				Without Fe-bentonite			
	Stress reduction by ion concentration		Stress reduction by smectite dissolution		Stress reduction by ion concentration,		Stress reduction by smectite dissolution	
	MPa	%	MPa	%	MPa	%	MPa	%
Point A	0.0006	0.1%	0.36	7.2%	0.006	0.1%	0.17	3.4%
Point B	0.08	8%	0.68	13.7%	0.06	1.1%	0.6	12%

3.3.3 THMC results with the dual-structure model

BExM was implemented in TOUGHREACT-FLAC3D and a series of THMC simulations were conducted for both "high T" and "low T" using FEBEX bentonite as EBS. Coupled THMC model with BExM was not conducted for Kunigel-VI because the parameterization of BExM for Kunigel-VI bentonite requires addition modeling effort and reliable data to calibrate some of key parameters whereas parameters for BExM for FEBEX bentonite have been well calibrated (e.g. Sánchez et al., 2012). It is also noted that the chemical model in the THMC model using BExM for FEBEX bentonite presented in this sections is the same as in Zheng et al. (2015), which did not considered the iron related reactions as articulated in Section 3.2.3. The reason is that Fe-bentonite interaction does not have significant effect on smectite alteration (as shown earlier in Section 3.3.2).

3.3.3.1 THMC simulation results

As section 3.2.3 illustrates, the chemical-mechanical coupling is implemented in the dual-structure model. It allows us to evaluate how the chemical changes may affect the mechanical behavior of the EBS bentonite in terms of effective/net and total stress. The effects considered in the model come from three components, volume fraction of smectite, exchangeable cation concentration, and osmotic suction.

We simulated a series of generic repository cases (described in Figure 3.2) with both high temperature ("high T") and low temperature ("low T") subjected to THMC processes (noted as "THMC"), in which C-M coupling is considered. The material for buffer is using FEBEX bentonite, whose mechanical behavior is computed with BExM. To account for the effects resulted by chemical reactions, we also simulated another scenario under the same loading conditions but without C-M coupling (noted as "THM"). Since the coupling is one-way, i.e. the mechanical behavior does not affect the fluid, thermal transports or chemical reactions. The evolution of temperature, liquid saturation and pore pressure is the same for result by "THMC" computation with high temperature and the one by "THM" with high temperature. The same situation is obtained with two "low T" cases. Figure 3.13 shows the temperature changes, and Figure 3.14 displays the evolution of liquid saturation and Figure 3.15 shows the evolution of pore pressure at point A and B for both "low T" and "high T" cases. At point A, the temperature can reach up to 200 °C in "high T" case and to 95 °C in "low T" case at around twenty years, and

then it decreases again to the ambient temperature, 25 °C. Point B has lower temperature than point A since it is far from the heater. The temperature at point B goes up to 170 °C in "high T" case and to 80 °C in "low T" case at around twenty years, and then it decreases again to the ambient temperature, 25 °C. As Figure 3.14 shows, the liquid saturation at point A decreases firstly due to the drying process by the heater nearby. The material has been dried more during the high temperature case, inducing greater reduction in liquid saturation. Around one year, the bentonite at point A reaches the lowest saturation in both "high T" and "low T" cases. Then, the material is hydrated from the surrounding rocks to reach fully saturation status (about twenty years for "high T", fifteen years for "low T"). For point B, which is close to host rocks, the hydration starts at the beginning of the simulations. In "high T" case, the drying process near the heater helps the material at point B hydrate even faster. The bentonite reaches fully saturation at round five years in "high T" case, while it takes about eight years to saturate the material in "low T" case. There is no much difference of pore pressure between point A and point B. Since the point B is closer to host rocks than point A, the pore pressure at point B increases earlier than point A. In both "high T" and "low T" cases, pore pressures reach the peaks at around one hundred years (about 10.5 MPa in "high T", 3MPa in "low T"). After the peaks, pore pressures decreases to 2 MPa at around thirty thousand years, then they increase again.
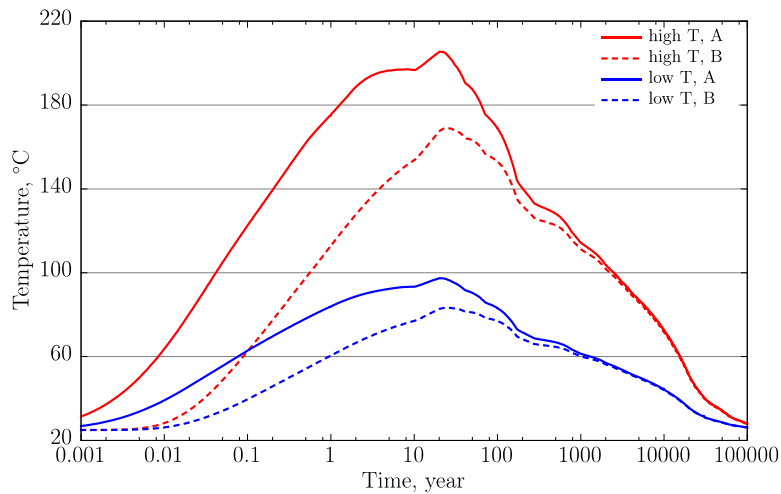
Figure 3.13. Simulation results of temperature evolution at point A and B with FEBEX bentonite for the "low T" and "high T" scenarios, respectively.

135
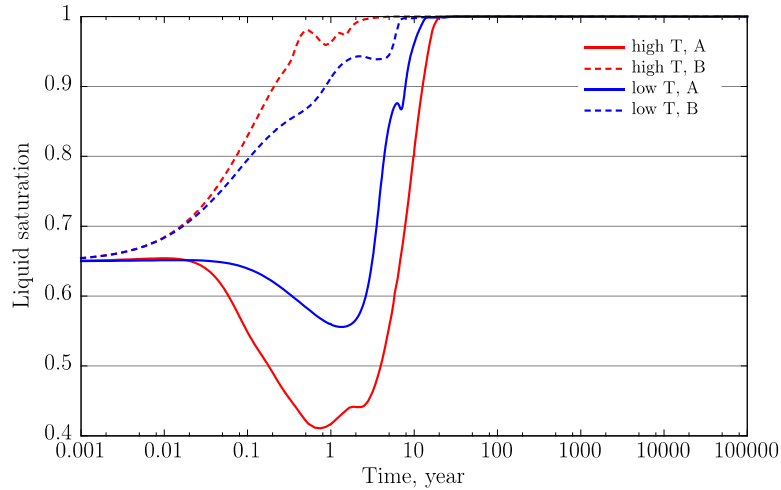
Figure 3.14. Simulation results of liquid saturation at point A and B with FEBEX bentonite for the "low T" and "high T" scenarios, respectively.
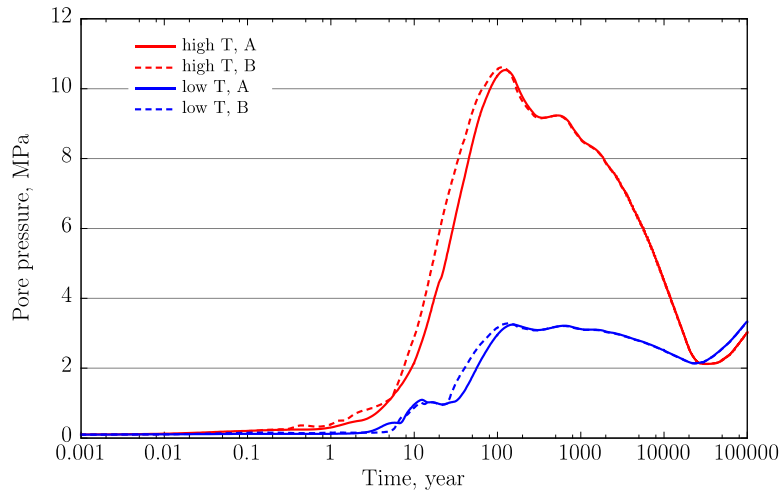
Figure 3.15. Simulation results of pore pressure at point A and B with FEBEX bentonite for the "low T" and "high T" scenarios, respectively. Note that before the material is fully saturated, the pore pressure is gas pressure, after fully saturation of the bentonite, the pore pressure refers to liquid pressure.

Figures 3.16 and 3.17 show the mean total stress changes at point A and B for both "low T" and "high T" cases. For both "THM" and "THMC" cases at point A, peak stresses in bentonite are about 4.5 MPa for the "low T" cases and 13 MPa for the "high T" cases, all at around one hundred years. Then the total stresses decrease until thirty thousand years, after when the stresses increase again to reach the hydrostatic status. The difference of stresses between "THM" and "THMC" cases are very small (less than 0.5 MPa), but it can be concluded that with the effects of chemical reaction, the total stresses decrease in both "high T" and "low T" cases at point A, inducing that the swelling capacity of the bentonite is reduced. For point B, the behavior is different. Peak stresses in bentonite at point B are about 6 MPa for the "low T" case and 14.5 MPa for the "high T" case, both at around one hundred years. The reason that stresses at point B are higher than stresses at point A is because point B is close to the surrounding Opalinus clay, which is subjected to high compression stress. In "low T" cases, the stress at point B by

136

"THMC" computation is lower than the result by "THM" calculation, but the opposite result is obtained in "high T" cases. This phenomenon is caused from the combined results of three components of chemical reactions. The effects due to each component are investigated in the next section.
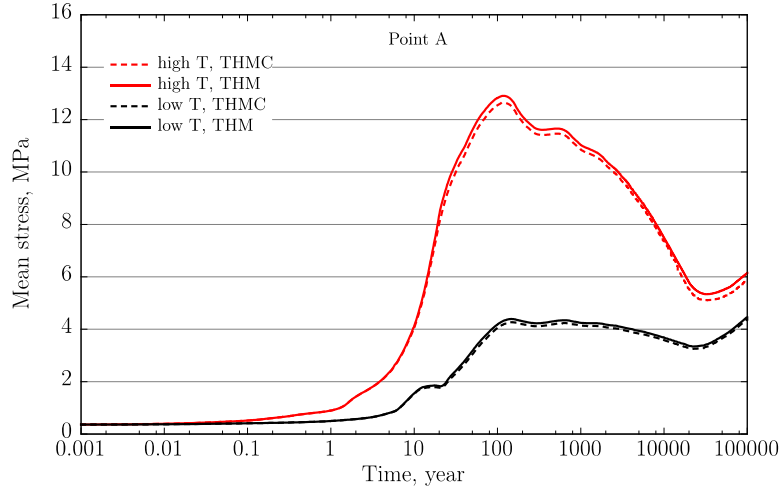
Figure 3.16. Simulation results of mean total stress at point A with FEBEX bentonite for the "low T" and "high T" scenarios, respectively.
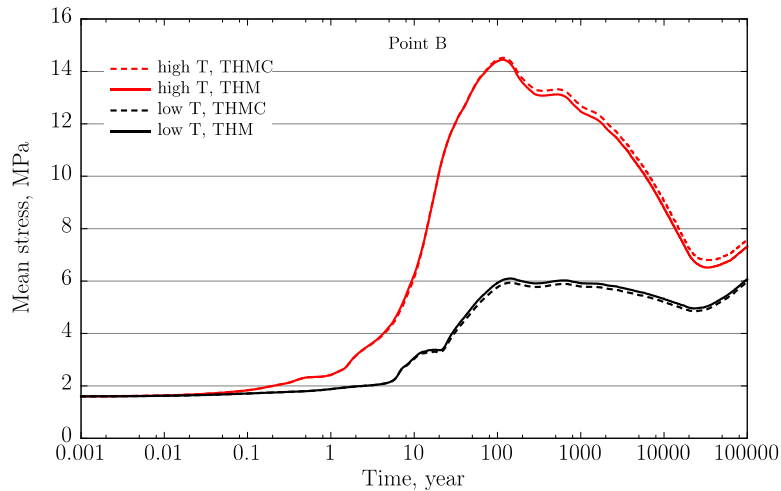
Figure 3.17. Simulation results of mean total stress at point B with FEBEX bentonite for the "low T" and "high T" scenarios, respectively.

Swelling stress is not clear in the simulation with the dual-structure model, because the micro-swelling strain is calculated directly in the framework of the model. Moreover, the non-linear plasticity induced from both micro- and macro-structures increases the difficulty to distinguish the swelling stress from the total stress. We present the mean effective/net stress (mean net stresses for unsaturated bentonite, and mean effective stress for fully saturated bentonite) during the simulation to illustrate the accumulation of stress in the solid skeleton of bentonite (Figures 3.18 and 3.19). At point A, mean effective/net stresses in "high T" cases (about 4 MPa at peak) are higher than the ones in "low T" (about 1.4 MPa at peak), and "THMC" cases have lower stresses than the corresponding "THM" cases as well. At the beginning of the simulation,

137

bentonite is unsaturated. Thus, the net stress is plotted and it goes up to the peak stress at around twenty years when the material reaches fully saturation (Figure 3.18). Then effective stress is plotted instead. Since the pore pressures increase much from twenty years to one hundred years (about 6 MPa increase in "high T" and 2 MPa increase in "low T"), all effective stresses reduce until the turning point where pore pressures reach the peak and start to decrease at around one hundred years. Then the effective stresses in "low T" cases become stable only with small changes, while the effective stresses in "high T" cases show the opposite changes against the evolution of pore pressures. Similar behaviors can be found with the point B, where the mean effective/net stresses reach the highest stress 4.5 MPa in "high T" cases and 2.7 MPa in "low T" cases. However, after the bentonite is fully saturated, the effective stresses at point B do not decrease as much as the ones at point A, and then the effective stresses increase to the highest stress which is more than the stresses at twenty years.
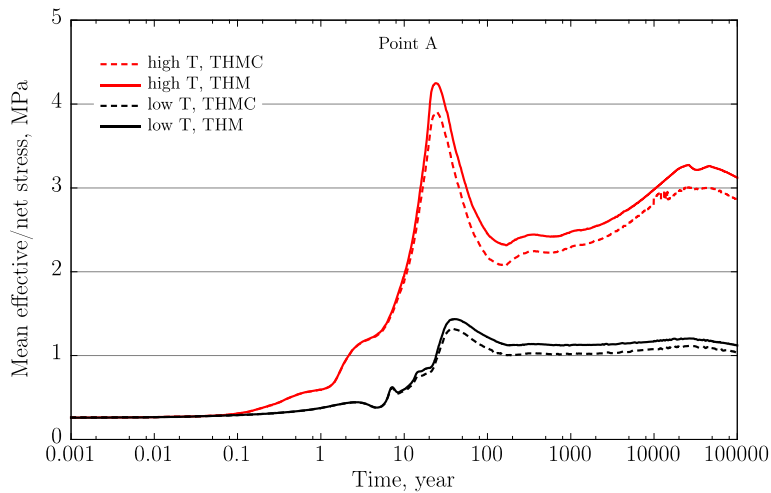
Figure 3.18. Simulation results of mean effective/net stress at point with FEBEX bentonite for the "low T" and "high T" scenarios, respectively.
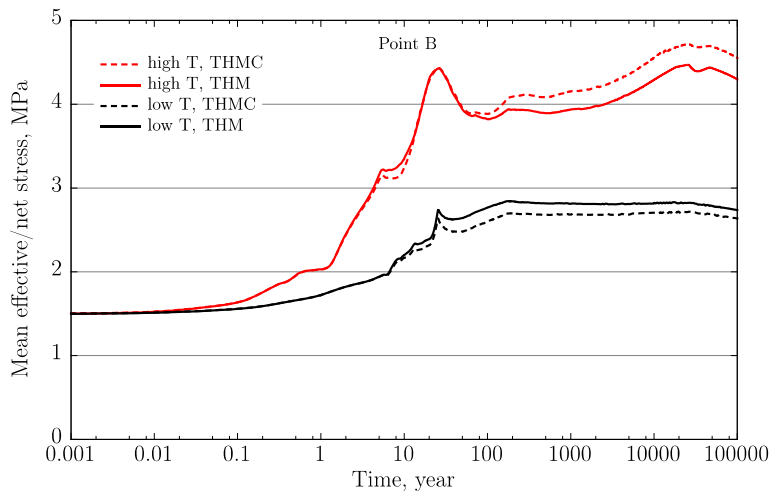
Figure 3.19. Simulation results of mean effective/net stress at point B with FEBEX bentonite for the "low T" and "high T" scenarios, respectively.

138

3.3.3.2   *Effects of chemical changes on stress*

The difference in calculated stresses between THMC and THM in Figures 3.18 and 3.19 clearly demonstrate the effect of chemical change on stress. Three chemical changes including the change in the volume fraction of smectite, change in exchanged cations and ionic strength contribute distinctively to the stress evolution in bentonite. In the current model, dissolution of smectite leads to decrease in the volume fraction of smectite (Figure 3.20), which tends to decrease the stress; β_m depends on the concentration of the exchanged Na, K, Ca and Mg, the enrichment of exchanged sodium in the interlayer leads to the increase of β_m (Figure 3.21), which tends to increase stress. The infiltration of more concentrated water from clay formation to EBS bentonite leads to the increase in ionic strength of pore water in bentonite and subsequently osmotic suction, which tends to lower the stress. The relative importance of these three effects varies temporally and spatially and between cases ("high T" versus "low T"), and the combination of these three effects determines whether chemical change enhances or suppresses the stress. In order to delineate the contribution of each effect on stress, in addition to the THMC that considers all three effects, notated "THMC(f_s, β_m, s_o)" in the following figures, we also conducted simulations that take into account each individual effect independently of the others. These simulations are referred as "THMC(f_s)" that only the effect of volume fraction of smectite was considered, "THMC(β_m)" that only the effect of exchanged cations was considered and "THMC(s_o)" that only the effect of ionic strength via osmotic suction was considered.
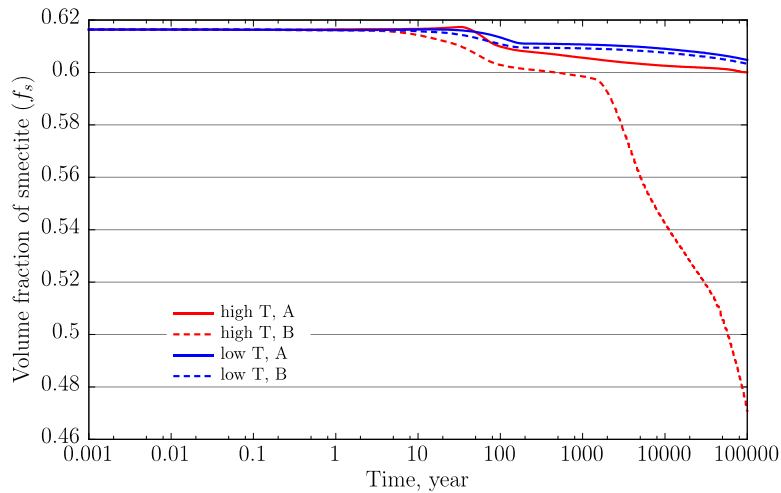
Figure 3.20. The evolution of the volume fraction of smectite at points A and B with FEBEX bentonite for the "low T" and "high T" scenarios, respectively.
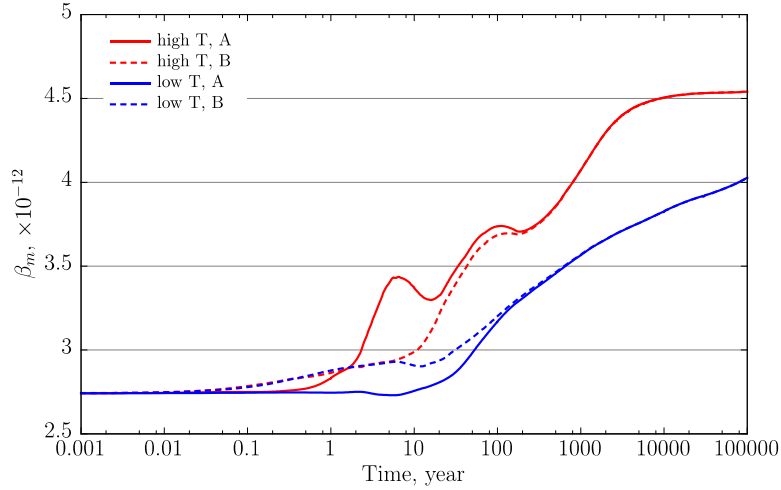
Figure 3.21. Simulation results of the evolution of $\boldsymbol{\beta_m}$ at points A and B with FEBEX bentonite for the "low T" and "high T" scenarios, respectively.
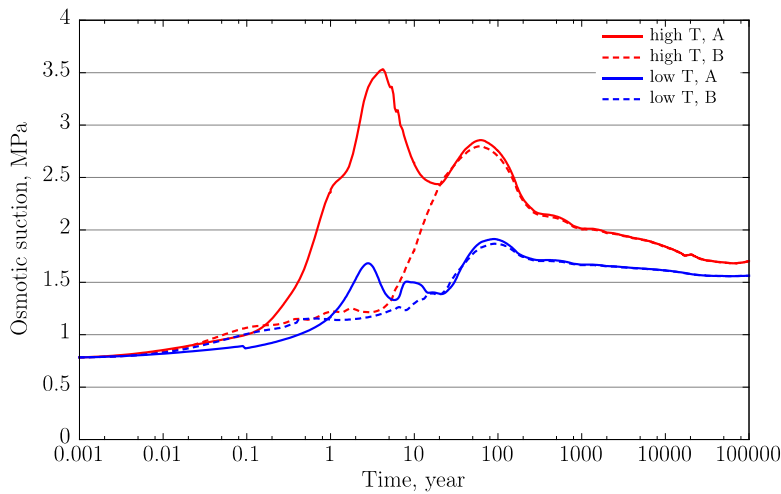
Figure 3.22. Simulation results of the osmotic suction at points A and B with FEBEX bentonite for the "low T" and "high T" scenarios, respectively.

Figure 3.22 shows the total stress evolution at point A for "high T" cases with C-M coupling schemes that includes different coupling schemes. "THM" means no C-M coupling, while "THMC(f_s, β_m, s_o)" indicates the C-M coupling with (f_s, β_m, s_o) effect is computed in the simulation. Overall, chemical effect leads to lower stress. By enlarging the curves between one hundred and ten years and one hundred and twenty years, it is found that the stress calculated without any C-M coupling ("THM") almost overlaps with the one with only the effect of volume fraction of smectite ("THMC(f_s)"), indicating that changes in volume fraction of smectite has only minimal effect on stress. The stress computed with only exchanged cation concentration ("THMC(β_m)") is higher than the "THM", which reveals that exchanged cations have positive effects on stress. The water infiltration from host rock leads to an increase of ionic strength of pore water in bentonite barrier which in turn cases the increase in osmotic suction (Figure 3.22). As a result, the swelling capacity of bentonite decreases, which is manifested by the reduction of

140

the total stress for the case of "THMC(s_o)", i.e. a negative effect. Eventually, the negative effect of ionic strength via osmotic suction on stress outplays the positive effect of exchanged cations on stress, and consequently chemical changes result in lower stress overall (Figure 3.23).
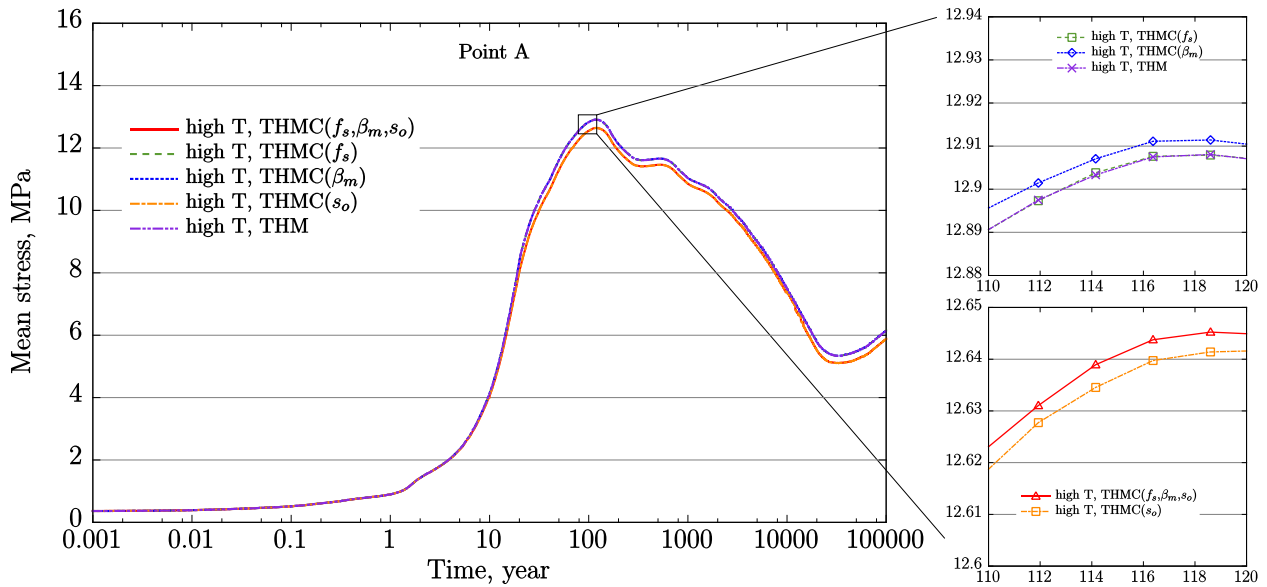
Figure 3.23. Simulation results of mean total stress at point A with FEBEX bentonite for the "high T" scenarios. Different C-M couplings are considered and computed.

The total stress evolutions at point A in "low T" cases are similar. The effect of osmotic suction is dominant and chemical changes overall lead to a decrease in stress. However, it is noteworthy that the difference between results by "THM", "THMC(f_s)" and "THMC(β_m)" are negligible (Figures 3.24).
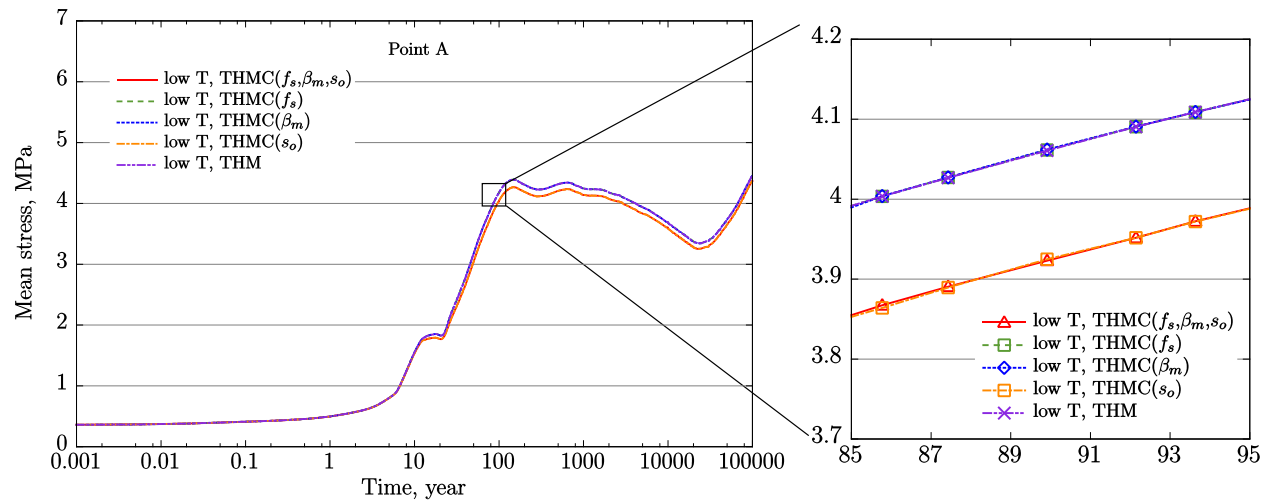
Figure 3.24. Simulation results of mean total stress at point A with FEBEX bentonite for the "low T" scenarios. Different C-M couplings are considered and computed.
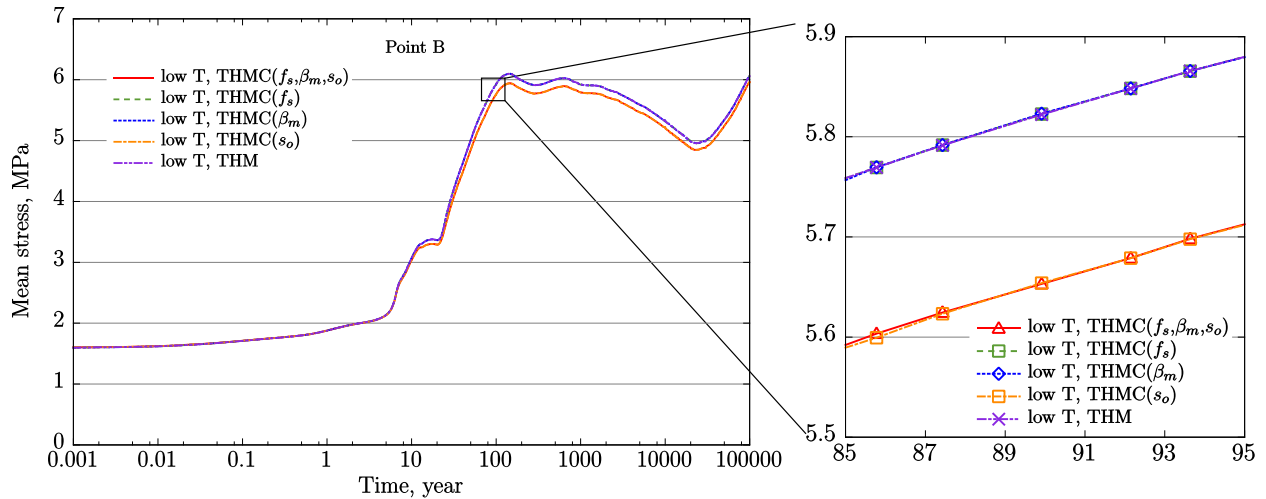
Figure 3.25. Simulation results of mean total stress at point B with FEBEX bentonite for the "low T" scenarios. Different C-M couplings are considered and computed.

Same observation can be obtained for the total stress at point B for "low T" cases (Figure 3.24). But the stress evolution at point B for "high T" is an outlier (Figure 3.25) — chemical effect as a whole lead to higher stress than the "THM" model, which is because that the effect of osmotic suction dominates whereas the effects induced by f_s and β_m are quite small. In comparison with the osmotic suction evolution at point A, the osmotic suction at point B went through different route (see Figure 3.22) — before the osmotic suction peaks at around one hundred years, point A went through up and down from 1 to ten years whereas point B underwent monotonic increase. The historical difference at point A and B was carried for longer simulation time due their effect on the bulk modulus. As a result, in terms of chemical effect on stress, point A and B exhibit different behavior: chemical effect as a whole lead to higher stress than the "THM" model at point B whereas the mean stress at point A computed with chemical effect is lower than the mean stress in "THM" model.
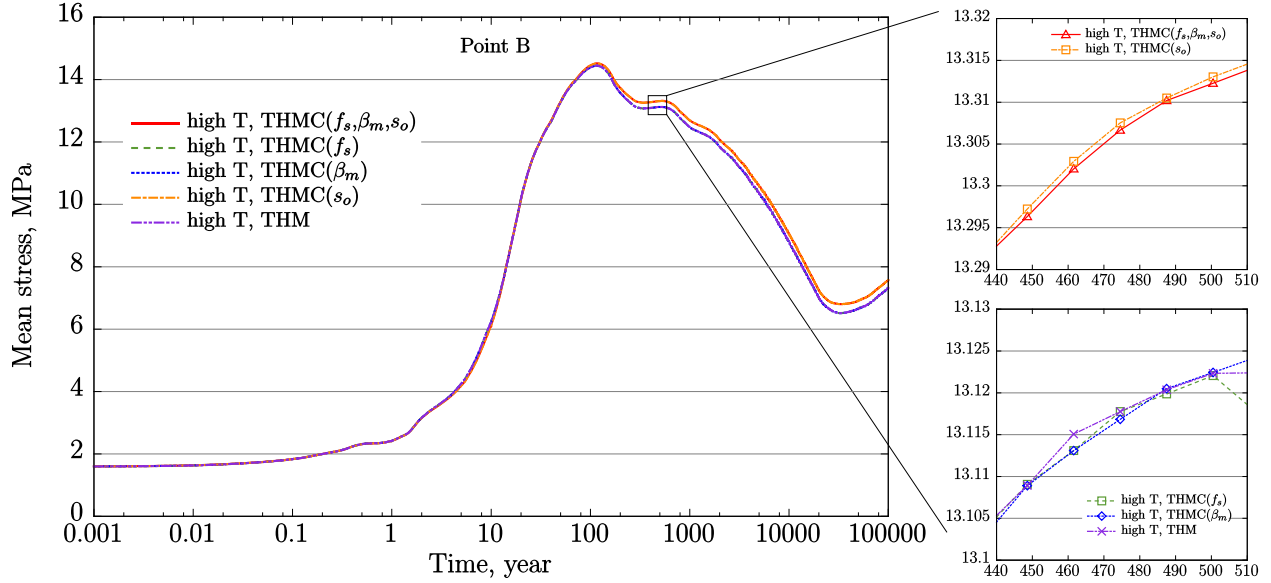
Figure 3.26. Simulation results of mean total stress at point B with FEBEX bentonite for the "high T" scenarios. Different C-M couplings are considered and computed.

3.3.3.3 Sensitivity to β_m

The current β_m calculated directly from the concentration of exchanged cations are three orders of magnitude smaller than that used by Sanchez et al. (2012). Thus, we introduce a factor α_β to correct β_m: $\beta'_m = \alpha_\beta \beta_m$. Here, 10^3 is used for α_β such that β_m will be in the same order of that in Sanchez et al. (2012). Note that in Sanchez et al. (2012) β_m is constant but in our model it is a function of exchange cations and therefore evolves spatially and temporally. In order to evaluate the effect of changing β_m, we conducted two sets of simulations, one is THMC model with C-M coupling that consider different effect as in section 3.3.3.2, the other is a THM simulation with β_m = 0.021 MPa^{-1} as in Sanchez et al. (2012. Another point, E, in the middle of the bentonite is picked for plotting stress evolutions (Figure 3.27). Larger β_m enlarges the effect of exchanged cations on stress. Therefore, "THMC(β_m)" that consider only the effect of exchanged cations has stress about 1 MPa higher than the "THM" case. Case "THMC(s_o)" has stress about 0.7 MPa lower than the "THM" case, indicating that osmotic suction suppress the stress. The results from case "THMC(f_s)" overlaps with the result by "THM", indicating that the dissolution of smectite has minimal effect on stress. The positive feedback of exchanged cations on stress outplay the osmotic suction and chemical change overall lead to an increase in stress.

143
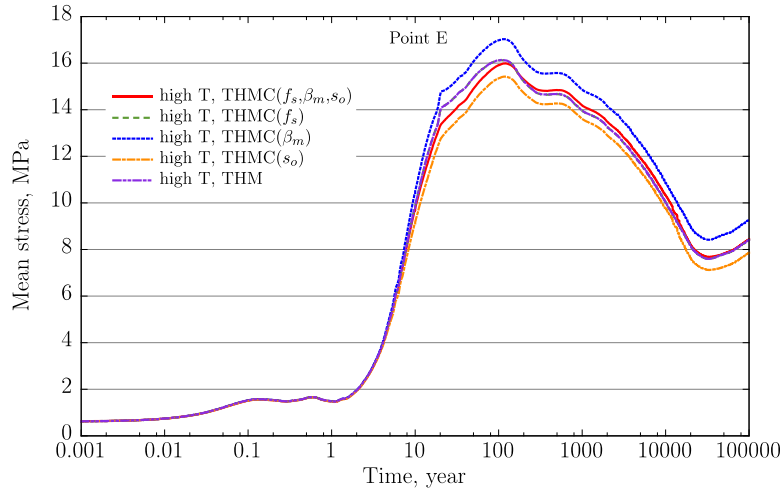
Figure 3.27. Simulation results of mean total stress at point E with FEBEX bentonite for the "high T" scenarios. Different C-M couplings are considered and computed.

3.4   Conclusions

3.4.1   Summary of current modeling work

Since FY13, we have been using coupled THMC modeling to evaluate the chemical alteration and associated mechanical changes in a generic repository to consider the interaction between EBS bentonite and the NS clay formation. Two main scenarios were developed for comparison: a "high T" case in which the temperature near the waste package can reach about 200 ºC and a "low T" scenario in which the temperature peaks at about 100 ºC. Conducting coupled THMC modeling proved challenging. The coupling between chemical and mechanical processes is the key part of THMC model that allow us to evaluate the impact of chemical changes on mechanical behavior. In FY16, THMC models utilize dual structure Barcelona Expansive Clay Model (BExM) (Sánchez et al., 2005) to link mechanical process with chemistry, allowing us to simultaneously incorporate the effects of exchangeable cations, ionic strength of pore water and abundance of swelling clay on the swelling stress of bentonite. In addition, the corrosion of steel canister was considered in the chemical model to evaluate whether the iron-bentonite interaction would aggravate the negative impact on swelling stress through the formation of Fe bearing clay minerals.

Coupled THMC models using BExM were developed for a generic case using FEBEX bentonite as EBS and Opalinus clay as NS. The following observations have been concluded from the model results: this newly developed model is used to predict the chemical-mechanical coupling in the geologic repositories for radioactive waste. The chemical effects on mechanics can be found as:

- The chemical changes as a whole reduce both total stress and effective/net stress in the bentonite buffer except the positions near the confinement rocks in the "high T" cases. However, the difference between the result computed with C-M coupling ("THMC") and the result without C-M coupling ("THM") is very small (less than 0.5 MPa).

144

- Three chemical changes, including the change in the volume fraction of smectite, change in exchanged cations and ionic strength contribute distinctively to the stress evolution in bentonite. In the current model, dissolution of smectite leads to decrease in the volume fraction of smectite which decrease the stress; because the enrichment of exchanged sodium in the interlayer, the change in exchanged cations cause the increase in stress; the infiltration of more concentrated water from clay formation to EBS bentonite leads to the increase in osmotic suction and subsequently lowers the stress. The relative importance of these three effects varies temporally and spatially and between cases ("high T" versus "low T"), and the combination of these three effects determines whether chemical change enhances or suppresses the stress.
- The effect of chemical change on stress is very sensitive to the parameters that are related to the chemical-mechanical coupling.
- In comparison with the THMC that used extended linear swelling model (Zheng et al., 2015), THMC model using BExM showed much less chemical effect on stress. The first reason is that exchanged cations which was not able to be taken into account by extended linear swelling model, is now considered in BExM. For FEBEX bentonite, change in exchanged cations has positive effect on the stress, which cancel out the negative effect due to the change of ionic strength (via osmotic sunction) and consequently the chemical change overall has much less effect on stress in THMC model using BExM than that in the THMC that used extended linear swelling model. The second reason is that the chemical-mechanical coupling via BExM, the dissolution of smectite was factored in directly via the volume fraction of smectite by modifying the bulk modulus for micro-structure, but in BExM, bulk modulus is a function of stress and change significantly in the model, the bulk modulus changes by smectite dissolution was overshadowed by the stress change.

Interaction between corroded steel canister and bentonite was taken into account in a THMC model for FEBEX bentonite using extended linear swelling. The corrosion process was simplified and the model focused on the possibility of forming Fe bearing clay minerals. Based on literature survey, we included vermiculite, berthierine, saponite as the potential Fe-clay mineral forming in the model, but none of them is formed. However, including Fe-bentonite interaction leads to slightly more precipitation of chlorite and dissolution of smectite, which drives down the swelling stress reduction slightly. As far as the dissolution of smectite and swelling stress reduction is concerned, including Fe-bentonite interaction does not seem to be very important.

3.4.2   Future Work

The current coupled THMC model greatly improves our understanding of the coupled processes contributing to chemical and mechanical alteration in EBS bentonites and NS argillite formations and answers questions regarding the thermal limit of EBS bentonite in clay repository. However, more questions remain to be answered regarding the THMC alteration of bentonites and clay formations under high temperature. Further refinement of current models and improvements for the TOUREACT-FLAC3D simulator are needed in the future. In the remaining months of FY16 and FY17 the following activities are proposed:

- The current dual-structure model contains some limitations based on its physical assumptions. Moreover, the number of parameters for BExM is much more than other mechanical models, which increases the difficulty to calibrate the model for specific materials. The model needs to be simplified to improve its numerical robustness and to apply easily on different materials.
- The THMC model using BExM will be utilized in more numerical analysis with other buffer material such as Kunigel-VI bentonite. In current model, THMC model using BExM was only conducted for FEBEX bentonite because BExM had been calibrated for FEBEX bentonite and its concept fit better bentonite with high smectite content. However, the applicability of BExM for bentonite with low smectite such as Kunigel-VI bentonite need to be tested and how chemical-mechanical coupling via BExM work out for Kunigel-VI need to be evaluated.
- The geochemical model for the Fe-bentonite interaction will be refined and calibrated against data. In the current model, no significant iron-related bentonite alteration was found despite some laboratory and field studies have shown formation of iron-clay minerals. The geochemical conceptual model and thermodynamic data base are the key to raise our confidence on the model. In the FY17, the geochemical model for Fe-bentonite interaction will be tested from data obtained in an eighteen years' in situ test and then simulations with higher temperature and long time will be conducted.
- Current models show precipitation of silicate minerals during illitization, which could result in the cementation of bentonite and subsequently lead to change in the mechanical properties of bentonite. Although the formation of silicate minerals is only about 3-4%, the change of mechanical properties as result of cementation needs to be quantified before we can safely conclude that silicate cementation won't significantly affect the mechanical properties.

3.5   References

Bethke C M (2002) The geochemists workbench release 4.0: A users guide to RXN, ACT2, TACT, REACT, and GTPLOT.

Birgersson M., Wersin p. (2004) Reactive Transport Modelling of Iron-Bentonite Interactions, an Update for the Olkiluoto Case, KBS-3H

Bossart P. (2011) Characteristics of the Opalinus Clay at Mont Terri, http://www.mont-terri.ch/internet/mont-terri/en/home/geology/key_characteristics.html

Bucher, F., and Müller-Vonmoos, M. (1989) Bentonite as a containment barrier for the disposal of highly radioactive waste. Applied Clay Science, 4(2): 157–177.

Casciello, E., J. W. Cosgrove, M. Cesarano, E. Romero, I. Queralt and J. Vergés 2011. Illite-smectite patterns in sheared Pleistocene mudstones of the Southern Apennines and their implications regarding the process of illitization: A multiscale analysis. Journal of Structural Geology 33(11): 1699-1711.

Chen, Y., C. Zhou and L. Jing 2009. Modeling coupled THM processes of geological porous media with multiphase flow: Theory and validation against laboratory and field scale experiments. Computers and Geotechnics 36(8): 1308-1329.

Cheshire, M. C., F. A. Caporuscio, M. S. Rearick, C. Jové-Colón and M. K. McCarney 2014. Bentonite evolution at elevated pressures and temperatures: An experimental study for generic nuclear repository designs. American Mineralogist 99(8-9): 1662-1675.

Cuadros, J. 2006. Modeling of smectite illitization in burial diagenesis environments. Geochimica et Cosmochimica Acta 70(16): 4181-4195.

ENRESA 2000. Full-scale engineered barriers experiment for a deep geological repository in crystalline host rock FEBEX Project, European Commission: 403.

Fernández, A. M., B. Baeyens, M. Bradbury and P. Rivas (2004). Analysis of the porewater chemical composition of a Spanish compacted bentonite used in an engineered barrier. Physics and Chemistry of the Earth, Parts A/B/C 29(1): 105-118.

Fernández, A. M., Turrero, M. J., Sánchez, D. M., Yllera, A., Melón, A. M., Sánchez, M., Peña, J., Garralón, A., Rivas, P., Bossart, P. and Hernán, P. (2007) On site measurements of the redox and carbonate system parameters in the low-permeability Opalinus Clay formation at the Mont Terri Rock Laboratory. Physics and Chemistry of the Earth, Parts A/B/C 32(1-7): 181-195 .

Fernández, A., Cuevas, J., Rivas, P., 2001. Pore water chemistry of the FEBEX bentonite. Mat. Res. Soc. Symp. Proc. 663, 573–588.

Gaston D, Newman C, Hansen G, Lebrun-Grandie D. MOOSE: A parallel computational framework for coupled systems of nonlinear equations. Nucl Eng Des 2009; 239(10): 1768–1778.

GENS, A. 2010 Soil environment interactions in geotechnical engineering. Géotechnique 60, 3-74

Guimarães LDN, Gens A, Olivella S (2007) Coupled Thermo-Hydro-Mechanical and Chemical Analysis of Expansive Clay Subjected to Heating and Hydration. Transport in Porous Media 66(3): 341-372.

Guimarães LDN, Gens A, Sánchez M, Olivella S (2013) A chemo-mechanical constitutive model accounting for cation exchange in expansive clays. Géotechnique 63, 221–234

Hicks, T.W., White, M.J. and Hooker, P.J. (2009) Role of Bentonite in Determination of Thermal Limits on Geological Disposal Facility Design, Report 0883-1, Version 2, Falson Sciences Ltd., Rutland, UK, Sept. 2009.

Horseman S.T. and McEwen, T. J. (1996) Thermal constrains on disposal of heat-emitting waste in argillaceous rocks, Engineering Geology 41, 5-16.

Itasca, 2009. FLAC3D, Fast Lagrangian Analysis of Continua in 3 Dimensions, Version 4.0, Minneapolis, Minnesota, Itasca Consulting Group.

JNC, Japan Nuclear Cycle Development Institute. (1999) H12: project to establish the scientific and technical basis for HLW disposal in Japan: supporting report 2 (respiratory design and engineering Technology). Japan Nuclear Cycle Development Institute, Tokyo.

Kamei, G., M. S. Mitsui, K. Futakuchi, S. Hashimoto and Y. Sakuramoto 2005. Kinetics of long-term illitization of montmorillonite—a natural analogue of thermal alteration of bentonite in the radioactive waste disposal system. Journal of Physics and Chemistry of Solids 66(2–4): 612-614.

Karnland, O., Olsson, S. and Nilsson, U. (2006) Mineralogy and sealing properties of various bentonites and smectite-rich clay materials, SKB Technical Report TR-06-30.

Kim J, Sonnenthal E, Rutqvist J (2015) A sequential implicit algorithm if chemo-thermo-poro-mechanics for fractured geothermal reservoir. Computers & Geosciences, 76; 59–71.

Komine, H., and Ogata, N. (1996) Prediction for swelling characteristics of compacted bentonite. Canadian Geotechnical Journal, 33: 11–22.

Landolt D., Davenport A., Payer J., Shoesmith D., (2009) A Review of Materials and Corrosion Issues Regarding Canisters for Disposal of Spent Fuel and High-level Waste in Opalinus Clay, Technical Report 09-02.

Laredj, N., Missoum, H. and Bendani, K. (2010) Modeling the effect of osmotic potential changes on deformation behavior of swelling clays. Journal of Porous Media 13(8): 743-748.

Lasaga, A. C., J. M. Soler, J. Ganor, T. E. Burch and K. L. Nagy 1994. Chemical weathering rate laws and global geochemical cycles. Geochimica et Cosmochimica Acta 58: 2361-2368.

Lauber, M., B. Baeyens and Bradbury, M. H. (2000) Physico-Chemical Characterisation and Sorption Measurements of Cs, Sr, Ni, Eu, Th, Sn and Se on Opalinus Clay from Mont Terri. PSI Bericht Nr. 00-10 December 2000 ISSN 1019-0643.

Liu, H.H., J. Houseworth, J. Rutqvist, L. Zheng, D. Asahina, L. Li, V. Vilarrasa, F. Chen, S. Nakagawa, S. Finsterle, C. Doughty, T. Kneafsey and J. Birkholzer. (2013) Report on THMC modeling of the near field evolution of a generic clay repository: Model validation and demonstration, Lawrence Berkeley National Laboratory, August, 2013, FCRD-UFD-2013-0000244.

Lloret A, Villar MV, Sánchez M, Gens A, Pintado X, Alonso EE. Mechanical behaviour of heavily compacted bentonite under high suction changes. Géotechnique 2003; 53(1):27–40.

Martin, F., S. Perrin, M. Fenart, M. Schlegel and C. Bataillon 2014. On corrosion of carbon steels in Callovo-Oxfordian clay: complementary EIS, gravimetric and structural study providing insights on long term behaviour in French geological disposal conditions. Corrosion Engineering, Science and Technology 49(6): 460-466.

Montes-H, G., B. Fritz, A. Clement and N. Michau 2005. Modelling of geochemical reactions and experimental cation exchange in MX80 bentonite. Journal of Environmental Management 77(1): 35-46.

Mosser-Ruck, R. and M. Cathelineau 2004. Experimental transformation of Na, Ca-smectite under basic conditions at 150 C. Applied Clay Science 26(1): 259-273.

Mosser-Ruck, R., M. Cathelineau, D. Guillaume, D. Charpentier, D. Rousset, O. Barres and N. Michau 2010. EFFECTS OF TEMPERATURE, pH, AND IRON/CLAY AND LIQUID/CLAY RATIOS ON EXPERIMENTAL CONVERSION OF DIOCTAHEDRAL SMECTITE TO BERTHIERINE, CHLORITE, VERMICULITE, OR SAPONITE. Clays and Clay Minerals 58(2): 280-291.

Nagra 2002: Project Opalinus Clay, Safety report, Nagra Technical Report 02-05, Nagra

Nitao J (1996) Reference Manual for the NUFT Flow and Transport Code, Version 1.0 Earth Sciences Department Lawrence Livermore National Laboratory.

Noorishad J, Tsang CF (1996) ROCMAS-simulator: a thermohydro-mechanical computer code. In: Stephansson O, Jing L, Tsang C-F, editors. Coupled Thermo-hydro-mechanical processes of fractured media, vol. 79. Elsevier: Developments in Geotechnical Engineering, 551–8.

Ochs, M., Lothenbach, B., Shibata, M. and Yui, M. (2004) Thermodynamic modeling and sensitivity analysis of porewater chemistry in compacted bentonite. Physics and Chemistry of the Earth, Parts A/B/C 29(1): 129-136.

Olivella S, Carrera J, Gens A, Alonso EE (1994) Nonisothermal multiphase flow of brine and gas through saline media. Transp Porous Media 15: 271–93.

Pacovsky, J., Svoboda, J., Zapletal, L., 2005. Saturation development in the bentonite barrier of the mock-up CZ geotechnical experiment. Clay in Natural and Engineered Barriers for Radioactive Waste Confinement—Part 2. Physics and Chemistry of the Earth 32(8–14), 767–779.

Pusch R. and Karnland, O. (1996) Physico/chemical stability of smectite clays, Engineering Geology 41: 73-85.

Pusch, R. and Madsen, F. T. (1995) Aspects on the illitization of the kinnekulle bentonites. Clays and Clay Minerals 43(3): 261-270.

Pusch, R., Kasbohm, J. and Thao, H. T. M. (2010) Chemical stability of montmorillonite buffer clay under repository-like conditions—A synthesis of relevant experimental data. Applied Clay Science 47(1–2): 113-119.

Ramírez, S., J. Cuevas, R. Vigil and S. Leguey 2002. Hydrothermal alteration of "La Serrata" bentonite (Almeria, Spain) by alkaline solutions. Applied Clay Science 21(5–6): 257-269.

Rutqvist J, Börgesson L, Chijimatsu M, Kobayashi A, Nguyen TS, Jing L, Noorishad J, Tsang CF (2001) Thermohydromechanics of partially saturated geological media – Governing equations and formulation of four finite element models. Int. J. Rock Mech. & Min. Sci. 38, 105–127.

Rutqvist, J. and Tsang, C.-F. (2002). Coupled Thermohydromechanical Analysis of FEBEX in Situ test with ROCMAS, Swedish Nuclear Power Inspectorate Research Team Report to DECOVALEX Task 1 Coordinator, Part B-THM modeling of the bentonite. Lawrence Berkeley National Laboratory, Berkeley, CA, USA.

Rutqvist, J., Y. Ijiri and H. Yamamoto 2011. Implementation of the Barcelona Basic Model into TOUGH–FLAC for simulations of the geomechanical behavior of unsaturated soils. Computers & Geosciences 37(6): 751-762.

Rutqvist, J., Zheng, L., Chen, F., Liu, H.-H. and Birkholzer, J. (2013). Modeling of Coupled Thermo-Hydro-Mechanical Processes with Links to Geochemistry Associated with Bentonite-Backfilled Repository Tunnels in Clay Formations. Rock Mechanics and Rock Engineering: 1-20.

Rutqvist, J., Zheng, L., Chen, F., Liu, H.-H. and Birkholzer, J. (2014) Modeling of Coupled Thermo-Hydro-Mechanical Processes with Links to Geochemistry Associated with Bentonite-Backfilled Repository Tunnels in Clay Formations. Rock Mechanics and Rock Engineering: 47(1): 167-186.

Saaltink MW, Batlle F, Ayora C, Carrera J, Olivella S (2004) RETRASO, a code for modeling reactive transport in saturated and unsaturated porous media. Geologica Acta 2(3): 235–251.

Sánchez, M., A. Gens and S. Olivella (2012). THM analysis of a large-scale heating test incorporating material fabric changes. International Journal for Numerical and Analytical Methods in Geomechanics 36(4): 391-421.

Sánchez, M., A. Gens, L. J. D. N. Guimarães and S. Olivella 2005. A double structure generalized plasticity model for expansive materials. International Journal for numerical and analytical methods in geomechanics 29: 751-787.

Shibata, T., M. Watanabe, N. Taniguchi and A. Shimizu 2014. Modelling of carbon steel corrosion under oxygen depleted environment. Corrosion Engineering, Science and Technology 49(6): 435-441.

Soler, J. M. 2001. The effect of coupled transport phenomena in the Opalinus Clay and implications for radionuclide transport. Journal of Contaminant Hydrology 53: 63-84.

Sonnenthal, E. Chapter 5 in: Birkholzer, J. Rutqvist, E. Sonnenthal, and D. Barr, Long-Term Permeability/Porosity Changes in the EDZ and Near Field due to THM and THC Processes in Volcanic and Crystalline-Bentonite Systems, DECOVALEX-THMC Project Task D Final Report, 2008.

Steefel CI (2001) GIMRT, Version 1.2: Software for Modeling Multicomponent, Multidimensional Reactive Transport. Users Guide. Livermore, California, Lawrence Livermore National Laboratory.

Taron J, Elsworth D, Min KB (2009) Numerical simulation of thermal–hydrologic–mechani-cal–chemical processes in deformable, fractured porous media, International Journal of Rock Mechanics Mining Sciences, 46: 842–854.

Thury, M., 2002. The characteristics of the Opalinus Clay investigated in the Mont Terri underground rock laboratory in Switzerland. Comptes Rendus Physique 3(7-8), 923-933.

Wang W, Rutqvist J, Görke UJ, Birkholzer JT Kolditz O (2011) Non isothermal flow in low permeable porous media: A comparison of Richards' and two-phase flow approaches. Environmental Earth Sciences, 62: 1197–1207.

Wersin P., Johnson, L.H. and McKinley, I.G. (2007) Performance of the bentonite barrier at temperature beyond 100oC: A critical review, Physics and Chemistry of the Earth 32: 780-788.

Wersin, P., A. Jenni and U. K. Mäder 2015. INTERACTION OF CORRODING IRON WITH BENTONITE IN THE ABM1 EXPERIMENT AT ÄSPÖ, SWEDEN: A MICROSCOPIC APPROACH. Clays and Clay Minerals 63(1): 51-68.

Wettingen, Switzerland

Wolery, T. J. 1993. EQ3/6, A software package for geochemical modelling of aqueous systems (Version 7.2). , Lawrence Livermore National Laboratory.

Xu, T., E. Sonnenthal, N. Spycher and K. Pruess 2006. TOUGHREACT: A Simulation Program for Non-isothermal Multiphase Reactive Geochemical Transport in Variably Saturated Geologic Media. Computers and Geosciences 32: 145-165.

Xu, T., Spycher, N., Sonnenthal, E., Zhang, G., Zheng, L. and Pruess, K. (2011) TOUGHREACT Version 2.0: A simulator for subsurface reactive transport under non-isothermal multiphase flow conditions. Computers & Geosciences 37(6): 763-774.

Zhang R, Yin X, Winterfeld PH, Wu YS (2012) A fully coupled model of nonisothermal multiphase flow, geomechanics, and chemistry during co2 sequestration in brine aquifers. Proceedings of the TOUGH Symposium, 838–848.

Zheng L, Samper J (2008) A coupled THMC model of FEBEX mock-up test. Physics and Chemistry of the Earth, Parts A/B/C 33, Supplement 1: S486-S498.

Zheng L., Rutqvist J. Kim, K. and Houseworth J. (2015), Investigation of Coupled Processes and Impact of High Temperature Limits in Argillite Rock. FCRD-UFD-2015-000362, LBNL-187644.

Zheng, L., J. Samper and L. Montenegro 2011. A coupled THC model of the FEBEX in situ test with bentonite swelling and chemical and thermal osmosis. Journal of Contaminant Hydrology 126(1–2): 45-60.

Zheng, L., Li, L., Rutqvist, J., Liu, H. and Birkholzer, J.T., (2012). Modeling Radionuclide Transport in Clays. Lawrence Berkeley National Laboratory. FCRD-URD-2012-000128

Zheng,L. Jonny Rutqvist, Carl Steefel, Kunhwi Kim, Fei Chen, Victor Vilarrasa, Seiji Nakagawa, Jiangtao Zheng, James Houseworth, Jens Birkholzer. (2014) Investigation of Coupled Processes and Impact of High Temperature Limits in Argillite Rock. FCRD-UFD-2014-000493, LBNL-6719E

4. Understanding the THMC Evolution of Bentonite in FEBEX-DP Coupled THMC Modeling and Examination of the Structure of Bentonite

4.1 Introduction

The clay and crystalline radioactive water repository typically involves a multi-barrier system. In addition to the natural barrier system (NBS), i.e. the host rock and its surrounding subsurface environment, it also has an engineered barrier system (EBS). The EBS represents the man-made, engineered materials placed within a repository, including the waste form, waste canisters, buffer materials, backfill, and seals.

The most common buffer material for EBS is compacted bentonite, which features low permeability and high retardation of radionuclide transport. The safety functions of EBS bentonite include limiting transport in the near field; damping the shear movement of the host rock; preventing the sinking of canisters (if emplaced in the center of the tunnel), limiting pressure on the canister and rock, and reducing microbial activity. To assess whether EBS bentonite can maintain these favorable features when undergoing heating from the waste package and hydration from the host rock, we need a thorough understanding of the thermal, hydrological, mechanical, and chemical evolution of bentonite under disposal conditions. While numerous laboratory experiments, field tests, and numerical models have been conducted to improve the understanding of each individual process or coupled THC/THM processes, there is a lack of studies on coupled THMC processes due to the challenges of conducting experiments and developing models that can cover all the THMC processes. Recently in the UFD program, coupled THMC models have been developed for a generic disposal system in clayey host rock with EBS bentonite (Liu et al., 2013; Zheng et al., 2014; Zheng et al., 2015b). However, model validation was difficult for lack of THMC data from long-term, large-scale experiments. The FEBEX (Full-scale Engineered Barrier EXperiment) *in situ* test, which has been operated for eighteen years, provides a unique opportunity of validating coupled THMC models.

In the FEBEX *in situ* test, two heaters surrounded by bentonite blocks about 0.7 m thick were emplaced in a tunnel excavated in granite. The heaters were switched on in 1997. In 2002, heater 1 was dismantled; in 2015, the second heater was dismantled in the FEBEX-DP project, which is comprised of extensive THMC and biological characterization of bentonite, and development of numerical models. LBNL/DOE joined the FEBEX-DP project in FY15. The ultimate goal is to use THMC data from FEBEX-DP to validate THMC models and therefore enhance our understanding of coupled THMC process. In this section, we describe our progress in FY16, which includes the development of coupled THMC models that interpret the THM data and predict the chemical evolution in bentonite, and synchrotron X-ray microtomography measurements of the bentonite samples to examine the microstructure of bentonite that suffered eighteen years of *in situ* heating and hydration.

4.2 A Brief Description of FEBEX Experiments

FEBEX (**F**ull-scale **E**ngineered **B**arrier **Ex**periment in Crystalline Host Rock) is a research and demonstration project that was initiated by ENRESA (Spain). THE FEBEX objective was to study the behavior of components in the near-field for a high-level radioactive waste (HLW)

repository in crystalline rock. Specifically, the project aimed to demonstrate the feasibility of fabricating and assembling the EBS and developing methodologies and models for evaluation of the thermo-hydro-mechanical (THM) and thermo-hydro-chemical (THC) behavior of the near-field (ENRESA, 2000). These objectives were to be attained through the combination of *in situ* and mock-up tests, and numerous small-scale laboratory tests, and THC/THM modeling. The project was initially scheduled for a period of seven years, from 1994 to 2001, but was extended several times as the experiments continued. Figure 4.1 shows the history of FEBEX projects, with different project names representing different operational stages.
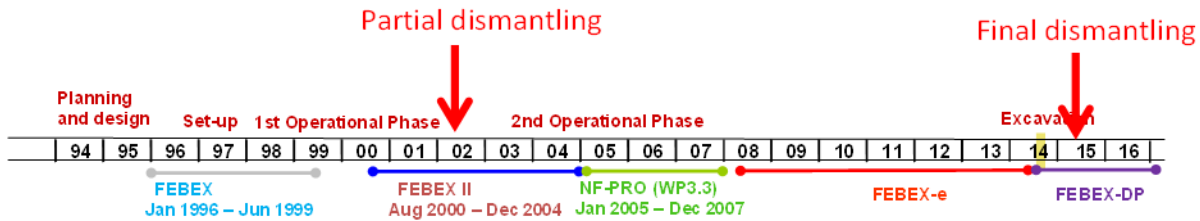
Figure 4.1. The operational stages of FEBEX *in situ* test (Vomvoris, personal communication).

The centerpiece of FEBEX experiments is, of course, the *in situ* test conducted at the Grimsel underground laboratory, Switzerland. The test consists of five basic units: the drift, the heating system, the bentonite barrier, the instrumentation, and the monitoring and control system (Figure 4.2). The drift is 70.4 m long and 2.28 m in diameter. The test area, which was sealed with a concrete plug, is located at the last 17.4 m of the drift where heaters, bentonite and instrumentation were installed. The main elements of the heating system are two heaters (#1 and #2), 1 m apart, which simulate full-sized canisters. Heaters were placed inside a cylindrical steel liner. Each heater is made of carbon steel, measures 4.54 m in length and 0.9 m in diameter, and has a wall thickness of 0.1 m. Heaters were operated at a constant power output of 1200 W/heater during the first 20 days and 2000 W/heater for the following 33 days. Afterwards, the heaters were switched to a constant-temperature control mode to maintain a maximum temperature of 100 ℃ at the steel liner/bentonite interface.

The bentonite barrier is made of blocks of highly compacted bentonite, situated in vertical sections normal to the axis of the tunnel. The cross section of bentonite barrier is shown in Figure 4.3. The dimension of fabricated bentonite blocks are shown in Figure 4.3 (right) and Table 4.1. There were gaps between blocks, but the volume of gaps has not been reliably estimated. Although the dismantling of bentonite barrier revealed that all gaps were sealed, these gaps might affect the initial hydration of bentonite, but such effect is difficult for model to take into account. The average values of the initial dry density and the water content of compacted bentonite blocks are 1.7 g/cm^3 and 14.4%, respectively.
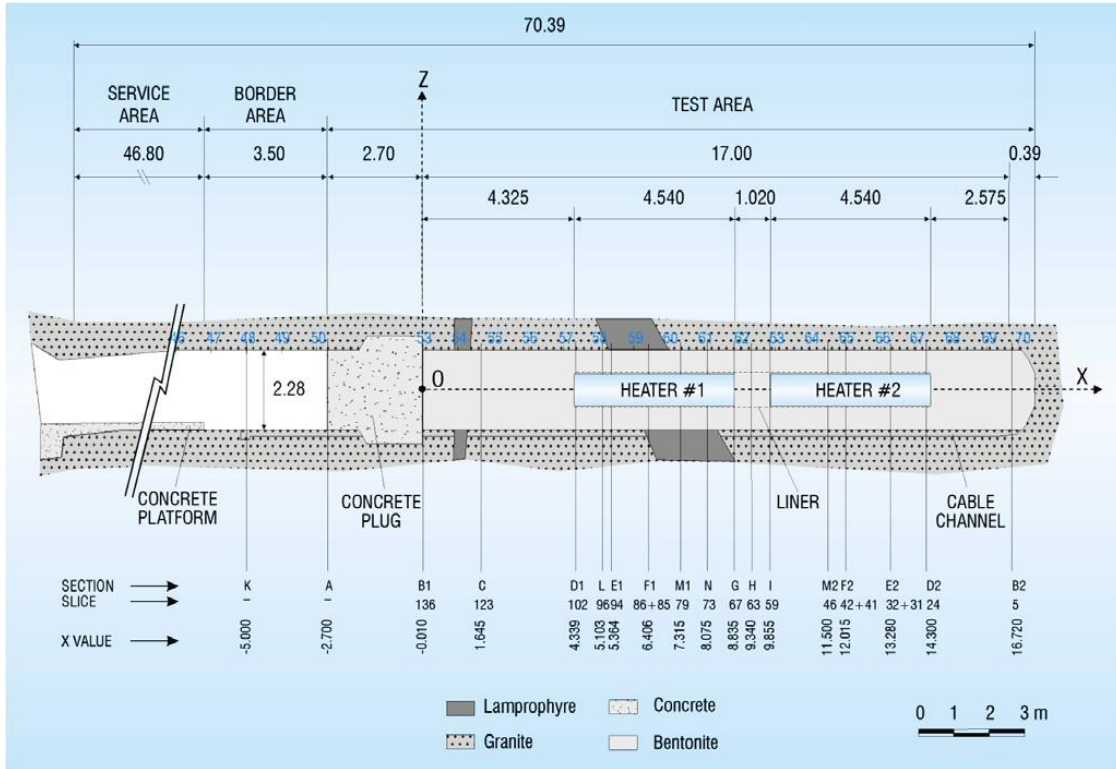
Figure 4.2. The initial configuration of the FEBEX *in situ* test at the Grimsel underground laboratory (Switzerland) (ENRESA, 2000).
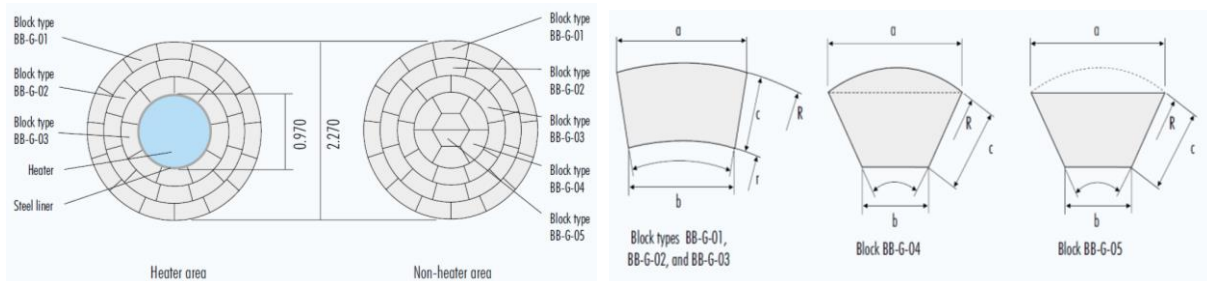
Figure 4.3. The geometry of clay barrier (left) and the type of bentonite blocks (right) with dimensions listed in Table 4.1 (ENRESA, 2000).

Table 4.1. Dimensions for bentonite blocks (ENRESA 2000)

Type	a mm	b mm	c mm	Thicknes mm	R mm	r mm	α
BB-G-01	$470.0^{2.0}_{5.0}$	$380.0^{2.0}_{4.0}$	$214.0^{2.0}_{3.0}$	$125.0^{2.0}_{2.0}$	1 133	919	24º
BB-G-02	$473.0^{2.0}_{5.0}$	$361.0^{2.0}_{4.0}$	$214.0^{2.0}_{3.0}$	$125.0^{2.0}_{2.0}$	917	703	30º
BB-G-03	$478.0^{2.0}_{5.0}$	$330.0^{2.0}_{3.0}$	$214.0^{2.0}_{3.0}$	$125.0^{2.0}_{2.0}$	701	487	40º
BB-G-04	$483.0^{2.0}_{5.0}$	$240.0^{2.0}_{3.0}$	$240.0^{2.0}_{3.0}$	$125.0^{2.0}_{2.0}$	485	—	60º
BB-G-05	$483.0^{2.0}_{5.0}$	$240.0^{2.0}_{3.0}$	$240.0^{2.0}_{3.0}$	$125.0^{2.0}_{2.0}$	—	—	60º

The *in situ* test began on February 27, 1997. Heater #1 was switched off in February 2002 and dismantled from May to September in 2002. The buffer and all components were removed up to a distance of 2 meters from heater #2 to minimize disturbance of the non-dismantled area. A dummy steel cylinder with a length of 1 m was inserted in the void left by heater #1 in the center of the buffer. The description of the partial dismantling operation is given in Bárcena et al. (2003). A comprehensive post-mortem bentonite sampling and analysis program was performed on the solid and liquid phases to check the physical and chemical changes induced by the combined effect of heating and hydration and to test THM and THC model predictions (ENRESA 2006a,b). The layout of the sampling sections for THC and THM measurements after the dismantling of heater #1 is given in Figure 4.4.
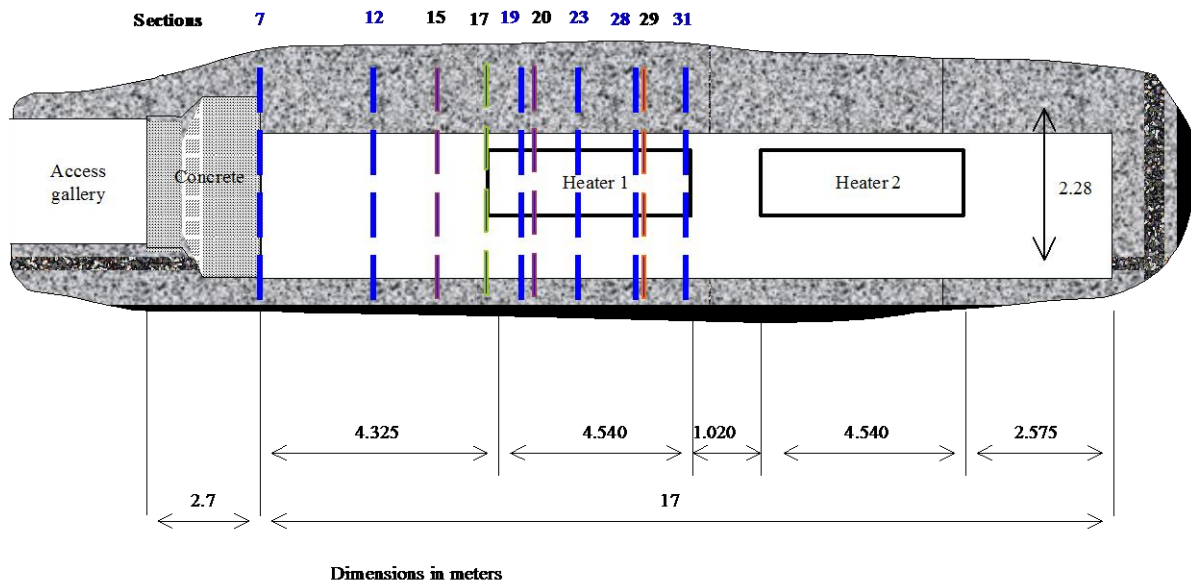
Figure 4.4. Layout of the sampling sections during the dismantling of heater 1 in 2002. In blue color are the common sections for THC and THM analyses (Fernandez and Rivas, 2003)

154
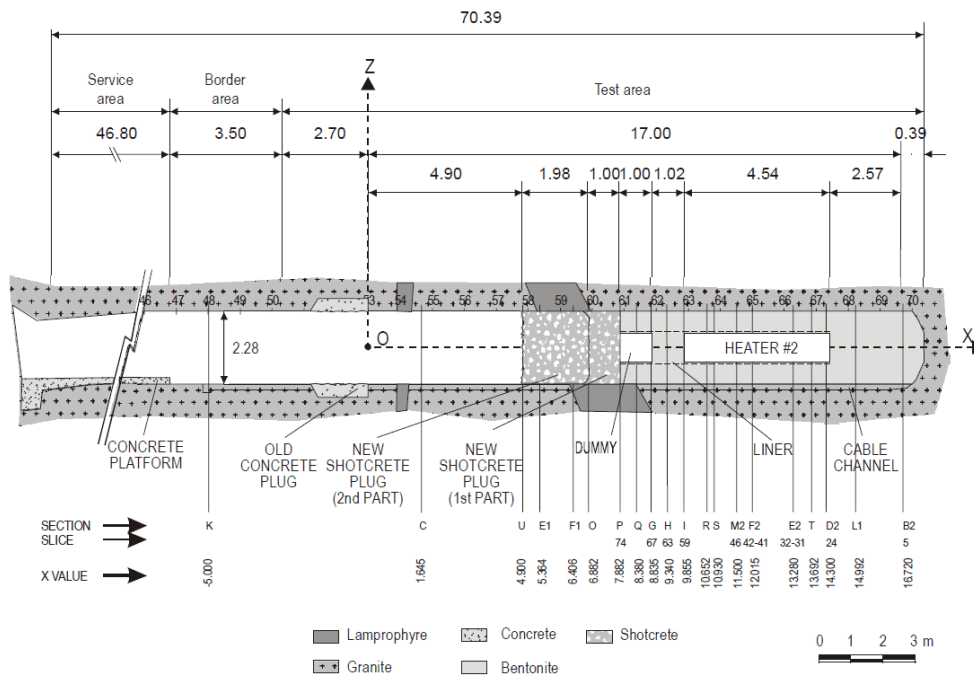
Figure 4.5. *In situ* test configuration following dismantling of heater 1 (Huertas et al., 2005)

After the dismantling of heater #1, the tunnel was plugged with shotcrete (Figure 4.5) and heater #2 was kept working under normal conditions to maintain a constant 100 °C at the steel liner/bentonite interface. In 2014, considering that changes in the state of bentonite buffer was very slow and it was unlikely for bentonite to reach fully saturation in the project lifetime, the decision was made to turn off and dismantle heater #2. The objective of the second dismantling operation, carried out throughout 2015, was to dismantle all the remaining parts of the *in situ* test, including heater #2. This operation included carrying out a complete sampling of the bentonite, rock, relevant interfaces, sensors, metallic components and tracers to allow the analysis of the barriers' condition after ~eighteen years of heating and natural hydration. On April 24, 2015, heater #2 was switched off. After a short cool off time period, dismantling was carried out from the shotcrete towards the bentonite section by sections (see Figure 4.6) and samples were taken for THMC and microbiological characterization. Details about the dismantling of heater #2 are given in Garcia-Sineriz et al. (2016). Preliminary THM characterization revealed that the bentonite away from the heater is fully saturated (see Figure 4.7), but the bentonite at the vicinity of heater #2 has not been fully saturated yet — gravimetric water content is around 17-19% (see Figure 4.7) and water saturation is about 80% near the heater (see Figure 4.8).

155
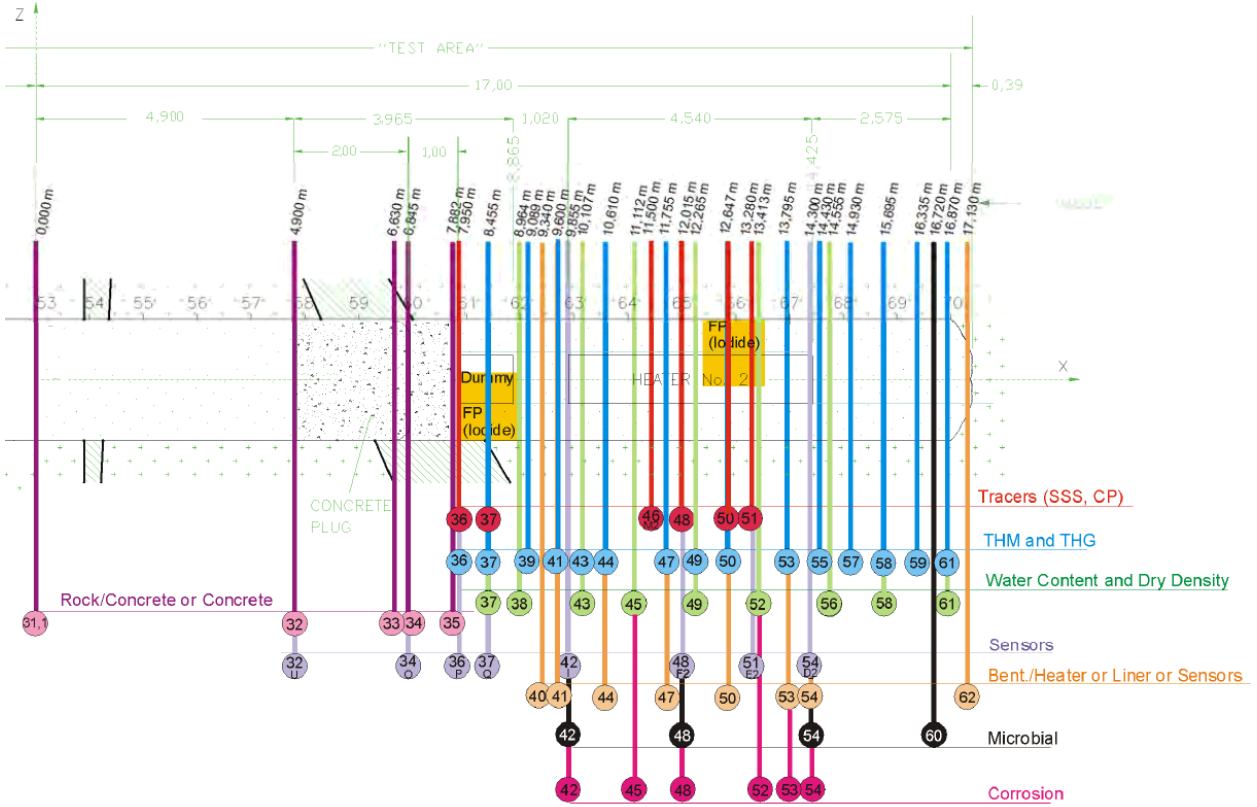
Figure 4.6. Section layout during the dismantling operation of heater #2 (Detzner and Kober, 2015)
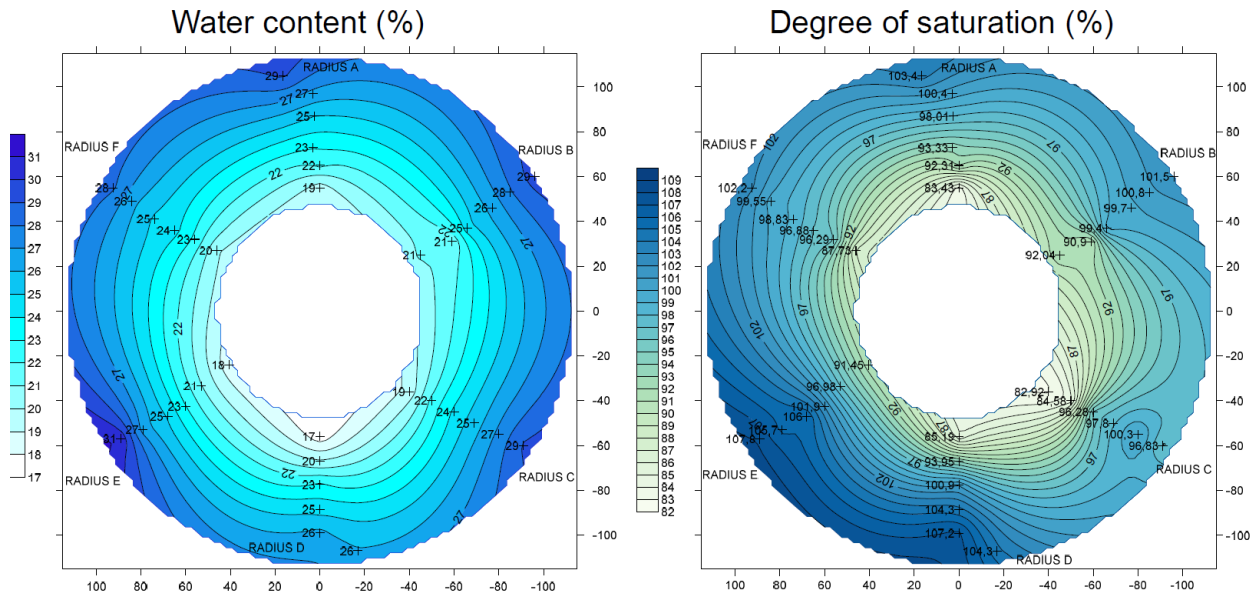
Figure 4.7. Spatial distribution of water content (left) and degree of saturation (right) at section 49 (see Figure 4.5 for the position of section 49) (Villar, weekly email communication).
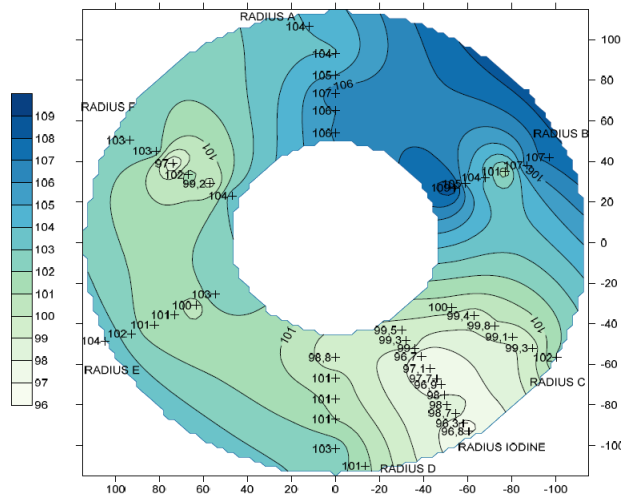
Figure 4.8. Spatial distribution of degree of saturation (right) at section 37 (see Figure 4.5 for the position of section 37) (Villar, weekly email communication).

The long-term FEBEX *in situ* test with comprehensive THMC data provides a unique opportunity to validate coupled THMC models and strengthen our understanding of coupled processes in bentonite. In addition, experiments at different scales with the same type of bentonite are also very useful to evaluate the key parameters obtained at different scales and study the scaling effect of modeling THMC processes. Up to now, several THM/THC models have been developed to interpret the FEBEX experiments, including the THM model for the mock-up test (Sánchez et al., 2005; 2012a) and *in situ* test (Sánchez et al., 2012b), and THC models for the small scale heating and hydration experiment (Zheng et al., 2010), mock-up test (Zheng and Samper, 2008), and *in situ* tests (Samper et al., 2008a; Zheng et al., 2011; Zheng et al., 2015b).

4.3 Model Development

In FY15, the THC model was developed and tested against temperature, relative humidity and chemical data collected after the dismantling of heater #1. In FY16, the THMC model was developed based on the THC model by adding mechanical processes and compared with data collected during the dismantling of both heater #1 and heater #2.

4.3.1 Simulator

The numerical simulations are conducted with TOUGHREACT-FLAC3D, which sequentially couples the multiphase fluid flow and reactive transport simulator, TOUGHREACT (Xu et al., 2011), with the finite-difference geomechanical code FLAC3D (Itasca, 2009). The coupling of TOUGHREACT and FLAC was initially developed in Zheng et al. (2012) to provide the necessary numerical framework for modeling fully coupled THMC processes. It was equipped with a linear elastic swelling model (Zheng et al., 2012; Rutqvist et al., 2013) to account for swelling as a result of changes in saturation and pore-water composition and the abundance of swelling clay (Liu et al., 2013; Zheng et al., 2014). A recent addition to the code is the capability of simulating Non-Darcian flow (Zheng et al. 2015b) and thermal osmosis.

157

4.3.2   Modeling Setup

As shown in Figure 4.7, the hydration of bentonite is fairly symmetrical, and radial symmetry has also been observed for heating (as shown later in Figures 4.11 to 4.15). We therefore use an axi-symmetrical mesh (Figure 4.9) to save computation time so that we can focus on the key coupling processes. However, such a model can only be used to interpret and predict the THMC behavior in the "hot sections", i.e. sections of bentonite block surrounding the heater including sections 41-54 (or more typically section 49) in Figure 4.6. 3-D models that have both "hot" and "cold" sections (such as sections 55-62 in Figure 4.6) could be developed in the future.
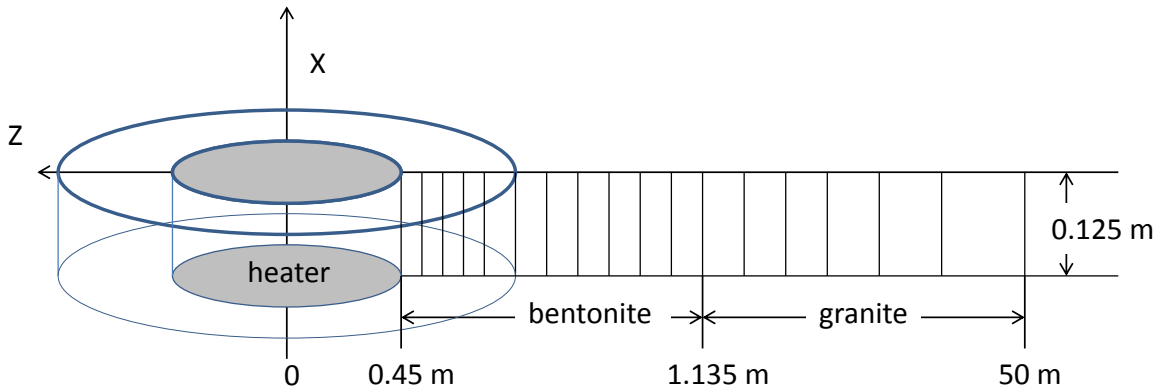
Figure 4.9. Mesh used for the model, not to the scale.

The model considers two material zones for the bentonite and granite. The first two nodes (1 and 2) are located on the external wall of the heater (r = 0.45-0.46 m). Bentonite is located within 0.45 m < r < 1.135 m. The remaining domain up to 50 m is used to simulate the granite. The simulation time starts on February 27, 1997 and ends on July 1, 2015, a total of 6,698 days (18.3 years).

The initial temperature is uniform and equal to 12 ℃. A constant temperature of 100 ℃ is prescribed at the heater/bentonite interface (r = 0.45 m) while temperature is assumed to remain constant at its initial value of 12 ℃ at the external boundary (r = 50 m) because the thermal perturbation induced by the heaters does not extend to this boundary.

The bentonite has initially a gravimetric water content of 14% which corresponds to a saturation degree of 55% and a suction of 1.11×10^5 kPa. The boundary conditions for flow include: 1) no flow at r = 0.45 m and 2) a prescribed liquid pressure of 7 bars at r = 50 m.

4.3.3   The TH model

The model considers non-isothermal two phase (air and water) flow, with each individual phase fluxes given by a multiphase version of Darcy's Law. For the vapor flow in the air phase, in addition to Darcy flow, mass transport can also occur by diffusion and dispersion according to Fick's law. Thermal behavior is relatively well understood because it is less affected by coupled processes in comparison with hydrological and chemical processes and the relevant parameters can be reliably measured. In current model, both conductive (Fourier's law) and convective heat flux are considered in the model and thermal conductivity is the key parameter. Figure 4.10 shows the measured thermal conductivity for FEBEX bentonite as a function of degree of water saturation.
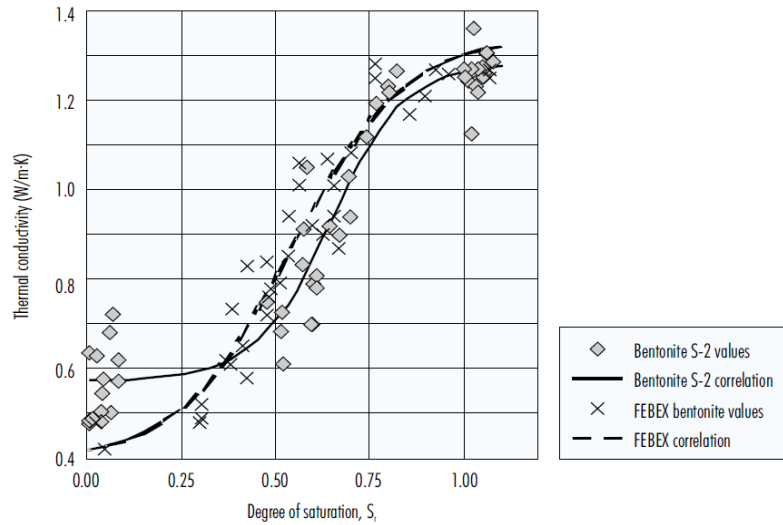
Figure 4.10. Thermal conductivity of FEBEX bentonite as a function of degree of saturation (ENRESA, 2000). Also shown is thermal conductivity for bentonite S-2 which has similar properties to FEBEX bentonite.

Because over the span of water saturation that FEBEX bentonite went through (from an initial degree of water saturation 55-59% to 100%), the thermal conductivity/water saturation relationship can sufficiently be represented by a linear relationship; we use a linear relationship implemented in TOUGH2 (Pruess et al., 1999):

$$K_{th} = K_{wet} + S_l(K_{wet} - K_{dry}) \qquad (2)$$

where K_{wet} is the thermal conductivity under fully saturated conditions, K_{dry} is the thermal conductivity under dry conditions, and S_l is the liquid saturation degree. K_{wet} and K_{dry} are given in Table 4.1.

In previous modeling work (e.g. Sánchez et al., 2012b; Zheng and Samper, 2008), significant effort has been invested to find out why the hydration of FEBEX bentonite is slower than predicted by the typical Darcy flow model. Several processes have been proposed to explain the discrepancy between measured data and predictions by the Darcy flow model. These include the permeability decrease due to the dual-structural behavior of bentonite (Sánchez et al., 2005, 2012b), thermal osmosis, in which a moisture flux induced by the thermal gradient in the bentonite is in the opposite direction of water infiltration from the granite (Zheng et al., 2011), and permeability decrease due to swelling (Zheng and Samper, 2008), and Non-Darcian flow (Liu and Birkholzer, 2012).

In Zheng et al. (2015b), a TH model with Non-Darcian flow was developed and the threshold gradient, the key parameter for Non-Darcian flow, was calibrated based on a small scale column test for FEBEX bentonite. However, including Non-Darcian flow into the TH model led to a significant underestimation of the relative humidity data in the entire bentonite barrier (even in bentonite near the bentonite/granite interface). Although the relevance of Non-Darcian behaviour is clear for saturated flow in clay rock (Liu and Birkholzer, 2012 and references cited therein), Zheng et al. (2015b) showed two issues that prevented us from clearly delineating the contribution of Non-Darcian flow to water flow in unsaturated clay or bentonite. First and

159

foremost, the calibration of the relative permeability and retention curves overshadows the effect of Non-Darcian flow. The non-linear relationship between water flux and hydraulic gradient, which motivates the relevance of Non-Darcian behavior to water flow, is already accounted for, at least partially, by the relative permeability (which in turn is a function of the retention curve) in the flux-gradient relationship for unsaturated flow. However, in most modelling exercises, relative permeability is calibrated based on a Darcy-type flow. As a result, the calibration of the parameters associated with relative permeability overshadows the contribution of Non-Darcian flow— the parameters for relative permeability might be "over-calibrated" so that the effect of Non-Darcian flow looks irrelevant. For FEBEX bentonite, the relative permeability and retention curve were calibrated based on a Darcy type of flow model (ENRESA, 2000), which essentially obviates Non-Darcian flow for unsaturated bentonite. Thus, if Darcian flow is added on top of relative permeability that is calibrated based on Darcy flow, we double count the non-linearity between flux and gradient, and consequently the model significantly underestimates the water inflow from granite to bentonite. Second, Cui et al. (2008) reported that threshold gradients are different for different capillary pressure. Further research is needed to take into account the effect of capillary pressure when a threshold gradient is calculated. However, even though we can improve our threshold gradient calculation by taking into account capillary pressure, it is unlikely to eliminate the aforementioned issue of process uncertainties versus parameter uncertainties. Based on the findings from Zheng et al. (2015b) in the models presented in this report, Non-Darcian flow was not considered.

The key parameters affecting the hydration of bentonite are the permeability of granite, the relative permeability and retention curves of bentonite, the vapor diffusion coefficient and permeability of bentonite. In Zheng et al. (2015b), the most plausible values for these parameters were discussed and illustrated with sensitivity analyses and listed in Table 4.1.

Granite is a fractured medium and should ideally be represented by fractures and matrix. Just as previous models for *in situ* tests (Samper et al., 2008a; Sánchez et al., 2012b), current model also assumes granite is a homogeneous porous medium, which requires us to use an equivalent permeability. Based on the total water flow at the entire test zone (17.4 m, see Figure 4.3) (ENRESA, 2000), the permeability of granite is around 5×10^{-18} to 8×10^{-18} m^2. ENRESA (2000) also reports that the most frequent permeability is 1×10^{-18} but deems it is more representative of rock matrix. Zheng et al. (2011) used 8×10^{-18} m^2, Kuhlman and Gaus (2014) estimated a permeability of 6.8×10^{-19} m^2, and Sanchez et al. (2012b) used a surprisingly small value, 8.18×10^{-21} m^2. Based on the published values, it seems that permeability between 7×10^{-19} to 8×10^{-18} m^2 is plausible. Based on the evaluation in Zheng et al. (2015b), a permeability of 2×10^{-18} m^2 is used (Table 4.1).

The capillary pressure (retention curve) is calculated by van Genuchten function as:

$$P_{cap} = -\frac{1}{\alpha}\left(\left[S^*\right]^{-1/m} - 1\right)^{1-m}$$

4.2

where P_{cap} is the capillary pressure (Pa), $S^* = (S_l - S_{lr})/(1 - S_{lr})$ and S_l is the water saturation, S_{lr} is the residual water saturation. S_{lr} is 0.1 for bentonite and 0.01 for granite. The values of α and m are given in Table 4.1. The retention curve was fairly well studied for FEBEX bentonite. For

example, ENRESA (2000) presented the retention curve for both drying and wetting path and van Genuchten function (van Genuchten, 1980) were derived with a *m* ranging from 0.3 to 0.6. Kuhlman and Gaus (2014) estimated an *m* of 0.3 and Zheng et al. (2011) and Sánchez et al. (2012b) use an *m* of 0.18, which is slightly lower.

The effective permeability of bentonite has been under scrutiny by modelers (e.g. Zheng et al., 2011) due to its critical role in determining the hydration of bentonite. It is the product of intrinsic permeability (k) (or saturated permeability, absolute permeability) and relative permeability (k_r). Relative permeability using $k_r = S_l^3$ (where S_l is water saturation degree) has been consistently used by different models (Zheng et al., 2011; Sánchez et al., 2012b; Kuhlman and Gaus, 2014) and we use the same function here. The plausible saturated permeability for FEBEX bentonite in the initial state could be in a range from 1×10^{-21} to 9×10^{-21} m^2 based on various sources (Zheng et al., 2011; Sánchez et al., 2012b; Kuhlman and Gaus, 2014; Chen et al., (2009) and we use 2.15×10^{-21} m^2 in the model. However, as demonstrated by Zheng et al. (2015b), a constant intrinsic permeability for bentonite could not explain the relative humidity data in the entire thickness of the bentonite barrier. In the next section, we will discuss the change of permeability as a result of mechanical changes in bentonite.

Table 4.2. Thermal and hydrodynamic parameters.

Parameter	Granite	Bentonite
Grain density [kg/m^3]	2700	2780
Porosity ϕ	0.01	0.41
Saturated permeability [m^2]	2.0×10^{-18}	2.15×10^{-21}
Relative permeability, k_{rl}	$k_{rl} = S$	$k_{rl} = S^3$
Van Genuchten $1/\alpha$ [1/Pa]	4.76×10^{-4}	1.1×10^{-8}
Van Genuchten m	0.7	0.45
Compressibility, β [1/Pa]	3.2×10^{-9}	5.0×10^{-8}
Thermal expansion coeff. [1/^{o}C]	1.0×10^{-5}	1.5×10^{-4}
Dry specific heat [J/kg-^{o}C]	793	1091
Thermal conductivity [W/m-^{o}C] dry/wet	3.2/3.3	0.47/1.15
Effective vapor diffusion coefficient (m^2/s)	1.03×10^{-4}	1.03×10^{-4}

4.3.4 Mechanical Model

In current models, we tested two mechanical models for bentonite: a linear swelling model and dual structure Barcelona expansive clay model (BExM).

4.3.4.1 Linear swelling model

The linear swelling models have been used in the generic model evaluation of bentonite barrier in Zheng et al. (2015a; b). The advantage of this method is its simplicity and easy calibration of key parameters, but the disadvantage is that it does not describe correctly the transient of state of swelling. For nonisothermal behavior of unsaturated soils, we may partition the total incremental strain into elastic (ε^e), plastic (ε^p), suction (ε^s), thermal strains (ε^T) and chemical strains (ε^c) (Zheng et al., 2015b):

$$d\varepsilon = d\varepsilon^e + d\varepsilon^p + d\varepsilon^s + d\varepsilon^T + d\varepsilon^c \qquad 4.3$$

where the suction strain represents the strain associated with changes in suction and chemical strain represents the strains associated with change in chemical conditions, including changes in ion concentration and abundance of swelling clays.

A linear elastic swelling model essentially defines the suction stress as a function of water saturation:

$$d\varepsilon^s = \beta_{sw} dS_l \qquad 4.4$$

where S_l is the water saturation and β_{sw} is a moisture swelling coefficient.

Under mechanically constrained conditions and considering the linear relationship between swelling stress and suction strain, $d\sigma_s = 3K d\varepsilon^s$, we have a swelling stress that is linearly proportional to the saturation:

$$d\sigma_s = 3K\beta_{sw} dS_l \qquad 4.5$$

where K is the bulk modulus. Equation (4.5) is what was used for EBS bentonite in Rutqvist et al. (2011). In this report, β_{sw} is 0.238, calibrated based using the swelling pressure of 5 MPa for FEBEX bentonite under full saturation. The swelling pressure for FEBEX bentonite ranges from 4.5 MPa (Castellanos et al., 2008) to 7 MPa (ENRESA, 2000).

The porosity change in bentonite is given by the following state-surface expression (Lloret and Alonso, 1995):

$$e = A + B\ln\sigma' + C\ln(\psi + p^a) + D\ln\sigma'\ln(\psi + p^a) \qquad 4.6$$

where e is the void ratio, which is equal to the volume of voids divided by the volume of the solids; p^a is the atmospheric pressure (Pa), σ' is the mean effective stress (Pa); ψ is the suction (Pa), and A, B, C and D are empirical constants which for the FEBEX compacted bentonite are equal to A = 0.91, B = - 0.0552, C = - 0.0606413 and D = 0.00479977.

The stress-dependence of permeability for low-permeability sedimentary rock is fairly well known and has been studied extensively (e.g. Ghabezloo et al., 2009; Kwon et al., 2001). Many empirical relationships have been put forward to describe the permeability changes with effective stress. One of them is the exponential law (David et al., 1994), which is used in the current model:

$$k = k_0 \exp[-\gamma(\sigma - \sigma_0)] \qquad\qquad 4.7$$

where k is the permeability at the effective stress σ, k_0 is the permeability at initial stress σ_0 and is equal to 2.15E-21 m²; γ is the stress sensitivity coefficient and equal to 1E-7 Pa^{-1} in the current model based on the calibration against THM data.

4.3.4.2   *Dual structure Barcelona expansive clay model (BExM)*

The dual structure Barcelona Expansive Clay model (BExM) (Alonso et al., 1999; Sánchez et al., 2005) provide a more mechanistic way to describe the mechanical behavior of bentonite and have been used to simulate the FEBEX mockup test (Sánchez et al., 2012a) and *in situ* test (Sánchez et al., 2012b). The dual structure BExM was also implemented in TOUGHREACT-FLAC3D and used in the report to simulate the mechanical behavior of the FEBEX *in situ* test.

In the dual structure model, the macrostructure is modeled with a constitutive model for unsaturated soils, such as the Barcelona Basic Model (BBM). The microstructure is incorporated to extend BBM to a dual structure model, which enables simulating the behavior of expansive soils, such as the dependency of swelling strains and swelling pressures on the initial stress state and on the stress path, strain accumulation upon suction cycles and secondary swelling. Thus, in the dual structure model, the total volume (V), the total void ratio (e), and porosity (ϕ) of the material are divided into a micro-structural part and a macro-structural part. The micro-structure can swell to invade the macro-porosity, depending on the mechanical confinement and load level. This is relevant when considering permeability changes during the soil swelling, because fluid flow takes place mostly through the macro-porosity, which is not proportional to the total strain and deformation of the expansive soil. Equations to describe the mechanical behavior of micro-structural and macro-structural levels and the interaction between structural levels are given in Section 2.

The parameters of BExM utilized for these studies are summarized in Table 4.2. The set of parameters are calibrated based on compacted bentonite by Lloret et al. (2003), and are used in the numerical analysis for the Mock-up test by Sanchez et al. (2012a). In Lloret et al. (2003), the simulation is one-dimensional, which can be treated as an isotropic case in 3D. However, the lateral displacements are constrained in oedometer test but the vertical loading is controlled by

stresses. Thus, the stress status in oedometer test is anisotropic and the assumption of isotropy is not appropriate for this test. In Sanchez et al. (2012a), between numerical results and observed behavior during experiments are in agreement, the macro-structural bulk modulus of bentonite can reach as high as 2 GPa. Based on the report by Rutqvist and Tsang (2002), the bulk modulus of FEBEX bentonite should be in the order of $10 - 100$ MPa. Therefore, the bulk modulus values evolve too high during the simulation of Sanchez et al. (2012a). Here we determine the parameters related to macro-structural bulk modulus, κ, which gives reasonable bulk modulus (in the order of 10 MPa~1000 MPa), from the observed results during experiment. In order not to affect the hydraulic effects on macro-structures, we increase the value of the parameter κ_s to keep the same ratio of $\frac{\kappa}{\kappa_s}$ as Lloret et al. (2003) and Sanchez et al. (2012) used in their simulations.

Table 4.3. Parameters used for combination of loading paths tests (Lloret et al., 2003; Sánchez et al., 2012).

Parameters defining the Barcelona basic model for macrostructural behavior

$\kappa = 0.018$	$\kappa_s = 0.0036$	$\lambda(0) = 0.08$	$p_c = 0.5$ MPa	$r = 0.90$	$\zeta = 1$ MPa^{-1}	$p_0^* = 6.5$ MPa
$\alpha_a = 1$	$\alpha_0 = 1 \times 10^{-5\circ}$C^{-1}					

Parameters defining the law for microstructural behavior

$\alpha_m = 0.021$ MPa^{-1} $\quad \beta_m = 2.3 \times 10^{-3}$ MPa^{-1} $\quad \chi = 1$

Interaction functions

$$f_c = 1 + 0.9 \tanh\left[20\left(\frac{p_r}{p_0} - 0.25\right)\right] \qquad f_s = 0.8 - 1.1 \tanh\left[20\left(\frac{p_r}{p_0} - 0.25\right)\right]$$

$e_{macro} = 0.21$ $\qquad\qquad\qquad\qquad\qquad\qquad e_{micro} = 0.48$

Note that the parameters (κ and κ_s) related to macro-structural bulk modulus are higher than original ones used in (Lloret et al., 2003; Sánchez et al., 2012a). All other parameters are set to zero.

4.3.5   Chemical Model

The establishment of the chemical model requires first the knowledge of initial chemical conditions in bentonite and granite, i.e., the initial mineralogical and pore water compositions. Extensive mineralogical characterization had been conducted by ENRESA (2000) and Fernández et al. (2004). Ramírez et al. (2002) also reported the mineralogical composition of FEBEX bentonite, which is slightly different from that reported by ENRESA (2000). In this report, we take the average of mass fraction reported in ENRESA (2000), Fernández et al. (2004) and Ramírez et al. (2002) and transformed the mass fraction to volume fraction (ratio of the volume for a mineral to the total volume of medium) using a porosity of 0.41 (see Table 4.3). Note the minerals that have zero volume fractions are the secondary minerals that could be formed. Detailed mineralogical composition of granite has not been found in current literature search, probably because the chemical conditions in granite are not supposed to be actively changed by repository conditions. Previous THC models for the *in situ* test (Samper et al., 2008a; Zheng et al., 2011) only include quartz in the minerals assemblage in granite. Siitari-Kauppi et al. (2007) reported that Grimsel granite is composed of quartz, K-feldspar, plagioclase and a small amount of "dark material". In the current model, we consider quartz, K-feldspar, plagioclase in granite with their volume fractions listed in Table 4.3.

Table 4.4. Mineral volume fraction (dimensionless, ratio of the volume for a mineral to the total volume of medium) FEBEX bentonite (ENRESA, 2000; Fernández et al., 2004; Ramírez et al., 2002) and granite (Zheng et al., 2011).

Mineral	**FEBEX Bentonite**	**Granite**
Calcite	0.00472	0
Smectite	0.546	0.
Chlorite	0.0024	0
Quartz	0.012	0.37
K-Feldspar	0.0059	0.35
Plagioclase	0	0.27
Dolomite	0.0	0
Illite	0.0	0
Kaolinite	0.0	0
Siderite	0.0	0
Ankerite	0.0	0

FEBEX bentonite blocks have an initial gravimetric water content of 13.5–14% (ENRESA 2000). As described in Bradbury and Baeyens (2003), obtaining the pore-water chemistry of compacted bentonite with such low water content is difficult. Because the concentration of ions for the initial state of compacted bentonite cannot be measured directly, indirect measurement methods must be used. Squeezing and aqueous extract are the most commonly used methods. Squeezing is a straightforward method — pore-water is squeezed out and concentrations are measured. However, pore water cannot be extracted by squeezing from clay samples with gravimetric water contents less than 20% (Fernández et al. 2001, 2004), which means that squeezing cannot be done for FEBEX bentonite blocks. In an aqueous extract test, a crushed sample is placed in contact with water at a low solid/liquid ratio (ranging from 1:16 to 1:1). After establishing equilibrium, the solid phase is separated and the liquid phase is analyzed (Fernández et al., 2001). Geochemical modeling was needed to retrieve the aqueous ion concentrations at low water content (Zheng et al., 2008). Therefore, any uncertainties associated with the geochemical models affect the evaluation of initial aqueous concentration levels at low water content (the water content at the initial state). The model presented in this report uses the pore water composition (see Table 4.4) inferred by Fernández et al. (2001) from aqueous extract data. The pore water composition for granite (Table 4.4) is taken from Zheng et al. (2011).

Table 4.5. Pore-water composition (mol/kg water except for pH) of FEBEX bentonite (Fernández et al., 2001) and granite (Zheng et al., 2011).

	EBS Bentonite: FEBEX	**Granite**
pH	7.72	8.35
Cl	1.60E-01	1.31E-05
SO_4^{-2}	3.20E-02	7.86E-05
HCO_3^-	4.1E-04	3.97E-04
Ca^{+2}	2.2E-02	1.81E-04
Mg^{+2}	2.3E-02	1.32E-06
Na^+	1.3E-01	3.76E-04
K^+	1.7E-03	7.80E-06
Fe^{+2}	2.06E-08	2.06E-08
$SiO_2(aq)$	1.1E-04	6.07E-04
AlO_2^-	1.91E-09	3.89E-08

In the chemical model, we consider aqueous complexation, cation exchange, surface complexation and mineral dissolution/precipitation. Aqueous complexes and their disassociation constants for reactions that are written in terms of the primary species in Table 4.4 are listed in Table 4.5. These thermodynamic data were taken from Data0.dat.YMPv4.0, an EQ3/6 (Wolery, 1993) database qualified by the U.S. Department of Energy for the Yucca Mountain project. Surface protonation reactions are given in Table 4.6 and cation exchange reactions are given in Table 4.7.

Table 4.6. Aqueous complexes and their dissociation constants

Species	Log K (25°C)	Species	Log K (25°C)
OH^-	13.99	$MgHCO_3^+$	-1.03
Al^{+3}	-22.88	$CO_2(aq)$	-6.34
$HAlO_2(aq)$	-6.45	CO_3^{-2}	10.33
$NaAlO_2(aq)$	0.75	$CaCO_3(aq)$	7.01
$AlOH^{+2}$	-17.87	$KCl(aq)$	1.50
$Al(OH)_2^+$	-12.78	$MgCl^+$	0.14
$Al(OH)_3(aq)$	-6.72	$MgSO_4(aq)$	-2.38
$CaCl^+$	0.70	$NaSO_4^-$	-0.81
$CaCl_2(aq)$	0.65	KSO_4^-	-0.88
$CaSO_4(aq)$	-2.10	$NaHSiO_3(aq)$	8.30
$NaCl(aq)$	0.78	$CaOH^+$	12.85
$FeCl^+$	0.17	$NaOH(aq)$	14.15
$FeHCO_3^+$	-2.04	$NaCO_3^-$	9.82
$FeCO_3(aq)$	4.88	$NaHCO_3(aq)$	-0.17
$FeCl_4^{-2}$	1.94	$CaHCO_3^+$	-1.04

Table 4.7. Surface protonation reactions on montmorillonite (Bradbury and Baeyens, 2005)

Surface complexation	Log K
$mon\_sOH_2^+ = mon\_sOH + H^+$	-4.5
$mon\_sO^- + H^+ = mon\_sOH$	7.9
$mon\_w1OH_2^+ = mon\_w1OH + H^+$	-4.5
$mon\_w1O^- + H^+ = mon\_w1OH$	7.9
$mon\_w2OH_2^+ = mon\_w2OH + H^+$	-6
$mon\_w2O^- + H^+ = mon\_w2OH$	10.5

Table 4.8. Cation exchange reactions on montmorillonite and illite (Bradbury and Baeyens, 2005)

Cation exchange reaction	$K_{Na/M}$
$Na^+ + mon-H = mon-Na + H^+$	1
$Na^+ + mon-K = mon-Na + K^+$	0.0775
$Na^+ + 0.5\ mon-Ca = mon-Na + 0.5Ca^{+2}$	0.302
$Na^+ + 0.5\ mon-Mg = mon-Na + 0.5Mg^{+2}$	0.302

Table 4.9.Equilibrium constants for mineral precipitation/dissolution

Primary Mineral	log(K)	Secondary Mineral	log(K)
Calcite	1.85	Siderite	1.543
Smectite-Na	-34.62	Dolomite	2.524
Quartz	-3.75	Ankerite	-1.035
K-feldspar	-22.91	Illite	-47.33
Albite	-20.133	Chlorite	4.298
Anorthite	-19.19	Kaolinite	-39.9

The equilibrium constants for precipitation/dissolution of primary minerals (minerals that are present initially) and secondary minerals are listed in Table 3.8. Note that plagioclase is a solid solution with albite and anorthite as its end members. In the current model, we assume plagioclase contains 10% anorthite and 90% albite so that there is quasi-equilibrium between pore water and plagioclase.

Mineral dissolution/precipitation is kinetically controlled. The kinetic law for mineral dissolution/precipitation is given in Xu et al. (2011). The kinetic rates and surface areas for the minerals considered in the model were taken mostly from Xu et al. (2006) (Table 4.9). However, the illitization rate (the rate of illite precipitation and smectite dissolution) was calibrated (Liu et al., 2013) based on the measured illite percentage in an illite/smectite (I/S) mixed layer from Kinnekulle bentonite, Sweden (Pusch and Madsen, 1995).

Table 4.10. Kinetic properties for minerals considered in the model (Xu et al., 2006).

Mineral	A (cm^2/g)	Parameters for Kinetic Rate Law							
		Neutral Mechanism		Acid Mechanism			Base Mechanism		
		k_{25} (mol/m^2-s)	E_a (kJ/mol)	k_{25} (mol/m^2-s)	E_a (kJ/mol)	n(H$^+$)	k_{25} (mol/m^2-s)	E_a (kJ/mol)	n(H$^+$)
Quartz	9.8	1.023×10^{-14}	87.7						
K-feldspar	9.8	3.89×10^{-13}	38	8.71×10^{-11}	51.7	0.5	6.31×10^{-12}	94.1	-0.823
Kaolinite	151.6	6.91×10^{-14}	22.2	4.89×10^{-12}	65.9	0.777	8.91×10^{-18}	17.9	-0.472
Illite	1.18×10^4 [1]	1.66×10^{-13}	105 [2]						
Chlorite	9.8	3.02×10^{-13}	88	7.76×10^{-12}	88	0.5			
Calcite	3.5	1.63×10^{-7}	23.5						
Dolomite	12.9	2.52×10^{-12}	62.76	2.34×10^{-7}	43.54	1			
Ankerite	9.8	1.26×10^{-9}	62.76	6.46×10^{-4}	36.1	0.5			
Smectite - Na	1.18×10^4 [1]	1.66×10^{-13}	105 [2]						

[1] Calibrated based on the field illitization data (Liu et al., 2013)

[2] From Pusch and Madsen (1995)

4.4   Model Results

The ultimate goal of using coupled THMC model to interpret the data collected in the FEBEX *in situ* test is to understand the THMC evolution of bentonite under the repository condition so that we can use most plausible processes and parameters to describe the behavior of bentonite. Once the coupled THMC model that can simultaneously match the measured temperature, relative humidity, water content, stress, aqueous concentrations, and minerals phase change, we can further use it to predict the long term (e.g. one hundred thousand years as required by most performance assessment) under different conditions, such as under higher temperature as was done by Zheng et al. (2015a).

The THC model developed in FY15 (Zheng et al., 2015b) was expanded to include mechanical processes using both linear swelling model and dual structure BExM. In this section, we first present model results from THMC model using the linear swelling model (denoted in the following sections as THMC-LS) and then discuss the results from the model that uses the dual structure BExM (referred as THMC-BExM in the following sections).

4.4.1   THMC model using linear swelling model

4.4.1.1   THM data and model results

In the FEBEX *in situ* test, some data were collected real time by the sensors buried in the bentonite block such as temperature, relative humidity and stress; and some of them had to be measured in the laboratory using the bentonite sample that were taken after dismantling of test sections, including water content, dry density, concentration of ions in pore water and mineralogical composition. Table 4.10 list some key dates of the FEBEX *in situ* test to facilitate the discussion of the model results. The dismantling of heater #1 in 2002 and heater #2 in 2015 provides two snapshots of measured water content, dry density, and concentrations of ions in pore water and mineralogical composition, which are very valuable for understanding the temporal evolution of these key data, as shown later in the report. Note that concentrations of ions in pore water and mineralogical composition have been analyzed by the other partner of FEBEX-DP project and are not available yet.

Table 4.11. Timeline of FEBEX in situ test.

Event	Date	Time (day)	Time (year)
Commencement of heating	2/27/1997	0	0.0
Shutdown of Heat #1	2/2/2002	1827	5.0
Sampling after heat #1 was dismantled	5/2/2002	1930	5.3
Shutdown of heat #2	4/24/2015	6630	18.2
Sampling after heat #2 was dismantled	7/3/2015	6700	18.3

Figures 4.11 through 4.14 compare the measured temperatures to two simulation results: a TH model and a THMC model with linear swelling (THMC-LS). Because the current model simulates only the "hot" sections that are normally located at the middle of the 4.5 m long heater, we used temperature measured at section F2 and E2 (see Figure 4.3) surrounding heater #2 to constrain the thermal calculation. Starting February 27, 1997, a constant power of 1200 W was applied to each heater for 20 days and then a constant power of 2000 W for another 33 days. After that, the system was switched to the constant temperature mode, allowing the power to fluctuate freely, but the maximum temperature at the surface of steel liner of the heater was maintained at 100 $^{\circ}$C. After the shutdown of heater #1 on February 2, 2002 (1827 days), the temperature field changed, as manifested by the temperature evolution after 1827 days in Figures 4.11 to 4.14. Unfortunately, the thermal sensors at radial distances of 0.48 m and 1.09 m failed shortly after 1827 days, but the temperature data from some sensors at a radial distance of 0.8 m (Figure 4.12) and 1.05 m (Figure 4.13) show the decrease in temperature after the shutdown of heater #1. The model results match well with the temperature data at all the radial distances. Near the steel liner, e.g., radial distance of 0.48 m in Figure 4.11, the temperature is almost the same as at the surface of the steel liner, but it decreases noticeably at a radial distance of 1.09 m (very close to the bentonite/granite interface) after the shutdown of heater #1 (Figure 4.14). The current model is a 1-D axi-symmetrical model that is designed to simulate the conditions of "hot" sections. In order to account for the heat dissipation from "hot" sections to "cold" sections

170

(located outside of the heater in X direction, such as sections B1 and B2 in Figure 4.3) , we used a semi-analytical solution implemented in TOUGH2 (Pruess et al., 1999) with an adjusted heat exchange surface area to match the temperature data. After 1827 days, the heat exchange surface area was adjusted again to match the data to mimic further heat loss from heater #2 when heater #1 was removed. In general, a fairly good match between the models and data was achieved.

The temperature profiles calculated by TH and THMC model differ only slightly at locations away from the heater. The reason is that thermal conductivity is a function of degree of water saturation and the TH and THMC models give different degrees of water saturation.
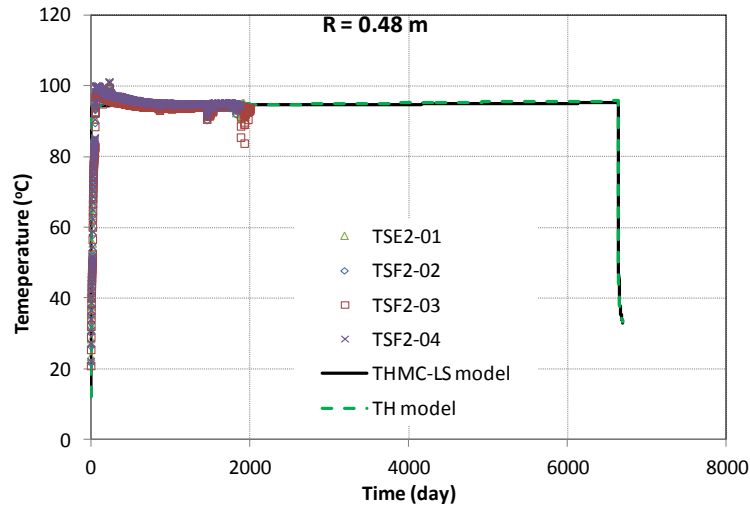
Figure 4.11. Measured temperature by sensors located at a radial distance of 0.48 m in sections E2 and F2 and model results from the TH model and THMC model with linear swelling (THMC-LS).
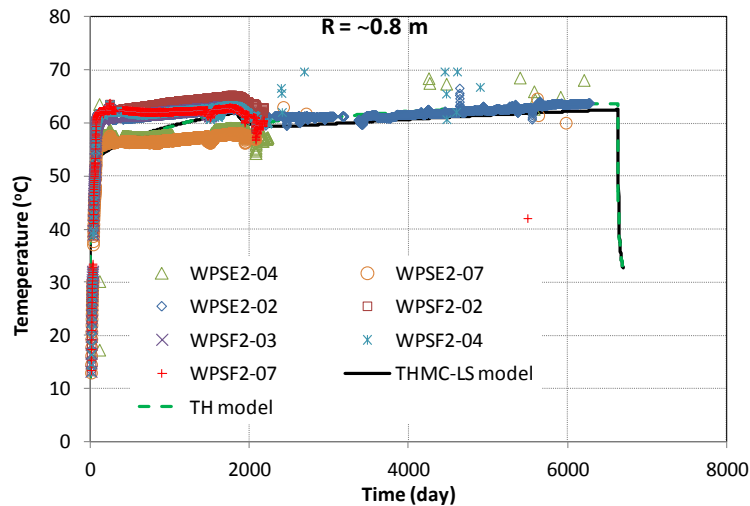
Figure 4.12. Measured temperature by sensors located at a radial distance of 0.8 m in sections E2 and F2 and model results from the TH model and THMC model with linear swelling (THMC-LS).

171
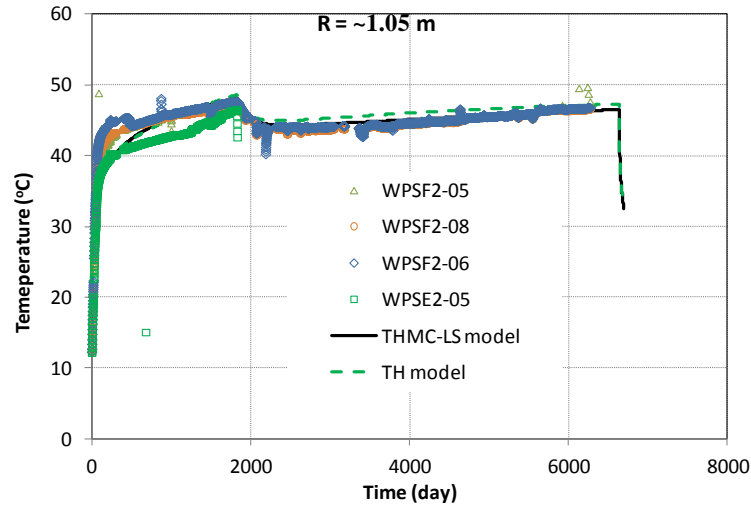
Figure 4.13. Measured temperature by sensors located at a radial distance of 1.05 m in sections E2 and F2 and model results from the TH model and THMC model with linear swelling (THMC-LS).
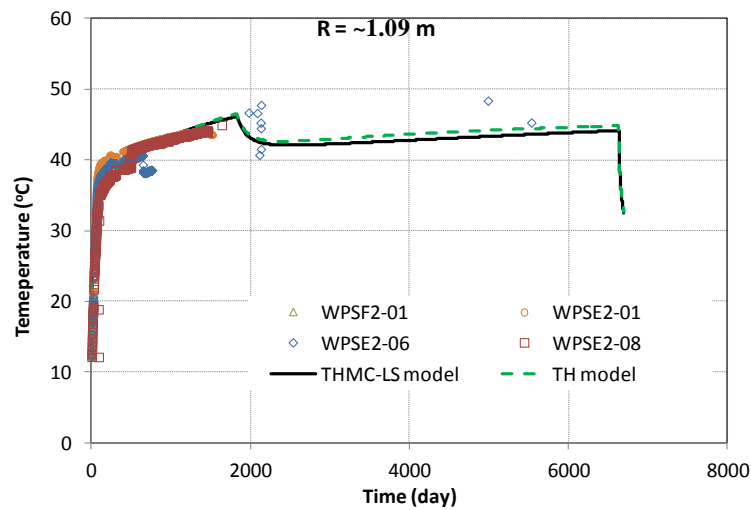
Figure 4.14. Measured temperature by sensors located at a radial distance of 1.09 m in sections E2 and F2 and model results from the base TH model.

Relative humidity, water content and dry density are three types of hydrological data that are available so far for comparing with model results. Water content and dry density were measured two times: one was after the dismantling of heater #1 (in 2002, 5.3 years after the start of heating) and the other was after the dismantling of heater #2 (in 2015, 18.3 years after the start of heating).

172

For the water content and dry density data, in this report we select data from sections 18, 28 and 29 (Zheng et al., 2011) (see Figure 4.4 for their locations) and sections 22 and 27 (Daucousse and Lloret, 2003) whose locations are given in Figure 4.15.
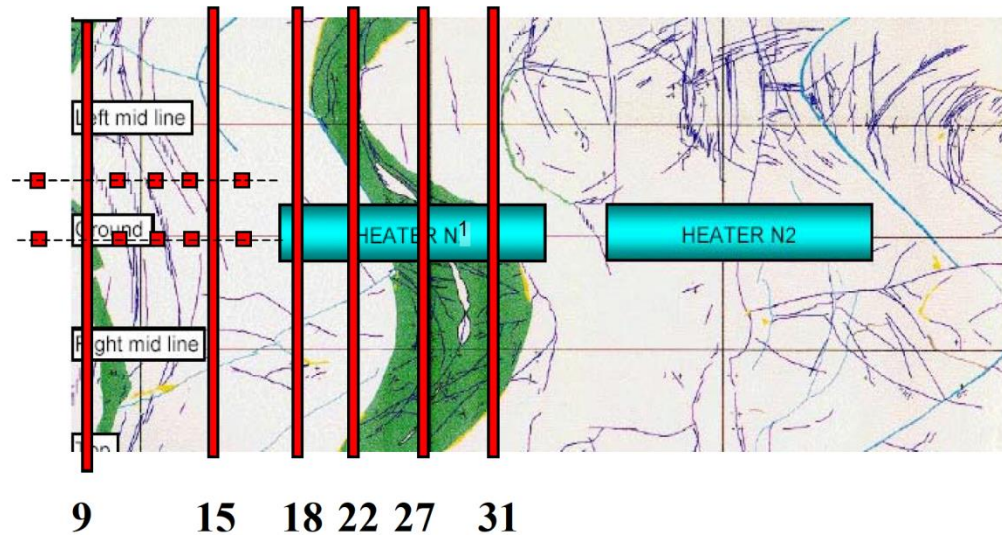
Figure 4.15. Layout of the sampling sections for water content and dry density measurement during the dismantling of heater #1 in 2002 (Daucousse and Lloret, 2003).

After about five years heating and hydration, bentonite near the heater remains fairly dry, with water contents close to the initial value, whereas bentonite near the granite become fully saturated and have water content ranging from 25% to 35% (Figure 4.16). The TH model with a constant porosity apparently fails to match the measured data at 5.3 years— model underestimates the water content data near the granite and overestimates the data in the middle of bentonite barrier. If the porosity is constant, the water content of fully saturated sample is 25%, higher measured water content near granite clearly indicates the swelling of bentonite upon hydration from the granite. The THMC model that accounts the swelling of bentonite and subsequent porosity and permeability clearly outperforms the TH model and matches reasonably well the data at 5.3 years. As the heating and hydration continues in the bentonite barrier surrounding heater #2, water contents near the heater kept increasing and reached about 18-19% at 18.3 years upon the dismantling of heater #2, but water contents near the granite (about 0.2 m from the bentonite/granite interface) at 18.3 years remained similar to that at 5.3 years because the bentonite had become fully saturated in early time and no more swelling is allowed in the confined gallery. Water content data at 18.3 years are nicely matched by the THMC model across the entire length of the bentonite barrier, but significantly overestimated by the TH model from a radial distance of 0.45 to 0.8 m and underestimated by the TH model from a radial distance of 0.8 m to the bentonite/granite interface.
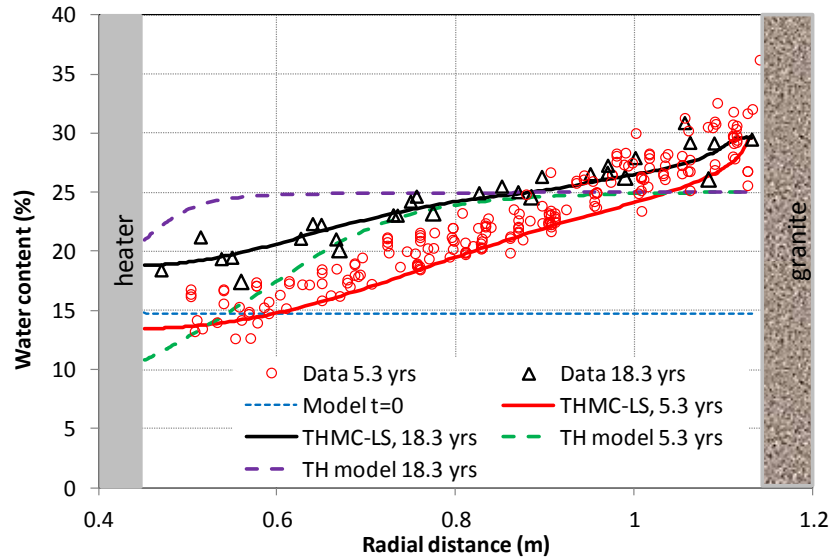
Figure 4.16. Measured water content data at sections 19, 28 and 29 (Zheng et al., 2011) and sections 22 and 27 (Daucousse and Lloret, 2003) after the dismantling of heater #1 ("data 5.3 yrs") and at section 49 after the dismantling of heater #2 ("data 18.3 yrs") and model results from the TH model (Zheng et al., 2015b), THMC model with linear swelling (THMC-LS).

The swelling of bentonite due to the hydration is clearly manifested by the measured dry density data. Initially the FEBEX bentonite blocks have a dry density of 1.7 g/cm^3. Considering the gaps between the bentonite blocks, the average dry density of the bentonite barrier shortly after the test started could be around 1.65 g/cm^3. After 5.3 and 18.3 years, the dry density ranges from 1.4-1.6 g/cm^3 near the granite, which indicate the swelling of bentonite. For bentonite near the heater, dry density is around 1.65-1.75 (Figure 4.17), indicating compression from the outer rings of the barrier. Model results show that the dry density at 5.3 years is higher than that at 18.3 years whereas measured data do not show any clear difference between 5.3 years and 18.3 years. As bentonite continues getting hydrated from granite and water content kept increasing from 5.3 years to 18.3 years, it is more conceivable that dry density decreases with time. One reason that measured dry densities at 5.3 and 18.3 years do not show clear difference might be measurement procedure. Dry density cannot be measured under *in situ* conditions in which the bentonite blocks were compressed by a confining stress of about 7-8 MPa. When samples were taken out of the gallery, they essentially underwent an unloading process which altered the volume of samples, i.e. the dry density measured in the laboratory does not necessary represent the *in situ* conditions anymore. The THMC model seems to match the dry density profile after 18.3 years pretty well (Figure 4.17).

174
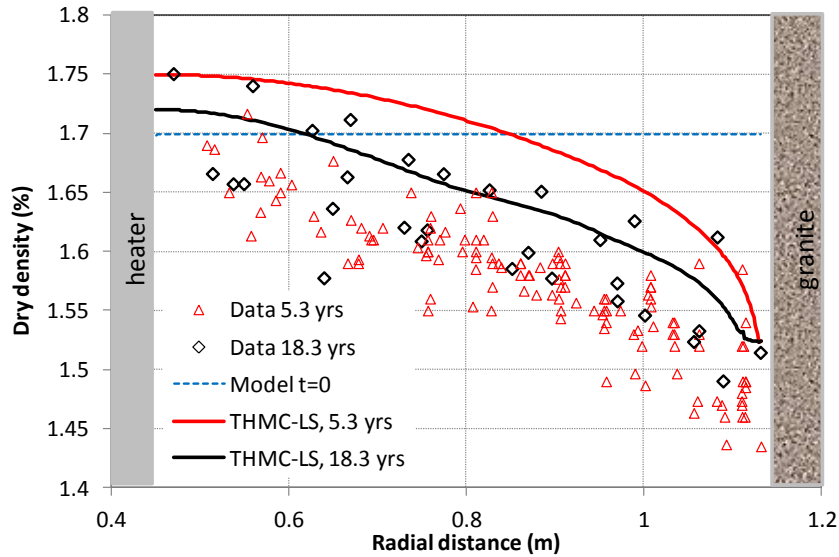
Figure 4.17. Measured dry density data at sections 22 and 27 (Daucousse and Lloret, 2003) after the dismantling of heater #1 ("data 5.3 yrs") and at section 49 after the dismantling of heater #2 ("data 18.3 yrs") and model results from THMC model with linear swelling (THMC-LS).

Assuming the solid phase in bentonite is not compressible, porosity can be calculated from dry density with a grain density of 2.78 g/cm^3, which are called 'inferred porosity data" in Figure 4.18. Model results show increase of porosity due to the swelling upon the continuous hydration of bentonite and match well the 'inferred porosity data" at 18.3 years (Figure 4.18). Similar to dry density data, porosity data do not show any difference between 5.3 years and 18.3 years. In Figures 4.17 and 4.18, the TH model with a constant porosity of 0.41 apparently cannot fit the measured dry density and porosity and is therefore not shown here.
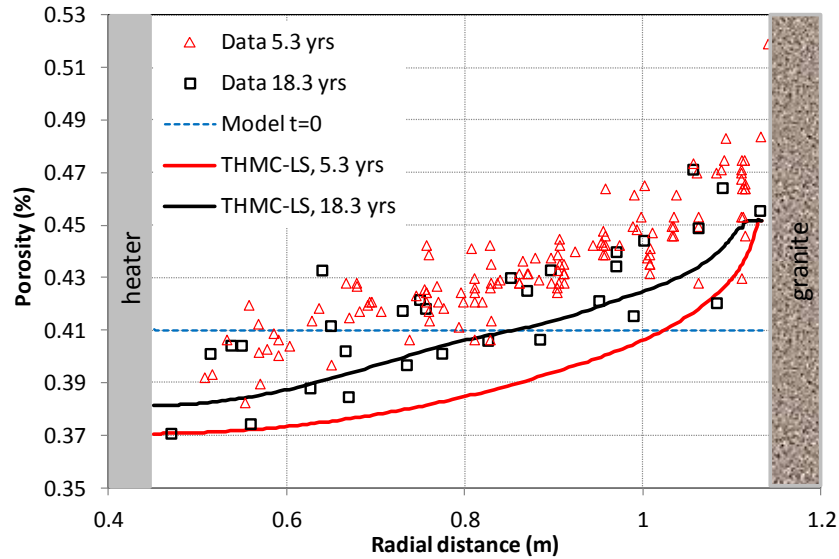
Figure 4.18. Inferred porosity data at sections 22 and 27 (Daucousse and Lloret, 2003) after the dismantling of heater #1 ("data 5.3 yrs") and at section 49 after the dismantling of heater #2 ("data 18.3 yrs") and model results from THMC model with linear swelling (THMC-LS).

Unlike water content and dry density, relative humidity data were measured real time by sensors at various positions in the bentonite. These data were grouped by the radial distance of the sensors. Previous modeling exercises (e.g. Zheng et al., 2011) showed that relative humidities near the heater have been overestimated and were the key data to test the models. Unfortunately, most sensors for relative humidities failed for the sections around heater #2, especially near the heater. For example, as shown in Figure 4.19, sensors at section E2 (WCSE2-03, WCSE2-04) at a radial distance of ~0.52 m only provide data until 147 days. We therefore have to rely on the relative humidity data measured at section E1 (located around heater #1) to constrain our model. A fairly good match between model results and relative humidity was achieved. The TH model overestimates the measured relative humidities after about 1000 days and seems not provide a correct trend of the evolution of relative humidity. A better fit between the model and data was obtained by the THMC model. In the THMC model, permeability decrease due to swelling is responsible for the lower calculated relative humidity near the heater. Another important parameter that controls the relative humidity is the vapor diffusion coefficient. In the base-case THMC model, the vapor diffusion coefficient is 1.03×10^{-4} m^2/s, which is about 5-10 fold larger than a typically measured value (e.g., LaManna and Kandlikar, 2011). In a sensitivity run based on the THMC-LS model, a vapor diffusion of 2×10^{-5} m^2/s is used and the model results significantly overestimate the data. It is not uncommon to use higher-than-normal vapor diffusion coefficient to interpret moisture movement in unsaturated medium under non-isothermal conditions, a phenomenon that was called enhanced vapor diffusion (Clifford and Webb, 1996).

176

Figure 4.19. Measured relative humidity by sensors located at a radial distance of 0.52 m in sections E2 and E1 and model results from the TH model (Zheng et al., 2015b), THMC model with linear swelling (THMC-LS) and a sensitivity run that is based on THMC-LS but has a vapor diffusion coefficient that is 5 times lower.

Measured relative humidities in the middle of the bentonite barrier (radial distance of 0.8 m, Figure 4.20) and at the outer rings of the bentonite barrier (Figure 4.21 and 22) were adequately matched by both the TH and THMC-LS models. One interesting observation is that the THMC model, albeit having decreased permeability due to swelling at the outer ring area, shows rapid increase in relative humidity near the granite boundary, which actually matches the measured data better than the TH model.

Figure 4.20. Measured relative humidity by sensors located at a radial distance of ~0.8 m in sections E1, E2, F1 and F2 and model results from the TH model (Zheng et al., 2015b) and THMC model with linear swelling (THMC-LS).
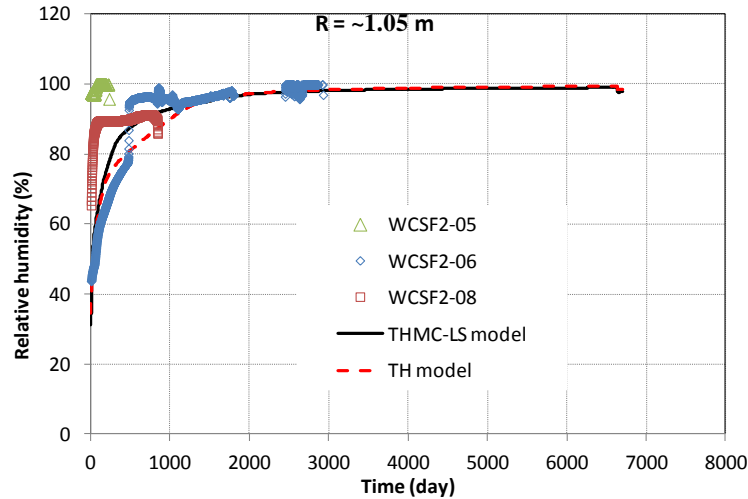
Figure 4.21. Measured relative humidity by sensors located at radial distance of ~1.05 m in section F2 and model results from the TH model (Zheng et al., 2015b) and THMC model with linear swelling (THMC-LS).
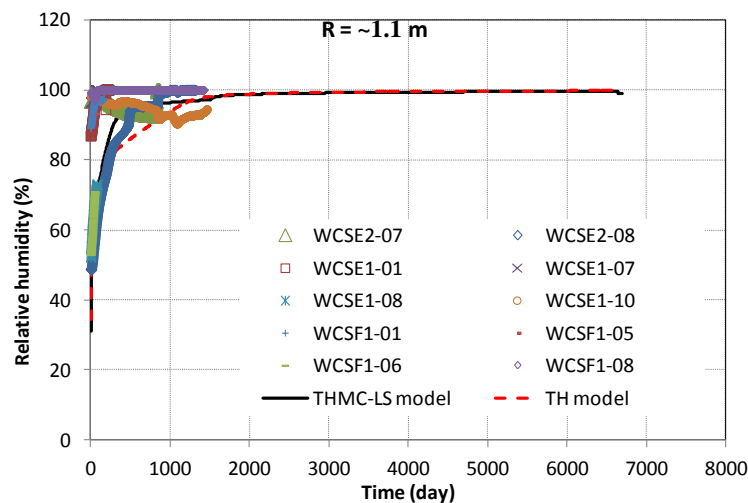
Figure 4.22. Measured relative humidity by sensors located at radial distance of ~1.1 m in sections E1, E2 and F1 and model results from the TH model (Zheng et al., 2015b) and THMC model with linear swelling (THMC-LS).

Sensors for measuring stress were also emplaced in the bentonite block. Although a majority of them stopped functioning, we still were able to extract data at two radial distances: one is 0.5 m, very near the heater and the other is 1.1 m, right at the bentonite/granite interface. No data were available for bentonite in the middle of the barrier. Figures 4.23 and 4.24 show the measured stress and model results. The total stresses in bentonite gradually increase as more water infiltrated into the bentonite. The swelling of bentonite creates a compressive force in the confined gallery, which eventually reaches a plateau as the bentonite barrier is close to being fully saturated, as shown clearly by the data and model result at radial distance of 1.1 m and to a lesser degree by the data at a radial distance of 0.5 m. It is expected that after the entire bentonite barrier becomes fully saturated, the stress field is fairly homogenous. The THMC model matches

178

reasonably the data near the granite (Figure 4.24) but overestimates the data near the heater (Figure 4.23). However, it is noteworthy that the stress at a radial distance of 0.5 m might have similar uncertainties of measured stress at radial distance of 1.1 (see Figure 4.24).
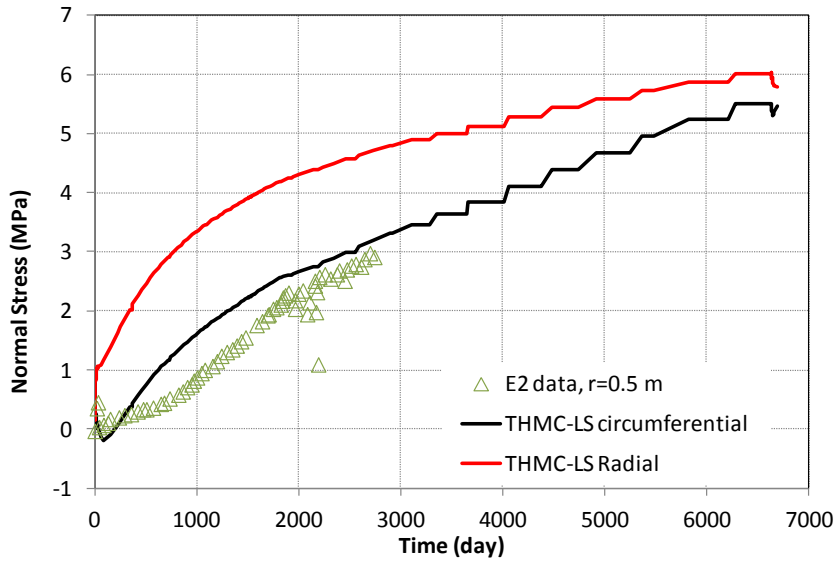
Figure 4.23. Measured stress by sensors located at a radial distance of ~0.5 m in section E2 and THMC model with linear swelling (THMC-LS).
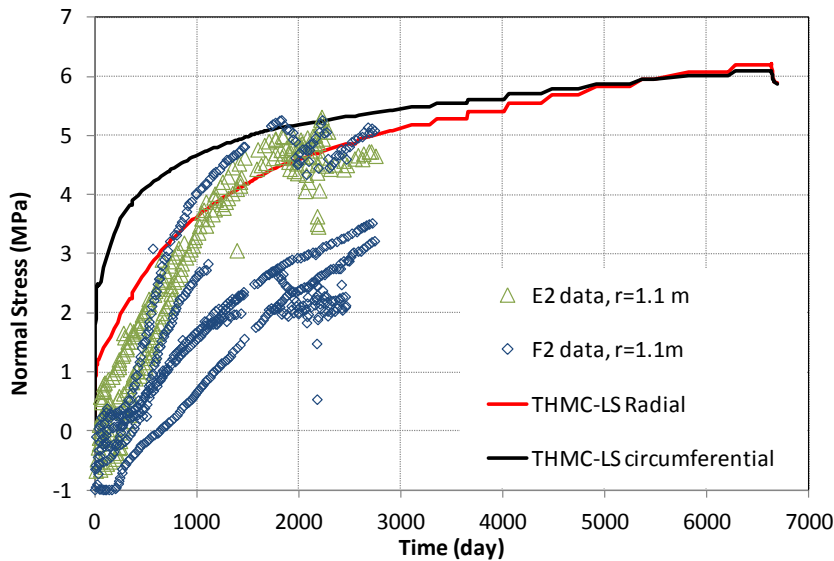
Figure 4.24. Measured stress by sensors located at radial distance of ~1.1 m in sections E2 and F2 and THMC model with linear swelling (THMC-LS).

4.4.1.2   *Chemical data and model results*

The two dismantling events in the FEBEX *in situ* test provide a unique opportunity to check the both the spatial and temporal evolution of the geochemistry in bentonite.

After the dismantling of heater #1 in 2002, samples were taken along several radii in each section (Zheng et al., 2011). Bentonite samples were taken for THC analyses from three sections surrounding the heater #1: 19, 28, and 29 (see Figure 4.4 for their locations). Each sampling section consists of an outer, central and inner layer of bentonite blocks. Bentonite blocks were preserved immediately after their extraction in plastic films, with two layers of aluminized PET sheets and vacuum-sealed plastic bags. Protection against mechanical damage was used to ensure the integrity of the material (ENRESA, 2006a). Aqueous extract tests (AET) were used to obtain pore water chemistry for compacted FEBEX bentonite. AET is a method to quantify the total content of soluble salts of a clay sample. A *1:R* AET consists on adding to a mass M_s of powdered clay sample a mass of distilled water equal to R times M_s. The clay sample and water are stirred during a period of time, usually 2 days, during which water and clay are allowed to equilibrate. Chemical analyses are performed on the supernatant solution after phase separation by centrifugation (Sacchi et al., 2001). In addition to dilution, chemical reactions take place during pore water extraction, which changes the concentrations of dissolved species in a complex nonlinear manner. This makes it difficult to derive the chemical composition of the original pore water from the aqueous extract data (Bradbury and Baeyens, 1998; Sacchi et al., 2001). The inference of dissolved concentrations for reactive species requires geochemical modeling based on mineralogical data (Fernández and Rivas, 2005; Zheng et al., 2008). Aqueous extract tests and concentration of exchangeable cations are available for sections 19, 28 and 29 (Fernández and Rivas, 2003). Aqueous extract data from sections 29 and 19 were interpreted by inverse geochemical modeling (Zheng et al., 2008) and used to test the model predictions (Zheng et al., 2011).

After the dismantling of heater #2 in 2015, a similar procedure was taken to measure the pore water composition and mineralogical composition. Because these data won't be available until the end of 2016, in this report, we still use the chemical data obtained after the dismantling of heater #1 to evaluate our THMC models.

Chloride, as a conservative species, is only controlled by the transport processes, i.e. advection and dispersion, which is subsequently dictated by the THM model rather than chemical reactions. In Zheng et al. (2015b), when the THC model failed to match the profile of chloride concentration measured at 5.3 years, it was postulated that adding mechanical processes and the resulting porosity and permeability changes would diminish such a mismatch. Therefore, in FY16, great effort was therefore dedicated to develop coupled THMC and THM models; they seem to be sufficiently calibrated as shown in the previous sections. However, as shown in Figure 4.25, the THMC model is still unable to match chloride data—it overestimates the concentrations near the granite and underestimates concentrations near the heater. The decrease in permeability at the outer rings of the bentonite barrier in the THMC model leads to less water infiltration and thus less dilution, which is why the THMC model has higher chloride concentration near the granite than the THC model. Less water infiltration also means less evaporation near the heater, which explains why the THMC model has lower chloride concentration near the heater than the THC model. As shown later in the report, finding the right permeability-porosity relationship or considering thermal osmosis might allow the THMC model to match both the THM and chemical data.

180
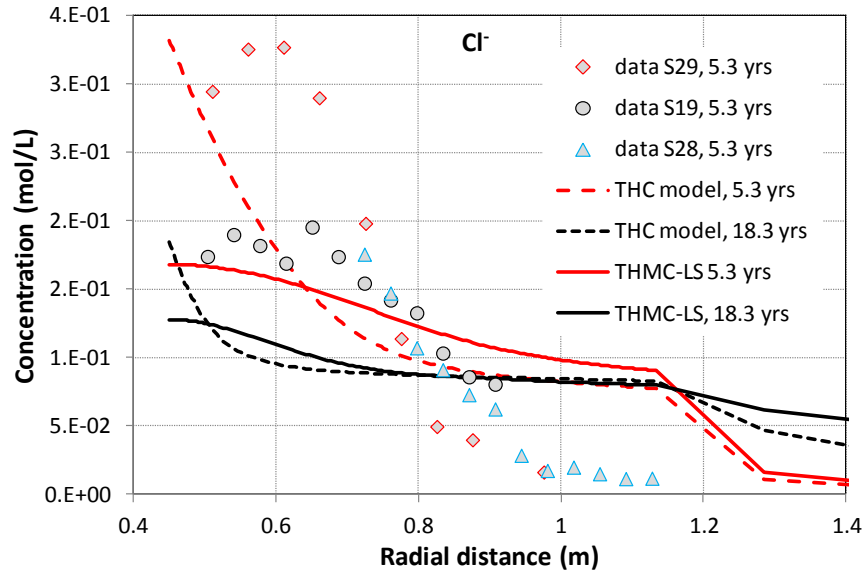
Figure 4.25. The concentration profile of chloride at 5.3 years (Zheng et al., 2011) and model results from the THC model (Zheng at al., 2015b) and THMC model with linear swelling (THMC-LS).

The concentration profiles of major cations are shown in Figures 4.26 to 4.28. As revealed in Zheng et al. (2015b), the spatial concentration profile of major cations, albeit subject to chemical reactions including cation exchange and minerals dissolution/precipitation, is largely controlled by transport processes and follow the trend of chloride. Chemical reactions alter concentration levels but not the overall trend of the concentration profiles. Similarly, just as the THMC model overestimates the concentration of chloride near the bentonite/granite interface, it also overestimates the concentrations of sodium, calcium, magnesium, and potassium as well. In addition to the transport processes, sodium concentration could also be affected by cation exchange and dissolution of smectite. However, because the sodium concentration is much higher than other cations and the concentration perturbation of other cations is fairly small, the sodium concentration is not impacted noticeably by cation exchange, and the amount of smectite dissolved (Zheng et al., 2015) is also too small to meaningfully alter the sodium concentration. The THMC model predicts that the concentration of sodium keeps going down until 18.3 years.
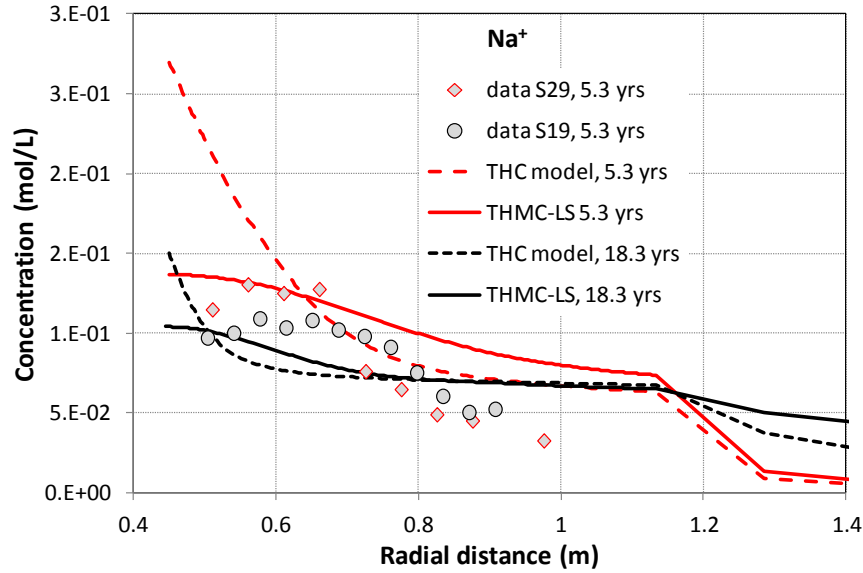
Figure 4.26. The concentration profile of sodium at 5.3 years (Zheng et al., 2011) and model results from the THC model (Zheng at al., 2015b) and THMC model with linear swelling (THMC-LS).

The THMC model, just like THC model, overestimates the measured calcium concentration across the entire bentonite barrier (Figure 4.27). In addition to the transport processes, the precipitation of dolomite and the dissolution of calcite also affect the concentration level of calcium. Eventually the model needs to delicately balance the pH, bicarbonate, calcium concentration, calcite dissolution, and dolomite precipitation to capture the concentrations of all of them.

Figure 4.27. The concentration profile of calcium at 5.3 years (Zheng et al., 2011) and model results from the THC model (Zheng at al., 2015b) and THMC model with linear swelling (THMC-LS).

Zheng et al. (2015b) showed that magnesium is involved in the dissolution/precipitation of smectite, the precipitation of dolomite, and cation exchange, but eventually these reactions seem to cancel each other out, and magnesium concentration is largely controlled by the transport processes just like chloride. The discrepancy between the THMC model and magnesium concentration data is similar to other cations (Figure 4.28).
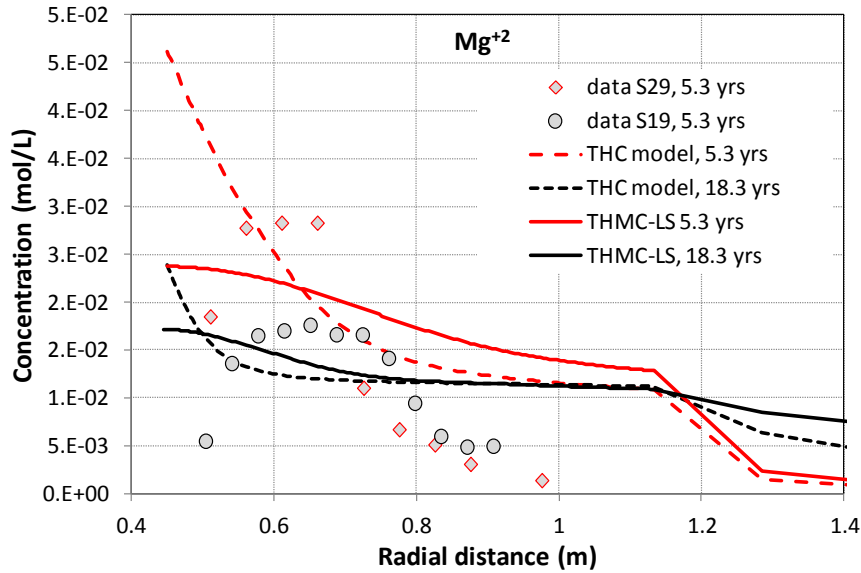
Figure 4.28. The concentration profile of magnesium at 5.3 years (Zheng et al., 2011) and model results from the THC model (Zheng at al., 2015b) and THMC model with linear swelling (THMC-LS).

The computed concentration of potassium from the THC model (Zheng et al., 2015b) that include chemical reactions is actually lower than that from a sensitivity run that did not consider any chemical reactions, suggesting that some reactions consume potassium in the pore water, which turned out to be the precipitation of illite. Although the THMC model overestimates slightly the potassium concentration near the granite, it seems to match the potassium concentration near the heater quite well.
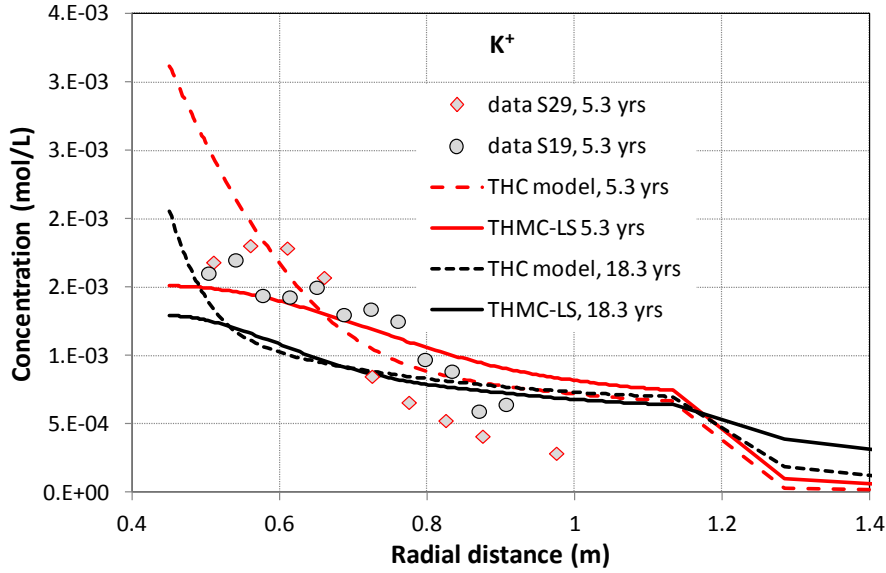
Figure 4.29. The concentration profile of potassium at 5.3 years (Zheng et al., 2011) and model results from the THC model (Zheng at al., 2015b) and THMC model with linear swelling (THMC-LS).
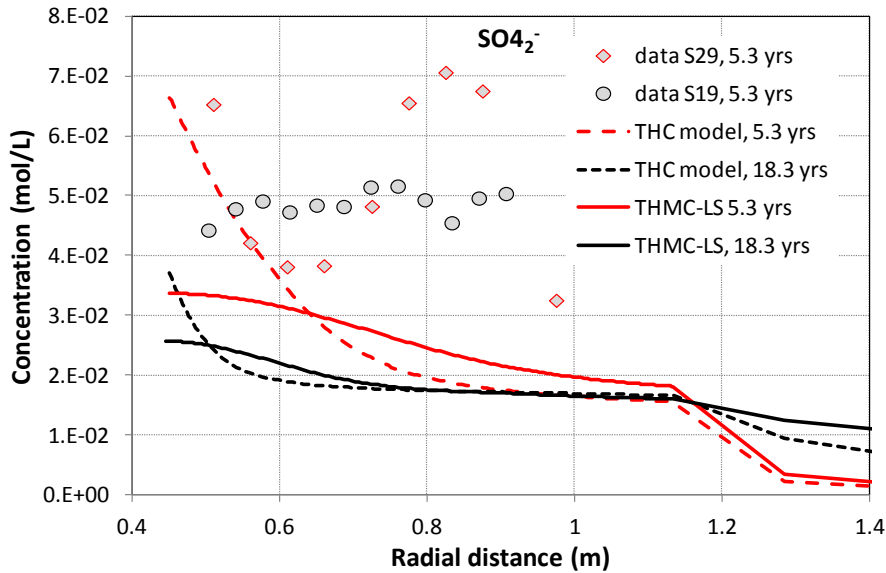
Figure 4.30. The concentration profile of sulfate at 1930 days (Zheng et al., 2011) and model results from the base model.

FEBEX bentonite contains a small amount of gypsum (ENRESA, 2000). But the amount is very small and gypsum is very soluble, so a small change in the water saturation may make gypsum disappear, which makes it debatable whether there is gypsum initially in the bentonite. The presence of gypsum had been one of the major uncertainties when the pore water compositions under *in situ* conditions were inferred from aqueous extract data (Zheng and Samper, 2008). Figure 4.30 shows the inferred data and model results. Unlike cations, the data for sulfate does not follow the trend of chloride, which indicated strong interference by chemical reactions. In the current model, no gypsum is present in the bentonite. Both the THC and THMC model results underestimate the data. Refinement of the current chemical model is warranted in the future.

184

It is usually very difficult to predict pH because it involves many reactions. For FEBEX bentonite, pH is mainly regulated by carbonate reactions involving calcite and dolomite and surface protonation reactions. Zheng et al. (2011) showed that surface protonation has strong pH buffering capacity and the model in this report confirms that observation. However, both the THC and THMC models still underestimate the measured pH slightly by 0.1-0.2 unit, which may be attributed to the uncertainties in the initial amount of calcite. Figure 4.32 shows the concentration profile of bicarbonate. Previous modeling work (e.g. Samper et al., 2008) showed that bicarbonate concentration is very sensitive to the alteration of calcite and dolomite and is coupled with pH changes. The current model does not consider the dissolution/exsolution of CO_2 gas, which may be a key reaction to explain the underestimation of pH and bicarbonate by the model. Also as mentioned above, inference processes using geochemical modeling were needed to obtain the chemical composition of pore water in bentonite under *in situ* conditions based on the measured concentrations by aqueous extract (Zheng et al., 2008a). However, during the aqueous extract, there was CO_2 exsolution that changed the inventory of total carbonate, which was difficult to capture accurately in the geochemical model that was used to infer the concentration under the *in situ* conditions (Zheng et al., 2008). This is another source of uncertainty regarding the pH and concentration of bicarbonate.
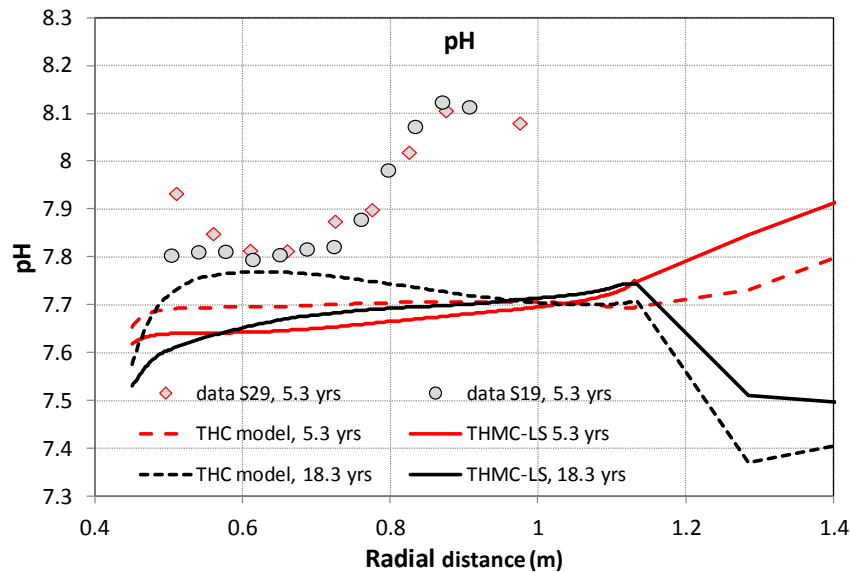
Figure 4.31. The profile of pH at 1930 days (Zheng et al., 2011) and model results from the base model.
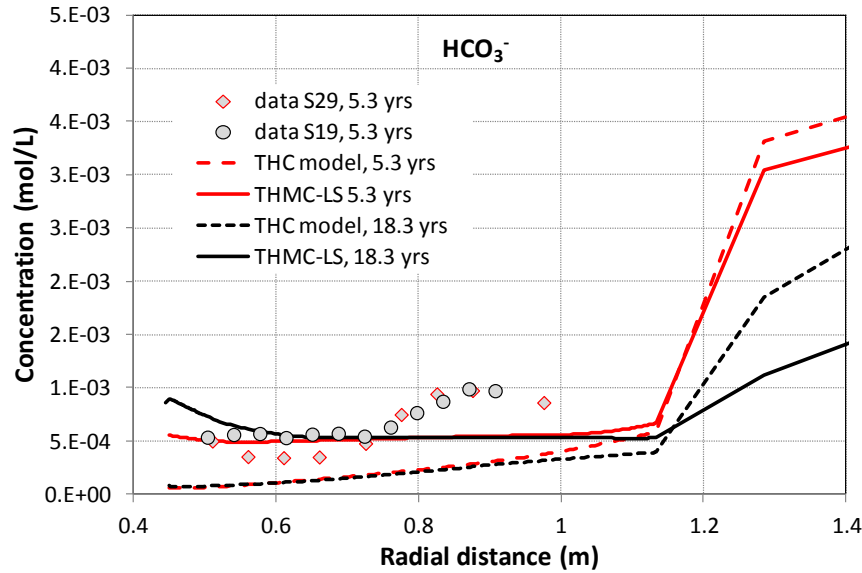
Figure 4.32. The concentration profile of bicarbonate at 1930 days (Zheng et al., 2011) and model results from the base model.

Regarding the evolution of concentration of major cations in pore water, after 18.3 years (Figures 4.25 to 4.32) the THMC model predicts lower concentrations across the entire bentonite barrier whereas the THC model predict lower concentration near the heater than that after 5.3 years, but concentrations near granite similar to the level of 5.3 years. Sulfate concentration will be further diluted as more water comes to saturate bentonite (Figure 4.30), but pH and bicarbonate at 18.3 years stay roughly the same level as at 5.3 years (Figures 4.31 and 4.32).

4.4.2   THMC model using BExM

Conceptually BExM divides the bentonite into a dual structure (Figure 4.33). Similar structural concept had been used by other modeler such as Bradbury and Baeyens (2003), Samper and Zheng (2008b) and Zheng and Samper (2015). Swelling take place predominantly in the micro-structure—water molecular enters into the inlayer space and cause an expansion of clay aggregates, and water flows occurs mainly through the macro-structure. The expansion of micro-structure compresses the space of macro-pore and therefore leads to a reduction in permeability. Such a reduction in permeability would be one of the major reasons that THMC can explain the water content data, which cannot be achieved by TH model. Figure 4.34 shows the measured water content at 5.3 years (dismantling of heater #1) and 18.3 years (dismantling of heater #2) and model results by the THMC model using linear swelling (THMC-LS) and BExM (THMC-BExM). Both models have similar water content results and match nicely the measured water content at 5.3 years. However, at 18.3 years, they deviate —THMC-BExM underestimates the water content data whereas the THMC-LS results match sufficiently the water content data. A close examination of the calculated spatial distribution of permeability (Figure 4.35) and porosity (Figure 4.36) at 5.3 years shows that THMC-BExM has lower permeability than THMC-LS but higher porosity than THMC-LS, which is why THMC-BExM and THMC-LS have similar water content results. At 18.3 years, THMC-BExM has similar total porosity to THMC-LS, but lower permeability THMC-LS, which explains why THMC-BExM computes lower water content than THMC-LS. Permeability and porosity changes will be further discussed in the next section.
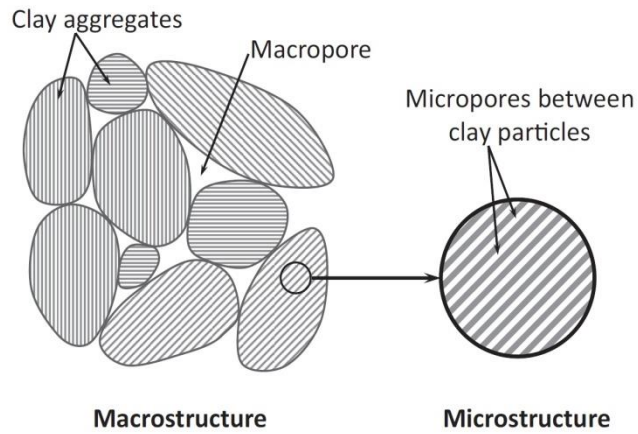
Figure 4.33. Schematic representation of the two structural levels considered in the dual structure BExM (Vilarrasa et al., 2015).
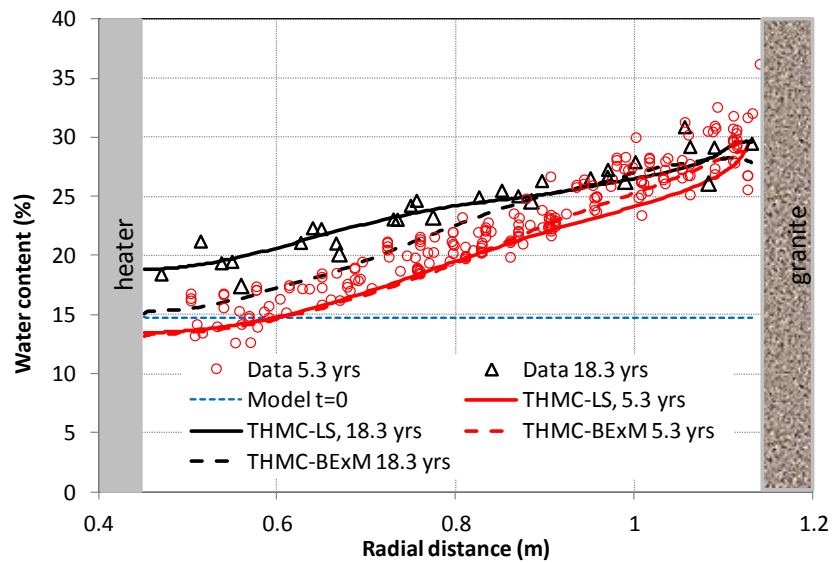
Figure 4.34. Measured water content at 5.3 years (dismantling of heater #1) and 18.3 years (dismantling of heater #2) and model results by the THMC model using linear swelling (THMC-LS) and BExM (THMC-BExM).
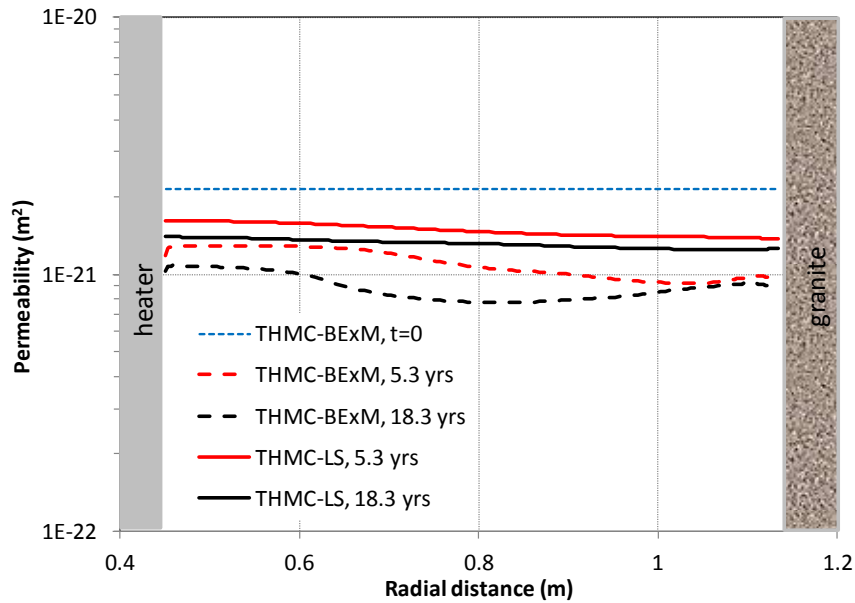
Figure 4.35. Spatial distribution of intrinsic permeability at time zero, 5.3 years (dismantling of heater #1) and 18.3 years (dismantling of heater #2) calculated by the THMC model using linear swelling (THMC-LS) and BExM (THMC-BExM).
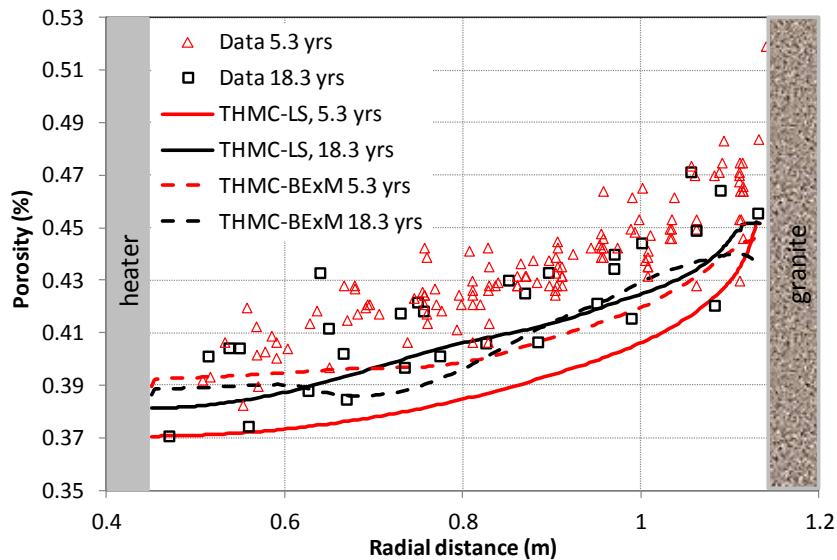
Figure 4.36. Measured porosity at 5.3 years (dismantling of heater #1) and 18.3 years (dismantling of heater #2) and calculated porosity by the THMC model using linear swelling (THMC-LS) and BExM (THMC-BExM).

Figure 4.37 shows the dry density data and model results, which have the following observations. First, the data is very scattered, which makes the interpretation difficult. A better measurement procedure might be needed. Second, although the THMC-LS model shows a decrease of dry density from 5.3 years to 18.3 years, observational data show no clear difference between 5.3 years and 18.3 years and neither do the model results by THMC-BExM. In BExM,

as suction keeps decreasing upon the hydration of bentonite, the micro-structure experiences swelling, but the macro-structure, depending on the local stress state at a given time, could be compressed or expanded, which is why in THMC-BExM, dry densities at 18.3 years are not always lower than that at 5.3 years. On the contrary, THMC-LS uses a linear swelling model, i.e., swelling strain is merely a function of water saturation. As a result, increase in water saturation from 5.3 years to 18.3 years leads to more swelling and subsequently higher porosity and lower dry density. Simply from the goodness-of-fit the measured data dry density, it seems that THMC-BExM outperforms THMC-LS and likely reflects the reality.
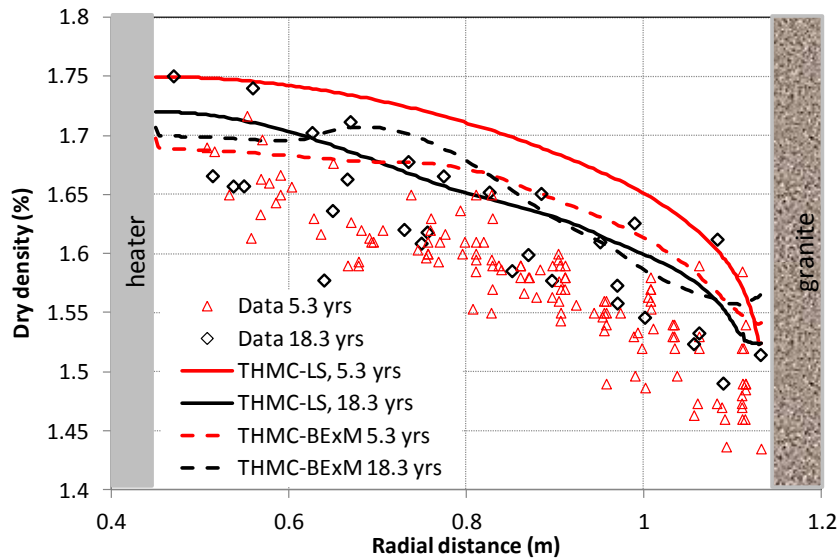
Figure 4.37. Measured dry density at 5.3 years (dismantling of heater #1) and 18.3 years (dismantling of heater #2) and model results by the THMC model using linear swelling (THMC-LS) and BExM (THMC-BExM).

There was about 70 days of cooling down period between the time that the heater #2 was switched off and bentonite samples were taken section by section due to operational reason. During this time period, temperature in the bentonite decreased to about 30 °C (Figure 4.38). This cooling off period, albeit seemingly very short compared with more than 18 years of operation of the test, has a significant impact on the spatial distribution of water content, as shown in Figure 4.39. Both THMC-LS and THMC-BExM show remarkable re-distribution of water content from 18.2 years to 18.3 years, which is featured by an increase in water content near the heater (roughly with a radial distance < 0.6 m) and a decrease in water content in the middle of bentonite barrier (radial distance from 0.6 to 0.9 m), indicating an moisture movement from the middle of the bentonite barrier towards the heater. Such a phenomenon might be caused by the deceased vapor diffusion upon the disappearance of thermal gradient, or the loss of thermal osmosis.
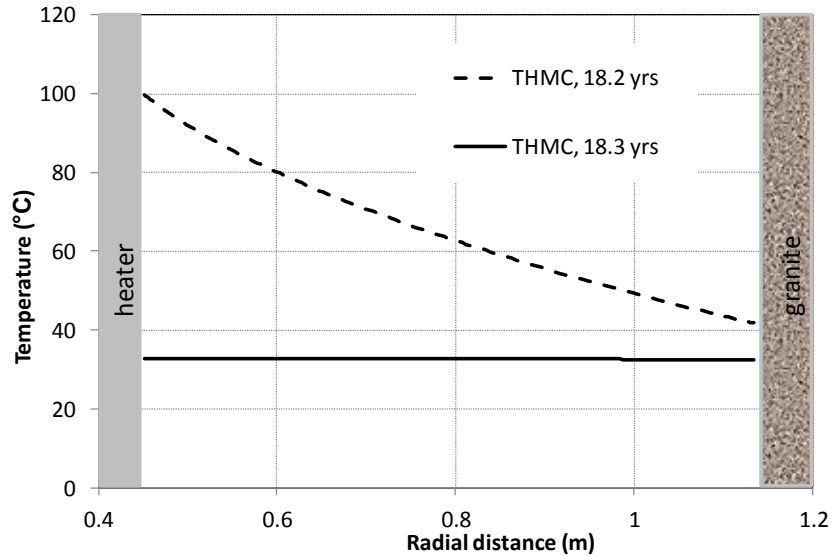
Figure 4.38. Calculated temperature at the time that heater #2 was switched off (18.2 years) and dismantling was conducted (18.3 years).
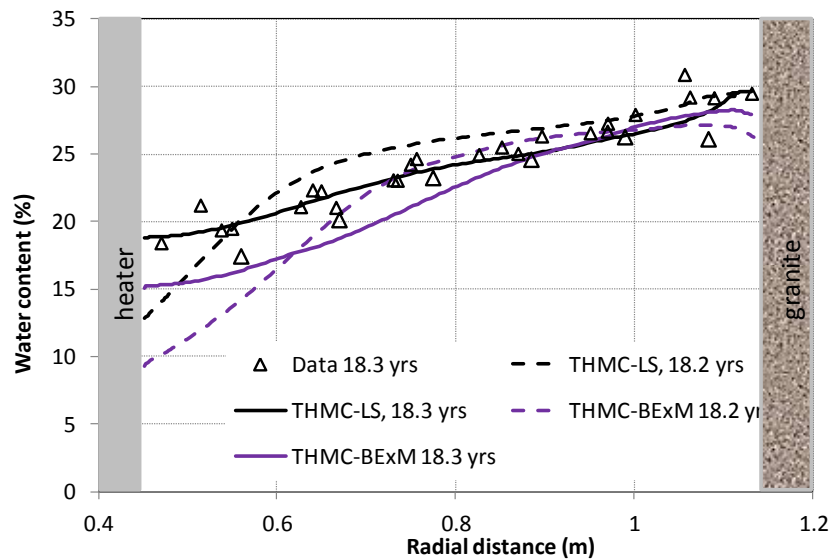
Figure 4.39. Measured dry density at 18.3 years (dismantling of heater #2) and model results by the THMC model using linear swelling (THMC-LS) and BExM (THMC-BExM) at the time that heater #2 was switched off (18.2 years) and dismantling was conducted (18.3 years).

Figures 4.40 to 43 depict the measured relative humidity and values computed with THMC-LS and THMC-BExM at four radial distances. THMC-BExM match nicely the relative humidity data near the heater (Figure 4.40) and outperforms the THMC-LS model, but underestimates slightly the data in the middle of the bentonite barrier (Figure 4.41) and underperforms slightly THMC-LS for the data in the middle of bentonite barrier. THMC-LS and THMC-BExM have similar calculated relative humidities at the outer rings of bentonite barrier and both of them match well with measured data.
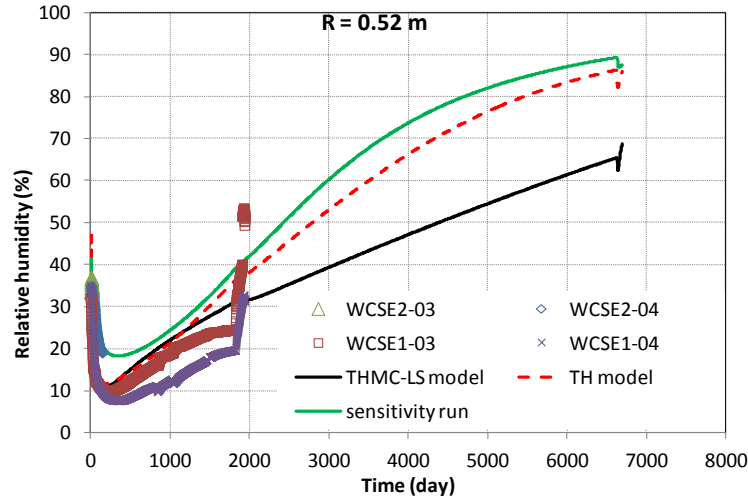
190
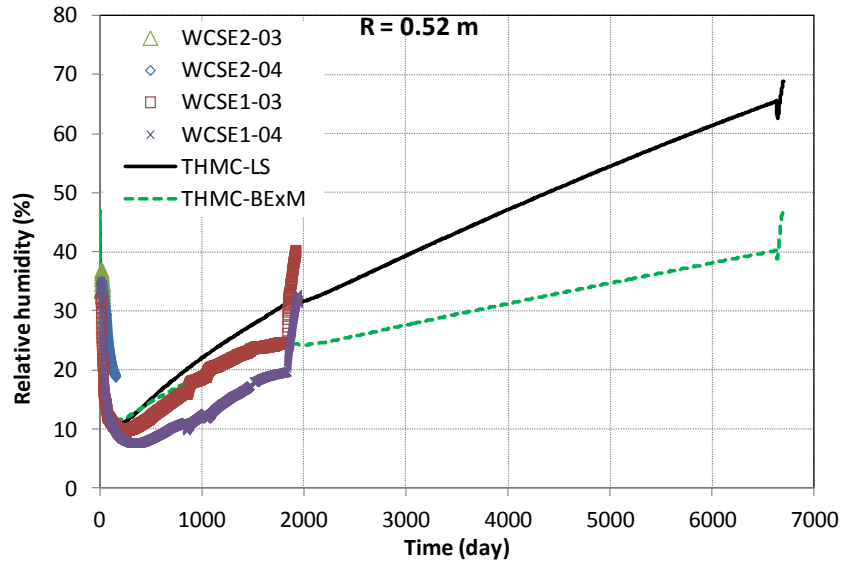
Figure 4.40. Measured relative humidity by sensors located at a radial distance of 0.52 m in sections E2 and E1 and model results from THMC model using linear swelling (THMC-LS) and BExM (THMC-BExM).
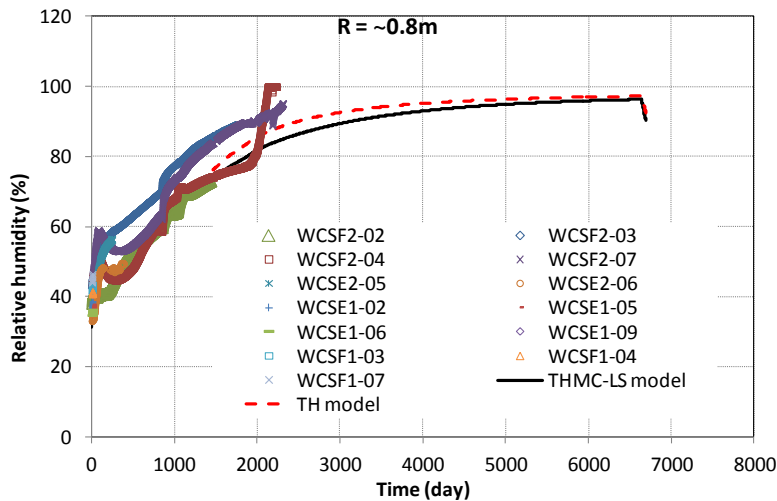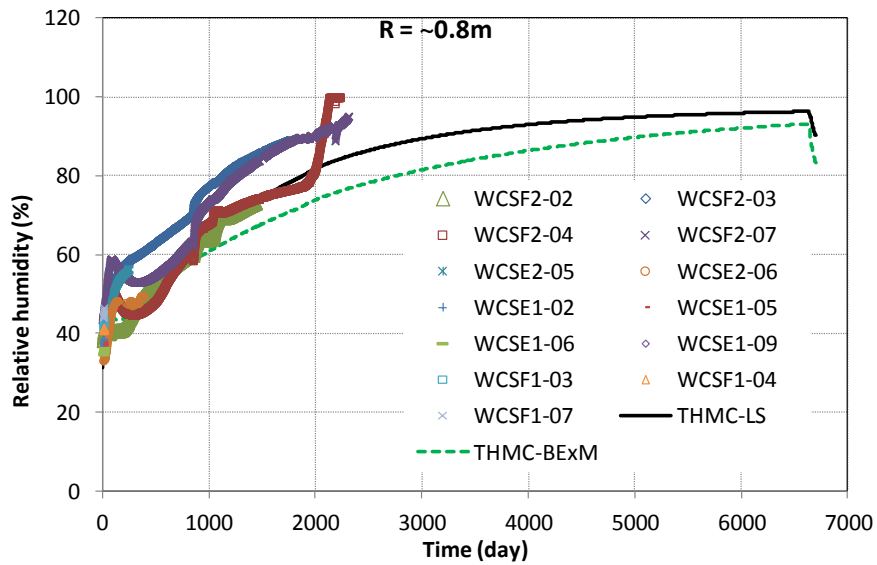

Figure 4.41. Measured relative humidity by sensors located at a radial distance of ~0.8 m in sections E1, E2, F1 and F2 and model results from THMC model using linear swelling (THMC-LS) and BExM (THMC-BExM).

191
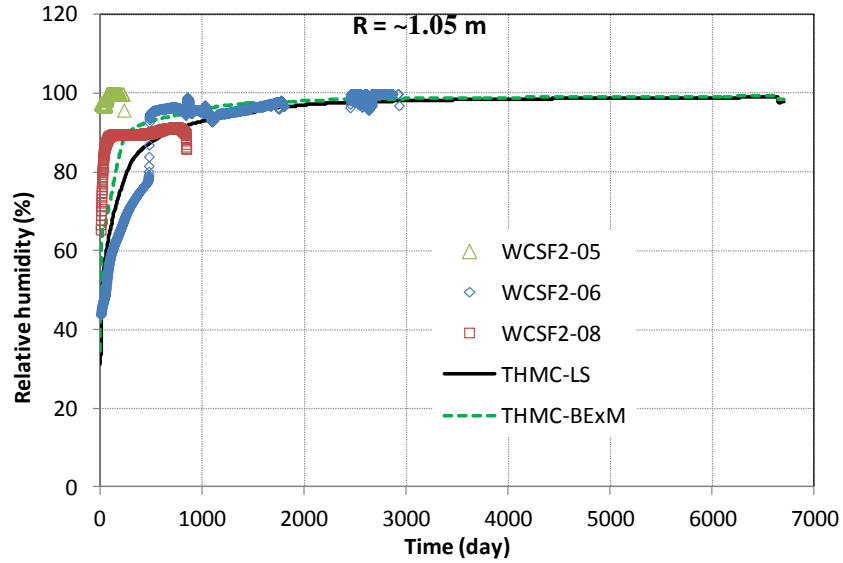
Figure 4.42. Measured relative humidity by sensors located at a radial distance of ~1.05 m in section F2 and model results from THMC model using linear swelling (THMC-LS) and BExM (THMC-BExM).
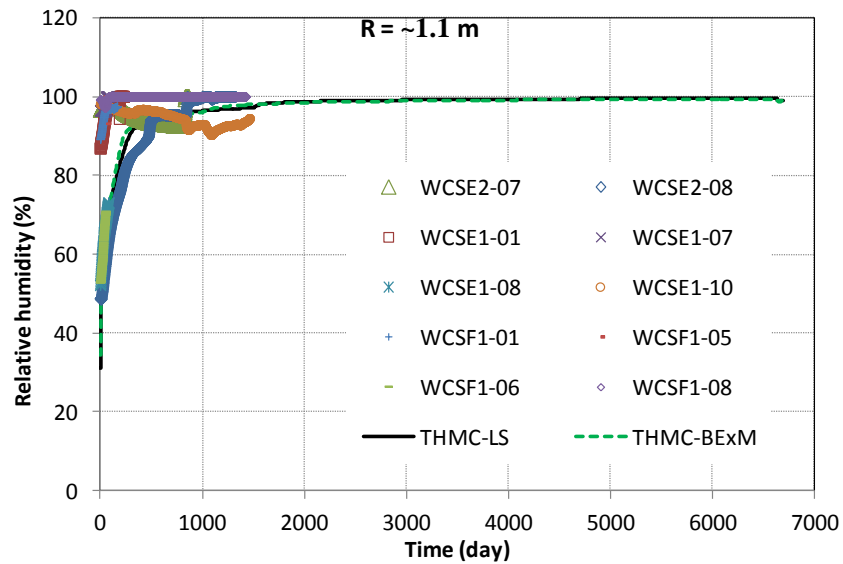
Figure 4.43. Measured relative humidity by sensors located at a radial distance of ~1.1 m in sections E1, E2 and F1 and model results from THMC model using linear swelling (THMC-LS) and BExM (THMC-BExM).

Figures 4.44 and 4.45 show the measured stress and model results by both THMC-LS and THMC-BExM. The expansion of bentonite gradually drives the stress to higher levels, but a rise in stress gradually slows down as the bentonite becomes fully saturated. BExM models that describe the swelling of bentonite more mechanistically, match better the stress increase in the early time than the linear swelling model that is known to be unable to describe the transient state of swelling.

192
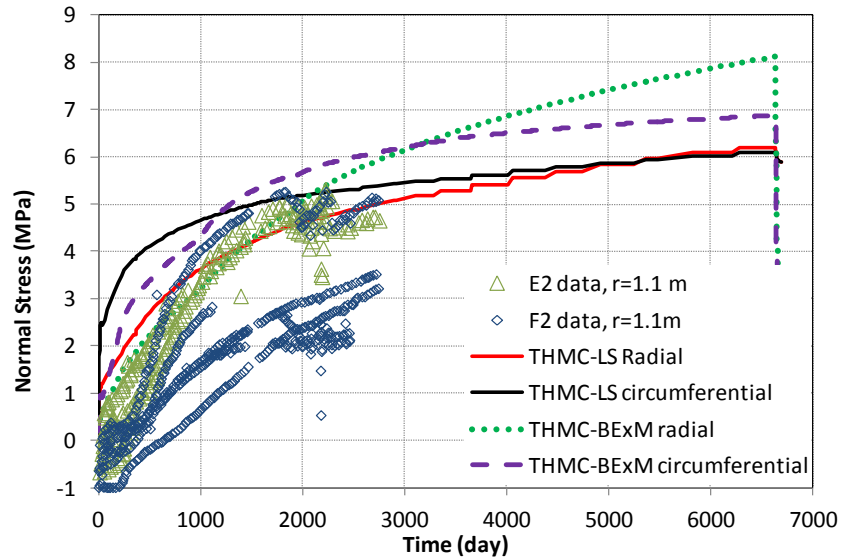
Figure 4.44. Measured stress by sensors located at radial distance of ~1.1 m in sections E2 and F2 and THMC model with linear swelling (THMC-LS).
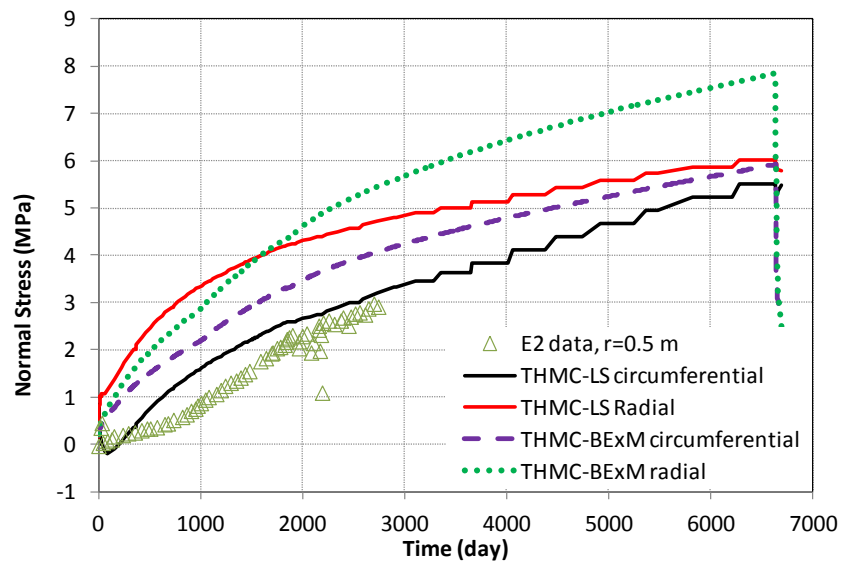
Figure 4.45. Measured stress by sensors located at a radial distance of ~0.5 m in section E2 and THMC model with linear swelling (THMC-LS).

In general, THMC-LS and THMC-BExM yield rather similar results in terms of water content, dry density, relative humidity and stress, despite the difference in calculated permeability and porosity. Considering uncertainties in the measured water content, dry density, relative humidity and stress data, both models seem to be sufficiently calibrated by the THM data and THMC-BExM maybe slightly better. However, as shown in Figure 4.47, THMC-BExM is facing the same problem the THMC-LSoverestimation of the chloride concentration near the granite and underestimation of its concentration near the heater. In fact, THMC-BExM is even worse than THMC-LS with its flatter spatial concentration profile. The fact that current THMC models, either using linear swelling or more complex BExM, reasonably match THM data but fail to

193

explain the chemical data, indicate that the current THMC model is flawed—either some critical coupling relationships were not correctly calibrated or some important processes are missing, which will be further discussed in the next section.
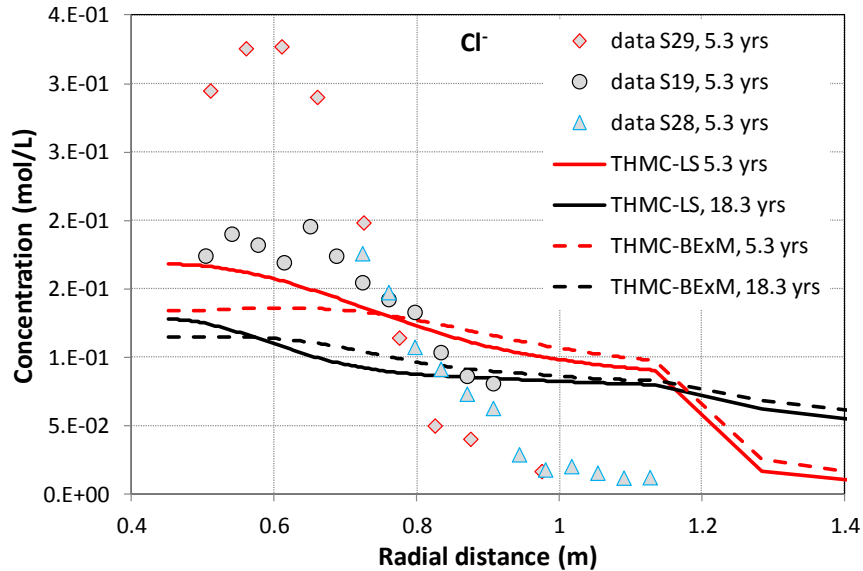
Figure 4.46. The concentration profile of chloride at 5.3 years (Zheng et al., 2011) and model results from the THMC model with linear swelling (THMC-LS) and BExM (THMC-BExM).

4.4.3   Effect of permeability change on chloride concentration

As discussed in Sections 4.4.1 and 4.4.2, the THMC models using either linear swelling (THMC-LS) or BExM (THMC-BExM) sufficiently match the THM data, but fail to match the concentration profile of chloride at 5.3 years. Chloride is a conservative species; its spatial distribution is controlled exclusively by advection and diffusion. In the THMC-LS and THMC-BExM model shown in Sections 3.4.1 and 3.4.2, the effective diffusion coefficient is 2E-9 m^2/s. In order to test if the match between the THMC model and chloride data can be improved by adjusting the diffusion coefficient, we conducted a sensitivity run in which the effective diffusion coefficient is reduced to 2E-10 m^2/s. As shown in Figure 4.48, the model with a lower diffusion coefficient significantly overestimates the concentration near the heater although it matches better the concentration near the bentonite/granite interface. More important, neither model is able to match the shape of concentration front (concentration profile from radial distance 0.7 m to 0.9 m). The sensitivity analysis shows that discrepancies between THMC model and chloride data cannot be resolved by adjusting diffusion, which means that advection is not properly calculated in the THMC models. Because advection is totally dependent on the water movement in the bentonite, in this section we re-visit the permeability change in the THMC model to see if we can solve the dilemma that THMC models match the THM data but not the chemical data.
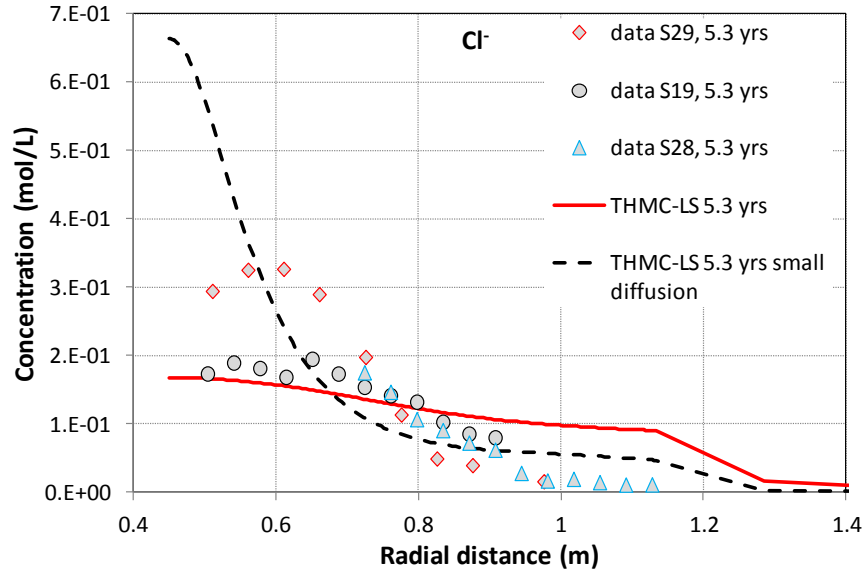
Figure 4.47. The concentration profile of chloride at 5.3 years (Zheng et al., 2011) and model results from the THMC model with linear swelling (THMC-LS) and a sensitivity run in which the effective diffusion coefficient is 2E-10 m²/s.

For water flow in unsaturated medium, flux is related to pressure gradient via an effective permeability, which is the product of intrinsic permeability (k) (or saturated permeability, absolute permeability) and relative permeability (k_r). The relative permeability function of $k_r = S_l^3$ has been used for FEBEX bentonite (Zheng et al., 2011; Sánchez et al., 2012b; Kuhlman and Gaus, 2014), however, there are uncertainties in the relative permeability function (Table 4.11): different exponent values were obtained in different tests, ranging from 1.1 to 4.46. In two sensitivity runs shown in Figure 4.49, we used two relative permeability functions with exponent equal to 1.1 and 4, respectively. The concentration profile is flatter if the exponent in the relative permeability function is higher (e.g., equal to 4 in Figure 4.49) and steeper if the exponent in the relative permeability function is higher (e.g., equal to 1.1 in Figure 4.49), but adjusting the relative permeability function is not able match the shape of the concentration front.

Table 4.12. Exponent in relative permeability law obtained from different type of tests (ENRESA, 2000)

Test	Value of n, in $k_r = S_r^n$
Water infiltration in small teflon cells	4.64
Water infiltration in bentonite in contact with granite	3.50
Heat and water flow experiment 1	3.06
Heat and water flow experiment 2	1.10
Heat and water flow experiment 3	1.68
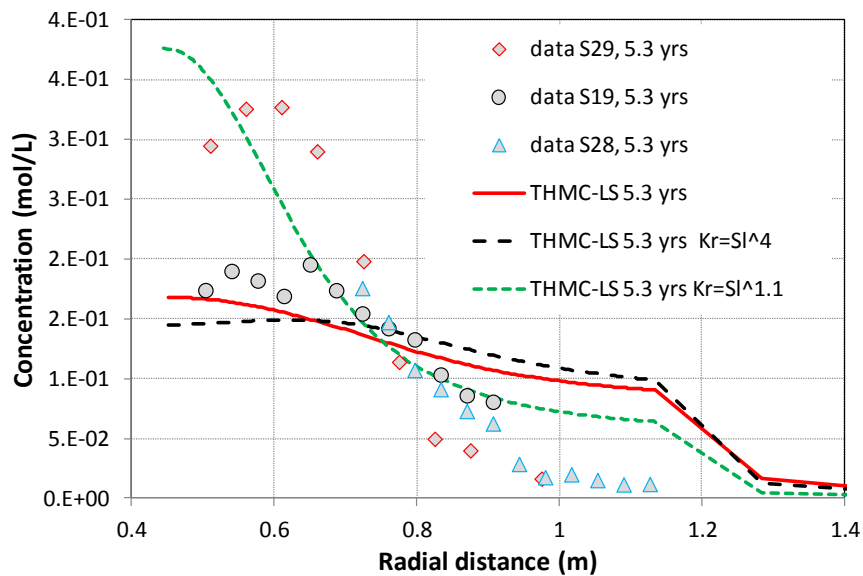
Figure 4.48. The concentration profile of chloride at 5.3 years (Zheng et al., 2011) and model results from the THMC model with linear swelling (THMC-LS) and sensitivity runs in which the exponent in the relative permeability functions are 4.4 and 1.1, respectively.

After failing to match the concentration profile by adjusting the diffusion coefficient and the relative permeability function, we checked the intrinsic permeability. Intrinsic permeability is usually measured under saturated condition and it is a function of total porosity (Figure 4.50) or dry density (Figure 4.51) for FEBEX bentonite. The data from Villar (2002) can be fitted with Equation 4.8:

$$k \ = \ \exp[19(\emptyset - 2.9) \qquad\qquad 4.8$$

And the data from ENRESA (2000) can be fitted by Equation 4.9:

$$\log k = -2.96\rho_d - 8.57$$

4.9

Based on measured dry density 18.3 years (Figure 4.17), we can calculate the permeabilities across the bentonite barrier at 18.3 years based on Equations 4.8 and 4.9, which are shown in Figure 4.52. Also shown in Figure 4.52 are the permeabilities from THMC models using linear swelling (THMC-LS) or BExM (THMC-BExM). We can see the THMC models exhibit a different trend than the data — from granite toward the heater, the data show a gradual decrease whereas the models show a gradual increase. Although it is known that permeability values measured in the laboratory are different (typically smaller) than that revealed by large scale model due to a scaling effect, the fact that the model and data exhibit distinct spatial trends in Figure 4.52 clearly reveals that the permeability-porosity relationship used in THMC-BExM or permeability-stress relationship used in THMC-LS needs to be revised to match not only the THM data but also chemical data.
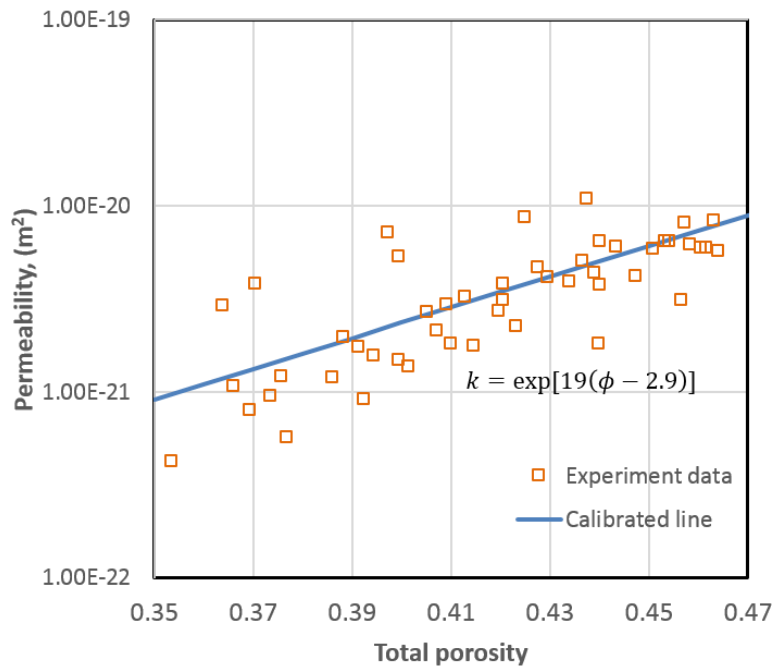
Figure 4.49. Intrinsic permeability as a function of total porosity (Villar, 2002)
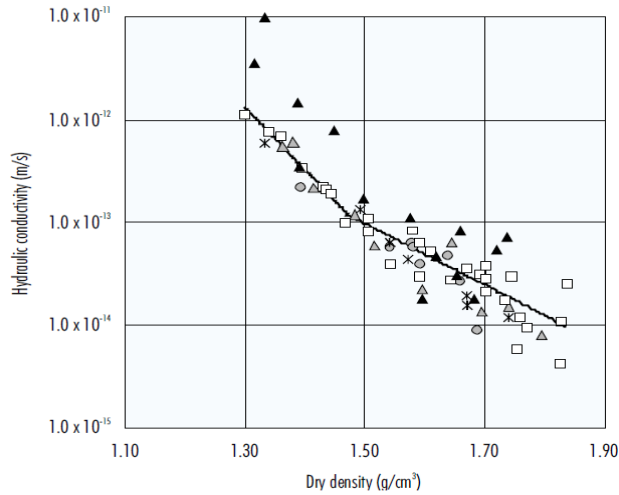
Figure 4.50. Intrinsic permeability as a function of dry density, which can be fitted with $\log k = -2.96\rho_d - 8.57$ (ENRESA, 2000).
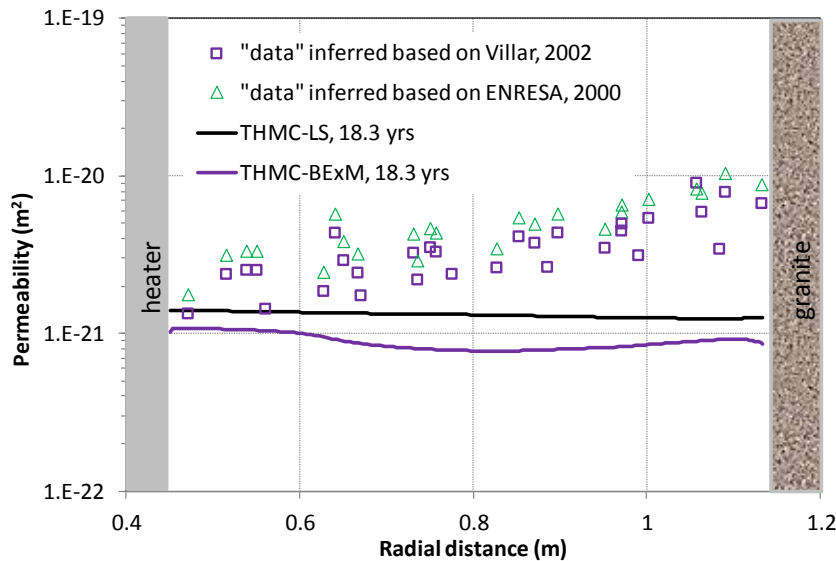
Figure 4.51. Intrinsic permeability calculated from dry density data based on Equation 4.7 ("data inferred based on Villar, 2002) and based on the Equation 4.8 (data inferred based on ENRESA, 2000) and the computed permeabilities from THMC-LS and THMC-BExM.

 We therefore conducted a simulation using Equation 4.10 for permeability changes:

$$\log k = (-2.96\rho_d - 8.57)/\alpha \qquad\qquad 4.10$$

Equation 4.10 is modified from Equation 4.9 by adding a factor α of 2.45 to account for the scaling effect (difference in permeability between laboratory measured and field calibrated

198

values). This simulation, named "Model B" in Figure 4.53, is based on the THMC-LS model presented in Section 3.4.1. It provides an overall decent match of chloride data at 5.3 years and especially at the concentration front. However, from the middle of the bentonite (radial distance of 0.7) towards the heater, the concentration data plateaus whereas the model results show a monotonic rise. Model B predicts very low concentrations in most parts of the bentonite barrier and very high concentrations close to heater after 18.3 years. Figure 4.54 shows the measured water content and results from "Model B". Although model B matches nicely the measured water content at 5.3 years, it overestimates the data at 18.3 years. In summary, using the revised function for permeability change as has been done in "Model B" leads to a better fit the chloride concentration data but a worse fit to the water content data. An additional process is probably needed for the model to match both THM and chemical data.
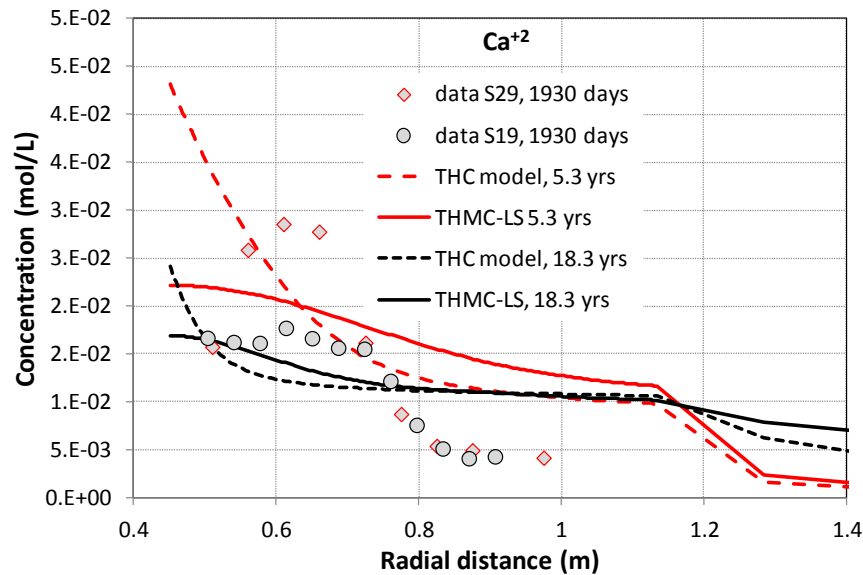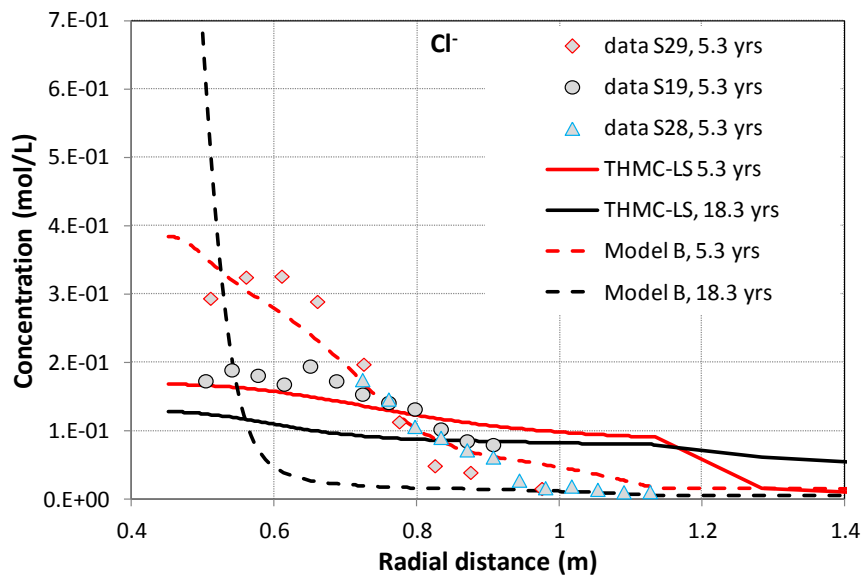

Figure 4.52. The concentration profile of chloride at 5.3 years (Zheng et al., 2011) and model results from the THMC model with linear swelling (THMC-LS) and sensitivity runs (model B) using the Equation 4.9 for permeability change.
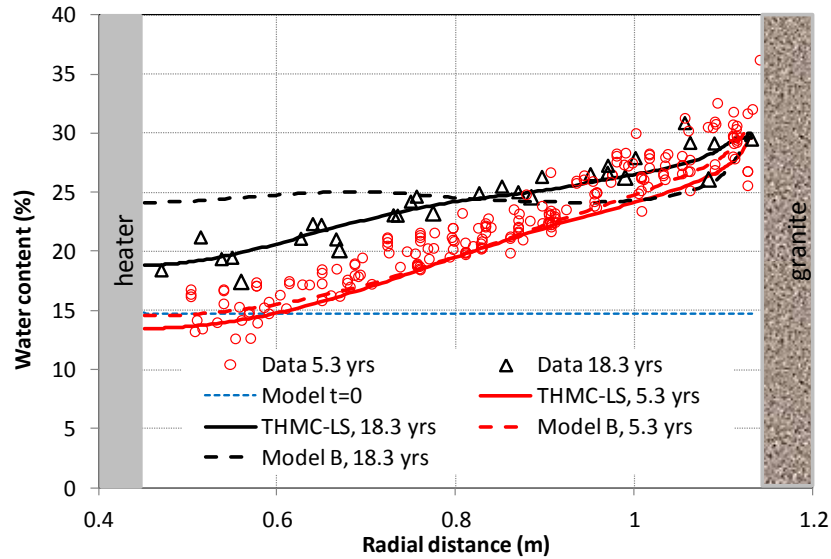
Figure 4.53. Measured water content at 5.3 years (dismantling of heater #1) and 18.3 years (dismantling of heater #2) and model results by the THMC model using linear swelling (THMC-LS) and Model B which is based on THMC-LS but using different function for permeability change.

4.5 Quantitative characterization of the fracture network in the FEBEX samples via Synchrotron X-ray Micro-CT

4.5.1 Introduction

In a radioactive waste repository with bentonite backfilled engineered barrier system, bentonite barrier undergoes simultaneously heating and hydration. The hydration leads to swelling, which helps the bentonite to seal gaps and pre-existing micro-fractures, while the heating could lead to desiccation of bentonite and creates micro-fractures. How these two competitive processes play out in the long run is important for estimating the permeability change in bentonite. Theoretical and empirical relationships for permeability change have been tested in the models for the FEBEX *in situ* test. Although the comparison between model and THMC data has been very helpful in calibrating the "right" relationships (or key parameters for the relationships), uncertainties in other processes and interaction of coupled processes might results in non-unique sets of parameters that could lead to equal or similar reasonable fit between model and data. Checking the microstructure of the bentonite buffer will serve as additional evidence to delineate the right permeability change functions and increase the predictability of models. Bentonite samples were taken from the FEBEX *in situ* test after the dismantling of heater #2. In this section, we describe a series of synchrotron X-ray micro CT (SXR-µCT) experiments to examine the microstructure of bentonite.

4.5.2   The technique

SXR-μCT has so far proven to be a very valuable tool for studying the fracture network of these samples. While some sample conservation and preparation issues might be present, the basically non-destructive aspect of the technique puts SXR-μCT at an advantage to other imaging methods such as scanning electron microscopy (SEM). In electron microscopy the sample is (usually) kept in vacuum under an electron beam, and in such conditions some dehydration is guaranteed to occur. But also measurements in environmental SEM's would still require a non-trivial sample preparation: the sample would need to be cut to create a flat surface for the analysis, and the surface would be of course the part of the sample most subject to artifacts due to cutting. The surface itself is also the part of the sample more prone to dehydration, given its immediate contact with the atmosphere. In addition to that, there is of course the issue of having to deal with 2D data. For all these reasons, we used XR-μCT to look at the interior of the sample, undisturbed as much as possible, in a non-destructive fashion. The collected data can be used for 3D visualization of the samples via software rendering, where operations such as virtual cuts are possible to investigate the interior of the sample, but the data can be used to characterize the microstructure of the sample in a quantitative fashion, using a variety of morphometric parameters (see e.g. Zandomeneghi et al., 2010). A quantitative characterization is especially important when looking at differences within a series of samples.

The experiments were carried out at the 8.3.2 beamline at the Advanced Light Source (ALS) at LBNL (MacDowell et al., 2012). The experiment consists of placing the sample on a rotating stage, and taking radiographs over 180 degrees of rotation, at given angular intervals. Software based on the concept of the filtered-back projection will provide as a result, starting from the radiographs, a virtual volume of the sample in the form of a stack of horizontal "slices" (e.g. Kak and Slaney, 1988).

In these experiments the samples were measured with monochromatic X-rays (34 keV), 650 ms of exposure time, collecting 2049 projections, with a continuous tomography and "local area" (sample larger than the field of view) setup. The advantage of using a sample larger than the field of view in this specific context is important: the outer part of the sample is not actually measured, but that part of the sample is the one theoretically more subject to issues due to the sample preparation, so instead of performing a conventional tomographic measurement and then extensively croping the dataset, we decided to use this strategy to be able to acquire a larger usable dataset with each measurement. The resulting voxel size of these measurements was 3.22 μm and the usable datasets were cylinders of 1820 vx (= 5.86 mm) diameter and 500 vx (= 1.61 mm) height.

Two measurements at higher resolution (0.633 μm voxel size) were carried out as well. Higher resolution measurements were done to check the presence of smaller fractures, which would have been missed at the lower resolution. Still, this resolution only allows the measurement on a very small sample, raising serious issues about its representativeness, also given the heterogeneity of the material at that scale.

201

In addition to the static experiments, an *in-situ* experiment involving the heating of the sample to monitor the development of cracks had been also carried out. The sample was heated up to ~180 °C for 8 minutes, sealed (but vented) in an unconfined pressure state. This was carried out in order to both mimic a worst-case scenario (sudden heating), but also, and mostly, to check the mechanisms of crack nucleation and propagation under heating conditions typical of this material.

4.5.3 Sample selection and preparation

The samples were protected in vacuum-sealed bags that were delivered to LBNL from the source, until sampling for SXR-µCT took place. The sample was prepared by carefully cutting a ~1.5 cm piece from each of the bulk bentonite samples, making sure that the sample was not coming from the outer surface of the blocks. Just after cutting the sample, the fragments were immediately sealed in plastic wrap and aluminum foil to minimize as much as possible the loss of moisture, which would likely develop new cracks. Maximum care was paid not to expose the samples to air for any significant amount of time and not to generate new cracks in general. Smaller fragments (~4 mm) were chosen for higher resolution measurements. For the *in-situ* heating experiment, no plastic wrap was used.

The stability of the material over time was also further confirmed by the lack of appreciable motion artifacts in the collected datasets. This kind of artifact is very common in samples rich in highly hydrated clays or organic material measured in air.

From the selection of samples available, we decided to analyze two series:

1) The BD-48 series consists in two samples from section 48 around the heater (see Figure 4.6 for the position of section 48). We analyzed samples immediately adjacent to the heater (BD-48-3) and close to the host rock tunnel surface (BD-48-7). Section 48 is located right in the middle of theheater and underwent the strongest heating and the slowest hydration. Over the course of the test, the temperature at section 48 near the heater is around 100 °C and about 50 °C near the granite. Although water content and dry density were not measured for samples in section 48, water content and dry density measured for samples at section 49, which is next to section 48, can be used as a reliable reference of water content and dry density. Based on the data collected at the same radial distance from the central axis of gallery at section 49, sample BD-48-3 is likely to have a water content of 18-19% and a water saturation degree of 80%, whereas sample BD-48-7 is fully saturated with a water content of around 30%.

2) The BD-59 series includes samples from section 59 located near the end of the gallery and away from heater #2. Three samples from different positions were analyzed: close to the heater (BD-59-15), in the middle of the section (BD-59-8), and close to the host rock, in the outer rim (BD-59-3). The temperatures at section 59 have always been low during the entire testing period, which is around 22 °C and has no spatial variation.

In Figure 4.54 (left) the localization of the samples has been highlighted on the schematics of the BD-59 section. The samples from BD-48 are shown to the right, with the position of the heater in that section colored in red.
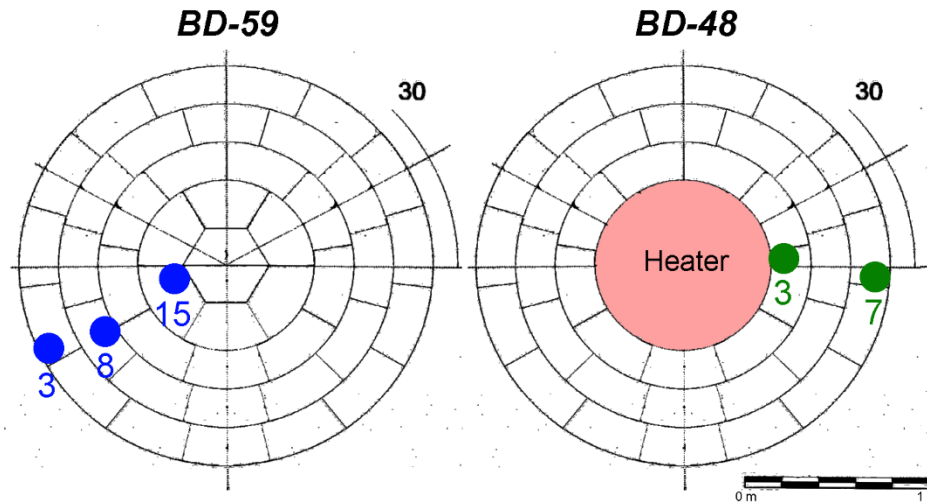
Figure 4.54. Location of the different samples: the series from the section outside the heater (section 59, sampling points in blue), and the series from the section with the heater (section 48, with measured sampling points marked in green) are shown within the pattern of the bentonite blocks.

4.5.4   Analysis strategy

The problem of fracturing in these samples has been addressed using different approaches aimed at different important issues. We can divide the work into three main parts:

1) Quantitative characterization of the fracture networks in the different samples: Which parameters can we use to describe the fracture networks in a quantitative fashion? Is the resolution vs. field of view ratio good enough for this characterization? Is there any appreciable heterogeneity among different samples?
2) Effect of dehydration: What is the effect of strong dehydration on the fracture network? Can we identify specific mechanisms of crack nucleation and propagation?
3) The effect of resolution: high resolution means the ability of finding smaller scale features such as micro- and nano- fractures. But it also means a much smaller volume investigated. What are we missing from the main measurements? Is this higher resolution really important from a practical point of view?

To answer the questions listed above we developed specific analysis strategies taking advantage of the experimental setup available at the X-ray imaging synchrotron beamline 8.3.2 at the ALS.

4.5.5 Results

Listed below are the results obtained addressing the three different main parts.

4.5.5.1 *Quantification of the fracture network*

The micro-structure of bentonite is represented by the fracture network in the sample and the quantification of the fracture network is the main topic for this research. We want to be able to associate a quantitative parameter to each sample such that we can understand the variation of the fracture network for samples at different locations. To reach this goal, we selected three points at different positions with respect the distance from the tunnel wall in section 59, which has no heater in the center, and two samples from section 48, which has a heater in the center. To monitor the variability of the fracture network in the same positions we have chosen three different samples for each position, and a total of 15 samples were analyzed.

The analysis of the tomographic datasets was carried out using an automated Fiji (Schindelin et al., 2012) script, minimizing human intervention and assuring that each sample was analyzed in the exact same way. The main target for the script was to obtain volumes where the medial axis of the fractures was labeled, in each point, with the local thickness (Dougherty and Kunzelmann, 2007), a value related to the aperture. The resulting volumes include all the information about the frequency and size distributions of the fracture network.

In the figures presented in this chapter, the sample names follow this structure: "SectionName"_"BlockNumber"_SampleNumber", so e.g., BD48_3_2 is the 2nd sample measured from the block #3 of the section BD-48.
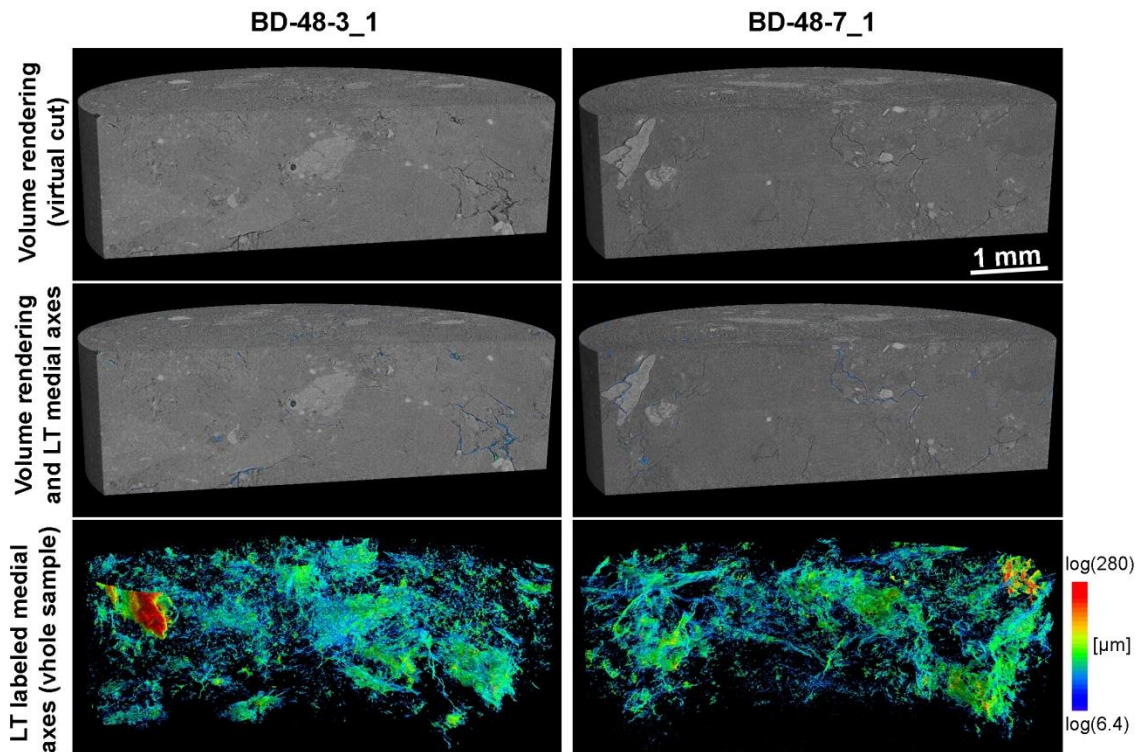
Figure 4.55. Graphical results of the micro-CT analysis of two samples from section 48: BD-48-3 (near the heater) and BD-48-7 (near the granite).

From the results in Figure 4.56, we can appreciate that the samples are pervaded by a network of thin fractures, with sizes in the order of the few tens of microns. In the volume renderings we can see that the fractures are present in the clay matrix, some cut across larger crystalline particles (quartz, feldspar, etc.), and some fractures are located along the interfaces of the crystals with the clay-rich matrix. From this observation it seems safe to assume that there are different mechanisms involved in the development of the fractures. In the middle of Figure 4.56, the superimposing of the medial axes of the fractures (labeled with the values of the local thickness - LT- in each voxel) serves as a check to confirm that the script finds all the fractures above the actual resolution, and the labeling with the LT values is correct.

In the lower sections, only the rendering of the labeled medial axes is shown. A color log scale for the aperture values has been chosen since the vast majority of the aperture values are small, so in a log scale it is easier to appreciate the small variations in aperture in the fracture network. This also serves as a comparison to the final plots where a log scale was chosen for the same reason.

The same approach was used to analyze the other 9 samples (3 for each position) from section 59, and the graphical results are shown in Figure 4.57.
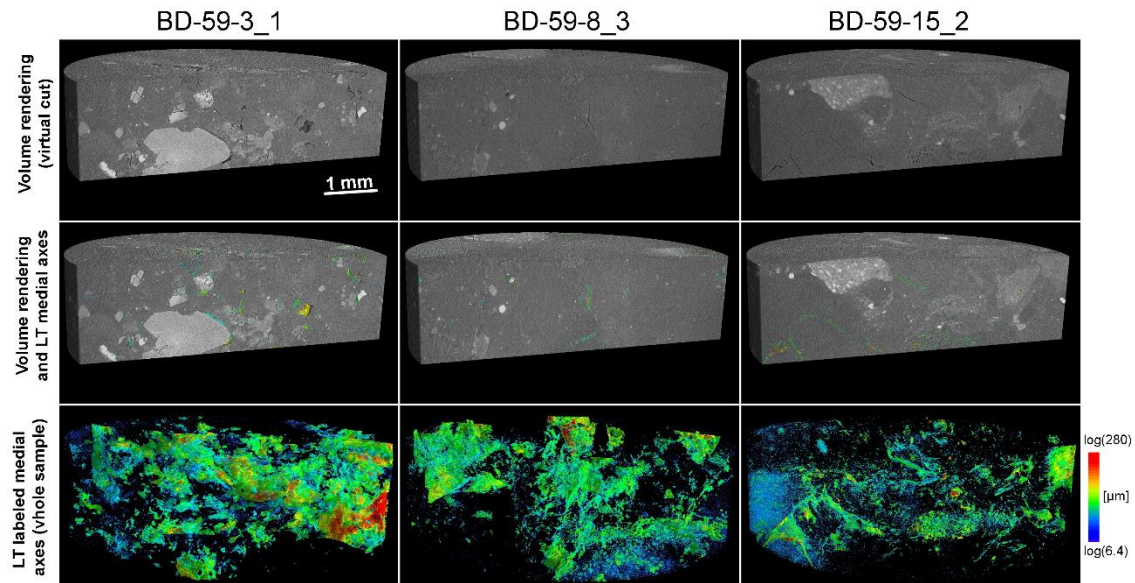
Figure 4.56. Graphical results of the analysis of two samples from the section 59: BD-59-3 sample (near the granite), BD-59-8 (half radius) and BD-59-15 (center). See Figure 4.55 for more precise sample location information.

Similar to the observations in samples BD-48-3 and BD-48-7, samples from section 59 present an extensive fine fracture network, with different kinds of fractures of (aggregate-matrix detaching, pure desiccation cracks of the clay matrix, etc.). It is also noteworthy to point out that there is a small amount of microporosity apparently not related to modifications in the microstructure of the material, but with the nature of the aggregate particles in the bentonite. An example is visible in the left side of the sample BD-59-15 in Figure 4.57.

More details about the characteristics of the fracture network can be seen in Figure 4.58, where a thin horizontal slice of a sample (from BD-59-3) is shown superimposed with a smaller volume of the fractures (as a white isosurface) to emphasize the structure and provide context for the fracture network. A zoom of a detail of the slice, but with the LT labeled medial axes is also shown to highlight the different kinds of fractures present. It is easy to see that fractures run inside broken aggregate particles (e.g., top right), and that they connect different aggregate particles, but thin fractures are also present in the clay matrix. From Figure 4.58 it is also possible to appreciate again that the calculation of the medial axes and the fracture aperture-related values seem to be correct.
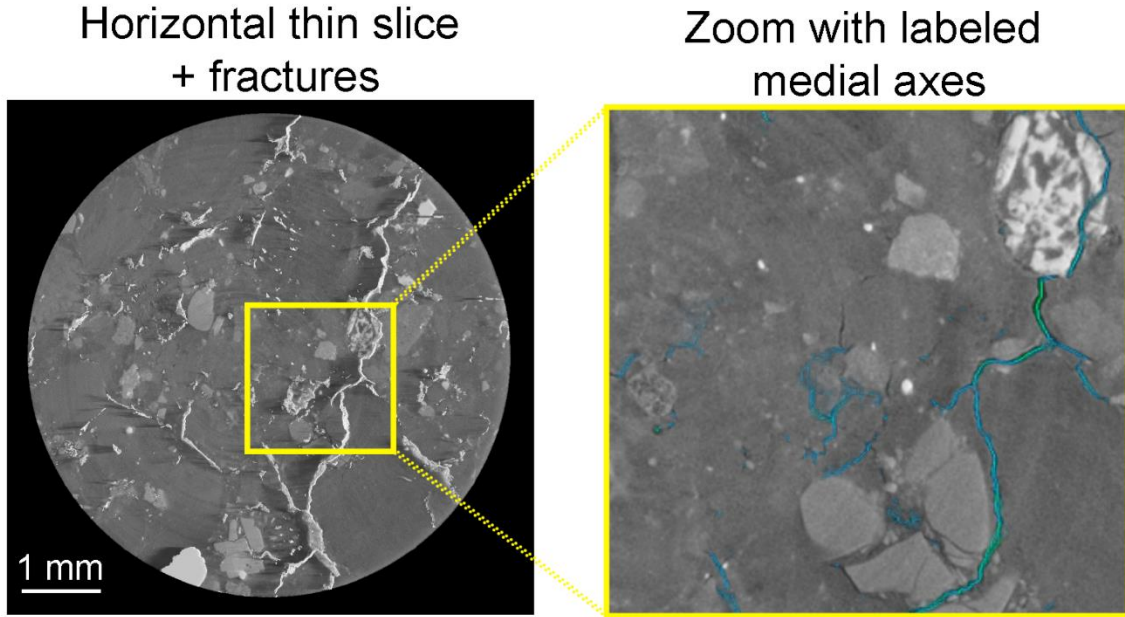
Figure 4.57. Highlighting different features of the fracture network in a sample from BD-59-3.

Having available 15 volumes, 3 for each point in the two sections, allowed us to carry out some analysis trying to characterize the networks in a more quantitative fashion. For each sample a frequency plot of apertures has been calculated, and the results are shown in Figure 4.59.
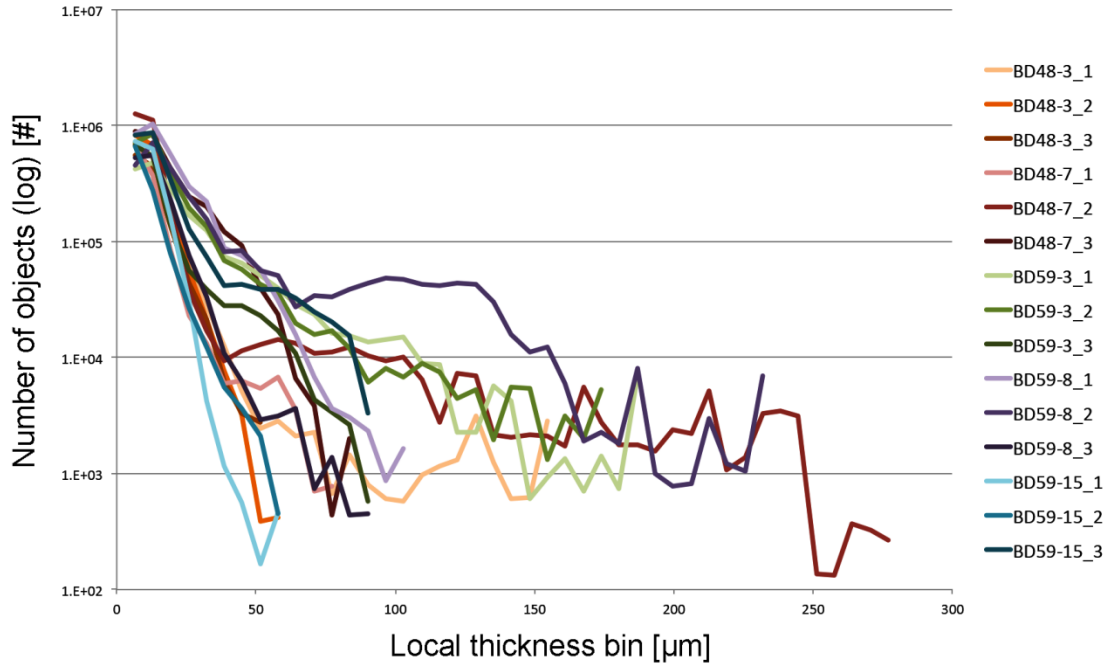
Figure 4.58. Local Thickness (LT) frequency plots (in absolute values) for all the 15 samples.

From Figure 4.59 it is possible to observe that at the largest LT values the samples are very different, in a seemingly chaotic fashion, but also the largest values of LT (i.e. large cracks) are very uncommon. The most interesting observation can be done in the range from 25 to 45 μm, where a bifurcation of the trends of the plots seems to be present. This is an interesting interval since for smaller than 25 μm size bins, the size starts to be too close to the resolution, and the morphometric parameters start to be less reliable. Below the 25 μm size the microporosity of a few aggregates also starts to be important and potentially impacts the reliability of the calculation (this issue is discussed in terms of reliability of the shape-preferred orientation morphometric analysis in Voltolini et al. 2011). The number of points in the medial axes of the fractures below the 45 μm size is also very large, making the analysis more reliable from a purely statistical point of view. Obtaining statistically reliable results would be more challenging for the larger fractures, with bins larger than 100 μm, for example.
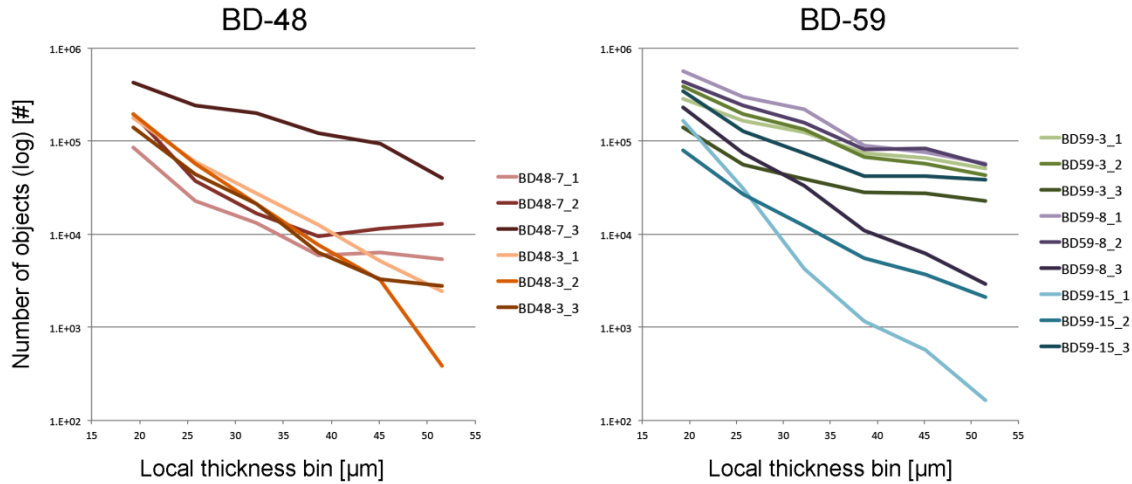
Figure 4.59. LT frequency plots in a smaller interval for the two different sections separated.

The fracture aperture distributions in this interval are roughly linear (in log scale), and a linear regression for each sample has been calculated. The slope of the fitted line (angular coefficient) provides direct information about the ratios of small vs. large fractures. For example, smaller values of the angular coefficient mean that a large amount (exponentially proportional) of microfractures are present in the sample, close to the resolution value of our measurements, while higher values highlight the presence of larger cracks.

To summarize the results, the average of the values of the 3 volumes (since measurements were done in triplicate: each position in the sections had 3 different samples measured) was calculated as well, so the values plotted refer to a total volume of ~ 130 mm^3, for each position sampled. As can be appreciated by the plots in Figures 4.6 and 4.7 the variability of the samples in the same block can be rather high. This calculation was done to see if there was any difference of the samples related to its position relative to the heater (section in the heater vs. section outside the heater), but also to see if there was any difference related to the distance from the wall of the tunnel. Differences in hydration values have been reported from *in situ* measurements during the tests, so these values could be related to different extent of fracturing.

The values below in Figure 4.60 show what seems to be a correlation of the angular coefficient relative to the distance to the granite contact, but the variability of the values is quite different from sample to sample, so while this trend shows some consistency, a much larger number of measurements should be carried out to fully validate this finding.
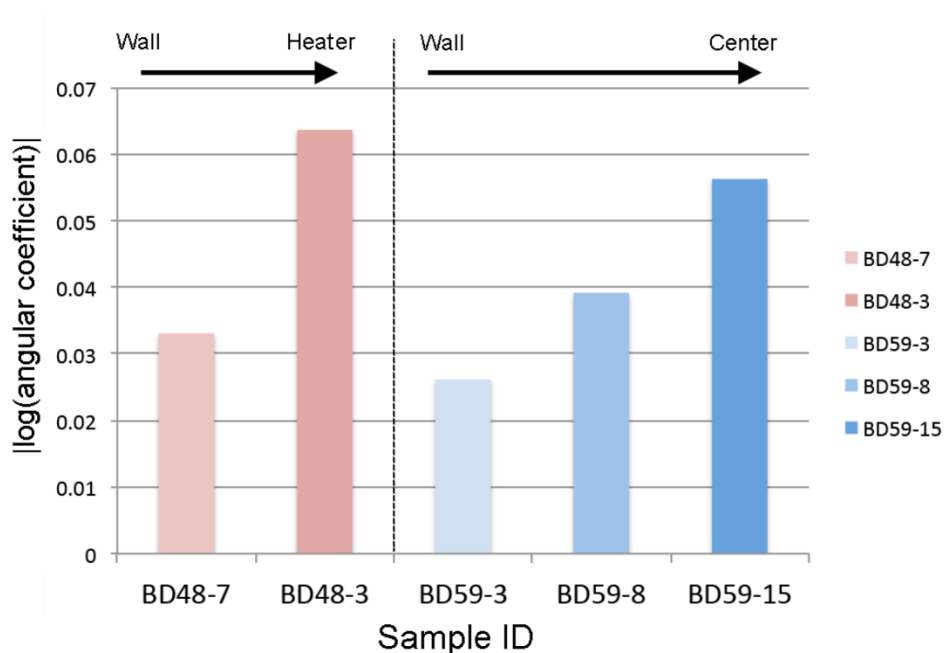
Figure 4.60. Angular coefficients (average of the 3 measured for each point) of the linear regressions of the plots shown in Figure 4.58.

Figure 4.60 shows that the |slope| of the linear regression curve increases with the distance from the wall, which seems to indicate that the samples closer to the wall tend to have a larger amount of large fractures compared to the samples close to the heater or to the center of the section. The sample close to the heater (BD-48-3) has the largest relative amount of the smallest microfractures of all the samples. This analysis seems to suggest that the slight decrease in humidity promotes the relative creation of smaller microfractures, while no evident trend is observable looking at the absolute values.

4.5.5.2   Dehydration-Induced Fracturing: SXR-μCT in situ Heating

The most likely fracturing mechanism in these samples is likely due to the shrinkage caused by the loss of water. In the FEBEX *in situ* test, the bentonite near the heater underwent (see section 4.4.1.1) a fairly long time period (about 3000 days) of desaturation—relative humidity decreased from the initial 40% to 8% after 500 days and took about 2500 days to recover to the initial values, and then gradually got hydrated and reached a relative humidity about 80-90% by the end of test (about 6700 days). Questions raised include whether fractures are developed during the desaturation period and whether those fractures vanished after the moisture content in bentonite increases. The desaturation of bentonite near the heater in FEBEX *in situ* test or in a typical repository condition occurs in a confined condition and is accompanied by the rise of stress. Although it is extremely difficult to monitor the development of fractures under the same conditions, in this report, we have performed an *in situ* SXR-μCT measurement of a sample from BD-59-3 subject to heating at a relatively high temperature under unconfined conditions, hopefully to shed light on the fracturing mechanism while we are fully aware the difference between the laboratory and field conditions. The sample was mounted, sealed in aluminum foil onto the rotating stage of the SXR-μCT beamline and a baseline scan was done. After the baseline scan, the sample was heated with a hot air blower to ~ 180 °C for 8 minutes. After the

heating a final measurement of the sample was done again. The visual results are presented in Figure 4.61.
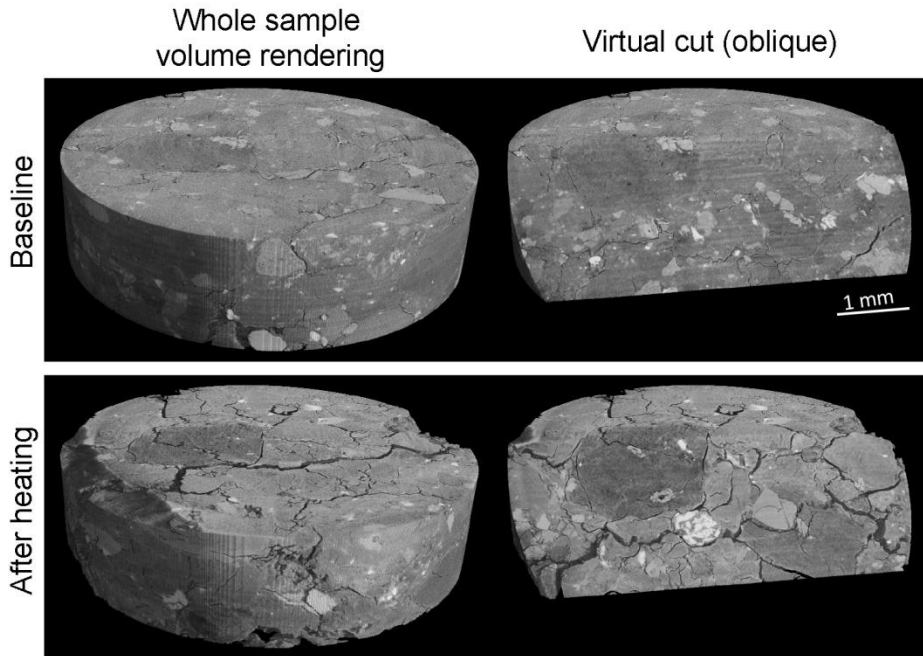
Figure 4.61. Sample from BD-59-3 before and after heating. A virtual cut of the sample is also shown to better appreciate the interior of the sample.

The results displayed in Figure 4.61 clearly show a dramatic increase in the number and size of the fractures. Different fracturing mechanisms can be observed here as well, with fractures connecting different aggregate particles, running along their interfaces, but through them as well. In addition to that, an extensive network of small fractures also develops in the clay-rich parts of the sample.

Although we have observed rapid development of fractures after heating it is noteworthy that such a case would be very unlikely in a real case scenario, where a constant supply of moisture should be provided by the host rock, so that the migration of moisture would be limited by the surrounding material; and the confining stress of the bentonite barrier would make the development of fractures more difficult. Nevertheless such an experiment does give an insight of development of fractures in bentonite, i.e., fractures would be created along the interfaces of clay aggregates and through the aggregates as well.
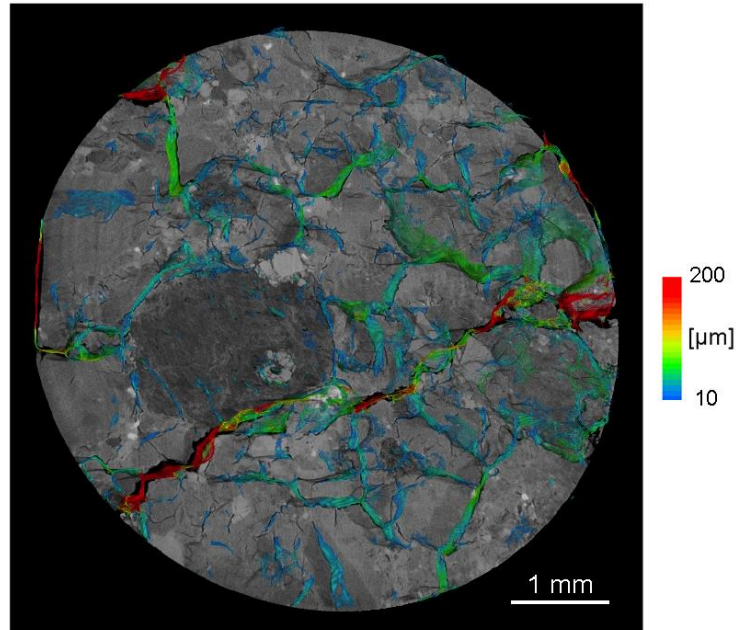
Figure 4.62. Thin horizontal slice of the sample BD-59-3 after heating. A thicker volume of the LT labeled medial axes of the fractures has been superimposed to highlight the topological features of the fractures network.

The development of the fracture network after heating is rather dramatic. As shown in Figure 4.62, samples after heating have much larger aperture values (the scale in this figure is linear, since there was no need to use a logarithmic scale as for the previous fracture network datasets) and a more pervasive fracture network was developed than what was observed in the sample before heating. Major fractures running across the whole sample are present, with a very large number of small fractures (see the blue values), which create a very dense network of connected fractures.

An analysis focusing on the quantitative comparison of the fracture networks before and after the heating process is still ongoing.

4.5.5.3   *High resolution SXR-μCT*

The analyses presented in Section 4.5.5.1 used a resolution of 3.22 μm, trying to balance the sample size and the imaging resolution, finding the best compromise between the smallest fractures we were able to detect, while trying to maximize the actual volume of the sample analyzed. The parameters measured show significant variability, but also some weak trends depending of the sample. Because measuring and analyzing very large numbers of volumes would be highly impractical due to the time required for both the measurement and the analysis, in section 4.5.5.1, we focused on checking fracture apertures distributions for various samples with duplicates using a resolution of 3.22 μm. However, such resolution may not allow us to detect nanoscale features, which are known to be important for clay-rich materials. All the imaging techniques, by their very nature, deal with the resolution vs. field of view issue: high-resolution means smaller volume, therefore the statistical meaningfulness rapidly decreases. On the other hand, large volumes analyzed at low resolution might miss some fundamental

characteristics. In this context we have decided to carry out a measurement at much higher resolution (633 nm per voxel) on the sample BD48-7. Given the higher resolution the usable volume investigated is a ~1 mm large cylinder.

The main target is to see how much of the smaller features, below the resolution of the measurements described in Section 4.5.5.1, are missed using the lower resolution scans, and to check if those are important.

The graphical results are shown in Figure 4.63, where the segmented volume of the voids (fractures + micropores) has been highlighted in red.
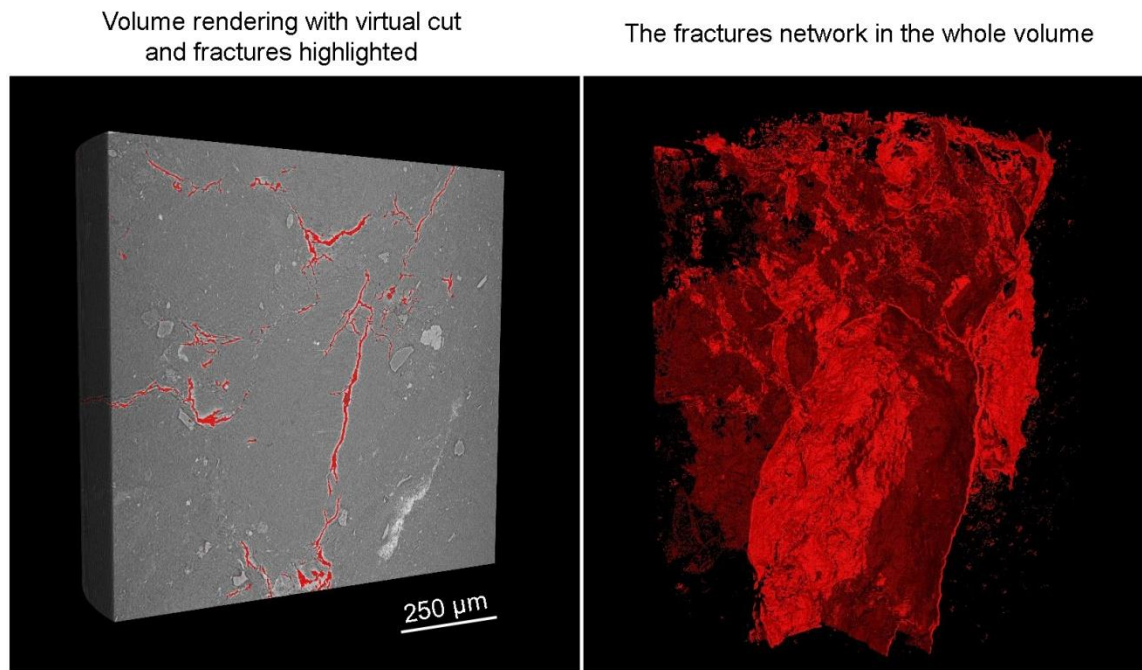
Figure 4.63. Results from the high-resolution SXR-μCT measurement on sample BD-48-7. The voids have been highlighted in red.

Figure 4.63 shows that the separation of the voids (fractures and micro- and nano-pores) looks correct. From a simple qualitative point of view it is possible to see that the amount of fractures with aperture values close to the resolution is relatively low. This observation, if confirmed by a quantitative analysis, would be very important since it would tell that very high-resolution measurements are not strictly necessary to obtain a comprehensive description of the fracture network. On the other hand, some features visible only at this resolution are present: more specifically nanoporosity present in some specific aggregate particles becomes visible, and measurable, at this resolution. Another important topic is the overall quality of the data used to obtain the quantitative description of the fracture network: being described by a much larger amount of voxels, the fractures in this sample are easier to analyze, and with greater accuracy, providing better quality results. In addition, having information at this scale would help in getting more accurate information about the connectivity. The resolution of the measurements in 4.5.5.1 has been proven good enough to obtain a sufficiently accurate description of the aperture distributions of the fractures in the sample, but the connectivity of fractures can be on smaller

scales that even if their importance from a volumetric point of view is negligible, and while their detection may have limited utility for the purposes of many topological parameters aimed at the description of the framework, some physical properties, such as permeability, can be impacted by the presence of nanometric connections building a connected, and thus significantly more permeable, material. Hence, it is important to have high-resolution datasets in case permeability models are to be employed to model realistic hydraulic properties for these samples.

A comprehensive characterization of the fracture network in this volume, to compare it directly with a low-resolution volume from the same sample, is ongoing.

4.6 Summary and Future Work

4.6.1 Coupled THMC Modeling of FEBEX *in situ* Test

The FEBEX *in situ* test that lasted more than eighteen years is extremely valuable for validating the coupled THMC model and deepening our understanding of the evolution of the bentonite barrier over the course of heating and hydration. In the FEBEX-DP project, heater #2 was dismantled and extensive THMC characterization was conducted. LBNL/DOE joined the FEBEX-DP in FY15. The ultimate goal is to use THMC data from FEBEX-DP to validate THMC models and therefore enhance our understanding of coupled THMC processes in bentonite.

In FY15, TH model with Non-Darcian flow and the THC model were developed and sensitivity to key parameters was conducted. Model results showed that including Non-Darcian flow into the TH model led to a significant underestimation of the relative humidity data in the entire bentonite barrier. In FY16, the THC model was extended to THMC models and mechanical processes were simulated using both linear swelling model and dual structure BExM. The results from THMC models match reasonably the measured temporal evolution of temperature, relative humidity and stress at several compliance points in the bentonite barrier and the measured spatial distribution of water content and dry density at 5.3 years when the heater #1 was dismantled and at 18.3 years when the heater #2 was dismantled. However, the THMC models failed to explain the spatial profile of concentration at 5.3 years. The major findings from current modeling work are as follows:

- As expected, the THMC model outperformed the THC model in terms of matching measured THM data. Permeability and porosity changes due to mechanical process (swelling) were the key to matching all the THM data.

- The THMC model using complex double structure BExM (THMC-BExM) did not clearly outperform the THMC model using linear swelling model (THMC-LS) in terms of matching the measured data. THMC-BExM led to a slightly better fit of measured relative humidities and stress near the heater and a slightly worse fit to the measured water content and dry density at 18.3 years. Although BExM is a more mechanistic approach and describes structural details of bentonite (the micro- and macro-structure of bentonite), it failed to manifest its superiority to the simple linear swelling model, which is probably due to that the THM data including relative humidity, stress, dry density and water content are all macroscopic such that these data cannot delineate the more mechanistic BExM from a linear swelling model.

213

- Although the THMC models successfully matched the THM data, they failed to desirably match the measured concentration profile of conservative species (chloride) at 5.3 years and subsequently the concentration profile of reactive species. The concentration profiles of cations (calcium, potassium, magnesium and sodium) were largely shaped by transport processes despite that their concentration levels were affected by mineral dissolution/precipitation and cation exchange. The concentration profile of pH, bicarbonate and sulphate were largely determined by chemical reactions.

- Revising the function for permeability changes in the THMC model improved the goodness-of-fit to chloride concentration profile but deteriorated the fit to water content data. It seemed there was a dilemma that the THMC model cannot match both the THM and chemical data simultaneously, suggesting that additional processes might be needed in the conceptual model.

- The THMC model predicted that concentration levels of major cations and anions at 18.3 years when the heater #2 was dismantled would continue going down in most parts of the bentonite barrier except the area very close to the heater, where the concentration would go up, which will be compared with concentration data that are expected to be available by the end of 2016.

- In the remaining months of FY16 and FY17, the following work is planned:

- Thermal osmosis, a moisture movement driven by the thermal gradient, has already been incorporated in the simulator TOUGHREACT-FLAC3D. We will test if the THMC model with thermal osmosis can match both the THM data and the concentration profile of chloride.

- Once the THMC model is calibrated against THM data and measured concentration data at 5.3 years, it will be used to interpret the concentration data for 18.3 years that are expected to be available by the end of 2016.

- The chemical model will be fine-tuned, especially regarding redox condition evolution in the bentonite barrier and bentonite-canister interaction, and evolution of gases such CO_2, CH_4 and H_2.

Ultimately, after the THMC models for FEBEX *in situ* test are fully validated with data, they will be used to explore THMC changes in the long run under higher temperature.

4.6.2   Quantitative characterization of the fracture network in the FEBEX samples

Although the comparison between model and THMC data has been very helpful in calibrating the "right" relationships (or key parameters for the relationships), uncertainties in other processes and interaction of coupled processes might results in non-unique sets of parameters that could lead to equal or similar reasonable fit between model and data. Checking the microstructure of the bentonite buffer will serve as additional evidence to delineate the right permeability change functions and increase the predictability of models. Bentonite samples were taken from the FEBEX *in situ* test after the dismantling of heater #2. In FY16, we have conducted a series of synchrotron X-ray microCT (SXR-μCT) examination of the microstructure of bentonite samples. The major accomplishments are as follows:

- A total of 5 samples from different locations were examined with three duplicates for each sample. Fracture networks for each sample were obtained and quantified. We found that the variability among duplicates from the same location in bentonite barrier is significant, mostly linked to the heterogeneity of the material. Nevertheless some weak correlation has been found: the ratio of large to small aperture fractures is larger from samples with higher water content (they are also close to the bentonite/granite interface). In other words, samples closer to the bentonite/granite interface tend to have a larger amount of large fractures, whereas samples close to the heater or to the center of the section tends to have larger amount of small fractures. While a truly statistically meaningful validation of this result is still needed, this correlation is clearly present in our sample survey. It is noteworthy that a larger amount of measurements would be experimentally impractical to carry out, and the quantitative analyses of 5 different samples with 3 duplicates for each sample that were accomplished in this report is already something not commonly found in the XR-µCT literature.
- XR-µCT imaging was also conducted for a sample at the "as is" state (the state that we received from the FEBEX *in situ* test) and a heated state. Comparison between the fracture network before and after heating showed heating completely modified the microstructure of the material, generating a pervasive network of fractures, both very large in size with a thick network of small ones especially in the clay aggregates of the sample, but whether this is due to the heating itself or moisture loss over the course of heating needs further study. While we are fully aware that the sample was heated under different conditions than what would be expected in the field, such an exercise seems to emphasize the importance of keeping bentonite well hydrated to ensure a good sealing effect.
- During the experiment, we also addressed some important technical issues: (1) we have found *the best resolution vs. field of view compromise, and representativeness issues as well*. We have tried to maximize the analyzed volume while avoiding losing important details due to too low resolution. (2) *We have successfully developed a protocol/software for the analysis of the fracture network, focusing on the aperture value distributions.*

At this stage, the results suggest that SXR-µCT is an ideal tool for checking the micro-structure of clay-based backfill for nuclear waste repository, and providing some quantitative parameters to directly compare different samples. This opens new opportunities to advance the research in the bentonite barrier such as:

- *Testing the behavior of different candidate sealing materials before deploying them.* This includes advanced characterization (multi-technique, when needed) and *in situ* experiments. As an example, analyses could be conducted to check different clay vs. aggregate ratios, different type of clays, the use of surfactants / antiflocculants / interlayer exchangeable molecules / etc. to obtain clay aggregates with different mechanical properties and/or response to dehydration, or even completely different sealing materials. The ability of *in situ* heating also provides the unique opportunity to see directly the modification of the sample during the loss of moisture. XR-µCT can also be coupled with other XR scattering-based techniques when a precise correlation with the hydration state of the clay structure (wide-angle X-ray powder diffraction) or the size of the clay tactoids (small-angle X-ray scattering) needs to be directly correlated with the development of desiccation cracks (e.g. Suuronen et al. 2014).

- *Using the measured datasets to build predictive tools.*
  Besides the visualization and quantitative characterization of the sealing materials, SXR-µCT is also able to provide 3D volume datasets which can be used in a digital rock physics context: if the volume(s) obtained are meaningful, in terms of resolution vs. field of view, for measuring a given property, specific software able to calculate those properties (such as permeability, invasion of non-wetting fluids, diffusion, etc.) from the datasets are available or under development. This ability of calculating some physical properties of the samples following the SXR-µCT measurement would end the path that started from the scientific question and would result with a predictive tool available to the scientific community.

4.7   References

Alonso, E. E., J. Vaunat and A. Gens 1999. Modeling the mechanical behaviour of expansive clays. Engineering Geology 54: 173-183.

Bárcena, I., Fuentes-Cantillana, J.L. & García-Siñeriz, J.L. (2003). Dismantling of the Heater 1 at the FEBEX "in situ" test. Description of operations. Enresa Technical Report 9/2003.

Bear, J., (1972). Dynamics of fluids in porous media. American Elsevier Publishing Company Inc, New York. ISBN 0-486-65675-6.

Bradbury, B., Baeyens, B., (2003). Porewater chemistry in compacted resaturated MX-80 bentonite. Journal Contaminant Hydrology 61, 329–338.

Bradbury, M. H. and B. Baeyens (2005). Modelling the sorption of Mn(II), Co(II), Ni(II), Zn(II), Cd(II), Eu(III), Am(III), Sn(IV), Th(IV), Np(V) and U(VI) on montmorillonite: Linear free energy relationships and estimates of surface binding constants for some selected heavy metals and actinides. Geochimica et Cosmochimica Acta 69(4): 875-892.

Bradbury, M.H., Baeyens, B., (1998). A physicochemical characterisation and geochemical modelling approach for determining porewater chemistries in argillaceous rocks. Geochimica et Cosmochimica Acta 62, 783–795.

Castellanos, E., M. V. Villar, E. Romero, A. Lloret and A. Gens 2008. Chemical impact on the hydro-mechanical behaviour of high-density FEBEX bentonite. Physics and Chemistry of the Earth, Parts A/B/C 33, Supplement 1(0): S516-S526.

Chen, Y., Zhou, C., Jing, L., (2009). Modeling coupled THM processes of geological porous media with multiphase flow: theory and validation against laboratory and field scale experiments. Computers and Geotechnics 36 (8), 1308–1329.

Clifford K.H. and Webb S.W. (1996). A Review of Porous Media Enhanced Vapor-Phase Diffusion Mechanisms, Models, and Data – Does Enhanced Vapor-Phase Diffusion Exist? Sandia National Laboratories Albuquerque, NM. SAND96-1198

Cui YJ, Tang AM, Loiseau C, Delage P (2008). Determining the unsaturated hydraulic conductivity of a compacted sand-bentonite mixture under constant-volume and free-swell conditions. Physics and Chemistry of the Earth 33, S462-S471

Daucousse D. Lloret A. (2003) Results of "in situ" measurements of water content and dry density, Technical report, Polytechnic University of Catalonia, 70-UPC-L-5-012.

David C, Wong T-F, Zhu W, Zhang J. (1994) Laboratory measurement of compaction-induced permeability change in porous rocks: Implications for the generation and maintenance of pore pressure excess in the crust. Pure Appl. Geophys. 1994;143:425-456.

Detzner K. and Kober F. (2015) FEBEX-DP drilling and sampling report sections 32-34, Internal report, AN15-714, NAGRA.

Dougherty, R. and Kunzelmann, K.H., 2007. Computing local thickness of 3D structures with ImageJ. Microscopy and Microanalysis, 13(S02), pp.1678-1679.

ENRESA (2000). Full-scale engineered barriers experiment for a deep geological repository in crystalline host rock FEBEX Project, European Commission: 403.

ENRESA, (2006a). FEBEX: Updated final report. ENRESA Tech. Publ. PT 05-0/2006, 589 pp.

ENRESA, (2006b). FEBEX: Final THG modelling report. ENRESA Tech. Publ. PT 05-3/2006, 155 pp.

Fernández, A. M., B. Baeyens, M. Bradbury and P. Rivas (2004). Analysis of the porewater chemical composition of a Spanish compacted bentonite used in an engineered barrier. Physics and Chemistry of the Earth, Parts A/B/C 29(1): 105-118.

Fernández, A., Rivas, P., (2003). Task 141: post-mortem bentonite analysis. geochemical behaviour. CIEMAT/DIAE/54520/05/03, Internal Note 70-IMA-L-0-107 v0.

Fernández, A.M., Cuevas, J., Rivas, P. (2001). Pore water chemistry of the FEBEX bentonite. Mat. Res. Soc. Symp. Proc. 603, 573-588.

Fernández, A.M., Rivas, P., (2005). Pore water chemistry of saturated FEBEX bentonite compacted at different densities. In: Alonso, E.E., Ledesma, A. (Eds.), Advances in Understanding Engineered Clay Barriers. A.A Balkema Publishers, Leiden, The Netherlands, pp. 505–514.

Garcia-Sineriz, J.L., Abós, H., Martínez, V., De la Rosa, C., Mäder, U. and Kober, F. (2016): FEBEX-DP Dismantling of the heater 2 at the FEBEX "in situ" test. Nagra Arbeitsbericht NAB 16-011. p. 92

Ghabezloo S, Sulem J, Guédon S, Martineau F. Effective stress law for the permeability of a limestone. Int. J. Rock Mech. Min. Sci. 2009;46:297-306.

Huertas, F. B. de la Cruz, J. L. Fuentes-Cantillana, et al. (2005). Full-Scale Engineered Barriers Experiment for a Deep Geological Repository for High-Level Waste in Crystalline Host Rock – Phase II. EUR 21922

Itasca, (2009). FLAC3D, Fast Lagrangian Analysis of Continua in 3 Dimensions, Version 4.0, Minneapolis, Minnesota, Itasca Consulting Group.

Kak, A.C. and Slaney, M., 1988. Principles of computerized tomographic imaging (pp. 5-47). IEEE press.

Kwon O, Kronenberg AK, Gangi AF, Johnson B. Permeability of Wilcox shale and its effective pressure law. J. Geophys. Res.-Sol. Ea. 2001;106:19339-53.

Kuhlman U., Gaus I. (2014). THM Model validation modelling of selected WP2 experiments:Inverse Modelling of the FEBEX in situ test using iTOUGH2. DELIVERABLE-N°: D3.3-1, NAGRA.

LaManna, J. M. and S. G. Kandlikar 2011. Determination of effective water vapor diffusion coefficient in pemfc gas diffusion layers. International Journal of Hydrogen Energy 36(8): 5021-5029.

Liu, H.-H. and J. Birkholzer (2012). On the relationship between water flux and hydraulic gradient for unsaturated and saturated clay. Journal of Hydrology 475: 242-247.

Liu, H.H., J. Houseworth, J. Rutqvist, L. Zheng, D. Asahina, L. Li, V. Vilarrasa, F. Chen, S. Nakagawa, S. Finsterle, C. Doughty, T. Kneafsey and J. Birkholzer. (2013). Report on THMC modeling of the near field evolution of a generic clay repository: Model validation and demonstration, Lawrence Berkeley National Laboratory, August, 2013, FCRD-UFD-2013-0000244.

Lloret A, Villar MV, Sánchez M, Gens A, Pintado X, Alonso EE. Mechanical behaviour of heavily compacted bentonite under high suction changes. Géotechnique 2003; 53(1):27–40.

Lloret, A., Alonso, E.E., 1995. State surfaces for partially saturated soils, In proceedings of the International Conference on Soils Mechanics and Foundation Engineering, Balkema, pp. 557-562.´

MacDowell, A.A., Parkinson, D.Y., Haboub, A., Schaible, E., Nasiatka, J.R., Yee, C.A., Jameson, J.R., Ajo-Franklin, J.B., Brodersen, C.R. and McElrone, A.J., 2012, October. X-ray micro-tomography at the Advanced Light Source. In SPIE Optical Engineering+ Applications (pp. 850618-850618). International Society for Optics and Photonics.

Pruess, K., C. Oldenburg and G. Moridis (1999). TOUGH2 User's Guide, Version 2.0, Lawrence Berkeley National Laboratory, Berkeley, CA.

Pusch, R. and Madsen, F. T. (1995). Aspects on the illitization of the kinnekulle bentonites. Clays and Clay Minerals 43(3): 261-270.

Ramírez, S., J. Cuevas, R. Vigil and S. Leguey (2002). Hydrothermal alteration of "La Serrata" bentonite (Almeria, Spain) by alkaline solutions. Applied Clay Science 21(5–6): 257-269.

Rutqvist, J., Y. Ijiri and H. Yamamoto 2011. Implementation of the Barcelona Basic Model into TOUGH–FLAC for simulations of the geomechanical behavior of unsaturated soils. Computers & Geosciences 37(6): 751-762.

Rutqvist, J., Zheng, L., Chen, F., Liu, H.-H. and Birkholzer, J. (2013). Modeling of Coupled Thermo-Hydro-Mechanical Processes with Links to Geochemistry Associated with Bentonite-Backfilled Repository Tunnels in Clay Formations. Rock Mechanics and Rock Engineering: 1-20.

Sacchi, E., Michelot, J.L., Pitsch, H., Lalieux, P., Aranyossy, J.F., (2001). Extraction of water and solution from argillaceous rock for geochemical characterisation: methods, processes, and current understanding. Hydrogeology Journal 9, 17–33.

Samper, J., L. Zheng, A. M. Fernández and L. Montenegro (2008b). Inverse modeling of multicomponent reactive transport through single and dual porosity media. Journal of Contaminant Hydrology 98(3–4): 115-127.

Samper, J., L. Zheng, L. Montenegro, A. M. Fernández and P. Rivas (2008a). Coupled thermo-hydro-chemical models of compacted bentonite after FEBEX in situ test. Applied Geochemistry 23(5): 1186-1201.

Sánchez, M., A. Gens and L. Guimarães (2012a). Thermal–hydraulic–mechanical (THM) behaviour of a large-scale in situ heating experiment during cooling and dismantling. Canadian Geotechnical Journal 49(10): 1169-1195.

Sánchez, M., A. Gens and S. Olivella (2012b). THM analysis of a large-scale heating test incorporating material fabric changes. International Journal for Numerical and Analytical Methods in Geomechanics 36(4): 391-421.

Sánchez, M., A. Gens, L. J. D. N. Guimarães and S. Olivella (2005). A double structure generalized plasticity model for expansive materials. International Journal for numerical and analytical methods in geomechanics 29: 751-787.

Schindelin, J., Arganda-Carreras, I., Frise, E., Kaynig, V., Longair, M., Pietzsch, T., Preibisch, S., Rueden, C., Saalfeld, S., Schmid, B. and Tinevez, J.Y., 2012. Fiji: an open-source platform for biological-image analysis. Nature methods, 9(7), pp.676-682.

Siitari-Kauppi, M., Leskinen, A., Kelokaski, M., Togneri, L. Alonso, U., Missana, T., García - Gutiérrez, (2007). Physical Matrix Characterisation: Studies of Crystalline Rocks and Consolidated Clays by PMMA Method and Electron Microscopy as Support of Diffusion Analyses. CIEMAT Technical Report, 1127, December 2007.

Suuronen, J.P., Matusewicz, M., Olin, M. and Serimaa, R., 2014. X-ray studies on the nano-and microscale anisotropy in compacted clays: Comparison of bentonite and purified calcium montmorillonite. Applied Clay Science, 101, pp.401-408.

Van Genuchten, M. T. 1980. A closed-form equation for predicting the hydraulic conductivity of unsaturated soils. Soil science society of America journal 44(5): 892-898.

Vilarrasa, V., J. Rutqvist, L. B. Martin and J. Birkholzer 2015. Use of a Dual-Structure Constitutive Model for Predicting the Long-Term Behavior of an Expansive Clay Buffer in a Nuclear Waste Repository. International Journal of Geomechanics 0(0): D4015005.

Villar, M.V. 2002. Thermo-hydro-mechanical characterisation of a bentonite from Cabo de Gata: a study applied to the use of bentonite as sealing material in high-level radioactive waste repositories. ENRESA, Madrid. Technical Publication 01/2002.

Voltolini, M., Zandomeneghi, D., Mancini, L. and Polacci, M., 2011. Texture analysis of volcanic rock samples: quantitative study of crystals and vesicles shape preferred orientation from X-ray microtomography data. Journal of Volcanology and Geothermal Research, 202(1), pp.83-95.

Wolery, T. J., (1993). EQ3/6, A software package for geochemical modelling of aqueous systems,Version 7.2. Lawrence Livermore National Laboratory, USA.

Xu, T., E. Sonnenthal, N. Spycher and K. Pruess (2006). TOUGHREACT: A Simulation Program for Non-isothermal Multiphase Reactive Geochemical Transport in Variably Saturated Geologic Media. Computers and Geosciences 32: 145-165.

Xu, T., Spycher, N., Sonnenthal, E., Zhang, G., Zheng, L. and Pruess, K. (2011). TOUGHREACT Version 2.0: A simulator for subsurface reactive transport under non-isothermal multiphase flow conditions. Computers & Geosciences 37(6): 763-774.

Zandomeneghi, D., Voltolini, M., Mancini, L., Brun, F., Dreossi, D. and Polacci, M., 2010. Quantitative analysis of X-ray microtomography images of geomaterials: Application to volcanic rocks. Geosphere, 6(6), pp.793-804.

Zheng L., Rutqvist J. Kim, K. and Houseworth J. (2015b), Investigation of Coupled Processes and Impact of High Temperature Limits in Argillite Rock. FCRD-UFD-2015-000362, LBNL-187644.

Zheng, L. and J. Samper (2008). A coupled THMC model of FEBEX mock-up test. Physics and Chemistry of the Earth, Parts A/B/C 33, Supplement 1: S486-S498.

Zheng, L. and J. Samper (2015). Dual-continuum multicomponent reactive transport with nth-order solute transfer terms for structured porous media. Computational Geosciences 19(4): 709-726.

Zheng, L. Jonny Rutqvist, Carl Steefel, Kunhwi Kim, Fei Chen, Victor Vilarrasa, Seiji Nakagawa, Jiangtao Zheng, James Houseworth, Jens Birkholzer. (2014). Investigation of Coupled Processes and Impact of High Temperature Limits in Argillite Rock. FCRD-UFD-2014-000493, LBNL-6719E

Zheng, L., J. Rutqvist, J. T. Birkholzer and H.-H. Liu 2015a. On the impact of temperatures up to 200 °C in clay repositories with bentonite engineer barrier systems: A study with coupled thermal, hydrological, chemical, and mechanical modeling. Engineering Geology 197: 278-295.

Zheng, L., J. Samper and L. Montenegro (2008). Inverse hydrochemical models of aqueous extracts tests. Physics and Chemistry of the Earth, Parts A/B/C 33(14–16): 1009-1018.

Zheng, L., J. Samper and L. Montenegro (2011). A coupled THC model of the FEBEX in situ test with bentonite swelling and chemical and thermal osmosis. Journal of Contaminant Hydrology 126(1–2): 45-60.

Zheng, L., J. Samper, L. Montenegro and A. M. Fernández (2010). A coupled THMC model of a heating and hydration laboratory experiment in unsaturated compacted FEBEX bentonite. Journal of Hydrology 386(1–4): 80-94.

Zheng, L., Li, L., Rutqvist, J., Liu, H. and Birkholzer, J.T., (2012). Modeling Radionuclide Transport in Clays. Lawrence Berkeley National Laboratory. FCRD-URD-2012-000128

5. Discrete Fracture Network (DFN) Approach for THM Damage Modeling in Argillaceous Rock

In this section, we present LBNL's activities related to development, testing, and applications of a discrete fracture network (DFN) approach for modeling THM induced damage and fracturing in argillaceous rocks. In argillaceous rocks, fractures are major factors that change hydrological and mechanical properties of the rock materials. Although clay-rich formations usually exhibit low intrinsic rock permeability with very limited fracture permeability, under certain conditions permeable fracture networks occur leading to the increase of rock permeability (Cosgrove, 2001; Bossart et al., 2004). Herein, two classes of fracturing processes are investigated: 1) fracture propagation induced by fluid overpressure; and 2) fracture-damage due to stress redistribution around an excavation in the excavation damage zone (EDZ).

The former class may involve rather vigorous hydro-mechanical interactions of fluid contents within clay-rich formations. In various scenarios of pressure change of fluid contents, limited fluid flow arises very slowly due to the low permeability of rock matrix. Consequently, the rock systems are not in pressure equilibrium, and the pressure conditions can trigger fault reactivation and hydraulic fracturing (Gonçalvès et al., 2004). Geologic evidence of natural fractures suggests that the Mercia Mudstone within the Bristol Channel Basin in the UK was subject to repeated episodes of natural hydraulic fracturing over its 250 million year history (Cosgrove, 2001). Also, fluid-driven fracturing processes are often addressed in many geo-engineering applications. For example, hydraulic fracturing and stimulation of fracture networks are utilized by the energy industry (e.g., shale gas extraction, enhanced geothermal systems) to increase permeability of geological formations (Freeman et al., 2011; Zimmermann and Reinicke, 2010). From the opposite perspective, related to underground storage of nuclear waste or CO_2, fracturing of the repository rock could be detrimental for geo-environmental issues due to increasing the risk of contaminant leakage (Bossart et al., 2004; Chiaramonte et al., 2008).

As the latter class, fractures in the EDZ have been routinely observed in clay-rock underground research laboratories (URLs) in Europe, including the Opalinus Clay at Mont Terri URL, Switzerland, Boom Clay at MOL in Belgium, and the Callovo-Oxfordian Clay at Bure in France (Volckaert et al., 2004). These fractures mainly form as a consequence of static and dynamic stress disturbance by excavation (Bossart et al., 2002). However, other effects, such as shrinkage caused by ventilation dry-out during the pre-closure phase, and thermal pressurization and gas evolution expected after closure, may also result in fracturing (Blümling et al., 2007). The EDZ not only exhibits fracturing along tunnel surfaces, but can contain fracture damage in thin zones (<~1 m) around drifts, which has been verified from measurements of permeability in that area (Bossart et al., 2004). The connectivity of fractures along a tunnel has been observed in the HG-A test at Mont Terri, Switzerland, where a test tunnel section, backfilled with sand and sealed by a packer, was saturated and a series of water injection tests were performed. In the test results, non-uniform pressure increases along the packer sleeve were monitored, which indicates preferential fluid flow paths formed by heterogeneous fracture damage around the excavation zone (Lanyon et al., 2009).

This report covers an overview of the modeling approach, including coupled THM processes in the simulation code and representation of mechanical anisotropy, in Sections 4.1. The simulation code combines TOUGH2 with the rigid-body-spring network (RBSN) model, which enables a discrete representation of fractures and fracture networks in rock formations. In Section 4.2, the

TOUGH-RBSN code is validated against the laboratory experiments for hydraulic fracture propagation in rock-analogue samples and sensitivity analyses are conducted through qualitative comparisons of simulations results for which reservoir configurations are changed. Section 4.3 presents anisotropic failure characteristics in the simulations of uniaxial compression tests and a tunnel excavation process in the presence of discrete faults, in which the simulation results are compared with the theory and the field-test observations.

5.1   Methodology

5.1.1   Model discretization

The computational domain for both the TOUGH2 and RBSN calculations is tessellated using a Voronoi diagram (Okabe et al., 2000). The discretization process is carried out basically in three steps: 1) nodal point insertion; 2) Delaunay tessellation; and 3) Voronoi discretization. Within the domain, nodal points are positioned in regular or irregular formation. For random point generation, a minimum allowable distance l_{min} is used to define the desired nodal density of the unstructured grid. The Delaunay tessellation is conducted based on the nodal positions, where each Delaunay edge defines the nodal connection of the corresponding lattice element. Through the dual Voronoi tessellation, the spatial domain is collectively filled with discrete polyhedral cells that render the elemental volumes. More detailed procedure of the domain partitioning is presented elsewhere (Yip et al., 2005; Asahina and Bolander, 2011).

The Voronoi discretization is not only an effective method for partitioning a spatial domain, but is also an essential part of the RBSN model formulation. The Voronoi diagram serves to scale the element coefficients for the system equations. Also, the availability of sharing the same grid geometry for the TOUGH2 and RBSN models enables a tight coupling without any spatial interpolation of primary variables.

For the discrete fracture network (DFN) approach, fractures and such discontinuities are explicitly modeled within the Voronoi grid. Voronoi cells generally represent the matrix component in a geomaterial constitution, and pre-existing or newly generated fractures are placed on the Voronoi cell boundaries. The geometry of fracture networks (e.g., orientation, length, curvature) can be obtained by observational mapping data, computer-generated statistical reproductions, or mechanical simulation results. An example of the discretization procedure in 2D modeling involving a straight fracture is as follows:

  i.   Generate a Voronoi unstructured grid for the spatial domain.
 ii.   Overlay the reference fracture trajectory onto the grid.
iii.   Test all connections of natural neighboring nodes to check if they cross the fracture. For example, compare connections ij and jk in Figure 5.1.
 iv.   The collection of the Voronoi cell boundaries corresponding to the nodal connections that cross the reference fracture (such as ij) forms discretized fractures.
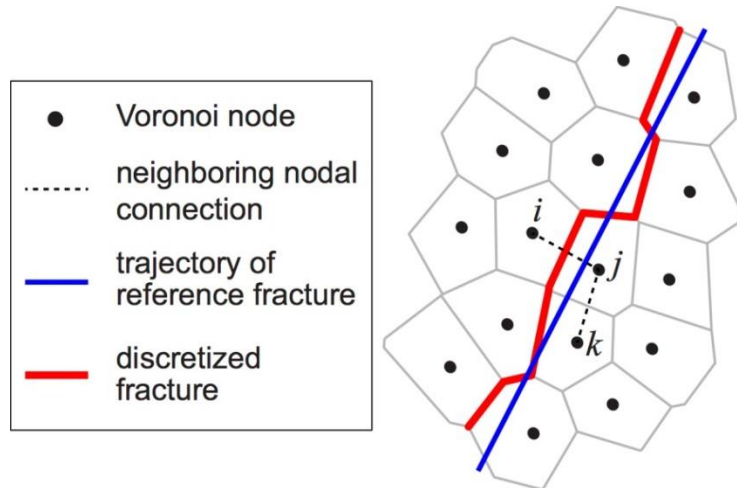
Figure 5.1. Fracture mapping and discretization within an unstructured Voronoi grid.
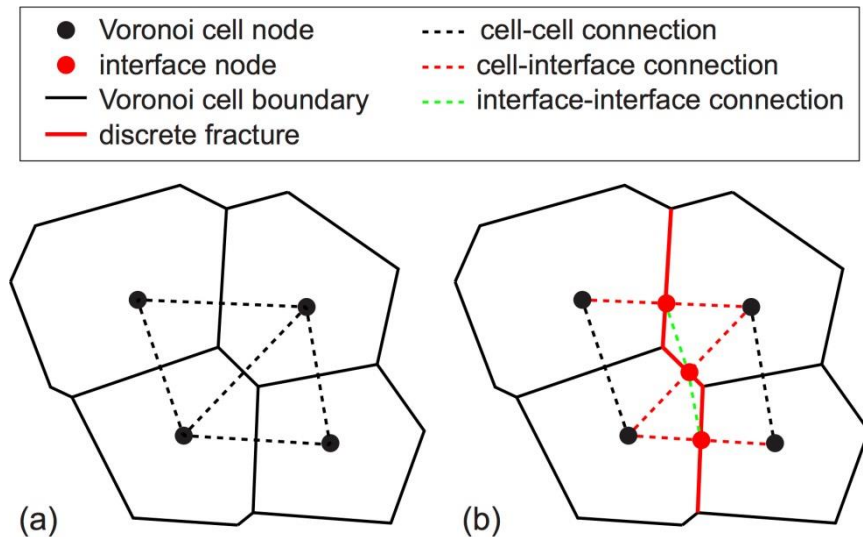
Figure 5.2. Introduction of interface nodes and additional connections for flow through discrete fractures: a) original Voronoi cell nodes and connections; and b) insertion of interface nodes and connections.

By repeating the above process for multiple fractures, a network of discrete fractures can be generated. This fracture discretization process is completely automated and can be easily extended to more complicated geometries in 3D modeling. However, the grid size should be carefully chosen to obtain a sufficiently accurate representation of the reference fracture. With a finer grid, the discretized fractures correspond more closely to the reference fracture, but the computational expense may be increased.

In the TOUGH2 simulations using a grid structure of the ordinary Voronoi discretization, flow and mass transfer are enacted only through the connections of the neighboring Voronoi nodes (called cell-cell connections in Figure 5.2 (a). However, if fracturing occurs within the matrix, substantial flow may arise through the fracture path. For the DFN approach, a modification of the grid structure is proposed, in which dynamic formation of flow channels along the fractures is facilitated by introducing additional interface nodes and the associated connections. As shown in Figure 5.2 (b), an interface node is inserted where the cell-cell connection intersects the

Voronoi cell boundary. The original cell-cell connection is divided into two cell-interface (and vice versa) connections by the interface node. In addition, the connections between the interface nodes are established to activate flow channels in discrete fractures.

Fluid flow through fractures is assumed to conform with Darcy's law (Witherspoon et al., 1980), and hydrological properties (e.g., porosity and permeability) of a discrete fracture can be evaluated from the grid geometry and the fracture aperture width. The fracture aperture can be either assigned as a pre-existing fracture property or explicitly measured from the mechanical-damage computation of the RBSN model. A parallel-plate mode (Bear 1972) is applied to define fracture permeability, which is related to a hydraulic aperture within the validity of cubic law for Darcy flow.

5.1.2 Hydrological and mechanical coupling in TOUGH-RBSN

This section describes the linkage between the TOUGH2 simulator and the RBSN approach. The hydrological and mechanical codes are sequentially coupled to each other, where the general procedure is similar to that applied for the TOUGH-FLAC simulator (Rutqvist et al., 2002; Rutqvist, 2011). However, the TOUGH-RBSN coupling modules have been substantially modified to account for the fluid flow through discrete fractures.
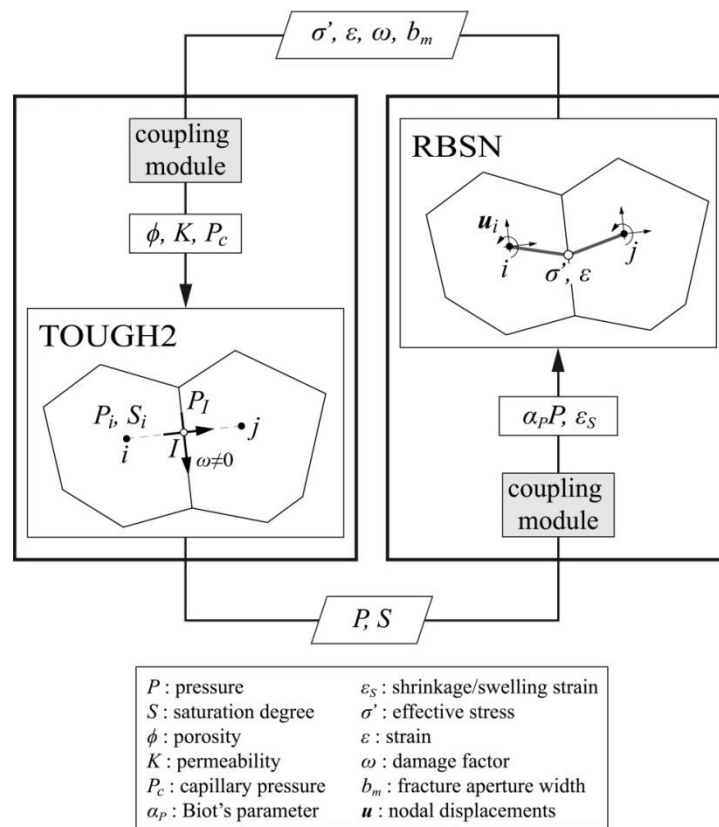
Figure 5.3. Flow diagram of the TOUGH-RBSN coupling procedure.

Figure 5.3 shows a schematic flow diagram of the coupling procedure between the TOUGH2 and RBSN codes. Coupling modules are implemented in each side of the modeling codes, by which material properties and mechanical boundary conditions are updated with the outputs of primary

224

variables of physical quantities. As aforementioned, an advantage from sharing the same Voronoi grid geometry in the TOUGH-RBSN simulator is that the primary variables are highly correlated at the same nodal position and thus the data exchange between the two models is straightforward during the coupling procedure.

First, the TOUGH2 to RBSN link supplies pressure and degree of saturation to update the mechanical quantities. From the pore pressure P, the effective (grain-to-grain) stress σ_n', applied to the normal spring of a lattice element, is calculated using Biot's theory (Biot and Willis 1957):

$$\sigma_n' = \sigma_n + \alpha_p P \qquad 5.1$$

where σ_n is the total normal stress obtained from overall loading, including external loads; α_p is Biot's effective stress parameter. Note that tensile stress is taken to be positive for the sign convention in this report. The effective stress in a lattice element ij can be calculated by averaging the pressure at nodes i and j, for which Equation (5.1) is transformed into an incremental form:

$$\Delta\sigma' = \Delta\sigma + \alpha_p(\Delta P_i + \Delta P_j)/2 \qquad 5.2$$

where ΔP_i and ΔP_j are the pressure increments at nodes i and j, respectively. If the element ij corresponds to an interface node I for the activated fluid flow through the fracture, the effective stress increment can be described as

$$\Delta\sigma' = \Delta\sigma + \alpha_p \Delta P_I \qquad 5.3$$

where ΔP_I is the pressure increment at node I in the TOUGH2 model. Also, the shrinkage/swelling effect due to the local changes of liquid saturations can be taken into account:

$$\Delta\varepsilon_s = \alpha_s(\Delta S_i + \Delta S_j)/2 \qquad 5.4$$

where ε_s is shrinkage/swelling strain; and α_s is the hydraulic shrinkage coefficient. If a poroelastic geomaterial is subjected to confinement conditions, the effective stress can be affected by the swelling/shrinking strain as

$$\Delta\sigma' = \Delta\varepsilon_s E \qquad 5.5$$

where E is the Young's modulus.

Next, the RBSN to TOUGH2 link supplies the effective stress and the strain calculated in the lattice element to update the hydrological properties of the corresponding TOUGH2 grid blocks i and j. Porosity, permeability, and capillary pressure are generally related with the effective stress and strain values (Rutqvist and Tsang, 2002).

If fracturing occurs at element ij (i.e., $\omega \neq 0$), the associated fracture node I and additional connections are activated in the TOUGH2 model. The permeability of an individual fracture depends on the hydraulic aperture b_h (Witherspoon et al., 1980). According to a parallel-plate model, the fracture permeability is defined as $b_h^2/12$. The hydraulic aperture is coupled to the mechanical aperture b_m (Rutqvist et al., 1998, 2000):

$$b_h = b_{hr} + f b_m \qquad 5.6$$

where b_{hr} is the residual hydraulic aperture and $f \leq 1.0$ is a dimensionless factor that accounts for the slowdown of flow in a natural rough fracture in comparison to the ideal case of parallel smooth fracture surfaces. However, herein f is set equal to unity for simplicity.

5.1.3   Implementation of Mechanical Anisotropy in the RBSN Models

Most sedimentary and metamorphic rocks (e.g., shales and slates) have directional fabrics such as bedding, foliation, and flow structures, which result in anisotropic features in bulk-scale mechanical responses. For example, Opalinus Clay rocks exhibit transversely isotropic elastic properties, in which Young's modulus is greater in the direction parallel to bedding than normal to the bedding (Bossart, 2012). Anisotropic features may also be observed in failure responses. In this study, a novel scheme for geomechanical models is introduced to represent those anisotropic features without the need of cumbersome manipulation of the grid geometry to be aligned to the bedding fabric.

5.1.3.1   Anisotropy in Elasticity

Figure 5.4 shows the arrangements of spring sets within a Voronoi grid and the corresponding lattice elements. A 2D description is provided herein for simplicity, but this scheme has been developed within 3D modeling framework. In the ordinary RBSN model, the spring sets are oriented to their individual local coordinates defined by the Voronoi diagram. However, in the new scheme, all the spring sets are aligned to the principal bedding direction. The spring coefficients are defined in global fabric coordinates, where two orthogonal N- and P-axes are normal and parallel to bedding, respectively. For a lattice element with the cross-section area A_{ij} and the element length h_{ij}, two translational spring coefficients k_N, k_P, and one rotational spring coefficient k_ϕ are calculated by using transversely isotropic Young's moduli related to the bedding direction:

$$k_N = E_N \frac{A_{ij}}{h_{ij}}, \;\; k_P = E_P \frac{A_{ij}}{h_{ij}}, \;\; k_\phi = E_N \frac{I_\phi}{h_{ij}} \tag{5.7}$$

where I_ϕ is the second moment of area of the element cross-section, and E_N and E_P are Young's moduli normal and parallel to bedding, respectively.

As seen in Figure 5.4, three distinct coordinate systems are considered for representation of kinematic quantities: global X-Y coordinates based on domain construction; local x-y coordinates for individual elements; and global N-P coordinates related to the orientation of fabric. For each spring set, the spring stiffness matrix is established in N-P coordinates:

$$\mathbf{k}_b = \begin{bmatrix} k_N & & \\ & k_P & \\ & & k_\phi \end{bmatrix} \tag{5.8}$$

Although the derivation is invariant to coordinate systems, it is more convenient for matrix formulation to represent and manipulate the stiffness quantities in local x-y coordinates rather than in global N-P coordinates. Thus the spring stiffness matrix, $\mathbf{k}_b$, is transformed to local x-y coordinates using following coordinate transformation (McGuire and Gallagher, 1979):

$$\mathbf{k}_s = \mathbf{\gamma}^T \, \mathbf{k}_b \, \mathbf{\gamma} \qquad\qquad 5.9$$

where $\mathbf{\gamma}$ is the 3×3 coordinate transformation matrix from local (*x-y*) to global fabric (*N-P*) coordinates:

$$\mathbf{\gamma} = \begin{bmatrix} Nx & Ny & 0 \\ Px & Py & 0 \\ 0 & 0 & 1 \end{bmatrix} \qquad\qquad 5.10$$
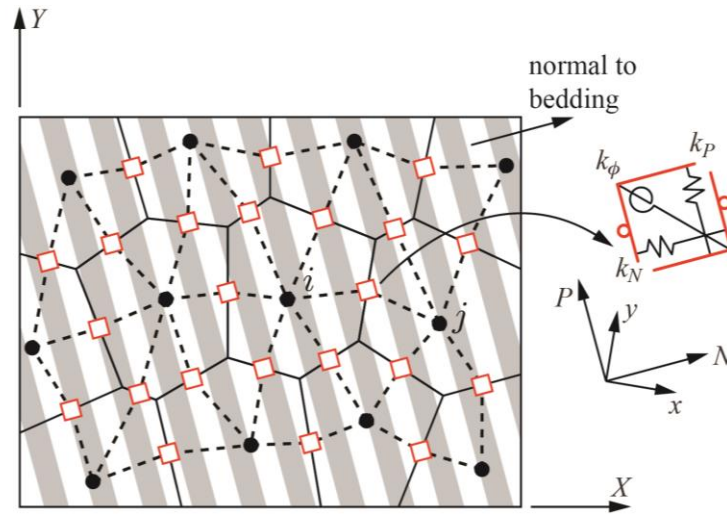
Figure 5.4. Arrangements of the spring sets in the identical lattice structure, where the spring coefficients comply with transversely isotropic elastic properties.

The first 2×2 entries in **γ** are the direction cosines between the bedding direction and the local coordinate axes. The element stiffness matrix, $\mathbf{k}_e$ (with respect to local x-y coordinates), is obtained by post- and pre-multiplication of $\mathbf{k}_s$ by the geometric transformation matrix that relates the generalized relative displacements at the spring set to the nodal displacements. Detailed formulation is presented elsewhere (Bolander and Saito, 1998; Berton and Bolander, 2006).

Finally, the element stiffness matrix is transformed to global coordinates:

$$\mathbf{K}_e = \mathbf{\Gamma}^T \, \mathbf{k}_e \, \mathbf{\Gamma} \qquad\qquad 5.11$$

where **Γ** is the coordinate transformation matrix from global domain *X-Y* to local *x-y* coordinates.

5.1.3.2   *Stress tensor calculations and weak-plane failure model*

Determination of local failure of a lattice element starts from evaluating the stress state based on the stress tensor calculation. The calculation of stress tensor at a Voronoi cell node is possible by considering the equilibrium conditions of the spring forces. Sets of the spring forces are applied at the boundaries surrounding a Voronoi cell (Figure 5.5 (a)), and nodal force components F_{nn}, F_{ns}, and F_{nt} can be calculated for an arbitrary section passing through the Voronoi cell node (Figure 5.5(b)) with its corresponding local *n-s-t* coordinates (Figure 5.5(c)), which satisfy the equilibrium condition with all the forces acting on the remaining cell boundaries. Moment contributions to equilibrium are not considered here. By dividing these force components by the cut-face area A_{cut}, whose normal direction is in *n*-axis, the corresponding stress components σ_{nn}, σ_{ns}, and σ_{nt} can be obtained:

$$\sigma_{nn} = F_{nn}/A_{cut}$$

$$\sigma_{ns} = F_{ns}/A_{cut} \qquad\qquad 5.12$$

$$\sigma_{nt} = F_{nt}/A_{cut}$$
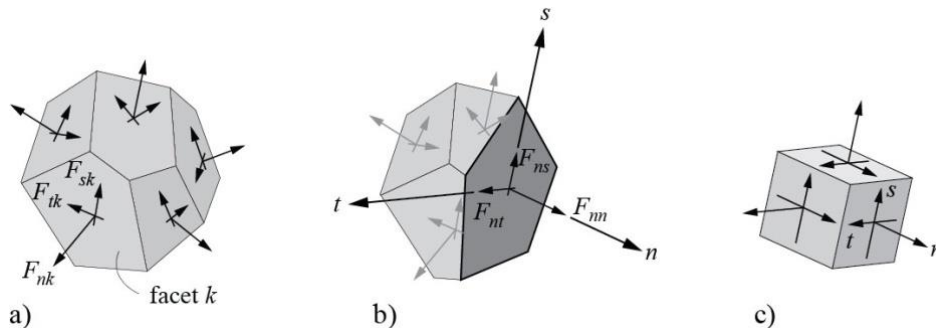
Figure 5.5. a) components of spring force local coordinates; b) a set of nodal forces satisfying the equilibrium; and c) complete stress tensor at Voronoi cell node (Adopted from Yip et al., 2005).
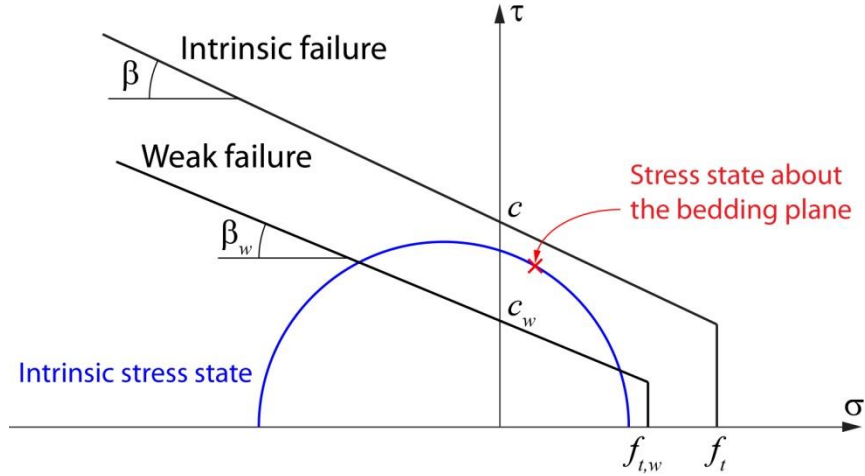
Figure 5.6. Weak-plane failure model with two different Mohr-Coulomb type criteria for intrinsic failure and weak failure.

By repeating this process for two other mutually perpendicular sections (Figure 5.5c), the full stress tensor is obtained:

$$\boldsymbol{\sigma} = \begin{bmatrix} \sigma_{nn} & \sigma_{ns} & \sigma_{nt} \\ & \sigma_{ss} & \sigma_{st} \\ Symm. & & \sigma_{tt} \end{bmatrix} \qquad 5.13$$

Consequently, the stress tensor of the inter-element is calculated by averaging the corresponding nodal stress tensor matrices:

$$\bar{\boldsymbol{\sigma}} = (\boldsymbol{\sigma}_i + \boldsymbol{\sigma}_j)/2 \qquad 5.14$$

where $\boldsymbol{\sigma}_i$ and $\boldsymbol{\sigma}_j$ are the stress tensors at the neighboring nodes i and j, respectively.

From the calculated $\bar{\boldsymbol{\sigma}}$, the Mohr circle of a lattice element can be drawn on the $\tau - \sigma$ coordinates, which will be assessed by Mohr-Coulomb type criteria to determine local failure as shown in Figure 5.6. Herein, the weak-plane model is used to represent strength anisotropy. The model assumes that the inherent strength is the same in all directions of a rock material, except for one set of parallel planes where the strength is lower. Since the bedding planes in sedimentary rocks may be planes of weakness, the model has a physical basis, and therefore it is quite important in spite of its simplicity. Two different sets of strength parameters are necessary to define the failure envelopes, which are explicitly available from typical laboratory test results. First, intrinsic strength parameters (cohesive strength c, friction angle β, and tension cut-off f_t) define a failure envelope that represents isotropic failure in all directions except the direction of bedding. If the stress state of a lattice element is such that the Mohr circle exceeds the envelope, the material will undergo failure like as it is an isotropic material, so called intrinsic failure. For the anisotropic failure on the bedding planes, the weak plane criterion is given by lower values of the cohesion c_w, friction angle β_w, and tensile strength $f_{t,w}$. The stress state about the bedding plane is represented as one point on the Mohr circle, which is compared with the weak plane criterion. If the stress point falls outside the envelope, failure will occur along the weak plane. Figure 5.6 demonstrates a determination of weak failure in which the stress state only violates the weak plane criterion.

229

5.2 Hydraulic Fracturing in Rock-Analogue Samples

5.2.1 Model Description

The coupled HM modeling involves hydraulic fracture propagation in a laboratory experimental program which has been supported by the Assistant Secretary for Fossil Energy, Office of Natural Gas and Petroleum Technology, through the National Energy Technology Laboratory. The laboratory tests have been conducted using soda-lime glass blocks in which fractures are artificially generated to provide some analogy to fractured rock materials. A complex pre-existing fracture network is designed and fabricated within the specimens (Figure 5.7 (a)), for which a laser-engraving technique is utilized to generate defects (Stewart et al., 2012). The fracture formation is described as a planar cloud of thermally induced, isolated micro-cracks.

For model preparation, a 90 mm square domain with a 3.2 mm diameter borehole at the center is discretized, and the pre-existing fractures are replicated by mapping the designed pattern onto the unstructured grid, as described in Section 5.1.1. Figure 5.7 (b) depicts details of the fracture network modeled in the Voronoi grid. Mechanical properties of the glass material are set as follows: Young's modulus E=73.8 GPa, tensile strength f_t=11.3 MPa; cohesive strength c=8.5 MPa; and internal friction angle β=25° for the Mohr-Coulomb failure criterion. It is simply assumed that the glass material is impermeable, non-porous, and incompressible. Also, all the interface nodes, which represent fractures in the TOUGH2 simulation, are initially set to be impermeable. For an activated pre-existing fracture or a newly generated fracture, the corresponding interface node undergoes a permeability increase, which is calculated based on the hydraulic aperture as suggested by Equation (5.6).

The specimen is subjected to anisotropic confining stresses, $\sigma_x : \sigma_y$= 4.83:7.24 MPa, and water is injected into the borehole at a constant rate. Because the glass is prone to brittle fracturing, the injection rate should be carefully considered to induce observable fracture propagation. The injection rate is 3.8×10^{-5} cm^3/s per unit centimeter thickness, which is roughly estimated from the injection volume history in the actual tests.
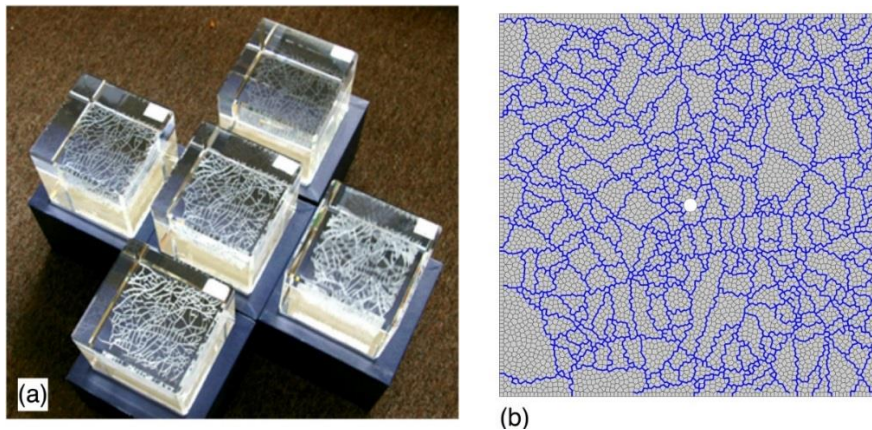
Figure 5.7. Physical and numerical representations of complex pre-existing fractures: a) 3D laser-engraved fractures in glass blocks with different opaqueness of their fracture network reflecting different mechanical properties of these fractures; and b) mapping of the fracture network onto an unstructured Voronoi grid.

5.2.2   Hydraulic Fracture Fropagation in Intact glass Blocks

Hydraulic fracturing simulations are performed for intact glass blocks to determine other unknown parameters through a calibration process. By setting the mechanical properties of the pre-existing fracture elements same as those of the glass domain, the fractured glass block can convert into the intact glass block while preserving the grid geometry and modeling configurations described in Section 5.2.1. With the given injection rate, the compressibility of the borehole is adjusted to 5.0×10^{-9} Pa^{-1}. The injection pressure evolution is plotted in Figure 5.8, where the simulated pressurization rate, denoted by the slope of the ascending branch, is fitted to the experimental result for an intact borehole. The preset/calibrated hydrological properties are listed in Table 5.1.

Figure 5.9 shows snapshots of the fracture traces and the pressure distributions over time. The breakdown point is captured at time t_0, from which the time lapse during fracture propagation is counted as $\tau = t - t_0$. Two fracture branches stretch out from the borehole and propagate mainly in the direction parallel to the maximum confining stress. As the fractures advance, the injected fluid transfers into the empty space created by the fractures. The fracture paths reflect higher pressure contrasting to the surrounding glass matrix, and accordingly the injection pressure decreases at the borehole. Further fracture growth occurs at one branch reaching the upper boundary in two seconds. Such rapid and instantaneous fracture propagation makes it difficult to observe details of interactions between pre-existing fractures and hydraulic fractures in the experiments.
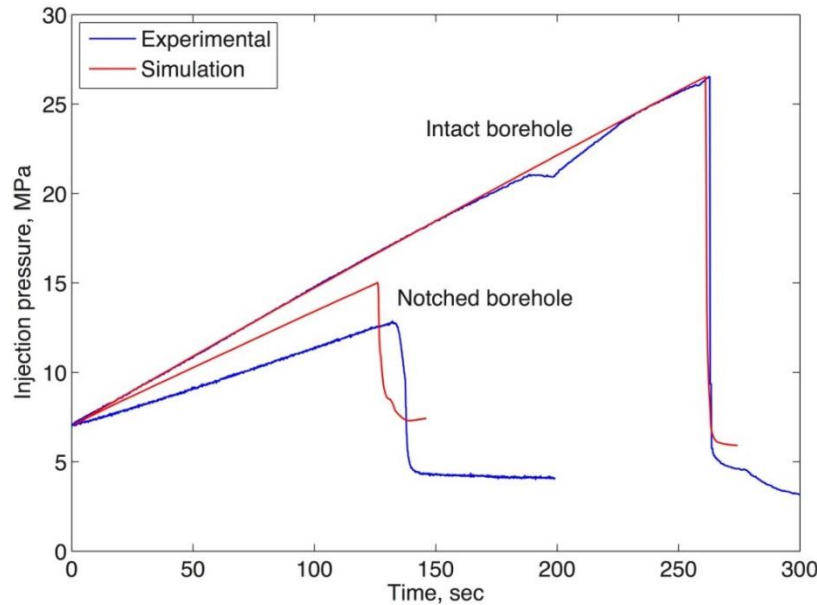
Figure 5.8. Injection pressure evolutions for hydraulic fracturing of intact glass blocks.

Table 5.1 Hydrological properties of glass, fracture, and borehole domains.

		Permeability (m²)	Porosity (-)	Compressibility (Pa⁻¹)
Glass		0	0	0
Fracture	Pre-existing	0	0	0
	Activated	$b_h^{12}/12^†$	0.8	3.0×10^{-8}
Borehole		1.0×10^{-9}	0.8	5.0×10^{-9}

[†]The permeability of an activated fracture depends on the hydraulic aperture width, which is evaluated by Equation (5.6) with an assumption for the residual hydraulic aperture $b_{hr}= 0.25$ μm.
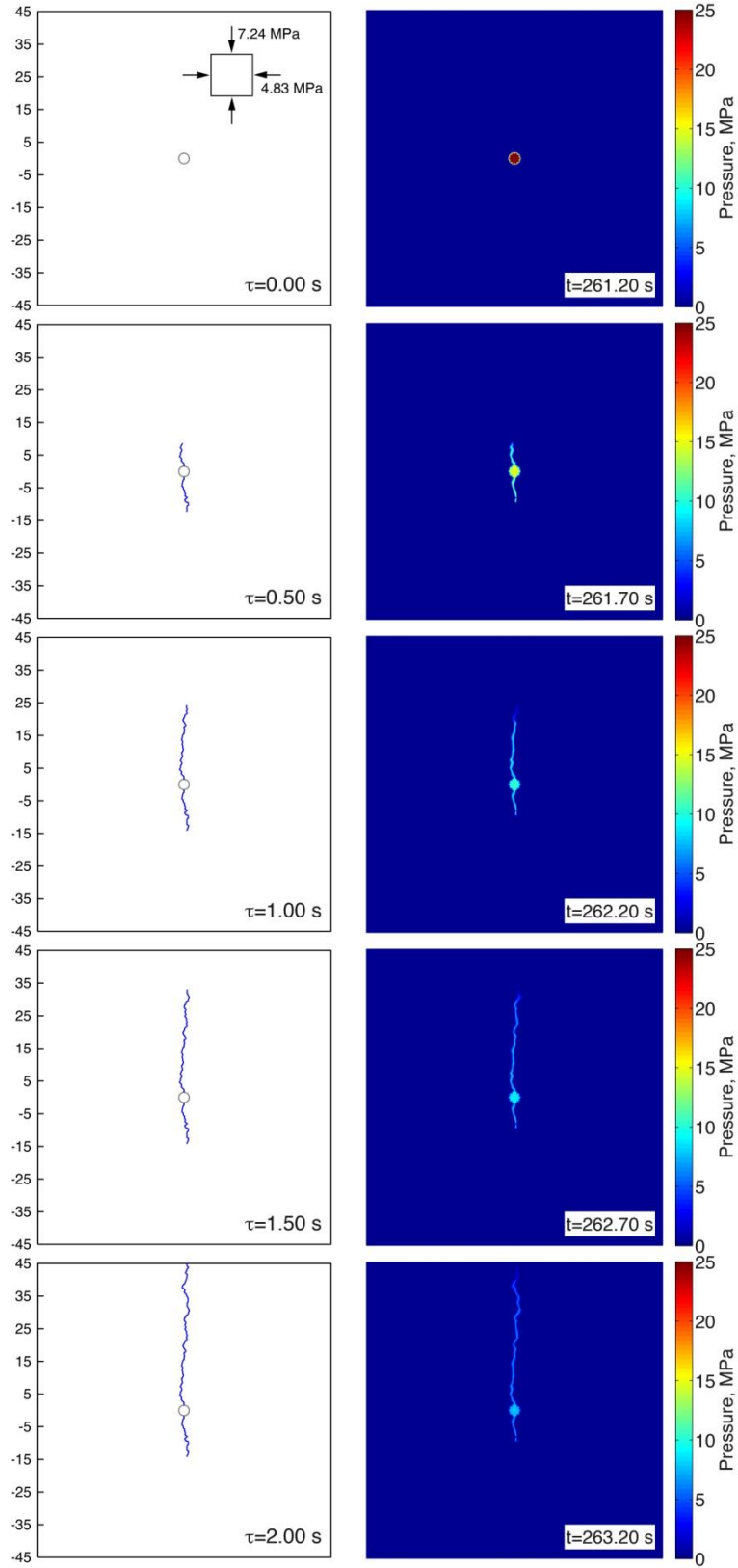
Figure 5.9. Snapshots of the fracture traces and the pressure distributions during fracture propagation from the intact borehole.

233
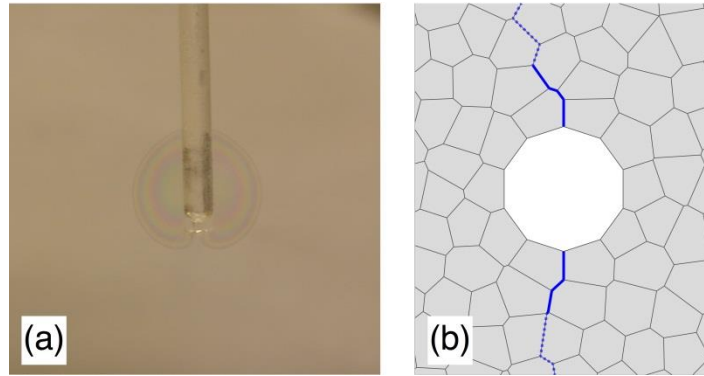
Figure 5.10. Introduction of initial notches around the borehole: a) pre-cracking of a test sample; and b) modeling of the notches by selecting fractured segments (illustrated by blue solid lines).

To stabilize the fracture growth, pre-cracks or notches are introduced around the borehole. Strain singularity and stress concentration arise at the crack tips (Rice, 1968), which is expected to advance the fracture initiation with a lower triggering pressure and thus provide a gradual fracture propagation. In the experimental program, a small flaw is generated by mechanically compressing a rubber plug at the bottom of the borehole. This method generates stable pre-cracks by pressurizing the borehole wall (Figure 5.10 (a)). The orientation of the flaw can be controlled to some degree by applying confining stresses to the specimen during the pressurization. In the numerical models, notches or other types of discontinuities (e.g., defects, fault planes, etc.) are represented by breaking/damaging the elements. From the resulting fracturing paths for the intact borehole presented in Figure 5.9, the fractured interface segments are manually picked to introduce the notches around the borehole (Figure 5.10 (b)), in which the mechanical resistance is completely removed in tension and small permeability and porosity are introduced.

The injection pressure evolution of the notched borehole is plotted and compared with that of the intact borehole in Figure 5.8. The injection pressure increases at a lower rate in the pre-peak region, which is attributed to infiltration of the injected fluid into the notches. The breakdown occurs at a lowered peak pressure as expected and the pressure is gradually released in the post-peak region, which implies slower fracture propagation with the notched borehole. Both the simulations and the laboratory tests demonstrate that the fracture growth is slower in the case of the notched borehole. However, a disagreement exists on the peak pressure and the pressurization rate between the simulation and experimental results. These quantitative discrepancies may be because it is difficult to precisely measure the length of the pre-cracks and therefore they may not be correctly represented in the model.

A comparison between Figures 5.9 and 5.11 explicitly explains the effects of the notched borehole on the rate of fracture growth. The fracturing speed is significantly reduced with the notched borehole, in which about 5 to 10 times longer period of time is taken for the same extent of fracture propagation. Moreover, a low level of the triggering and driving pressure evolves during the fracturing process with the notched borehole, and therefore the fracture is arrested after reaching a certain length (at $\tau=8.00$ s) and then the fracture front proceeds very slowly while the fluid injection is continued at a constant rate.
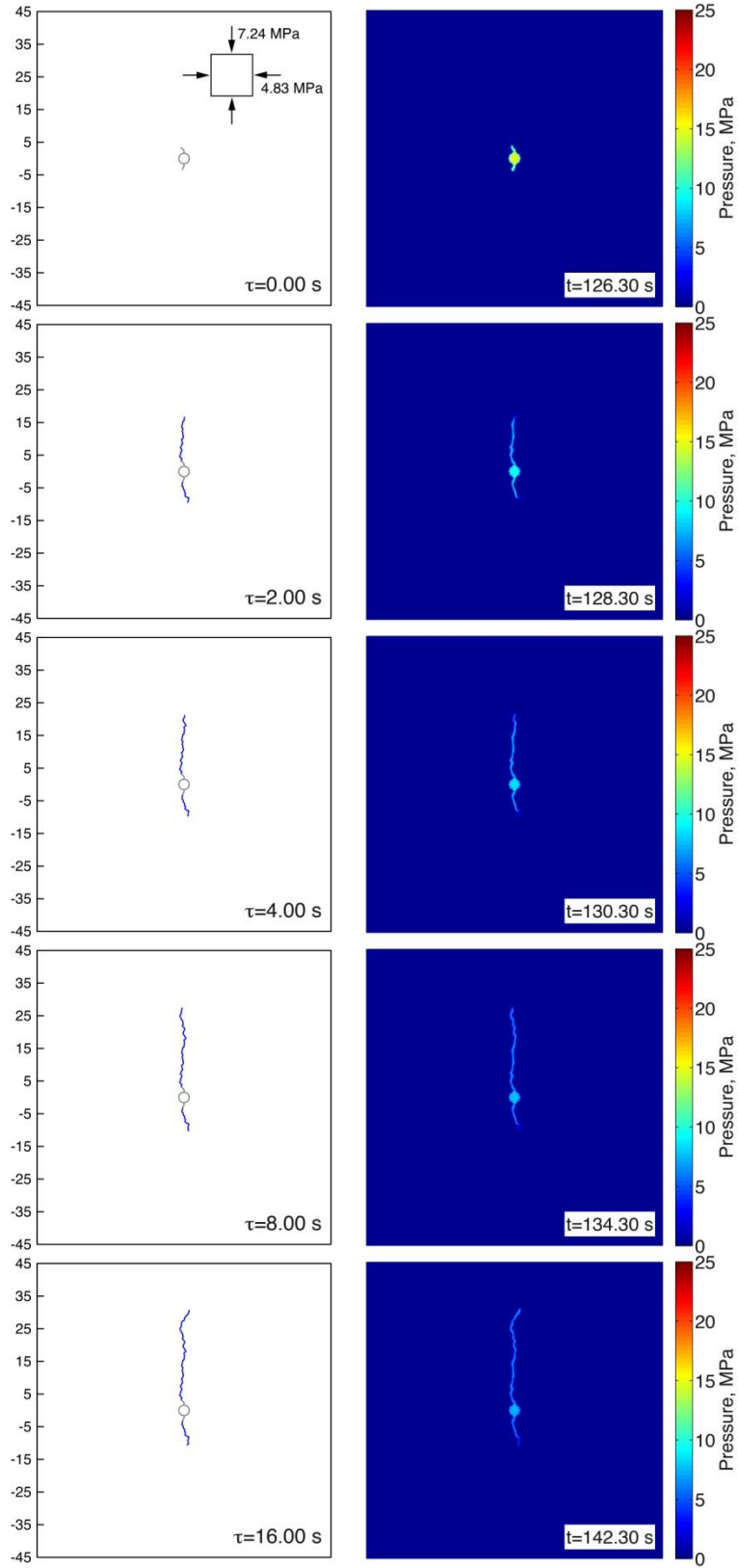
Figure 5.11. Snapshots of the fracture traces and the pressure distributions during fracture propagation from the notched borehole.

235

5.2.3 Hydraulic Fracture Propagation in a Glass Block Containing Pre-Existing Fractures

Within the same model description presented in Section 5.2.1, a fractured glass block is modeled by assigning weaker and more compliant mechanical properties to the lattice elements which correspond to the pre-existing fractures. The mechanical properties of the pre-existing fractures can be varied based on the expected weakening in accordance with the density of the etched micro-cracks in the test samples, which is reflected by the opaqueness of the fracture network in Figure 5.7 (a). For the simulation presented in this section, Young's modulus, the tensile strength, and the cohesive strength are initially reduced by half from those of the intact glass material, whereas the internal friction angle is retained. The notches around the borehole are modeled in the same way described in Section 5.2.2, but from the result of a preliminary simulation the fractured segments are taken at different locations mainly corresponding to the pre-existing fractures. Hydrological properties of the material domains conform to the values in Table 5.1. Note that the pre-existing fractures are assumed to be initially impermeable, thus they do not affect the hydrological behavior unless activated, whereas the notches are regarded as activated fractures (See Table 5.1).

The resulting fracture trace shows that the direction of hydraulic fracturing is influenced by a combination of the anisotropic stress condition and the degraded mechanical properties of the pre-existing fracture network (Figure 5.12 (a)). Two main fractures propagate from the borehole in the direction sub-parallel to the maximum confining stress with a slight perturbation due to the local heterogeneity of pre-existing fractures. The fracture branches mostly follow the activated pre-existing fractures (depicted by blue lines), and at some locations cut-throughs are made by newly generated fractures (depicted by red lines). The overall shape of the simulated fracture trace agrees well with the visualized hydraulic fracturing paths in the laboratory test, where a red fluorescent dye is mixed with the injected fluid for better visibility of fracturing paths (Figure 5.12 (b)).
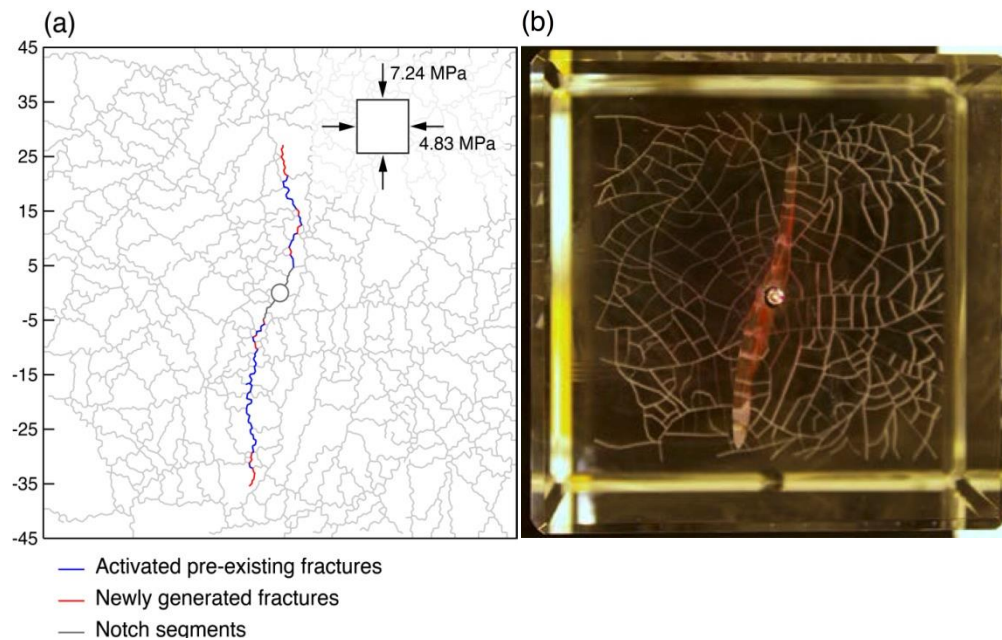
Figure 5.12. A comparison between a) the simulated fracture trace within the pre-existing fractures and b) the visualization of hydraulic fractures in the laboratory test.

5.3 Simulations of Damage and Fracture in Opalinus Clay Rocks

5.3.1 Uniaxial compression tests

The modeling scheme proposed in Section 5.1.3 is verified through simulation of uniaxial compression tests for various orientations of bedding planes. Consider 2D configurations of a cylindrical core sample subjected to unconfined uniaxial compression, in which the loading direction forms an angle relative to the bedding plane, θ (see Figure 5.13). The simulations consider seven cases of the loading angle: $\theta = 0°, 15°, 30°, 45°, 60°, 75°, 90°$. Boundary conditions are assigned at top and bottom layers of cells. Incremental loading is applied at the top layers by displacement control and the bottom layers are fixed. Herein the anisotropic mechanical properties of the rock material are adopted from the experimental results for the Opalinus Clay (Bossart, 2012), which are arranged in Table 5.2.
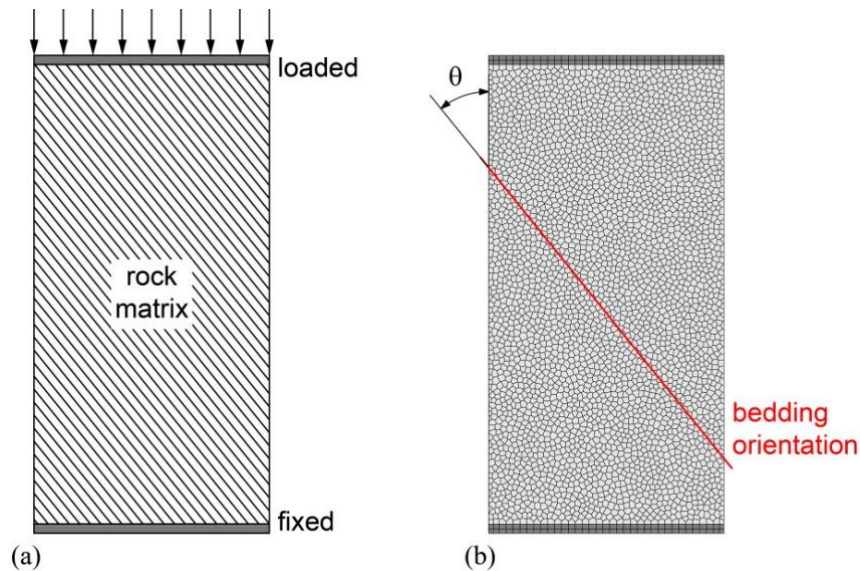
Figure 5.13. 2D specimen for uniaxial compression test: a) schematic drawing of the test program; and b) model discretization.

Table 5.2. Anisotropic mechanical properties of the Opalinus Clay (Bossart, 2012).

Mechanical properties	Parallel to bedding	Normal to bedding
Young's modulus (GPa)	15.5	9.5
Uniaxial tensile strength (MPa)	2.0	1.0
Cohesion (MPa)	5.5	2.2
Internal friction angle (degrees)	25	25
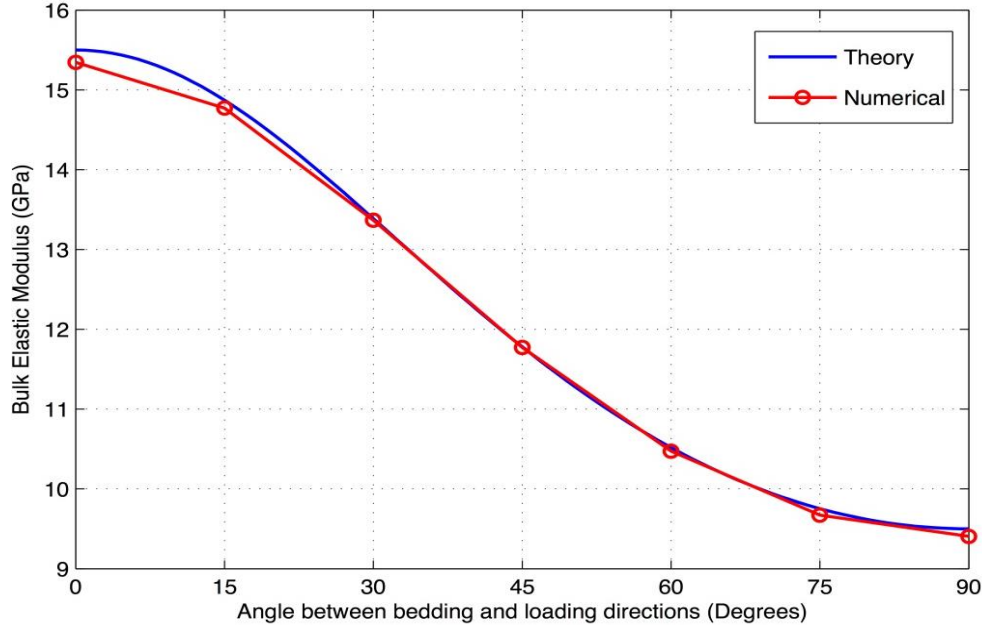
Figure 5.14. Variation of elastic modulus of Opalinus Clay with different loading angles.

The anisotropy of the elastic properties can be found in bulk elastic moduli. Theoretically, the bulk elastic modulus for loading angle θ is obtained by (Pariseau, 2006):

$$\frac{1}{E} = \frac{\cos^4 \theta}{E_P} + \left(\frac{1}{G_{12}} - \frac{2 \nu_{12}}{E_P}\right) \sin^2 \theta \, \cos^2 \theta + \frac{\sin^4 \theta}{E_N} \qquad 5.15$$

where G_{12} is shear modulus and ν_{12} is Poisson ratio. An approximation of the relationship between shear modulus and Young's moduli for an anisotropic system with $\nu = 0$ is given as

$$G_{12} = 1/\left(\frac{1}{E_P} + \frac{1}{E_N}\right) \qquad 5.16$$

With this assumption for Equation (5.15), the theoretical variation in bulk elastic modulus is depicted in Figure 5.14. Simulated elastic moduli show a are in agreement with the theoretical evaluations.

For the weak-plane failure model proposed in Section 5.1.3.2, the two different failure criteria limit the maximal compressive principal stresses at their critical stress states, which can be theoretically derived with an assumption of unconfined loading configurations:

$$\sigma_1 = 2 \frac{c \cos \beta}{1 - \sin \beta} \qquad 5.17$$

for the intrinsic failure criterion (cohesion c, friction angle β) and

$$\sigma_{1,w} = 2 \frac{c_w \cos \beta_w}{\sin 2\theta \cos \beta_w - (\cos 2\theta + 1)\sin \beta_w} \qquad 5.18$$

for the weak failure criterion (cohesion c_w, friction angle β_w, respectively. The minimum value between the two limit stresses is chosen to be uniaxial compressive strength for a specific loading angle θ. The Variation of the theoretical values as a function of loading angle is plotted in Figure 5.14. From the simulation results, peak stress values of the stress-strain response curves

238

can be regarded as uniaxial compressive strengths. The simulated strengths are perfectly matched with the theoretical values.
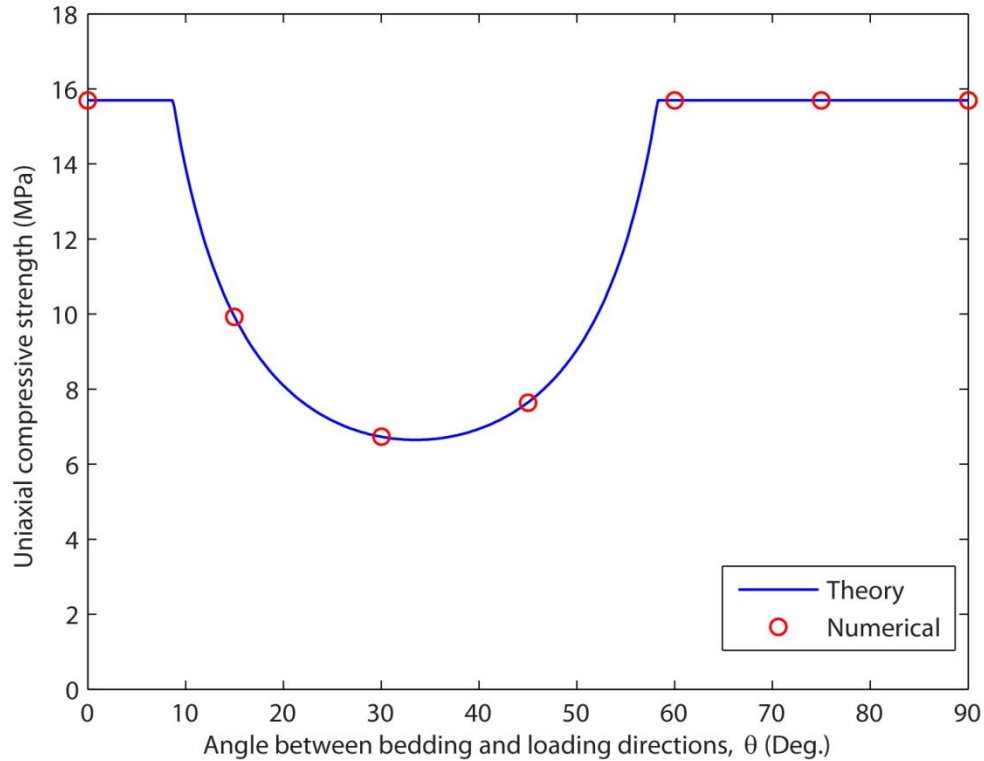
Figure 5.15. Variation of elastic modulus of Opalinus Clay with different loading angles.

5.3.2   EDZ Formations in the HG-A Microtunnel

This section presents the validity of the modeling scheme for anisotropic failure behavior observed in the field site, the HG-A microtunnel. The 1-m diameter microtunnel is located at the Mont Terri underground research laboratory (URL) near Saint-Ursanne, Switzerland. The rock of the test site is relatively homogeneous in meter-scale, but pronounced bedding was discovered at finer scales (Marschall et al., 2006). The rock formation is highly fractured with frequencies of 0.3 to 1 m, although the fracture permeability is not significant, which indicates that fractures are mostly closed under natural stress conditions (Marschall et al., 2006; 2008).

One main purpose of the HG-A test is to provide data on the geomechanical and hydrogeologic effects of the excavation damage zone (EDZ). Although the long-term physical features observed in the test are related to coupled hydro-mechanical processes, as an initial study, herein the problem is simplified by assuming a constant uniform pore pressure such that fracture damage is simulated using the mechanical modeling of the RBSN approach exclusively. This assumption is valid up until the point at which mechanical deformation occurs much more quickly than water flow processes in the rock formation, where mechanical equilibrium is held within a rapid (undrained) excavation (Liu et al., 2013).

Figure 5.16 (a) shows excavation damage of the microtunnel. Partial damage and exfoliations have occurred along the microtunnel wall, which are mainly attributed to the anisotropic strength characteristics of the rock. The relative weakness orthogonal to the bedding and the weakness

239

near faults intercepting the tunnel, as depicted in Figure 5.16 (b), result in the non-uniform damage around the excavation wall.
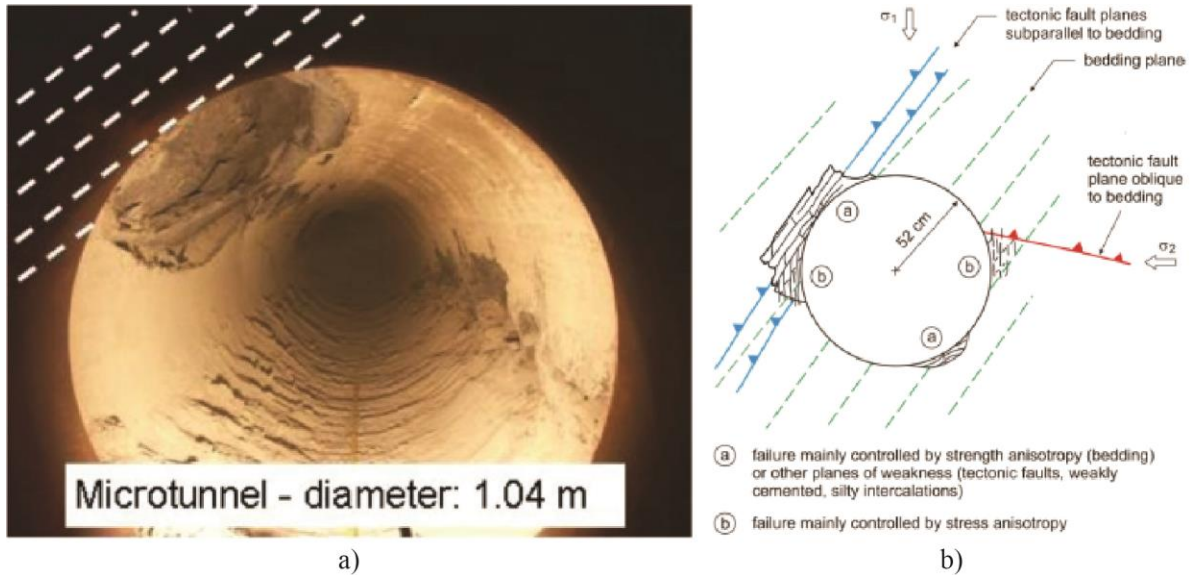
Figure 5.16. a) Excavation damage viewing from the HG-A Niche towards back end (Marschall et al., 2006); and b) Conceptual diagram of the damage zone (Lanyon et al., 2009; Marschall et al., 2006).

This study is focused on investigating the effects of the faults on the failure characteristics. As shown in Figure 5.17, 2D computational domain with dimension of 10-m square is discretized with a gradual nodal density, where a circular subdomain for excavation is defined at the center. The bedding planes are assumed to be aligned at 45° from the horizontal axis similarly to the orientation of fabric shown in Figure 5.16 (b). The anisotropic elastic and strength properties of the rock matrix conform to the parameters listed in Table 5.2. The observed fault planes are precisely modeled into a grid (see Figure 5.17b), for which the weaker strength parameters are assigned: tensile strength $f_{t,f} = 0.5$ MPa; cohesion $c_f = 1.0$ MPa; and friction angle $\beta_f = 23°$.

Far-field confining stresses are applied at the boundary edges: 5.5 MPa in the horizontal direction and 6.5 MPa in the vertical direction (Martin and Lanyon, 2003), and the pore pressure of 1.5 MPa is applied over the domain at the initial stage. A one-step preliminary simulation is conducted to grasp the initial stress state for the given stress and pressure configurations, so the main simulation starts with the undeformed condition. An excavation process can be demonstrated by gradually reducing the elastic parameters, internal stress and pressure in the excavation zone over the loading steps. Herein, an exponential function is adopted, by which the values will be decreased to about 10^{-6} of the initial configurations after 100 loading steps.

Figure 5.18 presents the resulting failure patterns. Damage occurs mainly around the excavation zone, and more brisk failures are found at the tunnel wall where its tangent is sub-parallel to the bedding planes, which has been found in the field observations (Figure 5.16). The effects of fault planes on the failure patterns can be interpreted in comparison between Figures 5.18 (a) and 5.18

(b). The matrix domain is homogenous in the material composition, thus the failure pattern is quite symmetric without fault planes (Figure 5.18 (a)), which may be attributed to the anisotropic strength properties. However, in the presence of faults (Figure 5.18 (b)), distinct shear fracture develops along the fault planes, and then fractures grow from the fault planes. One kind of distinguishing characteristics in the fracture pattern with fault planes is that the fracture growth is limited by the fault planes. The resulting fracture pattern is not symmetric due to the stress contour perturbed by the fault planes.
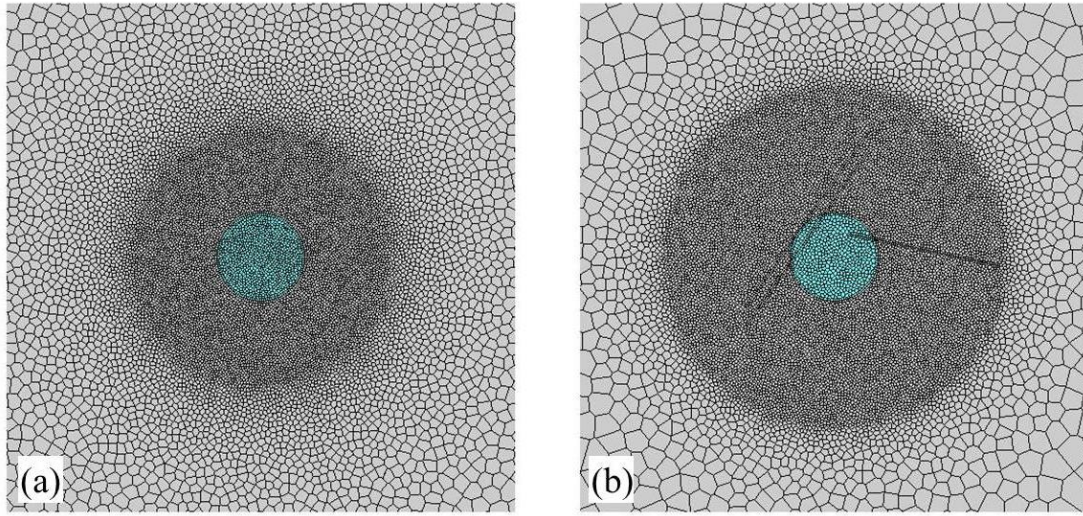
Figure 5.17. Discretizations of the computational domain for the HG-A test simulations: a) without fault planes; and b) with fault planes explicitly modeled into the grid.
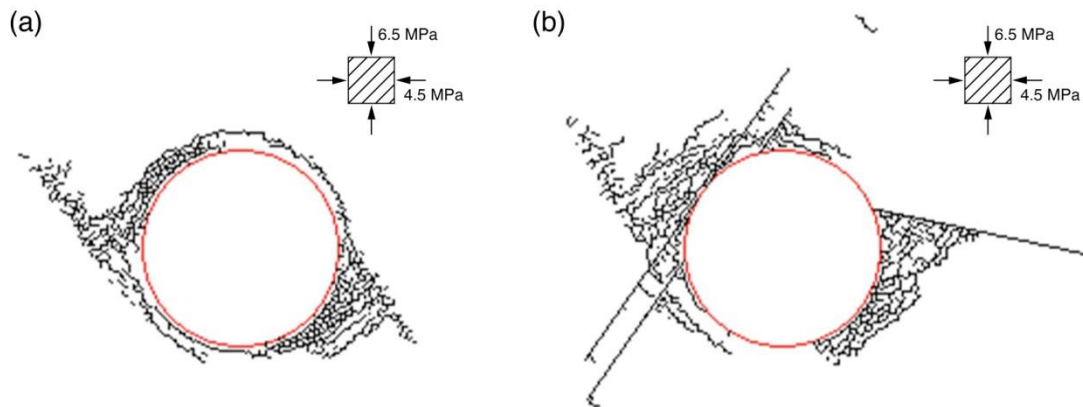
Figure 5.18. Resulting failure patterns around the tunnel excavation zone: a) without fault planes; and b) with fault planes.

241

5.4   Development of Dynamic Simulation Code

In dynamic modeling of mechanical behavior, the motion of the system is governed by a differential equation based on Newton's second of law of motion. The particle-lattice model, considered in this work, consists of Voronoi cells with mass and inertial moments, which are interacting with their neighbors via spring connections constructed by the RBSN theory. Figure 5.19 shows a free-body diagram of a Voronoi cell subjected to external load applied at the node and local internal forces generated at the spring sets. Each cell has six nodal degrees of freedom in 3D global coordinates. Let us consider the external load vector $\mathbf{p}(p_X, p_Y, p_Z, \tau_X, \tau_Y, \tau_z)$ and a local internal force vector $\mathbf{f}_k(f_{nk}, f_{sk}, f_{tk}, m_{nk}, m_{sk}, m_{tk})$ for a Voronoi facet k. The rotational components of the internal spring force vector (i.e., m_{nk}, m_{sk}, m_{tk}) are omitted for visibility in Figure 5.19 (b). The internal spring force terms in the local coordinates are transformed into the global coordinates and assembled into a global vector $\mathbf{f}$:

$$\mathbf{f} = \sum_{k=1}^{n} \mathbf{\Gamma}_k{}^T \mathbf{f}_k \tag{5.19}$$

where $\mathbf{\Gamma}_k$ is a 6×6 matrix for coordinate transformation from global X-Y-Z to local n-s-t for individual Voronoi facets.

The governing equation for nodal displacements and rotations varying with time can be constructed as

$$\mathbf{J}\ddot{\mathbf{u}} + \mathbf{f} = \mathbf{p}(t) \tag{5.20}$$

where $\ddot{\mathbf{u}}$ is a second derivative of displacement vector (i.e., acceleration). $\mathbf{J}$ is the inertia matrix containing mass and moment of inertia tensor of the Voronoi cell, which can be expressed with the corresponding sub-matrices $\mathbf{M}$ and $\mathbf{I}$:

$$\mathbf{J} = \begin{bmatrix} \mathbf{M} & 0 \\ 0 & \mathbf{I} \end{bmatrix} = \begin{bmatrix} m & & & & & \\ & m & & & 0 & \\ & & m & & & \\ & & & I_{XX} & I_{XY} & I_{XZ} \\ & 0 & & I_{YX} & I_{YY} & I_{YZ} \\ & & & I_{ZX} & I_{ZY} & I_{ZZ} \end{bmatrix} \tag{5.21}$$

The mass and inertial moment terms are calculated from the geometrical properties of the Voronoi cell. The polyhedral cells are mostly in irregular shape so that it demands a generalized method to compute the volume, centroidal position, and inertia tensor of an arbitrary polyhedron. In the proposed method, a polyhedron can be treated as the combination of pyramids defined by the cell facets and the cell node, which are regarded as the pyramid bases and the apex, respectively. Consequently, the geometrical properties of the polyhedral cell can be easily computed by combining those of all pyramids. Construction of the inertia matrix is essential to calculate the acceleration vector:

$$\ddot{\mathbf{u}} = \mathbf{J}^{-1}[\mathbf{p} - \mathbf{f}] \tag{5.22}$$

Herein, the resultant acceleration is used to explicitly derive higher-order kinematic information (i.e., velocity and displacement). The solution in Equation (5.22) can be rewritten in the discretized form at time $t_{n+1} = (n+1)\Delt$:

$$\ddot{\mathbf{u}}_{n+1} = \mathbf{J}^{-1}[\mathbf{p}_{n+1} - \mathbf{f}_{n+1}] \qquad\qquad 5.23$$

where the resultant internal force $\mathbf{f}_{n+1}$ applied to the spring sets is explicitly related to the nodal displacement $\mathbf{u}_{n+1}$, which is derived by integrating the known kinematic information up to time n:

$$\mathbf{u}_{n+1} = \mathbf{u}_n + \dot{\mathbf{u}}_n\Delta t + \frac{\ddot{\mathbf{u}}_n}{2}\Delta t^2 \qquad\qquad 5.24$$
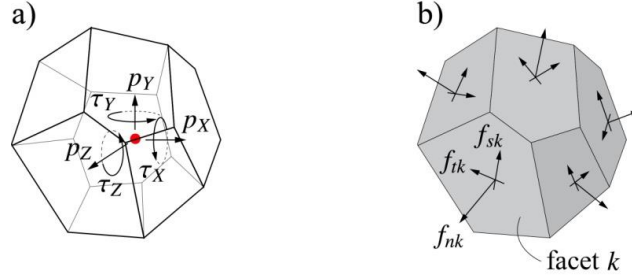
Figure 5.19. Free-body diagram of a Voronoi particle for dynamic equilibrium condition: a) external force terms; and b) internal forces corresponding to the RBSN spring forces.

Then, the unknown velocity $\dot{\mathbf{u}}_{n+1}$ is derived using the calculated $\ddot{\mathbf{u}}_{n+1}$:

$$\dot{\mathbf{u}}_{n+1} = \dot{\mathbf{u}}_n + \frac{\ddot{\mathbf{u}}_{n+1}+\ddot{\mathbf{u}}_n}{2}\Delta t \qquad\qquad 5.25$$

If there are velocity-dependent terms involved in the force calculation such as a damping force, the internal force $\mathbf{f}_{n+1}$ is not simply fixed until the velocity $\dot{\mathbf{u}}_{n+1}$ converges. For that case, an additional "predictor-corrector" iteration algorithm is necessary during these explicit time integrations.

As an ongoing development stage, the simulation code has been established with modern programming features (e.g., dynamic memory allocation, modularized program blocks) implemented in Fortran 90. New data structures will provide better computational efficiency and simple code management for extension and modification. Also, the calculation of the inertial tensor of an arbitrary polyhedron is included in the code. The Voronoi-based particles are the most fundamental elements for dynamic modeling, so it is crucial to obtain their geometrical properties for solving the governing ODEs. The solution phase is implemented using explicit time integration algorithms (e.g., velocity Verlet scheme), which will ease converting the serial computing to a parallelized version. High performance computation libraries, such as PETSc and Polymec, can be adopted for parallelization of the simulation code.

5.5 Summary and Future Work

In this work we are implementing an effective two-way coupling between the TOUGH2 simulator and the RBSN approach for the application of damage and fracturing in argillaceous rocks. In FY16 we have continued our work on modeling damage and deformation in anisotropic rock and around tunnels, but have also made substantial effort in simulation of fluid driven fracture propagation. The work on fluid driven fracture propagation forms the groundwork for another future application related to gas migration in bentonite and clay rocks. The simulator

currently provides a discrete representation of hydrological (fluid flow through fracture networks) and mechanical (fracture initiation and propagation) responses. The permeability of an individual fracture is rigorously evaluated from the grid geometry and the fracture aperture width.

In addition to the TOUGH-RBSN linkage, an improvement in the RBSN modeling scheme has been achieved to extend the applicability of the model to general geomaterials that exhibit mechanical anisotropy. In a new approach, elastic spring coefficients and strength parameters are systematically formulated for individual lattice elements based on the bedding orientation, and a simple but efficient weak-plane failure model is adopted to represent the anisotropic fracture response with fabric-dependent strength parameters.

The TOUGH-RBSN code and the developed algorithms for fluid driven fracturing has been applied to predictive and interpretative simulations for hydraulic fracturing of the laboratory experiment samples. The hydraulic fractures reproduced in the simulations compare favorably to the experimental results with respect to the injection pressure evolutions and the resulting fracture paths. As for the mechanical anisotropy, uniaxial compression tests on Opalinus Clay have been simulated in order to demonstrate the validity of the new modeling scheme. Thereafter, updated simulations of EDZ formations for the Mont Terri HG-A microtunnel have been conducted. Qualitative comparisons show that the simulation results closely match field observations, in which non-uniform failure patterns attributed to the anisotropic mechanical characteristics form around the excavation zone and the presence of fault planes significantly influences the failure patterns.

In summary, in FY16 we have further developed TOUGH-RBSN with the goal of producing an efficient tool for understanding the variety of characteristics in THM processes in argillaceous rocks, including fracture damage and fluid driven fracture propagation. The series of simulations presented in this report section demonstrate the current TOUGH-RBSN capabilities for modeling tightly coupled HM processes and the RBSN approach for mechanical anisotropy in elastic and fracture responses. For the ongoing development, a refinement could be made into the TOUGH-RBSN code to rigorously evaluate the change of fracture porosity as a response of the mechanical fracture aperture change, which will be addressed in future work. In addition, the ongoing work on the dynamic version and porting that version to high performance computing will provide an avenue for modeling larger scale problems, including 3D complex fracture geometry.

For FY17, recommended work is as follows:

- We plan to complete the dynamic simulation framework, and verification and validation of the simulation code will be provided through geomechanics examples including fracturing processes. Also, by high performance computing in the dynamic simulation code, our modeling capacities will be extended to full 3D large scale problems.

- More realistic simulations will be available by setting the fracture porosity dependent on the fracture aperture width in the TOUGH-RBSN coupling modules.

- Relating to the DECOVALEX-2019 task, TOUGH-RBSN code can be applied to the gas migration in bentonite clay, in which the clay material often dilates to create preferential

flow pathways. We will attempt to demonstrate such preferential pathways using the discrete modeling approach.

- Swelling of a ductile/expanding shale matrix will be simulated to investigate the time-dependent deformation of the rock, including fracture closure/sealing, which significantly impacts on the hydrological properties of the rock material.

5.6 References

Asahina, D. and Bolander, J.E. 2011 Voronoi-based discretizations for fracture analysis of particulate materials, *Powder Technology*, 213, 92–99.

Bear, J. 1972 *Dynamics of Fluids in Porous Media*, Elsevier, New York, New York.

Berton, S. and Bolander, J.E. 2006 Crack band model of fracture in irregular lattices, *Computer Methods in Applied Mechanics and Engineering*, 195, 7172–7181.

Biot, M.A. and Willis, D.G. 1957 The elastic coefficients of the theory of consolidation, *Journal of Applied Mechanics*, 24, 594–601.

Blümling, P., Bernier, F., Lebon, P., and Martin, C.D. 2007 The excavation damaged zone in clay formations time-dependent behaviour and influence on performance assessment, *Physics and Chemistry of the Earth*, 32, 588–599.

Bolander, J.E. and Saito, S. 1998 Fracture analyses using spring networks with random geometry, *Eng. Fract. Mech.*, 61, 569–91.

Bossart, P. 2012 Characteristics of the Opalinus Clay at Mont Terri, http://www.montterri.ch/internet/montterri/en/home/geology/key_characteristics.parsys.49924.DownloadFile.tmp/characteristicsofopa.pdf.

Bossart, P., Meier, P.M., Moeri, A., Trick, T., and Mayor, J.C. 2002 Geological and hydraulic characterisation of the excavation disturbed zone in the Opalinus Clay of the Mont Terri Rock Laboratory, *Engineering Geology*, 66(1–2), 19–38.

Bossart, P., Meier, P.M., Moeri, A., Trick, T., and Mayor, J.-C. 2004 Structural and hydrogeological characterisation of the excavation-disturbed zone in the Opalinus Clay (Mont Terri Project, Switzerland), *Applied Clay Science*, 26, 429–448.

Chiaramonte, L., Zoback, M.D., Friedmann, J., and Stamp, V. 2008 Seal integrity and feasibility of CO_2 sequestration in the Teapot Dome EOR pilot: geomechanical site characterization, *Environ. Geol.*, 54, 1667–1675.

Cosgrove, J.W. (2001) Hydraulic Fracturing during the Formation and Deformation of a Basin: A Factor in the Dewatering of Low-Permeability Sediments, *AAPG Bulletin*, 85(4), 737–748.

Freeman, C.M., Moridis, G.J., and Blasingame, T.A. (2011) A numerical study of microscale flow behavior in tight gas and shale gas reservoir systems, *Transport in porous media*, 90(1), 253–268.

Gonçalvès, J., Violette, S., and Wendling, J. (2004) Analytical and Numerical Solutions for Alternative Overpressuring Processes: Application to the Callovo-Oxfordian Sedimentary Sequence in the Paris Basin, France, *Journal of Geophysical Research*, 109, 14.

Lanyon, G.W., Marschall, P., Trick,T., de La Vaissière, R., Shao, H. and Leung, H. (2009) Hydromechanical evolution and self-sealing of damage zones around a microtunnel in a claystone formation of the Swiss Jura Mountains, *ARMA*, 09-152.

Liu, H.H., Houseworth, J., Rutqvist, J., Zheng, L., Asahina, D., Li, L., Vilarrasa, V., Chen, F., Nakagawa, S., Finsterle, S., Doughty, C., Kneafsey, T. and Birkholzer, J. (2013) Report on *THMC modeling of the near field evolution of a generic clay repository: Model validation and demonstration*, (FCRD-UFD-2013-000244), U.S. DOE Used Fuel Disposition Campaign.

Marschall, P., Distinguin, M., Shao, H., Bossart, P., Enachescu, C. and Trick, T. (2006) Creation and evolution of damage zones around a microtunnel in a claystone formation of the Swiss Jura Mountains, *Society of Petroleum Engineers*, SPE-98537-PP.

Marschall, P., Trick, T., Lanyon, G.W., Delay, J. and Shao, H. (2008) Hydro-mechanical evolution of damaged zones around a microtunnel in a claystone formation of the Swiss Jura Mountains, *ARMA*, 08-193.

Martin, C.D. and Lanyon, G.W. (2003) Measurement of in-situ stress in weak rocks at Mont Terri Rock Laboratory, Switzerland, *International Journal of Rock Mechanics & Mining Sciences*, 40, 1077–1088.

McGuire, W. and Gallagher, R.H. (1979) *Matrix Structural Analysis*, John Wiley & Sons, New York.

Okabe, A., Boots, B., Sugihara, K., and Chiu, S.N. (2000) *Spatial Tessellations: Concepts and Applications of Voronoi Diagrams*, 2nd ed., Wiley, NYC, 696 pages.

Pariseau, W.G. (2006) *Design Analysis in Rock Mechanics*, Taylor & Francis, London, UK.

Rice, J.R. (1968) A path independent integral and the approximate analysis of strain concentration by notches and cracks, *Journal of Applied Mechanics*, 35 (2), 379–386.

Rutqvist, J. (2011) Status of the TOUGH–FLAC simulator and recent applications related to coupled fluid flow and crustal deformations, *Computers & Geosciences*, 37(6), 739–750.

Rutqvist, J. and Tsang, C.-F. (2002) A study of caprock hydromechanical changes associated with CO_2-injection into a brine formation, *Environmental Geology*, 42, 296–305.

Rutqvist, J., Noorishad, J., Tsang, C.-F., and Stephansson, O. (1998) Determination of fracture storativity in hard rocks using high-pressure injection testing, *Water Resources Research*, 34 (10), 2551–2560.

Rutqvist, J., Tsang, C.-F., and Stephansson, O. (2000) Uncertainty in the maximum principal stress estimated from hydraulic fracturing measurements due to the presence of the induced fracture, *International Journal of Rock Mechanics and Mining Sciences*, 37, 107–120.

Rutqvist, J., Wu, Y.-S., Tsang, C.-F., and Bodvarsson, G. (2002) A modeling approach for analysis of coupled multiphase fluid flow, heat transfer and deformation in fractured porous rock, *International Journal of Rock Mechanics & Mining Sciences*, 39, 429–442.

Stewart, R.R., Dyaur, N., Omoboya, B., de Figueiredo, J.J.S., Willis, M., and Sil, S. (2012) Physical modeling of anisotropic domains: Ultrasonic imaging of laser-etched fractures in glass, *Geophysics*, 78(1), D11-D19.

Volckaert, G., Bernier, F., Sillen, X., Van Geet, M., Mayor, J.-C., Göbel, I., Blümling, P., Frieg, B., and Su, K. (2004) Similarities and differences in the behaviour of plastic and indurated clays, *The Management and Disposal of Radioactive Waste: Euradwaste '04*, Luxembourg.

Witherspoon, P. A., Wang, J. S. Y., Iwai, K., and Gale, J. E. (1980) Validity of cubic law for fluid flow in a deformable rock fracture, *Water Resources Research*, 16, 1016–1024.

Yip, M., Mohle, J., and Bolander, J. (2005) Automated modeling of three-dimensional structural components using irregular lattices, *Computer-Aided Civil and Infrastructure Engineering*, 20, 393–407.

Zimmermann, G., and Reinicke, A. (2010) Hydraulic stimulation of a deep sandstone reservoir to develop an Enhanced Geothermal System: Laboratory and field experiments, *Geothermics*, 39(1), 70–77.

6.   Summary

(1) THM modeling: FE heater test and DECOVALEX (Section 2)

UFD and LBNL greatly benefit from participating in these international activities for developing expertise and testing advanced models for coupled THM processes to be used for predicting long-term THM evolution of a multibarrier nuclear waste repository system, involving backfilled emplacement tunnels in argillite host formations. In FY16, we have been able to successfully complete the DECOVALEX-2015 modeling associated with the Mont Terri HE-E experiment and Horonobe EBS experiment, and for the first time been able to analyze field data from the largest ongoing underground heater test in the worlds; the Mont Terri FE experiment. The main accomplishments in FY16 include the improvement of the implementation and efficiency of the Barcelona Expansive Model (BExM) in TOUGH-FLAC as well as the interpretative modeling of field data from all the three underground heater experiments included in LBNL's international commitments on heater experiments.

The interpretative analyses of heater experiments, as well as the evaluation of the outcome of predictive modeling have confirmed that temperature and moisture evolution can be predicted with confidence. Related to the evolution of moisture content and buffer resaturation some questions remain related to the thermally driven diffusion, how strong this process is and why we observe some apparent inconsistencies between the modeling of different experiments; we observed some difference in moisture evolution between the Mont Terri HE-E and FE experiments that should be studied further.

Related to the mechanical evolution of the buffer, it is well known this is more complex as it depends on a number of processes such as swelling, pore pressure and thermal expansion that in turn depends on the evolution of saturation, temperature, pressure and 3D geometrical mechanical confinement effects. No mechanical measurements were conducted in the buffer for the HE-E experiment, whereas the stress in the buffer has not yet been developed very much in the case of the Horonobe EBS experiment and Mont Terri FE experiment. The stress in the buffer will take years to develop and this should be modeled in the future, especially related to the Mont Terri FE experiment which is comprehensively monitored regarding mechanical changes in both buffer and host rock.

In the remaining months of FY16 and FY17, the following activities are recommended:

- We plan to continue our work on participating in major international underground heating experiments, by continuing modeling of the Mont Terri FE experiment as one of the international modeling teams and starting on a new modeling tasks in the new DECOVALE-2019 project. These commitments in the new DECOVALEX-2019 project will replace our previous commitments related to the Mont Terri HE-E and Horonobe EBS experiments in the DECOVALEX-2015, which has been completed.

- The DECOVALEX-2019 tasks to be started in FY17 are denoted Task A and Task E in the new DECOVALEX-2019 project. Task A is related to gas migration in bentonite, and TOUGH-FLAC with dual-structure model is one of the approach that will be tested. Task E is related to upscaling of modeling results from small scale to one-to-one scale based in heater test data in Callovo-Oxfordian claystone (COx) at MHM underground research laboratory in France. This will be a perfect task for our development and application of the model capabilities we have developed and tested over the last few years within the UFD Campaign. Upscaling is an important issue for the repository design and safety calculation. The question is how to go from sample to a repository scale? This task will include modeling at difference scales, from laboratory scale to field scale heater experiments and all the way to repository scale.

- The FY17 work on the Mont Terri FE experiment will be focused on modeling of the mechanical evolution of the buffer and host rock, including the application of the BExM model at a large scale. It will be a great opportunity to apply and test the BExM at the larger scale on the FE experiment,

in particular because one the other international modeling teams is the University of Catalonia group in Barcelona, Spain that is the origin of the BExM model and they will apply BExM for the modeling of the Mont Terri FE experiment, but using a different numerical simulator. At the same time we will continue to validate and gain experiences in the use of the BExM.

- In addition to these tasks related to underground heater experiments, in FY17 we intend to study a few important technical issues that arose from the DECOVALEX-2015 work on HE-E and Horonobe experiments. The first, is related to the strength of thermally driven diffusion which did not seem consistent between different experiments, such as the HE-E and FE experiments. We will investigate different options of enhanced thermal diffusion which may resolve the small deviation between modeling and measurements of the evolution of relative humidity the buffer as observed for the HE-E experiment. The second is related to the small inconsistencies we observed in the early time stress evolution at the Horonobe EBS experiment. We now have longer term measurement data from the experiment and using this we plan to try different constitutive mechanical models, such as BBM instead of simple swelling, to investigate whether a more consistent mechanical behavior can be modeled.

- Finally, the implementation and application of a continuum damage model for the evolution of the excavation disturbed zone is another needed addition to the current model for the calculating the evolution of permeability along with damage as well as sealing and healing. Different approaches can be tested, including continuum damage models considering fracture evolution implicitly. Such a model can be benchmarked against discrete fracture modeling of damage zone fractures using TOUGH-RBSN. The goal is to build a pragmatic continuum model that can be validated against field experiments such as sealing experiments conducted in underground research laboratories.

(2)   Investigation of the impacts of high temperature limits with THMC modeling (Section 3)

Coupled THMC modeling have used to evaluate the chemical alteration and associated mechanical changes in a generic repository to consider the interaction between EBS bentonite and the NS clay formation. Two main scenarios were developed for comparison: a "high T" case in which the temperature near the waste package can reach about 200 ℃ and a "low T" scenario in which the temperature peaks at about 100 ℃. The coupling between chemical and mechanical processes is the key part of THMC model that allow us to evaluate the impact of chemical changes on mechanical behavior. In FY16, THMC models utilize dual structure (BExM) (Sánchez et al., 2005) to link mechanical process with chemistry, allowing us to simultaneously incorporate the effects of exchangeable cations, ionic strength of pore water and abundance of swelling clay on the swelling stress of bentonite. In addition, the corrosion of steel canister was considered in the chemical model to evaluate whether the iron-bentonite interaction would aggravate the negative impact on swelling stress through the formation of Fe bearing clay minerals.

Coupled THMC models using BExM were developed for a generic case using FEBEX bentonite as EBS and Opalinus clay as NS. The following observations have been concluded from the model results:

- The chemical changes as a whole reduce both total stress and effective/net stress in the bentonite buffer except the positions near the confinement rocks in the "high T" cases. However, the difference between the result computed with C-M coupling and the result without C-M coupling is very small (less than 0.5 MPa).

- Three chemical changes, including the change in the volume fraction of smectite, change in exchanged cations, and ionic strength, contribute distinctively to the stress evolution in bentonite. In current model, dissolution of smectite leads to decrease in the volume fraction of smectite which decrease the stress; because the enrichment of exchanged sodium in the interlayer, the change in exchanged cations cause the increase in stress; the infiltration of more concentrated water from clay formation to EBS bentonite leads to the increase in osmotic suction and subsequently lowers the stress. The relative importance of these three effects varies temporally and spatially and between

249

cases ("high T" versus "low T"), and the combination of these three effects determines whether chemical change enhances or suppresses the stress.

- The effect of chemical change on stress is very sensitive to the parameters related to the chemical-mechanical coupling.

- In comparison with the THMC that used extended linear swelling model (Zheng et al., 2015), THMC model using BExM showed much less chemical effect on stress. The first reason is that exchanged cations which was not able to be taken into account by extended linear swelling model, is now considered in BExM. For FEBEX bentonite, change in exchanged cations has positive effect on the stress, which cancel out the negative effect due to the change of ionic strength (via osmotic sunction) and consequently the chemical change overall has much less effect on stress in THMC model using BExM, than that in the THMC that used extended linear swelling model. The second reason is that the chemical-mechanical coupling via BExM, the dissolution of smectite was factored in directly via the volume fraction of smectite by modifying the bulk modulus for micro-structure, but in BExM, bulk modulus is a function of stress and change significantly in the model, the bulk modulus changes by smectite dissolution was overshadowed by the stress change.

- Interaction between corroded steel canister and bentonite was taken into account in a THMC model for FEBEX bentonite using extended linear swelling. The corrosion process was simplified and the model focused on the possibility of forming Fe bearing clay minerals. Based on literature survey, we included vermiculite, berthierine, saponite as the potential Fe-clay mineral forming in the model, but none of them is formed. However, including Fe-bentonite interaction leads to slightly more precipitation of chlorite and dissolution of smectite, which drives down the swelling stress reduction slightly. As far as the dissolution of smectite and swelling stress reduction is concerned, including Fe-bentonite interaction does not seem to be very important.

The current coupled THMC model greatly improves our understanding of the coupled processes contributing to chemical and mechanical alteration in EBS bentonites and NS argillite formations and answers questions regarding the thermal limit of EBS bentonite in clay repository. However, more questions remain to be answered regarding the THMC alteration of bentonites and clay formations under high temperature. Further refinement of current models and improvements for the TOUREACT-FLAC3D simulator are needed in the future. In the remaining months of FY16 and FY17 the following activities are proposed:

- The current dual-structure model contains some limitations based on its physical assumptions. Moreover, the number of parameters for BExM is much more than other mechanical models, which increases the difficulty to calibrate the model for specific materials. The model needs to be simplified to improve its numerical robustness and to apply easily to different materials.

- The THMC model using BExM will be utilized in more numerical analysis with other buffer material such as Kunigel-VI bentonite. In current model, THMC model using BExM was only conducted for FEBEX bentonite because BExM had been calibrated for FEBEX bentonite and its concept fit better bentonite with high smectite content. However, the applicability of BExM for bentonite with low smectite content such as Kunigel-VI bentonite need to be tested and how chemical-mechanical coupling via BExM work out for Kunigel-VI need to be evaluated.

- The geochemical model for the Fe-bentonite interaction will be refined and calibrated against data. In the current model, no significant iron-related bentonite alteration was found despite some laboratory and field studies have shown formation of iron-clay minerals. The geochemical conceptual model and thermodynamic data base are the key to raise our confidence on the model. In FY17, the geochemical model for Fe-bentonite interaction will be tested from data obtained in an eighteen years' *in situ* test and then simulations with higher temperature and long time will be conducted.

- Current models show precipitation of silicate minerals during illitization, which could result in the cementation of bentonite and subsequently lead to change in the mechanical properties of bentonite. Although the formation of silicate minerals is only about 3-4%, the change of mechanical properties as result of cementation needs to be quantified before we can safely conclude that silicate cementation won't significantly affect the mechanical properties.

(3) Understanding the THMC evolution of bentonite in FEBEX-DP— Coupled THMC modeling and examination of the structure of bentonite (Section 4)

Coupled THMC modeling

The FEBEX *in situ* test whichlasted more than eighteen years is extremely valuable for validating the coupled THMC model and deepening our understanding of the evolution of the bentonite barrier over the course of heating and hydration. In the FEBEX-DP project, heater #2 was dismantled and extensive THMC characterization was conducted. In FY16, the THC model was extended to THMC models and mechanical processes were simulated using both linear swelling model and dual structure BExM. The results from THMC models match reasonably the measured temporal evolution of temperature, relative humidity and stress at several compliance points in the bentonite barrier and the measured spatial distribution of water content and dry density at 5.3 years when the heater #1 was dismantled and at 18.3 years when the heater #2 was dismantled. However, the THMC models failed to explain the spatial profile of concentration at 5.3 years. The major findings from current modeling work are as follows:

- As expected, the THMC model outperformed the THC model in terms of matching measured THM data. Permeability and porosity changes due to mechanical process (swelling) were the key to match all the THM data.

- The THMC model using complex double structure BExM (THMC-BExM) did not clearly outperform the THMC model using linear swelling model (THMC-LS) in terms of matching the measured data. THMC-BExM led to a slightly better fit of measured relative humidities and stress near the heater and a slightly worse fit to the measured water content and dry density at 18.3 years. Although BExM is a more mechanistic approach and describes structural details of bentonite (the micro- and macro-structure of bentonite), it failed to manifest its superiority to the simple linear swelling model, which is probably due to that the THM data including relative humidity, stress, dry density and water content are all macroscopic such that these data cannot delineate the more mechanistic BExM from a linear swelling model.

- Although the THMC models successfully matched the THM data, they failed to desirably match the measured concentration profile of conservative species (chloride) at 5.3 years and subsequently the concentration profile of reactive species. The concentration profiles of cations (calcium, potassium, magnesium and sodium) were largely shaped by transport processes despite that their concentration levels were affected by mineral dissolution/precipitation and cation exchange. The concentration profile of pH, bicarbonate and sulphate were largely determined by chemical reactions.

- Revising the function for permeability changes in the THMC model improved the goodness-of-fit to chloride concentration profile but deteriorated the fit to water content data. It seemed there was a dilemma that the THMC model cannot match both the THM and chemical data simultaneously, suggesting that additional processes might be needed in the conceptual model.

- The THMC model predicted that concentration levels of major cations and anions at 18.3 years when the heater #2 was dismantled would continue going down in most parts of the bentonite barrier except the area very close to the heater, where the concentration would go up, which will be compared with concentration data that are expected to be available by the end of 2016.

In the remaining months of FY16 and FY17, the following work is planned:

- Thermal osmosis, a moisture movement driven by the thermal gradient, has already been incorporated in the simulator TOUGHREACT-FLAC3D. We will test if the THMC model with thermal osmosis can match both the THM data and the concentration profile of chloride.

- Once the THMC model is calibrated against THM data and measured concentration data at 5.3 years, it will be used to interpret the concentration data for 18.3 years that are expected to be available by the end of 2016.

- The chemical model will be fine-tuned, especially regarding redox condition evolution in the bentonite barrier and bentonite-canister interaction, and evolution of gases such CO_2, CH_4, and H_2.

- Ultimately, after the THMC models for FEBEX *in situ* test are fully validated with data, they will be used to explore THMC changes in the long run under higher temperature.

Quantitative characterization of the fracture network in the FEBEX samples

Although the comparison between model and THMC data has been very helpful in calibrating the "right" relationships (or key parameters for the relationships), uncertainties in other processes and interaction of coupled processes might results in non-unique sets of parameters that could lead to equal or similar reasonable fit between model and data. Checking the microstructure of the bentonite buffer will serve as additional evidence to delineate the right permeability change functions and increase the predictability of models. Bentonite samples were taken from the FEBEX *in situ* test after the dismantling of heater #2. In FY16, we have conducted a series of synchrotron X-ray microCT (SXR-μCT) examination of the microstructure of bentonite samples. The major accomplishments are as follows:

- A total of five samples from different locations were examined with three duplicates for each sample. Fracture networks for each sample were obtained and quantified. We found the variability among duplicates from the same location in bentonite barrier is significant, mostly linked to the heterogeneity of the material. Nevertheless, some weak correlation has been found: samples closer to the bentonite/granite interface tend to have a larger amount of large fractures, whereas samples close to the heater or to the center of the section tends to have larger amount of small fractures. While a truly statistically meaningful validation of this result is still needed, this correlation is clearly present in our sample survey.

- During the experiment, we also addressed some important technical issues: (1) we have found the best resolution vs. field of view compromise. (2) We have successfully developed a protocol/software for the analysis of the fracture network, focusing on the aperture value distributions.

In the remaining months of FY16 and FY17, the following experimental work is planned:

- (SXR-μCT) examination will be conducted for more samples at different locations to overcome the heterogeneity and find statistically defensible relationship between microstructure and physical parameters such as water content.

- The measured datasets will be used to build predictive tools. Besides the visualization and quantitative characterization of bentonite, SXR-μCT is also able to provide 3D volume datasets which can be used in a digital rock physics context: if the volume(s) obtained are meaningful, in terms of resolution vs. field of view, for measuring a given property, specific software able to calculate those properties (such as permeability, invasion of non-wetting fluids, diffusion, etc.) from the datasets are available.

(4) Discrete Fracture Network (DFN) Approach for THM Damage Modeling in Argillaceous Rock (Section 5)

In FY16 we further developed TOUGH-RBSN with the goal of producing an efficient tool for understanding the variety of characteristics in THM processes in argillaceous rocks, including fracture damage and fluid driven fracture propagation. The series of simulations presented in this report section demonstrate the current TOUGH-RBSN capabilities for modeling tightly coupled HM processes and the RBSN approach for mechanical anisotropy in elastic and fracture responses. For the ongoing development, a refinement could be made into the TOUGH-RBSN code to rigorously evaluate the change of fracture porosity as a response of the mechanical fracture aperture change, which will be addressed in future work. In addition, the ongoing work on the dynamic version and porting that version to high performance computing will provide an avenue for modeling larger scale problems, including 3D complex fracture geometry.

The TOUGH-RBSN code and the developed algorithms for fluid driven fracturing have been applied to predictive and interpretative simulations for hydraulic fracturing of the laboratory experiment samples. The hydraulic fractures reproduced in the simulations compare favorably to the experimental results with respect to the injection pressure evolutions and the resulting fracture paths. As for the mechanical anisotropy, uniaxial compression tests on Opalinus Clay have been simulated in order to demonstrate the validity of the new modeling scheme. Thereafter, updated simulations of EDZ formations for the Mont Terri HG-A microtunnel have been conducted. Qualitative comparisons show that the simulation results closely match field observations, in which non-uniform failure patterns attributed to the anisotropic mechanical characteristics form around the excavation zone and the presence of fault planes significantly influences the failure patterns. For FY17, recommended work is as follows:

- We plan to complete the dynamic simulation framework, and verification and validation of the simulation code will be provided through geomechanics examples including fracturing processes. Also, by high performance computing in the dynamic simulation code, our modeling capacities will be extended to fully 3D large scale problems.

- More realistic simulations will be available by setting the fracture porosity dependent on the fracture aperture width in the TOUGH-RBSN coupling modules.

- Relating to the DECOVALEX-2019 task, TOUGH-RBSN code can be applied to the gas migration in bentonite clay, in which the clay material often dilates to create preferential flow pathways. We will attempt to demonstrate such preferential pathways using the discrete modeling approach.

- Swelling of a ductile/expanding shale matrix will be simulated to investigate the time-dependent deformation of the rock, including fracture closure/sealing, which significantly impacts on the hydrological properties of the rock material.

7. Acknowledgents

Experimental studies of Engineered Barrier Systems conducted at Los Alamos National Laboratory (FY16) (PART III)

1. Introduction

The U.S. Department of Energy has designed the Used Fuel Disposition Campaign to investigate the design and safety function of generic nuclear geologic repositories in a variety of geologic settings. The evaluation of engineered barrier system (EBS) concepts and interaction with the wall rock (i.e., natural barriers), waste canisters, or other EBS interfaces are important to the long term performance and safety of geologic repositories (Nutt et al., 2011, Jove-Colon et al., 2011). The European community, especially the French, have investigated bentonite stability in contact with steel under a variety of experimental conditions in an attempt to replicate repository conditions (Pusch 1979; Madsen 1998; Meunier et al. 1998; Guillaume et al. 2003; Wersin et al. 2007; Mosser-Ruck et al. 2010; Ferrage et al. 2011). The majority of their research was focused on lower temperature environments and atmospheric pressures. Our experimental program for FY16 aims to characterize how EBS components react and change in the presence of Opalinus Clay at reasonable high temperature (300 ^{o}C, 150 Bar) in-situ repository conditions.

1.1 Background

One of the more accepted ideas for high-level nuclear waste disposal is to emplace the steel waste canister in a geological repository with a bentonite barrier between the canister and host rock (Pusch 1979; Meunier et al. 1998). Bentonite is used to provide 1) a physical barrier to prevent fluid seeping in from natural surroundings and interacting with the waste package, 2) a chemical barrier by attenuating actinide migration if a release occurs. Furthermore, the bentonite's swelling capacity has the capability of self-sealing if cracks develop within the bentonite due to shrink-swell phenomena. However, there remain large uncertainties regarding the long-term stability of bentonite at potential repository conditions, particularly, under prolonged periods of high thermal loads. There have been numerous investigations on the stability of bentonites under various repository conditions and in contact with various metals replicating possible canister compositions (Pusch 1979; Madsen 1998; Meunier et al. 1998; Guillaume et al. 2003; Wersin et al. 2007; Mosser-Ruck et al. 2010; Ferrage et al. 2011).

This report summarizes the various authigenic minerals occurring within hydrothermal experiments replicating a high temperature repository environment. The emphasis is on; 1) Opalinus wall rock interactions with EBS backfill, 2) copper alteration and corrosion rates, and 3) steel/bentonite interface phase reactions. The intent of Section 1 will examine various reactions that include unprocessed Wyoming bentonite, the clay/metal interface, and the metal/clay/host rock components. Much of the characterization and discussion on the early EBS (1-12) results have been published in Cheshire et al. (2013; 2014). Characterization of both the pre-run materials and post experiment phases of experiments EBS-1 through -17 were discussed in Caporuscio, et al. (2015) to better describe the processes that progress during the hydrothermal reactions. In addition to expanded analyses of the earlier reactions, experiments on host-rock (Opalinus Clay) interaction were conducted to further our understanding of this complex system. Those experimental starting materials are shown in Table 1 The initial Opalinus clay synthetic groundwater depicted in Table 2.

Table 1 Initial components and reaction conditions for EBS experiments in the presence of Opalinus Clay.

Experiment	Clay, g	Brine, g	EBS Component	Run temp, °C	Run time
OPALINUS CLAY EXPERIMENTS					
EBS-14	14.86	128.1	**Opalinus Clay**	300	6 weeks
EBS-15	14.72	158.5	Opal - 316SS	300	6 weeks
EBS-17	14.44	155.2	Opal – Cu	300	
					6 weeks
EBS-18	12.77	117.0	Opal – LCS	300	6 weeks
					6 weeks
EBS-19	14.82	120.0	Opal – 304SS	300	

Table 2: Synthetic groundwater chemistry used in the Opalinus Clay experiments. All values were measured at 25 C (n.m. = not measured)

	Type Solution	Actual Solution
Species	mg/L	mg/L
Ca^{2+}	421	426
Cl^-	5672	6470
CO_3^{2-}	162	n.m.
K^+	221	225
Na^+	3885	3846
Si	5	1
SO_4^{2-}	2305	998
Sr^{2+}	27	0.16
TDS	11502	12153
pH	7.24	7.50
Experiment Used		EBS 14, 15, 17

Section 2 will be a summary of copper alteration and reaction rates, as first described in Caporuscio et al. (2015). Section 3 which describes the mineral interface between bentonite backfill and steel was also summarized by Caporuscio et al. (2015) and will be expanded to include a description of pit corrosion occurring on low carbon steel (EBS-18).

1.2   Methods

Analytical methods (Experimental Setup, Mineral characterization, and aqueous geochemical analyses) remain unchanged from Caporuscio et al. (2014). They are listed in Appendix A for convenience.

Post-reaction copper foils were mounted in epoxy then polished exposing the cross-sectioned surfaces. These foil mounts were then imaged using two different methods; SEM and reflected light microscopy. For each EBS run 17 to 25 images were taken for each method. These image locations were mapped and chosen to give a random distribution of the corrosion in the foils. All images were saved and analyzed in Photoshop. Each image had 7-20 data points extracted from it. The thickness of the chalcocite layer and the depth of the corrosion pitting were measured and then labeled for future analysis. Corrosion rates were determined by dividing the average corrosion pit depth by the number of days in the run.

2.   Results

2.1   EBS 18 Experiment

This section focuses on experiment EBS 18 (bentonite –Opalinus Clay- low carbon steel) has detailed results in Appendix B (water chemistry), Appendix C (XRD analysis), Appendix D (electron microprobe data), and Appendix E – (SEM images). The aqueous geochemistry results of Appendix B have the following elements of note. Both Ca and Fe go into solution beginning at the 3-week mark (half way through the experiment). The Ca stays in solution, however Fe precipitates upon quenching. Potassium (K) and Na go into solution earlier in the experiment, and both elements begin to precipitate at the two-week mark (analcime growth). The trend of SiO_2 is more ambiguous, where filtered and unfiltered cations do not trend together. There is early solution of SiO_2, however SiO_2 then forms solids (Quartz growth) beginning at the second week. Note that there is a dramatic increase in sulfate anions (pyrite breakdown) from the second week till the end of the experiment.

Analysis of the reaction products by QXRD (Appendix C) are not well constrained. Furthermore, the results are in part at odds with electron microprobe analyses and SEM EDX analyses. Although clinoptilolite and feldspar match other analytical method characterization, the muscovite, ferrosilite and chlorite determinations are suspect. Samples are presently being rerun by a facility that specializes in clay mineralogy.

Appendix D shows the results of microprobe analyses. Clinoptilolite and analcime-wairakite zeolites are characterized. Abundant authigenic quartz was observed but analyses were not conducted. The rest of the microprobe analyses were performed on the steel / bentonite interface. Interior to the pit corrosion (Appendix E, images E.7 and E.8) the mineral formed is goethite, directly at the steel clay boundary are discontinuous sulfide grains (unable to analyze due to small size), and finally proximal to the steel layer is a layer of Fe-saponite. Images of the saponite are in Appendix E.

SEM / EMS backscattered images depicted in Appendix E were characterized by EDX for mineral identification. Images E.1 and E.2 portray analcime-wairakite euhedral isometric crystals. Clinoptilolite is shown in images E.3 and E.4. Radial growth plagioclase is seen in

image E.5. Fe-saponite / low carbon steel interface is depicted in image E.6. Pit corrosion of the low carbon steel in shown in images E.7 and E.8.

2.2   Copper Corrosion.

2.2.1   Copper Reaction with Bentonite

The primary corrosion product for all experiments was chalcocite (Cu_2S) with minor covellite (CuS) appearing in some runs (EBS-17) (Appendix C, C.2.). Chalcocite formed a hexagonal morphology ranging from discrete plates to completely coalesced patches on the copper surface (Appendix E.9. A & C). Chalcocite crystallized on the copper surfaces due to available H_2S from the decomposition of pyrite in the hydrothermal environment. It is evident that the formation of these surface bound minerals was from the direct crystallization from solution in the localized environments surrounding the metal plates.

There were minor amounts of an unknown fibrous material associated with the copper surface (Appendix E.9.B.). Corrosion seemed to take place with an initial dissolution of the copper developing dissolution features on the copper surface (Appendix E.9.A.).

2.2.2   Copper Corrosion

The thickness of the chalcocite layer and the depth of the corrosion pits varied with both temperature profile and experiment duration. In most of the experiments the chalcocite forms a thick layer over a corroded/pitted layer. This layer is visible both in the SEM images of Cu corrosion (Appendix E, E.10) and the reflected light images (Appendix E, E.11). A notable exception to this is the Opalinus Clay run, EBS-17, where the chalcocite layer was found to be either absent or extremely thick. For the ramped temperature experiment, EBS-4, the average chalcocite thickness was 3.0(1) μm. In the isothermal experiments in both bentonite (EBS-11) and Opalinus Clay (EBS-17), the layer was thicker, 8.2(4) μm and 5.6(4) μm respectively. The chalcocite layer was thinner in the six-month long-term cooling run (EBS-16) with a depth of only 2.6(1) μm.

Chalcocite layer thickness generally correlated with the amount of pit corrosion the Cu foil had undergone, but also depended on the sulfur content of the system. The initial overall thicknesses of the copper foils were ~ 63 μm. For EBS-16 and EBS-17, the width of the corrosion pitting was also measured to give an approximate aspect ratio for the corrosion pits. Both the thickness of the chalcocite and the depth of the pits formed approximately normal distributions for all EBS runs, giving confidence that a random distribution was measured. The only run differing from this pattern was EBS-17, which exhibited two different corrosion environments. One averaged a corrosion pit depth of 9 μm, which is in alignment with the copper corrosion measurements on other EBS runs. The other behavior resulted in significant pitting depths up to and above 25 μm. For the four experiments a total of 849 measurements were made, 414 of the chalcocite layer and 445 of the pit depths. The short-term isothermal experiments in both bentonite and Opalinus Clay yielded similar average pit corrosion depths, 13.5(6) μm and 13.1(6) μm respectively. The ramped experiment (EBS-4) incurred less corrosion, having an average pit depth of only 5.7(2) μm. However, the six-month experiment (EBS-16) copper foils developed only 4.3(1) μm corrosion depths, which is similar to that of EBS-4, but sustained over a much longer period of time. Pitting corrosion was restricted to the exterior surfaces of the rolled copper foil. The surfaces within the rolled copper foil were protected from the brine and thus did not suffer significantly from either chloride or sulfide attack.

Corrosion rates (Appendix F, Table F.1) were determined by dividing the average corrosion pit depth by the number of days in the run. Corrosion rates from the two isothermal experiments on bentonite and Opalinus Clay are within experimental error of each other and displays the highest corrosion rates measured. Copper foils from the Opalinus Clay experiments exhibited several regions of extreme corrosion (Appendix E, E.10 D and Appendix E, E.11 D). These parts of the copper foil were corroded > 50% and show deep channeling in the Cu foil. The corrosion rate for the five-week ramped experiment (EBS-4) was half that of the isothermal experiments, 0.16(6) μm/day for the ramped versus ~ 0.31 μm/day for the isothermal experiments. The six-month long-term cooling experiment had a much smaller average corrosion rate of 0.024(8) μm/day. This is consistent with the reduced corrosion found in the long-term experiment.

The nature of corrosion pitting in the copper foils was similar for all experiments. The average aspect ratio of the width to the depth of the corrosion pits found in the experiment with the least corrosion, the six-month extended cooling run, was 1.4(9). The run with the most corrosion, the six week Opalinus Clay run, had a nearly identical aspect ratio of 1.3(8). The similarity of these aspect ratios indicates that although more rapid corrosion is occurring during the six-week experiment, the pit shapes are unaffected by rate and retains the same nature regardless of the amount of corrosion the copper foil has undergone. A wide variety of corrosion pit structures exist, but extremely deep corrosion pits are just as common as shallow wide ones.

2.3   Steel /Bentonite Interface Mineralogy

304 SS. 304SS underwent uniform interface reaction during the 300°C experiments. Post-reaction 304 SS formed a layer of smectite and chlorite covering the surface of the steel plate (Appendix E., E.12. A & B). However, smectite was the only phyllosilicate associated with the reaction site products in the six week, 300°C reaction (Appendix E., E.12. C & D). The primary type smectite associated with the steel surface appears to be an Fe-saponite. Smectite expands upon ethylene glycol saturation to 16.8 Å (with 002 at 8.35 Å) suggesting no significant amount of mixed-layering is present. Pentlandite ((Cu, Ni, Fe)-sulfide) appears to have formed sparingly in both 304 SS experiments along with an unknown fibrous material (Appendix E., E.12. A & B). The smectite and chlorite morphologies tend to be fairly consistent producing a bladed to micaceous habit with a rose-like texture (Appendix E., E.12). The initial montmorillonite has a distinctly different morphology (foily; Appendix E., E.12C) suggesting smectite associated with the 304SS is newly formed. The interface reaction products have thicknesses ranging from 9 to 44 μm with crystallites occurring perpendicular to 304SS substrate (Appendix E., E.12. D). There was no significant change in the interface layer thicknesses with increased reaction time at 300°C. Chemical analyses of post-reaction 304SS and the smectite mantle indicates there was a slight Fe transfer from the 304SS forming a Cr-enriched steel outer layer and a Fe-rich smectite and chlorite coating (Appendix E., E.13). The reaction products do include varying degrees of Cr and Ni substitutions. Accurate chemical formula for the interface reaction products are not possible due to the intimate mixing of multiple phases. The average bulk chemistry of the corrosion layer is provided in Appendix F.2. Fe-rich phyllosilicates that formed on steel plates in the ramped experiments have two 06ℓ diffraction bands 1.536 and 1.523 Å (9.138 and 9.216 Å b-parameters), corresponding to trioctahedral chlorite and smectite (Appendix C, C.2.). It is uncertain which minerals species correspond to the b-parameters as there is overlap in the unit-cell parameters between the Mg, Fe-saponites (9.120 (Mg^{2+}) to 9.30 (Fe^{2+}) Å) and chlorite (9.228 to 9.294 Å) species (Kohyama et al. 1973; Moore and Reynolds 1997). The Fe-smectite

produced in the six week, 300°C experiment has a 1.547 Å (9.282 Å b-parameters) 06ℓ diffraction band, consistent with Fe-saponite (Kohyama et al. 1973).

316SS. 316 SS underwent exfoliation corrosion during the ramped and isothermal, 300°C experiments. Post-reaction 316 SS formed smectite dominated interface reaction products with some chlorite covering the surface of the steel plate (Appendix E, E.14. A & B). However, smectite was the only phyllosilicate associated with interface reaction products in the six week, 300°C reaction (Appendix E, E.14. C& D). The primary type smectite associated with the steel surface appears to be an Fe-saponite. Smectite expands to 16.8 Å (with 002 at 8.44 Å) upon ethylene glycol saturation suggesting no significant amount of mixed-layering is present. However, the six weeks, 300°C smectite product expands to 16.3 Å (002 at 8.25 Å) upon ethylene glycol saturation indicating a possible decrease in swelling capacity. A pentlandite-like ((Cu, Ni, Fe)-sulfide) material appears to have also been formed in both 316SS experiments along with what appears to be fibrous sulfides (Appendix E, E.14.D). The smectite and chlorite morphologies tend to be fairly consistent producing a bladed to micaceous habit with a rose-like texture (Appendix E, E.14). The interface reaction products have thicknesses ranging from 20 to 40 μm with crystallites occurring perpendicular to 316SS substrate (Appendix E, E.15 and E.16). There was no significant change in the interface reaction layer thicknesses with increased reaction time at 300°C. Chemical analyses of post-reaction 316SS and mantling products indicates there was significant Fe leaching from the 316SS forming a Cr-enriched steel outer layer up to 4 μm thick. The Cr-enriched layer also underwent oxidation and sulfidation producing a noticeable alteration zone (Appendix E, E.15). Smectite and chlorite coatings were enriched in iron most likely from the iron leached from the 316SS (Appendix E, E.16). Fe-rich phyllosilicates that formed on steel plates in the ramped experiments have 06ℓ diffraction bands 1.535 (9.210 Å b-parameters), corresponding to a trioctahedral phyllosilicate (Appendix C, C.4.; Kohyama et al. 1973; Moore and Reynolds 1997). It is uncertain which minerals species correspond to the b-parameters, however the b-parameter is probably related to an Fe-saponite due to a smectite dominance in the corrosion products. The Fe-smectite produced in the six week, 300°C experiment has a fairly broad 1.54 Å (9.24 Å b-parameters) 06ℓ diffraction band, consistent with Fe-saponite (Kohyama et al. 1973).

Low-carbon steel. Low-carbon steel underwent pitting corrosion during the ramped and isothermal, 300°C experiments. Post-reaction low-carbon steel developed a smectite coating the steel plate surfaces (Appendix E., E17). Unlike the 304SS and 316SS, there was no evidence of any chlorite phases present in the interface reaction product of the low-carbon steel. The primary type smectite associated with the steel surface appears to be an Fe-saponite. Smectite expands to 16.6 Å (with 002 at 8.32 Å) upon ethylene glycol saturation suggesting no significant amount of mixed-layering is present. Also, pyrrhotite ($Fe_{1-x}S$) platelets formed concurrently with the smectite phases as determined their spatial distribution (Appendix E., E17C). Smectite morphology is varied between a honeycombed texture and rose-like texture with a bladed to micaceous habit (Appendix E., E17 B & D). In addition to the small scaled textures, there is an overlying botryoidal texture with the interface reaction products (Appendix E., E17 C). These interface reaction products have thicknesses ranging from 13 to 56 μm with additional ~ 7 μm corrosion pits. The bladed to micaceous crystallites tend to occur with the longer dimensions perpendicular to the steel substrate (Appendix E., E17 and E18). Chemical analyses of post-reaction low-carbon steel and interface reaction products indicate no chemical fractionation associated with the phase transformation process. Accurate chemical formula for the interface

reaction products are not possible due to the intimate mixing of multiple phases. The average bulk chemistry of the interface reaction layer is provided in Appendix F, Table F.3. There does appear to be oxidation and sulfidation associated with the surface (Appendix E., E18). Smectite is enriched in iron most likely due to the iron dissolved from the steel (Appendix E., E18). The Fe-rich smectite has 06ℓ diffraction bands of 1.547 Å (9.264 Å b-parameters), corresponding to a trioctahedral smectite (Appendix C., C.5); Kohyama et al. 1973; Moore and Reynolds 1997).

3 Discussion

3.1 EBS 18 Experiment

Cheshire et.al. (2014) wrote a comprehensive work on silicate phase transformations and Caporuscio et.al. (2015) summarized the previous experiments produced for the Argillite EBS experimental research program. Therefore, discussions will be limited to the EBS 18 experiment produced this year. As noted, equipment issues had put the laboratory in stand down mode for over one year, reducing the number of experiments produced. This experiment (EBS-18) sat pressurized at 140 bar and room temperature for 9 months waiting for the equipment issues to be resolved.

To summarize, EBS-18 was run isothermally at 300 ºC for 6 weeks at 150 bar pressure. The components are bentonite clay, Opalinus Clay, Opalinus Clay synthetic groundwater, low carbon steel coupons, and Fe/Mt solid buffer. The phyllosilicates produced in this experiment are equivalent to previous isothermal 300 ºC experiments. The starting montmorillonite converted to smectite (Figure E.3), while the clay material in contact with the steel coupons altered to Fe saponite (Figure E.6). The zeolite phases produced in this experiment include both clinoptilolite (Figure E.3 and E.4.) and an analcime$_{37}$-wairakite$_{63}$ isometric zeolite Figures E.1. and E.2.). When plotted on Si/Al vs percent analcime diagram (see below), certain trends become obvious. There is a clear solid solution series from EBS 14 to EBS 16, with silica increasing slightly toward the analcime end-member. All samples on the trend line were isothermal experiments at 300 ºC. EBS-12 and EBS 18 fall slightly above this line. Sample EBS 12 was slightly under saturated in brine, and sample EBS 18 was held at high pressure for 9 months, as discussed above. This co-existence of both clinoptilolite and "wairakite" within EBS 18 may also be due to long-term pressurization of the reactant material. It is believed that the clinoptilolite was allowed to recrystallize from the original small grains and also incorporate the remnant glass shards into the clinoptilolite. In addition, the data cluster with a Si/Al ratio between 4.5 and 5.0 (EBS 1, EBS 2, and EBS 6) seemingly relates to clinoptilolite and were either the ramped temperature experiment (held at 300 ºC for only a short time) or was the starting material (MR Bentonite) from Colony, Wyoming.
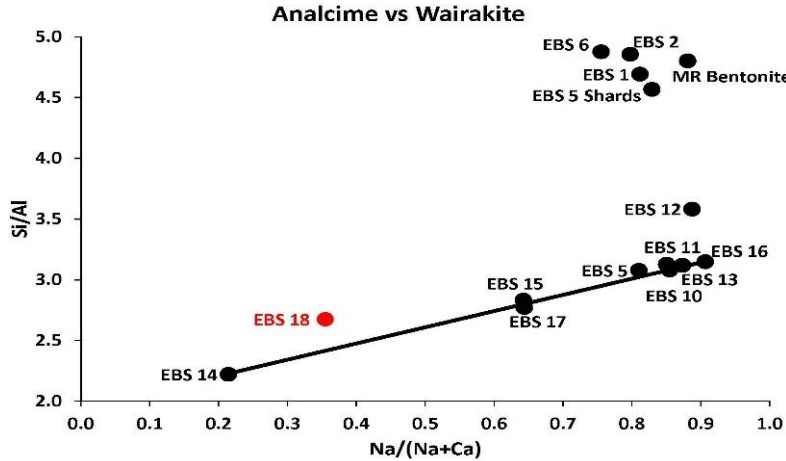
Figure 1. Graph of Si/Al ratio versus Na/(Na + Ca) composition of analcime-wairakite series. Trends are dependent on mineral bulk composition and temperature profile. The data cluster at high Si/Al for EBS 1, EBS 2, and EBS 6 appears to correspond to clinoptilolite. The EBS18 data point in red denotes a wairakite composition in the opalinus clay experiment (see text).

There is also abundant authigenic growth of quartz and plagioclase (Figure E.5.) in the run products of EBS-18. This mineral assemblage (wairakite + plagioclase + quartz + water) was characterized Liuo (1970) for the synthesis of ordered wairakite.

3.2   Copper Corrosion

3.2.1 Copper interactions

Copper corrosion in a sulfide-bearing, compacted bentonite environment has been suggested to be a function of both sulfate reducing bacteria growth conditions (e.g., available carbon, sulfate concentrations, and electron donors) and geochemical parameters effecting sulfide diffusion (e.g., bentonite density, fluid content, and ferrous iron concentrations) to the copper surfaces (Pederson 2010). Overall reactions associated with sulfide-induced copper corrosion involving chalcocite (Cu_2S) formation can be written as,

$$2Cu° + H_2S \rightarrow Cu_2S_{(s)} + 2e^- + 2H^+ \qquad (1a)$$

$$2Cu° + HS^- \rightarrow Cu_2S_{(s)} + 2e^- + H^+ \qquad (1b)$$

$$2Cu° + S^{--} \rightarrow Cu_2S_{(s)} + 2e^- \qquad (1c)$$
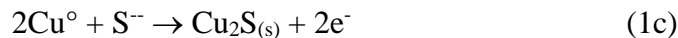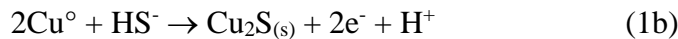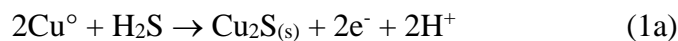
One reason for listing these three reactions is to denote the importance of H_2S, HS^-, and S^{--} on activating copper corrosion and the appearance of chalcocite ($Cu_2S_{(s)}$) as the product sulfide solid (Macdonald and Sharifi-Asl, 2011). Under anoxic and high temperature repository conditions, chloride and sulfide corrosion will be the primary (non-radiolytic) mechanism affecting copper waste canisters (King et.al, 2010). Biotic sulfate reduction mechanisms probably will be minimal at high-temperature conditions; therefore the dominant sulfide source is likely from sulfide minerals associated with the original bentonite barrier material or the wall rock. The electrochemical mechanisms of copper corrosion in the case of interactions with sulfide- and chloride-bearing solutions under anaerobic conditions have been advanced by Chen et al. (2010, 2011a); Chen et al. (2011b); King (2010); King and Lilja (2011); King et al. (2013). Macdonald

and Sharifi-Asl (2011) provides a comprehensive thermodynamic description of copper stability under various conditions including temperature effects. It is expected that in the presence of Cl-bearing pore solutions or brines, the predominant Cu aqueous complex under nominally anoxic conditions in the presence of bentonite clay and copper metal is $CuCl_2^-$ (King et al., 2013; Schwartz, 2008). The appearance of chalcocite in copper corrosion experiments quantifying the formation of sulfide films has stimulated investigations to understand the effects of such film on the copper surface such as the influence on corrosion rates and mechanisms, and the level of protectiveness (Chen et al., 2011a). According to Chen et al. (2010, 2011a), the suggested reaction leading to the formation of chalcocite in Cu-Cl solutions can be expressed as:

$$CuCl_2^- + HS^- \rightarrow Cu_2S_{(s)} + 4Cl^- + H^+ \tag{2}$$

The stepwise mechanism proposed by these authors involves adsorption of the Cu $(HS)_{ads}$ species and its subsequent decomposition to $CuCl_2^-$ and HS^- leading to $Cu_2S_{(s)}$ precipitation as described by reaction (2). However, other mechanisms based on the interaction with Cu-Cl solutions can potentially explain $Cu_2S_{(s)}$ film growth in the presence of Cu^+ and HS^- (e.g., $2Cu^+ + 2HS^- = Cu_2S_{(s)} + H_2S$). Chen et al. (2010) proposed a mechanism for $Cu_2S_{(s)}$ film growth with low porosity during the corrosion process. Although Chen et al. (2010) study suggest that growth of a porous $Cu_2S_{(s)}$ film can be described as diffusion-limited, the heterogeneous nature of the bentonite clay cover on the copper surface (in addition to porous $Cu_2S_{(s)}$) could allow for sufficient porosity for the transport of HS^- and copper aqueous species interacting with both $Cu_2S_{(s)}$ and copper metal interfaces. This observation is indicated by the growth habit of $Cu_2S_{(s)}$ between clay crystals identified in the current experimental work. Mitigating sulfide-induced corrosion might be achieved by maintaining a high bentonite density thereby restricting sulfide diffusion (Pederson 2010). However, given the dynamic nature of bentonite swelling, its porous nature, and moisture transport in the clay EBS such mitigation could be difficult to achieve.

The equilibria between copper metal, $Cu_2S_{(s)}$, and $CuCl_2^-$ can be represented by the following reactions:

$$Cu° + H_2S + CuCl_2^- = Cu_2S_{(s)} + 2Cl^- + H_2 \tag{3a}$$

$$Cu° + HS^- + CuCl_2^- + \tfrac{1}{2}H_2 = Cu_2S_{(s)} + H_2S + 2Cl^- \tag{3b}$$
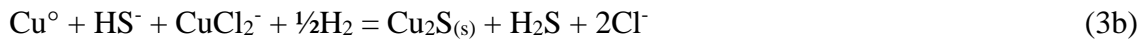
The Eh potential for the invariant point equilibria between copper metal, $Cu_2S_{(s)}$, and $CuCl_2^-$ at 200 and 300 °C are depicted as Pourbaix diagrams in Figure E.19 (a,b). As shown in these diagrams, the Eh potentials are relatively low at the three-phase invariant point, which decreases with increasing temperature. Moreover, the computed equilibrium pH at this invariant point shifts toward near-neutral values with increasing temperature. These diagrams were generated using the CHNOSZ software package (Dick, 2008) and associated thermodynamic database. The diagram was generated assuming activities of SO_4^{--}, Cl^-, and Cu^+ of 1.0×10^{-6}, 0.2, and 1.0×10^{-6}, respectively. The aqueous species activities were constrained by the solute concentrations used in these experiments. Thermodynamic data for $Cu_2S_{(s)}$ in CHNOSZ is sourced to Helgeson et al. (1978).

One question regarding copper surface alteration is whether surface passivation occurs when considering in the long-term barrier material performance of a repository system. There was no substantial change in the mineral thicknesses or surface coverage on copper between the ramped and isothermal, 300°C experiments. The studies by Chen et al. (2010, 2011a) indicate similar mineral surface growth at lower temperatures. Mineral growth restrictions during

experiments could possibly be from copper passivation, but can also be explained by depletion in the corrosive species or surface transport. In the case of copper, as sulfide is depleted from the system chloride (in an anoxic environment) becomes the primary corrosive agent, subsequently altering the corrosion rate (King et al. 1992; Carlsson 2008). However, further work needs to be conducted to determine if surface passivation does develop in this system or rather a change in the chemical environment has altered the corrosion rates.

3.2.2 Corrosion Rates

A multitude of studies have investigated copper corrosion rates. Many of these previous experiments focused on the corrosion of Cu in the air or seawater in application to industrial and naval uses (Kass 1990; Nunez et al. 2005; Sandberg et al. 2006). Copper corrosion has been studied with respect to sulfur and chlorine content in the context of both nuclear repositories and other saline industrial applications (Escobar et al. 1999; Abghari 2013; Bojnov and Makela 2003; Taniguchi and Kawasaki 2008; Chen et al. 2010, 2011a; Kumpulainen et al. 2011). Since long-term experiments on the scale of nuclear repository lifetimes are not possible, archeological findings on the wear of copper artifacts give the best long-term corrosion rates available (Demchenko et al. 2004; Hallberg 1988). The long-term corrosion rates found from these artifacts range from 0.01 to 1.51 μm/yr. The atmospheric and marine corrosion rates are even smaller than this, ranging from 0.0012 to 0.8 μm/yr. in marine water and atmosphere respectively (Nunez et al. 2005). While these rates provide a basic guideline for the corrosion of copper in the nuclear repository, these experiments are not specialized enough to give specific insight into the lifetime of the Cu canister in an EBS.

A handful of experiments have delved into the specific conditions found in repository environments: bentonite clay pack, saline groundwater and elevated temperatures/pressures. Kim et al. (2007) investigated copper corrosion in wet bentonite with synthetic and natural groundwater for 170 to 1231 days at 70°C. These long-term bentonite and saline brine experiments yielded corrosion rates an order of magnitude or more (0.18-0.87 μm/yr.) below those found during the EBS runs in this study (8.8-116 μm/yr.). Kumpulainen et al. (2011) mixed MX-80 bentonite with 0.5 M NaCl solution for 8.2 years yielding a lower corrosion rate (0.035 μm/yr.) compared to the rates from Kim et al. (2007) and much smaller than rates determined from this study. While both Kim and Kumpulainen's experiments used materials found in an EBS, they did not implement environmental controls such as high temperature and MPa-scale pressures.

Rosborg et al. (2005; 2011) investigated copper bentonite combinations with saline ground water. Their studies yielded corrosion rates between 2.3-20 μm/yr. for one 4.25 years experiment (range is due to measurement technique), which is in agreement with the long-term rate (EBS-16) found in this study. Rosborg et al. (2011) showed that bentonite mixed with oxic saline groundwater for 3 and 4.2 years, yielded copper corrosion rates of 0.4 and 1.6 μm/yr., respectively. These rates are lower compared to the corrosion rates from the current study, but are of the same magnitude as the long-term (180 days) rate found in EBS-16. Taniguchi and Kawasaki (2008) studied mixtures of bentonite and sand with varying NaS_2 concentration at 80°C. As a control they also included a study of copper corrosion in a simple solution with varying NaS_2 concentration. They found corrosion rates increased with increasing NaS_2 concentrations, 15 μm/yr. at 0.1 M NaS_2 and 0.55 μm/yr. at 0.001 M NaS_2. These results validate that sulfur concentrations play a major part in the corrosion process and that relatively high

corrosion rates found in this study are likely influenced by the sulfur content of the brine and packing material during the run.

3.2.3 Factors Influencing Corrosion

Several environmental and compositional factors contribute to the higher corrosion rates found in this study. First of all, previous experimental data was collected at significantly lower temperatures than those used in this study. Full EBS experimental data including P-T-t conditions, and chemistry data can be found in Caporuscio, et.al. (2015). For example, EBS-4 started at 25°C and increased to 300°C (573 K) before cooling. The other copper EBS runs all reached 300°C at the outset of the experiment. The highest temperature recorded in similar experiments is 80°C (353 K) used by Taniguchi and Kawasaki (2008) followed by 70°C (343 K) used by Kim et al. (2007). The experiments of Rosborg et al. (2005; 2011) did not use elevated temperatures. Elevated temperatures increase corrosion rates, especially at neutral to lower pH (Antonijevic and Petrovic 2008; Boulay and Edwards 2001). High temperatures used in this study were chosen to closely simulate a high heat load nuclear repository. The 299°C temperature estimate for a nuclear repository given by Greenberg and Wen (2013) indicate high temperatures better simulate the corrosion activity in a new repository. Other, slower, corrosion rates will only come into play as the heat dissipates over 100 year timescales. Thus, higher corrosion rates found for all EBS test cases are a representation of maximum potential corrosion in the repository scenario we developed, early failure at high temperature / high aqueous water influx due to hydrostatic pressure.

The high corrosion rates measured during this study are also influenced by pressure. The pressure during experimental runs was 15-16 MPa for all EBS runs. Few experimental studies have dealt with corrosion rates at pressures in the MPa range. A study by Betova et al. (2003) investigated the effect of saline groundwater compositions on copper corrosion with no clay included. These experiments were run at 14 MPa and 80°C, which is a good estimate for pressure within a repository if not the temperature. Nuclear waste repositories will likely be 400 to 700 m deep and have to withstand an evenly distributed load of 7 MPa hydrostatic pressure from groundwater and a 7 MPa pressure from swelling of the bentonite (King et al. 2002). Betova et al. (2003) measured corrosion rates of 5.5-17 μm/yr. over six days. These rates are within an order of magnitude in agreement with the results from this study and indicate that elevated pressure may have more of an effect than previously estimated by King et al. (2002), who assumed the pressure effect to be ~ 10% based on theoretical estimates of equilibrium constants at pressure. Further experimental studies at pressure are needed to elucidate the effect of pressure on Cu corrosion.

The clay and brine composition also make a significant difference in corrosion rate. The brines used in the EBS 4, 11, 16 and 17 runs are listed in Table 1. The composition of the brine for the three bentonite runs (EBS 4, 11 and 16) was similar. The EBS-4 brine contained the highest concentration of Cl- while the EBS-16 brine contained the highest concentration of sulfate. Despite the relatively sulfur and chloride rich compositions, both EBS-4 and EBS-16 underwent less corrosion than EBS-11. This effect is likely due to the differences in temperature profile and is not a sign of different corrosion behavior. The brine used in the Opalinus Clay experiment (EBS-17) was especially high in both chloride and sulfur, an order of magnitude higher in concentration. Several previous studies have concluded that increasing Cl and sulfur content increases the copper corrosion rate (Taniguchi and Kawasaki 2008; Abghari et al. 2013).

The increased corrosion in EBS-17, which shows corrosion tracks penetrating over half of the copper foil in some areas, is due to compositional differences in both brine and in clay. Added to the significant amount of Cl^- and SO_4^{--} in the brine, these compositional differences explain the abundant corrosion of EBS-17. The corrosion of the outer copper foil of EBS-17 was uneven, leading to the interpretation that surface activation reactions by either chloride or sulfur species were inhibited or kinetically-hindered growth of $Cu_2S_{(s)}$ persisted locally throughout the foil's surface.

A final consideration for the corrosion rates measured is the duration of the experiments. A barrier system in a nuclear repository will be required to sustain for 10^5 to 10^6 years, but obviously no experiments can be run at those timescales. Extrapolation must then be used from measurements made on more human timescales in the laboratory. What timescale is best used becomes the essential question. Three experiment durations were used in this study: 5 weeks, 6 weeks and 6 months. The three 5-6 week experiments (EBS 4, 11 and 17) all yield corrosion rates between 0.16(6) - 0.32(15) μm/day. EBS-16, however, has a much lower corrosion rate, only 0.024(8) μm/day or 8.8(3) μm/year. A similar decrease in corrosion rate, although less dramatic, was observed by Kim et al. (2007). The wet bentonite with synthetic groundwater experiment lasting 188 days at 70°C had a corrosion rate of 0.87 μm/year while the experiment lasting 844 days yielded a corrosion rate of 0.18 μm/year, an 80% reduction in rate. These results indicate that the duration of the experiment does matter and that long-term experiments are necessary to provide the best corrosion rates for extrapolation to long timescales. In addition, the reduced corrosion rate with time suggests the chalcocite layer formation does create a passivation layer that may be effective at repository timescales.

3.3 Steel /Bentonite Interface Mineralogy

Results from these experiments have shown the more dynamic environment associated with this system is at the bentonite-metal interface. Fe-rich phyllosilicates (i.e., trioctahedral, Fe-rich saponite and chlorite) are crystallized on steel surfaces forming a reactive substrate with a high surface area compared to the original steel surfaces. It is evident that the formation of these surface bound minerals is from the direct crystallization from solution in the localized environments surrounding the metal plates. However, it is uncertain to what extent these authigenic minerals will have an effect on the repository system.

Synthetic Fe-saponites have been crystallized in dilute solutions and gels of silica, Fe-, Al-chlorides at temperatures up to 850°C and pH of 8.5 – 9.5 (Kloprogge et al. 1999). This is consistent with a partial dissolution of the steel plates contributing ferrous iron into a fluid phase with silica and aluminum, thereby facilitating Fe-saponite (smectite) crystallization with the steel surfaces acting as a growth substrate. Further, Fe-saponite alteration into chlorite has been suggested (Mosser-Ruck et al., 2010) in the presence of ferrous iron at temperatures approaching 300°C and near-neutral pH. The stainless steel interaction with bentonite via congruent dissolution/oxidation can be detailed by the following reactions.

Stainless steel dissolution

$$Fe_{1.22}Cr_{0.37}Ni_{0.22} \rightarrow 1.22Fe^{2+} + 0.37Cr^{3+} + 0.22Ni^{2+} + 3.99e^-$$

Smectite evolution

$$Fe^{2+} + Ni^{2+} + Cr^{3+} + H_2S_{(aq)} + (Na,K,Ca)_{0.33}(Al_{1.67},Fe^{3+}_{0.20},Mg_{0.13})Si_4O_{10}(OH)_2 \rightarrow (Fe,Ni,Cr)_9S_8 +$$

Smectite   pentlandite

$$(Na,K,Ca)_{0.33}Fe_3(Si_{3.67},Al_{0.33})O_{10}(OH)_2$$

Fe Saponite
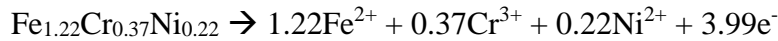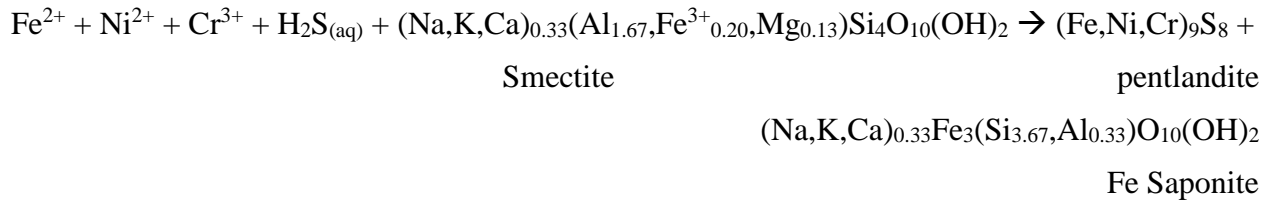
Low carbon steel interaction with clay at low temperature has been investigated by Necib et. al. (2016). They determined two corrosion rates, an active (up to 200 µm/yr.) and a passive (<30 µm/yr.) behavior. They attribute the high corrosion rate to an acidic pH transient (down to 4.5 pH) common to their experiments when pyrite breaks down. Their experiments were run at 85 ºC and 1 atm. Although the reactants in our samples were similar, the P, T conditions were radically different. Measurement of the deepest corrosion pit for experiment EBS 18 was 125 µm (Figure E.8), which would correlate to 1083 µm/yr. This 5-fold increase in corrosion rate for experiment EBS 18 may be due in part to the elevated P, T (150 bar, 300 ºC) conditions of our experiment. The other item of note is that the corrosion material inside the pit is goethite [Fe^{+3} O(OH)], an iron oxide phase indicative of highly oxidizing conditions. Perhaps this stage of corrosion is the result of microenvironments where water breaks down (hydrolysis) at the coupon surface and allows for oxidizing domains in a generally reducing environment. A second possibility is that the low carbon steel coupon began oxidizing while sitting at a pressure of 140 bar for 9 months before temperature was applied. The mechanism of pit corrosion in low carbon steel, along with corrosion rates for the three steel types (304, 326, LCS) would be a very strong focus area for continued study in EBS research.

4   Conclusions

This document summarizes the EBS18 experiment and gives preliminary water chemistry data for EBS 19. There is also a summary of 1) the research conducted on copper corrosion that includes corrosion rates and 2) a partial review of steel bentonite interface reactions and pit corrosion reactions in the low carbon steel coupons of EBS 18. Concepts developed so far include:

1) Illitization of smectites may be restricted due to the bulk chemistry of the overall system,

2) Pyrite within bentonite that may be used as backfill reacts readily in groundwater and the resulting H_2S(aq,g) reacts in a minor fashion with steel and aggressively with copper,

3) The interface between bentonite and steel develops a well characterized new mineral phase, Fe-saponite (especially at 300°C), that grows perpendicular to the steel surface,

4) Another Fe layered phyllosilicate, stilpnomelane, grows in the presence on native iron (one of our solid buffer materials), which alludes to the idea that oxygen fugacity may be quite variable, depending on scale,

5) Zeolites transform as temperature increases. Mine run bentonite contains clinoptilolite, and transforms to analcime at higher temperature, releasing both SiO_2 and water. Opalinus Clay upon heating develops wairakite along cracks and edges. The location of these new growth

zeolites is due to the impermeable nature of the shale. Mixtures of Opalinus Clay and Colony bentonite produce an intermediate composition Analcime-Wairakite solid solution phase, indicating ease of cation exchange for this zeolite. The experiment EBS 18 exhibited both clinoptilolite and analcime as stable phases.

6) Pit corrosion is the driving force in copper degradation. The copper reacts with H_2S (aq,g) to produce chalcocite and covellite. At latter times in the reaction pathway Cl may combine with copper to produce atacamite.

7) Systematic measurements (N>850) of copper corrosion cross sections have determined corrosion reaction rates at experimental temperatures and pressures. At 6-week duration, corrosion rates ranged from 0.12 to 0.39 micron/day, depending on heating profiles and bulk composition. However, in the 6-month experiment, the corrosion rate dropped by an order of magnitude, to 0.024 micron/day. We believe that complete coverage by the reaction product chalcocite pacifies the corrosion reaction.

8) Pit corrosion of low carbon steel was common in EBS 18 experiment, and resulted in a corrosion rate of 1083 µm/yr. Mineral products within the pits consisted primarily of goethite, indicative of a highly oxidizing micro environment.

Research needs to be emphasized in the following areas for FY17:

- Corrosion of steels must be the focus of the upcoming year
- Performed detailed geochemical modeling of FY13-FY16 experimental reactions
- International FEBEX-DP – hydrothermal treatment of FEBEX samples expanding the thermal range in addition to routine mineral/geochemical interrogations.
- Perform transmission electron microscope (TEM) investigation looking at very local chemical changes within a pit corrosion metal surface.

5   Acknowledgements

6 References

Abghari, B., 2013. Corrosion of Copper in Concentrated Aqueous Chloride under Anaeobic Conditions. Master's Thesis, University of Toronto, Department of Chemical Engineering and Applied Chemistry

Antonijevic, M.M. and Petrovic, M.B., 2008. Copper Corrosion Inhibitors. A review. Int. J. Electrochem. Sci., 3, 1-28

Betova, I., Beverskog, B., Bojinov, M., Kinnunen, P., Makela, K., Pettersson, S.-O., Saario, T., 2003. Corrosion of Copper in Simulated Nuclear Waste Repository Conditions. Electrochem. Solid-State Lett. 6, B19-B22

Bojinov, M., Makela, K., 2003. Corrosion of Copper in Anoxic 1M NaCl Solution. POSIVA OY, Olkiluoto, Finland

Boulay, N., Edwards, M., 2001. Role of temperature, chlorine, and organic matter in copper corrosion by-product release in soft water. Water Res., 35, 683-690

Caporuscio, F.A., Cheshire, M.C., Rearick, M.S., and Jove-Colon, C. (2014). - LANL Argillite EBS Experimental Program 2014. FCRD-USED-2014-000491.

Caporuscio, F.A., Cheshire, M.C., Palaich, S., Norskog, K., Jove-Colon, C., (2015) Argillite Disposal R&D-LANL 2015. Summary of baseline experiments for generic repository engineered barriers. Los Alamos National Laboratory FY 2015 – Deliverable UFD Work package # FCRD-UFD-2015-000356, LA-UR-15-26110

Carlsson, T., 2008. Interactions between copper corrosion products and MX-80 bentonite. Svensk Kärnbränslehantering Working Report. TR-08-46, 24

Chen, J., Qin, Z., Shoesmith, D., 2010. Kinetics of corrosion film growth on copper in neutral chloride solutions containing small concentrations of sulfide: J. Electrochem. Soc. 157, no. 10, C338-C345.

Chen, J., Qin, Z., Shoesmith, D., 2011a. Long-term corrosion of copper in a dilute anaerobic sulfide solution: Electrochim. Acta. 56, no. 23, 7854-7861.

Chen, J., Qin, Z., Shoesmith, D., 2011b. Rate controlling reactions for copper corrosion in anaerobic aqueous sulphide solutions: Corros. Eng. Sci Tech. 46, no. 2,138-141.

Cheshire, M.C., Caporuscio, F.A., Jové-Colón, C., and McCarney, M.K. (2013) Alteration of clinoptilolite into high-silica analcime within a bentonite barrier system under used nuclear fuel repository conditions. Proceeding from the 14th International High-Level Radioactive Waste Management Conference, 410-415.

Cheshire, M.C., Caporuscio, F.A., Jove-Colon, C., and McCarney, M.K. (2014) Bentonite Clay Evolution at Elevated Pressures and Temperatures: An experimental study for generic nuclear repositories. American Mineralogist, V99, pp1662-1675

Chipera, S.J. and Bish, D.L. (2002) FULLPAT: a full-pattern quantitative analysis program for X-ray powder diffraction using measured and calculated patterns. Journal of Applied Crystallography, 35, 744–749.

Chung, F.H. (1974) Quantitative interpretations of X-ray diffraction patterns of mixtures. I. Matrix flushing method for quantitative multicomponent analysis. Journal of Applied Crystallography, 7, 519-525.

Coombs, D.S. (1955) X-ray observations on wairakite and non-cubic analcime. Mineralogical Magazine, 30, 699-708.

Crerar, D.A., Susak, N.J., Borcsik, M., and Schwartz, S. (1978) Solubility of the buffer assemblage pyrite + pyrrhotite + magnetite in NaCl solution from 200 to 350°C. Geochimica et Cosmochimica Acta, 42, 1427-1437.

Demchenko, L.V., Zlobenko, B.P., Manichev, V.I., Kadoshnikov, V.V., Spasova, L.V., 2004. Corrosion of Archeological Artefacts from the Olviya Site in Ukraine. Mat. Res. Soc. Symp. Proc. 807, 1-6.

Dick, J. M., 2008, Calculation of the relative metastabilities of proteins using the CHNOSZ software package: Geochem. Trans. 9, 10.

Eberl, D.D., Velde, B., and McCormick, T. (1993) Synthesis of illite-smectite from smectite at Earth surface temperatures and high pH. Clay Minerals, 28, 49-60.

Escobar, I. S., Silva, E., Silva, C., Ubal, A., 1999. Proc. Fourth Inter. Conf. Copper 99-Cobre99, 1, 371

Ferrage, E., Vidal, O., Mosser-Ruck, R., Cathelineau, M., and Cuadros, J. (2011) A reinvestigation of smectite illitization in experimental hydrothermal conditions: Results from X-ray diffraction and transmission electron microscopy. American Mineralogist, 96, 207-223.

Greenburg, H.R. and Wen, J. (2013) Repository layout and host rock thermal gradient trade study for large waste packages in clay/shale: Using the DSEF thermal analytical model. LLNL-TR-639869-DRAFT, pp. 38.

Guillaume, D., Neaman, A., Cathelineau, M., Mosser-Ruck, R., Peiffert, C., Abdelmoula, M., Dubessy, J., Villieras, F., Baronnet, A., and Michau, N., (2003) Experimental synthesis of chlorite from smectite at 300 °C in the presence of metallic Fe. Clay Minerals, 38, 281-302.

Hallberg, R.O., Ostlund, P., Wadsten, T., 1988. Inferences from a corrosion study of a bronze cannon, applied to high level nuclear waste disposal. Appl. Geochem. 3, 273-280.

Helgeson, H. C., Delany, J. M., Nesbitt, H. W., and Bird, D. K., 1978, Summary and Critique of the Thermodynamic Properties of Rock-Forming Minerals: Am. J. Sci. 278. 1-229

Jové-Colón, C. F., Caporuscio, F. A., Levy, S. S., Sutton, M., Blink, J., Greenberg, H. R., Fratoni, M., Halsey, W. G., Wolery, T. J., Rutqvist, J., et al. (2011) Disposal Systems Evaluations and Tool Development - Engineered Barrier System (EBS) Evaluation (Fuel Cycle Research and Development). Sandia National Laboratory, FCRD-USED-2011-000132, 1-192.

Kass, J., 1990. Evaluation of copper, aluminum bronze, and copper-nickel container material for the Yucca Mountain Project. Proc. Corr. Nucl. Fuel Waste Containers. IAEA. RN:23004457. 87-107.

Kim, S.S., Chun, K.S., Kang, K.C., Baik, M.H., Kwon, S.H., Choi, J.W., 2007. Estimation of the corrosion thickness of a disposal container for high-level radioactive wastes in a wet bentonite. J. Ind. Eng. Chem. 13, 959-964.

King, F., 2005. Overview of the corrosion behavior of copper and steel used fuel containers in a deep geologic repository in the sedimentary rock of the Michigan Basin, Ontario: Ontario Power Generation, Nuclear Waste Management Division Report.

King, F., 2007. Status of the understanding of used fuel container corrosion processes – Summary of current knowledge and gap analysis (NWMO TR-2007-09): Canada, NWMO. 104.

King, F., Ahonen, L., Taxen, C., Vuorinen, U., Werme, L., 2002. Copper corrosion under expected conditions in a deep geological repository. POSIVA OY, Helsinki, Finland. 185

King, F., Lilja, C., Pedersen, K., Pitkänen, P., Vähänen, M., 2010. An update of the state-of-the-art report on the corrosion of copper under expected conditions in a deep geologic repository. Swedish Nuclear Fuel and Waste Management Co. (SKB), Technical Report TR-10-67, 180.

King, F., Lilja, C., 2011. Scientific basis for corrosion of copper in water and implications for canister lifetimes: Corr. Eng. Sci. Tech. 46, no. 2, 153-158.

King, F., Lilja, C., Vähänen, M., 2013. Progress in the understanding of the long-term corrosion behavior of copper canisters: J. Nucl. Mater. 438, no. 1, 228-237.

King, F., Litke, C.D., Ryan, S.R., 1992. A mechanistic study on the uniform corrosion of copper in compacted Na-montmorillonite/sand mixtures. Corr. Sci. 33, 1979-1995.

Kloprogge J.T., Evans, R., Hickey, L., Frost, R., 1999. Characterization and Al-pillaring of smectites from Miles, Queensland (Australia). Applied Clay Science V20. Issue 4-5 January 2002, 157-163

Kohyama, N., Shimoda, S., and Sudo, T. (1973) Iron-rich saponite (ferrous and ferric forms). Clays and Clay Minerals, 21, 229-237.

Kumplulainen, S., Kiviranta, L., Carlsson, T., Muurinen, A., Svensson, D., Sasamoto, H., Yui, M., Wersin, P., Rosch, D., 2011. Long-term alteration of bentonite in the presence of metallic iron. POSIVA OY, Eurajoki, Finland. Report 2010-71

Liuo, J.G. (1970) Synthesis and stability relations of Wairakite, CaAl2Si4O12 2H2O. Cont. Min. Pet., 27, 259-282

Macdonald DD, Sharifi-Asl S. 2011. Is copper immune to corrosion when in contact with water and aqueous solutions? Swedish Radiation Safety Authority, SSM, Report. 2011:09

Madsen, F.T. (1998) Clay mineralogical investigations related to nuclear waste disposal. Clay Minerals, 33, 109-129.

Meunier, A., Velde, B., and Griffault, L. (1998) The Reactivity of Bentonites: a Review. An Application to Clay Barrier Stability for Nuclear Waste Storage. Clay Minerals, 33, 187-196.

Moore, D. M. and Reynolds, R.C. (1997) X-ray Diffraction and the Identification and Analysis of Clay Minerals. Oxford University Press, New York, New York, pp. 377.

Mosser-Ruck, R., Cathelineau, M., Guillaume, D., Charpentier, D., Rousset, D., Barres, O., and Michau, N. (2010) Effects of Temperature, pH, and Iron/Clay and Liquid/Clay Ratios on Experimental Conversion of Dioctahedral Smectite to Berthierine, Chlorite, Vermiculite, or Saponite. Clays and Clay Minerals, 58, 280-291

Necib, S., Linard, Y., Crusset, D., Michau, N., Daumas, S., Burger, E., Romaine, A., and Schlegel, M.L. (2016) Corrosion at the carbon steel–clay borehole water and gas interfaces at 85 °C under anoxic and transient acidic conditions, Corros. Sci. http://dx.doi.org/10.1016/j.corsci.2016.04.039

Nunez, L., Reguera, E., Corvo, F., Gonzalez, E., Vazquez, C., 2005. Corrosion of copper in seawater and its aerosols in a tropical island. Corr. Sci. 47, 461-484

Nutt, M. Voegele, M., Jové-Colón, C.F., Wang, Y., Howard, R., Blink, J., Liu, H.H., Hardin, E., and Jenni, K. (2011) Used fuel disposition campaign disposal research and development road map (Fuel cycle research and development). Sandia National Laboratory, FCRD-USED-2011-000065, 1-121.

Pederson, K., 2010. Analysis of copper corrosion in compacted bentonite clay as a function of clay density and growth conditions for sulfate-reducing bacteria. J. Appl. Microbiol. 108, 1094-1104

Pearson, F.J., Arcos, D., Bath, A., Boisson, J.-Y., Fernandez, A.M., Gabler, H.-E., Gaucher, E., Gautschi, A., Griffault, L., Hernan, P., and Waber, H.N. (2003) Mont Terri Project-Geochemistry of water in the Opalinus Clay Formation at the Mont Terri Rock Laboratory. – Reports of the Federal Office for Water and Geology (FOWG), Geology Series No. 5.

Pouchou, J.L. and Pichoir, F. (1985) "PAP"($\phi\rho Z$) correction procedure for improved quantitative microanalysis. Microbeam Analysis. Ed. Armstrong, J.T. San Francisco Press, pp. 104-106.

Pusch, R. (1979) Highly compacted sodium bentonite for isolating rock-deposited radioactive waste products. Nuclear Technology, 45, 153-157.

Rosborg, B., Pan, J., Leygraf, C., 2005. Tafel slopes used in monitoring of copper corrosion in a bentonite/groundwater environment. Corr. Sci. 47, 3267-3279.

Rosborg, B., Kosec, T., Kranjc, A., Pan, J., Legat, A., 2011. Electrochemical impedance spectroscopy of pure copper exposed in bentonite under oxic conditions. Electrochem. Acta. 56, 7862-7870.

Sandberg, J., Wallinder, I.O., Leygraf, C., Le Bozec, N., 2006. Corrosion-induced copper runoff from naturally and pre-patinated copper in a marine environment. Corr. Sci. 48, 4316-4338.

Schwartz, M. O., 2008. High-level waste disposal, ethics and thermodynamics. Env. Geol. 54, no. 7, 1485-1488.

Seyfried, J.R., Janecky, D.R., and Berndt, M.E. (1987) Rocking autoclaves for hydrothermal experiments II. The flexible reaction-cell system. Hydrothermal Experimental Techniques. Eds. Ulmer, G.C. and Barnes, H.L. John Wiley & Sons, pp. 216 – 239.

Środoń, J. (1980) Precise identification of illite/smectite interstratifications by X-ray powder diffraction. Clays and Clay Minerals, 28, 401-411.

Taniguchi, N., Kawasaki, M., 2008. Influence of sulfide concentration on the corrosion behavior of pure copper in synthetic seawater. J Nucl. Mater. 379, 154-161

Wersin, P., Johnson, L.H., and McKinley, I.G. (2007) Performance of the bentonite barrier at temperatures beyond 100°C: A critical review. Physics and Chemistry of the Earth, 32, 780-788.

Update to Thermodynamic Database Development and Sorption Database Integration (Part IV)

1. Introduction

This part of the report summarizes research conducted at Lawrence Livermore National Laboratory (LLNL) within the Argillite Disposal R&D Work Package. The focus of this research is the thermodynamic modeling of Engineered Barrier System (EBS) materials and properties and development of thermodynamic databases and models to evaluate the stability of EBS materials and their interactions with fluids at various physico-chemical conditions relevant to subsurface repository environments. The development and implementation of equilibrium thermodynamic models are intended to describe chemical and physical processes such as solubility, sorption, and diffusion. The scope of the effort included the following:

- Illustrating the concepts developed by Wolery and Jove-Colon (FY15 effort) and applying them to mineralogic components of greatest interest to UFD research
- Testing the PhreeqcRM-PEST framework for surface complexation modeling as part of sorption database development.
- Supporting the involvement of the Used Fuel Disposition campaign in the Nuclear Energy Agency Thermodynamic Database Development (supported through the International Work Package)

The thermodynamic database development effort is a longterm investment by the Used Fuel Disposition (UFD) program. It includes reviewing and revising previously developed thermodynamic databases and expanding them to cover the needs of the repository types currently under consideration by the UFD program (i.e. clay, granite, deep borehole). The effort is a collaboration between LLNL and SNL.

Two manuscripts have been prepared as a result of the recent effort. In FY16, LLNL prepared a follow-on manuscript to that of Wolery and Jove-Colon's FY15 manuscript, creating a modified SUPCRT92 code data file, and producing a modified version of a water model consistent with the CODATA recommendations. This will provide a core for additional database development. As much as possible, the efforts of the NEA TDB effort and other investigators were leveraged. Information contained in the two manuscripts is described in the following section.

The second effort involves development of surface complexation and cation exchange databases for use in PA models. This effort is a continuation of FY15 work, in collaboration with Dr. V. Brendler (HZDR) and the RES^{3}T database development team. The goal of this effort is to develop a path forward for future sorption database development. The effort builds upon the RES^{3}T database effort by assembling digitized data collected from references contained in RES^{3}T and providing a modeling framework for fitting the digitized data to a self-consistent surface complexation model and associated database.

A third effort involves participation of Cynthia Atkins-Duffin (LLNL) in the Nuclear Energy Agency (NEA) Thermochemical Database (TDB) project. Dr. Atkins-Duffin is the UFD representative for thermodynamic database development efforts at the NEA in support of international nuclear waste repository research. This effort was supported through the International Work Package. However, a short summary is provided in this document.

2. Thermodynamic Database Development

The paper "Chemical Thermodynamic Data. I. The Concept of Links to the Chemical Elements and the Historical Development of Key Thermodynamic Data" by Thomas J. Wolery (LLNL) and Carlos F. Jové-Colón (SNL) was submitted to *Geochimica et Cosmochimica Acta* in December, 2015. Editorial decision (likely acceptance upon responding to reviewers' comments) was received in March, 2016). A significant part of this fiscal year's effort has been spent into responding to the comments of the Associate Editor and four reviewers, including shortening the paper from 99 to 70 pages. As of this writing (8/16/16), the paper is ready for resubmission. The current abstract from this paper is:

Chemical thermodynamic data remain a keystone for geochemical modeling and reactive transport simulation as applied to an increasing number of applications in the earth sciences, as well as applications in other areas including metallurgy, material science, and industrial process design. The last century has seen the development of a large body of thermodynamic data and a number of major compilations. The past several decades have seen the development of thermodynamic databases in digital form designed to support computer calculations. However, some problems with thermodynamic data appear to be persistent. One problem pertains to the use of inconsistent primary key reference data. Such data pertain to elemental reference forms and key, stoichiometrically simple chemical species including metal oxides, CO_2, water, and aqueous species such as Na^+ and Cl^-. A consistent set of primary key data (standard Gibbs energies, standard enthalpies, and standard entropies for key chemical species) for 298.15K and 1 bar pressure is essential. Thermochemical convention is to define the standard Gibbs energy and the standard enthalpy of an individual chemical species in terms of formation from the reference forms of the constituent chemical elements. We propose a formal concept of "links" to the elemental reference forms, as thermochemical convention. This concept involves a documented understanding of all reactions and calculations leading to values for a formation property (Gibbs energy or enthalpy). A valid link consists of two parts: (a) the path of reactions and corrections and (b) the associated data, which are key data. Such a link differs from a bare "key" or "reference" datum in that it requires additional information. Some or perhaps all of its associated data may also be key data. In evaluating a reported thermodynamic datum, one should identify the links to the chemical elements, a process which can be time-consuming and which may lead to a dead end (an incomplete link). The use of two or more inconsistent links to the same elemental reference form in a thermodynamic database will necessarily result in an inconsistency in the database. Thus, in constructing a database, it is important to establish a set of reliable links (generally resulting in a set of primary reference data) and then correct all data adopted subsequently for consistency with that set. Recommended values of key data have not been constant through history. We review some of this history through the lens of major compilations and other influential reports, and note a number of problem areas. Finally, we illustrate the concepts developed in this paper by applying them to some key species of geochemical interest, including liquid water, quartz and aqueous silica, and gibbsite, corundum, and the aqueous aluminum ion.

This paper describes a methodology for evaluating consistency in thermodynamic data and building thermodynamically consistent databases. It reviews nearly a century of thermodynamic data. It then applies the methodology to key data for (1) water, (2) quartz and aqueous silica, and (3) gibbsite, corundum, and the aluminum ion. Follow-on efforts will focus on further illustrating these concepts and applying them to mineralogic components of greatest interest to the UFD program.

A second manuscript, "Chemical Thermodynamic Data. II. Water in SUPCRT92 and Similar Codes: Thermochemical Properties in Relation to Equations of State" was recently prepared for submission to *Computers & Geosciences*. The abstract is

The properties of liquid water and steam are central to the thermodynamics of aqueous systems and phase relations among water and minerals. SUPCRT92 (Johnson et al., 1992) has been a useful tool for generating thermodynamic data to support geochemical modeling and reactive transport calculations. The code uses standard thermodynamic models for which the relevant data are mostly provided on the code's own thermodynamic data base. However, the thermodynamic properties of water are hard-coded. They are calculated in part from a two-phase, single-component fluid equation of state (EOS) model. SUPCRT92 uses the EOS developed by Haar et al. (1984) and, near the critical point, that of Levelt Sengers et al. (1983). These models account for the temperature and pressure dependence of the usual thermochemical properties (e.g., the standard Gibbs energy, enthalpy, and entropy). However, they use non-thermochemical reference conditions of u (specific internal energy, kJ kg-1) = 0 and s (specific entropy, kJ kg-1 K-1) = 0 at the triple point of water (273.16K and ~ 0.00611 bar). Results from these models must be translated to accord with thermochemical reference values for the standard enthalpy and entropy at 298.15K and 1 bar. In SUPCRT92, this is accomplished by the use of a "translation function" derived by Helgeson and Kirkham (1974a), which was built into earlier versions of the software and retained unchanged. This function presumes standard thermochemical data from Wagman et al. (1968), which are obsolete. The data for the original translation are comprised of compound constants that were further calculated using the older Keenan et al. (1969) EOS. Here we update the translation function for consistency with the standard thermochemical data recommended by CODATA (Cox et al., 1989). We do this for both the Haar et al. (1984) EOS and the more recent IAPWS-95 EOS (Wagner and Pruss, 2002). The IAPWS-95 EOS is analogously used to compute the thermochemical properties of water in two other codes, CHNOSZ (Dick, 2008; this also offers the Haar et al., 1984, EOS) and Cantera (Moffat and Jóve Colón, 2015). We calculated the "ideal gas" properties for both the Haar et al. (1984) EOS and the IAPWS-95 EOS. Results for the former basically confirm data given by other standard references (see for example Cox et al., 1989; and Chase, 1998). Results for the latter differ somewhat. The "H2O,g" model in SUPCRT92 for treating metastable vapor is not consistent with these results and should be discarded. Future database development should emphasize the use of the IAPWS-95 EOS, which is the current international standard, the EOS of Haar et al. (1984) being the previous standard). The gas-only EOS model given by Wagner and Pruss (2002) in their Section 3.1 should also be considered for dealing with metastable vapor.

This paper describes how to update the thermochemical data for water in SUPCRT92 for consistency with CODATA (Cox et al., 1989) and the equation of state (Haar et al., 1984, also known as IAPS-84) for water that is currently in SUPCRT92. The original SUPCRT implementation for calculating water properties as a function of temperature and pressure used an older equation of state and obsolete thermochemical data from NBS 270-3 (Wagman et al., 1968). That linkage ("translation function") was implemented in a nontransparent wat, with the thermochemical data being combined with data from the equation of state and the results stored as constants in a DATA statement. The paper addresses the needed update for two water equations of state, the IAPS84 currently in SUPCRT92 and the more recent IAPWS-95 one that is currently in two other pieces of software, CHNOSZ (Dick, 2008) and Cantera code suite (Moffat and Jove Colon, 2009). A simpler method for linking thermochemical data with a single-component fluid equation of state is also presented. The manuscript is presently being shortened, and submission to the journal is expected by the end of August, 2016.

We have made some other modifications to SUPCRT92, notably eliminating the obsolete direct access data file, creation of a SUPCRT data file converter (that converts from obsolete calorie units to Joule units), and changes to SUPCRT92 itself to do everything in Joule units. We will be comparing these modifications with SUPCRTBL (Zimmer et al., 2016), which is a SUPCRT92 modification that also uses Joule units and has been developed to use the Holland and Powell (2011) thermodynamic data for minerals. FY17 is expected to see a merge of these modified versions of SUPCRT92.

3. Surface Complexation and Ion Exchange Model and Database Development

The need to develop self-consistent surface complexation/ion exchange models, in concert with thermodynamic models, for nuclear waste repository performance assessment was identified many years ago (Bradbury and Baeyens, 1993). This issue was expressly identified in the recent NEA Sorption project reports (Davis et al., 2005; Ochs et al., 2012). However, significant progress on this issue has been made only recently in various international nuclear waste repository programs (e.g. (Bradbury and Baeyens, 2009), (Dresden-Rossendorf, 2013), (Geckeis et al., 2013)). Hybrid approaches have also been attempted (Bradbury et al., 2010). The best path forward for developing such databases remains an open question (Geckeis et al., 2013), particularly in cases where generic repositories are being investigated resulting in a need to model radionuclide behavior over a very broad range of solution and mineralogic conditions.

The RES³T project is a recent effort by HZDR to develop a digital open source thermodynamic sorption database. It includes mineral-specific surface complexation constants that can be used in additive models of more complex solid phases such as rocks or soils. It includes an integrated user interface to access selected mineral and sorption data and export data into formats suitable for other modeling software. Data records comprise mineral properties, specific surface areas, characteristics of surface binding sites and their protolysis constants, sorption ligand information, and surface complexation reactions (SC models include the Non-Electrostatic, Diffuse Double Layer, Constant Capacitance, Triple Layer, Basic Stern, and the 1-pK Model as extended to CD-MUSIC). The database also includes a comprehensive list of publications that are the primary sources of the surface complexation data. In total, the database includes over 130 minerals, 5000 surface complexation reaction constants, and 2800 references. The database provides a comprehensive list of reaction constants reported in the literature for a very large number of

radionuclide-mineral reaction pairs. However, this database project does not provide recommended values. It also does not capture the primary sorption data or provide information on the aqueous speciation constants used in determining those surface complexation constants. As a result, the RES³T project provides a foundation for developing a comprehensive surface complexation database but does not go so far as to provide one.

Three key issues prevent the application of the RES³T database in performance assessment and other radionuclide transport/risk assessment models. They are:

- An inability to integrate disparate data sets and surface complexation model constructs into single unified model and associated set of reaction constants
- An inability to produce self-consistent reaction constants based on a common set of aqueous speciation constants and surface properties.
- The absence of error propagation in the sorption data and/or database constants needed to assess model uncertainties.

To address these limitations, the inclusion of primary sorption data in the RES³T database is needed. This would allow for integration of all available literature data, error propagation, and database updating and ensure self-consistency between aqueous speciation, mineral solubility, and surface complexation databases.

In our FY14 progress report, we developed a test-case for U(VI) sorption to quartz and demonstrated how a self-consistent set of surface complexation constants could be produced from ~400 batch sorption data digitized from the published literature (10 publications in total). The minimization routine was performed using the FIT4FD software developed at LLNL (Zavarin et al., 2004) and based on the FITEQL software (Herbelin and Westall, 1994). However, this approach did not provide the flexibility needed to easily evaluate and test various surface complexation models. This LLNL software could only be used for a non-electrostatic model of the U(VI)-quartz system. One promising new approach identified in FY15 was the use of a recently released PhreeqC module, PreeqcRM (Charlton and Parkhurst, 2011; Parkhurst and Wissmeier, 2015). The module was developed to facilitate operator splitting approaches to reactive transport modeling. However, it was believed that the same code could be used in performing equilibrium calculations on individual batch sorption data. When linked to a parameter estimation software (e.g. PEST (Doherty, 2003)), the PhreeqcRM module could provide a framework for testing various surface complexation models on large sets of sorption data in a comprehensive manner.

This new approach was tested in FY16 on a small set of U(VI)-quartz sorption data. For the test-case, only one U(VI)-quartz dataset was used ((Arnold et al., 2000) identified as azbn00 using the reference formatting in RES³T); the code PhreeqC rather than PhreeqcRM was used in this case. The following describes the scheme used to run the fitting routine:

1. U(VI) and quartz were chosen as the test case
2. RES³T "Data assembly and formatting" query was run for Quartz and UO2<2+>
   a. Surface area, site density, and pKa's for each reference were collected
   b. All references and associated DOI's were collected
3. References and DOI's were used to access a digital copy of EACH original reference
4. Datathief software used to digitize data included in EACH original reference

5. PhreeqC input file was written such that each digitized sorption datapoint constituted a separate condition in the input file[1], including
    a. Solution composition
    b. Surface complexation reactive site density
    c. Mineral surface area
    d. Mineral concentration
6. PhreeqC output file was set to output total aqueous U(VI) concentration
7. PhreeqC thermodynamic database was set to thermo.com.V8.R6.230 file that is included in PhreeqC package
8. Surface complexation reactions were added to thermo.com.V8.R6.230 with estimated reaction constants
9. PEST control.pst file included all variables that will be fit during the minimization routine and all observational data (equilibrium U(VI) aqueous concentration) digitized from EACH original reference.
10. PEST template file was used to identify location of surface complexation variables in the thermodynamic databased used by PhreeqC
11. PEST instruction file was used to identify location of the PhreeqC output data that are used in the minimization routine (along with the observational data)
12. PEST was run to optimize surface complexation reactions for the U(VI)-quartz system.

The resulting fits to the data using the non-electrostatic model are comparable to the fits produced using LLNL's FIT4FD software (Figure 1). Thus, it appears that the approach developed in FY16 can provide a robust path forward for surface complexation database development. Importantly, the approach provides a unique opportunity to develop surface complexation modeling databases that can

1. Provide self-consistent fitted reaction constants based on large assemblies of data available in the literature.
2. Account for data uncertainty and goodness-of-fit to the overall uncertainty in model parameters.
3. Allow for updating the fitted surface complexation reaction constants as thermodynamic speciation and solubility databases evolve.
4. Provide a platform for testing various surface complexation models and assess their ability to capture observed sorption data reported in the literature in a comprehensive manner.

---

[1] In this case, only the data from one reference were used.
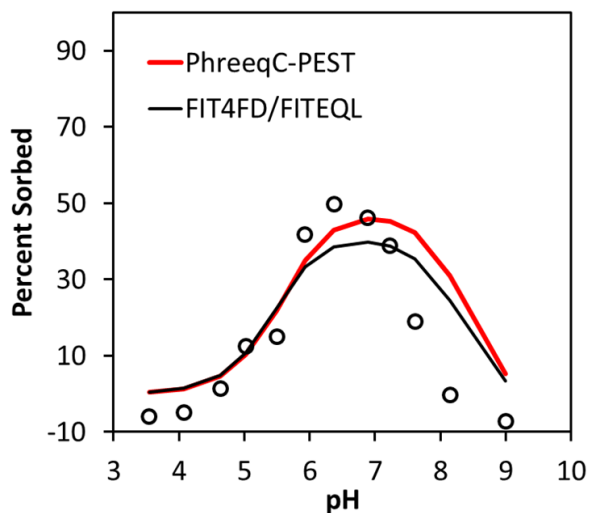
Figure 1. PhreeqC and FIT4FD non-electrostatic models fits to the data of (Arnold et al., 2000). The U(VI)-quartz sorption data were collected using 12.5 g/L quartz with a 0.2 m^2/g surface area and 4.8 sites/nm^2 estimates reactive site density. The total U(VI) concentration in all samples was 10^{-6} M.

4. Nuclear Energy Agency Thermodynamic Database Development

In FY16, Dr. Cindy Atkins-Duffin continued her participation in the Organization of Economic Cooperation and Development (OECD) Nuclear Energy Agency (NEA) Thermochemical Database (TDB) Project. Dr. Atkins-Duffin serves the United States representative to the Project's Management Board and is an elected member of the Board's Executive Group. The principal product of this activity is to make available a comprehensive, internally consistent, quality-assured and internationally recognized chemical thermodynamic database of selected chemical elements in order to meet the specialized modelling requirements for safety assessments of radioactive waste disposal systems. The Management Board and its Executive Group meet periodically to assess progress on the Project's approved plan of work and to suggest and approve technical contributors for both the conduct of the reviews and as peer reviewers of the work. The United States joins Belgium, Canada, Czech Republic, Finland, France, Germany, Japan, Spain, Sweden, Switzerland, and United Kingdom in the TDB Project.

The objective of the TDB Project is to produce a database that:

- Contains data for all the elements of interest in radioactive waste disposal systems;
- documents why and how the data were selected;
- gives recommendations based on original experimental data, rather than compilations and estimates;
- documents the sources of experimental data used;
- is internally consistent;
- treats all solids and aqueous species of the elements of interest for nuclear waste storage performance assessment calculations.

In 2014, the Project entered its fifth phase (2014-2018) of activities which include:

- Completion of the review of Ancillary Data (commonly used data required for use in calculations by all authors in reviews)
- Completion of second volume of Iron Data (thermochemical data of Iron is extensive. The review of Iron data was divided into two volumes. The first volume was completed in the fourth phase of the TDB.)
- Completion of the review of Molybdenum data.
- Initiate and complete an update of the Actinide data review.
- Initiate and complete a State-of-the-Art review of Cement chemistry and suggest options for including these findings in safety case efforts.
- Initiate and complete a State-of-the-Art review of High Ionic Strength thermochemical data and suggest options for including these findings in safety case efforts.

At the recent Executive Group meeting held in Paris on April 4-5, 2016, Maria-Eleni Ragoussi presented the status of all ongoing activities of the NEA-TDB project (Table 1). SOAR documents listed in Table 1 are "State of the Art Reports". In general, these reports assess the means by which various repository programs deal with non stoichiometric moieties/processes in performance assessment/safety cases. They are intended to provide users with an assessment of options. However, no recommendations are made about data or methods. In general these documents, while written under the NEA Guidelines, do not carry the same pedigree as the selected data in the more traditional NEA-TDB Volumes. A draft manuscript entitled "Fundamentals of the NEA Thermochemical Database and its influence over national nuclear programs on the performance assessment of deep geological repositories" by Maria-Eleni Ragoussi and David Costa was recently prepared for submission to the Journal and Environmental Radioactivity. The manuscript summarizes the 30 year effort by the NEA to develop comprehensive databases for use by the international nuclear waste repository science community and includes insights into how these and similar efforts may be more broadly applicable to environmental science research.

Table 1. Status of NEA-TDB Activities

Activity	Status	Final milestone
Ancillary Data Review	Most sections completed and currently under edition	Book to peer review summer 2016. Publication in 2017.
Fe – Part II Review	Most sections completed and currently under edition	Book to peer-review summer 2016. Publication in 2017.
Mo Review	Big part of single contributions concluded Completion expected during summer 2016	Book to peer-review end 2016. Publication in 2017.
SOAR Cements	Ongoing (initiated beginning 2014)	Completion of 1st draft mid 2018. Publication in 2019.
SOAR Pitzer	Ongoing (Initiated beginning 2015)	Completion of 1st draft end 2017. Publication in 2018.
Update Actinides	Ongoing (Initiated beginning 2015)	Completion of 1st draft end of 2016. Publication in 2017.

5. Planned FY17 Efforts

In FY17, we plan to continue our efforts in the development of thermodynamic databases in support of the UFD program. These include

- Illustrating the concepts developed by Wolery and Jove-Colon (Parts 1 and 2) and applying them to mineralogic components of greatest interest to UFD research, starting with a Part 3 paper re-analyzing the mineral data model of Helgeson et al. (1978).
- Testing the PhreeqC-PEST fitting routine using various surface complexation models (non-electrostatic, diffuse double layer, etc.) and applying the method to larger sets of sorption data (all U(VI)-quartz data available in the literature) in a comprehensive manner.
- Continued engagement with the NEA TDB project through the support of Dr. Atkins-Duffin as the UFD representative for international thermodynamic database development effort.

In addition to re-analyzing the mineral data of Helgeson et al., (1978), a Part 3 manuscript will be prepared and will update the thermochemical data for aqueous species and make comparisons with the mineral data of Holland and Powell (2011). We will create a modified SUPCRT92 data file, and produce a modified version of SUPCRT92 that contains key reference data based on the

CODATA (Cox et al., 1989) values or updated values known to be better. We expect to merge the improvements with others made in SUPCRTBL (Zimmer et al., 2016). This will provide a core for additional database development. As much as possible, we will leverage the efforts of the NEA TDB effort and other investigators. The Part 1 paper is now expected to be published in FY17. In FY17, we will also publish the Part 2 paper. We will be working on the Part 3 paper, with expected publication in early FY18.

6. Acknowledgments

7. References

Arnold, T., Zorn, T., Bernhard, G., and Nitsche, H., 2000. Applying the DDLM to model the sorption of uranium onto quartz and muscovite*Annual report 1999, Forschungszentrum Rossendorf e.V.* Institute of Radiochemistry, Dresden, Germany.

Bradbury, M. H. and Baeyens, B., 1993. A general application of surface complexation modeling radionuclide sorption in natural systems. *J. Colloid Interface Sci.* **158**, 364-371.

Bradbury, M. H. and Baeyens, B., 2009. Sorption modelling on illite. Part II: Actinide sorption and linear free energy relationships. *Geochim. Cosmochim. Acta* **73**, 1004-1013.

Bradbury, M. H., Baeyens, B., and Thoenen, T., 2010. Sorption Data Bases for Generic Swiss Argillaceous Rock Systems. Nagra, Wettingen, Switzerland.

Charlton, S. R. and Parkhurst, D. L., 2011. Modules based on the geochemical model PHREEQC for use in scripting and programming languages. *Computers & Geosciences* **37**, 1653-1663.

Davis, J., Ochs, M., Olin, M., Payne, T., and Tweed, C., 2005. Interpretation and prediction of radionuclide sorption onto substrates relevant for radioactive waste disposal using thermodynamic sorption models. OECD/Nuclear Energy Agency, Paris.

Doherty, J., 2003. PEST: Model-Independent Parameter Estimation. Watermark Numerical Computing.

Dresden-Rossendorf, H.-Z., 2013. RES³T - Rossendorf Expert System for Surface and Sorption Thermodynamics. RES³T - Rossendorf Expert System for Surface and Sorption Thermodynamics, Dresden, Germany.

Geckeis, H., Lützenkirchen, J., Polly, R., Rabung, T., and Schmidt, M., 2013. Mineral–Water Interface Reactions of Actinides. *Chemical Reviews* **113**, 1016-1062.

Herbelin, A. L. and Westall, J. C., 1994. FITEQL, A computer program for determination of chemical equilibrium constants from experimental data. Department of Chemistry, Oregon State University.

Ochs, M., Payne, T. E., and Brendler, V., 2012. Thermodynamic sorption modeling in support of radioactive waste disposal safety cases. A guideline document. OECD/NEA, Paris.

Parkhurst, D. L. and Wissmeier, L., 2015. PhreeqcRM: A reaction module for transport simulators based on the geochemical model PHREEQC. *Advances in Water Resources* **83**, 176-189.

Zavarin, M., Turner, G. D., and Westall, J. C., 2004. FIT4FD. Modification of the Program FITEQL to Facilitate Rapid Evaluation of Complex Datasets, Livermore (CA).

Fuel Matrix Degradation Model: Canister Corrosion and the Effect of Hydrogen on Used Fuel Degradation Rates (Part V)

1.   Introduction and Objective

Scientifically-based predictive models of waste form corrosion rates will provide reliable radionuclide source terms for use in repository performance assessments. Furthermore, demonstrating that there is a fundamentals-based, scientific basis for the waste form degradation process models is a key aspect for building confidence in the long-term calculations used for the repository safety case.

The objective of this project is to develop and implement a fundamentals-based process model for the degradation rate of used fuel that can be readily incorporated into the Generic Disposal System Analyses (GDSA) Performance Assessment (PA) code to provide radionuclide source terms throughout the service life of a disposal system. This model, referred to as the Fuel Matrix Degradation Model (FMDM), is based on the Canadian Mixed Potential Model (King and Kolar, 2003), but has been expanded and customized for application in the ongoing UFD R&D activities on disposal in Argillite and Crystalline rock media. The conceptual context for the FMDM within the generic performance assessment model is shown in Figure 1.
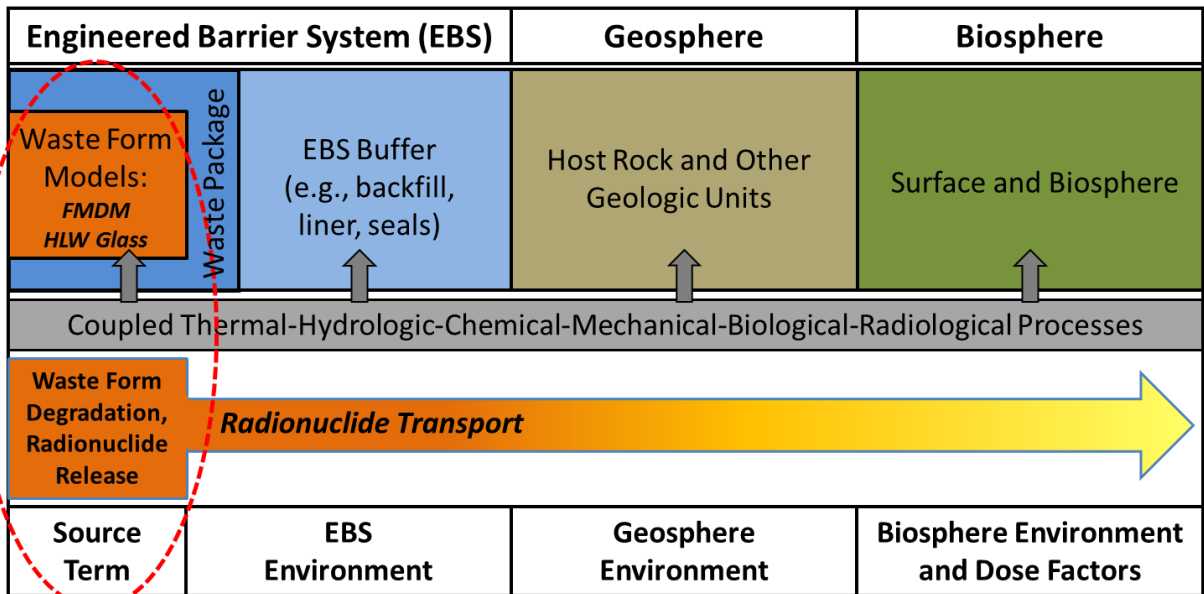
Figure 1. Conceptual diagram showing the context for the FMDM. Adapted from Mariner et al., 2015.

The continued development and implementation of the FMDM addresses two high level Features, Events, and Processes (FEPs) that are recognized as high R&D priorities for the UFD (Wang et al., 2014). The FEPs addressed by this model are 2.1.02 (waste form) and 2.1.03 (waste container), which correspond to the high priority research topics P19 (Development of waste form degradation model) and P20 (Development of new waste package concepts and models for evaluation of waste package performance for long-term disposal) identified by Wang et al., 2014.

The FMDM calculates the dissolution rate of used fuel as a function of the interfacial corrosion potential (E_{corr}) that is determined by the kinetic balance between all of the anodic and cathodic half reactions occurring at the fuel/solution boundary. The dissolution rate is relatively high under oxidizing conditions (high E_{corr}) but decreases dramatically at E_{corr} values lower than the U(IV)/U(VI) threshold potential, where only solubility-based chemical dissolution occurs. The FMDM accounts for:

- The generation of radiolytic oxidants as a function of fuel burn-up,
- the catalyzed oxidation of H_2, which protects the fuel from oxidative dissolution,
- the precipitation of secondary phases,
- the complexation of uranyl by carbonate,
- the oxidation of ferrous iron,
- temperature variations (by Arrhenius equations),
- the one-dimensional diffusion of all chemical species,
- the anoxic corrosion of steel components within a breached waste package to provide the flux of H_2 and ferrous iron, which, as discussed below, dominate fuel degradation process (*added and tested in FY-2016*).

Of these processes, the catalysis of H_2 oxidation on Nobel Metal Particles (NMP) on the fuel surface and the generation rate of radiolytic oxidants (determined by dose rate, which is related to fuel burn-up) are the most important for determining the degradation rate of the fuel (Jerden et al., 2015). Since the flux of H_2 to the fuel is determined by the anoxic corrosion rate of steel waste package components (e.g., Shoesmith, 2008), steel corrosion kinetics were added to the FMDM in FY-2016. The new electrochemical steel corrosion module is discussed in Section 2.

Specifically, the fuel degradation rate calculated by the FMDM accounts for oxidation of the fuel by radiolytic H_2O_2 (and its decomposition product O_2), the concentration of which is calculated using an analytical form of the radiolysis model developed at PNNL (Buck et al., 2014), and the burn-up/dose rate function described in Section 4 of this report. Fuel oxidation is counteracted by the catalytic oxidation of H_2 on NMP sites that are present on the fuel surface as a distinct phase.

It was shown in Jerden et al., 2015 that the FMDM accurately reproduces the experimental observation that relatively low concentrations of dissolved H_2 (~0.1mM) can inhibit the oxidative dissolution of the fuel. In the absence of oxidative dissolution, the fuel degrades by solubility based, chemical dissolution, which is over 4 orders of magnitude slower than oxidative dissolution (Röllin et al., 2001).

The present study, which focuses on the degradation behavior of uranium oxide used fuel, shows that interactions between the seepage water contacting the fuel and engineered barrier materials should be accounted for in waste form degradation models. As discussed in this report, it is

particularly important to account for chemical interactions between the corroding used fuel and steel waste package components that occur through a common solution.

Figure 2 is a conceptual diagram showing the key interfacial and bulk solution reactions included in the new version of the FMDM (FMDM Version 3) as well as other important source term processes that are not yet included, but may play a key role in radionuclide release and transport *(shown in dark red on Figure 2).*
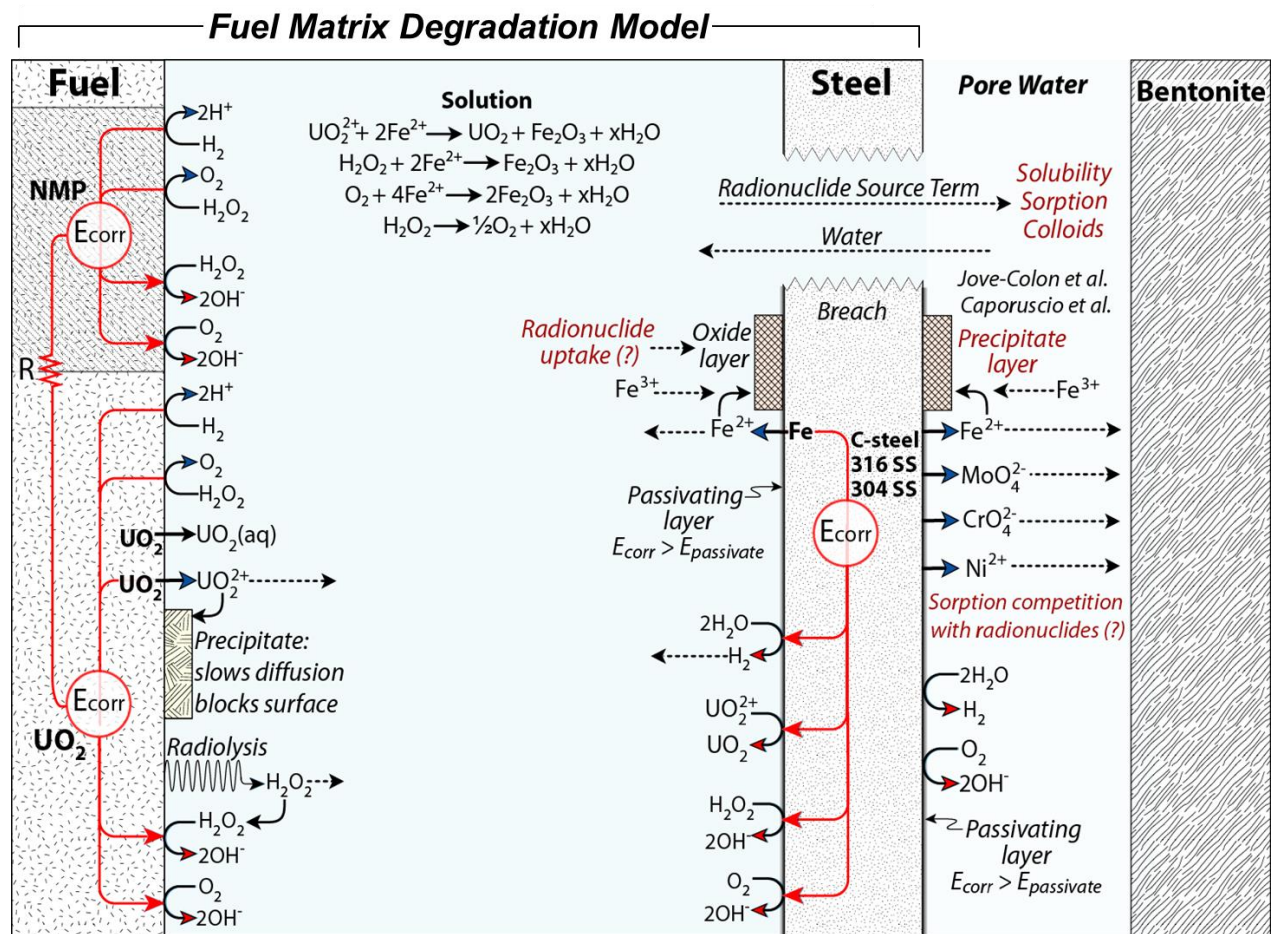
Figure 2. Conceptual diagram showing the context for the FMDM. Adapted from Mariner, P., Gardner, P., Hammond, G, Sevougian, D, Stein E., 2015, Application of Generic Disposal System Models, FCRD-UFD-2015-000126, SAND2015-10037, September 22, 2015, 209pp.

2. FY-2016 Extention of the Fuel Matrix Degredation Model: Electrochemical Steel Corrosion Module

Quantification of the long-term corrosion behavior of steels in relevant environmental conditions is central to developing a scientifically sound performance assessment model for nuclear waste repositories. As shown in Figure 3, the used fuel assemblies will be surrounded by and in close contact with steel components within the waste package and disposal canister.
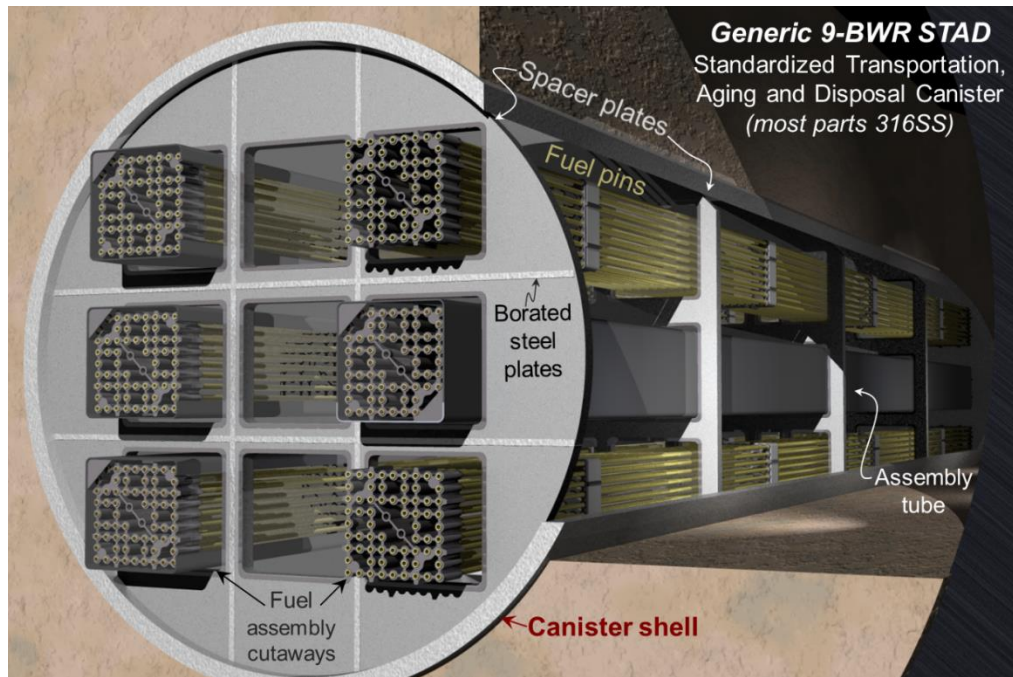
Figure 3. Conceptual diagram showing a generic BWR waste package.

Within a breached canister groundwater will infiltrate open spaces within the canister and begin to corrode steel components (Figure 4). This will set up a reaction front that will eventually contact the fuel rods. The steel will corrode and produce H_2 even if the infiltrating groundwaters are reducing. This is because the stability field of carbon steels and stainless steels lie below the stability field of water on an Eh vs. pH diagram (Figure 5). Therefore, as shown in both Figure 5a and Figure 6 (steel surface), metallic iron can be oxidized to Fe^{2+} by the reduction of water to H_2 + $2OH^-$. Assuming that the Zircaloy cladding has failed, the fuel will begin degrading by either relatively rapid oxidative dissolution or by relatively slow chemical dissolution. The dominant dissolution mechanism will be determined by the surface potential established by the solution contacting the fuel surface.
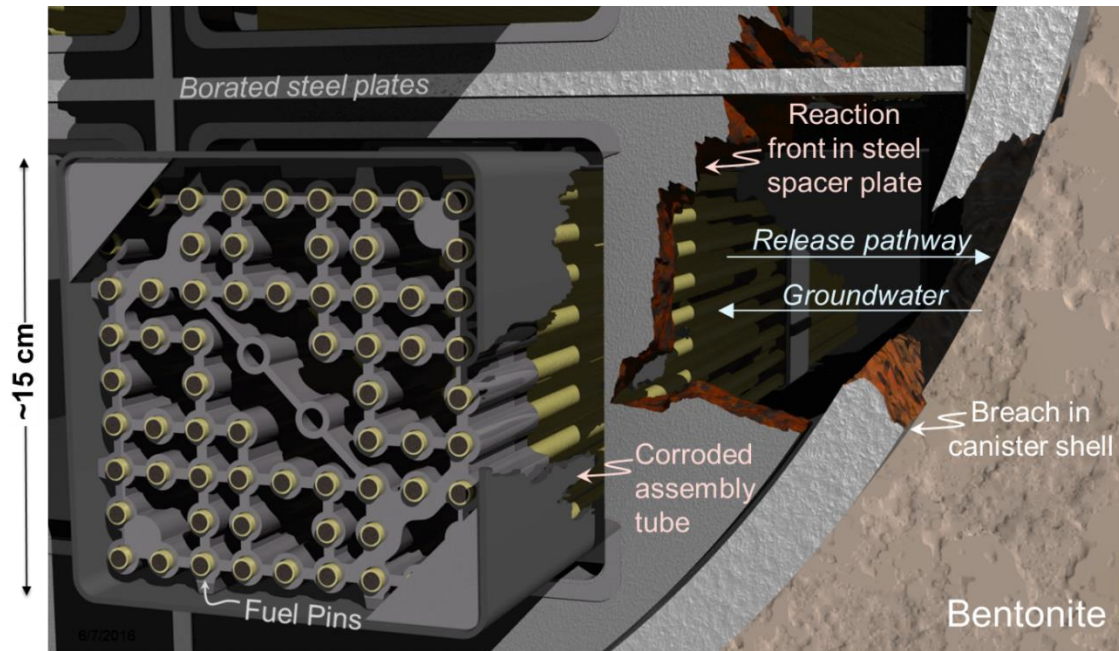
Figure 4. Conceptual diagram summarizing the key processes involved in radionucide release from a breached used fuel waste package. Following a breach groundwater will oxidize steel components and eventually reach fuel rods. The key thing to note is that the used fuel will degrade simultaneously with a number of different types of steels. The interactions between the steel corrosion reaction products H_2 and Fe^{2+} have been shown experimentally strongly effect the rate of fuel degradation (e.g., Shoesmith, 2008, Grambow, et al., 2010).
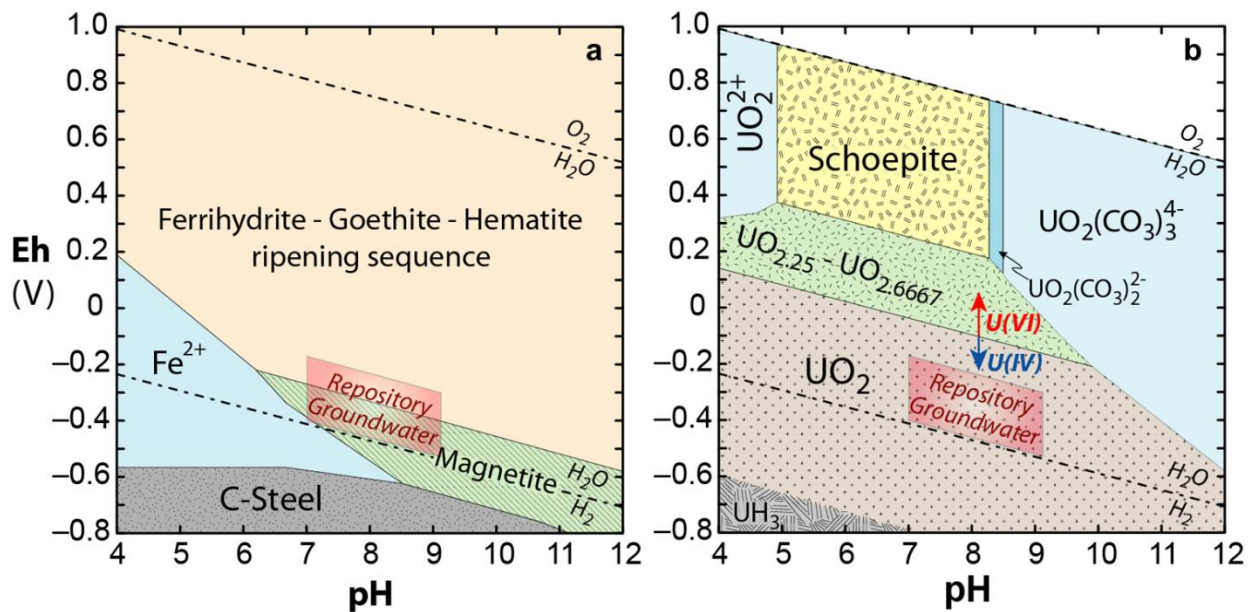
Figure 5. Eh – pH diagrams showing the conditions expected for groundwaters in a reducing crystalline rock or argillite repository (from Laaksoharju, et al., 2008). Figure 5a was drawn for 1×10^{-3} molar iron and the 5b was drawn for 1×10^{-6} molar uranium with 1×10^{-4} molar carbonate.

The rate of fuel degradation will ultimately be determined by the kinetic balance of five processes:

- The rate of radiolytic oxidant production (determined by dose rate, which is determined by fuel burn up and age).
- The rate of radiolytic oxidant reduction on fuel surface (cathodic reactions on fuel surface).
- The rate of U(IV) → U(VI) oxidation (anodic reactions on fuel surface).
- Rate of H_2 production by steel corrosion and H_2 flux to the NMP sites on the fuel surface.
- The rate of the oxidation of H_2 on the NMP catalytic sites (anodic reaction on fuel surface that anodically "protect" UO_2 from oxidation).

These processes are shown conceptually in Figure 6, which summarizes the reaction scheme for the FMDM.
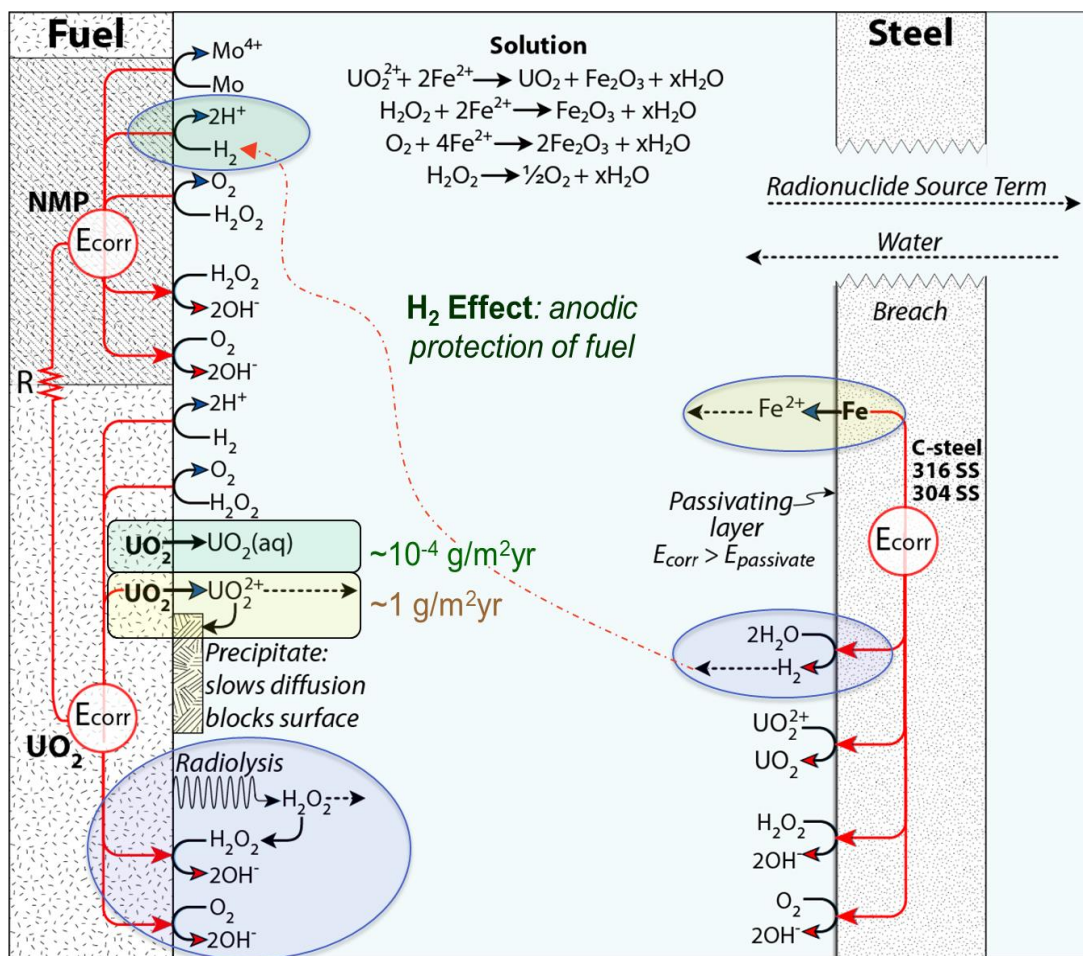
Figure 6. Schematic diagram showing the reaction scheme for the FMDM. The key processes in the model are highlighted in yellow (key anodic reactions), blue (key cathodic reactions) and green (the H_2 effect that can provide anodic protection of the UO_2 matrix from oxidative dissolution).

The mixed potential theory on which the FMDM is based Model (King and Kolar, 2003) is also ideal for quantifying steel corrosion because it accounts for the fundamental interfacial electrochemical reactions and couples those reactions with bulk solution chemistry. Therefore, as part of our FY-2016 work, we formulated, coded, and tested a relatively simple mixed potential model for steel corrosion and then added that model to the FMDM as a new module. The interfaces between the modules is presented in Figure 7.
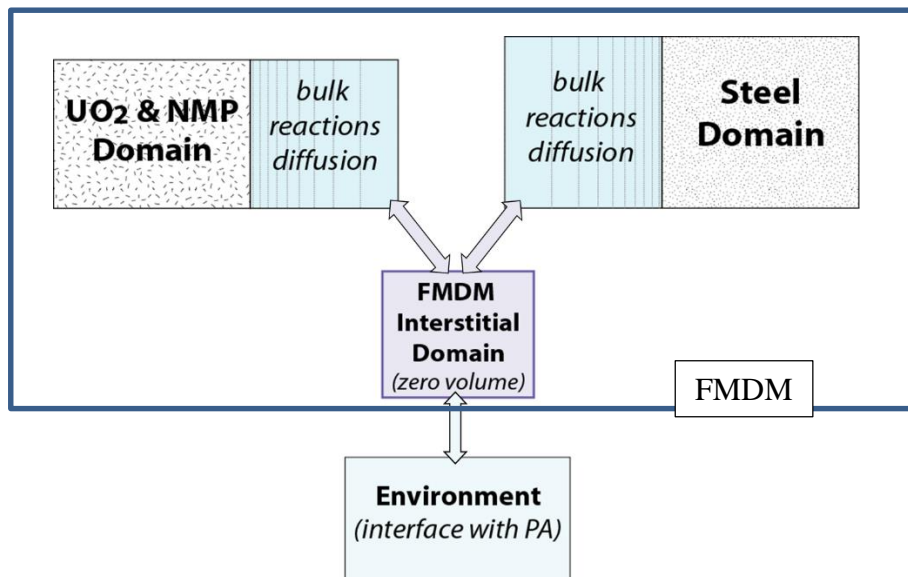
Figure 7. Schematic diagram showing the logic for how the steel surface was added to the FMDM.

There are several advantages to the approach of incorporating a separate steel corrosion module directly into the FMDM as shown in Figure 7:

- It directly couples fuel degradation and steel corrosion. This is vital, as it has been shown that, even at sub millimolar concentrations, the H_2 produced from the anoxic corrosion of steel can decrease the fuel dissolution rate by over four orders of magnitude (Jerden et al., 2015).
- directly coupling the fuel and steel degradation allows for the quantification of redox fronts that develop within the waste container due to the diffusion of radiolytic oxidants away from the fuel surface and the reactions of these oxidants with the steel surface and the resulting aqueous Fe^{2+} and H_2. This is also important because these redox fronts represent the Eh of the in-package solutions contacting the waste form and waste container internal components.
- This approach will allow the steel corrosion module to be readily implemented into the GDSA-PA PFLOTRAN model, as it will be incorporated into the FMDM, a version of which has already been integrated with PA.

As shown in Figure 7 the steel environment (steel surface plus bulk solution) are coupled to the fuel environment through a zero-volume interstitial domain, which can exchange mass fluxes with the fuel environment, the steel environment and the groundwater chemistry within the engineered barrier system adjacent to the waste package.

Within the FMDM no chemistry occurs in the interstitial domain or environment; those regions are zero-volume and only serve to provide an interface/outlet for the active fuel/NMP and steel domains. It is possible to control the interaction between domains by altering (1) the environmental concentrations, (2) the relative total areas of the two reactive domains, and/or (3) the leak rate from the interstitial domain to the environment. The environment domain serves as the input/output interface with the GDSA performance assessment model (the FMDM-PA interface is discussed in more detail below).

In parallel with the addition of the steel surface to the FMDM, the model parameter database was reviewed and updated. As part of this updating process several data gaps were identified to provide priorities for FY-2017 and future work. The main FMDM parameters and the important data gaps are summarized in Table 1.

Table 1. Summary of FMDM parameters and data gaps that need to be addressed in future work to improve the accuracy of the model.

Parameter	Description	Data needs to improve accuracy
Dimension of fuel environment	(mm – cm)	To be updated when dimensions of waste package are known
Nodes in fuel environment	(log-space grid: fine-spacing near surface)	To be updated when dimensions of waste package are known
Fuel surface coverage by NMP	(~1%)	From literature
Dimension of steel environment	(mm – cm)	To be updated when dimensions of waste package are known
Nodes in steel environment	(log-space grid: fine-spacing near surface)	To be updated when dimensions of waste package are known
Number of FMDM time steps	(100 – 1000)	Use to optimize PA interface
Fuel alteration layer porosity	(~50%)	From literature
Fuel alteration layer tortuosity	(~0.01)	From literature
Fuel alteration layer radiolysis factor	(*not used*)	*Could be activated to account for radionuclide uptake by U secondary phases*
Alpha particle penetration depth	(35μm)	From literature
Fuel burnup	(25 – 75 GWd/MTU)	**Input from PA**
Age of fuel (time out of reactor)	30 – 100 yrs	**Input from PA**
Resistance between fuel and NMP domains	(10^{-3} Volts/Amp)	Interpretation of literature
Temperature history	function	**Data need**: needs to be input from PA – will depend on repository scenario
Dose rate history	function	Based on MCNPX results of Radulescu, 2011
Spatial dose rate	function (decrease in dose rate with distance from fuel)	Based on MCNPX results of Radulescu, 2011
Rate constants for interfacial reactions in fuel and steel domains	See Figure 6 for summary of specific reactions	**Data need:** experiments needed due to lacking or inconsistent data in current literature on H_2 reactions on fuel and NMP and steel corrosion under relevant conditions
Charge transfer coefficients for interfacial half-cell reactions in fuel and steel domains	See Figure 6 for summary of specific reactions	**Data need:** experiments needed due to lacking or inconsistent data in current literature on H_2 reactions on fuel and NMP
Activation energys	T dependence: See Figure 6 for summary of specific reactions	**Data need:** experiments needed due to lacking or inconsistent data in current literature on H_2 reactions on fuel and NMP and steel corrosion under relevant conditions

Table 1. Continued.

Parameter	Description	Data needs to improve accuracy
Standard potentials for interfacial half-cell reactions: fuel and steel	See Fig. 6 for reactions	From literature
Relative area of fuel domain	Default 1:1, depends on waste package design	To be updated when dimensions of waste package are known
Relative area of steel domain	Default 1:1, depends on waste package design	To be updated when dimensions of waste package are known
Environmental leak rate (diffusion barrier factor)	Depends on waste package design, breach	Interpretation of literature
Environmental concentrations	(O_2, H_2, CO_3^{2-}, Fe^{2+})	**Input from PA**
Rate constants for bulk solution reactions in fuel, steel environments	See Figure 6 for summary of specific reactions	From literature
Activation energy for bulk solution reactions	T dependence, See Figure 6 for reactions	From literature
Passivation potential of steel surface	(85 V_{SCE}) as place-holder	**Data need:** experiments needed due to lacking or inconsistent data in current literature
Passivation corrosion current density	Calculated internally within FMDM	Function derived from literature
Radiolytic oxidant (H_2O_2) generation value (G_{cond})	Analytical function for conditional G_{H2O2} value from PNNL radiolysis model	Values based on radiolysis model results, Buck et al., 2013. *Would need to be updated, expanded for brine solutions (Cl, Br)*

3. Results From Test Runs of FMDM with Steel Corrosion Module as the Source of Hydrogen

A series of model runs were done using the updated FMDM over a range of relevant conditions assuming that the steel surface was pure iron metal (simulating carbon-steel). The focus of these runs was to quantify the sensitivity of the FMDM-predicted fuel degradation rate to the rate of steel corrosion. The conditions for these sensitivity calculations are listed below and examples of results are shown in Figures 8, 9 and 10.

- The variables that were changed for these sensitivity runs were: the interfacial rate constant for the oxidation of iron (reaction 1 below) and the age of the fuel.
  - The rate constant was varied from 10^{-3} to 1.0 mole/m^{2}yr (the actual value of this key parameter for different types of steels needs to be determined experimentally).
  - The age of fuel was varied from 20 to 200 years.
- Parameter values (see Table 1) for the fuel environment are from Jerden et al., 2015.
- Parameter values (see Table 1) for the steel environment are from King and Kolar, 2003.
- The environmental concentrations (constant concentration boundary) were [H_2] = 10^{-15} M, [O_2] = 10^{-9} M, [Fe^{2+}] = 10^{-9} M, [CO_3^{2-}] = 10^{-6} M.
- Temperature was held constant at 40°C for all runs.
- Fuel burnup was 50 GWd/tHM (gigawatt days per metric ton of initial heavy metal: U).

At the corrosion potential of carbon steel, under anoxic conditions, the corrosion rate-determining half-reactions are:

$$Fe^0 \rightarrow Fe^{2+} + 2e^- \tag{1}$$

$$2H_2O + 2e^- \rightarrow H_2 + 2OH^- \tag{2}$$

Mixed potential theory states that, at the corrosion potential, the net sum of the current densities of all anodic and cathodic reactions equals zero. That is, the corrosion potential is defined as the kinetic balance between anodic and cathodic reactions. Therefore, since (1) and (2) are the dominant reactions on the corroding steel, the rate of H_2 generation will equal the rate of steel corrosion (Fe oxidation) in units of moles H_2 per steel surface area per time at the corrosion potential. So the steel corrosion rates shown in Figures 8, 9 and 10 are directly proportional to the H_2 generation rates.
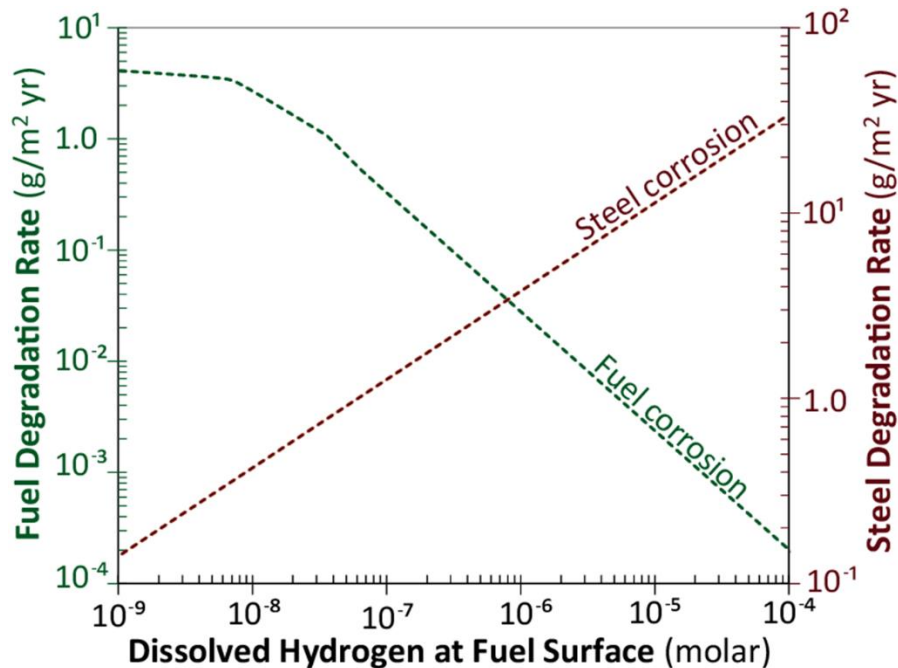
Figure 8. Used fuel and steel corrosion rates as functions of the concentration of dissolved H_2 in the common solution. This example is for a 200 year old fuel with a burnup of 50 GWd/tHM. The source of H_2 is the corrosion of steel and is thus its concentration is proportional to the steel corrosion rate (shown in red). For example, at a steel corrosion rate of ~1.5×10^{-1} g/m² yr the resulting dissolved H_2 concentration at the fuel surface is 10^{-9} molar and for a steel corrosion rate of ~30 g/m² yr the H_2 concentration at the fuel surface is 10^{-4} molar.

Figure 8 indicates that, over a relevant range of steel corrosion rates, the concentration of dissolved H_2 that reaches the fuel surface can vary considerably. The variation in H_2 concentrations produced by this range of steel corrosion rates causes the predicted fuel degradation rate to vary from 2×10^{-4} g/m² yr up to 4.0 g/m² yr over a range of nanomolar to 0.1 millimolar H_2 concentrations.

Figures 9 and 10 show the fuel degradation rates as a function of time when coupled with a range of relevant steel corrosion rates. The dashed curves in Figure 9 show the combined effects of radiolysis and steel corrosion and the solid curve shows the effects of radiolysis alone. As

mentioned above, for this simple but relevant case of carbon steel corrosion, the rate of iron oxidation is equal to the rate of H_2 production at the steel surface. The fuel degradation rate decreases slowly with time as the dose rate at the fuel surface decreases due to the decreasing production rates of the radiolytic oxidant H_2O_2 and associated O_2. That is, as the amount of radiolytic H_2O_2 decreases it takes less H_2 to anodically protect the fuel from oxidative dissolution. Therefore, the fuel degradation rate decreases to the chemical dissolution rate near 10^{-4} for all steel corrosion rates (see Figure 6 for reaction schematic).
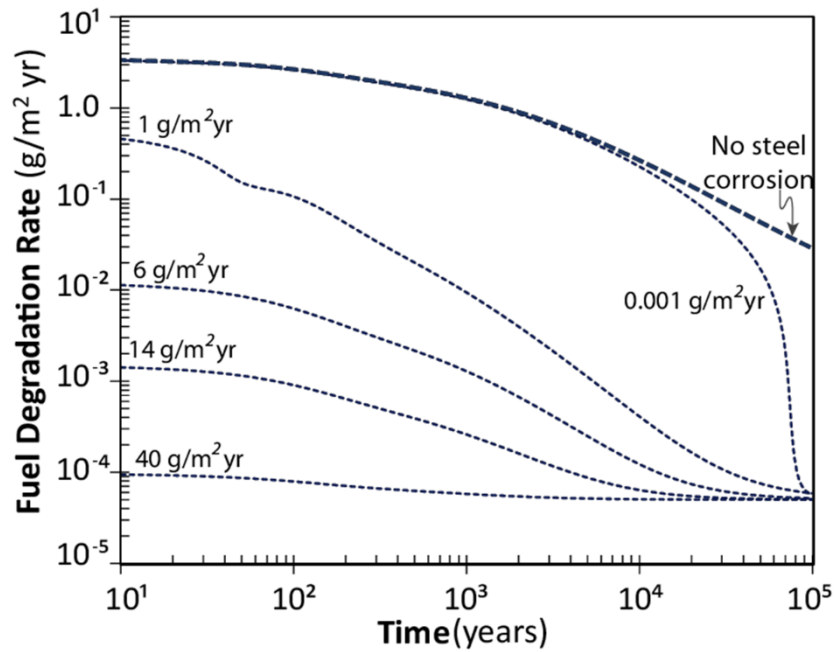
Figure 9. Results from the FMDM with the newly added steel corrosion module. All of these runs are for a 10 year old fuel with a burnup of 50 GWd/tHM. The rate of fuel degradation decreases with increasing steel corrosion rates due to the effect of H_2 which is produced at a rate proportional to steel corrosion (see Figure 6 for reaction summary).
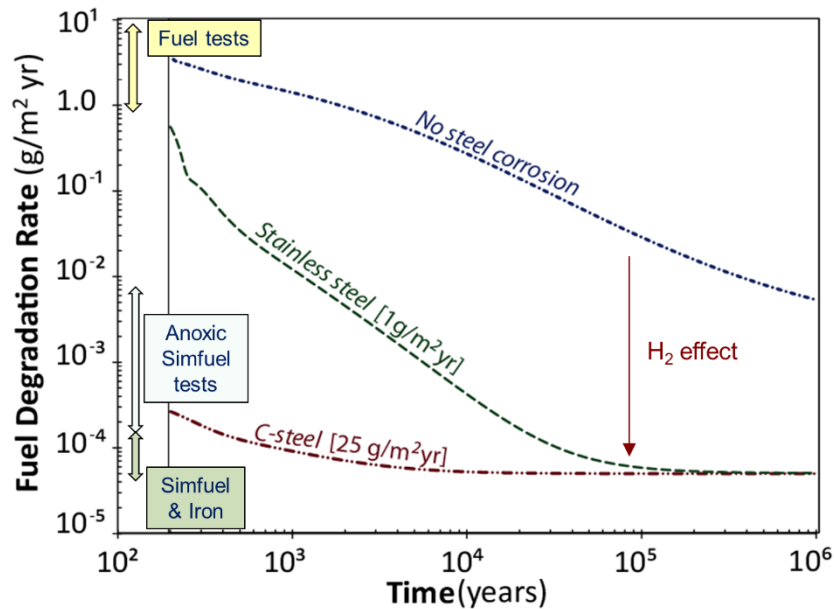
Figure 10. Results from the FMDM with the newly added steel corrosion module, comparing predictions with experimental ranges of degradation rates from relevant used fuel and simfuel tests. Fuel data from Cunnane 2004, Simfuel (U^{233} in UO_2) data from Ollila, 2008. These runs are for a 200 year old fuel with a burnup of 50 GWd/tHM.

Figure 10 also shows data ranges for used fuel and simulated fuel immersion tests. The fuel tests, compiled by Cunnane, 2004, were performed in oxidizing conditions using ~30 year old fuel that varied in burnup from 25 to 45 GWd/tHM. The temperature for these tests was varied from 25°C to 80°C, the pH varied from 7 to 9 and the solution was a buffered DIW with varying concentrations of dissolved carbonate (zero to millimolar). The simfuel tests (Ollila, 2008) involved the immersion of ^{233}U doped UO_2 in buffered DIW at pH 7 – 9 and 25°C to 90°C. These tests were performed under both anoxic conditions (argon purged) and reducing conditions (metallic iron added to tests).

The main conclusion drawn from Figure 10 is that, while there remains a need for focused electrochemical experiments to both measure parameter values and provide model validation data sets for the FMDM, it is encouraging that our initial results are roughly consistent with the data sets summarized in Figure 10 (within the test durations, which is on the order of months).

In order to assess the impact that the steel corrosion/H_2 effect will have on radionuclide source term calculations a hypothetical example was implemented using the radionuclide inventory for a 50 GWd/tHM BWR fuel provided by Carter et al., 2012. For this calculation the fuel dissolution rates from Figure 10 were multiplied by an assumed fuel specific surface area (9.5×10^{-4} m^2/g for fuel pellets in a typical BWR assembly, from Fillmore, 2003) to provide the fractional dissolution rate and then by the radionuclide inventory. For the example plots shown in Figures 11 and 12, the calculated activities of all isotopes were multiplied by biological toxicity factors from 10 CFR, Part 20, Appendix B.

Figure 11a shows the radionuclide source term for a case where there is no steel corrosion occurring during used fuel degradation (top line in Figure 10). Figure 11b shows a case that assumes that the first 30,000 years of fuel degradation is accompanied by carbon steel corrosion that generates relatively high H_2 concentrations (~10^{-4} molar) within the waste package. The

discontinuity at 30,000 years indicates the time at which all of the carbon steel has been consumed leading to the cessation of H_2 production and a corresponding increase in fuel dissolution rate. The time at which the carbon steel was all consumed was arbitrarily chosen and is likely unrealistic; however, it is still instructive in a qualitative sense to show how the consumption of steel can influence source term due to the H_2 effect.
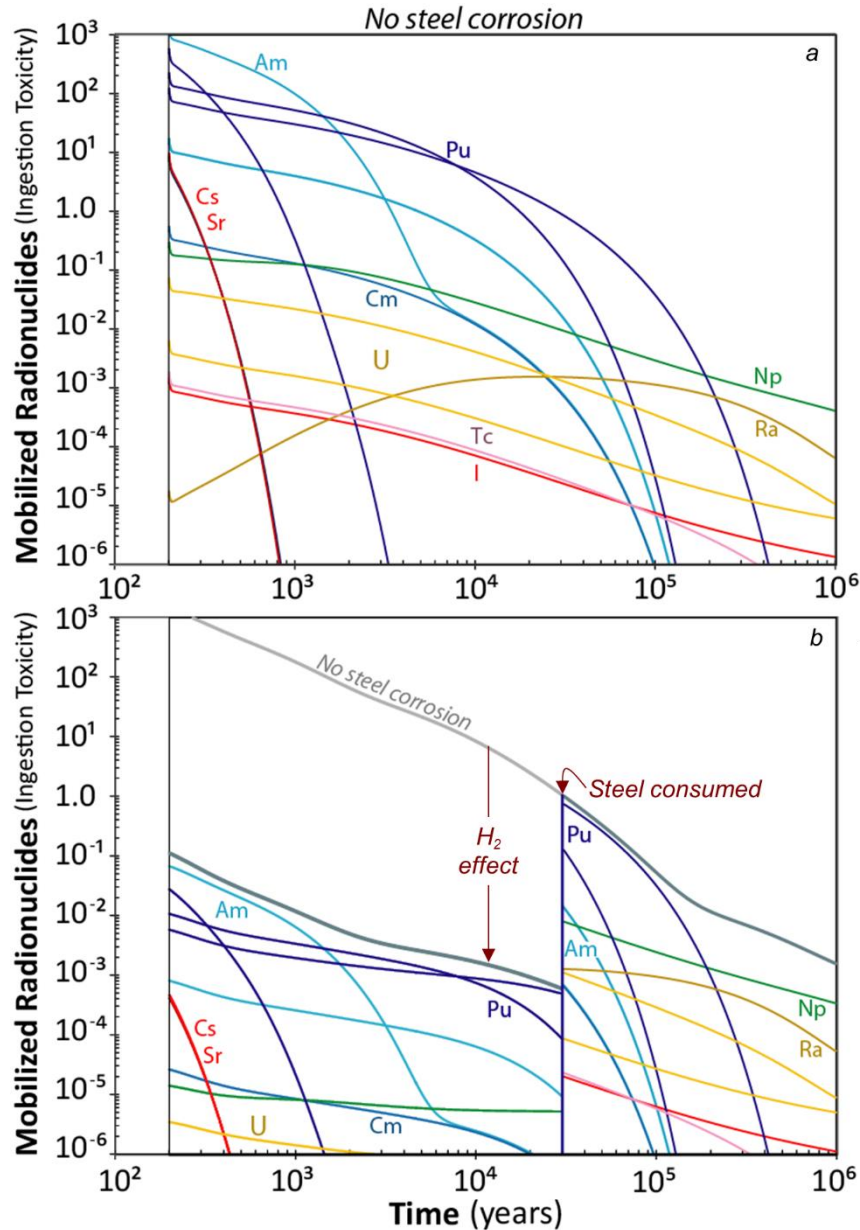
Figure 11. Hypothetical radionuclide source term for (a) the case with no steel corrosion, that is no H_2 generation during fuel degradation and (b) a case where carbon steel is corroding simultaneously with the used fuel for the first 30,000 years of the run. This example is for a 200 year old fuel with a burnup of 50 GWd/tHM. Specific isotopes are not labeled because the purpose of the plot is highlight the elemental output of this hypothetical source term example.

Perhaps a more realistic case is shown in Figure 12. In this figure it is assumed that carbon steel corrodes at a rate of 25 g/m^2 yr until it is all consumed at 3,000 years. At this point the more slowly corroding stainless steel (1 g/m^2 yr) dominates H$_2$ production rates resulting in a higher fuel degradation rate relative to the first 3,000 years. All steel assumed to be consumed by 40,000 years, resulting in the increase of fuel degradation rates due to the absence of H$_2$. Nevertheless, the benefit of accounting for steel corrosion in the FMDM calculations is revealed by integrating the curves to calculate the total mass that has dissolved.

Although the time frames for the FMDM test runs shown in Figures 11 and 12 are arbitrary and both the steel and fuel reaction parameters need to be validated by experiments, these hypothetical source term examples are qualitatively instructive. The most important observation is that, due to the H$_2$ effect, the radionuclide source term may be significantly attenuated. This indicates that having an accurate model for steel corrosion and the associated H$_2$ effect is essential for accurate source term calculations within the performance assessment model.
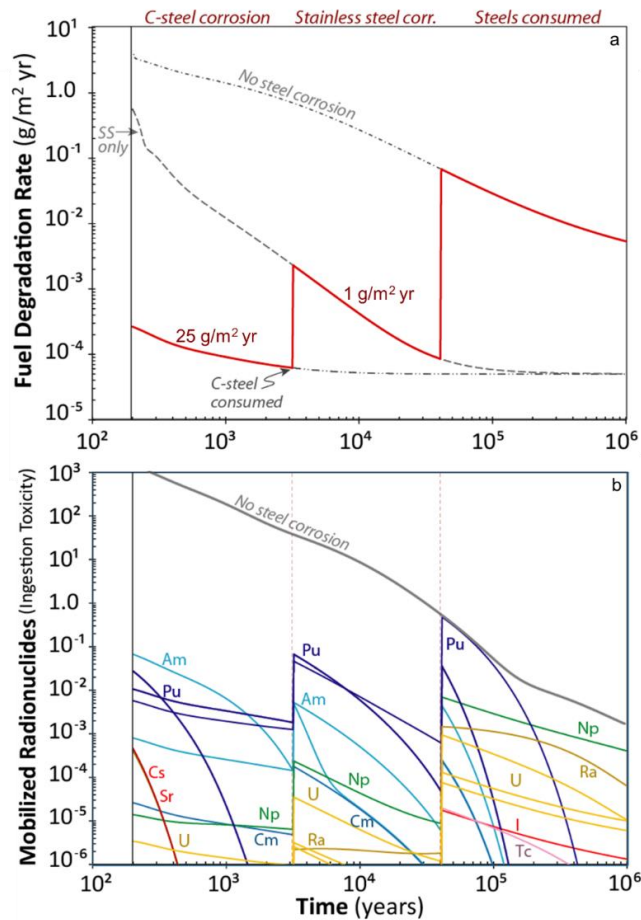
Figure 12. Hypothetical radionuclide source terms for the case where carbon steel corrosion dominates the first 3,000 years, followed by stainless steel until 40,000 years at which point all steel has been consumed (a). (b) shows the radionuclide source term for the case diagrammed in 12a. This example is for a 200 year old fuel with a burnup of 50 GWd/tHM. Specific isotopes are not labeled because the purpose of the plot is highlight the elemental output of this hypothetical source term example.

4. Integration of FMDM With the Generic Disposal System Analysis Performance Assesment (GDSA-PA) Model

Although the basic calculations in the FMDM were successfully integrated with GDSA PA reactive transport code PFLOTRAN in FY-2015 (Jerden et al., 2015), there remains a need to extend the code to encompass all chemical processes relevant to source term (e.g., the addition of the steel corrosion as a source of H_2) and optimize the FMDM code to improve performance. In addition to the extension of the FMDM to include the steel corrosion module (see Section 2 above), the FY-2016 integration work also focused on optimizing the FMDM code.

The basic information flow involved in the integration of the FMDM with PFLOTRAN is shown in Figure 13.
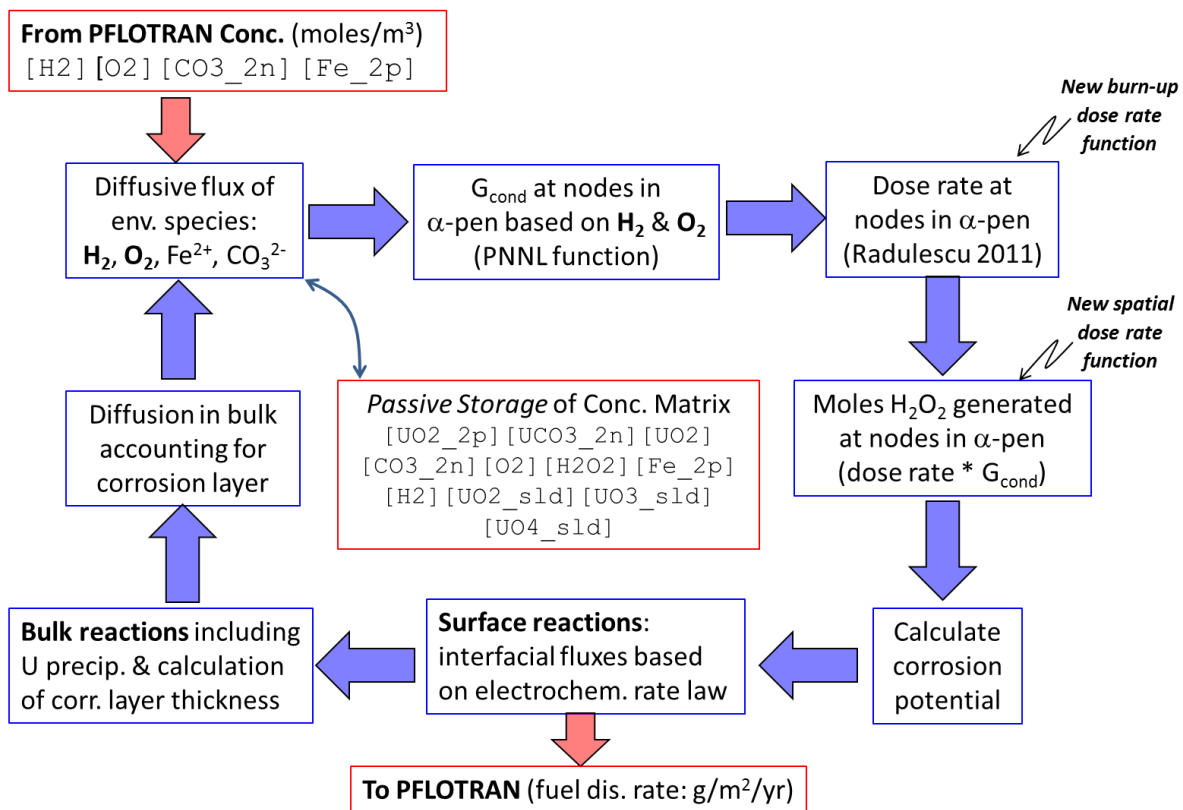
Figure 13. Conceptual flow diagram showing the individual calculations within a single time step of the FMDM. Note that the concentrations of all components must be stored and fed back to the FMDM at the beginning of each new time step. G_{cond} refers to the conditional generation value for H_2O_2, which determines the peroxide generation rate within the alpha radiation zone (α–pen). In the FMDM v.2.3 the conditional H_2O_2 generation value is calculated by an analytical function (G_{cond} is a function of [H_2] and [O_2]).

The FY-2016 FMDM (V.3) optimization work involved the following activities:

- The dose rate function was re-conditioned to avoid mathematical instability.
- Because Code profiling and sensitivity runs showed that the majority of the computing time of the FMDM is taking place in the bulk chemical reaction module, a plan for streamlining the reaction diffusion equations used in this module was formulated.
- A conceptual plan for integrating the FMDM (V.3) into PFLOTRAN was developed and is summarized in Figures 14 and 15 below.

Update of burnup (BU) - dose rate (RAD) function: The dose rates extrapolated to the fuel surface (distance equals zero) were correlated with the results of Radulescu 2011. The dose rate correlation from the Jerden et. al., 2015 report was replaced because of concerns with non-smooth transitions. For the new dose rate function, the main dose profile is represented using a logistic function, and the Am-241 in-growth was accounted for using a Gaussian. This expression should be globally valid, as long as the burn-up and age-of-fuel are greater than zero.

Figure 14 shows how the six process modules that make up the FMDM (V.3) are related to the GDSA PA model. All of the modules are coupled and the flow of information between them is summarized in Figure 13. The primary output of the FMDM is the fuel degradation rate in mass per surface area per time, which is used to define the radionuclide source term in PFLOTRAN. in addition to numerical inputs and outputs between FMDM and PFLOTRAN shown in Figure 14, there are also a number of places where model parameters need to be coordinated to avoid internal inconsistencies within the PA calculation. These points of coordination include:

- Time at which the waste package is breached.
- The temperature history of the waste package.
- The radionuclide inventory used in PFLOTRAN needs to be consistent with the burnup used in the FMDM.
- The solubility limits used in PFLOTRAN need to be consistent with the solubility limits for U(VI) secondary phases and iron oxides used in the FMDM.
- The specific surface area assumed in the PFLOTRAN source term model needs to be consistent with the relative surfaces of the fuel, steel and NMP domains within the FMDM.
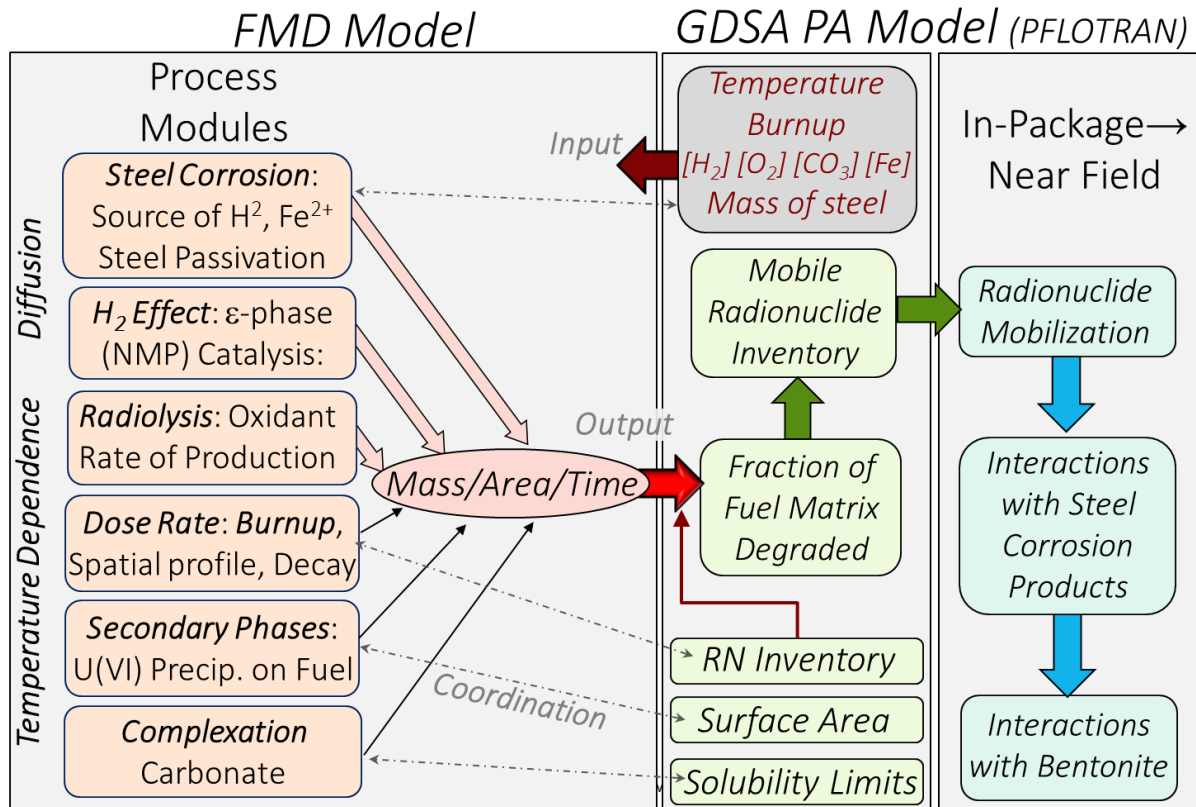
Figure 14. Conceptual diagram showing all of the active process modules in the latest version of the FMDM (V.3) and how they are integrated in terms of inputs and outputs with the PA model.

Figure 15 highlights the key objectives of work proposed for FY-2017 in the context of model integration. As discussed in this report, the effect of H_2 produced from the anoxic corrosion of steel will likely dominate the radionuclide source term for relevant repository scenarios. FY-2017 work will focus on quantifying parameter values and calibrating the steel corrosion and H_2 effect modules that are currently in the FMDM. This work will be done in parallel with efforts to optimize the serial performance of the FMDM to minimize run times. Once these modules are appropriately parameterized and tested, they will be added to the FMDM Fortran files that are called by PFLOTRAN to run within the GDSA PA model.
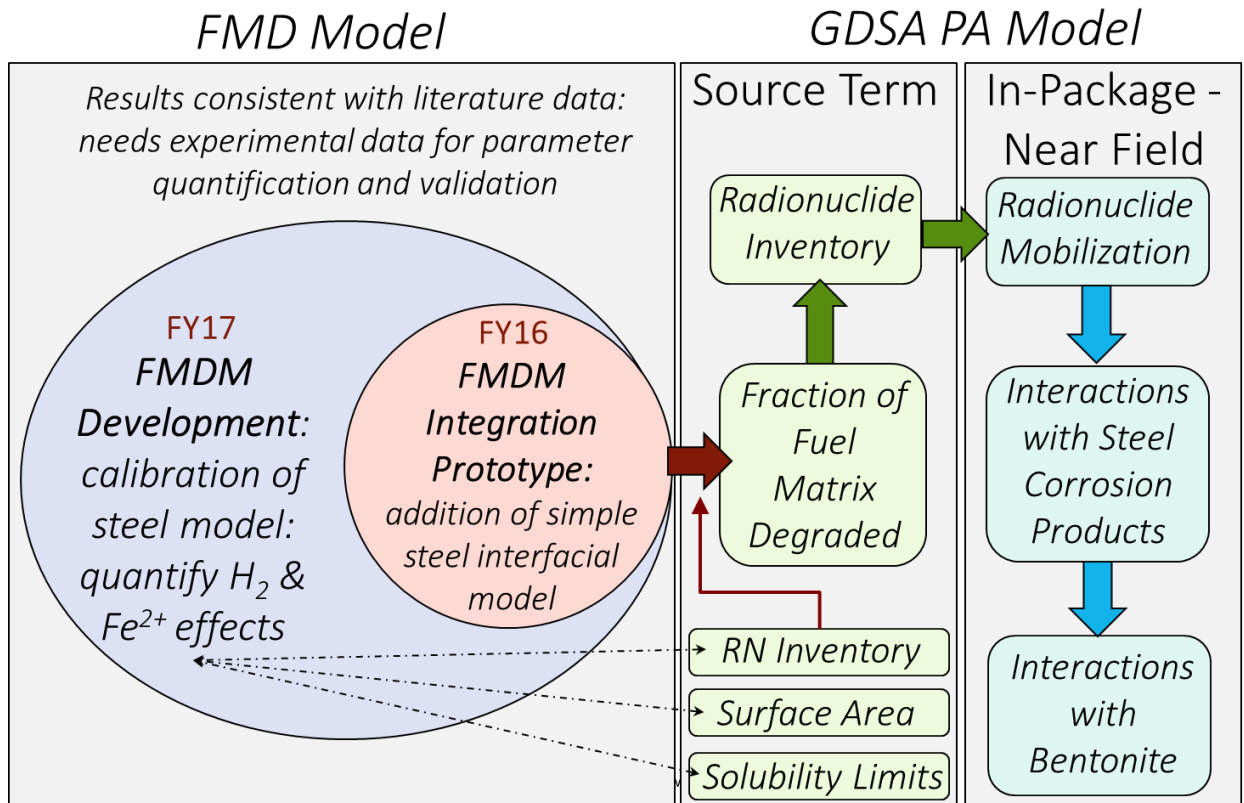
Figure 15. Conceptual diagram highlighting the major objective for FY-2017 in the context of integration with the GDSA PA modeling work.

5. Results from Scoping Experiments on Poisoning Catalytic Activity of Noble Metal Particles

To ensure that the process modules for used fuel degradation and steel corrosion accurately represent reality within the relevant ranges of repository conditions, the model development efforts need to be coupled with a focused experimental program to quantify key parameters and provide data sets for validation. Although the FY-2016 scope for this project did not include a deliverable for experimental work, scoping tests were performed using the radiological electrochemical testing facilities at Argonne National Laboratory (ANL) to provide confidence that the effect of H_2 on used fuel degradation is accurately represented in the FMDM and thus in the PA model.

As shown in Jerden et al., 2015, and in Section 2 above, the catalysis of H_2 oxidation on the NMPs attenuates the used fuel dissolution rate by as much as four orders of magnitude when dissolved H_2 concentrations reach approximately 0.1 mM. Because this NMP – H_2 catalysis process plays such a key role in determining the fuel dissolution rates and its mechanism is not yet fully understood, it is the subject of on-going electrochemical experiments designed to directly inform the process modeling efforts.

The experimental set up for the scoping tests consists of a 20 mL, three-electrode cell in which the experimental cover gas is continuously bubbled during the experiments (Figure 16). Multiple cells (experiments) are run simultaneously within an oven in a radiological laboratory. Multiple power supplies and potentiostats are available so that tests with two or more working electrodes (e.g., NMP and UO_2) can also be performed. The electrodes are characterized pre- and post-experiment by optical and Scanning Electron Microscopy (SEM). The solutions from selected tests are analyzed for electrode constituents (Ru, Mo, Pd, Rh, Tc, U, and other dopants such as REE) by Inductively coupled plasma mass spectrometry (ICP-MS).
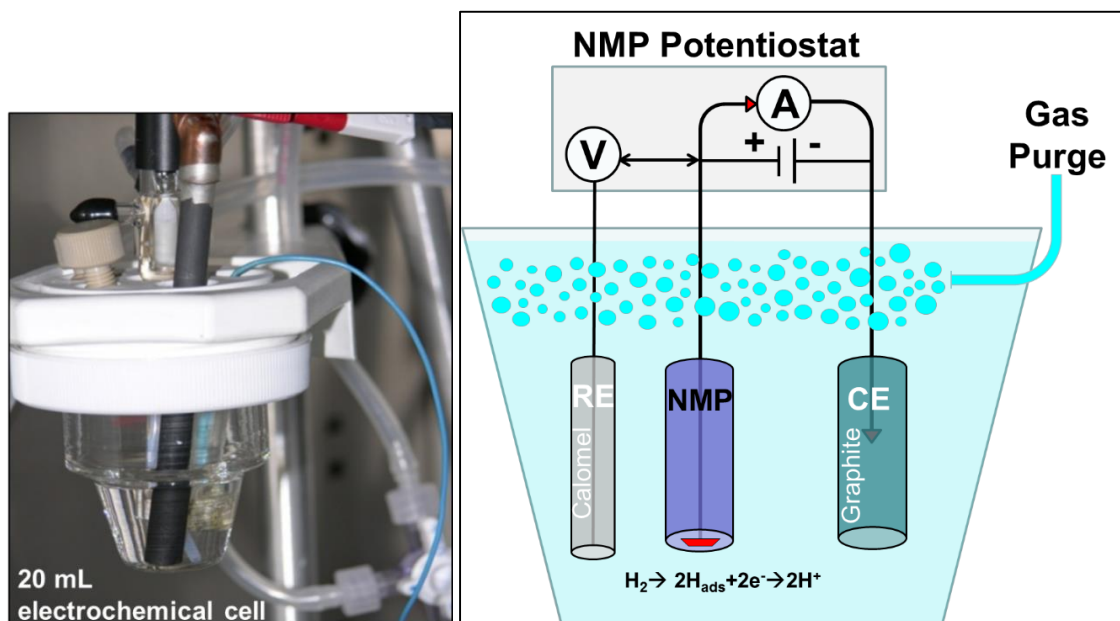
Figure 16. Photograph and schematic diagram of the type of cell used for the electrochemical experiments.

Tests performed in FY-2015 through FY-2016 focused on the interfacial reactions of H_2 with electrodes composed of a technetium bearing noble metal partial, which serves as a simulant for the fission product alloy present in spent fuel and modeled in the FMDM (NMP on Figures 2 and 6 above). Other tests were performed with electrodes made of the most abundant pure elements present in the NMP (Ru, Mo, and Pd). The NMP simulant electrode was made in house (Argonne) from an alloy produced by Steve Frank at Idaho National Laboratory that closely matches the composition and homogeneity (single alloy phase) of the NMP (ε-phase) found in used fuel. The NMP alloy used to make the electrode has a composition of $Ru_{56}Mo_{20}Rh_{11}Pd_{11}Tc_2$ and, based on characterization by SEM and energy dispersive x-ray analyses (EDS), appears to be composed of a single phase with trace amounts of TcO_2.

The EDS analyses of several locations on the NMP alloy used in our experiments show that this material falls within the compositional range of the fission product alloys generated in UO_2 light water reactor fuels (Figure 17).
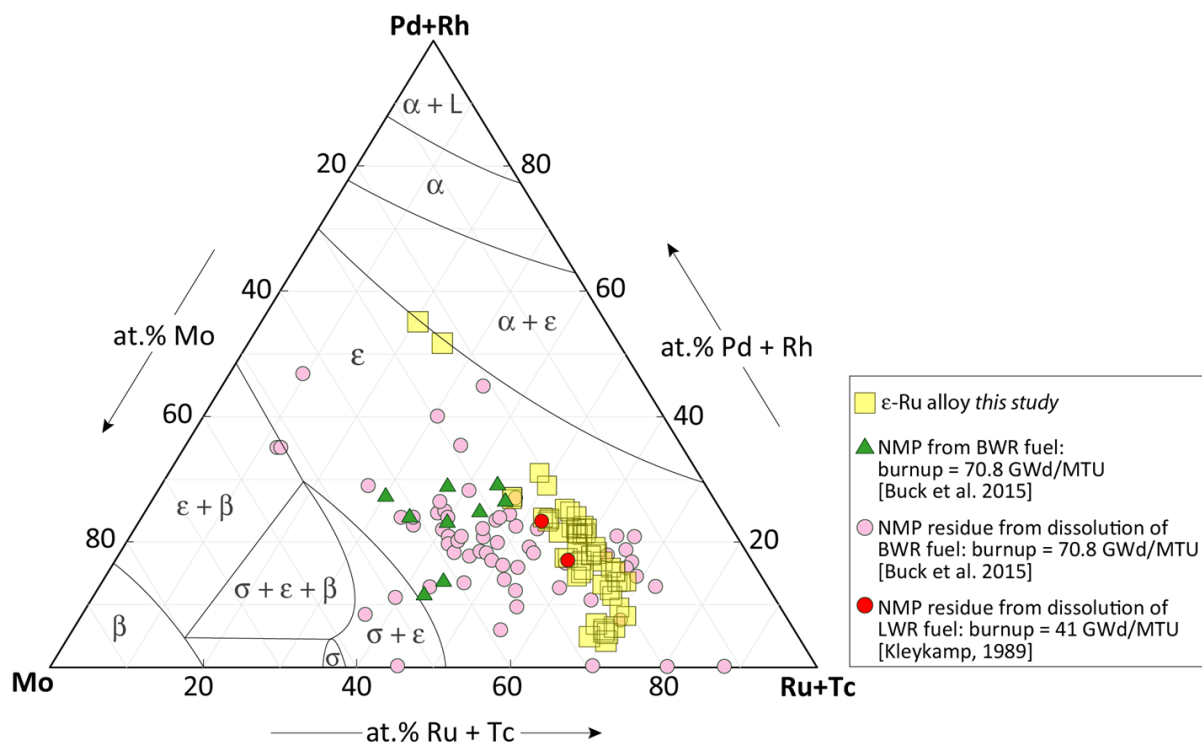
Figure 17. Energy dispersive x-ray analyses of the NMP alloy used in the scoping experimental studies (yellow squares). Note that the alloy falls within the ε-Ru phase field and is thus representative of the fission product alloy phase present in used fuel. The phase fields are for the 1700°C plot of this system from Kleykamp, 1989.

One of the most important experimental observations made regarding the role of H_2 in used fuel dissolution is that the presence of dissolved halides, particularly Br⁻, seems to counteract the H_2 effect (Metz et al., 2008). Although the mechanism is poorly understood, our new results (Figure 18) suggest that the NMP surfaces may be poisoned by halides and reduce their catalytic efficiency (i.e., counteract the protective H_2 effect). The effects of poisoning and alteration of the NMP surfaces are not currently accounted for in the FMDM, because these processes are not well

understood or quantified. However, due to the importance of the H_2 effect these processes are deemed high priorities for experimental investigations.

To investigate the reaction of H_2 on the NMP and other metal electrodes, scoping tests were performed in which the open circuit potential (OCP) of the electrode was measured for up to 80 hours in 1 mM NaCl purged by bubbling either air, Ar or 2% H_2 in Ar through the solution. The possible poisoning effect of Br^- was also investigated by performing the 2% H_2 cover gas tests in solutions containing 1 mM NaBr. The pH for all tests remained relatively constant at around 7.0. Typical results are shown in Figure 18.
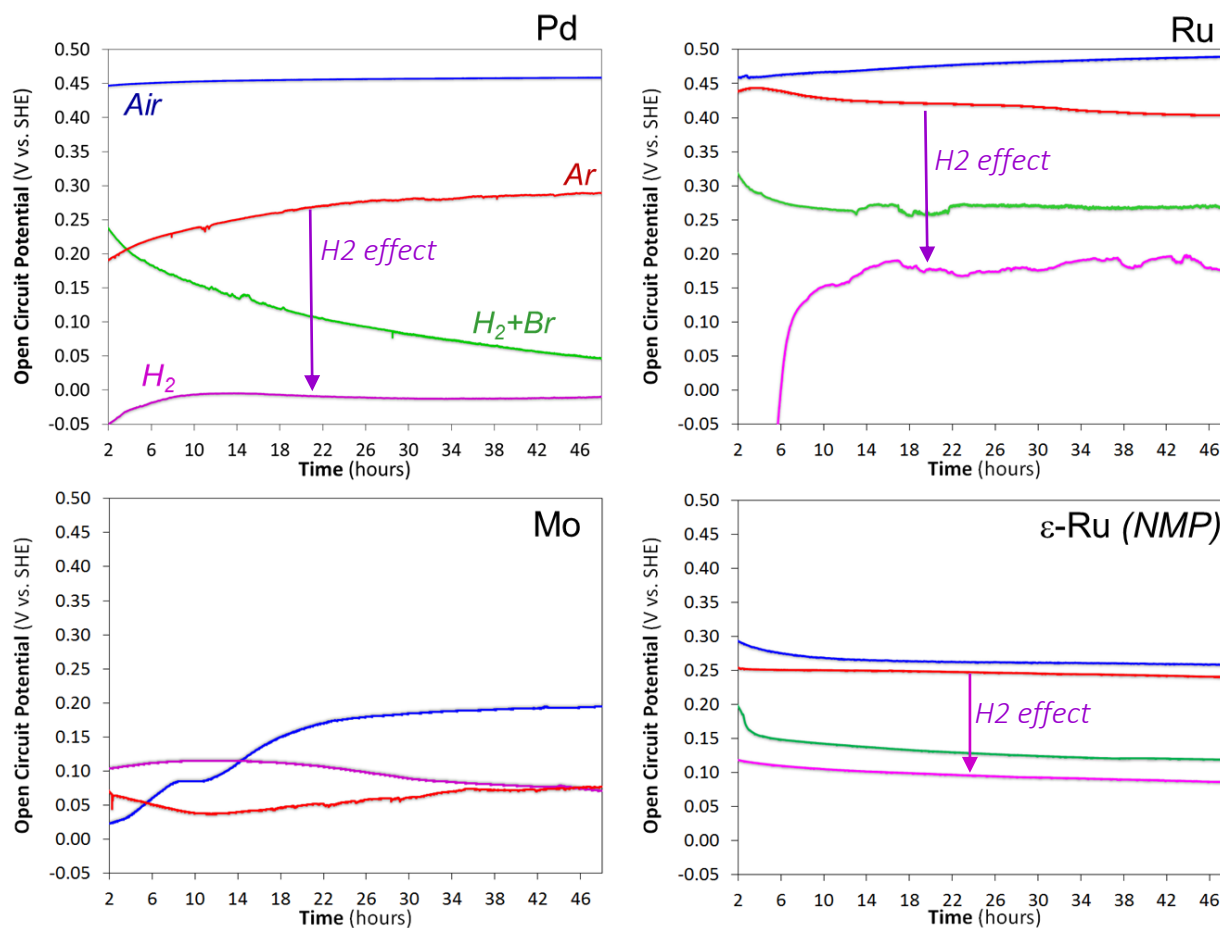
Figure 18. Results from scoping electrochemical tests showing the open circuit potentials of the $Ru_{56}Mo_{20}Rh_{11}Pd_{11}Tc_2$ (NMP) and pure Pd, Ru and Mo electrodes in 1 mM NaCl solution purged with air (blue curves), Ar (red curves), or H_2/Ar (violet curves) and 1 mM NaCl + 1 mM BrCl solution purged with H_2/Ar (green curves). Note that the presence of Br^- partially counteracts the H_2 effect on all of the electrode materials except for Mo. The Mo results were inconsistent due to the formation of an oxide layer (MoO_2) during the test.

The results of tests with the NMP electrode show a pronounced H_2 effect that causes a decrease in the open circuit potential from greater than 260 mV (vs. SHE) for the air cover gas tests down to around 100 mV for tests performed with 2% H_2 in Ar as the cover gas. That this large potential drop is not seen when the test is performed in pure Ar indicates that it is due to H_2 oxidation occurring on the NPM electrode. This shows that, under near neutral conditions, the NMP surface is hosting anodic reactions that can be generalized as:

$$H_2 \rightarrow 2H_{adsorbed} + 2e^- \rightarrow 2H^+ \tag{4}$$

As indicated by the green curves in Figure 18, the presence of 1 mM Br^- partially counteracts the H_2 effect, resulting in the NMP surface potential being approximately 60 mV higher than in its absence. The relative effects of both H_2 and Br^- on the OCP are significantly greater for reactions on the Ru and Pd electrodes; however, the results for the Mo electrode are confounded by the growth of an oxide layer (MoO_2) during the tests. It is likely that a thin (undetectable by SEM) MoO_2 layer is generated on the NMP electrode during the test.

Figure 19 shows the $Eh - pH$ diagrams for the main constituents of the NMP. Of particular interest in Figure 19 is the observation that the MoO_2 stability field overlaps the field for repository relevant conditions. This if interest because it implies that Mo within the NMP will likely oxidize when exposed to in-package solutions, which may impact the catalytic activity of the NMP surfaces. The $Eh - pH$ diagrams also indicate that sulfur may play an important role in the surface chemistry of Ru (the dominant element in the NMP) and thus should be accounted for in future experimental and modeling efforts.

Figure 19 also indicates that MoO_2 and perhaps Ru sulfides could play an important role in the evolution of the NMP surfaces under repository relevant solutions. This is important because the NMP surfaces are responsible for the H_2 effect that anodically protects used fuel from oxidation (see Figure 7 above). This indicates that future experimental and modeling efforts should account for the evolution of the NMP surface in relevant solutions.

The results in Figure 18 also show that even over short time frames (minutes) the presence of Br^- has an effect on the NMP – H_2 reaction. This is a significant observation as it identifies a key chemical process, that could counteract the protective H_2 effect that is not currently accounted for in the FMDM.
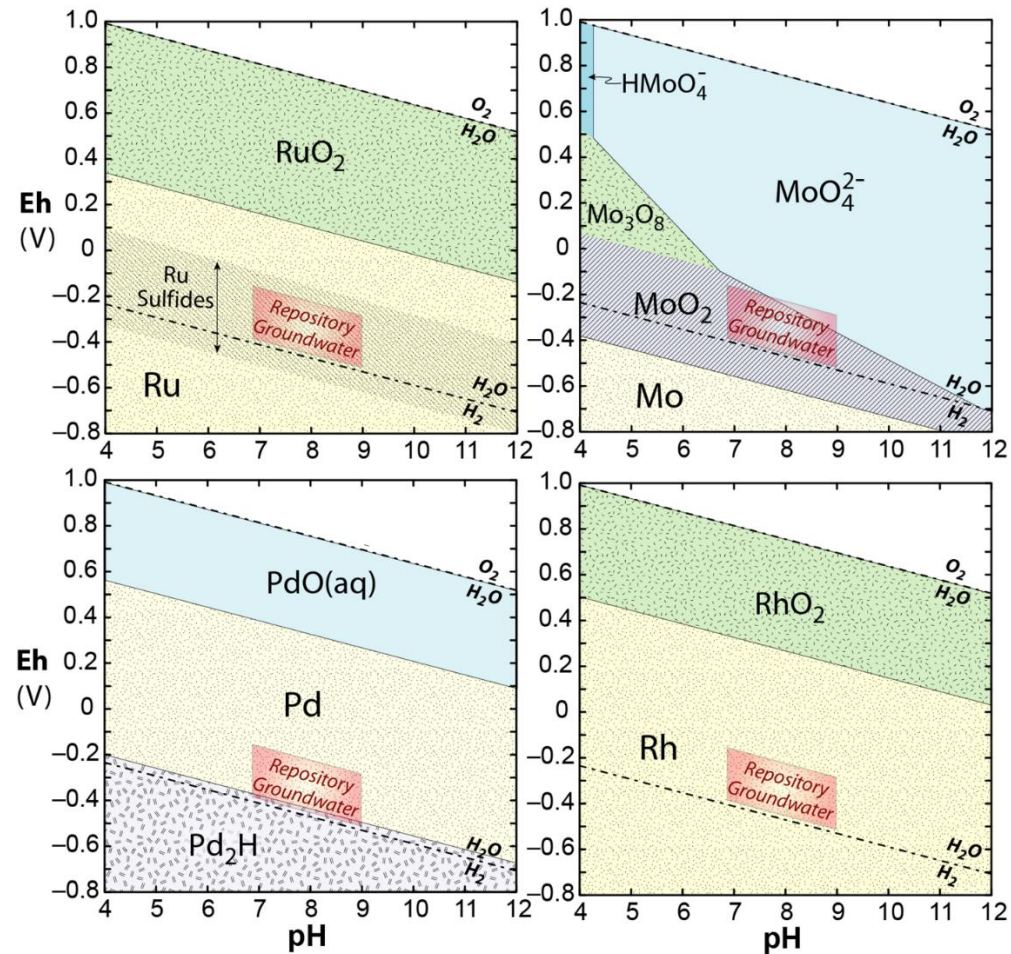
Figure 19. Eh – pH diagrams for the major constituents of the noble metal particle alloy (NMP) present in used fuel.

Future experimental work will also involve a series of electrochemical tests with simulated used fuel that consists of NMP in a UO_2 matrix. These tests will be used to generate a validation data set for the FMDM.

6.   Conclusions and Recommendations for Future Work

The primary purpose of this project is to develop a process model to calculate the degradation rate of used fuel based on fundamental underlying processes used to determine radionuclide source terms for reactive transport calculations in the Generic Disposal System Analysis PA model.

The main accomplishments for Argonne's FY2016 work on the Fuel Matrix Degradation Model (FMDM) development project are as follows:

- Formulated, coded and tested an electrochemical steel corrosion module that couples in-package steel corrosion with fuel degradation through the common solution. This module provides the kinetic source of H_2 that may control the used fuel dissolution rates under repository relevant conditions.

- Updated and optimized FMDM to improve the efficiency of integration with the GDSA PA model.
- Performed scoping electrochemical tests to build confidence in modeling the H_2 effect mechanism, which has been shown by both experiment and electrochemical modeling to significantly impact source term calculations when in-package steel components are corroding simultaneously with used fuel.

The key finding of the FY-2016 work was that the corrosion of steel canister materials will have a significant impact on the radionuclide source terms calculated by PA because of its role as the major source of the H_2, which attenuates the fuel degradation rate. The test runs with the updated FMDM indicate that the peak radionuclide source term from a breached waste package will likely be attenuated by the H_2 effect and the corrosion of steel components (the dominant source of H_2 in the system).

These processes have been added in the FMDM V.3; however, there remains a need for coupled experimental and process modeling work to accurately parameterize and validate the model. This future work is particularly important because the FMDM is currently being used to provide the radionuclide source term in the PA model. Thus, future improvements to the FMDM process model will have a direct impact on the accuracy of the existing GDSA PA model.

FY-2017 activities of particular importance are:

- Extend the FMDM Fortran – PFLOTRAN interface files to account for the corrosion of the steel components and the associated H_2 effect that anodically protects the fuel from oxidative degradation.
- Take next step in integration of FMDM with PA: demonstrate sensitivity of the Argillite PA model to key variables in the FMDM such as burnup, surface area, steel corrosion/H_2 production rates and the dissolved concentrations of H_2, O_2, carbonate and ferrous iron.
- Perform focused electrochemical experiments to determine the effect of halides and other possible poisons on the catalytic efficiency of the NMP. These tests will quantify processes that may counteract the protective H_2 effect.
- Account for the effect of poisons (e.g., Br, S) or other processes that counteract the protective H_2 effect in the FMDM.

Furthermore, the recognition and quantification of the interactions between the corrosion of steel waste package components and waste form degradation suggests that our models may provide important insights as to the types of steel that could be used to optimize the long-term performance of the waste package and canister materials.

7.   References

Buck E., Jerden, J., Ebert, W., Wittman, R., (2013) Coupling the Mixed Potential and Radiolysis Models for Used Fuel Degradation, FCRD-UFD-2013-000290.

Buck, E., Mausolf, E., McNamara, B., Soderquist, C., Schwantes, J., 2015, Nanostructure of Metallic Particles in Light Water Reactor Used Nuclear, *Journal of Nuclear Materials* 461, 2015, 236–243

Cunnane, J.C., 2004, CSNF Waste Form Degradation: Summary Abstraction, Bechtel SAIC Company LLC Technical Report, ANL-EBS-MD-000015 REV 02, August 2004

Fillmore, D.L., 2003, Parameter Selection for Department of Energy Spent Nuclear Fuel to be Used in the Yucca Mountain License Application, Idaho National Engineering and Environmental Laboratory Report, INEEL/EXT-03-01032 Revision 1, October 2003

Grambow, B., Bruno, J., Duro, L., Merino, J., Tamayo, A., Martin, C., Pepin, G., Schumacher, S., Smidt, O., Ferry, C., Jegou, C., Quiñones, J., Iglesias, E., Rodriguez Villagra, N., Nieto, J., Martínez-Esparza, A., Loida, A., Metz, V., Kienzler, B., Bracke, G., Pellegrini, D., Mathieu, Wasselin-Trupin, G., Serres, C., Wegen, D., Jonsson, M., Johnson, L., Lemmens, K., Liu, J., Spahiu, K., Ekeroth, E., Casas, I., de Pablo, J., Watson, C., Robinson, P., Hodgkinson, D., 2010, Model Uncertainty for the Mechanism of Dissolution of Spent Fuel in Nuclear Waste Repository, European Commission, Final Report for MICADO Project, EUR 24597, 2010.

Jerden J. Copple J., Frey K. Ebert W., 2014, Prototype Fortran Version of the Mixed Potential Process Model for Used Fuel Degradation, Used Fuel Disposition Campaign Milestone: M4FT-15AN0806012, October 15, 2014

Jerden J., Glenn Hammond, G., Copple J., Cruse, T., Ebert W., 2015, Fuel Matrix Degradation Model: Integration with Performance Assessment and Canister Corrosion Model Development, FCRD-UFD-2015- 000550, July 21, 2015

Jerden J. Frey K. Ebert W., 2015, A Multiphase Interfacial Model for the Dissolution of Spent Nuclear Fuel, *Journal of Nuclear Materials*, 462, 135–146

Joe T. Carter, J., Luptak, A., Gastelum, J., Stockman, C., Miller, A., 2012, Fuel Cycle Potential Waste Inventory for Disposition, FCR&D-USED-2010-000031 Rev 5, July 2012

King F. and Kolar M., (2003). The Mixed-Potential Model for UO_2 Dissolution MPM Versions V1.3 and V1.4., Ontario Hydro, Nuclear Waste Management Division Report No. 06819-REP-01200-10104 R00.

Kleykamp, H., Constitution and Thermodynamics of the Mo-Ru, Mo-Pd, Ru-Pd and Mo-Ru-Pd Systems, *Journal of Nuclear Materials*, 167 (1989), 49-63

Laaksoharju M., Smellie, J., Tullborg, E-L., Gimeno, M., Hallbek, L., Molinero, J., Waber, N., 2008, Bedrock hydrogeochemistry Forsmark site descriptive modeling SDM-Site Forsmark, SKB R-Report (R-08-47), SKB, Stockholm, Sweden

Mariner, P., Gardner, P., Hammond, G, Sevougian, D, Stein E., 2015, Application of Generic Disposal System Models, FCRD-UFD-2015-000126, SAND2015-10037, September 22, 2015, 209pp.

Metz V., Loida A., Bohnert E., Schild D., Dardenne K., (2008) Effects of Hydrogen and Bromide on the Corrosion of Spent Nuclear Fuel and γ-irradiated UO_2(s) in NaCl Brine, *Radiochim. Acta* 96, 637–648

NRC Regulations, Title 10, Code of Federal Regulations, PART 20—STANDARDS FOR PROTECTION AGAINST RADIATION, Appendix B to Part 20—Annual Limits on Intake (ALIs) and Derived Air Concentrations (DACs) of Radionuclides for Occupational Exposure; Effluent Concentrations; Concentrations for Release to Sewerage

Ollia, K., 2008, Dissolution of Unirradiated UO_2 and UO_2 Doped with ^{233}U in Low- and High-Ionic-Strength NaCl Under Anoxic and Reducing Conditions, Posiva Working Report 2008-50

Radulescu, G., (2011) Repository Science/Criticality Analysis, Oak Ridge National Laboratory, Reactor and Nuclear Systems Division, FTOR11UF0334, ORNL/LTR-2011, Oak Ridge National Laboratory, Oak Ridge, TN.

Röllin S., Spahiu K., Eklunda U., (2001), Determination of Dissolution Rates of Spent Fuel in Carbonate Solutions Under Different Redox Conditions with a Flow-through Experiment, *Journal of Nuclear Materials*, 297, 231–243

Shoesmith, D., 2008, The Role of Dissolved Hydrogen on the Corrosion/Dissolution of Spent Nuclear Fuel, Nuclear Waste Management Organization, Toronto, Ontario, Canada, TR-2008-19, November 2008.

Wang Y. et al., (2014) *Used Fuel Disposal in Crystalline Rocks: Status and FY14 Progress*, FCRD-UFD-2014-000060, SAND2014, Sandia National Laboratories, Albuquerque, NM.

Addition of Bromide to Radiolysis Model Formulation for Integration with the Mixed Potential Model (Part VI)

1.   Introduction

The U.S. Department of Energy Office of Nuclear Energy (DOE-NE), Office of Fuel Cycle Technology has established the Used Fuel Disposition Campaign (UFDC) to conduct the research and development activities related to storage, transportation, and disposal of used nuclear fuel (UNF) and high-level radioactive waste. Within the UFDC, the components for a general system model of the degradation and subsequent transport of UNF is being developed to analyze the performance of disposal options [Sassani et al., 2012]. Two model components of the near-field part of the problem are the ANL Mixed Potential Model and the PNNL Radiolysis Model. This report is in response to the desire to integrate the two models as outlined in [Buck, E.C, J.L. Jerden, W.L. Ebert, R.S. Wittman, (2013) "Coupling the Mixed Potential and Radiolysis Models for Used Fuel Degradation," FCRD-UFD-2013-000290, M3FT-PN0806058]

Details of the approach are intended to be sufficient for developing a module for calculating radiolytic generation of hydrogen peroxide with known concentration of H_2, O_2 and Br^-. The listings of the program and reactions considered in this report are given in the appendices.

2.   Radiolysis Model for Use in Used Fuel Oxidation

Previous work that reports the results of a radiolysis model sensitivity study [Wittman RS and EC Buck. 2012] showed that of the approximately 100 reactions [Pastina, B. and LaVerne, J. A., 2001] describing water radiolysis, only about 37 are required to accurately predict H_2O_2 to one part in 10^5. The intended application of that radiolysis model (RM) was to calculate H_2O_2 production for an electrochemical based mixed potential model (MPM) [Jerden, J., Frey, K., Cruse, T., and Ebert, W., 2013] developed to calculate the oxidation/dissolution rate of used nuclear fuel [Shoesmith, D.W., Kolar, M., and King, F., 2003] under disposal conditions where O_2 is expected to be at low concentrations and H_2 is generated from oxidation of steel containers. As an initial approximation, that model (MPM) was developed under the assumption that H_2O_2 is generated at a rate determined only by its radiolytic G-value. Ideally, for a full RM-MPM integration, the MPM would use a reaction kinetics based model to predict H_2O_2 for various water chemistries. As a further step in that direction, this report updates the previously reported steady-state behavior of a full RM under conditions where small concentrations of bromide [Br^-] are present.

2.1   Model Coupling Definition

The RM coupled kinetics/diffusion rate equations for H_2O_2 on discrete special zones (n) can be expressed in terms concentrations [H_2O_2]$_n$, fluxes J_n and dose rate $\dot{d}$ according to

$$\frac{d\left[H_2O_2\right]_n}{dt} + \frac{J_n^{(H_2O_2)} - J_{n-1}^{(H_2O_2)}}{x_n - x_{n-1}} = G_{H_2O_2}\dot{d}_n + (\text{reaction kinetics})_n \quad . \tag{1}$$

Assuming nonzero reaction kinetics and dose-rate only in the radiation zone (x_R) with diffusion out to the boundary (x_B), the steady-state solution to Eq. (1) after inserting Fick's Law fluxes containing diffusion constant D and boundary concentration [H_2O_2]$_B$ can be written:

$$\frac{D_{H_2O_2}}{x_R x_B}\left[H_2O_2\right] = G_{H_2O_2}\dot{d} + (\text{reaction kinetics}) + \frac{D_{H_2O_2}}{x_R x_B}\left[H_2O_2\right]_B \equiv G_{H_2O_2}^C \dot{d} \quad . \tag{2}$$

Equation 2 serves as the working definition of "conditional" G-value [Buck, et al., (2013)] ([H_2O_2]$_B$ = 0 is assumed). Here "conditional" refers to an effective H_2O_2 generation that is

conditional on the local water chemistry. Additionally, because each time-step of the MPM the radiolysis model would have effectively reached steady-state, Eq. (2) is assumed to define the interface between the RM and MPM – i.e. the MPM evaluates a new conditional G-value for its H_2O_2 production calculation at each time-step.

The next section describes an analytical simplification of the full RM to approximate $[H_2O_2]$ and Eq. (2) for use in the MPM and how $[H_2O_2]$ is affected by the presence of bromide.

Model Inclusion of Bromide Reactions

This section reviews how a simple analytical function for a conditional H_2O_2 G-value compares with the full radiolysis model and shows the added effect of including $[Br^-]$ related reactions. The Table 2-1 reactions contain the H_2O_2 generating mechanism of the full RM predictions. Without Br^- and for low O_2 concentration, reaction 33 shows how the presence of H_2 converts the $\cdot OH$ radical to the $\cdot H$ radical to accelerate H_2O_2 destruction lowering its conditional G-value. At higher O_2 concentrations, O_2 effectively competes for $\cdot H$ radicals to disable H_2O_2 destruction (reaction 27) (reaction numbers are those of the full RM and rate constants are from [Elliot, A.J.; McCracken, D.R. 1990] and [Kelm, M.; Bohnert, E. 2004]).

Table 2-1. Subset of reactions sufficient to represent the primary mechanisms for H_2O_2 generation in the full RM.

	Reaction	k_r
3	$H_2O_2 \rightarrow H^+ + \cdot HO_2^-$	1.1×10^{-1}
4	$H^+ + \cdot HO_2^- \rightarrow H_2O_2$	5.0×10^{10}
15	$\cdot HO_2 \rightarrow O_2^- + H^+$	1.3×10^6
16	$O_2^- + H^+ \rightarrow \cdot HO_2$	5.0×10^{10}
23	$e^- + H_2O_2 \rightarrow \cdot OH + OH^-$	1.1×10^{10}
26	$\cdot H + H_2O_2 \rightarrow \cdot OH + H_2O$	9.0×10^7
27	$\cdot H + O_2 \rightarrow \cdot HO_2$	2.1×10^{10}
33	$\cdot OH + H_2 \rightarrow \cdot H + H_2O$	4.3×10^7
34	$\cdot OH + H_2O_2 \rightarrow \cdot HO_2 + H_2O$	2.7×10^7
35	$\cdot HO_2 + O_2^- \rightarrow \cdot HO_2^- + O_2$	8.0×10^7
36	$H_2O_2 \rightarrow \cdot OH + \cdot OH$	2.5×10^{-7}
94	$Br^- + \cdot OH \rightarrow BrOH^-$	1.1×10^{10}
96	$Br^- + \cdot H \rightarrow BrH^-$	0.0×10^6
102	$Br^- + H_2O_2 \rightarrow Br^- + O_2^- + 2HO^+$	2.5×10^9
138	$BrOH^- \rightarrow Br^- + \cdot OH$	3.0×10^7
139	$BrOH^- \rightarrow \cdot Br + OH^-$	4.2×10^6

The net effect of this mechanism can be seen in Figure 2-1 where a reduction in H_2O_2 generation occurs for small O_2 and high H_2 concentration.
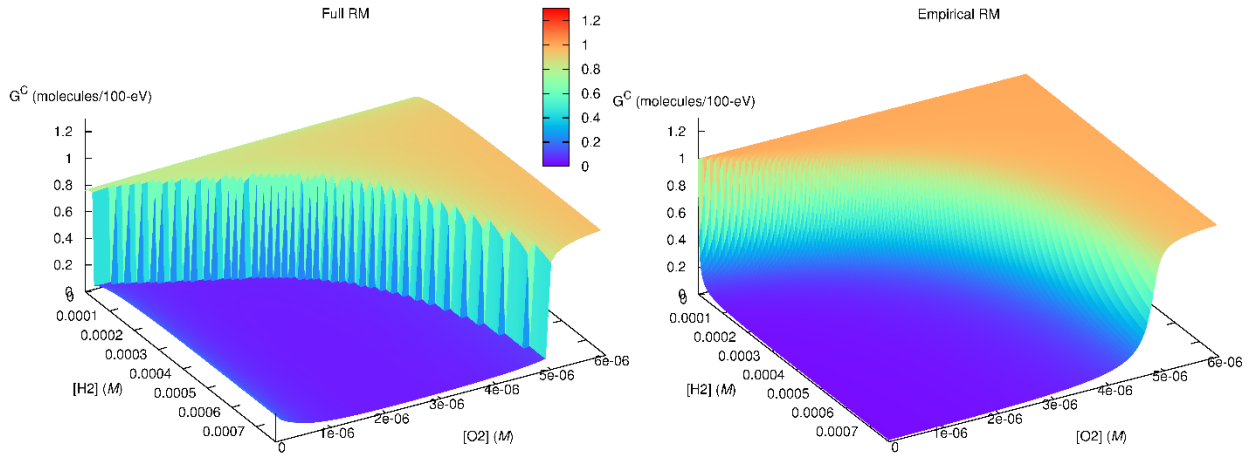
Figure 2-1. Comparison of Full RM and Empirical RM Steady-state conditional G-values at a dose rate of 160 rad/s.

The effect of even small concentrations of Br$^-$ can be seen in Figure 2-2. Figure 2-2 shows a slice through Figure 2-1 where [O$_2$] is fixed at 1 μM. The effect of high H$_2$ concentrations to lower the H$_2$O$_2$ conditional G-value is nearly removed with the presence of Br$^-$.
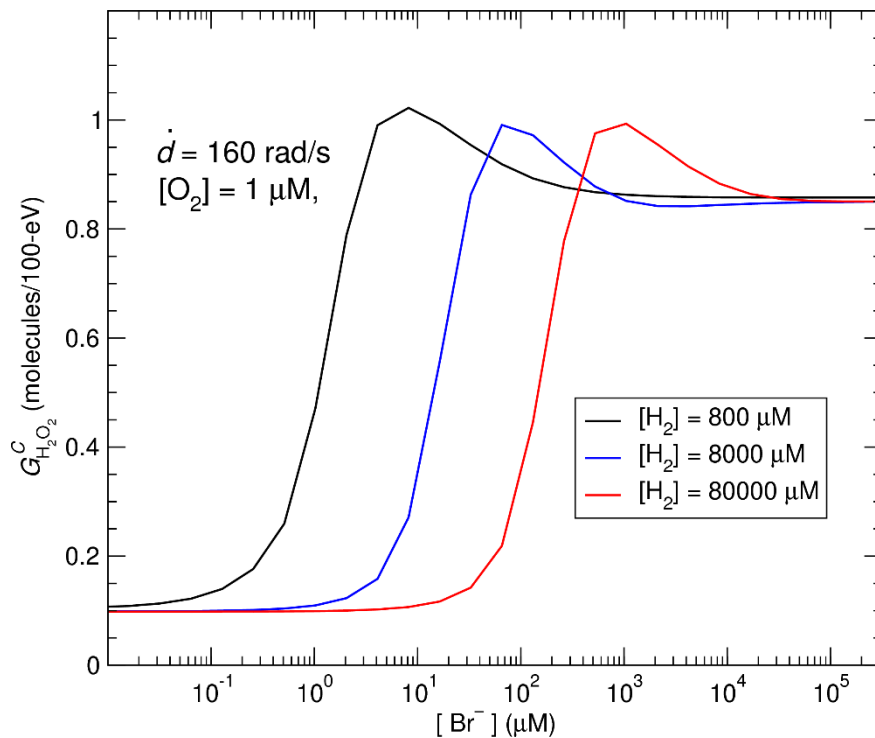
Figure 2-2. Effect of [Br$^-$] on the H$_2$O$_2$ conditional G-values in a ([H$_2$], [O$_2$]) region of suppressed H$_2$O$_2$ generation rate with Full RM.

It is interesting that even at a hydrogen pressure of 100 atm ([H$_2$] = 80000 μM) only 100-400 μM of Br$^-$ can bring G^C from 0.1 to nearly 1 molecule/100-eV. The main reason for the effect is reaction 92 in Table 2-1 [Kelm, M.; Bohnert, E. 2004]. By competing for the ·OH radical, Br$^-$

317

disables the mechanism for converting ·OH radicals to ·H radical, strongly lowering the rate of destruction of H_2O_2 destruction It should be mentioned that this mechanism does not operate for the chloride ion because of the smaller rate constant for reaction 39 (see Appendix G).

Based on Table 2.1 an empirical model was previously developed with a minimal number of reactions for use in the MPM. A summary of that model can be described by four "simplified" rate equations that dominate when hydrogen concentration is large. In the radiation zone assuming diffusion only for H_2O_2 and O_2, the four equations that incorporate reaction 92 are:

$$\tilde{D}_{H_2O_2}[H_2O_2] = \tilde{G}_{H_2O_2} - k_{26}[\cdot H][H_2O_2] - k_{36}[H_2O_2] \tag{3}$$

$$0 = \tilde{G}_{\cdot H} - k_{27}[\cdot H][O_2] - k_{23}[\cdot H][H_2O] + k_{33}[\cdot OH][H_2] \tag{4}$$

$$0 = \tilde{G}_{\cdot OH} - k_{33}[\cdot OH][H_2] - k_{94}[\cdot OH][Br^-] \tag{5}$$

$$\tilde{D}_{O_2}[O_2] = -k_{27}[\cdot H][O_2] + \tilde{D}_{O_2}[O_2]_B \tag{6}$$

where the bromide concentration is assumed to enter only through reaction 94 [Eq. (5)]. Additionally, if we assume the bromide concentration is the value in the radiation zone as with H_2, the conditional G-value can be expressed as the solution to a quadratic equation

$$G^C_{H_2O_2} = \frac{-C_1 + \left(C_1^2 - 4C_0C_2\right)^{\frac{1}{2}}}{2C_2} \tag{7}$$

where the coefficients are given by:

$$C_0 = -k_{23}k_{27}[H_2O]\tilde{D}^2_{H_2O_2} \tag{8}$$

$$C_1 = -\tilde{D}_{H_2O_2}\left[k_{26}k_{27}[O_2]_B\tilde{D}_{O_2} + k_{23}k_{26}[H_2O]\tilde{D}_{O_2} - 2k_{23}k_{27}[H_2O]\left(\tilde{D}_{H_2O_2} + k_{36}\right)\right]$$
$$+k_{26}k_{27}\tilde{D}_{H_2O_2}\left(\tilde{G}_{\cdot H} + \tilde{G}_{\cdot OH}F_{Br^-}\right) \tag{9}$$

$$C_2 = \left[k_{26}k_{27}[O_2]_B\tilde{D}_{O_2} + k_{23}k_{26}[H_2O]\tilde{D}_{O_2} - k_{23}k_{27}[H_2O]\left(\tilde{D}_{H_2O_2} + k_{36}\right)\right]\left(\tilde{D}_{H_2O_2} + k_{36}\right)$$
$$+k_{26}\left(k_{26}\tilde{D}_{O_2} - k_{27}\tilde{D}_{H_2O_2} - k_{27}k_{36}\right)\left(\tilde{G}_{\cdot H} + \tilde{G}_{\cdot OH}F_{Br^-}\right), \tag{10}$$

where

$$F_{Br^-} = \frac{k_{33}[H_2]}{k_{33}[H_2] + k_{94}[Br^-]}. \tag{11}$$

Unlike the pure water system, the presence of bromide introduces an additional dependence on hydrogen through Eq. (11). In this approximation some of the effect of H_2 is handled empirically by making $G_{\cdot H}$ and $G_{\cdot OH}$ dependent on $[H_2]$ according to:

318

$$G_{,\mathrm{H}} = (0.10 \text{ molecules}/100\text{-eV}) \left[1 - \exp\left(-\frac{[\mathrm{H}_2]F_{\mathrm{Br}^-}/0.1 \text{ atm}}{7.8 \times 10^{-4} M/\mathrm{atm}} \right) \right] \tag{12}$$

$$G_{,\mathrm{OH}} = (0.35 \text{ molecules}/100\text{-eV}) \left[1 - \exp\left(-\frac{[\mathrm{H}_2]F_{\mathrm{Br}^-}/0.3 \text{ atm}}{7.8 \times 10^{-4} M/\mathrm{atm}} \right) \right] \tag{13}$$

Additionally, in this approximation k_{23} is reduced by a factor of 56, k_{94} is increased by a factor of 10 and x_B is adjusted between 0.4 and 0.5~cm to compare reasonably well with the full radiolysis model kinetics-diffusion result. Appendix H gives the FORTRAN listing for evaluating the empirical RM. Figure 2-3 shows the conditional G-value as a function of $[\mathrm{H}_2]$ and $[\mathrm{O}_2]_B$ for the full RM and for the one calculated from Eqs. (7-13).
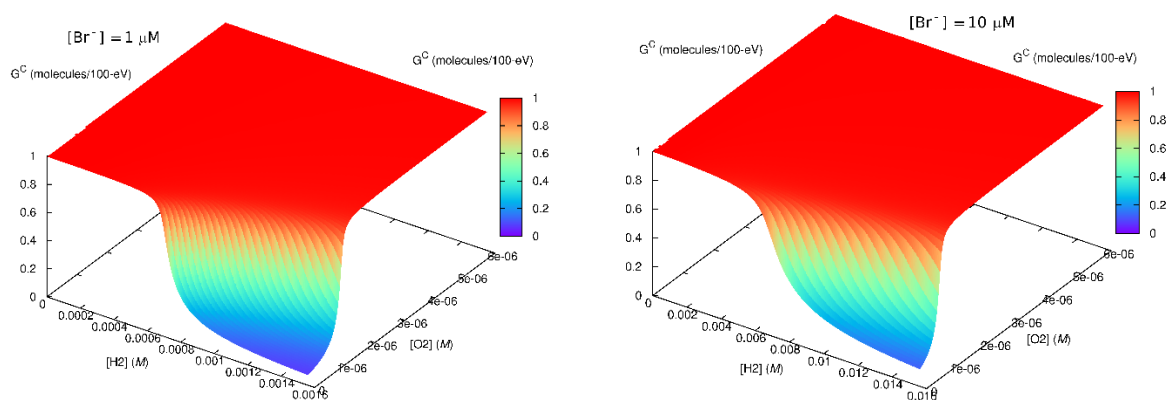
Figure 2-3. Effect of bromide ($[\mathrm{Br}^-] = 1$ µM and $[\mathrm{Br}^-] = 10$ µM) on Empirical RM Steady-state conditional G-values at a dose rate of 160 rad/s.

As in the case of Figure 2-1, a scaling behavior still occurs for Figure 2-3 where the shape of the concentration surface remains unchanged with the same scaling of dose rate, $[\mathrm{H}_2]$, $[\mathrm{O}_2]_B$ and now of $[\mathrm{Br}^-]$. The empirical RM with bromide was seen to have less accuracy in comparison with the full RM, but because of the absence of the direct $\mathrm{H}_2\mathrm{O}_2$ destructive reaction 102, the prediction of G^C appears to be normally conservative for regions where a larger G^C is expected. While it appears that more reactions and further complexity is required for greater accuracy, the Empirical RM is seen to retain the general features of the Full RM (Figure 2-4) and has the advantage of being quickly evaluated.

319
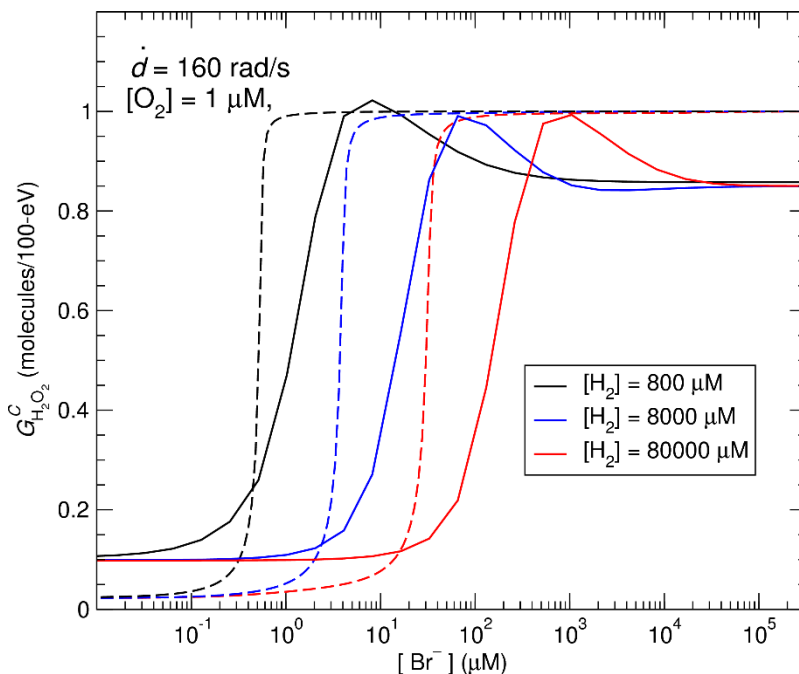
Figure 2-4. Effect of [Br$^-$] on the H$_2$O$_2$ conditional G-values in a ([H$_2$], [O$_2$]) region of suppressed H$_2$O$_2$ generation rate with Empirical RM (dashed) and Fill RM (solid).

2.2 Future Work

While a reasonable model for H$_2$O$_2$ generation with the presence of bromide can be constructed as in the pure water system, an accurate representation of the bromide effect on H$_2$O$_2$ seems to require the full radiolysis model. Future work will attempt to formulate a reduced model that more closely compares with the full model as well as incorporate carbonate chemistry. A future goal will be to represent a full RM with in the fuel degradation MPM, but as shown here, an empirical model is helpful for both simple calculation and for understanding the most relevant underlying mechanisms that are imbedded in the reactions.

3.   References

Brown PN, and AC Hindmarsh. 1989. "Reduced storage matrix methods in stiff ODE systems." *Journal of Applied Mathematics and Computing*, 31(May 1989):40-91.

Buck, E.C, J.L. Jerden, W.L. Ebert, R.S. Wittman, (2013) "Coupling the Mixed Potential and Radiolysis Models for Used Fuel Degradation," FCRD-UFD-2013-000290, M3FT-PN0806058.

Christensen, H., Sunder, S. (1996) An evaluation of water layer thickness effective in oxidation of UO_2 fuel due to radiolysis of water, *Journal of Nuclear Materials* 238: 70-77.

Elliot, A.J.; McCracken, D.R. 1990, "Computer modelling of the radiolysis in an aqueous lithium salt blanket: Suppression of radiolysis by addition of hydrogen," Fusion Eng. Des., 13, 21.

Freeze, G., Mariner, P., Houseworth, J., Cunnane, J., and F. Caporuscio, F. (2010). *Used Fuel Disposition Campaign Features, Events, and Processes (FEPs): FY10 Progress Report*, August 2010.

Hindmarsh AC. 1983. "ODEPACK, A Systematized Collection of ODE Solvers." In *Scientific Computing*, IMACS Transactions on Scientific Computation, Volume 1 edited by RS Stepleman, M Carver, R Peskin, WF Ames and WF Vichnevetsky, North-Holland, Amsterdam, pp 55-64.

Jerden, J., Frey, K., Cruse, T., and Ebert, W. (2012). *Waste Form Degradation Model Status Report: Electrochemical Model for Used Fuel Matrix Degradation Rate*. FCRD-UFD-2012-000169.

Jerden, J., Frey, K., Cruse, T., and Ebert, W. (2013). *Waste Form Degradation Model Status Report: ANL Mixed Potential Model, Version 1. Archive*. FCRD-UFD-2013-000057.

Jerden, James L., Frey, Kurt, and Ebert, William (2015), *A multiphase interfacial model for the dissolution of spent nuclear fuel*, Journal of Nuclear Materials, 462: 135-146.

King, F. and Kolar, M. (1999) *Mathematical Implementation of the Mixed-Potential Model of Fuel Dissolution Model Version MPM-V1.0*, Ontario Hydro, Nuclear Waste Management Division Report No. 06819-REP-01200-10005 R00.

King, F. and Kolar, M. (2002) *Validation of the Mixed-Potential Model for Used Fuel Dissolution Against Experimental Data*, Ontario Hydro, Nuclear Waste Management Division Report No. 06819-REP-01200-10077-R00.

Kelm, M., E. Bohnert (2004), *A kinetic model for the radiolysis of chloride brine, its sensitivity against model parameters and a comparison with experiments*, Institut für Nukleare Entsorgung, Forschungszentrum Karlsruhe GmbH, Karlsruhe.

King, F. and Kolar, M. (2003) *The Mixed-Potential Model for UO2 Dissolution MPM Versions V1.3 and V1.4*, Ontario Hydro, Nuclear Waste Management Division Report No. 06819-REP-01200-10104 R00.

Pastina, B. and LaVerne, J. A. (2001) Effect of Molecular Hydrogen on Hydrogen Peroxide in Water Radiolysis, *Journal of Physical Chemistry* A105: 9316-9322.

Poinssot, C. Ferry, C. M. Kelm, B. Grambow, A. Martinez, A., Johnson, L., Andriamoloolona, Z., Bruno, J., Cachoir, C., Cavedon, J.M., Christensen, H., Corbel, C., Jegou, C., Lemmens, K., Loida, A., Lovera, P., Miserque, F. de Pablo, J., Poulesquen, A., Quinones, J. Rondinella, V., Spahiu, K., and D. H. Wegen, (2004) S*pent Fuel Stability under Repository Conditions: Final Report of the European Project*, European Commission, 5th EURATOM FRAMEWORK PROGRAMME, 1998-2002.

Radulescu, G. (2011) *Radiation Transport Evaluations for Repository Science*, ORNL/LTR-2011/294, LETTER REPORT, Oak Ridge National Laboratory, August, 2011.

Sassani et al., 2012 *Integration of EBS Models with Generic Disposal System Models*, U.S. Department of Energy, Used Fuel Disposition Campaign milestone report: M2FT-12SN0806062, September, 7 2012

Shoesmith, D.W., Kolar, M., and King, F. (2003). A Mixed-Potential Model to Predict Fuel (Uranium Dioxide) Corrosion Within a Failed Nuclear Waste Container, *Corrosion, 59*, 802-816.

Wittman RS and EC Buck. 2012. "Sensitivity of UO_2 Stability in a Reducing Environment on Radiolysis Model Parameters." In *Actinides and Nuclear Energy Material, MRS Spring 2012 Proceedings*, vol. 1444, 3-8, ed. D Andersson, et al. Cambridge University Press, Cambridge, United Kingdom. DOI:10.1557/opl.2012.1449.

Appendix A
Methods and mineral characterization

a. Experimental Setup

The bentonite used in this experimental work is mined from a reducing horizon in Colony, Wyoming. The bentonite was pulverized and sieved to < 3 mm and used with a free moisture of ~15.5 wt. %. The groundwater solution was prepared using reagent grade materials dissolved in double deionised water. NaOH and HCl were added to adjust the initial solution pH. This solution was then filtered through a 0.45 μm filter and sparged with He before each experiment. The salt solution was added at 9:1 water: bentonite ratio. Initial components for wall rock experiments have been summarized in Table 1 of text.

A second series of experiments were performed to examine the bentonite system with host rock inclusion. Host-rock experiments focused on Opalinus Clay from the Swiss Underground Research Laboratory located at Mont Terri. The core was collected from BFE-A10 drill core (interval from 11 to 12 m and interval from 33 to 34 m from the borehole head). A portion of the Opalinus Clay was crushed and sieved with 10 mesh (~2 mm). Opalinus Clay to be used in experiments was reconstituted at 80 wt. % -10 mesh and 20 wt. % +10 mesh. Synthetic groundwater was chosen to replicate the groundwater composition that represents Opalinus Clay pore water (Table 2 of text, Pearson et al., 2003). The salt solution was added at 9:1 water: rock ratio.

The redox conditions for each system were buffered using a 1:1 mixture (by mass) of Fe_3O_4 and $Fe°$ added at 0.07 wt. % of the bentonite mass. Approximately 7 wt. % (of total solids mass) 304 stainless steel (NIST SRM 101g), 316 stainless steel (NIST SRM 160b), Cu-foil, and low-carbon steel (provided by Sandia National Laboratory) were added to the experiments to mimic the presence of a waste canister.

Reactants were loaded into either a flexible gold or titanium bag and fixed into a 500 mL Gasket Confined Closure reactor (Seyfried et al. 1987). Experiments were pressurized to 150 - 160 bar and were heated isothermally at 300 °C for 6 weeks Reaction liquids were extracted during the experiments and analyzed to investigate the aqueous geochemical evolution in relationship to mineralogical alterations. The sampled reaction liquids were split three-ways producing aliquots for unfiltered anion, unfiltered cation, and filtered (0.45 μm syringe filter) cation determination. All aliquots were stored in a refrigerator at 1°C until analysis.

b. Mineral Characterization

X-ray diffraction (XRD) analyses of experimental materials determined mineral compositions. Each sample was ground with 20 wt. % corundum (Al_2O_3) for quantitative XRD analysis of the bulk rock (Chung 1974). XRD measurements were conducted with a Siemens D500 diffractometer using Cu-Kα radiation. Data were collected from 2 to 70 °2θ with a 0.02 °2θ step-size and count times of 8 to 12 seconds per step. To better analyze the non-clay and clay fractions, the < 2 μm particles were separated via sedimentation in DI H_2O. An aliquot of the < 2 μm suspension was dropped on a zero-background quartz plate and dried. This oriented

mount was X-rayed from 2 to 40 °2θ at 8 to 12 s per step. The oriented mount was then saturated with ethylene glycol in a 60 °C oven for 24 hours and XRD analysis was repeated. A portion of the > 2 µm particles was ground with a mortar/pestle, deposited on a zero-background quartz plate, and X-rayed under the same parameters as the bulk powder material. The remaining > 2 µm portion was used for electron microscopy. Mineral identification and unit-cell parameters analysis was performed using Jade© 9.5 X-ray data evaluation program with ICDD PDF-4 database. Quantitative phase analysis (QXRD) was performed using FULLPAT (Chipera and Bish 2002). Illite-smectite composition of higher-ordered (R1-3) illite-smectites were modeled via ClayStrat+ (developed by Hongji Yuan and David Bish). Expandable component abundances for the disordered illite-smectites were calculated via the Δ°2Θ method (Środoń 1980; Eberl et al. 1993; Moore and Reynolds 1997). A regression from calculated data were used to calculate the % expandable (%Exp) component in each untreated and reacted bentonite. The equations are:

$$\%Exp = 973.76 - 323.45\Delta + 38.43\Delta^2 - 1.62\Delta^3 \text{ (Eberl et al. 1993, Eq. 3, } R^2=0.99),$$

with Δ corresponding to Δ°2Θ between the 002 and 003 peak positions for the oriented, ethylene glycol saturated samples.

Analytical electron microscopy was performed using a FEI™ Inspect F scanning electron microscope (SEM). All samples were Au/Pd-coated prior to SEM analysis. Imaging with the SEM was performed using a 5.0 kV accelerating voltage and 1.5 spot size. Energy dispersive X-ray spectroscopy (EDX) was performed at 30 kV and a 3.0 spot size.

Electron microprobe (EMP) analyses were performed at the University of Oklahoma using a Cameca SX50 electron microprobe equipped with five wavelength-dispersive spectrometers and PGT PRISM 2000 energy-dispersive X-ray detector. Petrographic characterization was performed by backscattered electron imaging coupled with energy-dispersive X-ray analysis, using beam conditions of 20 kV acceleration and 20 nA sample current. Quantitative analysis was performed by wavelength-dispersive spectrometry using 20 kV accelerating voltage, 20 nA beam current, and 2 µm spot size. Matrix corrections employed the PAP algorithm (Pouchou and Pichoir 1985), with oxygen content calculated by stoichiometry. Counting times were 30 seconds on peak for all elements, yielding minimum levels of detection (calculated at 3-σ above mean background) in the range of 0.01 to 0.03 wt. % of the oxides for all components except F (0.16 wt. %). All standards for elements in the silicates were analyzed using 30 second count times on peak, using K-alpha emissions. The standards and oxide detection limits are presented in Appendix A, with analytical data presented in Appendix B.

c. **Aqueous Geochemical Analyses**

Major cations and trace metals were analyzed via inductively coupled plasma-optical emission spectrometry (Perkin Elmer Optima 2100 DV) and inductively coupled plasma-mass spectrometry (Elan 6100) utilizing EPA methods 200.7 and 200.8. Ultra-high purity nitric acid was used in sample and calibration preparation prior to sample analysis. Internal standards (Sc, Ge, Bi, and In)

were added to samples and standards to correct for matrix effects. Standard Reference Material (SRM) 1643e Trace Elements in Water was used to check the accuracy of the multi-element calibrations. Inorganic anion samples were analyzed by ion chromatography (IC) following EPA method 300 on a Dionex DX-600 system. Aqueous geochemical results are presented in Appendix C.

Appendix B
Water ChemistrySample EBS-18
(Element Concentrations in ppm)

Lab ID	Date analyzed	Date Sampled	Al	B	Ba	Ca	Cl	Fe	K	Li	Mg	Mn
EBS-18 REACTION VESSEL	4/5/2016	2/17/2016	<0.02	<0.04	0.02	22	860	21	17	0.3	0.03	0.38
EBS 18 F	05/2/16	1/14/2016	1.1	3.25	0.18	17	---	<0.2	78	2	<0.2	0.02
EBS 18 F	05/2/16	1/28/2016	0.1	3.91	0.36	29	---	<0.2	96	1	9.8	0.06
EBS-18 F	4/5/2016	2/4/2016	<0.02	2.65	0.12	14	---	<0.2	62	1.5	<0.2	<0.02
EBS-18 F	4/5/2016	2/16/2016	<0.02	0.82	0.11	284	---	8	20	1.1	1.61	0.31
EBS-18-POST RUN F	4/5/2016	2/17/2016	<0.02	0.70	0.13	308	---	2	24	1.3	5.40	0.32
EBS 18 UF	05/2/16	1/14/2016	1.8	3.60	0.19	17	3761	<0.2	75	2	<0.2	0.03
EBS 18 UF	05/2/16	1/28/2016	0.2	4.73	0.35	28	4544	<0.2	97	1	9.7	0.06
EBS-18 UF	4/5/2016	2/4/2016	<0.02	3.10	0.13	14	2684	<0.2	66	1.6	0.21	0.04
EBS-18 UF	4/5/2016	2/16/2016	<0.02	0.71	0.11	290	1377	7	20	1.1	1.90	0.31
EBS-18-POST RUN UF	4/5/2016	2/17/2016	<0.02	0.57	0.13	309	1435	2	24	1.3	5.60	0.31

Lab ID	Date analyzed	Date Sampled	Na	Si	SiO2	SO4	Sr	Zn	TDS	Cation	Anion	Balance
EBS-18 REACTION VESSEL	4/5/2016	2/17/2016	511	70	150	45	0.10	<0.02	1628	25	25	0.00
EBS 18 F	05/2/16	1/14/2016	2109	99	211	---	0.2	0.19	2421	95	0	1.00
EBS 18 F	05/2/16	1/28/2016	2572	215	461	---	0.2	0.24	3174	116	0	1.00
EBS-18 F	4/5/2016	2/4/2016	1559	75	161	---	0.12	<0.02	1800	70	0	1.00
EBS-18 F	4/5/2016	2/16/2016	907	117	250	---	1.70	<0.02	1475	55	0	1.00
EBS-18-POST RUN F	4/5/2016	2/17/2016	1028	90	194	---	1.76	<0.02	1565	61	0	1.00
EBS 18 UF	05/2/16	1/14/2016	2165	84	179	16.95	0.2	0.24	6221	97	106	-0.05
EBS 18 UF	05/2/16	1/28/2016	2609	103	219	57.6	0.2	0.30	7571	117	129	-0.05
EBS-18 UF	4/5/2016	2/4/2016	1568	196	419	28	0.14	<0.02	4788	71	76	-0.04
EBS-18 UF	4/5/2016	2/16/2016	918	104	222	957	1.72	<0.02	3797	55	59	-0.03
EBS-18-POST RUN UF	4/5/2016	2/17/2016	999	80	170	1054	1.79	<0.02	4006	60	62	-0.02

B.1. EBS-18 Al
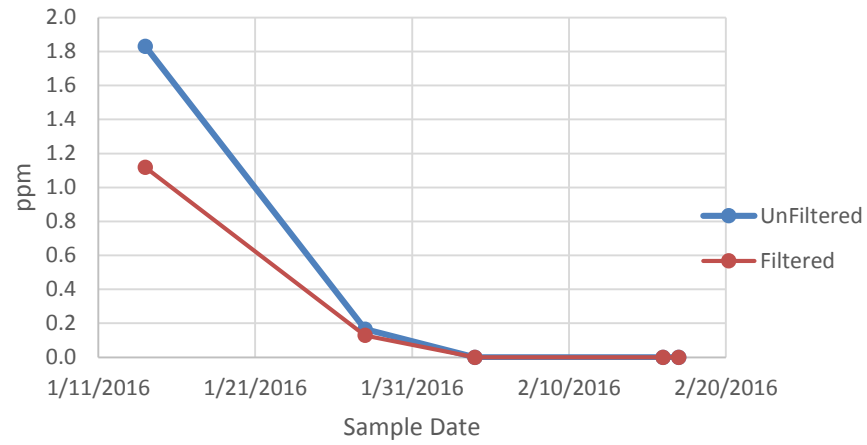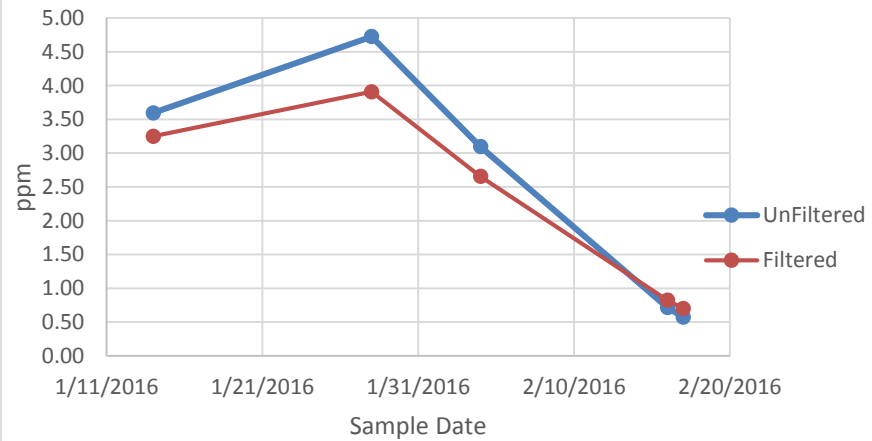
B.2. EBS-18 B

B.3. EBS-18 Ba
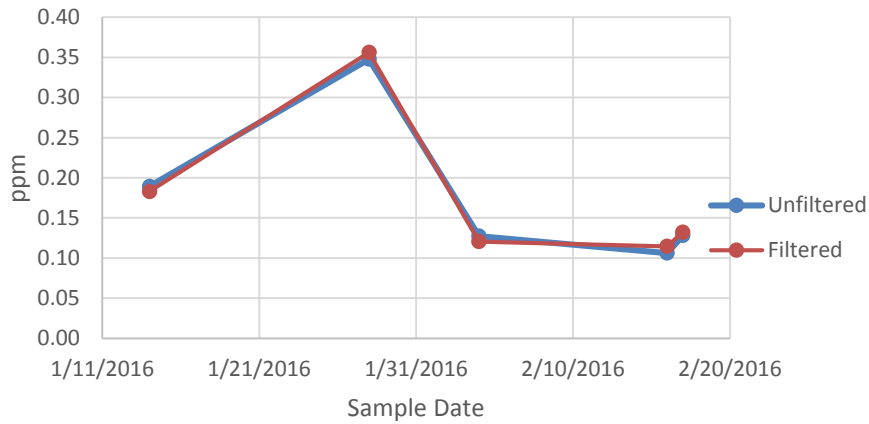
B.4. EBS-18 Ca
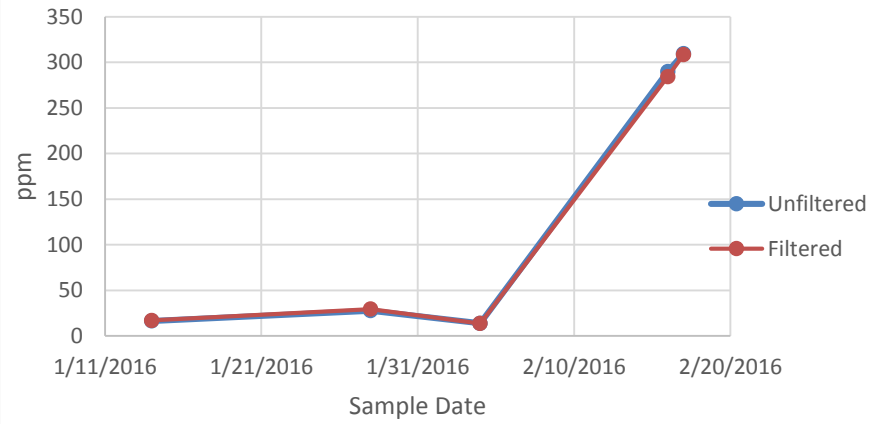
B.5. EBS-18 Fe
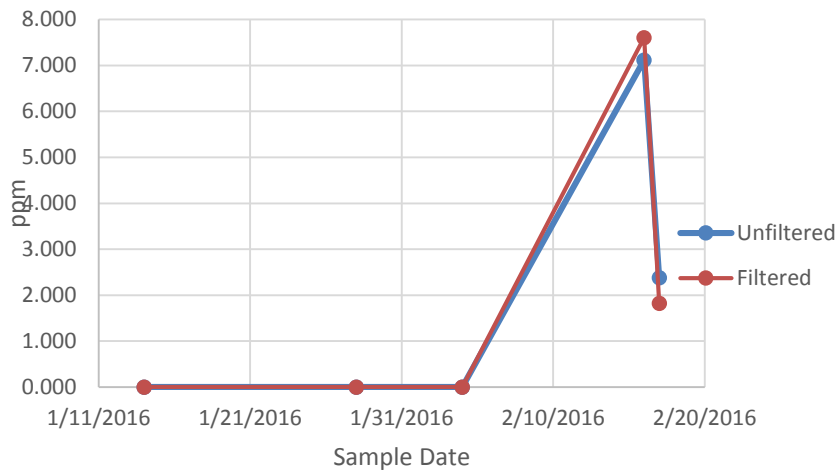
B.6. EBS-18 K
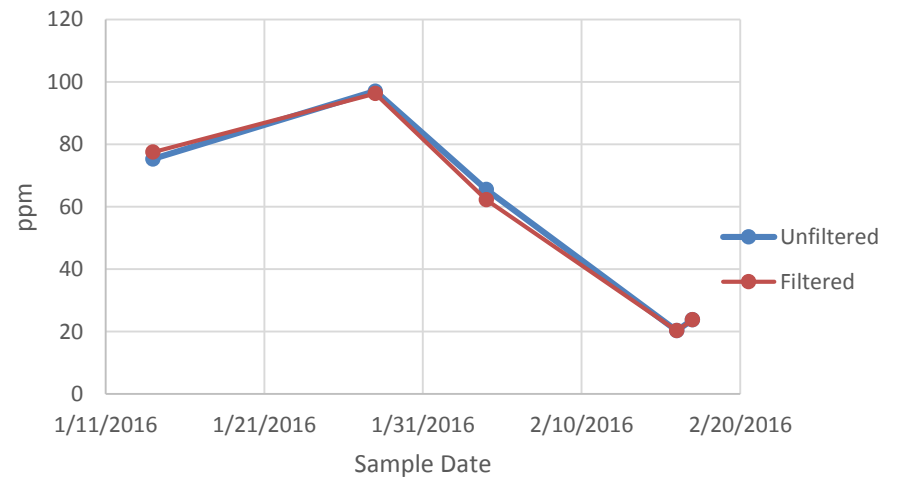
B.7. EBS-18 Li
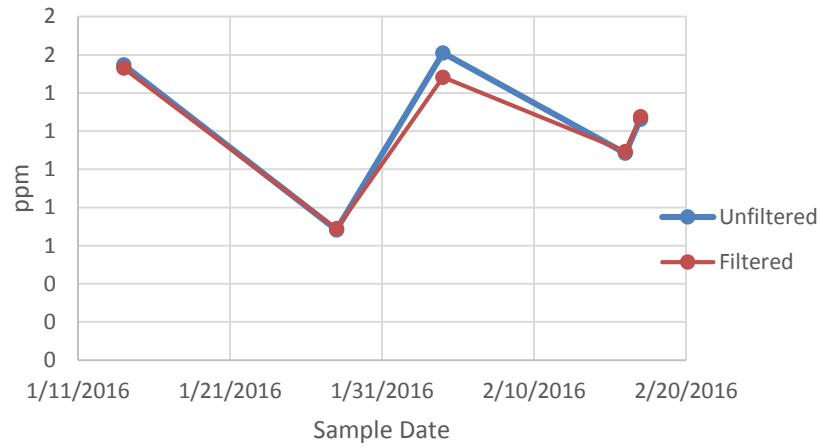
B.8. EBS-18 Mg
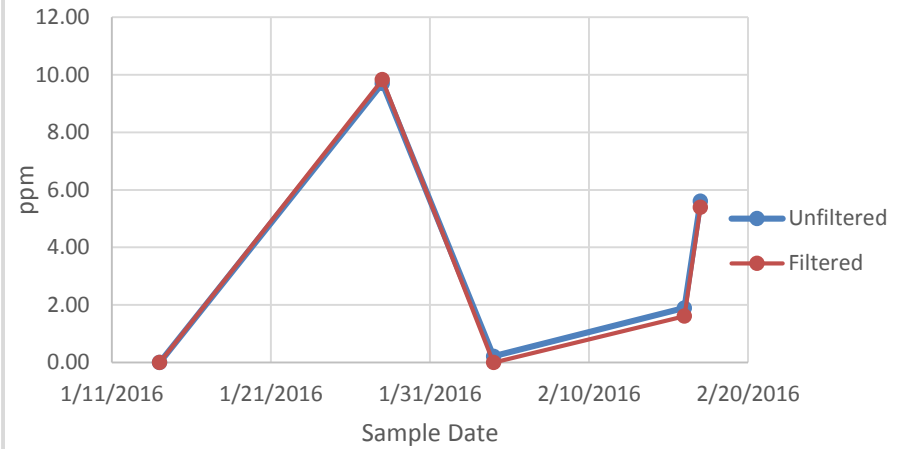
B.9. EBS-18 Mn
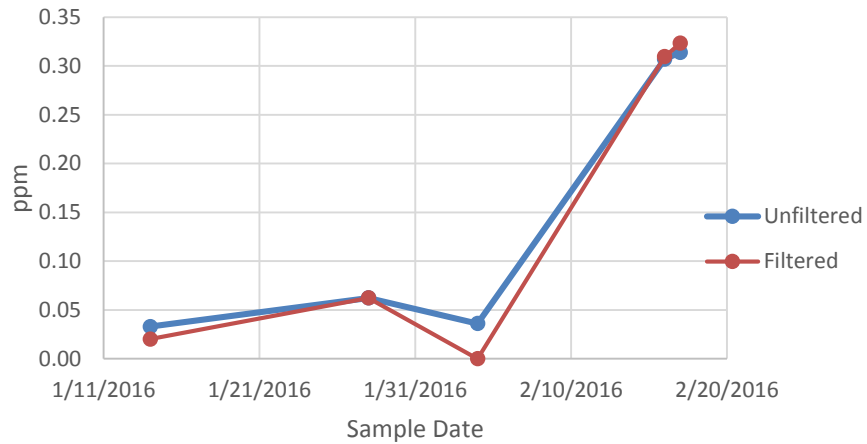
B.10. EBS-18 Na
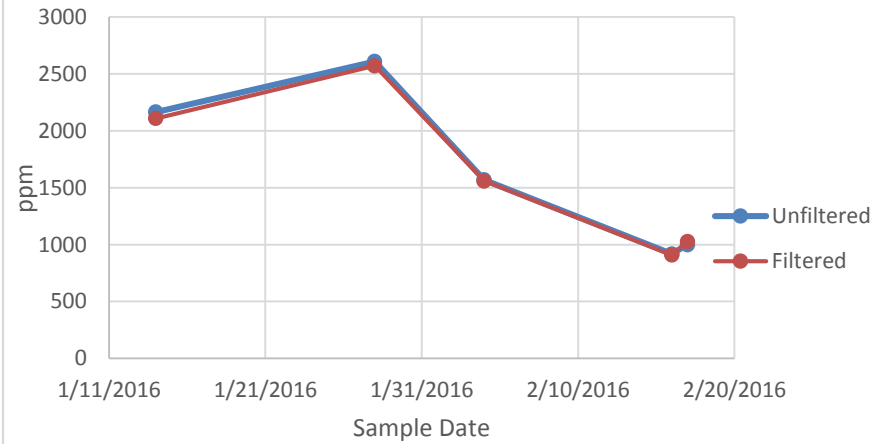
B.11. EBS-18 Si
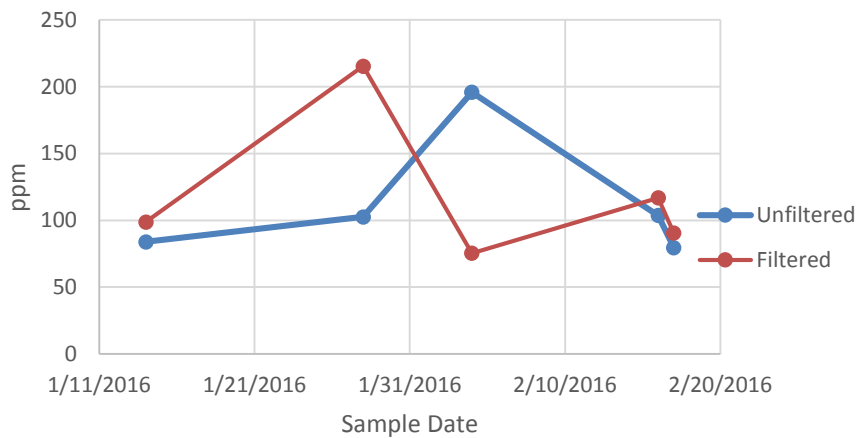
B.12. EBS-18 SiO2
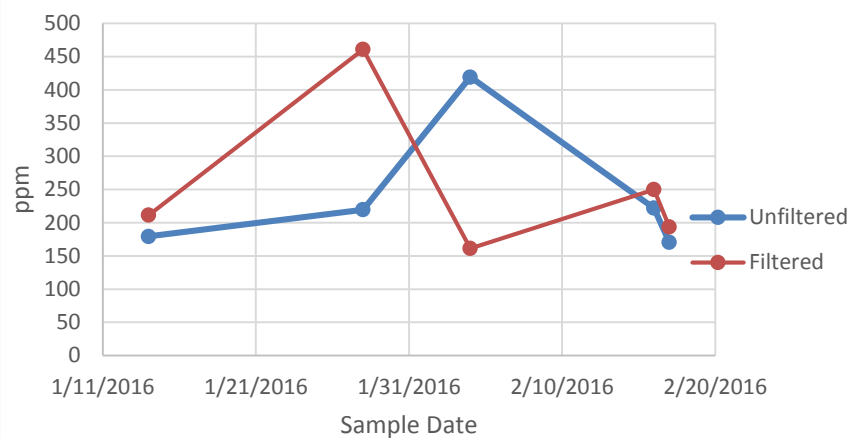
B.13. EBS-18 Sr
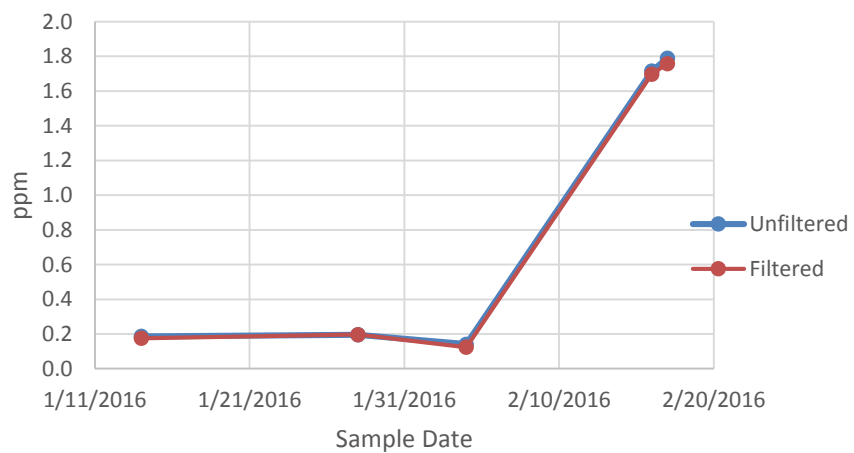
B.14. EBS-18 Zn
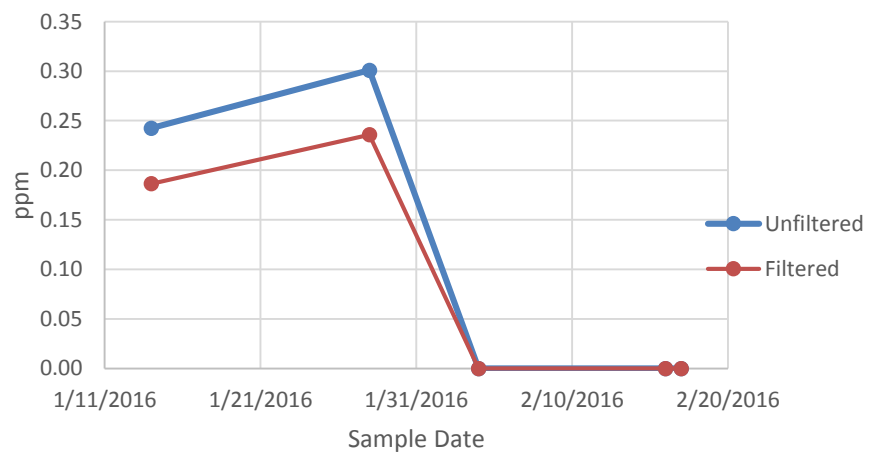
B.19. EBS-18 Total Anions
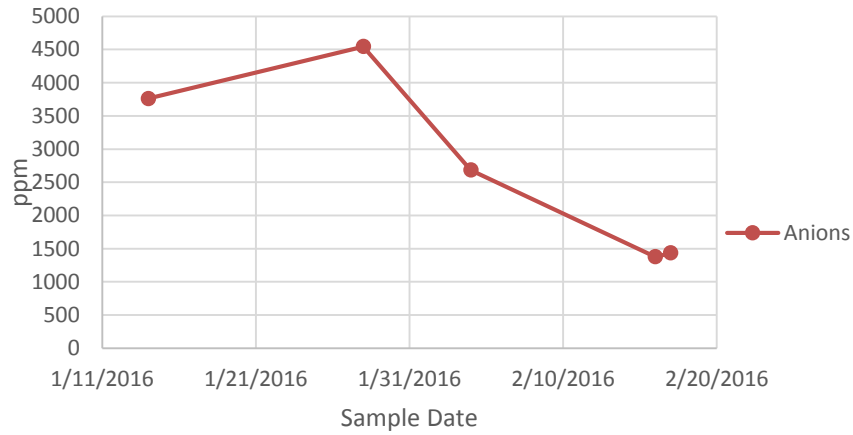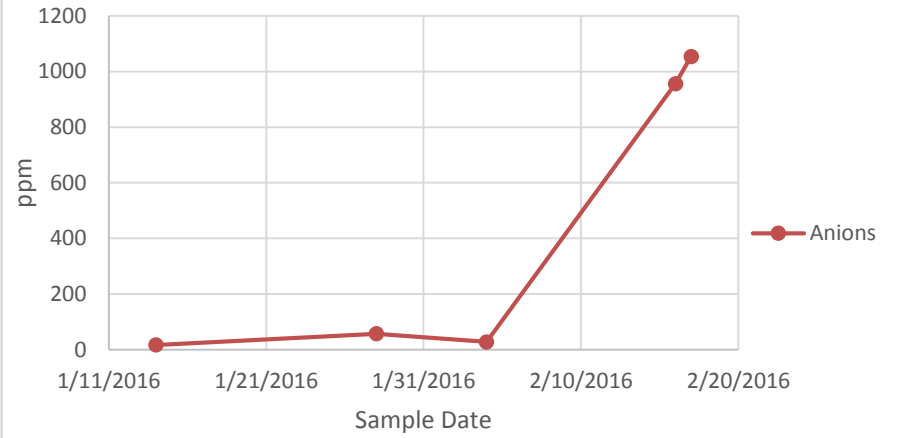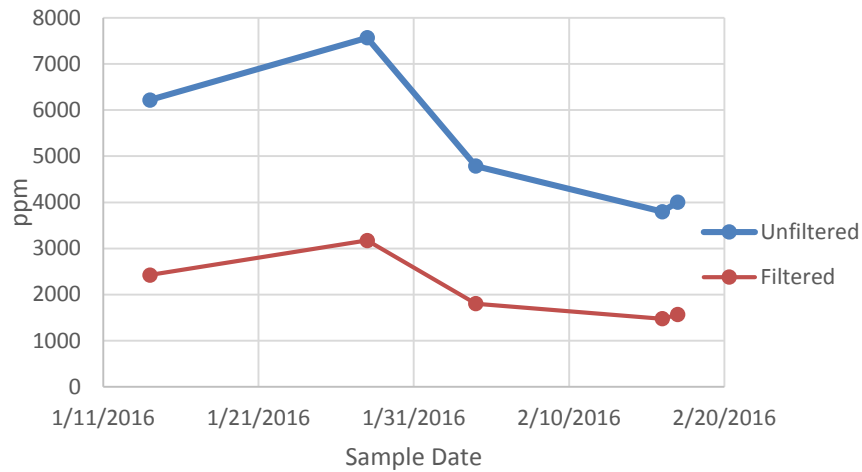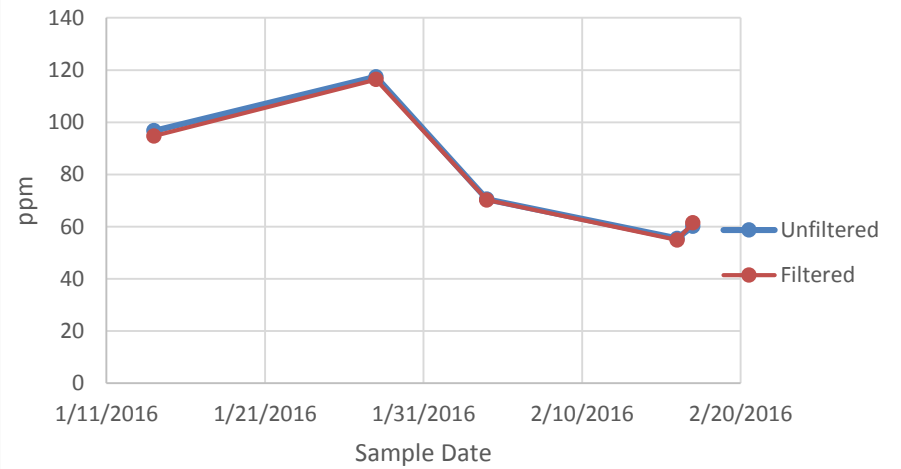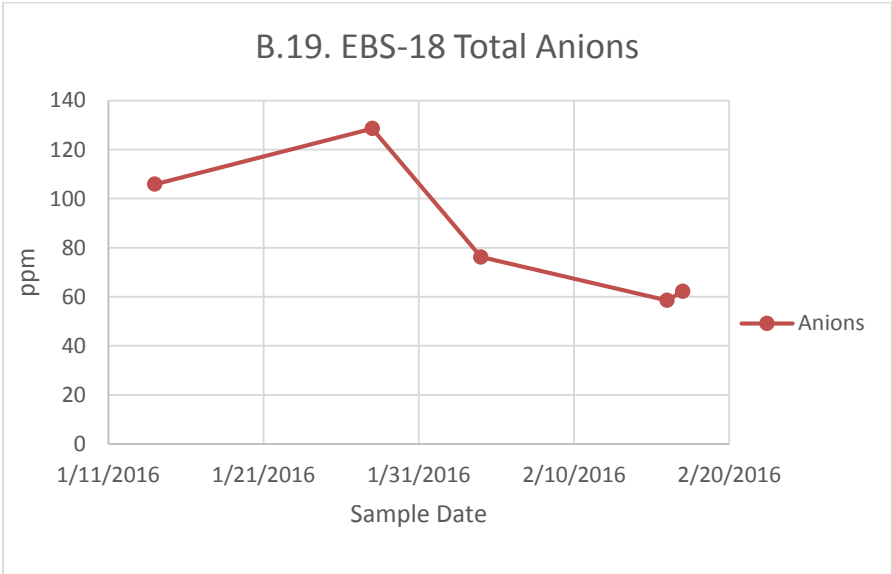
Appendix C
X-Ray Powder Diffraction Data

EBS-18
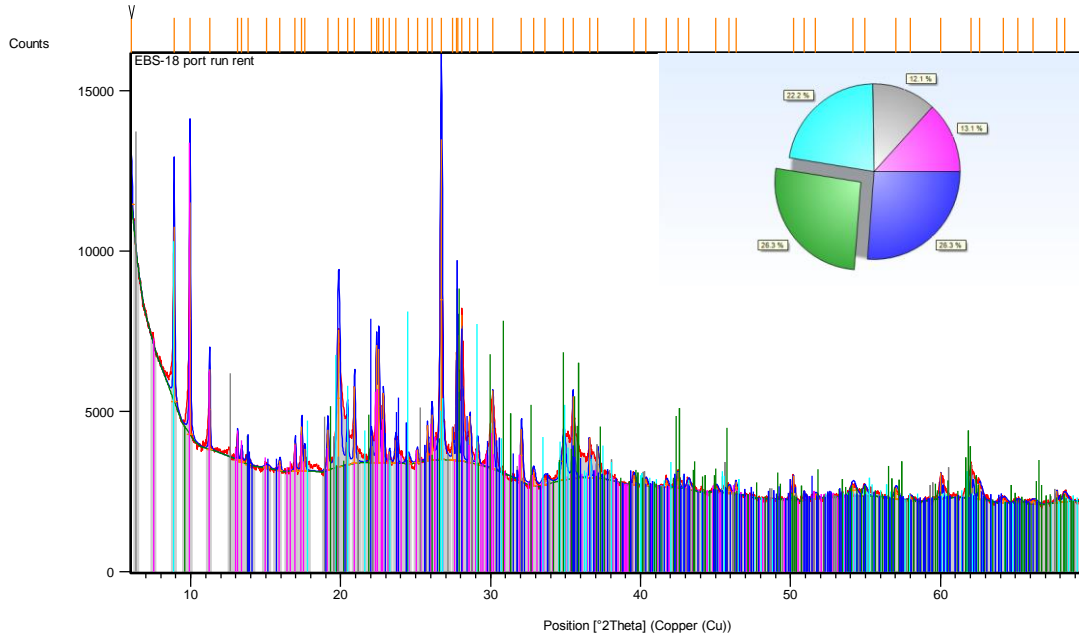
C.1. Semi quantitative analysis of EBS-18 matrix material

QXRD

Mineral Phase	Volume percentage
clinoptilolite	13
albite	26
ferrosilite	26
muscovite	23
chlorite	12
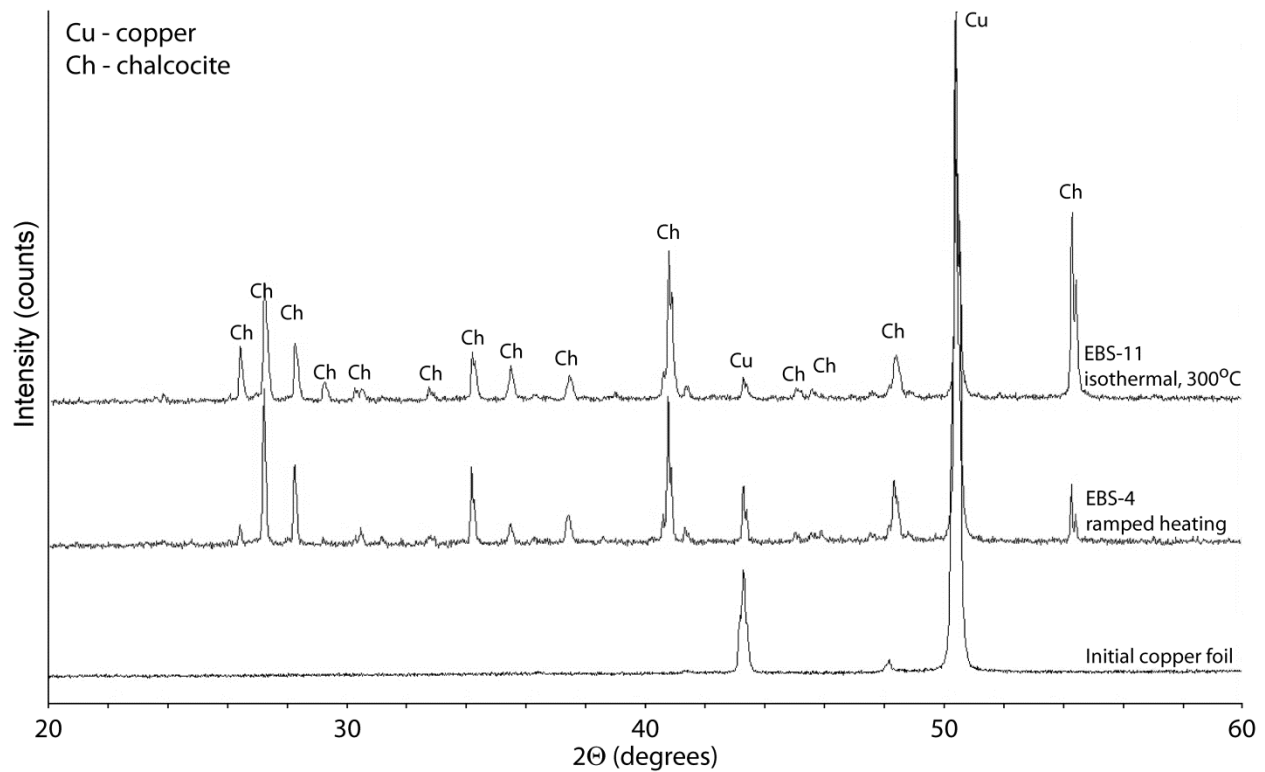
C.2. XRD plots for corrosion products on the copper foils used in the ramped heating (EBS-4) and six week, 300°C heating (EBS-11) experiments. Chalcocite (Cu_2S) is the principal corrosion phase.
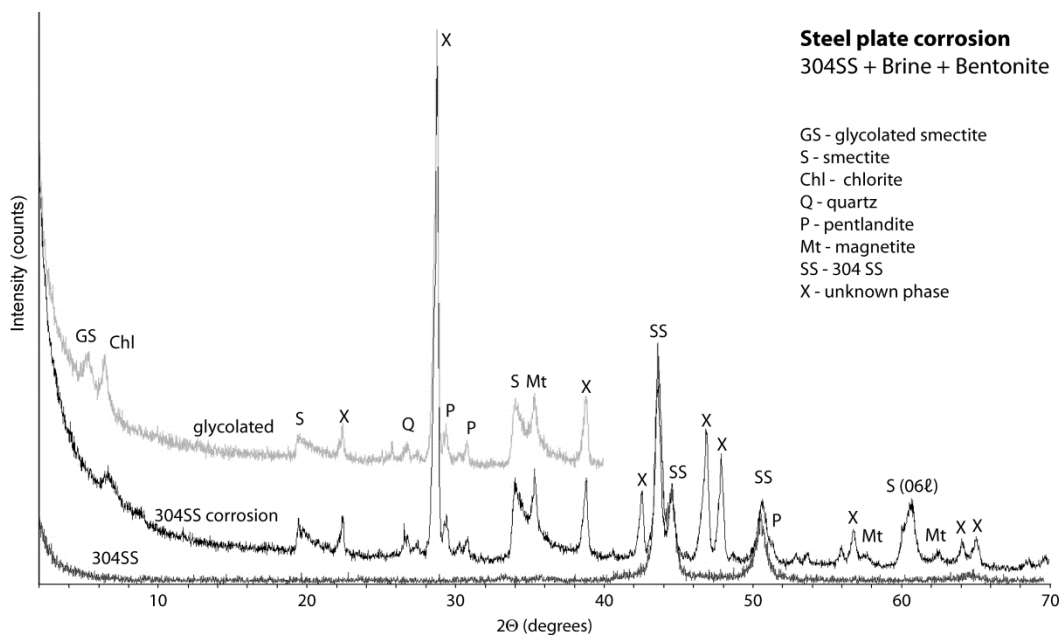
C.3. XRD patterns of the air-dried and ethylene glycol saturated corrosion products on the 304 SS plate used in the EBS-2 experiment. Smectite, chlorite, and a pentlandite-like material are the dominant interface reaction phases. Starting 304SS XRD plot is also shown for comparison.

337
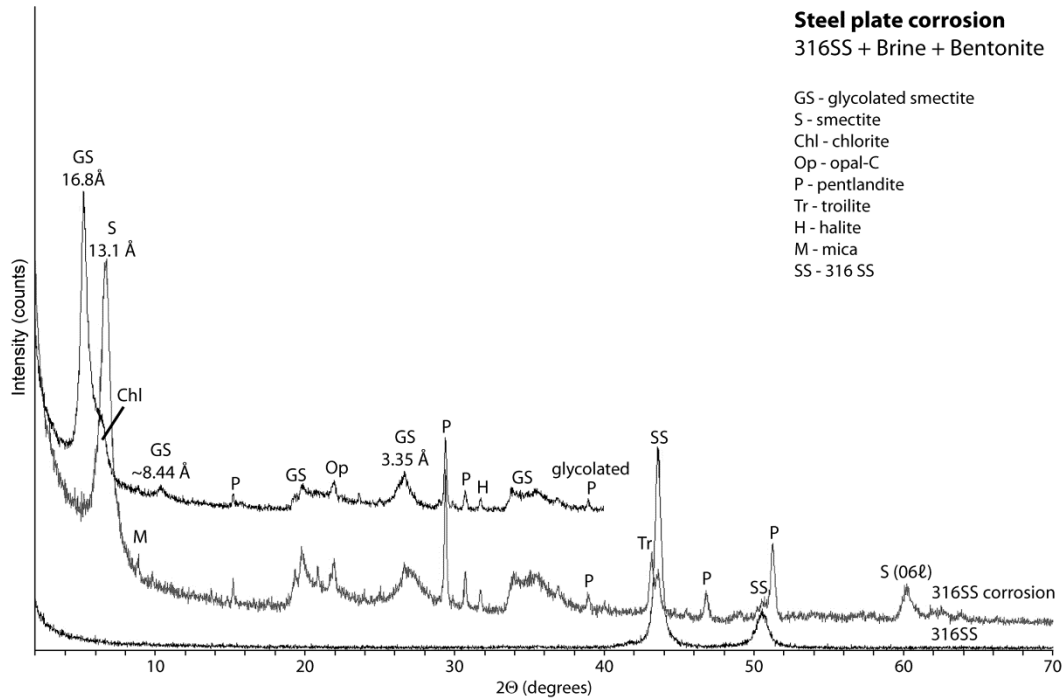
C.4. XRD patterns of the air-dried and ethylene glycol saturated interface reaction products on the 316SS plate used in the EBS-3 experiment. Smectite, chlorite, and a pentlandite-like material are the dominant corrosion phases. Starting 316SS XRD plot is also shown for comparison.
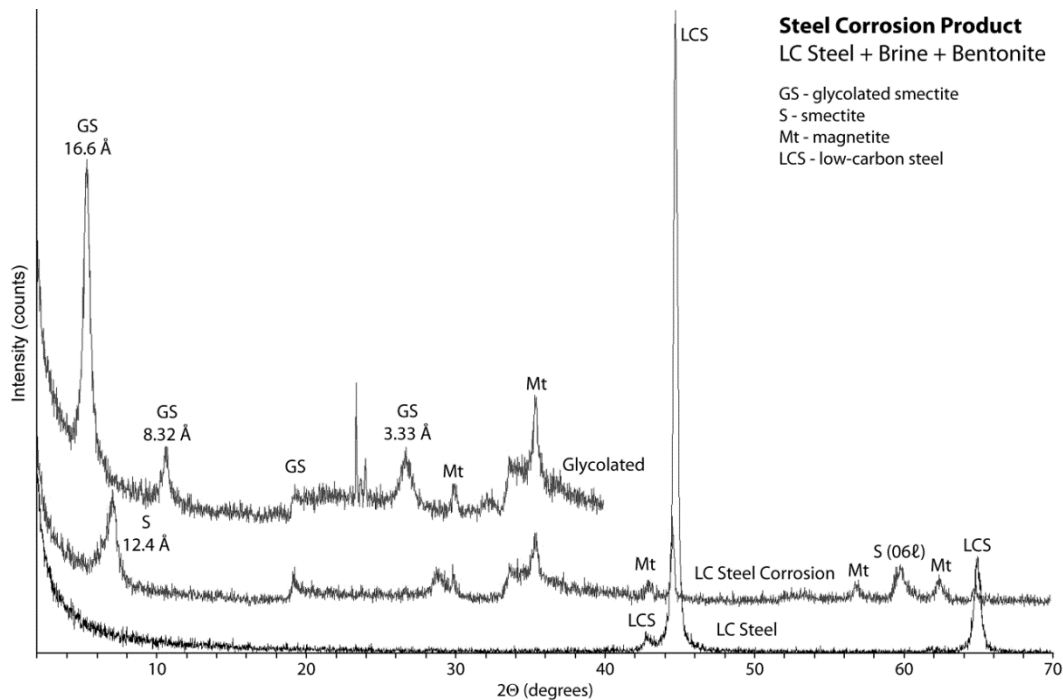
C.5. XRD patterns of the air-dried and ethylene glycol saturated interface reaction products on the low-carbon steel plate used in the EBS-6 experiment. Smectite is the dominant interface reaction phase. Magnetite is most likely from the starting magnetite materials used to control redox conditions. Initial low-carbon steel XRD plot is also shown for comparison.

Appendix D
Electron Microprobe data

		Weight Percent													
SAMPLE	Pt#	SiO2	TiO2	Al2O3	Cr2O3	FeO	NiO	MnO	MgO	CaO	Na2O	K2O	Cl	F	O=Hal	TOTAL
CLINOPTILOLITE																
EBS-18 Clinop	1	58.65	0.02	21.06	0.02	0.99	0.00	0.01	0.39	4.48	3.16	0.23	0.02	0.00	-0.01	89.03
EBS-18 Clinop	2	60.56	0.03	22.70	0.00	0.50	0.00	0.01	0.58	5.68	2.71	1.36	0.01	0.07	-0.03	94.21
EBS-18 Clinop	3	59.96	0.20	20.98	0.03	2.13	0.00	0.03	0.77	4.15	2.07	0.55	0.04	0.04	-0.03	90.95
EBS-18 Clinop	4	72.82	0.29	15.08	0.02	1.84	0.00	0.04	0.66	2.17	1.35	0.95	0.05	0.11	-0.06	95.37
EBS-18 Clinop	5	57.26	0.21	21.26	0.01	4.54	0.02	0.05	1.75	2.98	1.58	1.13	0.08	0.00	-0.02	90.87
AVE.		**61.85**	**0.15**	**20.22**	**0.01**	**2.00**	**0.00**	**0.03**	**0.83**	**3.89**	**2.17**	**0.84**	**0.04**	**0.04**	**-0.03**	**92.09**
Std Dev		**6.26**	**0.12**	**2.95**	**0.01**	**1.56**	**0.01**	**0.02**	**0.53**	**1.36**	**0.76**	**0.45**	**0.03**	**0.05**	**0.02**	**2.62**
18 Atoms per formula unit (sum excludes F & Cl)																
		Si	Ti	Al	Cr	Fe	Ni	Mn	Mg	Ca	Na	K	Cl	F		Sum
EBS-18 Clinop	1	6.437	0.001	2.724	0.002	0.090	0.000	0.001	0.065	0.526	0.673	0.032	0.004	0.000		10.552
EBS-18 Clinop	2	6.332	0.002	2.797	0.000	0.043	0.000	0.001	0.091	0.636	0.549	0.182	0.002	0.024		10.633
EBS-18 Clinop	3	6.459	0.016	2.663	0.002	0.192	0.000	0.003	0.124	0.479	0.433	0.076	0.007	0.014		10.447
EBS-18 Clinop	4	7.300	0.022	1.782	0.001	0.155	0.000	0.003	0.098	0.233	0.262	0.121	0.009	0.034		9.978
EBS-18 Clinop	5	6.272	0.017	2.744	0.001	0.416	0.001	0.005	0.286	0.350	0.335	0.158	0.015	0.000		10.585
AVE.		**6.560**	**0.012**	**2.542**	**0.001**	**0.179**	**0.000**	**0.003**	**0.133**	**0.445**	**0.450**	**0.114**	**0.008**	**0.014**		**10.439**
Std Dev		**0.42**	**0.01**	**0.43**	**0.00**	**0.14**	**0.00**	**0.00**	**0.09**	**0.16**	**0.16**	**0.06**	**0.01**	**0.01**		**0.27**
ANALCIME																

SAMPLE	Pt#	SiO2	TiO2	Al2O3	Cr2O3	FeO	NiO	MnO	MgO	CaO	Na2O	K2O	Cl	F	O=Hal	TOTAL
EBS-18 Anl	1	67.08	0.03	20.90	0.00	0.66	0.00	0.00	0.16	3.91	1.10	0.03	0.02	0.23	-0.10	94.12
EBS-18 Anl	2	62.99	0.02	20.17	0.00	0.80	0.01	0.00	0.17	3.98	2.22	0.06	0.03	0.06	-0.03	90.50
EBS-18 Anl	4	64.68	0.09	20.56	0.00	0.33	0.01	0.02	0.07	4.65	1.67	0.19	0.01	0.00	0.00	92.29
EBS-18 Anl	5	62.40	0.03	19.92	0.00	0.33	0.00	0.01	0.04	4.92	0.62	0.21	0.02	0.00	0.00	88.51
AVE.		64.29	0.04	20.39	0.00	0.53	0.00	0.01	0.11	4.37	1.40	0.12	0.02	0.07	-0.03	91.35
Std Dev		2.10	0.03	0.43	0.00	0.24	0.01	0.01	0.07	0.50	0.70	0.09	0.01	0.11	0.04	2.41

6 Atoms per formula unit (sum excludes F & Cl)

		Si	Ti	Al	Cr	Fe	Ni	Mn	Mg	Ca	Na	K	Cl	F		Sum
EBS-18 Anl	1	2.271	0.001	0.834	0.000	0.019	0.000	0.000	0.008	0.142	0.072	0.001	0.001	0.024		3.348
EBS-18 Anl	2	2.236	0.000	0.844	0.000	0.024	0.000	0.000	0.009	0.151	0.153	0.003	0.002	0.007		3.420
EBS-18 Anl	4	2.244	0.002	0.841	0.000	0.010	0.000	0.001	0.003	0.173	0.112	0.009	0.001	0.000		3.394
EBS-18 Anl	5	2.250	0.001	0.847	0.000	0.010	0.000	0.000	0.002	0.190	0.043	0.010	0.001	0.000		3.352
AVE.		2.250	0.001	0.841	0.000	0.015	0.000	0.000	0.006	0.164	0.095	0.006	0.001	0.008		3.379
Std Dev		0.02	0.00	0.01	0.00	0.01	0.00	0.00	0.00	0.02	0.05	0.00	0.00	0.01		0.03

SAMPLE	Pt#	SiO2	TiO2	Al2O3	Cr2O3	FeO	NiO	MnO	MgO	CaO	Na2O	K2O	Cl	F	O=Hal	TOTAL
Fe-Oxides (Goethite)																
EBS-18 Alt-1	1	1.03	0.00	0.24	0.67	70.38	0.53	0.78	0.00	0.03	0.09	0.00	6.66	0.00	-1.50	80.41
EBS-18 Alt-2	1	0.51	0.01	0.69	0.35	77.51	0.09	0.81	0.06	0.21	2.72	0.07	0.07	0.00	-0.02	83.09
EBS-18 Alt-2	2	8.28	0.01	2.61	0.61	64.35	0.44	0.32	0.38	2.11	1.20	0.08	0.17	0.00	-0.04	80.56

Sample	n	Si	Ti	Al	Cr	Fe	Ni	Mn	Mg	Ca	Na	K	Cl	F		Sum
EBS-18 Alt-3	1	8.35	0.01	2.72	0.67	68.62	0.50	0.55	0.59	3.35	0.92	0.09	0.13	0.06	-0.05	86.54
EBS-18 Alt-4	4	5.08	0.03	0.84	0.41	62.09	0.56	0.38	0.15	7.95	0.37	0.01	0.14	0.00	-0.03	78.00
AVE.		**4.65**	**0.01**	**1.42**	**0.54**	**68.59**	**0.43**	**0.57**	**0.24**	**2.73**	**1.06**	**0.05**	**1.43**	**0.01**	**-0.33**	**81.72**
Std Dev		**3.78**	**0.01**	**1.16**	**0.15**	**5.98**	**0.19**	**0.23**	**0.25**	**3.23**	**1.02**	**0.04**	**2.92**	**0.03**	**0.66**	**3.24**

22 Atoms per formula unit (sum excludes F & Cl)

Sample	n	Si	Ti	Al	Cr	Fe	Ni	Mn	Mg	Ca	Na	K	Cl	F		Sum
EBS-18 Alt-1	1	0.357	0.000	0.099	0.184	20.442	0.149	0.231	0.000	0.009	0.063	0.000	3.919	0.000		21.534
EBS-18 Alt-2	1	0.156	0.003	0.253	0.086	20.017	0.023	0.212	0.026	0.069	1.626	0.028	0.036	0.000		22.499
EBS-18 Alt-2	2	2.265	0.002	0.841	0.133	14.727	0.097	0.074	0.156	0.619	0.637	0.027	0.079	0.000		19.578
EBS-18 Alt-3	1	2.136	0.002	0.820	0.135	14.684	0.103	0.118	0.226	0.919	0.456	0.028	0.056	0.046		19.626
EBS-18 Alt-4	4	1.510	0.006	0.294	0.096	15.445	0.134	0.095	0.068	2.534	0.211	0.004	0.071	0.000		20.396
AVE.		**1.285**	**0.003**	**0.461**	**0.127**	**17.063**	**0.101**	**0.146**	**0.095**	**0.830**	**0.599**	**0.017**	**0.832**	**0.009**		**20.727**
Std Dev		**0.98**	**0.00**	**0.35**	**0.04**	**2.91**	**0.05**	**0.07**	**0.09**	**1.03**	**0.62**	**0.01**	**1.73**	**0.02**		**1.27**
Fe interface																
Fe-saponite																
EBS-18 Alt-1	2	29.55	0.03	13.18	0.27	44.29	0.02	0.16	1.61	0.05	0.16	0.02	0.33	0.06	-0.10	89.74
EBS-18 Alt-1	3	29.13	0.05	12.46	0.17	42.98	0.03	0.23	1.50	0.06	0.20	0.03	0.06	0.03	-0.03	86.95

		Si	Ti	Al	Cr	Fe	Ni	Mn	Mg	Ca	Na	K	Cl	F		Sum
EBS-18 Alt-2	3	22.66	0.04	10.52	0.13	50.31	0.03	0.52	1.26	1.63	1.08	0.08	0.28	0.01	-0.07	88.55
EBS-18 Alt-2	4	24.77	0.02	12.14	0.00	47.06	0.01	0.33	1.35	0.32	0.38	0.07	0.16	0.00	-0.04	86.62
EBS-18 Alt-3	2	14.90	0.00	6.55	0.65	52.17	0.53	0.38	1.28	1.86	0.39	0.04	0.11	0.00	-0.03	78.86
EBS-18 Alt-3	3	14.73	0.02	6.49	0.48	58.08	0.42	0.39	1.29	0.87	0.42	0.06	0.11	0.00	-0.02	83.35
EBS-18 Alt-4	1	17.99	0.00	8.14	0.64	55.76	0.15	1.25	1.37	0.33	0.14	0.03	0.13	0.00	-0.03	85.93
EBS-18 Alt-4	2	30.95	0.01	13.67	0.04	37.48	0.02	0.22	2.53	0.69	0.02	0.02	0.13	0.02	-0.04	85.79
EBS-18 Alt-4	3	16.42	0.00	7.25	0.15	58.50	0.05	0.60	1.34	0.57	0.10	0.01	0.04	0.00	-0.01	85.03
EBS-18 Alt-6	1	16.79	0.01	7.58	0.45	55.51	0.33	0.64	1.05	1.78	1.56	0.08	0.12	0.00	-0.03	85.92
EBS-18 Alt-6	2	18.31	0.01	9.68	0.07	55.43	0.02	0.54	1.36	1.53	0.67	0.04	0.14	0.02	-0.04	87.80
EBS-18 Alt-6	3	20.59	0.00	10.68	0.03	51.95	0.02	0.40	1.73	1.15	0.43	0.09	0.07	0.00	-0.02	87.14
EBS-18 Alt-6	4	27.24	0.05	9.58	0.00	35.68	0.03	0.28	1.13	0.94	0.37	0.13	0.60	0.01	-0.14	76.03
AVE.		21.85	0.02	9.84	0.24	49.63	0.13	0.46	1.45	0.91	0.45	0.05	0.17	0.01	-0.04	85.21
Std Dev		4.61	0.02	1.30	0.21	9.46	0.16	0.16	0.31	0.38	0.55	0.04	0.25	0.01	0.06	5.52
22 Atoms per formula unit (sum excludes F & Cl)																
Fe-saponite		Si	Ti	Al	Cr	Fe	Ni	Mn	Mg	Ca	Na	K	Cl	F		Sum
EBS-18 Alt-1	2	5.304	0.004	2.787	0.038	6.648	0.003	0.025	0.431	0.010	0.057	0.004	0.100	0.034		15.310
EBS-18 Alt-1	3	5.374	0.007	2.709	0.025	6.631	0.004	0.035	0.413	0.012	0.072	0.008	0.019	0.020		15.292

EBS-18 Alt-2	3	4.476	0.006	2.449	0.020	8.310	0.004	0.087	0.370	0.346	0.413	0.020	0.094	0.008		16.499
EBS-18 Alt-2	4	4.803	0.003	2.775	0.000	7.632	0.002	0.054	0.391	0.066	0.142	0.017	0.052	0.000		15.886
EBS-18 Alt-3	2	3.610	0.000	1.868	0.124	10.568	0.104	0.079	0.462	0.482	0.184	0.013	0.046	0.000		17.492
EBS-18 Alt-3	3	3.444	0.003	1.789	0.089	11.361	0.079	0.077	0.450	0.218	0.191	0.018	0.043	0.000		17.718
EBS-18 Alt-4	1	3.900	0.000	2.080	0.110	10.107	0.026	0.230	0.441	0.077	0.059	0.008	0.046	0.000		17.038
EBS-18 Alt-4	2	5.572	0.001	2.900	0.006	5.642	0.003	0.033	0.679	0.134	0.006	0.004	0.039	0.009		14.980
EBS-18 Alt-4	3	3.686	0.000	1.917	0.027	10.981	0.008	0.114	0.449	0.138	0.042	0.002	0.015	0.002		17.364
EBS-18 Alt-6	1	3.702	0.002	1.969	0.079	10.232	0.059	0.120	0.344	0.420	0.668	0.022	0.045	0.000		17.617
EBS-18 Alt-6	2	3.837	0.001	2.390	0.011	9.714	0.004	0.095	0.426	0.343	0.270	0.010	0.049	0.010		17.101
EBS-18 Alt-6	3	4.187	0.000	2.559	0.005	8.835	0.003	0.069	0.525	0.252	0.169	0.024	0.025	0.000		16.628
EBS-18 Alt-6	4	5.723	0.009	2.371	0.000	6.269	0.005	0.050	0.354	0.211	0.151	0.035	0.213	0.004		15.176
AVE.		4.432	0.003	2.351	0.041	8.687	0.023	0.082	0.441	0.208	0.186	0.014	0.061	0.007		16.469
Std Dev		0.93	0.00	0.25	0.04	1.76	0.03	0.03	0.08	0.09	0.24	0.01	0.09	0.00		1.05
STIPNOMELANE on iron strip																
EBS-18 Stilp	1	34.47	0.04	15.25	0.00	31.11	0.00	0.08	2.12	2.33	0.61	0.01	0.21	0.00	-0.05	86.22
EBS-18 Stilp	2	35.44	0.02	14.40	0.00	33.80	0.00	0.12	2.10	2.60	0.08	0.01	0.20	0.01	-0.05	88.79
EBS-18 Stilp	3	34.63	0.03	14.16	0.01	32.71	0.01	0.10	1.95	2.68	0.43	0.01	0.26	0.05	-0.08	87.03
EBS-18 Stilp	4	36.03	0.03	14.87	0.00	31.76	0.00	0.11	2.32	1.94	0.28	0.02	0.11	0.00	-0.02	87.47
EBS-18 Stilp	5	36.59	0.03	14.22	0.01	31.48	0.00	0.11	2.31	1.89	0.32	0.01	0.27	0.00	-0.06	87.24

SAMPLE	Pt#	SiO2	TiO2	Al2O3	Cr2O3	FeO	NiO	MnO	MgO	CaO	Na2O	K2O	Cl	F	O=Hal	TOTAL
Average		35.43	0.03	14.58	0.01	32.17	0.00	0.10	2.16	2.29	0.34	0.01	0.21	0.01	-0.05	87.35
Std Dev		0.90	0.01	0.47	0.01	1.09	0.00	0.01	0.16	0.37	0.19	0.01	0.07	0.02	0.02	0.93

8 Atoms per formula unit (sum excludes F & Cl)

		Si	Ti	Al	Cr	Fe	Ni	Mn	Mg	Ca	Na	K	Cl	F		Sum
EBS-18 Stilp	1	2.149	0.002	1.121	0.000	1.622	0.000	0.004	0.197	0.156	0.074	0.000	0.022	0.000		5.326
EBS-18 Stilp	2	2.169	0.001	1.039	0.000	1.730	0.000	0.006	0.192	0.170	0.010	0.000	0.021	0.002		5.316
EBS-18 Stilp	3	2.164	0.001	1.043	0.001	1.710	0.000	0.005	0.182	0.180	0.052	0.001	0.028	0.011		5.339
EBS-18 Stilp	4	2.202	0.001	1.072	0.000	1.624	0.000	0.006	0.212	0.127	0.033	0.001	0.011	0.000		5.278
EBS-18 Stilp	5	2.242	0.001	1.027	0.001	1.613	0.000	0.006	0.211	0.124	0.038	0.001	0.028	0.000		5.263
Average		2.19	0.00	1.06	0.00	1.66	0.00	0.01	0.20	0.15	0.04	0.00	0.02	0.00		5.30
Std Dev		0.04	0.00	0.04	0.00	0.06	0.00	0.00	0.01	0.03	0.02	0.00	0.01	0.00		0.03

SAMPLE	Pt#	SiO2	TiO2	Al2O3	Cr2O3	FeO	NiO	MnO	MgO	CaO	Na2O	K2O	Cl	F	O=Hal	TOTAL
EBS-18 Steel Alteration (transects)																
EBS-18 Alt-1	1	1.03	0.00	0.24	0.67	70.38	0.53	0.78	0.00	0.03	0.09	0.00	6.66	0.00	-1.50	80.41
EBS-18 Alt-1	2	29.55	0.03	13.18	0.27	44.29	0.02	0.16	1.61	0.05	0.16	0.02	0.33	0.06	-0.10	89.74
EBS-18 Alt-1	3	29.13	0.05	12.46	0.17	42.98	0.03	0.23	1.50	0.06	0.20	0.03	0.06	0.03	-0.03	86.95
Ave		19.90	0.03	8.63	0.37	52.55	0.19	0.39	1.04	0.05	0.15	0.02	2.35	0.03	-0.54	85.70
Std Dev		16.35	0.03	7.27	0.26	15.45	0.29	0.34	0.90	0.02	0.05	0.02	3.73	0.03	0.83	4.79

22 Atoms per formula unit (sum excludes F & Cl)

		Si	Ti	Al	Cr	Fe	Ni	Mn	Mg	Ca	Na	K	Cl	F		Sum

		Si	Ti	Al	Cr	Fe	Ni	Mn	Mg	Ca	Na	K	Cl	F		Sum
EBS-18 Alt-1	1	0.357	0.000	0.099	0.184	20.442	0.149	0.231	0.000	0.009	0.063	0.000	3.919	0.000		21.534
EBS-18 Alt-1	2	5.304	0.004	2.787	0.038	6.648	0.003	0.025	0.431	0.010	0.057	0.004	0.100	0.034		15.310
EBS-18 Alt-1	3	5.374	0.007	2.709	0.025	6.631	0.004	0.035	0.413	0.012	0.072	0.008	0.019	0.020		15.292
Ave		**3.68**	**0.00**	**1.87**	**0.08**	**11.24**	**0.05**	**0.10**	**0.28**	**0.01**	**0.06**	**0.00**	**1.35**	**0.02**		**17.38**
Std Dev		**2.88**	**0.00**	**1.53**	**0.09**	**7.97**	**0.08**	**0.12**	**0.24**	**0.00**	**0.01**	**0.00**	**2.23**	**0.02**		**3.60**
EBS-18 Alt-2	1	0.51	0.01	0.69	0.35	77.51	0.09	0.81	0.06	0.21	2.72	0.07	0.07	0.00	-0.02	83.09
EBS-18 Alt-2	2	8.28	0.01	2.61	0.61	64.35	0.44	0.32	0.38	2.11	1.20	0.08	0.17	0.00	-0.04	80.56
EBS-18 Alt-2	3	22.66	0.04	10.52	0.13	50.31	0.03	0.52	1.26	1.63	1.08	0.08	0.28	0.01	-0.07	88.55
EBS-18 Alt-2	4	24.77	0.02	12.14	0.00	47.06	0.01	0.33	1.35	0.32	0.38	0.07	0.16	0.00	-0.04	86.62
Ave		**14.05**	**0.02**	**6.49**	**0.27**	**59.81**	**0.14**	**0.49**	**0.76**	**1.07**	**1.34**	**0.07**	**0.17**	**0.00**	**-0.04**	**84.70**
Std Dev		**11.63**	**0.01**	**5.68**	**0.27**	**13.98**	**0.20**	**0.23**	**0.64**	**0.95**	**0.98**	**0.00**	**0.09**	**0.01**	**0.02**	**3.57**

22 Atoms per formula unit (sum excludes F & Cl)

		Si	Ti	Al	Cr	Fe	Ni	Mn	Mg	Ca	Na	K	Cl	F	Sum
EBS-18 Alt-2	1	0.156	0.003	0.253	0.086	20.017	0.023	0.212	0.026	0.069	1.626	0.028	0.036	0.000	22.499
EBS-18 Alt-2	2	2.265	0.002	0.841	0.133	14.727	0.097	0.074	0.156	0.619	0.637	0.027	0.079	0.000	19.578
EBS-18 Alt-2	3	4.476	0.006	2.449	0.020	8.310	0.004	0.087	0.370	0.346	0.413	0.020	0.094	0.008	16.499
EBS-18 Alt-2	4	4.803	0.003	2.775	0.000	7.632	0.002	0.054	0.391	0.066	0.142	0.017	0.052	0.000	15.886
Ave		**2.93**	**0.00**	**1.58**	**0.06**	**12.67**	**0.03**	**0.11**	**0.24**	**0.27**	**0.70**	**0.02**	**0.07**	**0.00**	**18.62**
Std Dev		**2.16**	**0.00**	**1.22**	**0.06**	**5.85**	**0.04**	**0.07**	**0.18**	**0.26**	**0.65**	**0.01**	**0.03**	**0.00**	**3.05**

EBS-18 Alt-3	1	8.35	0.01	2.72	0.67	68.62	0.50	0.55	0.59	3.35	0.92	0.09	0.13	0.06	-0.05	86.54
EBS-18 Alt-3	2	14.90	0.00	6.55	0.65	52.17	0.53	0.38	1.28	1.86	0.39	0.04	0.11	0.00	-0.03	78.86
EBS-18 Alt-3	3	14.73	0.02	6.49	0.48	58.08	0.42	0.39	1.29	0.87	0.42	0.06	0.11	0.00	-0.02	83.35
Ave		12.66	0.01	5.25	0.60	59.62	0.49	0.44	1.05	2.03	0.58	0.06	0.12	0.02	-0.03	82.92
Std Dev		3.73	0.01	2.19	0.10	8.33	0.06	0.09	0.40	1.25	0.30	0.02	0.01	0.03	0.02	3.86

22 Atoms per formula unit (sum excludes F & Cl)

		Si	Ti	Al	Cr	Fe	Ni	Mn	Mg	Ca	Na	K	Cl	F		Sum
EBS-18 Alt-3	1	2.136	0.002	0.820	0.135	14.684	0.103	0.118	0.226	0.919	0.456	0.028	0.056	0.046		19.626
EBS-18 Alt-3	2	3.610	0.000	1.868	0.124	10.568	0.104	0.079	0.462	0.482	0.184	0.013	0.046	0.000		17.492
EBS-18 Alt-3	3	3.444	0.003	1.789	0.089	11.361	0.079	0.077	0.450	0.218	0.191	0.018	0.043	0.000		17.718
Ave		3.06	0.00	1.49	0.12	12.20	0.10	0.09	0.38	0.54	0.28	0.02	0.05	0.02		18.28
Std Dev		0.81	0.00	0.58	0.02	2.18	0.01	0.02	0.13	0.35	0.16	0.01	0.01	0.03		1.17

EBS-18 Alt-4	1	17.99	0.00	8.14	0.64	55.76	0.15	1.25	1.37	0.33	0.14	0.03	0.13	0.00	-0.03	85.93
EBS-18 Alt-4	2	30.95	0.01	13.67	0.04	37.48	0.02	0.22	2.53	0.69	0.02	0.02	0.13	0.02	-0.04	85.79
EBS-18 Alt-4	3	16.42	0.00	7.25	0.15	58.50	0.05	0.60	1.34	0.57	0.10	0.01	0.04	0.00	-0.01	85.03
EBS-18 Alt-4	4	5.08	0.03	0.84	0.41	62.09	0.56	0.38	0.15	7.95	0.37	0.01	0.14	0.00	-0.03	78.00
Ave		17.61	0.01	7.47	0.31	53.46	0.19	0.61	1.35	2.39	0.15	0.02	0.11	0.00	-0.03	83.69
Std Dev		10.59	0.01	5.26	0.27	10.96	0.25	0.45	0.97	3.71	0.15	0.01	0.05	0.01	0.01	3.81

22 Atoms per formula unit (sum excludes F & Cl)

		Si	Ti	Al	Cr	Fe	Ni	Mn	Mg	Ca	Na	K	Cl	F		Sum

347

		Si	Ti	Al	Cr	Fe	Ni	Mn	Mg	Ca	Na	K	Cl	F		Sum
EBS-18 Alt-4	1	3.900	0.000	2.080	0.110	10.107	0.026	0.230	0.441	0.077	0.059	0.008	0.046	0.000		17.038
EBS-18 Alt-4	2	5.572	0.001	2.900	0.006	5.642	0.003	0.033	0.679	0.134	0.006	0.004	0.039	0.009		14.980
EBS-18 Alt-4	3	3.686	0.000	1.917	0.027	10.981	0.008	0.114	0.449	0.138	0.042	0.002	0.015	0.002		17.364
EBS-18 Alt-4	4	1.510	0.006	0.294	0.096	15.445	0.134	0.095	0.068	2.534	0.211	0.004	0.071	0.000		20.396
Ave		**3.67**	**0.00**	**1.80**	**0.06**	**10.54**	**0.04**	**0.12**	**0.41**	**0.72**	**0.08**	**0.00**	**0.04**	**0.00**		**17.44**
Std Dev		**1.67**	**0.00**	**1.09**	**0.05**	**4.02**	**0.06**	**0.08**	**0.25**	**1.21**	**0.09**	**0.00**	**0.02**	**0.00**		**2.23**
EBS-18 Alt-5	1	11.80	0.02	4.57	0.68	62.53	0.34	1.11	0.96	0.70	0.44	0.03	0.24	0.04	-0.07	83.46
EBS-18 Alt-5	2	49.89	0.16	14.91	0.04	20.43	0.01	0.16	2.25	0.51	0.27	1.53	0.23	0.03	-0.07	90.41
EBS-18 Alt-5	3	42.21	0.63	22.20	0.00	16.20	0.00	0.15	2.84	0.47	0.14	3.47	0.13	0.17	-0.10	88.63
Ave		**34.63**	**0.27**	**13.89**	**0.24**	**33.05**	**0.12**	**0.48**	**2.02**	**0.56**	**0.29**	**1.68**	**0.20**	**0.08**	**-0.08**	**87.50**
Std Dev		**20.14**	**0.32**	**8.86**	**0.38**	**25.62**	**0.19**	**0.55**	**0.96**	**0.12**	**0.15**	**1.73**	**0.06**	**0.08**	**0.02**	**3.61**
22 Atoms per formula unit (sum excludes F & Cl)																
		Si	Ti	Al	Cr	Fe	Ni	Mn	Mg	Ca	Na	K	Cl	F		Sum
EBS-18 Alt-5	1	2.928	0.004	1.337	0.134	12.975	0.068	0.234	0.355	0.185	0.213	0.008	0.100	0.030		18.443
EBS-18 Alt-5	2	7.377	0.017	2.599	0.005	2.526	0.001	0.020	0.496	0.081	0.078	0.288	0.057	0.016		13.487
EBS-18 Alt-5	3	6.388	0.072	3.958	0.000	2.049	0.000	0.020	0.642	0.077	0.042	0.670	0.034	0.082		13.918
Ave		**5.56**	**0.03**	**2.63**	**0.05**	**5.85**	**0.02**	**0.09**	**0.50**	**0.11**	**0.11**	**0.32**	**0.06**	**0.04**		**15.28**
Std Dev		**2.34**	**0.04**	**1.31**	**0.08**	**6.18**	**0.04**	**0.12**	**0.14**	**0.06**	**0.09**	**0.33**	**0.03**	**0.04**		**2.75**
EBS-18 Alt-6	1	16.79	0.01	7.58	0.45	55.51	0.33	0.64	1.05	1.78	1.56	0.08	0.12	0.00	-0.03	85.92
EBS-18 Alt-6	2	18.31	0.01	9.68	0.07	55.43	0.02	0.54	1.36	1.53	0.67	0.04	0.14	0.02	-0.04	87.80

348

		Si	Ti	Al	Cr	Fe	Ni	Mn	Mg	Ca	Na	K	Cl	F		Sum
EBS-18 Alt-6	3	20.59	0.00	10.68	0.03	51.95	0.02	0.40	1.73	1.15	0.43	0.09	0.07	0.00	-0.02	87.14
EBS-18 Alt-6	4	27.24	0.05	9.58	0.00	35.68	0.03	0.28	1.13	0.94	0.37	0.13	0.60	0.01	-0.14	76.03
Ave		**20.73**	**0.02**	**9.38**	**0.14**	**49.64**	**0.10**	**0.46**	**1.32**	**1.35**	**0.76**	**0.08**	**0.23**	**0.01**	**-0.05**	**84.22**
Std Dev		**4.61**	**0.02**	**1.30**	**0.21**	**9.46**	**0.16**	**0.16**	**0.31**	**0.38**	**0.55**	**0.04**	**0.25**	**0.01**	**0.06**	**5.52**
22 Atoms per formula unit (sum excludes F & Cl)																
		Si	Ti	Al	Cr	Fe	Ni	Mn	Mg	Ca	Na	K	Cl	F		Sum
EBS-18 Alt-6	1	3.702	0.002	1.969	0.079	10.232	0.059	0.120	0.344	0.420	0.668	0.022	0.045	0.000		17.617
EBS-18 Alt-6	2	3.837	0.001	2.390	0.011	9.714	0.004	0.095	0.426	0.343	0.270	0.010	0.049	0.010		17.101
EBS-18 Alt-6	3	4.187	0.000	2.559	0.005	8.835	0.003	0.069	0.525	0.252	0.169	0.024	0.025	0.000		16.628
EBS-18 Alt-6	4	5.723	0.009	2.371	0.000	6.269	0.005	0.050	0.354	0.211	0.151	0.035	0.213	0.004		15.176
Ave		**4.36**	**0.00**	**2.32**	**0.02**	**8.76**	**0.02**	**0.08**	**0.41**	**0.31**	**0.31**	**0.02**	**0.08**	**0.00**		**16.63**
Std Dev		**0.93**	**0.00**	**0.25**	**0.04**	**1.76**	**0.03**	**0.03**	**0.08**	**0.09**	**0.24**	**0.01**	**0.09**	**0.00**		**1.05**

Appendix E
SEM images EBS-18

Copper and Steel corrosion images

det	mode	HV	mag □	WD	HFW	10 µm
ETD	SE	30.00 kV	10 000 x	10.0 mm	25.6 µm	
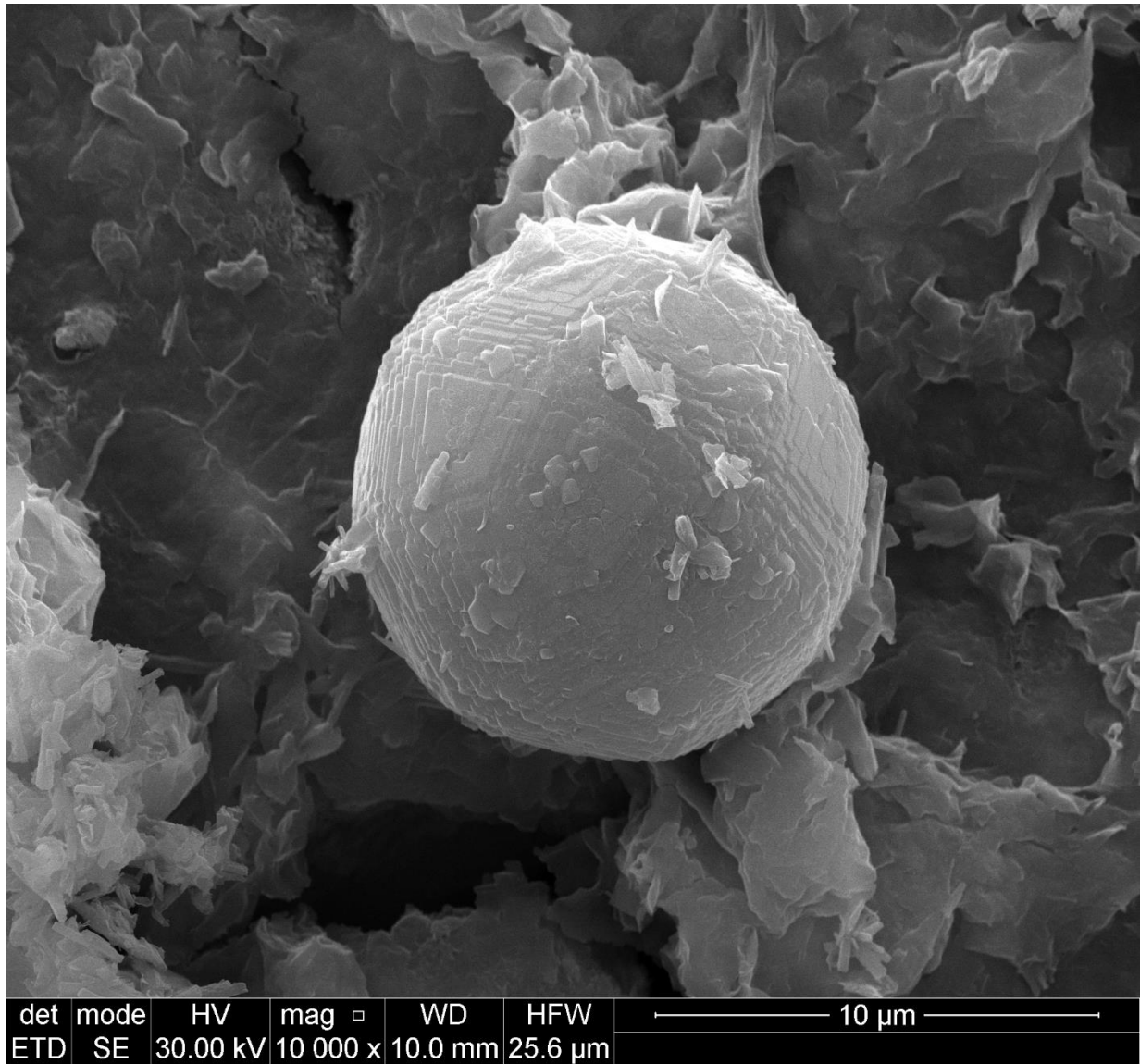
Figure E.1. Analcime – Wairakite zeolite in smectite matrix.

det	mode	HV	mag □	WD	HFW	100 μm
ETD	SE	30.00 kV	1 000 x	11.4 mm	256 μm	
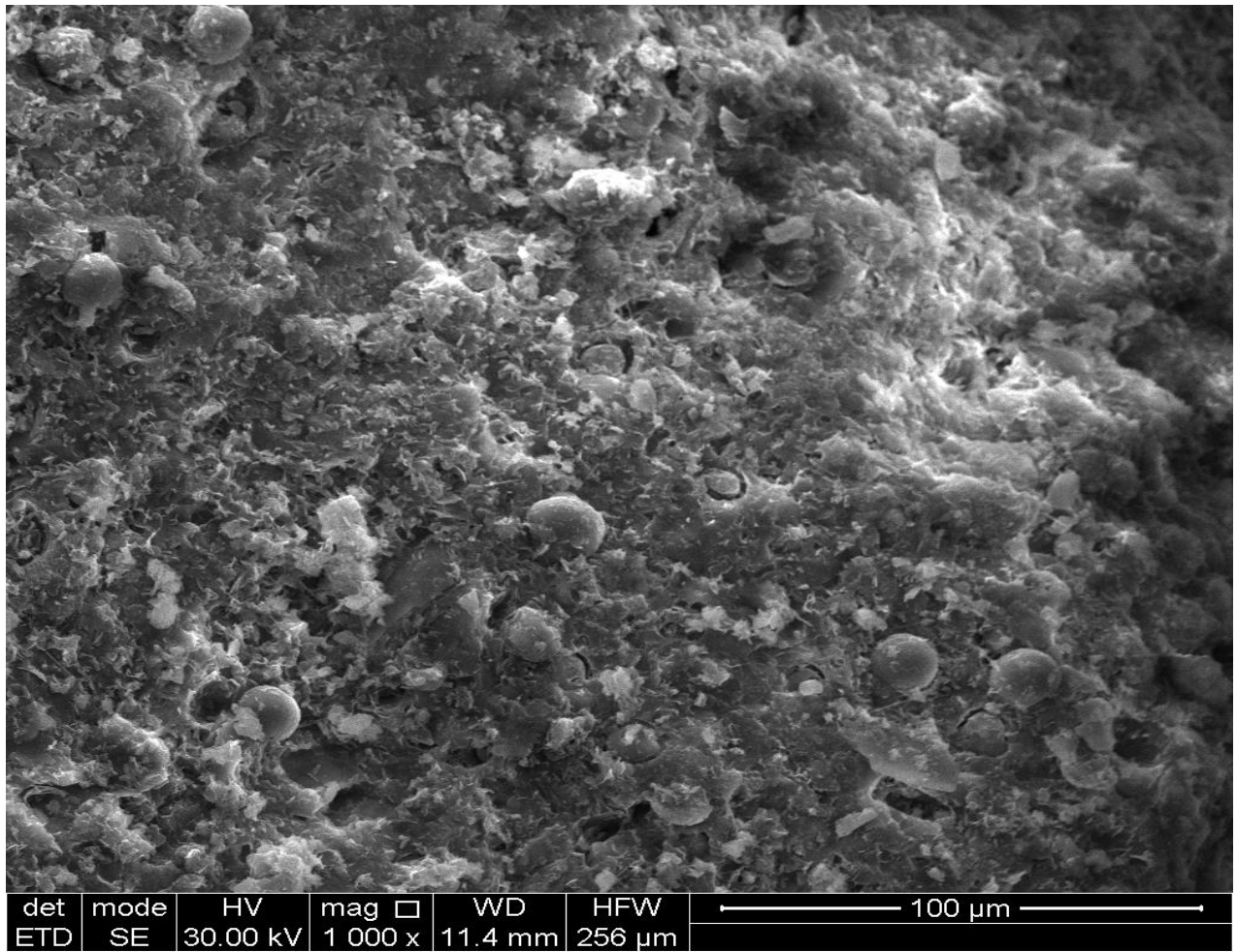
Figure E.2 Analcime – wairakite embedded in smectite groundmass.

det	mode	HV	mag ▫	WD	HFW	10 µm
ETD	SE	30.00 kV	10 000 x	10.0 mm	25.6 µm	
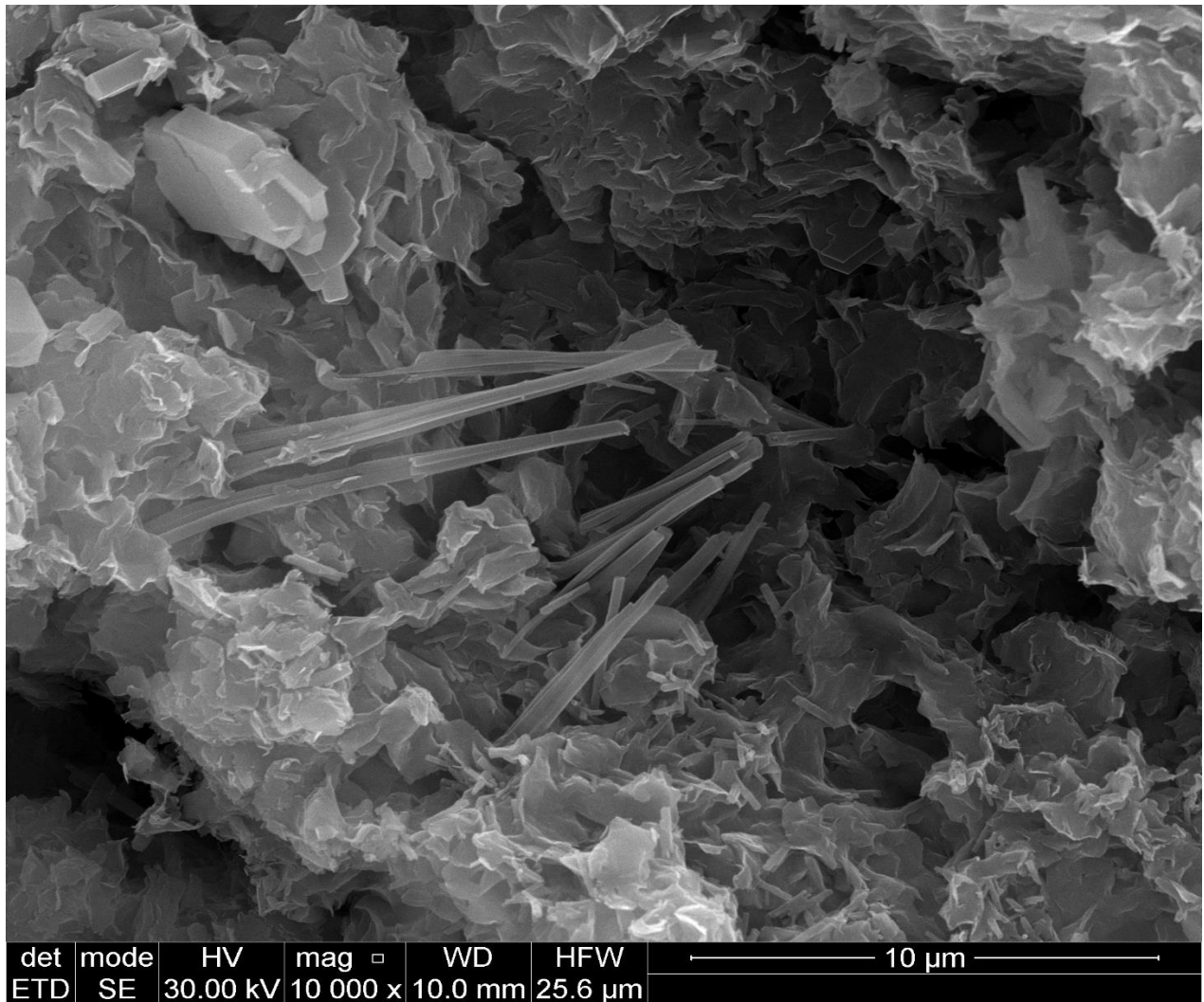
Figure E.3. Acicular clinoptilolite in smectite

det	mode	HV	mag □	WD	HFW	⊢—— 10 µm ——⊣
ETD	SE	5.00 kV	6 000 x	11.5 mm	42.7 µm	Squeeze-Out
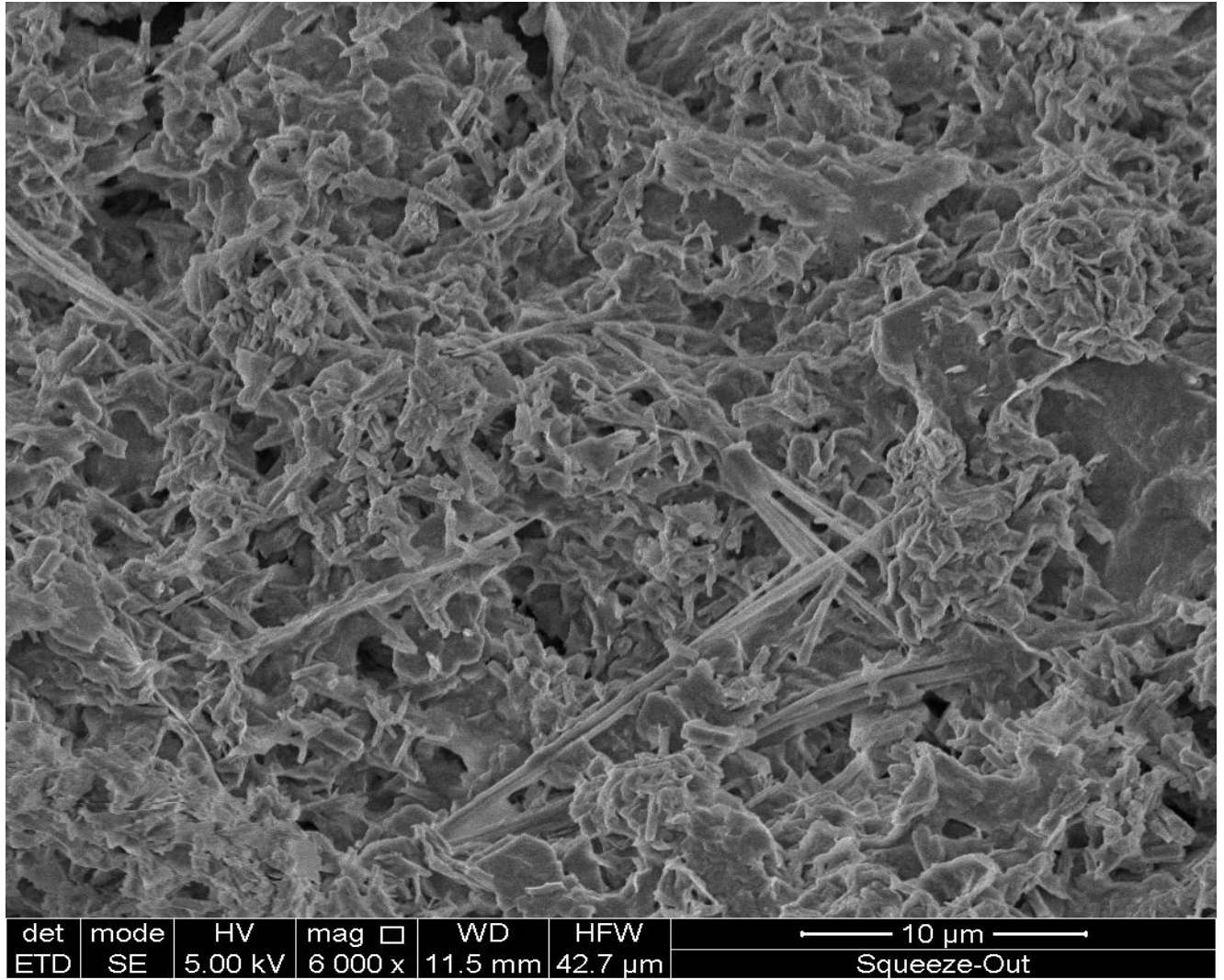
Figure E.4. Fibrous clinoptilolite and smectite

det	mode	HV	mag ☐	WD	HFW	
ETD	SE	30.00 kV	10 000 x	10.0 mm	25.6 µm	10 µm
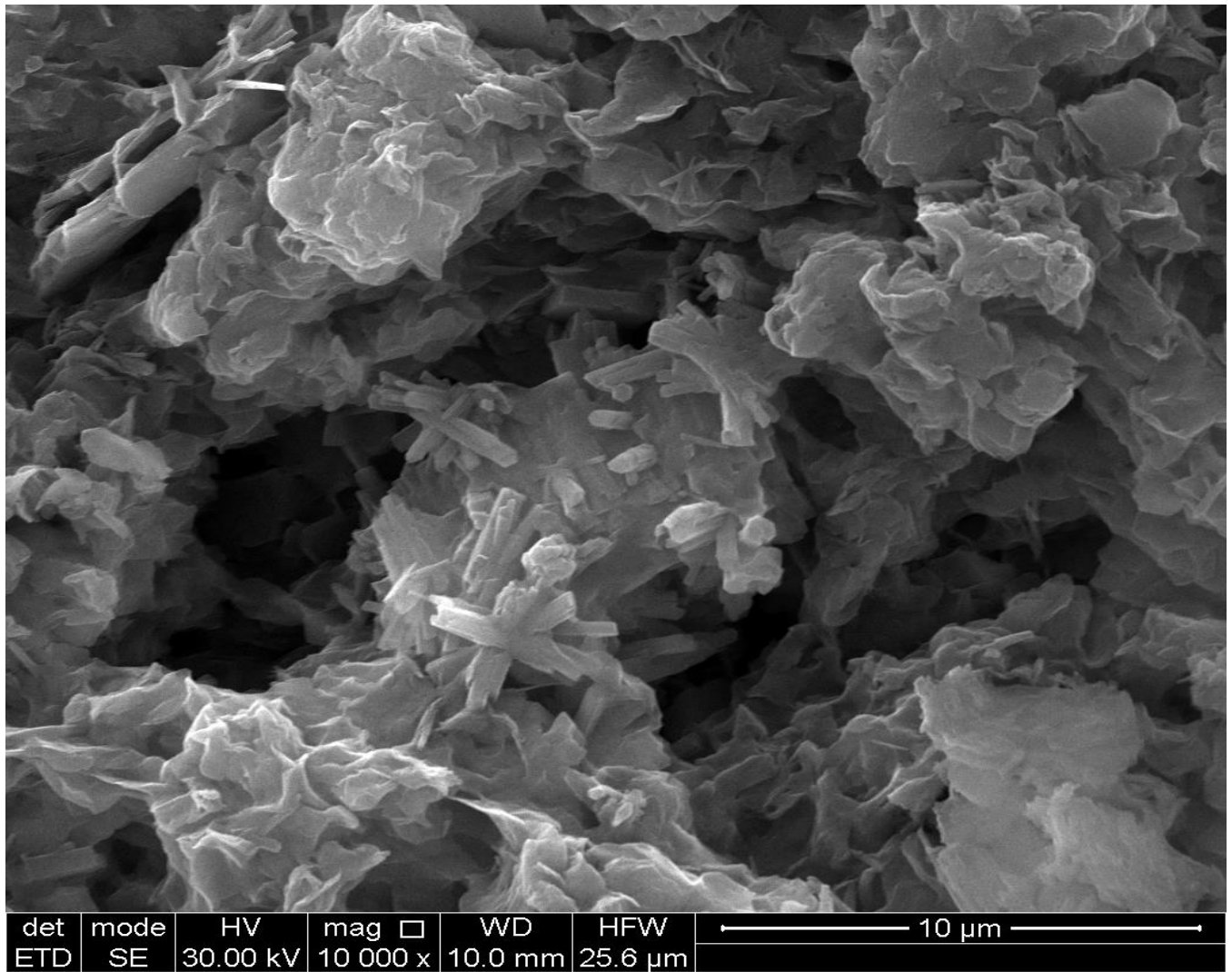
Figure E.5. Radial growth authigenic plagioclase

det	mode	HV	mag ☐	WD	HFW	← 100 μm →
ETD	SE	30.00 kV	1 000 x	10.3 mm	256 μm	

Figure E.6. Fe-saponite (fine grained material above black zone) grown on low carbon steel (lower grey mass).

Figure E.7. Note abundant pit corrosion in upper right region of low carbon steel sample.

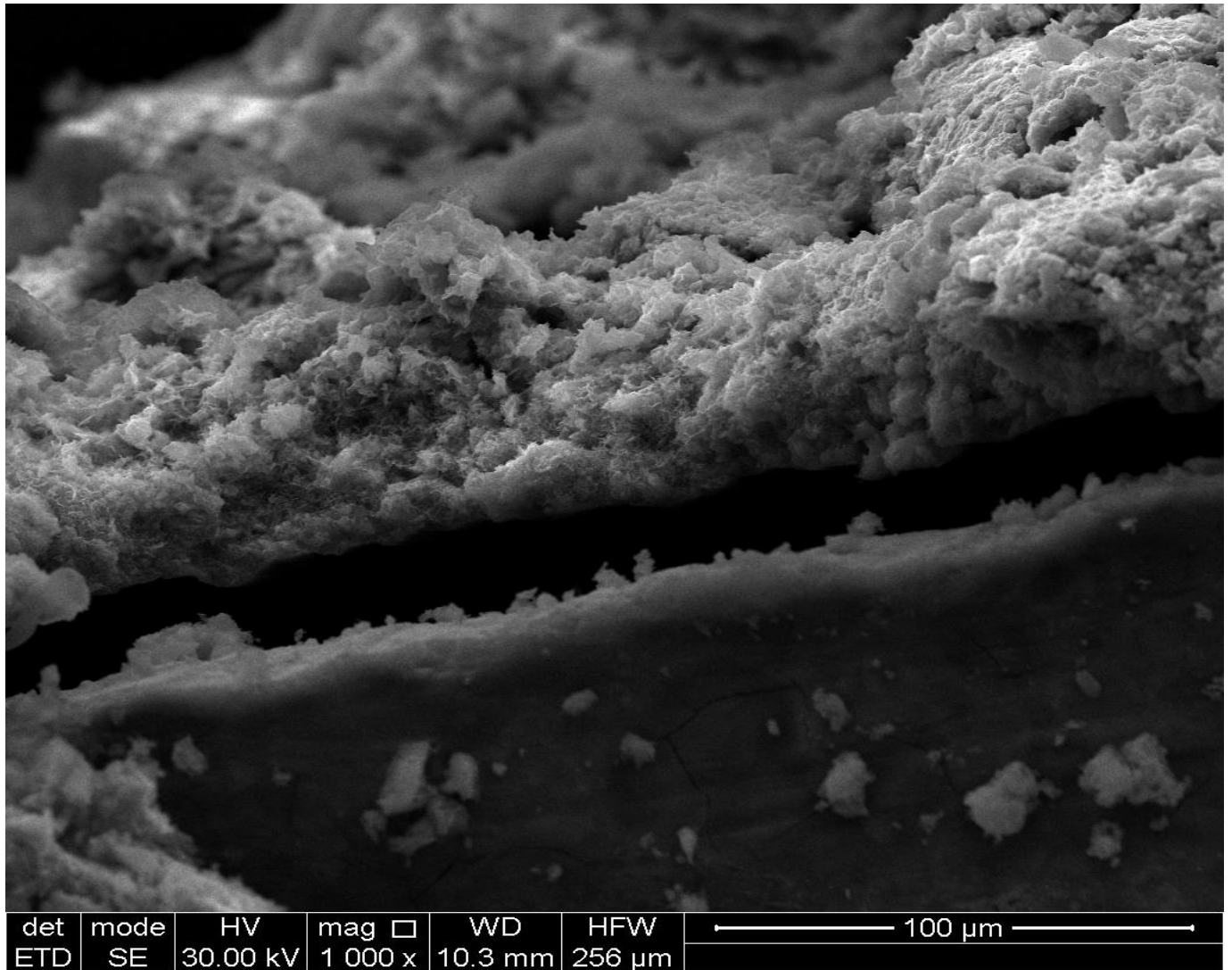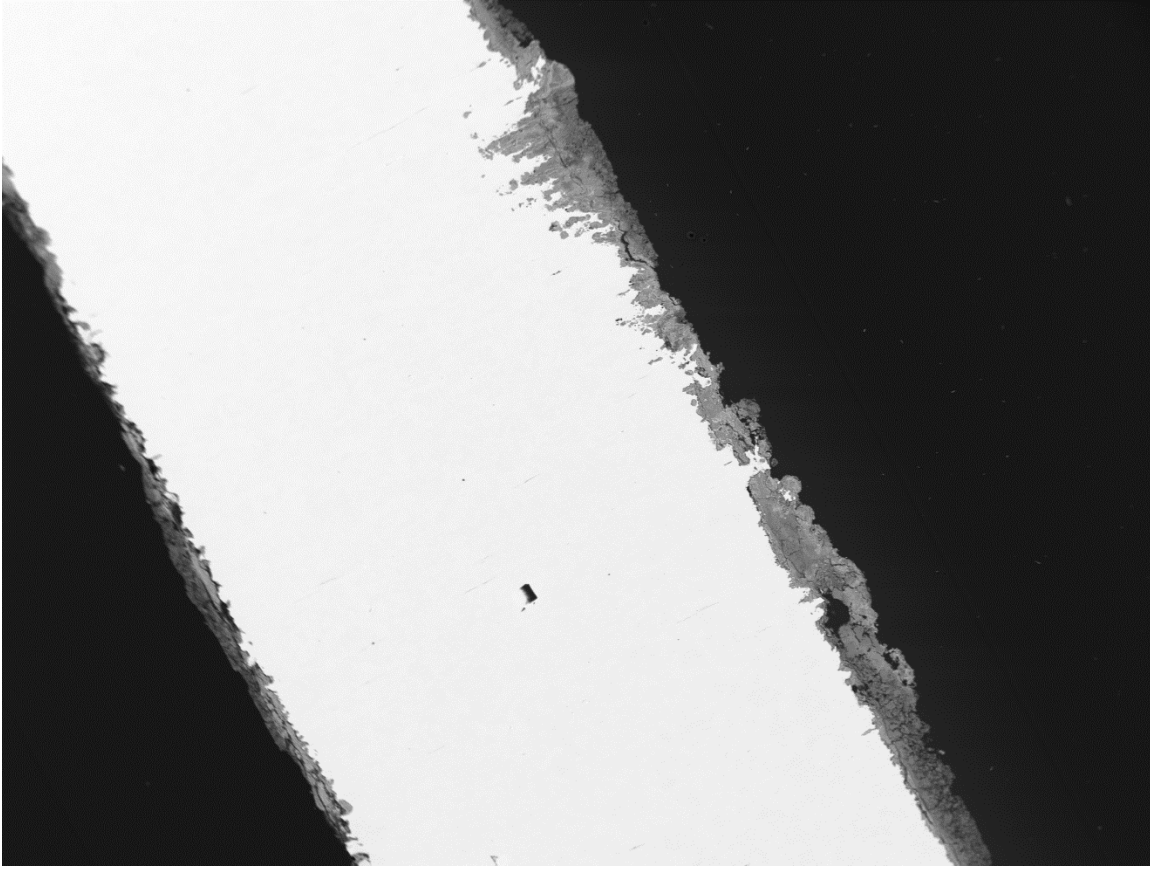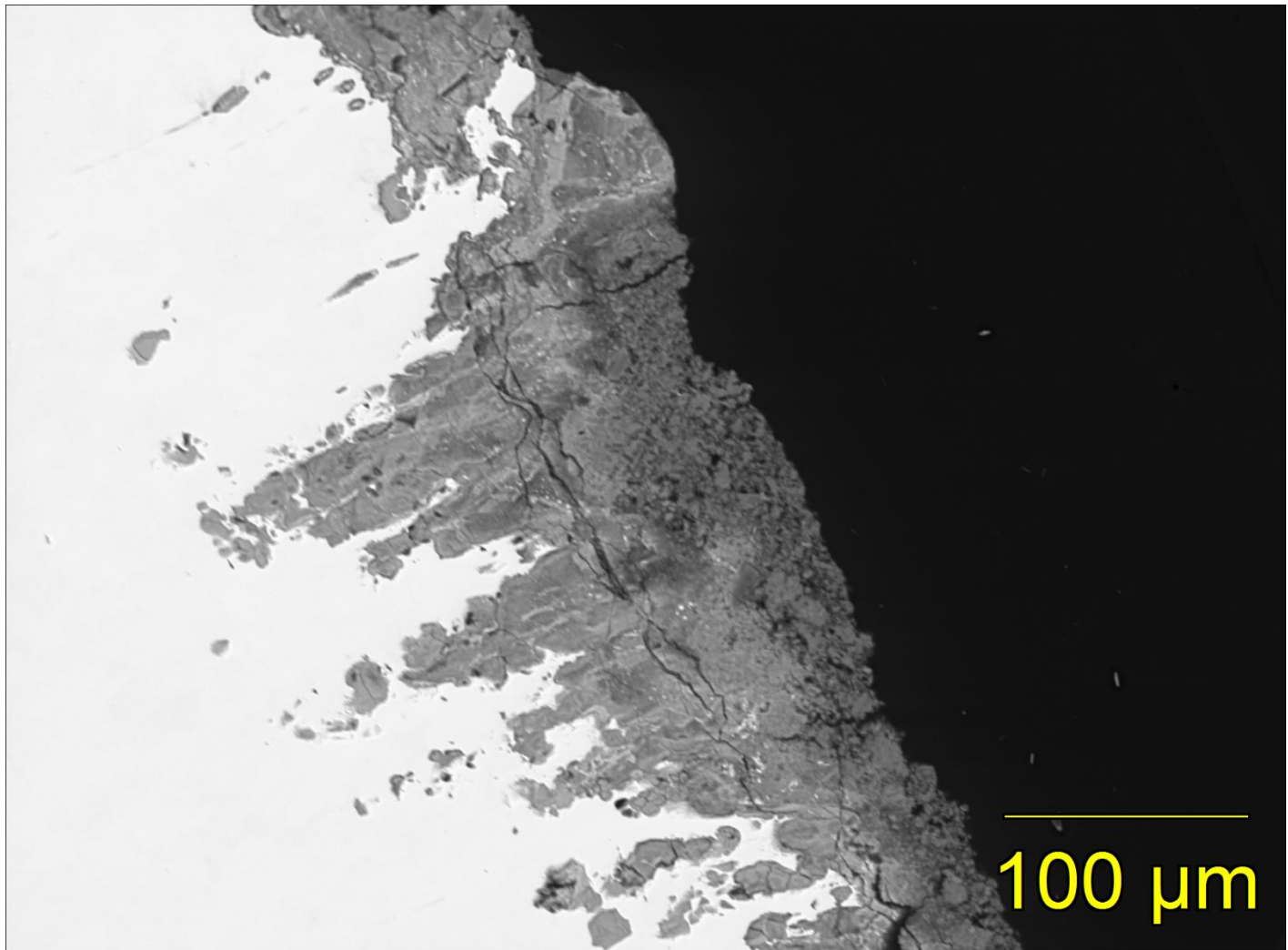**Figure E.8.** Pit corrosion of low carbon steel in experiment EBS-18. Depth exceeds 100 micron maximum and width is approximately 50 micron.
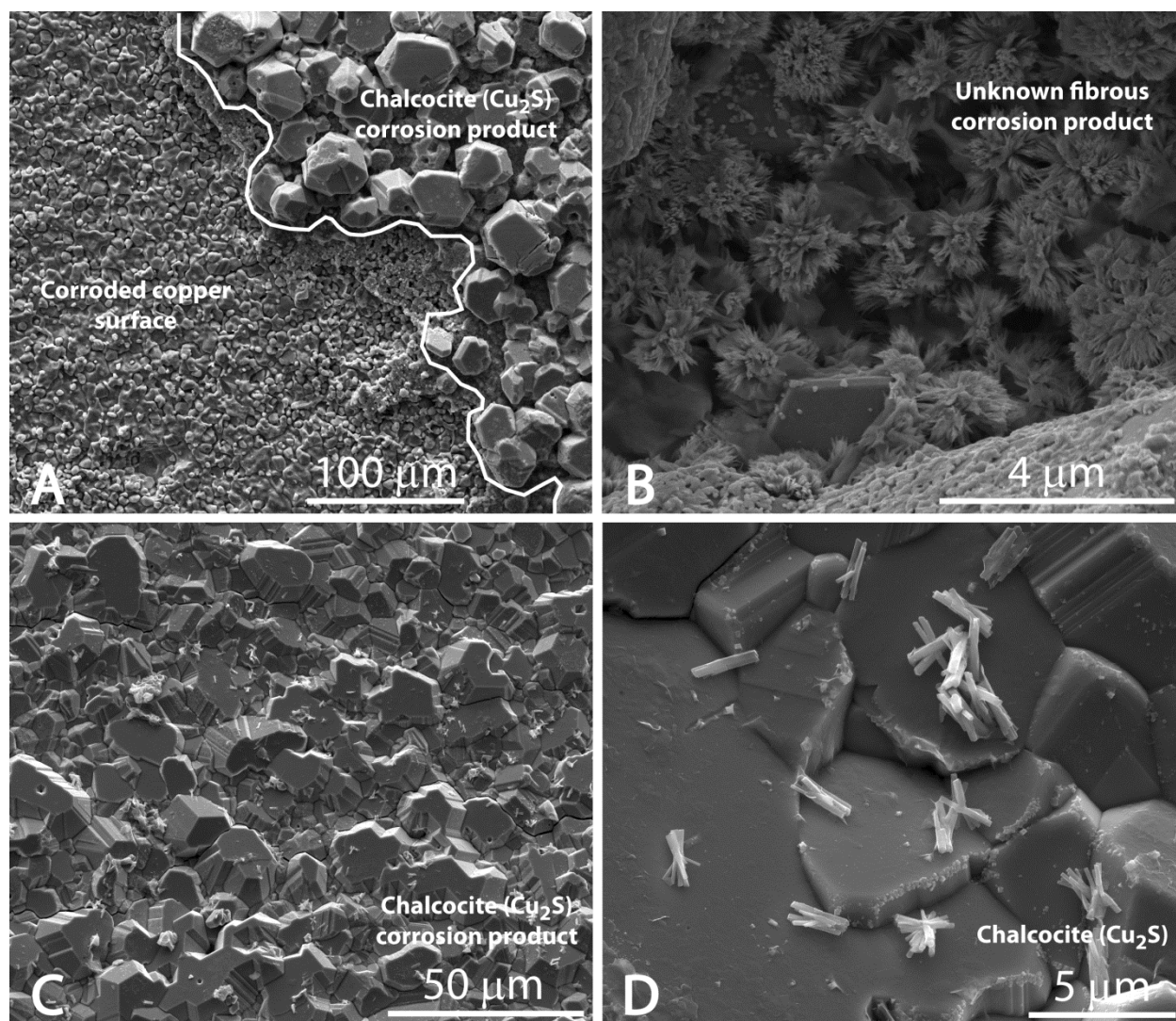
Figure E.9. SEM image (plan view) of copper surface showing corroded copper surfaces and various interface reaction products from both ramped (EBS-4) and isothermal, 300°C (EBS-8) heating profiles. A) Boundary between the corroded copper surface and chalcocite (Cu$_2$S) from EBS-4. B) Unknown fibers occurring on the copper surface in between chalcocite growths from EBS-4. These fibers might be a late-stage oxide or chloride corrosion product upon depletion of sulfide. C) Intergrown chalcocite from EBS-8. D) Atacamite (orthorhombic laths) resting on top of chalcocite crystals. Their growth is due to late stage scavenging of Cl from the brine.
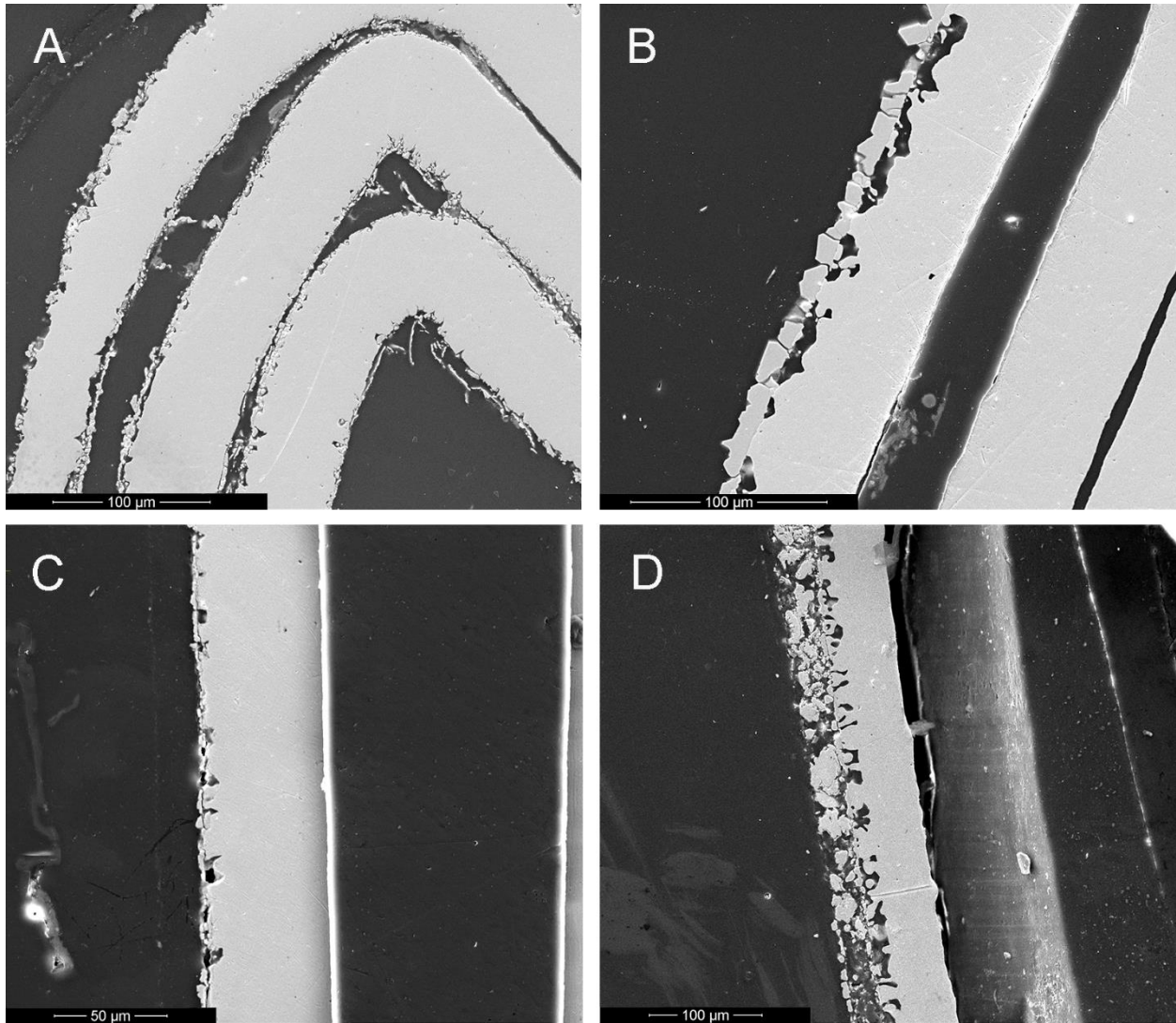
Figure E.10. SEM images from runs EBS-4 (A), EBS-11 (B), EBS-16 (C) and EBS-17(D). The overall thicknesses of the copper foils are ~ 63 μm. Surfaces within the rolled copper foil were relatively protected from sulfide attack.
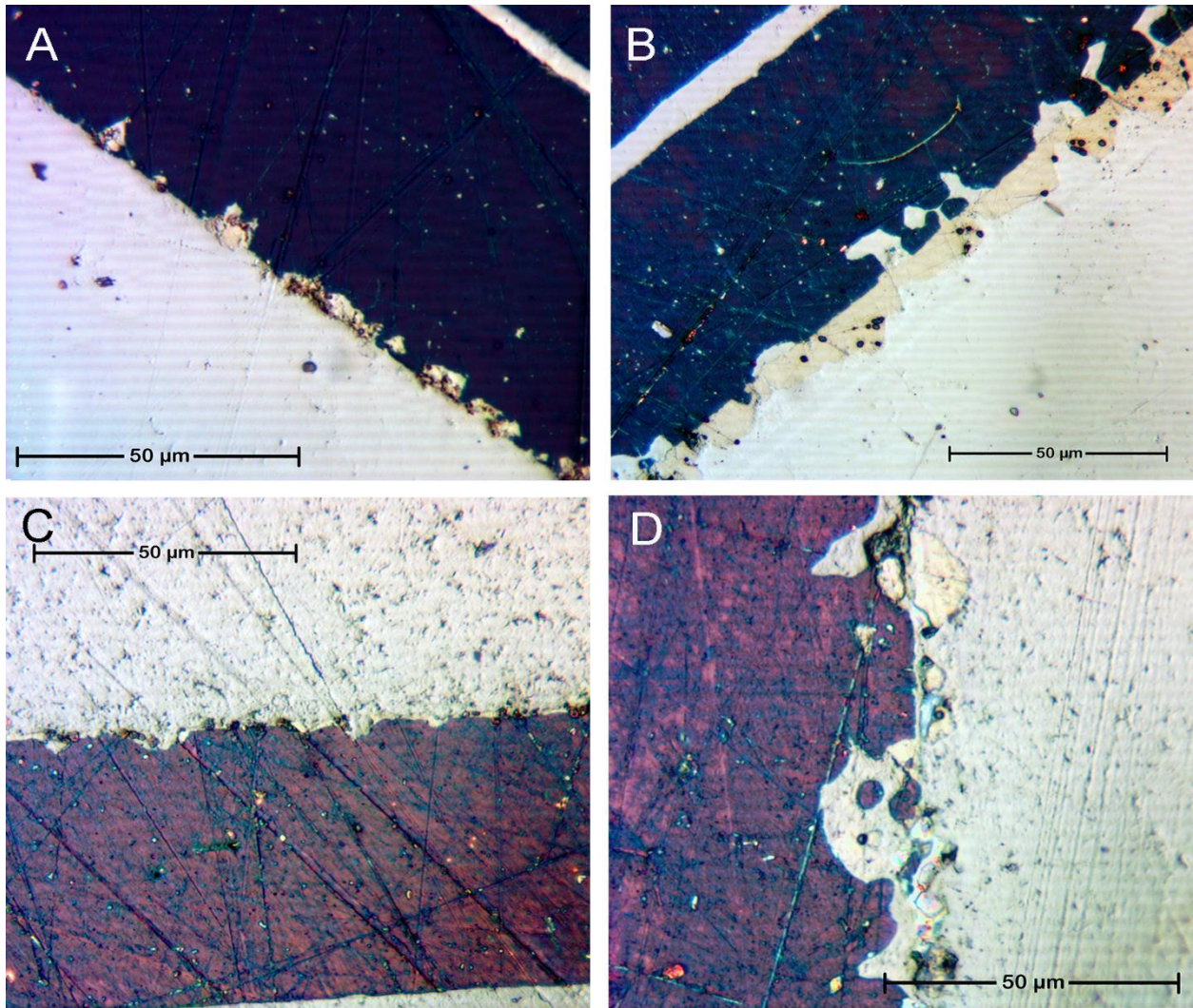
Figure E.11. Reflected light images of Cu corrosion. EBS-4 (A), EBS-11 (B), EBS-16 (C) and EBS-17 (D) with chalcocite layer (pale yellow). Copper color for images A and B, dark blue/black, images C and D, orange brown.
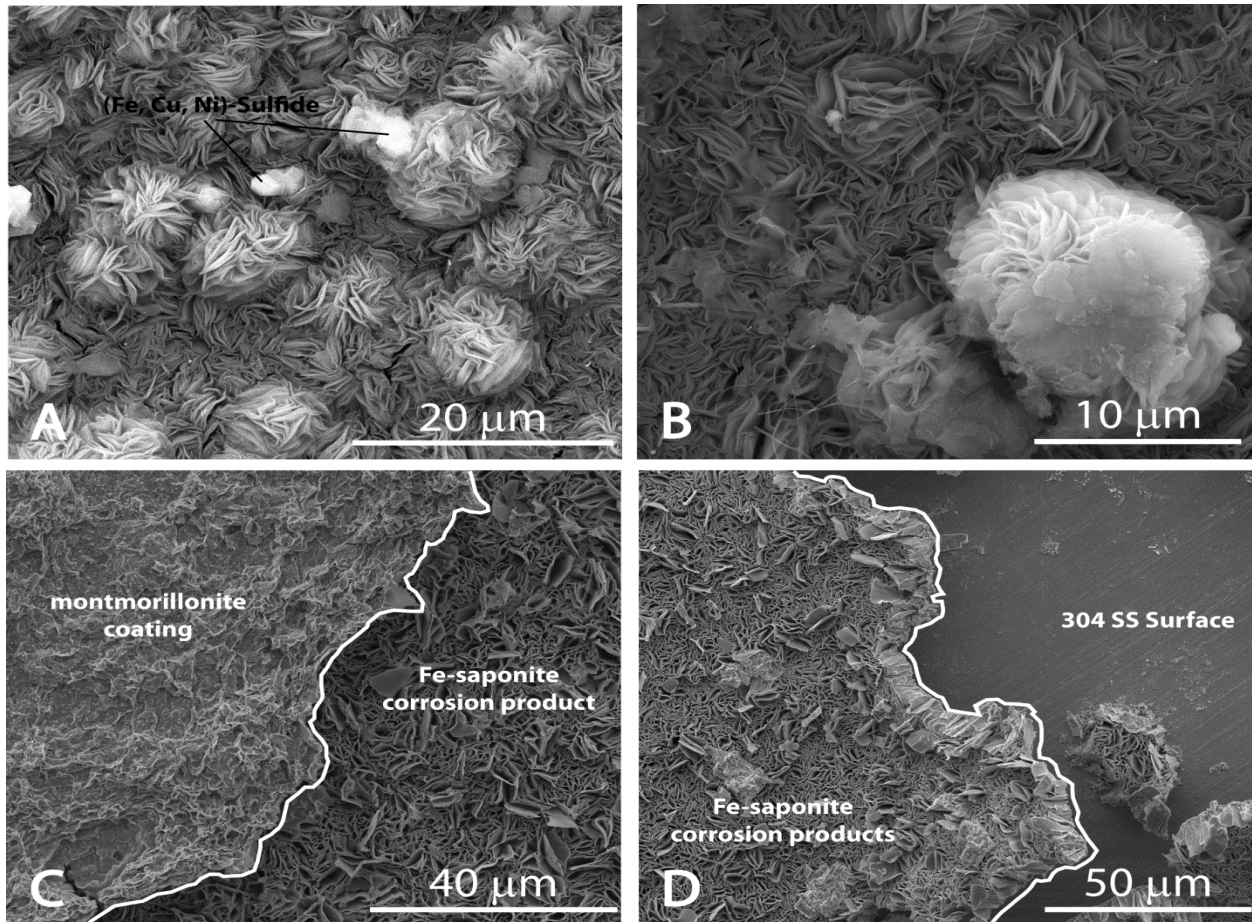
Figure E.12. SEM image (plan view) of Fe-phyllosilicates (saponite and chlorite) using 304 SS as a growth substrate from both ramped (EBS-2) and isothermal, 300°C (EBS-5) heating profiles. A) Fe-saponite and chlorite growths with later-stage pentlandite-like ((Fe, Cu, Ni)-sulfide) material from EBS-2. B) Unknown fibers overlaying rose-like Fe-saponite and chlorite interface reaction products from EBS-2. C) Montmorillonite coating on Fe-saponite showing the distinct morphology between the two smectites from EBS-5. D) Boundary between the Fe-saponite interface reaction product and 304 SS surface from EBS-5.
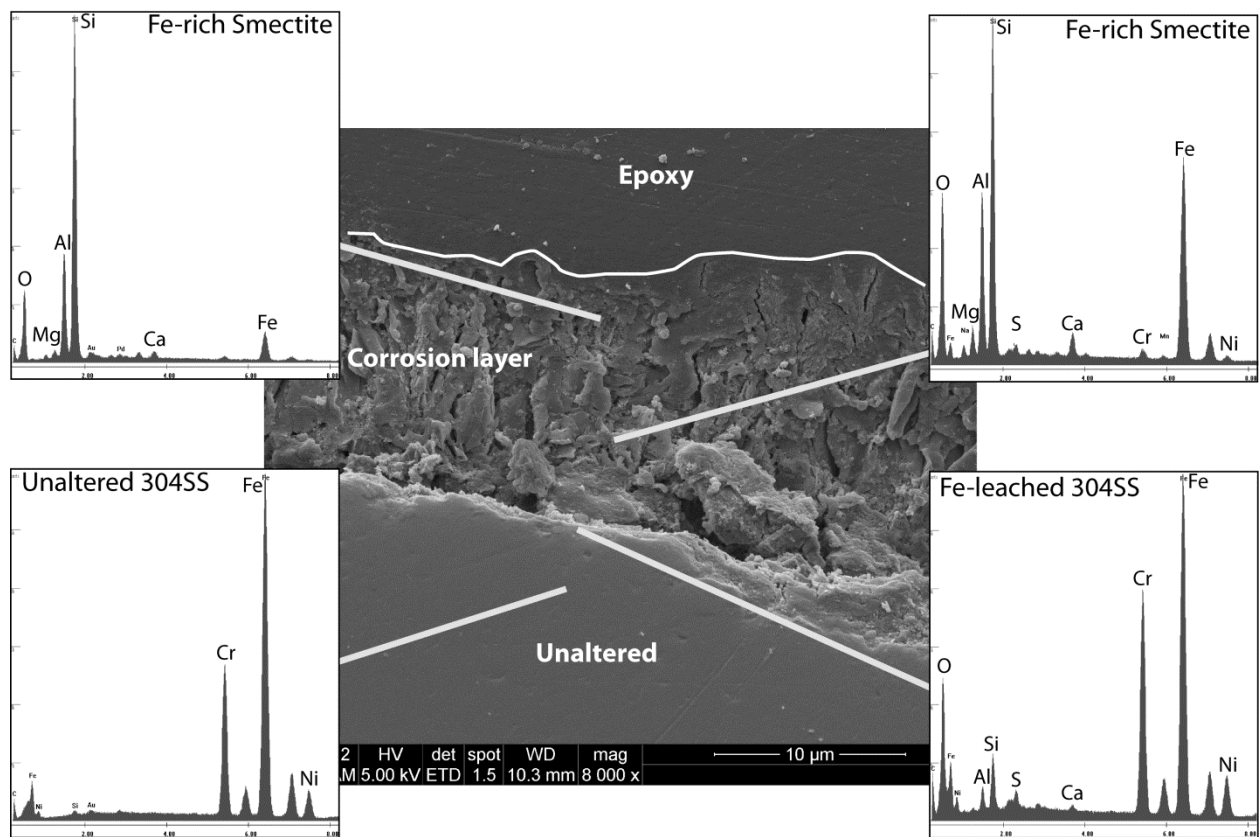
Figure E.13. SEM image of 304 SS cross-section showing Fe-saponite interface reaction products using steel surface as a growth substrate. EDX analyses of post-reaction 304SS and interface reaction products indicates Fe is leached from the 304SS forming a slightly Cr-enriched steel outer layer and an Fe-rich aluminosilicate (Fe-saponite/chlorite) coating. Uniform corrosion of the 304SS does not appear to develop significant incongruent dissolution.
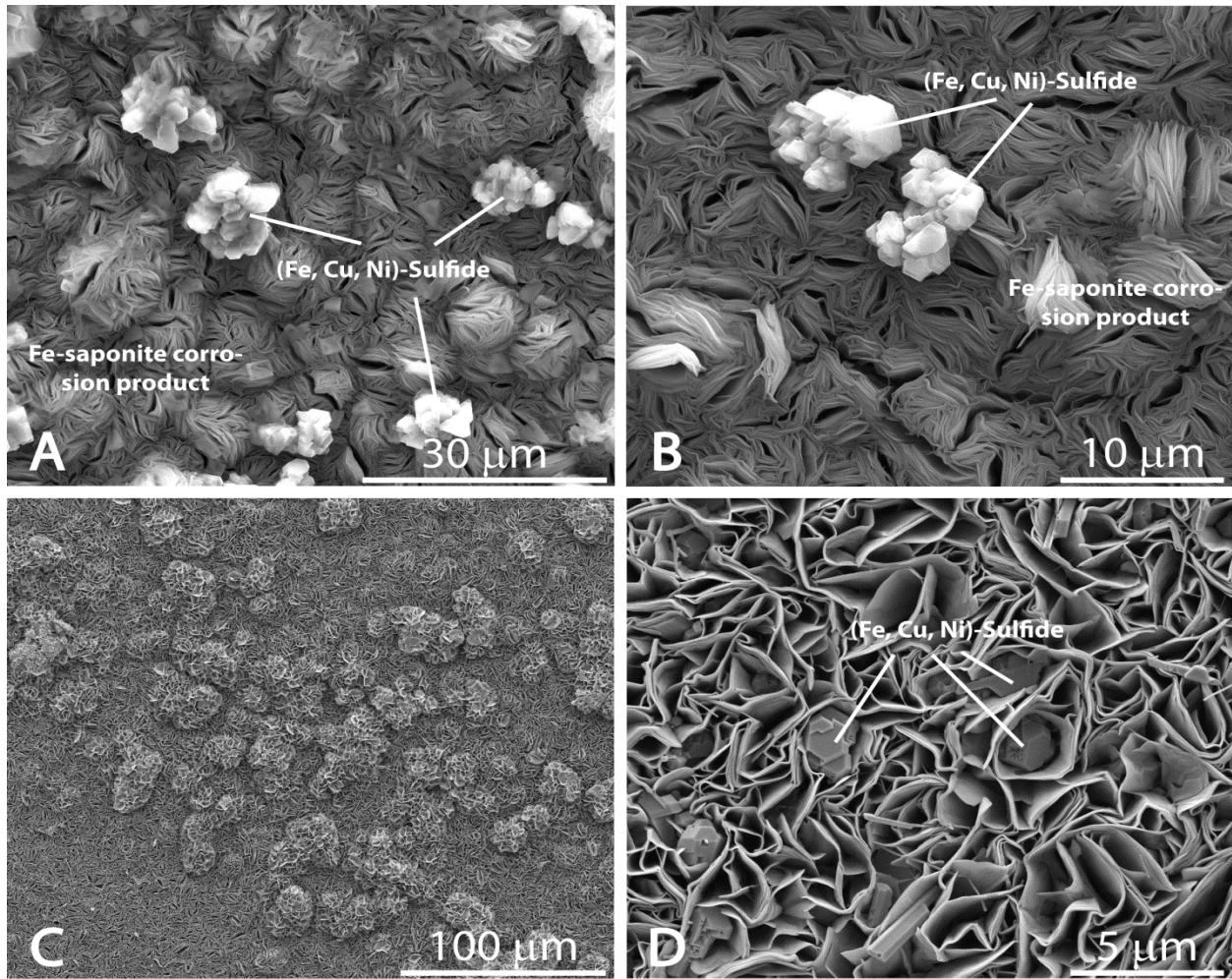
Figure E.14. SEM image (plan view) of Fe-saponite using 316SS as a growth substrate from both ramped (EBS-3) and isothermal, 300°C (EBS-10) heating profiles. A) Dense growth of Fe-saponite and chlorite with late-stage pentlandite-like ((Fe, Cu, Ni)-sulfide) material from EBS-3. B) Close-up of pentlandite-like ((Fe, Cu, Ni)-sulfide) material on Fe-phyllosilicates from EBS-3. C) Honeycomb and rose-like textures associated with Fe-saponite interface reaction products from EBS-10. D) Fe-saponite rose-like texture with pentlandite-like materials occurring between Fe-saponite foils from EBS-10.
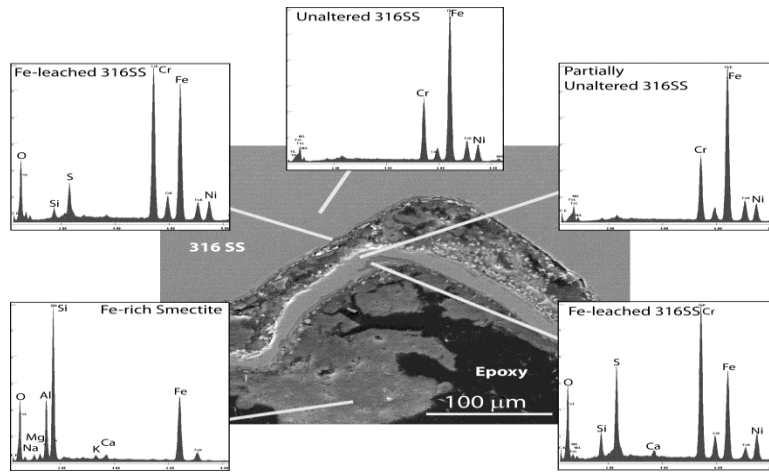
Figure E.15. SEM (secondary electron) image of 316SS cross-section showing Fe-saponite/chlorite growth due to exfoliation corrosion from EBS-3. Chemical analyses of post-reaction 316SS and interface reaction products indicates there was significant Fe leaching from the 316SS forming a Cr-enriched steel outer layer up to 4 μm thick.
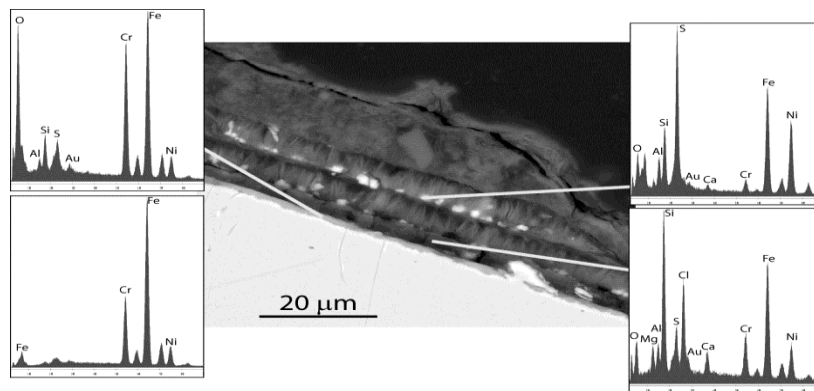
Figure E.16. SEM (back scatter) image of 316SS cross-section showing Fe-saponite/chlorite growth due to exfoliation corrosion from EBS-3. Chemical analyses of post-reaction 316SS and interface reaction products indicates there was significant Fe leaching from the 316SS forming a Cr-enriched steel outer layer up to 4 μm thick.
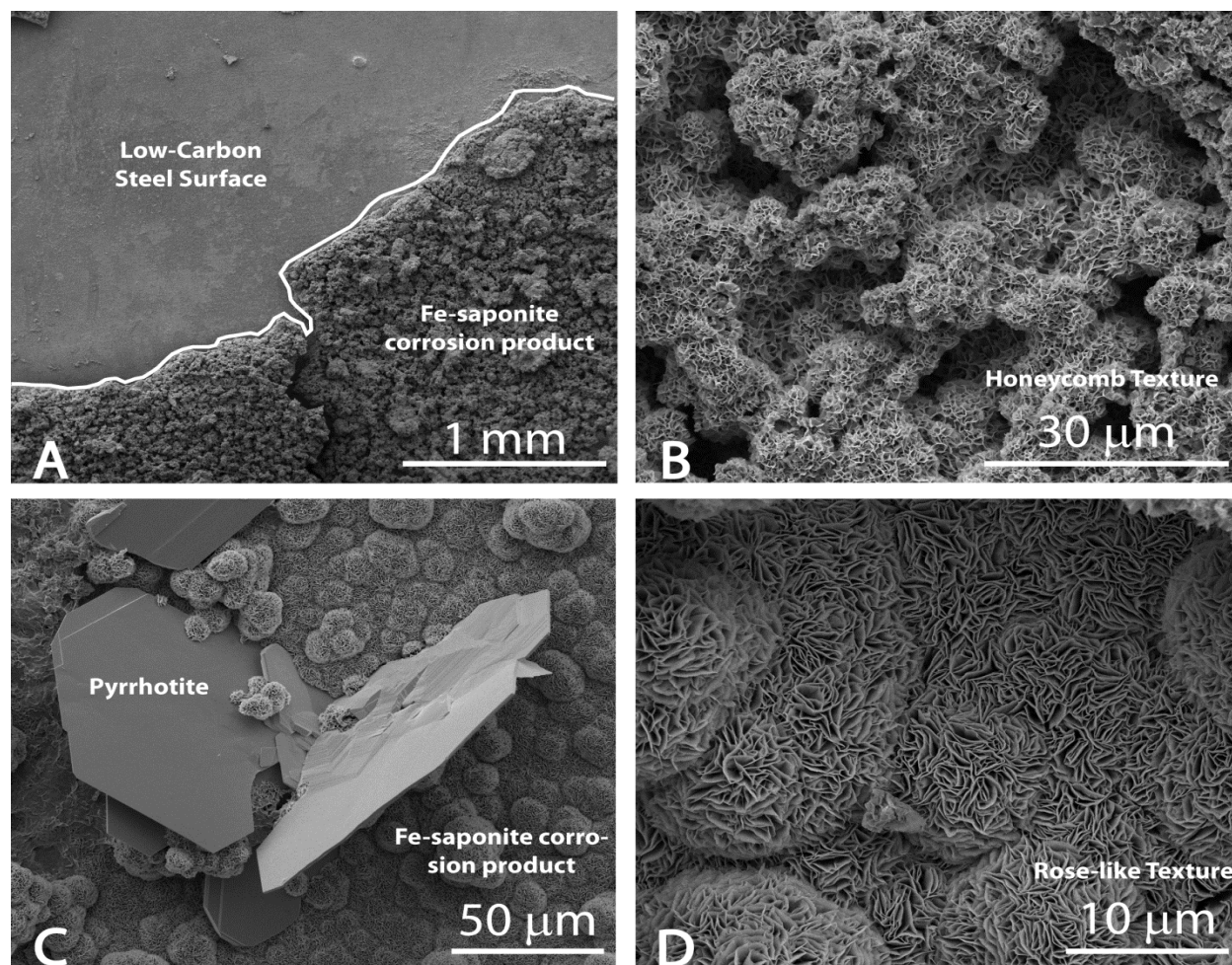
Figure E.17. SEM image (plan view) of Fe-saponite growth on low-carbon steel from the ramped (EBS-6) heating experiment. A) Boundary between the Fe-saponite interface reaction product and low-carbon steel surface. B) Honeycombed Fe-saponite. C) Botryoidal Fe-saponite interface reaction product with pyrrhotite platelets from EBS-6. D) Rose-like texture of Fe-saponite.
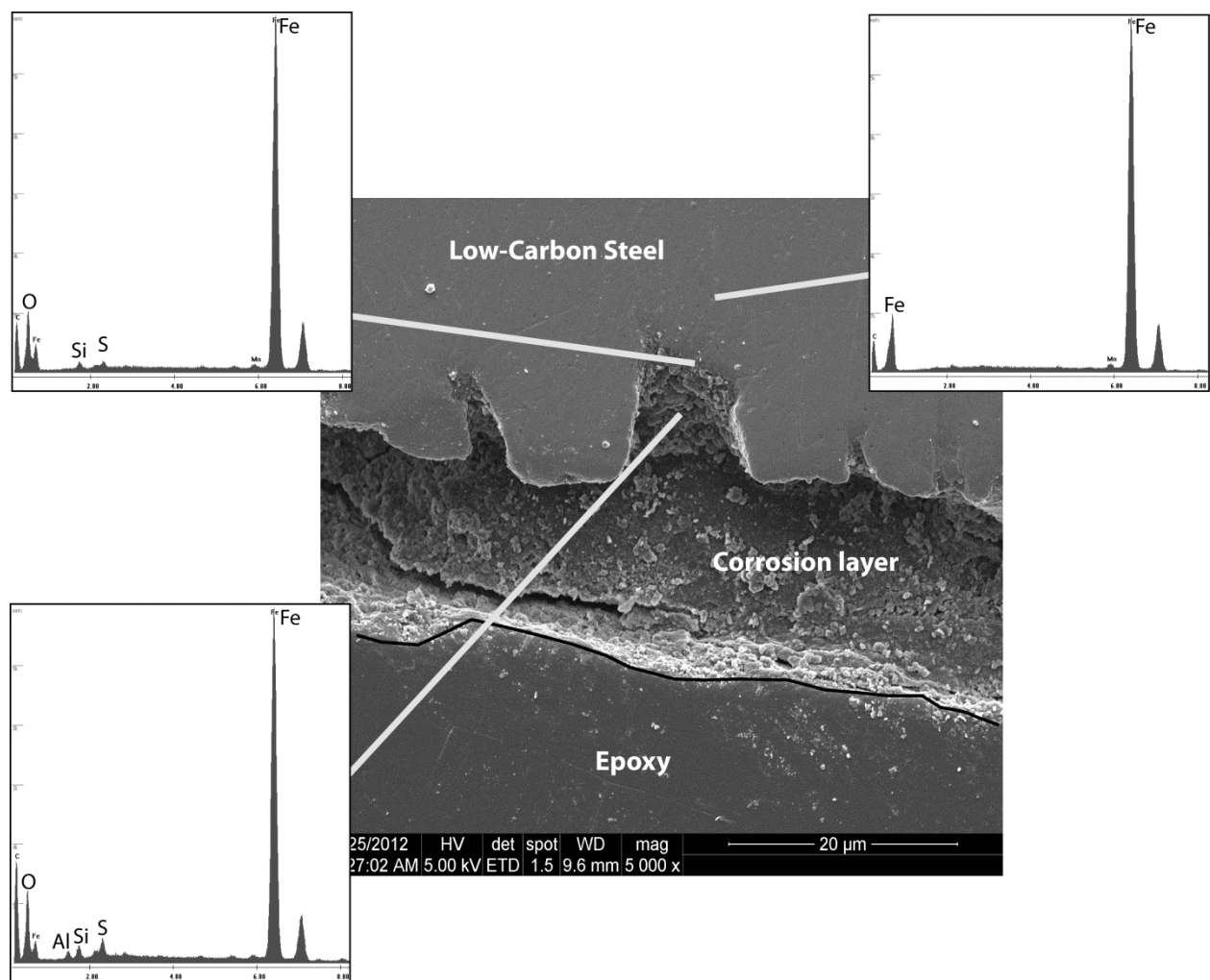
Figure E 18. SEM image of low-carbon steel cross-section showing Fe-saponite reaction products using steel surface as a growth substrate. EDX analyses of post-reaction low-carbon steel and interface reaction n surfaces show a slight oxidation and sulfidation of the surface (probably due to oxide and sulfide precipitates). EDX composition of the reaction product was not collected due to erosion of Fe-saponite during sample preparation. Extensive pitting corrosion of the low-carbon steel occurs during the ramped experiments (EBS-6).
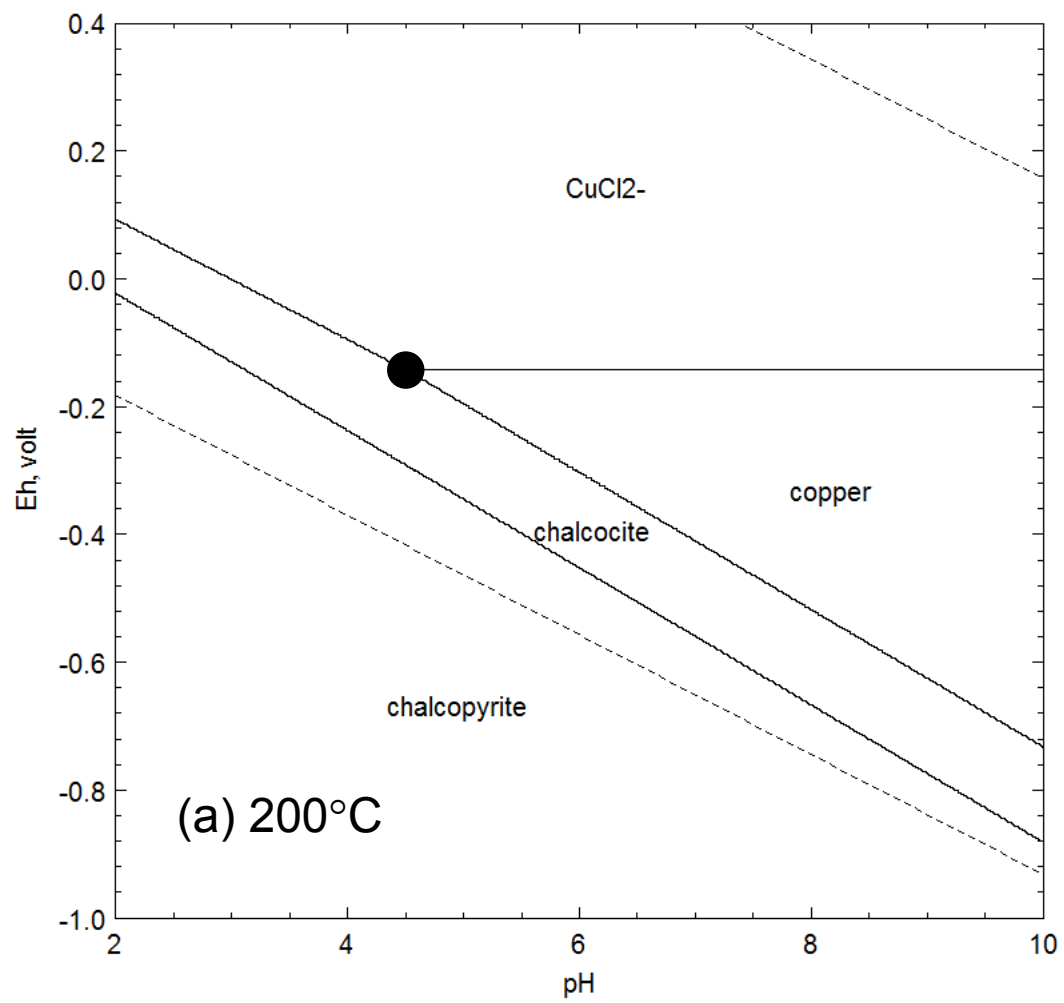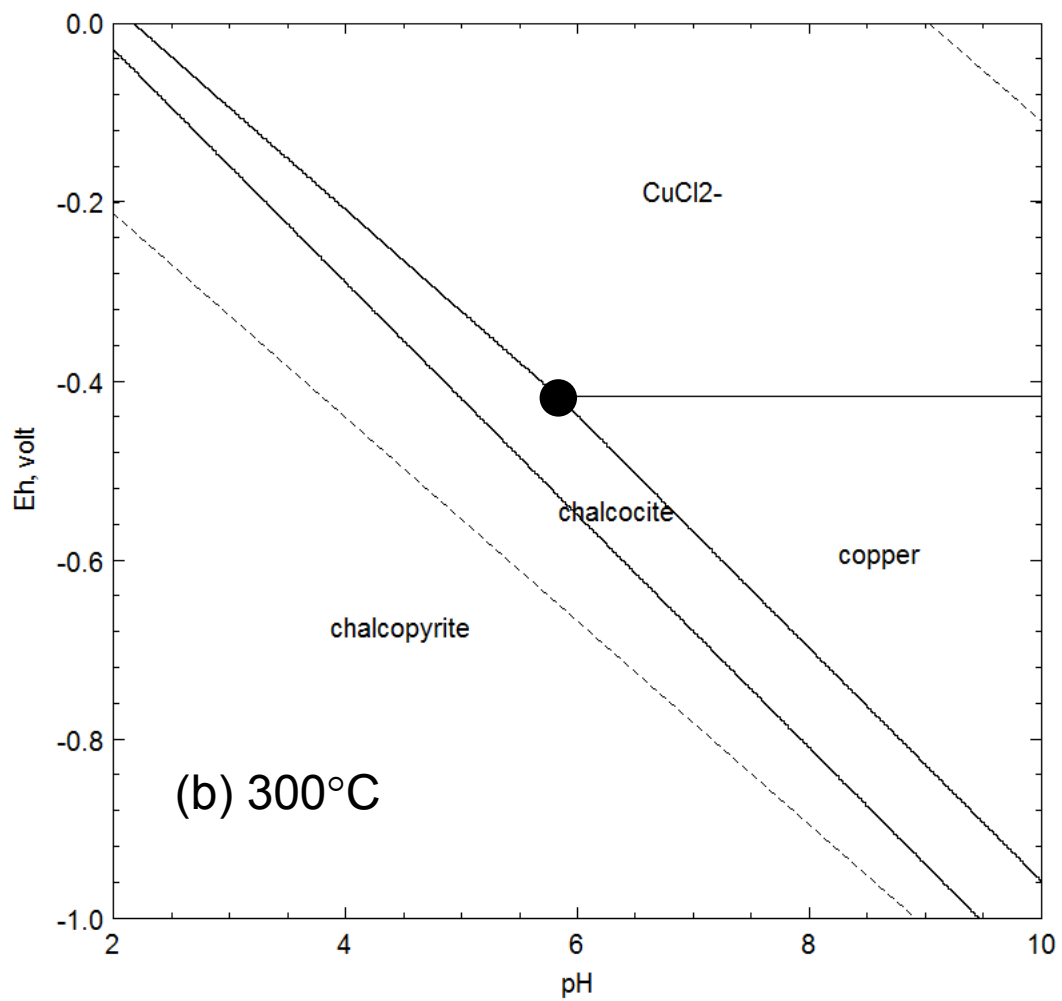
Figure E.19. Eh-pH diagram for the Cu-S-Cl-H$_2$O system at (a) 200 and (b) 300°C (see text). Dotted lines denote the stability of H$_2$O. The black dot represent the invariant points for copper-Cu$_2$S$_{(s)}$- CuCl$_2^-$ equilibrium

Appendix F
Miscellaneous tables

	Chalcocite Thickness (um)	Pit Depth (um)	Corrosion rate (um/day)
EBS-4	3.0(0.1)	5.7(0.2)	0.16(0.6)
EBS-11	8.2(0.4)	13.5(0.6)	0.32(0.2)
EBS-16	2.6(0.1)	4.3(10.)	0.024(0.01)
EBS-17	5.6(0.4)	13.1(0.6)	0.31(0.1)

Table F.1. Chalcocite thickness, pit depth and corrosion rate. Standard deviation in parentheses.

	SiO_2	Al_2O_3	Cr_2O_3	FeO*	MnO	MgO	NiO	CaO	Na_2O	K_2O	Total
EBS-2	33.47	13.14	1.25	31.03	0.38	1.98	1.26	1.31	1.60	0.62	86.04

Table F.2. Bulk chemical composition from the 304 SS corrosion layer developed from the ramped heating cycle (EBS-2)

	SiO_2	Al_2O_3	Cr_2O_3	FeO*	MnO	MgO	NiO	CaO	Na_2O	K_2O	Total
EBS-6	36.00	12.80	0.02	33.75	0.22	0.83	0.01	0.64	1.02	0.35	85.63

Table F.3. Bulk chemical composition (EMPA) from the low-carbon corrosion layer developed from the ramped heating cycle (EBS-6).

Appendix G
Reaction Listing for Full RM

```
Equilibrium constants:
H2O  <--> H+  + OH- : RKeq(2) = 10^(-13.999)
H2O2 <--> H+  + HO2-: RKeq(3) = 10^(-11.65)
OH   <--> H+  + O-  : RKeq(4) = 10^(-11.9)
HO2  <--> H+  + O2- : RKeq(5) = 10^(- 4.57)
H    <--> H+  + E-  : RKeq(6) = 10^(- 9.77)


      Reactions                         Rate constans (M^-n/s)
1     H+ + OH- = H2O                            1.4d11
2     H2O = H+ + OH-            rk( 2) = rk( 1)*RKeq(2)
3     H2O2 = H+ + HO2-          rk( 3) = rk( 4)*RKeq(3)
4     H+ + HO2- = H2O2                          5.0d10
5     H2O2 + OH- = HO2- + H2O                   1.3d10
6     HO2- + H2O = H2O2 + OH-   rk( 6) = rk( 5)*RKeq(2)/RKeq(3)
7     E- + H2O = H + OH-                        1.9d1
8     H + OH- = E- + H2O                        2.2d7
9     H = E- + H+               rk( 9) = rk(10)*RKeq(6)
10    E- + H+ = H                               2.3d10
11    OH + OH- = O- + H2O                       1.3d10
12    O- + H2O = OH + OH-       rk(12) = rk(11)*RKeq(2)/RKeq(4)
13    OH = O- + H+              rk(13) = rk(14)*RKeq(4)
14    O- + H+ = OH                              1.0d11
15    HO2 = O2- + H+            rk(15) = rk(16)*RKeq(5)
16    O2- + H+ = HO2                            5.0d10
17    HO2 + OH- = O2- + H2O                     5.0d10
18    O2- + H2O = HO2 + OH-     rk(18) = rk(17)*RKeq(2)/RKeq(5)
19    E- + H2O2 = OH + OH-                      1.1d10
20    E- + O2- + H2O = HO2- + OH-               1.3d10
21    E- + HO2 = HO2-                           2.0d10
22    E- + O2 = O2-                             1.9d10
23    H + H2O = H2 + OH                         1.1d1
24    H + H = H2                                7.8d9
25    H + OH = H2O                              7.0d9
26    H + H2O2 = OH + H2O                       9.0d7
27    H + O2 = HO2                              2.1d10
28    H + HO2 = H2O2                            1.8d10
29    H + O2- = HO2-                            1.8d10
30    OH + OH = H2O2                            3.6d9
31    OH + HO2 = H2O + O2                       6.0d9
32    OH + O2- = OH- + O2                       8.2d9
33    OH + H2 = H + H2O                         4.3d7
34    OH + H2O2 = HO2 + H2O                     2.7d7
35    HO2 + O2- = HO2- + O2                     8.0d7
36    H2O2 = OH + OH                            2.25d-7
37    OH + HO2- = HO2 + OH-                     7.5D9
38    HO2 + HO2 = H2O2 + O2                     7.0d5
39    OH + Cl- = ClOH-                          4.300D+09
40    OH + HClO = ClO + H2O                     9.000D+09
41    OH + ClO2- = ClO2 + H2O - H+              6.300D+09
42    E- + Cl = Cl- + H2O                       1.000D+10
43    E- + Cl2- = Cl- + Cl- + H2O               1.000D+10
44    E- + ClOH- = Cl- + OH- + H2O              1.000D+10
45    E- + HClO = ClOH-                         5.300D+10
46    E- + Cl2 = Cl2-                           1.000D+10
47    E- + Cl3- = Cl2- + Cl-                    1.000D+10
48    E- + ClO2- = ClO + OH- - H+               4.500D+10
49    E- + ClO3- = ClO2 + OH- - H+              0.000D+00
50    H + Cl = Cl- + H+                         1.000D+10
51    H + Cl2- = Cl- + Cl- + H+                 8.000D+09
52    H + ClOH- = Cl- + H2O                     1.000D+10
53    H + Cl2 = Cl2- + H+                       7.000D+09
54    H + HClO = ClOH- + H+                     1.000D+10
55    H + Cl3- = Cl2- + Cl- + H+                1.000D+10
56    HO2 + Cl2- = Cl- + HCl + O2               4.000D+09
57    HCl = Cl- + H+                            5.000D+05
58    HO2 + Cl2 = Cl2- + H+ + O2                1.000D+09
59    HO2 + Cl3- = Cl2- + HCl + O2              1.000D+09
60    O2- + Cl2- = Cl- + Cl- + O2               1.200D+10
61    O2- + HClO = ClOH- + O2                   7.500D+06
62    H2O2 + Cl2- = HCl + HCl + O2-             1.400D+05
63    H2O2 + Cl2 = HO2 + Cl2- + H+              1.900D+02
```

373

```
64      H2O2 + HClO = HCl + H2O + O2                      1.700D+05
65      OH- + Cl2- = ClOH- + Cl-                          7.300D+06
66      OH- + Cl2 = HClO + Cl-                            1.000D+10
67      H+ + ClOH- = Cl + H2O                             2.100D+10
68      H2O + Cl2O2 = HClO + ClO2- + H+                   2.000D+02
69      H2O + Cl2O2 = O2 + HClO + HCl                     0.000D+00
70      H2O + Cl2O = HClO + HClO                          1.000D+02
71      H2O + Cl2O4 = ClO2- + ClO3- + H+ + H+             1.000D+02
72      H2O + Cl2O4 = HClO + HCl + O4                     1.000D+02
73      O4 = O2 + O2                                      1.000D+05
74      Cl- + Cl = Cl2-                                   2.100D+10
75      Cl- + ClOH- = Cl2- + OH-                          9.000D+04
76      Cl- + HClO = Cl2 + OH-                            6.000D-02
77      Cl- + Cl2 = Cl3-                                  1.000D+04
78      Cl- + H+  = HCl    (assuming pKa = -3.9)          6.295D+01
79      ClOH- = OH + Cl-                                  6.100D+09
80      Cl2- = Cl + Cl-                                   1.100D+05
81      Cl2- + Cl2- = Cl3- + Cl-                          7.000D+09
82      Cl3- = Cl2 + Cl-                                  5.000D+04
83      ClO + ClO = Cl2O2                                 1.500D+10
84      ClO2 + ClO2 = Cl2O4                               1.000D+02
85      Cl2O2 + ClO2- = ClO3- + Cl2O                      1.000D+02
86      E- + ClO3- = ClR--                                1.600D+05
87      ClR-- + OH = OH- + ClO3-                          1.000D+10
88      ClR-- + O- = OH- + ClO3- - H+                     1.200D+09
89      HClO + HClO = Cl- + ClO2- + H+ + H+               6.000D-09
90      ClO2- + HClO = Cl- + ClO3- + H+                   9.000D-07
91      HClO + HClO = O2 + HCl + HCl                      3.000D-10
92      HClO4 = H+ + ClO4-    (a guess)                   1.000D+10
93      H+ + ClO4- = HClO4    (assuming pKa = -7)         1.000D+03
94      Br- + OH = BrOH-                                  1.100D+10
95      Br- + Br = Br2-                                   1.000D+10
96      Br- + H = HBr-                                    0.000D+06
97      Br- + O- = Br + OH- - H+                          2.200D+08
98      Br + BrO- = Br- + BrO                             4.100D+09
99      Br = BrOH- + H+ - H2O                             1.400D+00
100     Br + HO2 = H+ + Br- + O2                          1.600D+08
101     Br + OH- = BrOH-                                  1.300D+10
102     Br + H2O2 = Br- + O2- + H+ + H+                   2.500D+09
103     Br2- = Br + Br-                                   1.900D+04
104     Br2- + Br2- = Br- + Br3-                          3.400D+09
105     Br2- + BrO2- = BrO2 + Br- + Br-                   8.000D+07
106     Br2- + BrO- = BrO + Br- + Br-                     6.200D+07
107     Br2- + ClO2- = Br- + ClO2 + Br-                   2.000D+07
108     Br2- + H = H+ + Br- + Br-                         1.400D+10
109     Br2- + HO2 = H+ + Br- + Br- + O2                  1.000D+08
110     Br2- + O2- = Br- + Br- + O2                       1.700D+08
111     Br2- + E- = Br- + Br-                             1.100D+10
112     Br2- + H2O2 = Br- + Br- + HO2 + H+                1.900D+06
113     BrO- + OH = BrO + OH-                             4.200D+09
114     BrO- + O- = BrO + OH- - H+                        3.500D+09
115     BrO- + E- = Br- + O-                              1.500D+10
116     BrO2- + OH = BrO2 + OH-                           2.300D+09
117     BrO2- + BrO = BrO- + BrO2                         4.000D+08
118     BrO2- + O- = BrO2 + OH- - H+                      1.600D+09
119     BrO2- + E- = BrO + H2O - H+ - H+                  1.100D+10
120     BrO3- + OH = BrO3 + OH-                           0.000D+06
121     BrO3- + H = BrO2 + OH-                            2.000D+07
122     BrO3- + O- = BrO3 + OH- - H+                      0.000D+06
123     BrO3- + E- = BrO2 + OH- + OH- - H2O               3.400D+09
124     Br2 + H = Br2- + H+                               1.000D+10
125     Br2 + HO2 = H+ + O2 + Br2-                        1.300D+08
126     Br2 + O2- = O2 + Br2-                             5.000D+09
127     Br2 + Br- = Br3-                                  9.600D+08
128     Br2 + E- = Br2-                                   5.300D+10
129     HOBr + OH = BrO + H2O                             2.000D+09
130     HOBr + O2- = O2 + Br + OH-                        3.500D+09
131     BrO2 + OH = BrO3- + H+                            2.000D+09
132     BrO2 + BrO2 = BrO3- + BrO2- + H+ + H+ - H2O       4.000D+07
133     BrO2 + ClO2- = BrO2- + ClO2                       3.600D+07
134     Br3- + H = H+ + Br2- + Br-                        1.200D+10
```

```
135     Br3- + O2- = O2 + Br2- + Br-                    1.500D+09
136     Br3- = Br2 + Br-                                5.500D+07
137     Br3- + E- = Br2- + Br-                          2.700D+10
138     BrOH- = Br- + OH                                3.000D+07
139     BrOH- = Br + OH-                                4.200D+06
140     BrOH- + H+ = Br + H2O                           1.300D+10
141     BrOH- + Br- = Br2- + OH-                        1.900D+08
142     BrO + BrO = BrO- + BrO2- + H+ + H+ - H2O        2.800D+09
143     BrO + BrO2- = BrO- + BrO2                        4.000D+08
144     HOBr = H+ + BrO-                                1.580D+01
145     BrO- + H+ = HOBr                                1.000D+10
146     Br- + Cl2- = BrCl- + Cl-                        4.00D+09
147     BrCl- + Cl- = Cl2- + Br-                        1.10D+02
148     BrCl- = Cl- + Br                                8.50D+07
149     Br + Cl- = BrCl-                                1.00D+10
150     BrCl- + Br- = Br2- + Cl-                        8.00D+09
151     Br2- + Cl- = BrCl- + Br-                        4.30D+06
152     Br- + Cl2 = BrCl2-                              6.00D+09
153     BrCl2- = Cl2 + Br-                              9.00D+03
154     BrCl2- = BrCl + Cl-                             1.70D+05
155     BrCl + Cl- = BrCl2-                             1.00D+06
156     BrCl2- + Br- = Br2Cl- + Cl-                     3.00D+08
157     BrCl = HOBr + H+ + Cl- - H2O                    3.00D+06
158     HOBr + Cl- = BrCl + H2O - H+                    2.30D+10
159     BrCl = HClO + H+ + Br- - H2O                    1.15D-03
160     HClO + Br- = BrCl + H2O - H+                    1.32D+06
161     Br- + HOBr = Br2 + H2O - H+                     3.00D+09
162     Br2 = Br- + HOBr + H+ - H2O                     2.00D+00
163     Br- + HBrO2 = HOBr + HOBr - H+                  3.00D+06
164     HOBr + HOBr = Br- + HBrO2 + H+                  2.00D-05
165     Br- + BrO3- = HOBr + BrO2- - H+                 2.500D-7
166     HOBr + HBrO2 = Br- + BrO3- + H+ + H+            3.20D+00
167     HBrO2 + HBrO2 = HOBr + BrO3- + H+               3.00D+03
168     HOBr + BrO3- = HBrO2 + HBrO2 - H+               1.00D-08
169     HBrO2 + BrO3- = BrO2 + BrO2 + H2O - H+          4.20D+01
170     BrO2 + BrO2 = HBrO2 + BrO3- + H+ - H2O          4.20D+07
171     HBrO2 = BrO2- + H+                              5.00D+05
172     BrO2- + H+ = HBrO2                              1.35D+09
173     BrCl- + BrCl- = BrCl + Br- + Cl-                1.20D+09
174     Br2 + Cl- = Br2Cl-                              1.00D+07
175     Br2Cl- = Br2 + Cl-                              7.69D+06
176     BrCl + Br- = Br2Cl-                             1.00D+07
177     Br2Cl- = BrCl + Br-                             5.56D+02
```

Appendix H
FORTRAN Listing for Empirical RM

Emp-RM.f

```fortran
      implicit real*8 (a-h,o-z)

      ddot  = 160.d0           ! rad/s


      Brext = 1.d-6

      do i=0,200
      do j=0,200

      H2ext = 7.8d-4*dfloat(j)/100.d0        ! mole/L
      O2ext = dfloat(i)/2.d7 +  1.d-11     ! mole/L
      G2 = Gcond(ddot,O2ext,H2ext,Brext)

      write(*,*) H2ext,O2ext,G2

      enddo
      write(*,"(1x)")
      enddo


      STOP
      end

      FUNCTION Gcond(ddot,O2ext,H2ext,Brext)
      implicit real*8 (a-h,o-z)


      rk27  = 2.1d10          ! L/mole-s
      rk23  = 1.1d1/56.d0     ! L/mole-s   divided by 56
      rk26  = 9.0d7           ! L/mole-s
      rk36  = 0.0d0           ! L/mole-s
      rk33  = 4.3d7
      rk94  = 1.1d10 * 10.
      BrFact = rk33*H2ext/(rk33*H2ext + rk94*Brext)
      if(Brext.eq.0.) BrFact = 1.d0
      GH    = 0.100d0*(1.d0-dexp(-(H2ext*BrFact/7.8d-4)/.1d0))          ! molecules/eV
      GOH   = 0.350d0*(1.d0-dexp(-(H2ext*BrFact/7.8d-4)/.3d0))          ! molecules/eV
      CH2O  = 1.d3/18.d0      ! mole/L
      DO2   = 2.500d-05       ! cm^2/s
      DH2O2 = 1.900d-05       ! cm^2/s
      dx    = 3.5d-3          ! cm
      dN    = 0.475d0/dx
      GOH   =    GOH  * BrFact

         O2 =  O2ext + 2.d-6*Brext/(Brext+0.5d-6)
         H2 =  H2ext
         H2O = CH2O
         dk27  =  rk27
         dk23  =  rk23
         dk26  =  rk26
         dk36  =  rk36
      dkO2  =    DO2/(dN*dx**2)         !  1/s
      dkH2O2 =   DH2O2/(dN*dx**2)       !  1/s
      dot=   ddot*(1.d0/(1.602d-19*1.d4*6.022d23))


      A0 =       -dk23*dk27*H2O*dkH2O2**2

      A1 = -dkH2O2*(dk26*dk27*dkO2*O2+dk23*dk26*dkO2*H2O
     1  - 2.d0*(dk23*dk27*H2O)*(dkH2O2+dk36) )
     2  + dot*(gH+gOH)*dk26*dk27*dkH2O2

      A2 =  (dkH2O2+dk36)*(dk26*dk27*dkO2*O2+dk23*dk26*dkO2*H2O
     1  - (dk23*dk27*H2O)*(dkH2O2+dk36) )
     2  + dot*(gH+gOH)*dk26*(dk26*dkO2-dk27*dkH2O2-dk27*dk36)

      Gcond =  (-A1 + dsqrt(A1**2 - 4.d0*A2*A0))/(2.d0*A2)
c      Gcond = dkH2O2/(dkH2O2+dk36+dk26*dot*(gOH+gH)/
```

377

```
c    1      (dk23*H2O+dk27*O2))

     RETURN
     end

     SUBROUTINE NLconc(C1p,C1m,C0,dlam0,A,dN,dk)
     implicit real*8 (a-h,o-z)

     B = -(1.d0 - 1.d0/(A*C0) - dN*dlam0/(dk*A*C0))
     C = -1.d0/(A*C0)

     C1p = ( -B + dsqrt(B**2 - 4.d0*C) )/2.d0
     C1m = ( -B - dsqrt(B**2 - 4.d0*C) )/2.d0


     RETURN
     end
```